Synthesis and characterization of heteroleptic copper(I) complexes for solar energy conversion

Martina Sandroni

HAL Id: tel-01249991

https://tel.archives-ouvertes.fr/tel-01249991

Submitted on 4 Jan 2016

UNIVERSITÉ DE NANTES

FACULTÉ DES SCIENCES ET DES TECHNIQUES

_____

ÉCOLE DOCTORALE 3MPL

Année 2012

Synthesis and characterization of heteroleptic copper(I) complexes for solar energy conversion

Synthèse et caractérisation de complexes hétéroleptiques de cuivre(I) pour la conversion de l'énergie solaire

_____

THÈSE DE DOCTORAT
Discipline : Chimie fine
Spécialité : Chimie organique

Présentée
et soutenue publiquement par

Martina SANDRONI

Le 16 octobre 2012, devant le jury ci-dessous

Rapporteurs   Jean-François NIERENGARTEN, directeur de recherche, Université de Strasbourg
Nathan McCLENAGHAN, chargé de recherche, Université de Bordeaux
Examinateurs   Nicola ARMAROLI, docteur, ISOF – CNR, Bologna
Pietrick HUDHOMME, professeur, Université d'Angers
Membres invités   Errol BLART, maître de conférences, Université de Nantes
Yann PELLEGRIN, chargé de recherche, Université de Nantes

Directeur de thèse : Fabrice ODOBEL, directeur de recherche, Université de Nantes

Co-encadrant de thèse : Errol BLART, maître de conférences, Université de Nantes

Remerciements

Mes remerciements s'adressent tout d'abord à mon directeur de thèse, Fabrice Odobel, pour m'avoir donné l'opportunité de découvrir un domaine de la chimie très intéressant et varié, pour ses conseilles et son enthousiasme. Merci aussi pour la disponibilité montrée tout au long de ces trois années. Je tiens aussi à remercier Bruno Bujoli pour m'avoir accueillie au sein du laboratoire CEISAM.

Je remercie aussi mon co-encadrant, Errol Blart, en particulier pour les discussions sur les priorités dans la vie. Merci à Yann Pellegrin, qui m'a beaucoup appris (toujours de façon discrète et ouverte au dialogue) et avec qui c'est toujours un plaisir de discuter. Son aide a été déterminant pour la rédaction de cette thèse.

J'adresse également mes remerciements à Jean-François Nierengarten et Nathan McClenaghan, pour avoir accepté d'être rapporteurs de ce travail, et à Pietrick Hudhomme et Nicola Armaroli pour avoir accepté de le juger.

Ce travail de thèse a été accompli dans le cadre de l'ANR HeteroCop, et je voudrais remercier tous ceux qui en font partie : Mateusz Rebarz, Michel Sliwa, Olivier Poizat (LASIR, Université de Lille 1, merci pour m'avoir accueillie pour une semaine !), Narayan C. Bera, Megumi Kayanuma, Chantal Daniel (LCQ, Université de Strasbourg), Thibaut Stoll, Marcello Gennari, Jérôme Chauvin, Jérôme Fortage, Marie-Noëlle Collomb, Alain Deronzier (DCM Université J. Fourier, Grenoble). Ça a été un projet extrêmement intéressant, et je suis reconnaissante pour avoir eu l'occasion d'aborder la chimie des complexes de cuivre de différents points de vue.

Merci à tout le personnel du laboratoire CEISAM, et en particulier à Virginie Silvestre (RMN 500 MHz), Aurélien Planchat (diffraction des rayons-X), Julie Hemez (HR-MS) et Denis Loquet (analyse élémentaire) pour les analyses des molécules.

Pour tout ce qui est vie quotidienne au labo, je tiens à remercier tous les doctorants de l'équipe, passés (Julien B., Loïc, Clément), présents (Julien W., Ludovic) et futurs (Antoine) pour le temps passé ensemble et pour m'avoir appris la beauté de la langue française... Merci à mon co-bureau depuis trois ans, pas très loquace mais qui a des choses à dire. Et je n'oublie pas tous les doctorants du CEISAM avec qui on partage quotidiennement les couloirs, les déjeuners et les pauses café.

Last but not least, les gents qui de loin ou de près m'ont accompagné dans ce parcours : ma famille, les amis en Italie et ceux qui se sont éparpillés ailleurs, et le amis français qui sont une

partie importante des racines que j'ai mis ici. Carl, merci pour ton soutien, ça me donne beaucoup de stabilité et ça a été fondamental pendant les derniers mois.

Acronyms and abbreviations in alphabetical order

biQui	2,2'-biquinoline
biQuiCOOH	2,2'-biquinoline-4,4'-dicarboxylic acid
CR	Charge Recombination
CSS	Charge-Separated State
CV	Cyclic Voltammetry
dmp	2,9-dimethyl-1,10-phenanthroline; neocuproine
diMesPhen	2,9-dimesityl-1,10-phenanthroline
DMF	N,N-dimethylformamide
DMSO	dimethylsulfoxide
DPEphos	Bis(2-diphenylphosphinophenyl)ether
dpp	2,9-diphenyl-1,10-phenanthroline
dptmp	2,9-diphenyl-3,4,7,8-tetramethylphenanthroline
DPV	Differential Pulse Voltammetry
DSSC	Dye-Sensitized Solar Cell
ESI +/-	ElectroSpray Ionization positive/negative mode
Fc	Ferrocene
HOMO	Highest Occupied Molecular Orbital
HR-MS	High Resolution Mass Spectrometry
ILCT	Intra-Ligand Charge Transfer
LUMO	Lowest Unoccupied Molecular Orbital
MALDI +/-	Matrix Assisted LASER Desorption Ionization positive/negative mode
mesityl	2,4,6-trimethylphenyl
MLCT	Metal-to-Ligand Charge Transfer
MO	Molecular Orbital
NHE	Normal Hydrogen Electrode
SCE	Saturated Calomel Electrode
SPC	Single Photon Counting
SWV	Square Wave Voltammetry
TA	Transient Absorption
tbp	2,9-di-*tert*-butyl-1,10-phenanthroline
TBAPF$_6$	Tetrabutylammonium hexafluorophosphate
TFA	Trifluoroacetic acid
TTF	Tetrathiafulvalene
UV	Ultraviolet

Table of contents

General introduction

"If our black and nervous civilization, based on coal, shall be followed by a quieter civilization based on the utilization of solar energy, that will be no harmful to progress and to human happiness" (G. Ciamician, *Science* **1912**, *36*, 385)

These words, pronounced by Ciamician in 1912, summarize one of the main issues that humankind faces during this century: the energy problem. Currently, around 80% of energy resources are based on the combustion of fossil fuels. Resources shortage and growing pollution levels make it urgent to develop alternative energy sources, which have to be abundant, long-lasting and environmentally friendly. Solar energy appears to be an ideal candidate, as it provides the planet with about 10^4 times our annual energy consumption and it is furthermore more evenly distributed on earth than fossil fuels.

Unfortunately, solar energy cannot be used directly, and has to be converted into another form (heat, electricity or chemical potential). In particular, chemical approaches towards conversion into electricity and chemical potential have been extensively developed by the scientific community in the last decades. For both applications, a fundamental role is played by the photosensitizer, which has to absorb sunlight and produce a charge separated state. The electrons are then either collected in an external electrical circuit (photovoltaic devices) or used to run reactions, storing the photonic input into chemical bonds (artificial photosynthesis).

In this field, the most successful molecular systems are based on ruthenium(II) polypyridine complexes, that display well-suited and tuneable photophysical and electrochemical properties. Moreover, a great variety of structures can be synthesized thanks to the modular approach which is peculiar of coordination compounds. However, the use of ruthenium raises important issues like its high cost (related to the low abundance on the earth crust) and toxicity.

The aim of this thesis is to show that copper(I) can be a viable alternative to ruthenium(II) for solar energy conversion. Besides the abundance of copper on earth, its diimine complexes display valuable photophysical and electrochemical properties, together with a tetrahedral arrangement of the ligands allowing to build linear multicomponent arrays. The choice of the heteroleptic structure is motivated by the fact that it opens the way to directional charge transfer, a highly suitable feature when dealing with light conversion. At the heart of this topic is the HETPHEN synthetic strategy developed by Schmittel in 1997, that allows chemists to build stable heteroleptic copper(I) complexes.

The first chapter is an introduction describing the main aspects of artificial photosynthesis and reviewing the most important advancements of the research about copper(I) complexes.

Afterwards, in chapter 2, the effect of the coordination sphere structure (in particular concerning the steric hindrance) on the photophysical and electrochemical properties was investigated by means of model complexes. The study is then pursued using more elaborate ligands, containing an extended phenanthroline core and bromo groups.

In chapter 3, the enhancement of the absorption coefficient was addressed, since this is still a weak point of copper(I) complexes. The chosen strategy is the use of chromophoric push-pull styrylbipyridine ligands. The influence of different complementary ligands (diphosphine or diimine) was also assessed.

In chapter 4, the use of heteroleptic copper(I) diimine complexes to build rod-like molecular arrays for photoinduced electron transfer was developed. The aim was to build rod-like dyads and triads to test the possibility to generate a long-lived charge-separated state triggered by photoexcitation of a central copper(I) diimine sensitizer.

The last chapter focuses on the design of copper(I)-based sensitizers for dye-sensitized solar cells (DSSCs). Two new series of dyes containing different anchoring ligands will be presented and the photovoltaic performances were assessed and discussed.

This multidisciplinary work was carried out within the HeteroCop ANR project (09-BLAN-0183-01). The project involves four groups, each one in charge of a different aspect of the work:

- CEISAM, University of Nantes (M. Sandroni, Dr. Y. Pellegrin, Dr. E. Blart, Dr. F. Odobel): synthesis of the ligands and the complexes and preliminary physico-chemical characterizations (UV-Visible absorption, steady-state emission, electrochemistry and photovoltaic performances);
- LASIR, University of Lille 1 (Dr. M. Rebarz, Dr. M. Sliwa, Dr. O. Poizat): emission lifetime and quantum yield measurements, time-resolved spectroscopy;
- LCQ, University of Strasbourg (Dr. N.C. Bera, Dr. M. Kayanuma, Dr. C. Daniel): quantum mechanical calculations;
- DCM, Joseph Fourier University, Grenoble (T. Stoll, Dr. M Gennari, Dr. J. Chauvin, Dr. J. Fortage, Dr. M-N. Collomb, Dr. A. Deronzier): catalysts synthesis and characterization, photocatalytic hydrogen production assays (not described in this thesis).

The styrylbipyridine ligands presented in chapter 3 and 5 were synthesized by Dr. Huriye Akdas at the University of Rennes 1.

The photovoltaic properties of the complexes presented in chapter 5 were studied by Dr. Pellegrin.

CHAPTER 1

State of the art: artificial photosynthesis and copper(I) complexes

1.1. Solar energy conversion: introduction

The improvement of the living conditions of humankind is strongly connected with the access to energy.[1] The growth of world population and the increasing energy needs of developing countries lead to a global raise of the energy demand. At the same time, the currently most used energy sources are fossil fuels, which rise the double issue of availability and pollution. In fact, the available stocks are rapidly decreasing owing to their intense exploitation. For these reasons, the cost of fossil fuels is quickly growing. On the other hand, the hydrocarbon combustion releases large quantities of carbon dioxide in the atmosphere. CO_2 is a well-known greenhouse gas, and the rise of its concentration in the atmosphere is one of the main factors responsible for global warming.[2]

In order to preserve the equilibrium of the planet we are living on, and to guarantee access to energy to an even larger part of the world population, it appears necessary to develop alternative energy sources, which have to be sustainable and carbon neutral.[3]

Solar energy appears as an ideal candidate, and fulfils all these requirements. The amount of energy received in one year at the Earth surface corresponds to about ten thousand times our current annual energy consumption. However, solar energy, although very abundant, is discontinuous and needs to be stored and converted into a useful form, like electricity or fuel.

The most widespread way to store solar energy is certainly its transformation into high energy organic compounds starting from carbon dioxide and water, which is carried out by photosynthetic organisms and produces approximately $115 \cdot 10^9$ kg of biomass per year. This natural process has been an inspiration for the scientific community to elaborate new storage strategies.[4]

A nowadays well-established technology is constituted by batteries, where the energy is stored under the form of a redox gradient. In this field, major efforts have been devoted to the improvement of power density (the rate at which the charge can flow in and out of the battery), but the energy densities are still quite low ($\sim$ 0.1-0.5 MJ kg^{-1}), and are limited by the physical properties of the materials.[5] An interesting alternative, which is directly inspired by photosynthesis, is the

storage of energy in chemical bonds. Liquid fuels, in fact, have energy densities around 50 MJ kg^{-1}, and dihydrogen is even more efficient (140 MJ kg^{-1}).

In these introduction paragraphs, the natural photosynthetic process will be described, followed by the artificial approaches to fuel generation. In particular, the emphasis will be put on chemical approaches to solar energy conversion. Natural photosynthesis, occurring in plants, algae and cyanobacteria, converts sunlight, water and carbon dioxide into energy rich molecules such as carbohydrates or lipids. The goal of artificial photosynthesis, in the broadest sense, is to exploit *"the physics and chemistry underlying natural photosynthesis to harvest solar energy for technological purposes"*.[6] In this definition, it includes not only fuel photoproduction, but also the conversion of sunlight into electricity. The topic of photovoltaic energy, however, will not be addressed here but in the introduction of chapter 5.

The energy to drive photosynthesis is provided by sunlight, which is efficiently absorbed by the pigments present in the photosynthetic organisms.

$$CO_2 + H_2O + h\nu \rightarrow O_2 + biomass$$
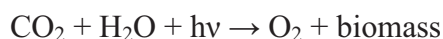
This reaction corresponds to the splitting of water into oxygen and hydrogen, where the latter, instead of being released in the atmosphere as a gas, is stored under the form of energy rich molecules. Photosynthesis is therefore a way to store the solar energy into chemical bonds.

The respiration is the reverse process, where "hydrogen" (stored under the form of high energy molecules) is combined with oxygen through a series of carefully controlled and efficient processes to provide metabolic energy.[7] An equivalent of respiration is the combustion reaction, where biomass combines with oxygen to provide energy with carbon dioxide release. For this reason, the combustion of biomass and biofuels is carbon dioxide neutral, if the biomass stock is properly restored.

If mankind could reproduce the same concept with simpler, artificial systems, immediate access to a large stock of fuel would be possible starting from inexpensive and abundant resources: water and sunlight.

1.1.1. Natural photosynthesis

The first studies about natural photosynthetic processes date back to the 17th century, and the research is still going on to elucidate all the aspects involved in this complex mechanism.

The whole photosynthetic reaction is very complex, as it leads to the synthesis of elaborate, energy rich organic molecules starting from simple building blocks: water and carbon dioxide. At the heart

of this process lies the splitting of water into oxygen and hydrogen: the former is released in the atmosphere where it is available for respiration and combustion, while the latter is combined with CO_2 to form sugars and other molecules. In this brief introduction, we will focus on the water splitting reaction by means of the absorption of photons, and on the energy and electron transfer chain providing light collection and charge separation to drive this reaction.

The photosynthetic reaction is carried out by different organisms, having a slightly different apparatus to perform it. However, some basic principles can be identified, that are common to all photosynthetic organisms:

- absorption of light energy by an antenna system, composed of pigments arranged in an ordered way thanks to a protein structure. The energy is then funnelled to a sensitizer (special pair) that initiates photoinduced electron transfer chain;
- charge separation through an electron transfer chain, with formation of highly oxidizing and reducing units at the two extremities;
- accumulation of charge equivalents by repetition of the above cycles, in order to perform the multielectron reactions necessary for water splitting;[8]
- catalysis with the redox equivalents produced upon photoinduced charge separation.

The photosynthetic apparatus is situated in the thylakoid membrane in the chloroplasts. Photosystem II (PSII) is responsible for light collection and water oxidation, and it is coupled with Photosystem I (PSI), where the electrons and protons resulting from the latter reaction are fixed as NADPH, a "bio-reductant" which is necessary for the carbon dioxide reduction to produce biomass.[7]

The antenna system is composed of pigment molecules (chlorophylls *a* and *b* and β-carotene) which are wrapped into a protein structure, in order to form an ordered superstructure suitable for funnelling the luminous energy to the **P680** (having a different structure in different organisms[9]). The electron transfer chain includes a pheophytin (**PH$_{D1}$**), two quinones (**Q$_A$** and **Q$_B$**) and a plastocyanin.

P680* is formed upon energy transfer from the antenna system. It is a highly reducing species and it is the starting point of the electron transfer chain which will provide a long-lived charge-separated state, necessary for the accumulation of the oxidizing and reducing equivalents (Fig. 1. 1). This electron transfer sequence is achieved through a redox gradient created by properly aligned and electronically tuned elements. A rapid electron transfer to the nearby pheophytin produces the first charge separated state **P680^{+}—PH$_{D1}$$^{-}$**. The negative charge is then rapidly transferred to a quinone, **Q$_A$**, leading to a rise of the charge-separated state lifetime by the increase of the distance between the two opposite charges. **P680^{+}** an extremely powerful oxidizer in the

world of living matter, with an oxidation potential of more than 1.12 V vs. NHE,[9] and is reduced by proton-coupled electron transfer from a tyrosine residue, which is then in charge of the oxidation of a cluster of four manganese ions. The OEC is a cluster containing four Mn^{2+} and one Ca^{2+} ion held together by a network of oxygenic bridges and water molecules. The structure was recently resolved by X-Ray crystallography,[10] but the operating mechanism has not been fully understood yet. The accumulation of four oxidizing equivalents in the Mn_4Ca cluster results in the oxidation of two water molecules to give one O_2 molecule, four electrons and four protons. The transport of the corresponding four reducing equivalents towards the PSI provides the energy to synthesize ATP from ADP. In Photosystem I, the energy of another red photon, absorbed by the **P700**, is used to start another electron transport chain finally resulting in the production of NADPH. ATP and NADPH are essential molecules for biomass synthesis and metabolic processes.

Fig. 1. 1. Schematic representation of the light-driven processes in natural photosynthesis.[7]

Before describing the artificial approaches to photosynthesis, it can be useful to make some considerations about the efficiency of this process.[7] Indeed, only a small part of the visible photons, which constitute 45% of the solar spectrum is used to drive the reactions resulting in biomass production. High energy photons are degraded with heat production to red photons ($\lambda = 680$ nm) in the antenna system, and used to excite **P680**. Moreover, each redox equivalent accumulated in the system requires the absorption of two red photons, at 680 (in **P680**) and 700 nm (in **P700**, PSI). The long electron transfer chains, and the absorption of the second photon in PSI are necessary to provide energy for the synthesis of ATP and NADPH. Moreover, a large number of reactions not directly involved in water splitting and biomass production occur in photosynthetic organisms, in order to ensure their organisation, metabolism, reproduction and protection from degradation. In light of all these data, the overall efficiency was theoretically estimated to be around 5%,[11,12] but

normally does not exceed 1-2%.[7] On a global basis, considering the ratio between the annual energy storage by photosynthetic processes and the solar energy arriving on the planet surface during the same amount of time, the efficiency can be estimated at 0.1%. However, if only the early stages of the process are taken into account, the efficiency is much higher, since it consists of highly efficient energy and electron transfer processes. Therefore, the artificial approach to photosynthesis concentrates on some useful reactions, with the aim to conceive efficient devices.

1.1.2. Useful hints from natural photosynthesis

In summary, natural photosynthesis relies on some basic principles, which can be used in order to develop the guidelines for the design of efficient artificial photosynthetic systems. The occurring processes are schematically represented by:

- efficient light collection by an antenna system: the energy is funnelled towards a sensitizer, provoking its excitation;
- long-range photoinduced electron transfer in the reaction centre: the charge-separated state lifetime is increased by moving the photoseparated charges away from each other. This is obtained through a chain of electron transfers in a spatially organised array that ensures the proper directionality to the charge movement;
- accumulation of oxidizing and reducing equivalents that allows the system to perform the multielectron reactions required for water splitting;
- presence of catalysts for both oxidation and reduction, ensuring storage of the redox equivalents and fast and efficient reactions.

The schematic representation of the photosynthetic array is given in Fig. 1. 2, where several approaches to the different aspects of artificial photosynthesis are highlighted. The whole photosynthetic process is very elaborate, and requires a sequence of several steps. For this reason, its faithful reproduction is an extremely hard task. In order to study and optimize each of the steps listed above, researchers usually address the different issues separately. Looking at literature reports, it is possible to identify several approaches to artificial photosynthesis, that can be roughly classified into four categories: systems reproducing light collection by the antenna effect, molecular arrays performing photoinduced long-distance charge transfer, systems for the photosensitization of molecular catalysts, and molecular catalysts for an efficient water splitting. Some systems, however, were able to reproduce artificially different aspects of the photosynthetic process. A few examples will be briefly mentioned in the next paragraphs.

Fig. 1. 2. Schematic representation of the photosynthetic process, and of the different approaches to artificial photosynthesis: ▬ study of the antenna effect; ▬ long-range photoinduced electron transfer; ▬ photosensitization of catalysts; ▬ catalysts for efficient water splitting.

1.1.2.a. Light collection by the antenna effect

The antenna effect plays an important role in photosynthesis since it allows the collection of a large number of photons by highly absorbing pigments, among which carotenes and especially chlorophylls. The collected energy is then funnelled to the reaction centre by means of efficient energy transfer steps to a dye playing the role of energy sink, producing the excitation of the latter that finally starts the electron transfer chain is PSII. This allows the natural photosynthetic apparatus to efficiently absorb a large part of the solar spectrum by a suitable mixture of dyes, and to overcome the intrinsic problem of the limited absorption of the reaction centre. An important feature is the spatial organization of the dyes, that provides directionality to the energy transfer. In the natural apparatus, it is given by the protein environment.

There are of course a few conditions to fulfil in order that the energy absorbed by the antennae is transferred to the final energy acceptor with quantum efficiency close to unity. Within the light harvesting complex of PSII, the energy transfer steps occur via the Förster resonant energy transfer mechanism (FRET), based on dipolar interactions between the donor and the acceptor. This energy transfer process can take place over long distances.

Taking inspiration from the natural pigments, some examples of carotenoid-based antennas were elaborated by T. and A. Moore, and D. Gust.[13] These molecules also play an important role in the photoprotection mechanism.

An interesting approach towards ordered arrays for light harvesting was put into shape by Balzani and Campagna, and was based on the use of dendrimers of ruthenium and osmium

complexes (Fig. 1. 3).[14] In these molecular structures, the properties of each component remain nearly unaltered, and the structural control allows to master their electrochemical and spectral properties. Meyer and colleagues elaborated Ru^{II}-Os^{II} arrays, where several Ru^{II} tris-bipyridine complexes are connected to an Os^{II} tris-bipyridine by functionalization of polystyrene or oligoprolyne strands (which provide spatial organization to the complexes).[15] It was demonstrated that these derivatized polystyrene assemblies support long-range energy transfer and can therefore act as "antennae" for the collection of visible light.

Fig. 1. 3. Left: structure of a decanuclear coordination metal dendrimer by Balzani and Campagna.[14] Right: electronic energy transfer processes occurring in polystyrene strands functionalized with ruthenium (white circles) and osmium complexes (black circles) by Meyer's group.[15]

Directly inspired from the natural antenna systems are the multiporphyrin arrays reported by Aida and co-workers (Fig. 1. 4).[16] The best properties, in terms of light harvesting and directional energy funnelling, were displayed by porphyrin dendrimers, which are characterised by the three-dimensional arrangement of a very large number of chromophores. An extensive research work about organic dendrimers was also performed by the Fréchet group.[17]

Gust and co-workers used instead an hexaphenylbenzene core (Fig. 1. 4) to spatially organize three different chromophores having complementary absorption spectra (bis(phenylethynyl)anthracene, borondipyrromethene and zinc porphyrin). Upon light absorption, the energy is rapidly transferred to the porphyrins, and it can be efficiently used to initiate a photoinduced electron transfer in a reaction centre (represented by a fullerene bound to the porphyrins through coordination bonds).[18]

Fig. 1. 4. Examples of artificial antennae of Aida and co-corkers (left)[16] and Gust and co-workers (right).[18]

An alternative approach for the construction of spatially organised molecular arrays was proposed by Lehn and co-workers, and exploited hydrophobic interactions to link the energy donor and the acceptor. The acceptor, a merocyanine dye, was included into the hydrophobic cavity of a cyclodextrin, covalently connected to the naphthoate donor.[19]

1.1.2.b. Molecular arrays for long-distance photoinduced charge transfer

This subject is perhaps the most widely studied one in the field of artificial photosynthesis, as charge separation in space is the principle allowing to provide long-lived photogenerated redox equivalents (as a consequence of the relatively slow recombination) with a high quantum yield. The latter are then used for to perform redox reactions. Hundreds of structures based on very different concepts that have been synthesized and thoroughly characterized. A more detailed overview of some relevant systems will be given in paragraph 4.1, but let us briefly introduce the basic concepts and approaches to obtain long-distance and long-lived excited states by using light energy.

In general, all these molecular assemblies are obtained by connecting a photosensitizer (S), responsible for light absorption, with an electron donor (D) and/or an electron acceptor (A). In this way, polyads are obtained and the photoinduced electron transfer processes are studied. Donor-sensitizer-acceptor (D—S—A) triads are the simplest example of polyads. Of course, the chromophore can also be at one extremity, like in the natural photosynthetic system (triads S—A_1—A_2 or D_2—D_1—S).

The absorption of a photon of the suitable wavelength (λ_{max}) promotes the sensitizer from the ground to the excited state, where it becomes both a better oxidant and a better reductant (see below, paragraph 1.2.1).[20] Depending on the redox potentials of the excited state, the excited

photosensitizer will be preferentially a powerful oxidant or reductant. The primary charge transfer will occur towards the electron acceptor for highly reducing S* (electron transfer) and towards the donor (hole transfer) for highly oxidizing S*. Then, the system undergoes a "dark" secondary charge transfer to give the long-lived D^+—S—A^- state. The interest in performing the second charge transfer is that, if the charges are separated by a long distance, the recombination reaction is slowed down (vide infra). This same principle provides the exceptionally long-lived charge-separated states involved in the natural photosynthetic process.

Fig. 1. 5. Reaction scheme for the formation of photoinduced charge-separated states in a D—S—A triad.

Among the many molecular systems that have been prepared, some families can be identified. First of all, the systems based on molecular moieties reminiscent of the biological systems, like β-carotene, porphyrins and quinones.[21,22] A great number of molecular assemblies, moreover, is based on the use of coordination compounds as sensitizers (Ru^{II}, Ir^{I}, Ir^{III}, Os^{II}, Re^{I}, Pt^{II}, Cu^{I}…),[23-29] in which the complexes are bound to electron donor and acceptor groups through covalent bonds. This approach is particularly appealing because it allows the construction of elaborate polyads by assembling the different units through coordination bonds in a modular way and will be examined in greater detail in chapter 4, where the topic of photoinduced charge transfer will be studied. It is important to observe that the great majority of these polyads based on coordination compounds contain rare and expensive metals, in particular ruthenium(II) complexes are by far the most extensively studied. It appears therefore important to investigate the possibility

of using more abundant and less expensive metals to build the chromophores, in view of practical applications of these compounds.

Another branch of this field deals with charge transfer processes occurring through non covalent bonds like hydrophobic interactions,[30] hydrogen bonding [31] or coordination bonds.[32,33]

1.1.2.c. Molecular catalysts for water splitting

An intense effort is also put in the research to find new catalysts to perform water splitting, and to improve their performances. A complete review of these systems is beyond the scope of this manuscript, so only a few systems will be mentioned.

Water oxidation is a very challenging task, since it is a four-electron process.

$$2 H_2O \rightarrow O_2 + 4 H^+ + 4 e^-$$

It can be efficiently obtained by the use of IrO_2 catalyst,[34] but this material has the non negligible drawback of being based on the extremely rare iridium. In order to move to cheaper materials, a cobalt phosphate catalyst was, for example, developed by the Nocera group.[35] Many important catalysts are based on ruthenium complexes. An example is the well-known ruthenium blue dimer, originally reported by T.J. Meyer and colleagues, whose structure is composed of two Ru bipyridine complexes bridged by an oxygen atom.[36] Monomeric[37] and dimeric[38] ruthenium complexes were also reported by Thummel and co-workers. Recently, the Sun group reported a monomeric ruthenium complex exhibiting very impressive catalytic properties, in particular a turnover frequency (300 s^{-1}) comparable with the rate of oxygen production in the natural OEC (Fig. 1. 6).[39]

TON 13
TOF 0.004 s^{-1}

TON 3200
TOF 7.7 s^{-1}

TON 8360
TOF 300 s^{-1}

Fig. 1. 6. Structure of three ruthenium-based catalysts for water oxidation, reported by the Meyer (left),[36] Thummel (centre)[37] and Sun (right)[39] groups.

Ir^{III} phenylpyridine aquo complexes exhibited a good catalytic activity in pure water, with turnover numbers around 2500.[40]

Quite recently, some systems based on the use of polyoxometalates comprising a M_4O_4 cubane core were reported by Hill and colleagues (M = Co), with a TOF > 5 s^{-1} at pH 8,[41] and by the groups of Scandola and Campagna (M = Ru).[42] These catalysts are directly inspired by the cluster present in the oxygen evolving centre.

Proton reduction to give molecular hydrogen can be efficiently catalysed by platinum nanoparticles. However, other systems are being considered in order to find efficient catalysts based on less rare and expensive elements. Some examples are shown in Fig. 1. 7.

Fig. 1. 7. Structures of some molecular proton reduction catalysts. From left to right cobaloximes, FeFe hydrogenase mimics, dimetallic molybdenum catalysts and Ni-based catalysts.

Taking inspiration from the natural [FeFe] hydrogenase enzymes, much work concentrates on the use of complexes containing two iron atoms bridged by two sulphur atoms (reminiscent of natural cysteine residues).[43] Recently, some systems based on mononuclear iron complexes were proposed by the Ott group.[44] Taking inspiration from the presence of nickel in natural hydrogenase enzymes, a series of Ni-containing catalysts was conceived by DuBois and colleagues.

Other widely studied proton reduction catalysts are cobaloximes, originally proposed by Espenson as electrochemical catalysts[45] and developed by many research groups in the last 25 years.[46,47] Several modifications of the cycle and of the axial ligands are possible, opening the way to a great deal of different structures.

Molybdenum was also used to conceive molecular catalysts for proton reduction: in particular sulphur bridged dimetallic structures were reported by DuBois and colleagues[48] and molybdenum-oxo polypyridine complexes were recently published by the Long group.[49]

1.1.2.d. Photosensitization of molecular catalysts

Active research is also going on to couple photosensitizers with water splitting catalysts. Such artificial systems rely on the use of a photosensitizer (PS) to reduce or oxidize the catalyst

(Cat) by photoinduced processes. The catalyst will then be able to perform water splitting and the photosensitizer is regenerated by the reaction with a sacrificial electron donor or acceptor.

This field was at first developed using "bimolecular" systems,[50-52] where the sensitizer and the catalyst are not bound to each other. In their seminal work published in 1977,[50] Lehn and Sauvage obtained hydrogen photoproduction using $[Ru(bpy)_3]^{2+}$ as the sensitizer and triethanolamine (TEOA) as the sacrificial electron donor. An electron relay ($[Rh(bpy)_3]^{3+}$) acted as electron relay to finally reduce the catalyst, platinum nanoparticles formed *in situ* by reduction of K_2PtCl_6. The mechanism for water reduction can involve either oxidative quenching of the excited photosensitizer, followed by regeneration by the electron donor (Fig. 1. 8), or a reductive quenching (electron transfer from the electron donor, followed by reduction of the relay by PS^-).

Fig. 1. 8. Schematic representation of the redox catalytic cycles in the photoreduction of water to hydrogen: oxidative quenching mechanism. D: sacrificial electron donor; PS: photosensitizer; R: electron relay; Cat: catalyst.

In order to optimize the electron transfer between the photosensitizer and the catalyst, PS-Cat systems, where the two units are linked by chemical bonds, were investigated. These systems work in solution and the majority of them are based on the use of a ruthenium(II)[53] or platinum(II)[54] sensitizer. For example, an interesting system for the accumulation of charges on a Mn cluster (reminiscent of the natural OEC) was proposed by Hammarström and colleagues: it was composed of a Mn_2 cluster covalently connected a to $[Ru(bpy)_3]^{2+}$ unit, with two secondary electron acceptors (NDI) to increase the charge-separated state lifetime (**(NDI)$_2$-Ru^{II}-(Mn^{II})$_2$**, Fig. 1. 9).[55] Unfortunately, even if the photo-accumulation of no less than three holes was achieved with this molecular system, the manganese cluster was irreversibly altered, and no catalysis, nor regeneration of the complex in its initial form could be obtained. Some PS-Cat arrays were proposed where two ruthenium complexes are connected by a ditopic ligand: one of the two metal centres performs the role of sensitizer and the second one of the catalyst.[56] Extensive work on Ru^{II}-Rh^{III} systems were also carried out in the Brewer group.[57]

Fig. 1. 9. Structure of three PS-Cat arrays: **(NDI)$_2$-Ru^{II}-(Mn^{II})$_2$**,[55] **Ru^{II}-Ru^{II}**[56] and **Ru^{II}-Rh^{III}-Ru^{II}**.[57]

More recently, semiconductors began to be used instead of sacrificial reactants, with the final aim to build an array working in water with no waste products. The semiconductors act at the same time as a solid support and as electron or hole reservoir to regenerate catalysts. Some works have been recently published on both water oxidation [58,59] and reduction.[60] These systems are based on photoelectrochemical cells, where the PS-Cat system is covalently grafted onto the electrode surface. An external bias is applied to the system in order to regenerate the photosensitizer after the photoinduced electron tranfer to, or from, the catalyst.

1.1.2.e. Systems mimicking the entire charge separation process

Artificial devices able to mimic the entire water splitting process are still lacking, but it is important to mention the work by Mallouk and colleagues,[59] who used a sensitizer-catalyst array with [Ru(bpy)$_3$]$^{2+}$ and IrO$_2$ to sensitize titanium dioxide in a photoelectrochemical cell (Fig. 1. 10). Upon light irradiation, electrons are injected from the ruthenium sensitizer into the conduction band of TiO$_2$, and the resulting hole shifts to IrO$_2$ nanoparticles, leading to water oxidation. The electrons provided by water oxidation on the anode side are collected at the platinum cathode to perform proton reduction. A small external bias is applied to provide enough driving force for the electron

collection in the external circuit. The water oxidation catalysis is extremely slow, but it constitutes however an extremely encouraging result towards the construction of the artificial leaf.

Fig. 1. 10. Schematic structure of the water splitting system of Mallouk and co-workers.[59]

1.2. Quantitative treatment of electron and energy transfer reactions

Solar energy conversion is based on the harvesting of luminous energy by a sensitizer. This energy is then either converted into a redox potential by a sequence of electron transfers (generation of a charge-separated state) or transferred to other molecules by means of energy transfer. In both cases, these photoinduced processes result in an excited state quenching of the sensitizer.

Let us consider an electron or energy donor (D) and an acceptor (A), the two groups are connected through a photochemically inert spacer. Upon excitation of a photoactive unit (D for example), the molecule can undergo different fates (Fig. 1. 11).

Fig. 1. 11. Schematic representation of the possible evolution of a dyad D-A after excitation of the D group. Intersystem crossing is not taken into account.

16

The possible processes are:

1) radiative relaxation of *D: *D-A → D-A + hv;
2) non radiative relaxation of *D: *D-A → D-A;
3) electron transfer to A, to yield a charge-separated state: *D-A → D$^+$-A$^-$;
4) electronic energy transfer to A: *D-A → D-*A.

The theoretical aspects of electron and energy transfer (points 3 and 4), the most important phenomena from the point of view of the subject of this thesis, are now briefly recalled. These topics are already the object of complete works,[61-64] so only the basic principles will be given here.

1.2.1. Photoinduced electron transfer

One of the possible fates for the relaxation of an electronically excited state is to undergo a photoinduced charge separation with a donor or an acceptor, present in solution or chemically bound to it.

The driving force for this redox reaction (*D-A → D$^+$-A$^-$) is given by the following equation (Rehm-Weller equation):[65]

$$\Delta G^0_{ET} = E_{D+/D*} - E_{A/A-} + corr \qquad \text{Eq. 1.1}$$

The correction term "corr" accounts for the electrostatic interactions between the charges (E_{CS}) and the redox potential correction (E_{redox}), if the solvent where the electrochemical data are recorded is different from the one where the photoinduced process occurs:

$$E_{CS} = \frac{-e^2}{4\pi\varepsilon_0\varepsilon_S R_{DA}} \qquad \text{Eq. 1.2}$$

$$E_{redox} = \frac{e^2}{4\pi\varepsilon_0}\left[\frac{1}{\varepsilon_S}\left(\frac{1}{2r_+} + \frac{1}{2r_-}\right) - \frac{1}{\varepsilon_r}\left(\frac{1}{2r_+} + \frac{1}{2r_-}\right)\right] \qquad \text{Eq. 1.3}$$

where "e" is the charge of electron, ε_0 is the vacuum permittivity, R_{DA} is the distance between donor and acceptor (Å), ε_s is the dielectric constant of the solvent where the photoinduced process is studied, ε_r is the dielectric constant of the solvent where the electrochemical measurements are recorded, r_+ is the radius of D$^+$ (Å) and r_- is the radius of A$^-$ (Å).

When photoexcited, the sensitizer becomes both a better oxidant and a better reductant (formation of a low energy hole and a high energy electron):

$$E_{D+/D*} = E_{D+/D} - E^{00} \qquad \text{Eq. 1.4}$$

$$E_{D*/D-} = E_{D/D-} + E^{00} \qquad \text{Eq. 1.5}$$

The occurrence of oxidative quenching (electron transfer to an electron acceptor) or reductive quenching (electron transfer from a donor) of the excited state depends on the oxidation and reduction potentials of the sensitizer and of the other electroactive groups in its environment, provided of course that the lifetime of the excited state is long enough to allow the various electron transfer steps to take place.

From Eq. 1.1 it can be deduced if the reaction is thermodynamically allowed ($\Delta G^0 < 0$) or not, but no information about the kinetics of the electron transfer is provided.

The kinetic aspect of the photoinduced electron transfer was widely studied by R. A. Marcus in the 1950's.[61,66-68] This theoretical treatment deals with the rate constant of electron transfer reactions, and was elaborated for weakly coupled, or non adiabatic, systems (see below). The rate constant for an electron transfer reaction between a donor D and an acceptor A is given by:

$$k_{ET} = \frac{2\pi}{\hbar} |V_{DA}|^2 \frac{1}{\sqrt{4\pi\lambda k_B T}} \exp\left(-\frac{(\Delta G^0 + \lambda)^2}{4\lambda k_B T} \right)$$

Eq. 1.6

The potential energy surfaces of the two states involved in the electron transfer reactions are represented in Fig. 1. 12.

Fig. 1. 12. Potential energy parabolas of *D−A and D$^+$−A$^-$. ΔG^0, $\Delta G^{\neq}$, λ and V_{DA} are illustrated. In weakly coupled systems considered here, the electronic coupling V_{DA} is small and the two surfaces can be seen as separate surfaces (non adiabatic electron transfer).

Let us now consider the different elements appearing in the equation.

- V_{DA} is the electronic coupling between D and A, originating from the orbital overlap of the two units, and thus decreasing exponentially with increase of the distance r_{DA}. In this case, weakly coupled systems are considered (Fig. 1. 12), where the electronic coupling is small if compared to thermal energy: $V_{DA} < k_B T$.

- λ is the reorganization energy, *i.e.* the energy that would be required to move the nuclei of the reactants and the solvent molecules to the positions that they occupy in the relaxed charge-separated state (product) without actually transferring the electron. This contribution can be split into two terms: λ_{in} and λ_{out}, that can be evaluated by using Eq. 1.7 and Eq. 1.8. These two additive contributions respectively stem from the internal changes in bond lengths and angles (λ_{in}) within the D-A assembly, and from the redistribution of the solvent molecules around the dyad adjusting to the variations of the local electric field. Globally, the λ value is strongly dependent on the structural changes of the system upon electron transfer, on the r_{DA} distance and on the dielectric properties of the solvent.

$$\lambda_{in} = \tfrac{1}{2} \sum (k_i \, \Delta q_i^2) \qquad\qquad \text{Eq. 1.7}$$

$$\lambda_{out} = \frac{\Delta e^2}{4\pi\varepsilon_0}\left(\frac{1}{\varepsilon_{op}} - \frac{1}{\varepsilon_s}\right)\left(\frac{1}{2a_D} + \frac{1}{2a_A} - \frac{1}{r_{DA}}\right) \qquad\qquad \text{Eq. 1.8}$$

In the two equations above: k_i is the vibrational force constant of the "i" normal mode and Δq_i are the nuclear displacements of the normal vibrations; Δe is the charge transferred by one electron, ε_{op} and ε_s are the optical and static dielectric constants of the solvent (considered as a continuum medium), a_D and a_A are the radii of D and A considered as hard spheres and r_{DA} is the distance.

- ΔG^0 is the total free energy change that the system undergoes upon moving from the excited state D*-A to the relaxed D$^+$−A$^-$ state, indicating if the reaction is thermodynamically allowed or not. Another important parameter is the activation energy $\Delta G^{\neq}$, that can be calculated from ΔG^0 and λ.

$$\Delta G^{\neq} = \frac{\left(\Delta G^0 + \lambda\right)^2}{4\lambda} \qquad\qquad \text{Eq. 1.9}$$

Interestingly, if Eq. 1.6 is considered, upon increase of ΔG^0 (for constant V_{DA} and λ) the k_{ET} value reaches a maximum value for $-\Delta G^0 = \lambda$. In this case, the transition to the D$^+$−A$^-$ state is barrierless. For higher driving forces, the rate constant starts decreasing, indicating the so-called Marcus inverted region (Fig. 1. 13). The existence of this region was demonstrated experimentally in 1984[69] and is useful for slowing down the charge recombination in the charge-separated state (in fact, the ΔG^0 for charge recombination is normally very high).

Fig. 1. 13. Illustration of the normal and inverted region for the electron transfer rate predicted by R.A. Marcus. The maximum rate is obtained for $-\Delta G^0 = \lambda$.

Concerning the electron transfer mechanism, it can be of different nature depending on the D−A distance and the role of the spacer.

In the *hopping* mechanism, occurring for short distances, there is a weak interaction between the orbitals of D and A ($S_{DA} \neq 0$; S is the overlap integral) and the electron is transferred directly from *D to A. The rate constant decreases exponentially with the energetic gap between the initial and final state (ΔE).[67]

In the *superexchange* mechanism, there is no direct interaction between D and A ($S_{DA} = 0$). However, a non zero overlap can exist between the orbitals of D and those of the spacer, and between those of A and those of the spacer. These overlaps indirectly lead to an electronic communication between D and A. The intermediate D^+-S^--A (S: spacer), participates to create an electronic communication, but is never populated (virtual state) and the electron transfer occurs directly from D to A. The energy gap dependence of the rate constant is weaker than in the previous case, as k_{ET} is inversely proportional to ΔE^2.

1.2.2. Energy transfer

Excited-state quenching by energy transfer occurs between units possessing isoenergetic states, in order to obey the law of conservation of energy. For the energy transfer to happen, the energy difference between D and *D has to be higher than that between A and *A. The two different mechanisms for energy transfer differentiate on the basis of the interaction between D and A, and have a different D-A distance dependence. Förster and Dexter energy transfer mechanisms are schematically represented in Fig. 1. 14.

Fig. 1. 14. Representation of the frontier orbitals of the energy donor (D) and acceptor (A), and of the Förster and Dexter energy transfer mechanisms.

1.2.2.a. Förster mechanism

The Förster or dipolar mechanism is based on dipole interactions between the *D → D and A → *A transitions. The energy transfer occurs thanks to the interaction between the two oscillating dipoles. This mechanism necessitates a good overlap between the emission spectrum of the energy donor and the absorption spectrum of the acceptor.

Fig. 1. 15. Overlap between the emission of the donor (Em) and the absorption of the acceptor (Abs).

The overlap function is defined as:

$$J(\lambda) = \int f_D(\lambda)\varepsilon_A(\lambda)\lambda^4 d\lambda \qquad \text{Eq. 1.10}$$

Where f_D is the emission intensity of the donor and ε_A is the molar extinction coefficient.

This mechanism has no stringent requirements concerning spatial proximity of D and A, as evidenced by the rate constant for the energy transfer Eq. 1.11. In fact, it occurs through space, even on long distances (until 100 Å). Energy transfer occurs between states with the same spin multiplicity.

$$k_F = 8.8 \cdot 10^{-25}\left(\frac{\phi_D J(\lambda)K^2}{n^4\tau_D R_{DA}^6}\right) \qquad \text{Eq. 1.11}$$

Φ_D and τ_D are the quantum yield and excited-state lifetime of the donor, $J(\lambda)$ is the spectral overlap defined above, K is the dipole orientation factor (which is maximized if the two dipoles oscillate on parallel planes), n is the refractive index of the solvent and R_{DA} is the donor-acceptor distance. K and R_{DA} can be obtained by molecular modelling.

1.2.2.b. Dexter mechanism

On the other hand, the Dexter, or double electron exchange, mechanism requires orbital overlap, and therefore decreases rapidly with the D-A distance, also depending on the nature of the spacer. The excited-state quenching occurs by a double electron exchange: an electron transfers from *D to the LUMO of A while another transfers from A to the HOMO of *D, resulting in the formation of excited *A (Fig. 1. 14). Importantly, the two electron shifts are simultaneous, and no ionic intermediates can be detected.

The rate constant for this mechanism is expressed by Eq. 1.12:

$$k_D = \frac{2H_{DA}^2}{h}\sqrt{\frac{\pi^3}{\lambda RT}}\exp\left(\frac{-\Delta G^{\neq}}{RT}\right) \qquad \text{Eq. 1.12}$$

$\Delta G^{\neq}$ is the activation energy of the process, λ is the reorganization energy (λ_{in} and λ_{out}) and H_{DA} is the matrix representing the electronic coupling between D and A. This factor decays exponentially with the distance, and is responsible for the fast decay of this energy transfer mechanism when D and A are moved far away from each other.

$$H_{DA} = H_{DA}^0\exp\left(-\frac{\beta}{2}(r - r_0)\right) \qquad \text{Eq. 1.13}$$

H_{DA}^0 is the electronic coupling at the r_0 distance, β is the attenuation factor and depends on the nature of the bridge linking D and A, r is the D-A distance and r_0 is the distance between D and A at

the Van der Waals radius contact. The exponential dependence on r is the reason of the rapid decay of the Dexter contribution with the distance.

1.3. Copper

As seen in the introduction, the world of artificial photosynthesis is strongly dominated by ruthenium complexes. The aim of this thesis is to conceive and develop new molecular arrays based on the remarkably cheaper and more abundant copper. Due to their better photophysical properties, from the point of view of solar energy conversion, this introduction chapter focuses on copper(I) complexes, that exhibit relatively intense absorption and fairly long-lived emissive excited states. In particular, copper(I) diimine complexes are considered as promising compounds to perform solar energy conversion.[70] In the following paragraphs, an overview of some interesting systems based on copper(I) will be presented, to introduce some useful concepts that are of interest for this thesis. Copper is present in the Earth crust in a concentration of about 50 ppm, and can be found in its native state or in different oxidized forms. In minerals, it can be found for example as a sulfide (chalcopyrite, chalcocyte), a carbonate (azurite, malachite) or an oxide (cuprite).[71] Used by mankind for 10000 years, the production trend is continuously rising and in particular since the beginning of the 20th century. The world production of this metal was around $15 \cdot 10^6$ tons in 2005. This abundance reflects in a relatively low cost if compared to that of rare metals like ruthenium (10^{-3} ppm in the earth crust). This metal is usually found in +1 and +2 oxidation states, even though copper(III) and copper(IV) can be found in some cases.[72,73]

Copper plays a crucial role in biological redox systems, particularly those associated with oxidation or oxygen transfer like cytochrome c oxidase, galactose oxidase or superoxide dismutase. A typical example is that of blue copper proteins in the electron transfer chain from substrates to oxygen.[74] These compounds are particularly useful to illustrate the role of the ligand surroundings in determining the properties of the complexes, and the different structural properties of copper(I) and copper(II).[75] A tetrahedral environment is favoured for the Cu^I ion, while Cu^{II} is more stable in a tetragonal coordination. In blue copper proteins, the Cu^{II} ion is forced by the protein environment to be in a tetrahedral coordination, which enhances the absorption coefficient and drastically lowers the reorganization energy upon electron transfer (thus increasing the reaction rate, according to Marcus theory). Remarkably, also the reduction potentials are carefully matched to those of the adjacent units in the electron transport chain, as a result of evolution pressure.

1.4. Homoleptic copper(I) bis-phenanthroline complexes

Since the discovery of the room temperature luminescence of copper(I) diimine complexes by McMillin ([Cu(**dmp**)$_2$]$^+$, **dmp** = 2,9-dimethyl-1,10-phenanthroline) and Sauvage ([Cu(**dpp**)$_2$]$^+$, **dpp** = 2,9-diphenyl-1,10-phenanthroline),[76,77] there is a growing interest in the photophysical and structural properties such compounds, which have been investigated by a large number of groups.[70,78,79] The presence of relatively long-lived excited states opens the way to a rich photochemistry, which is not possible with completely non emissive compounds such as [Cu(**phen**)$_2$]$^+$ (**phen** = 1,10-phenanthroline).

Various aspects of copper(I) diimine complexes will now be covered, in order to provide useful elements that will be used throughout this thesis work.

1.4.1. Structure

In copper(I) diimine complexes, the metal is characterized by a d^{10} electronic configuration. The completely filled external electronic shell results in a symmetrical distribution of the electron density, which favours tetrahedral arrangement of the ligands around the metallic ion. As will be explained in detail later on, structural properties have a strong influence on copper(I) complex photophysical and electrochemical properties. For this reason, it is important to analyse the possible distortions from the tetrahedral symmetry that can occur in solution and in the solid state. Typically, phenanthroline ligands have a bite angle around 82° and average Cu-N distances are around 2.0 Å.[78]

The structure of a tetrahedral diimine complex is shown in Fig. 1. 16. θ_x, θ_y and θ_z are the angles defined by the two ligands.

Fig. 1. 16. Left: structure of a copper(I) bisphenanthroline complex in its ground state with indication of the (i) wagging, (ii) rocking and (iii) flattening distortions.[78] Right: orientation of the axes, with the two ligands lying in the xy and xz planes. θ_x: flattening; θ_y: wagging; θ_z: rocking.

In a perfectly tetrahedral structure, $\theta_x = \theta_y = \theta_z = 90°$. Their values are used to define, in distorted structures, the flattening, wagging and rocking distortions, respectively, as indicated in the figure above.

The parameter ξ_{CD} (combined distortion)[70,78] was proposed in order to include all the distortions in the same value, and is defined by the Eq. 1.14:

$$\xi_{CD} = \frac{(90°+\theta_x)(90°+\theta_y)(90°+\theta_z)}{180^3}$$
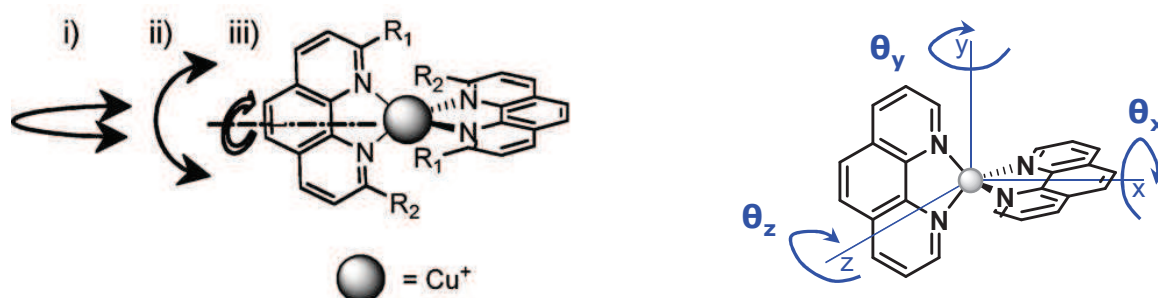
Eq. 1.14

In a tetrahedral system, $\xi_{CD} = 1$, while the value decreases for distorted structures. The θ values can be obtained from X-ray or calculated structures.

Several explanations were put forward to clarify the forces that control the complexes geometry, and two main contributions were identified. Originally, the strong influence of packing forces within the crystal was identified, mediated by intermolecular stacking between the ligands bound to adjacent metal centres.[80,81] For this reason, counterions were observed to play a role in determining the solid state electronic spectrum: bulkier ions reduce the intermolecular interactions and thus reduce the packing forces within the crystal. In complexes with aryl substituents, however, intramolecular stacking also comes into play as pointed out by Sauvage and co-workers for the case of [Cu(**dpp**)$_2$]$^+$,[82] but the presence of the aryl groups was proven not to be a sufficient condition to have such rocking distortion leading to a pyramidal geometry.[81] When the free rotation of the aryl rings is restricted, like in the case of complexes with 2,9-diphenyl-3,4,7,8-tetramethylphenanthroline (**dptmp**, see Fig. 1. 19), the structure exhibits a reduced flattening distortion.[81]

Concerning solution structure, since the packing forces are suppressed, they are mainly due to intramolecular interactions. Homoleptic complexes with 2,9-dialkyl substituted phenanthroline ligands tend to exhibit a nearly tetrahedral structure in solution, while the 2,9-diaryl substituted undergo severe distortions due to the π-stacking between the aryl rings.

Structural difference between copper(I) and copper(II) complexes is now briefly mentioned, because it has major consequences on the photophysical and electrochemical properties of these compounds. Copper(II), in fact, has a d^9 configuration, and tends to have a tetragonal geometry. The distortion is due to the increase of the overlap between the σ-donating orbitals of the ligands and the d_{xy} orbital of the copper ion, formally half-occupied in the d^9 electronic configuration.[78] Moreover, increase of the coordination number from 4 to 5, upon binding of a ligand in the axial position, is a usual process, that finally leads to an overall pyramidal structure. If we consider the structure reported in Fig. 1. 16, this structural change is sometimes claimed to be a Jahn-Teller distortion with flattening of the tetrahedral geometry (decrease of the dihedral angle between the two ligand

planes, θ_x). Therefore, the presence of bulky substituents in the 2 and 9 positions of the phenanthroline ring, which prevents the flattening deformation, has direct consequences on the relative stability of the two oxidation states.[83]

1.4.2. Absorption properties

The UV-Visible absorption spectrum of copper(I) diimine complexes is characterized, in the UV portion, by the π-π* transitions typical of the phenanthroline ligands. These intense bands have molar extinction coefficients around 5-$6 \cdot 10^4$ $M^{-1}cm^{-1}$. At lower energies (the blue part of the visible region) is the broad and less intense metal-to-ligand charge transfer (MLCT) transition, with a maximum wavelength around 450 nm and molar extinction coefficients ranging from $3 \cdot 10^3$ to $1.5 \cdot 10^4$ $M^{-1}cm^{-1}$.[84] These transitions occur at low energy because the 3d orbitals of the copper(I) ion are high in energy and easily accessible, and phenanthroline possesses low-lying empty π* orbitals, that can accept an electron. The localized nature of the transition, leading formally to a $[Cu^{II}(phen)(phen^{\bullet -})]^+$ excited state, was assessed by Raman spectroscopy and by transient absorption studies.[85,86] The HOMO and HOMO-1 are mainly composed of metal centered, $d_{xz,yz}$ orbitals, while the LUMO is constituted of ligand-centered π orbitals, bonding in the ligand region and antibonding in the metal region.[87] Since nearly 50% of the solar spectrum reaching the earth surface is composed of visible photons (against only 2-3% of UV photons), this MLCT band is particularly interesting from the point of view of solar energy conversion.

The MLCT structure of the excited state is very reminiscent of ruthenium polypyridine complexes, underlining the great potential of copper(I) complexes as substitutes to the former. Moreover, the copper(II) nature of the excited state is bound to have consequences on the behaviour of the excited state; those will be developed in detail below.

From an analysis of the MLCT absorption, three different contributions can be identified:[88] following the terminology proposed by Ichinaga and colleagues, they are termed bands I, II and III in order of increasing energy (Fig. 1. 17, left). Band I is usually found at wavelengths above 500 nm, band II between 430 and 480 nm and band III, whose λ_{max} is situated at 390-420 nm, is often hidden by the onset of other bands. Band I can be assigned to a $S_1 \leftarrow S_0$ transition, while band II, more intense, corresponds to a $S_2 \leftarrow S_0$ transition.[89] The relative intensity of the three contributions to the overall spectrum is strongly dependent on the complex symmetry, which is in turn influenced by the geometry in the ground state.[70] In particular band I is quite intense in the spectrum of complexes having D_2 symmetry, i.e. flattened structure.[81] A good example is the case of complexes with 2,9-bisaryl substituted phenanthrolines, like **dpp** (2,9-diphenylphenanthroline). Since $[Cu(\textbf{dpp})]^+$ was first published, in 1983,[77] its peculiar absorption behaviour has been pointed out.

The spectrum displays a broad shoulder at 550 nm, absent in the spectrum of $[Cu(\mathbf{dmp})_2]^+$. The same behaviour was observed for catenates and other complexes bearing aryl substituents on the phenanthroline ligands.[90,91] Interestingly, the low energy shoulder nearly disappears in the electronic spectrum of $[Cu(\mathbf{dptmp})_2]^+$ (**dptmp** = 2,9-diphenyl-3,4,7,8-tetramethyl-1,10-phenanthroline)[92] because the methyl groups at the 3 and 7 positions limit the extent of the flattening distortion at the ground state (Fig. 1. 17, right).
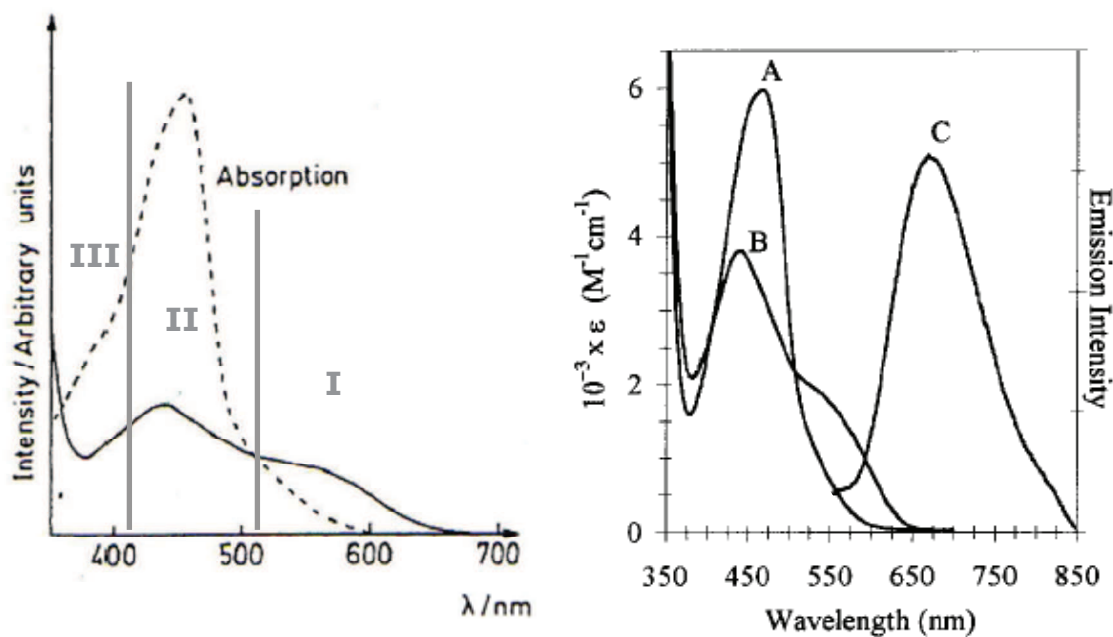
Fig. 1. 17. Left: Absorption spectra of $[Cu(\mathbf{dmp})_2]^+$ (- - -) and $[Cu(\mathbf{dpp})_{-2}]^+$ (—), the bands I, II and III are indicated in grey.[77] Right: absorption spectra of $[Cu(\mathbf{dpp})_2]^+$ (A) and $[Cu(\mathbf{dptmp})_2]^+$ (B).[92] C: emission spectrum, not pertinent. All the spectra are recorded in dichloromethane.

Concerning absorption spectra in the solid state, it was observed that flattening distortion from the tetrahedral symmetry, due to intra- or intermolecular forces, plays a major role in determining the shape of the spectrum. If the dihedral angle between the phenanthrolines is close to 90°, the solid appears as a red to orange powder. Conversely, if the angle is much smaller, a low energy contribution appears and the solids are violet.[81] On the contrary, rocking distortion has a smaller impact on the absorption properties.

1.4.3. Emissive excited states

Luminescence properties of copper(I) diimine complexes were discovered in 1980 by McMillin and co-workers, for [Cu(**dmp**)$_2$]$^+$.[76] These compounds exhibit a very broad and red-shifted emission around 700 nm, with very low intensity (quantum yield around 10^{-4}). Luminescence measurements conducted in different solvents evidenced a strong quenching in polar solvents, like acetonitrile or methanol, where the above mentioned compound did not emit any more.

The accepted explanation for this behaviour is the so-called exciplex quenching (graphically represented in Fig. 1. 18), proposed by McMillin and colleagues.[83,93] This phenomenon is due to the remarkably different geometry and coordination number for Cu^I and Cu^{II} complexes. In fact, as the lowest energy absorption has an MLCT character, in the excited state the copper(I) ion is formally oxidized to copper(II) and the complex undergoes a severe flattening that opens the way to the attack by a coordinating molecule, such as the solvent or the counteranion. In particular, potentially coordinating solvents like acetonitrile or DMF, or counteranions like nitrate efficiently quench the luminescence of these complexes.[79] Moreover, according to Jörtner's energy gap law, the nonradiative rate constant increases exponentially with the decrease of the energy gap between the ground and the excited state. The stabilization of the tetragonal MLCT state by formation of an exciplex results thus in a strong luminescence quenching.[87]
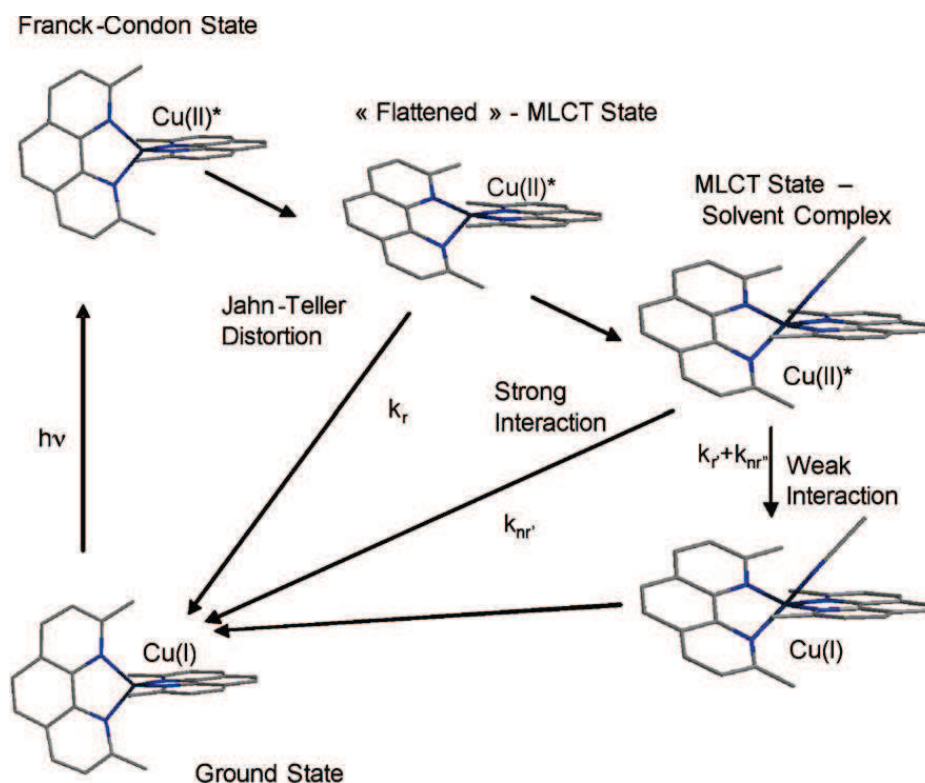
Fig. 1. 18. Excited-state processes for a [Cu(**dmp**)$_2$]$^+$ complex, interacting with an acetonitrile solvent molecule. [78]

Bulky groups at the 2 and 9 positions efficiently increase the excited-state lifetime thanks to a double steric effect. On one hand they prevent the complex from flattening, and thus from reducing its energy content, and on the other hand they screen the copper ion from the attack of solvent molecules leading to exciplex formation.[94] A particularly interesting compound is [Cu(**dpp**)$_2$]$^+$ (**dpp** = 2,9-diphenyl-1,10-phenanthroline).[77] This complex displays long-lived luminescence (310 ns in CH_2Cl_2 at room temperature), explained by an effective protection of the copper ion (formally in +2 oxidation state after excitation) from the attack of nucleophiles in solution. This fact was also proved by studying the structural properties of [Cu(**dpp**)$_2$]$^+$ and [Cu(**dpp**)$_2$]$^{2+}$ (used as a model of the excited state): the latter shows four-coordination, a rare phenomenon for Cu^{II} complexes which indicates a very hindered coordination sphere.[95] Another example of extremely bulky, strongly luminescent complex is given by [Cu(**dtbp**)$_2$]$^+$ (**dtbp** = 2,9-di-*t*-butyl-1,10-phenanthroline), which has a lifetime of 3.3 μs in dichloromethane solution.[96] The emission properties, however, are compensated by an easy ligand displacement to release the strains in the coordination cage. The structures of the ligands are given in Fig. 1. 19.

dmp
τ = 90 ns

dpp (R: H)
τ = 310 ns

dptmp (R: CH$_3$)
τ = 480 ns

dbp (R: H)
τ = 150 ns

dbtmp (R: CH$_3$)
τ = 920 ns

dtbp
τ = 3300 ns
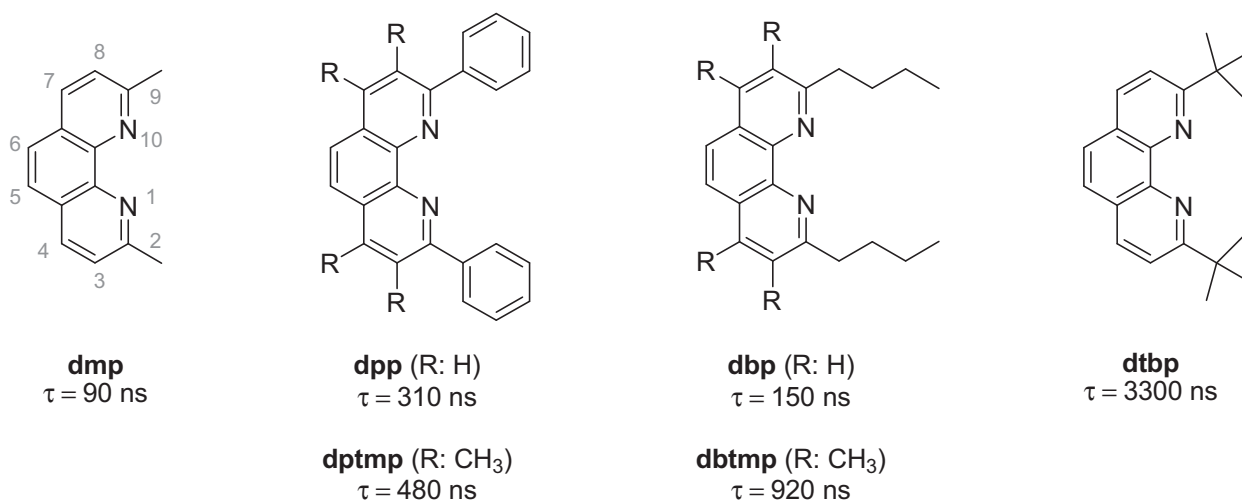
Fig. 1. 19. Structure of some ligands and emission lifetime of the corresponding copper(I) homoleptic complexes.[77,84,96] The atom numbering of the phenanthroline core is reported on the **dmp** ligand.

The excited-state structure is also influenced by the presence of substituents in positions 3 and 8 of the phenanthroline core. These groups markedly influence the geometry of the complexes, providing a strain that lowers the flattening distortion of the relative complexes in the excited state. The phenyl groups are forced to twist with respect to the phenanthroline core providing a more effective shielding of the metallic ion in the excited state.[92]

The study of the temperature dependence of the emission spectra of a series of copper(I) diimine complexes, among which [Cu(**dmp**)$_2$]$^+$, evidenced a blue shift and an increase of the

luminescence quantum yield upon increasing T.[97] This rather unusual behaviour was explained through a "two-state" model, considering the thermal equilibrium between two emissive MCLT states, singlet and triplet. The energy difference between the two is estimated to be between 1500 and 2000 cm^{-1},[76,98] so that at room temperature the majority of the molecules is in the triplet state, but the singlet can be reached by thermal activation. The radiative rate constants of the two states are very different (10^7 s^{-1} for ^{1}MLCT and 10^3 s^{-1} for ^{3}MLCT), and the emission mainly results from the deactivation of the singlet state, even if it is definitely less populated. This contributes to explain why copper(I)-phenanthroline complexes are generally speaking weakly luminescent.

1.4.4. Probing the excited state distortion: pulsed spectroscopic techniques

As introduced before, understanding the geometrical and electronic structure of the excited state is a fundamental instrument to rationalize and control the excited-state properties of copper(I) complexes. DFT calculations carried out on dialkyl substituted [Cu(NN)$_2$]$^+$ structures anticipate a severe flattening of the complex in the MLCT excited state, with a decrease of the dihedral angle between the two phenanthrolines from around 90º (ground state) to around 70º (excited state). At the same time, Cu-N distances shorten slightly.

Important experimental data on the excited-state distortion have been obtained by means of pump-probe spectroscopic techniques, allowing to follow the evolution of the molecules on very short timescales after excitation. These spectroscopic techniques use a first laser pump in the visible region ($\lambda_{max} \sim 450$ nm), followed by a probe pulse of different energy, depending on the aspects that are examined. The majority of the studies concentrate on the use of X-ray (XANES, EXAFS) or visible probe pulses (transient absorption spectroscopy). Time-resolved fluorescence also provides important information.

X-ray pump-probe techniques as XANES (X-ray Absorption Near Edge Spectroscopy) gave strong evidence for exciplex formation, with coordination of a fifth ligand after the structural distortion from tetrahedral geometry. Interestingly, solvent coordination was observed both in acetonitrile [87] and toluene,[99] albeit with different strengths. More recent results, obtained with a quantitative analysis of XANES data coupled with calculated spectra, evidence a significant rocking distortion in the exciplex structure.[100]

Pump-probe experiments based on visible transient absorption and time-resolved fluorescence measurements also helped to shed more light on the excited-state dynamic processes and the influence of bulky groups that rigidify the coordination sphere.[89,94,101] Extensive studies conducted on the simple model [Cu(**dmp**)$_2$]$^+$ afforded a precise picture of the different processes occurring in the first instants after excitation (Fig. 1. 20).[89] Right after the laser pulse (exciting in

the $S_1 \leftarrow S_0$ band, in the red side of the MLCT), the system remains in the "tetrahedral" Franck-Condon state for a short finite time due to the presence of a shallow minimum in the potential energy surface of the excited state. If the higher singlet states are populated (excitation at λ_{max}), the internal conversion to S_1 occurs on an ultrafast timescale. The decay to the flattened excited state occurs with a short time constant of around 0.8 ps, and is followed by ISC to the lowest triplet state in around 10 ps. Interestingly, intersystem crossing occurs on a relatively slow timescale, much slower than for Ru^{II} bipyridine complexes for example (40 fs), due to the lower spin-orbit coupling for Cu^{I} complexes and to the structural distortion occurring in the ^{1}MLCT state.[102] The kinetic constants below 20 ps appear to be solvent independent.

Transient absorption studies combined with TD-DFT calculations correlated the evolution of the ^{3}MLCT transient absorption with the dihedral angle between the two ligands planes. The structural flattening provokes in fact a blue-shift and a narrowing of the TA band.[87]
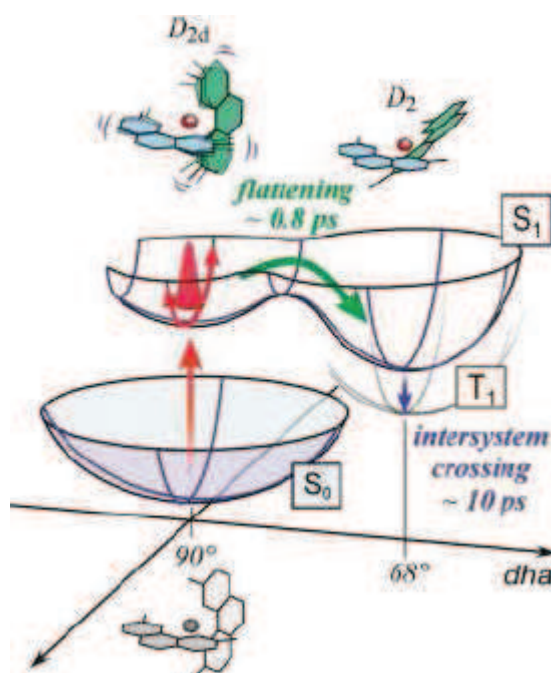
Fig. 1. 20. Diagram of the potential energy surfaces of the ground and excited states of $[Cu(\mathbf{dmp})_2]^+$, with indication of the photoinduced structural change in terms of flattening angle.[89]

If the flattening distortion is prevented by the presence of very bulky groups at the 2 and 9 positions of the phenanthroline, for example in $[Cu(\mathbf{dtbp})_2]^+$ (**dtbp** = 2,9-di-*t*-butyl-1,10-phenanthroline, Fig. 1. 19), a different behaviour is observed.[94] In this case there is no short time component and the intersystem crossing to the T_1 state is more rapid, as proven by the time-resolved fluorescence data. The complex has an outstanding excited-state lifetime of 1.9 μs in dichloromethane.

All in all, it appears mandatory to functionalize the phenanthroline core in α of the chelating nitrogen atoms with sterically challenging groups to obtain excited states with long lifetimes. This is an inescapable feature to design an efficient photosensitizer for light conversion into chemical energy. But thermodynamics play a major role too, as will be exposed now.

1.4.5. Ground and excited states redox properties

The electrochemical properties of copper(I) complexes are fundamental to understand their behaviour in photoinduced processes and, just like for the luminescence, they are strongly related to the different geometrical structure of Cu^I and Cu^{II}.

The reduction of usual copper(I) diimine complexes occurs at quite low cathodic potentials, usually between -1.5 and -1.7 V vs. SCE in acetonitrile.[91,103] The extra electron is located in a ligand-centred π* orbital (as confirmed also by quantum mechanical calculations).

The oxidation process consists in the removal of an electron from the copper-centred HOMO. The oxidation of copper(I) into copper(II) is accompanied by a severe flattening of the pseudo-tetrahedral structure, in order to evolve towards the more stable tetragonal coordination. Thus it is not surprising that bulky groups at the 2 and 9 positions of the phenanthroline ligands, that prevent the flattening distortion, destabilize the copper(II) form of the complex and shift anodically the potential of the $Cu^{II/I}$ redox couple. Moreover, from an electrochemical point of view, this couple is "quasi-reversible", which indicates that there is an important structural change between the forward and the backward electron transfers at the electrode.[104,105] Assuming that there are no electron donating nor withdrawing ligands, the $Cu^{II/I}$ oxidation potential can be used as a tool to evaluate the rigidity of the coordination sphere.[91,92]

Electron-withdrawing ligands have also been used, and they shift both the oxidation and the reduction potentials towards anodic values. Some examples are represented in Fig. 1. 21.
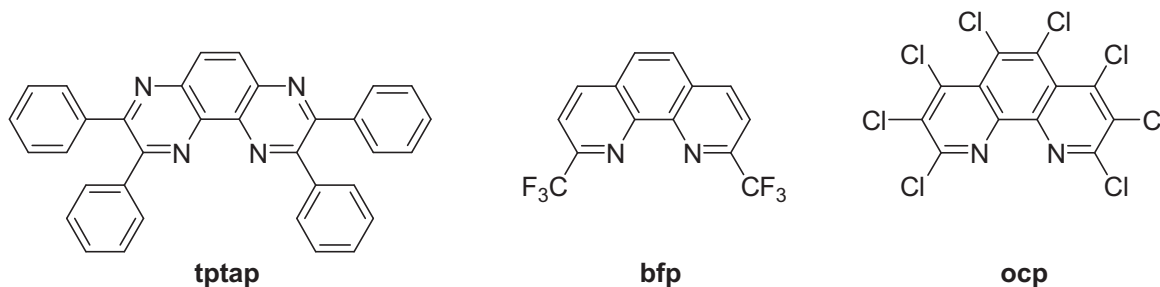
Fig. 1. 21. Structure of **tptap** (2,3,6,7-tetraphenyl-1,4,5,8-tetraazaphenanthrene),[106] **bfp** (2,9-bis(trifluoromethyl)-1,10-phenanthroline)[107] and **ocp** (octachloro-1,10-phenanthroline).[108]

Electrochemical data coupled to the analysis of absorption and emission spectra allow us to calculate the excited state redox potentials (Eq. 1.4 - 1.5). Let us consider for example the properties of $[Cu(dpp)_2]^+$, a well-studied complex which exhibits quite intense and long-lived luminescence.
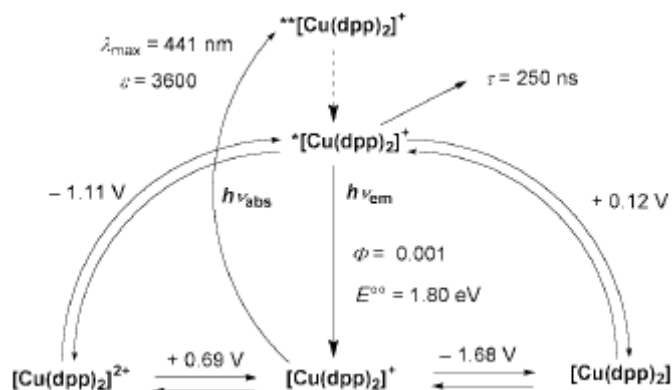
Fig. 1. 22. Photophysical and electrochemical properties of $[Cu(dpp)_2]^+$, reported vs. SCE.[77,84] * Lowest energy excited state. ** State populated by excitation in correspondence of the absorption maximum, by spin-allowed transition.

It can be observed that this species is a powerful reductant in the excited state, even more than the extensively used $[Ru(bpy)_3]^{2+}$ ($E_{S+/S*}$ = - 0.85 V).[84] This property is due to a quite low oxidation potential in the ground state, compensating the lower energy content of the excited state. On the contrary, copper(I) complexes are known to be quite poor photooxidants, as shown by the low $E_{S*/S-}$ potential.

In light of the data reported above, it is not surprising to find more reports about oxidative quenching of copper(I) diimine complexes than about reductive quenching. The first reports of photoinduced bimolecular electron transfer consider the excitation of $[Cu(dmp)_2]^+$, which was used to reduce cobalt(III) complexes in ethanol/water;[109-111] Ni(III) and Mn(III) were also used as electron acceptors.[112] Photoinduced electron transfer to viologens showed that the copper(I) complexes exhibited even better properties than ruthenium(II) complexes.[113] Reductive quenching of excited copper(I) complexes was achieved using complexes with electron withdrawing ligands, like $[Cu(tptap)_2]^+$ reported above, and ferrocene derivatives as the electron donors.[106]

A peculiar characteristic of copper(I) complexes, when photoinduced electron transfer is concerned, is the large reorganization energy due to the remarkable structural changes in passing from Cu^I to Cu^{II}. The λ value for $[Cu(phen)_2]^+$ was calculated to be around 2.4 eV by Gray and colleagues.[74,114] Since the lowest energy excited state has an MLCT nature (which can be described as $[Cu^{II}(phen)(phen^{\bullet-})]^+$), a reductive quenching is expected to have a considerably higher λ_i factor (according to Marcus' formalism) than oxidative quenching. This is due to the fact that an oxidative quenching consists in the removal of an electron from an orbital with mainly π^* character, the

copper ion being already in the +2 oxidation state, while reductive quenching consists in the population of a dσ* orbital and related structural change of the coordination sphere.[90,107]

1.5. Copper(I) diphosphine complexes

The research on copper(I) diphosphine complexes began more recently, if compared to that on diimine complexes. However, these complexes show extremely interesting luminescence properties, that paved the way to their use for the construction of different kinds of devices. The properties of this family of complexes will be described, followed by a brief overview of some applications. Mixed N^P ligands were also investigated,[70] but they will not be described here.

1.5.1. Mixed diphosphine-diimine complexes

The discovery, in 2002, of the astonishing luminescence properties of [Cu(**DPEphos**)(**dmp**)]BF_4 (Fig. 1. 23) and [Cu(**DPEphos**)(**dbp**)]BF_4 fostered numerous studies about the properties of this class of compounds.[115] These two molecules exhibit very long excited-state lifetimes (14.3 and 16.1 μs, respectively) and rather high emission quantum yields (around 0.15). The phosphine ligand has in fact a much wider bite angle than phenanthroline derivatives (around 115º), which acts on the excited-state lifetime in two ways. First of all by efficiently screening the complex from exciplex quenching, and secondly by preventing the excited-state flattening, that constitutes an energy loss and therefore increases the nonradiative rate constant according to the energy gap law.[116] Unlike [Cu(NN)$_2$]$^+$ complexes (where NN is phenanthroline or a 2,9-disubstituted phenanthroline) **DPEphos** copper(I) complexes exhibit luminescence even in coordinating solvents like acetonitrile or methanol.[116]

Cu-P(1)	2.2691 Å
Cu-P(2)	2.2728 Å
Cu-N(1)	2.104 Å
Cu-N(12)	2.084 Å
PCuP^NCuN	97.7º
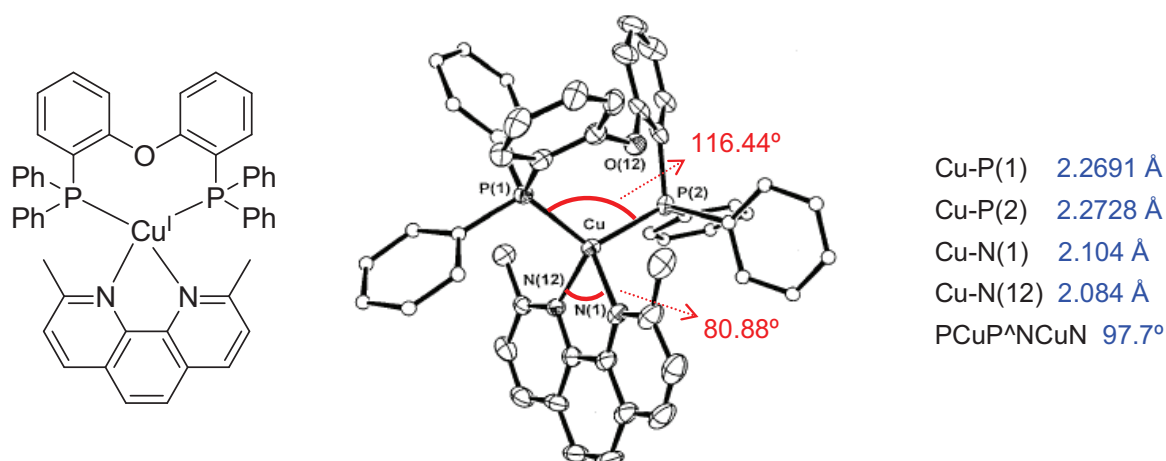
Fig. 1. 23. X-ray structure of [Cu(**DPEphos**)(**dmp**)]BF_4, with some angles and bond distances.[116]

The high steric hindrance of **DPEphos** also has remarkable consequences on the electrochemical properties of the complexes, indeed the redox potential of the $Cu^{II/I}$ couple is anodically shifted ($E_{1/2} \sim 1.4$ V vs. Ag/AgCl) with respect to copper(I) diimine complexes. The electron withdrawing character of the diphosphine ligand is also responsible for this shift.[117]

The X-ray structure of the complexes shows that the ether O atom is at a nonbonding distance (Cu-O > 3.1 Å),[116] and that the molecules display very limited flattening distortion, with the exception of [Cu(**DPEphos**)(**phen**)]BF$_4$ which has important intermolecular stacking interactions in the solid. In general, moreover, a less hindered structure is expected to be more flexible and therefore more prone to undergo distortions in solution too. The P-Cu-P angle measures about 115º, which is much closer to the 109º angle present in a perfect tetrahedral structure than the small bite angles of diimine ligands (phenanthroline or bipyridine).[117]

The electronic absorption spectrum displays scarcely intense, high energy MLCT transitions around 360 nm ($\varepsilon \sim 3000$ $M^{-1}cm^{-1}$). At higher energies, the absorption is dominated by intense ligand-centred bands. The localization of the frontier orbitals is obtained from quantum mechanical calculations: the HOMO is centred on the copper(I) ion, with important contributions of the phosphine ligand, while the LUMO is localized on the phenanthroline ligand like in copper(I) bis-diimine complexes.[117-119] Theoretical studies also point out that the absorption transitions are best described in terms of multiconfigurations, using linear combinations of occupied and virtual orbitals.[118] Moreover, the participation of a copper(I) d orbital in the lowest lying electronic transition is considered to play an important role in inducing efficient spin-orbit coupling and therefore improving the phosphorescence quantum yield.[120]

The astonishing luminescence properties of copper(I) diphosphine complexes are at the origin of the success of these compounds for different applications, mentioned in paragraph 1.5.3.

The bulky **binap** ligand was also tested, in combination to phenanthroline, bipyridine or neocuproine, but low emission was obtained, probably because this ligand is less effective in screening the excited complex from the attack of solvent molecules.[121]

1.5.2. Bis(diphosphine) complexes

Homo- and heteroleptic complexes containing exclusively diphosphine ligands (see Fig. 1. 24) were also studied.[122,123] The formation of homoleptic structures occurs for ligands with a relatively small bite angle, like diphenylphosphinobenzene (**dppb**) or diphenylphosphinomethane (**dppm**). In the case of bulky ligands, **DPEphos**, diphenylphosphinoethane (**dppe**) or diphenylphosphinopropane (**dppp**), having wider bite angles, the steric factors destabilize the homoleptic species favouring the formation of heteroleptic complexes with smaller complementary

ligands. As seen before for [Cu(PP)(NN)]$^+$ species, these complexes exhibit low intensity absorption bands in the near UV, conferring a yellow colour to the molecules both in the solid state and in solution. Luminescence properties are less impressive than those shown by the previous series, with an emission quantum yield around 10^{-4}, but [Cu(**DPEphos**)(**dppb**)]$^+$ (Fig. 1. 24; Φ = 2%; τ = 2.4 μs) showed a good performance when incorporated into an electroluminescent light emitting device.[123] Emission studies about the homoleptic [Cu(**dppb**)$_2$]$^+$ evidenced a temperature dependence of the luminescence behaviour similar to that of copper(I) diimine complexes: a decrease of emission intensity and energy upon temperature decrease. A two-state model was therefore assumed.

dppb   **dppm**: n=1   [Cu(**DPEphos**)(**dppb**)]$^+$ **dppQx**
                dppe: n=2
                dppp: n=3
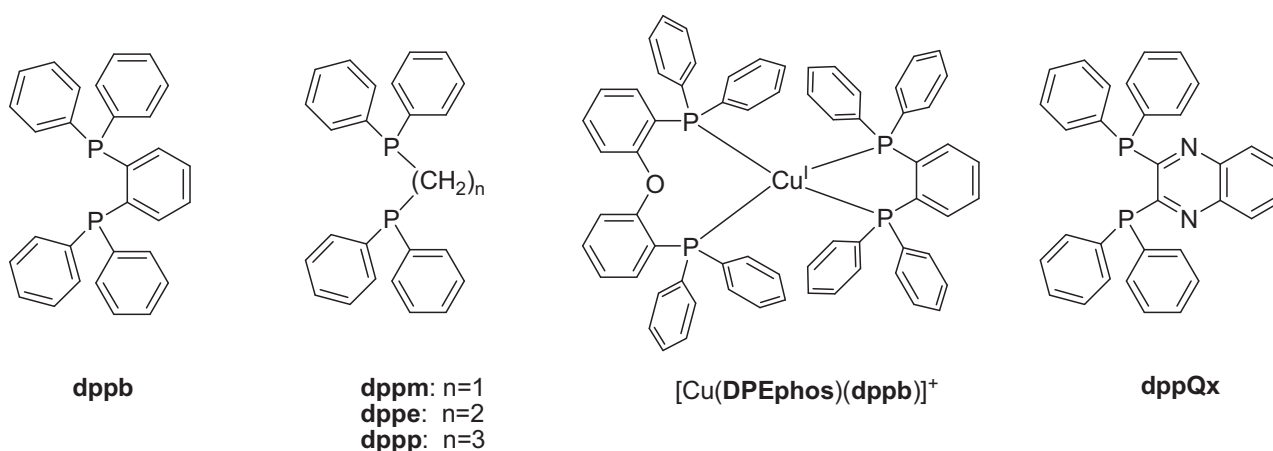
Fig. 1. 24. Structure of some diphosphine ligands and of complex [Cu(**DPEphos**)(**dppb**)]$^+$.[122,123]

Other scarcely hindering diphosphine ligands were proposed, for example 2,3-bis(diphenylphosphino)quinoxaline (**dppQx,** Fig. 1. 24).[124] This ligand is similar to diphenylphosphino benzene for the rigid structure and the size of the chelating unit. Unfortunately, its copper(I) complexes, even when **DPEphos** is used as the complementary ligand, did not show emission, which was explained as a ligand-induced quenching.

1.5.3. Applications of luminescent copper(I) diphosphine complexes

The outstanding luminescence properties displayed by copper(I) diphosphine complexes were exploited for different applications. In the quest for possible substitutes for Ir^{III} complexes as electrophosphorescent emitters in organic light-emitting diodes (OLEDs), many copper(I) diphosphine complexes were proposed. Interestingly, some of them provided a device efficiency comparable to that obtained with Ir^{III} emitters.[125-127] Recently, some neutral copper(I) complexes, obtained by combining DPEphos and an anionic complementary ligand, have been

synthesized.[128,129] Besides their good luminescence properties, the neutral charge allows to envisage sublimation processes to assemble the devices. The use of these compounds has also been investigated for the use in light-emitting electrochemical cells.[130]

Another field of application of strongly emissive copper(I) diphosphine complexes is oxygen sensing, where these compounds exhibited good sensitivity factors and short response times.[131,132]

1.6. Clusters

Another family of copper(I)-containing compounds is constituted by clusters.[133,134] These structures are usually composed of several copper(I) cations, bound to halide anions and organic ligands, and have general formula $Cu_nX_nL_m$ (X: halogenide; L: organic ligand).[70] Their main characteristic is constituted by the presence of direct metal-metal bonding. Depending on the ratio of the reactants (Cu^I, halide, organic ligand), clusters can exist in different structures, for example cubanes, $[CuXL_2]_2$ dimers or staircase polymers. Since copper(I) complexes are quite labile, and tend to undergo a rapid ligand exchange in solution, thermodynamic stability is the driving force for the formation of new species. Moreover, the potential energy surface for these molecules is quite flat, favouring the interconversion between different structural motifs.

Cuprous clusters with different organic ligands were the object of structural and photophysical characterization. In particular, the attention focussed on cuprous iodide clusters. Originally, pyridine ligands were used,[133,135] but the investigation extended also to alkynyl[136] and phosphine ligands.[137,138]
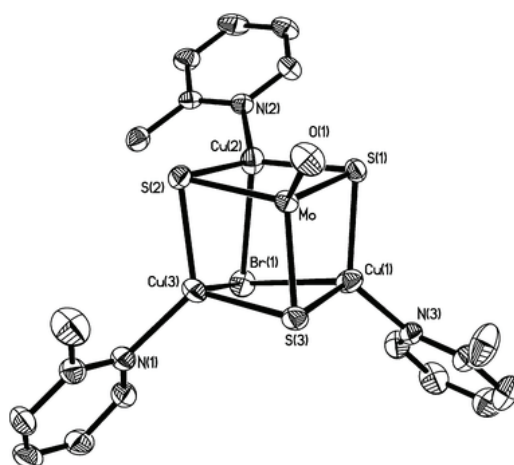
Fig. 1. 25. Cubane structure of a copper cluster with pyridine ligands.[135]

An important characteristic of copper(I) clusters is their intense luminescence, which exhibit a peculiar thermochromic behaviour, with two emission bands whose relative intensity depends on

37

the temperature. The emission originates from two excited states: a ligand-to-ligand charge-transfer state (XLCT: halogenide → ligand L) that dominates at low temperature, and a mixture between an XMCT (halogenide-to-metal CT) and a CC (cluster-centred transition, involving metal orbitals) that is recorded at room temperature.

1.7. Elaborated supramolecular structures based on copper(I)

Due to their suitable tetrahedral coordination sphere, copper(I) complexes have been extensively used for the elaboration of structurally elaborated supramolecular structures. Looking at literature, two different classes of compounds can be identified. The first one is constituted by mechanically interlocked molecules (MIMs), whose study was abundantly developed by Sauvage and colleagues in the early 1980s. The second class includes structures like nano-grids and polygons, and was extensively studied by Lehn first, followed by many other groups.

The HETPHEN (HETeroleptic PHENanthroline) approach towards the synthesis of stable heteroleptic copper(I) complexes will finally be described, as it is a fundamental concept that will be used for the elaboration of all the coordination compounds presented in this thesis.

1.7.1. Mechanically interlocked molecules

Mechanically interlocked molecules are supramolecular systems where the subunits are kept together as a consequence of their topology, without direct bonds between the units, analogous to two adjacent links in a chain. The first syntheses for this kind of molecules were based on a statistical approach and led to extremely low yields after complicated syntheses.[139] Sauvage's idea of using metal-templated synthesis was a real breakthrough in the field, and allowed to prepare extremely elaborated supramolecular structures like rotaxanes, catenanes and knots (Fig. 1. 26). Detailed reviews have been written that give a good overview of the research advancement on this topic,[140] so only the basic principles will be given here.

The metal-templated synthesis of interlocked molecules is based on two steps. At first, the elements are put in the suitable relative position by means of the coordination to the metal ion, with generation of the cross-over points. The tetrahedral coordination of copper(I) is particularly useful at this stage, as it allows to keep the two elements nearly perpendicular to each other. Afterwards, new covalent bonds are formed that provide the interlocked system (ex. stoppering reaction for rotaxanes, ring closing for catenanes). Most importantly, the mechanical bond is maintained even if the templating metal ion is removed. From the point of view of Cu^I complexes synthesis, here the

preparation of heteroleptic structures is achieved by means of circular ligands, where the formation of the homoleptic species is impeded by the presence of the ring.

Mechanically interlocked molecules have been used for the construction of many molecular machines, where the motion is triggered by chemical, electrochemical, photochemical or thermal stimuli.[141]
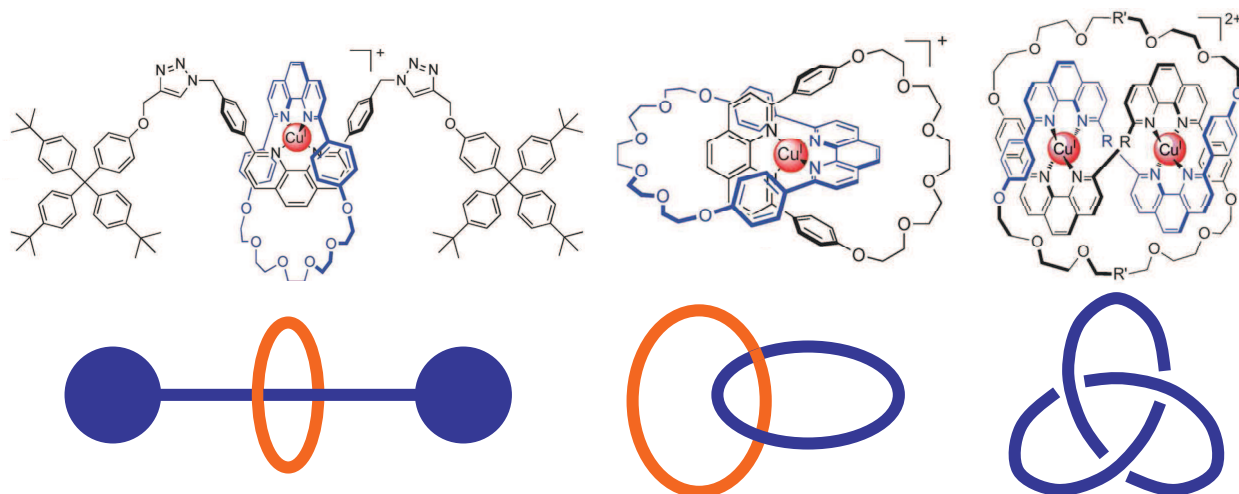
Fig. 1. 26. Schematic structure of metal-assembled rotaxane, catenane and knot, with examples.[140]

1.7.2. "Open" structures

The fundamental difference of this class of molecules with respect to the previous one is that the metal ion has an important structural role in the supramolecular assemblies, that are completely destroyed if the latter is removed from the coordinating cavity. Self-assembling supramolecular structures are interesting for different kinds of applications, among which information storage[142] or encapsulation of small molecules.[143]
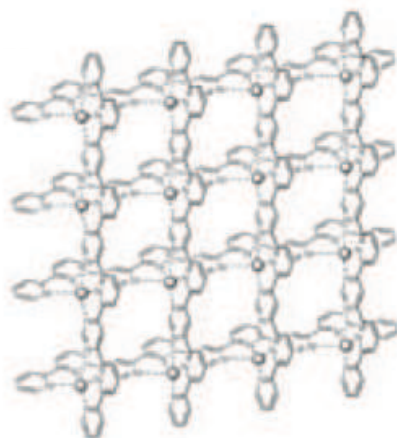
Fig. 1. 27. Structure of a nanogrid.[142]

39

The construction of such structures involves the use of multitopic ligands (containing pyridines, phenanthroline, bipyridines, catechols, terpyridines, …)[144] which are held together by coordination to metallic ions. As in the previous paragraph, Cu^I has been extensively used due to its tetrahedral coordination and mild synthetic conditions for the coordination reaction.

Among the published structures, we can find helicates,[145] circular helicates,[146] grids,[142] ladders, racks, cylinders [147] and cages.[143] In this case, as the formation of homoleptic complexes is usually possible upon ligand scrambling, the formation of heteroleptic structures was achieved by using highly hindered ligands, as it will be explained in the following paragraph.

1.7.3. Heteroleptic copper(I) diimine complexes: the HETPHEN approach

The extreme lability of Cu^I complexes prevented for long time the isolation of pure heteroleptic copper(I) diimine species. The fast ligand scrambling in solution, when two different ligands are present, leads in fact to a statistic mixture of the three possible coordination complexes.[105] This problem was solved in 1997 by Schmittel and Ganz,[148] who proposed an approach based on the combination of two 2,9-disubstituted phenanthrolines giving pure heteroleptic species. The protocol, called HETPHEN (HETeroleptic PHENanthroline) consists in combining a highly hindered ligand with another one bearing less bulky groups in the 2 and 9 positions of the phenanthroline core (Fig. 1. 28).
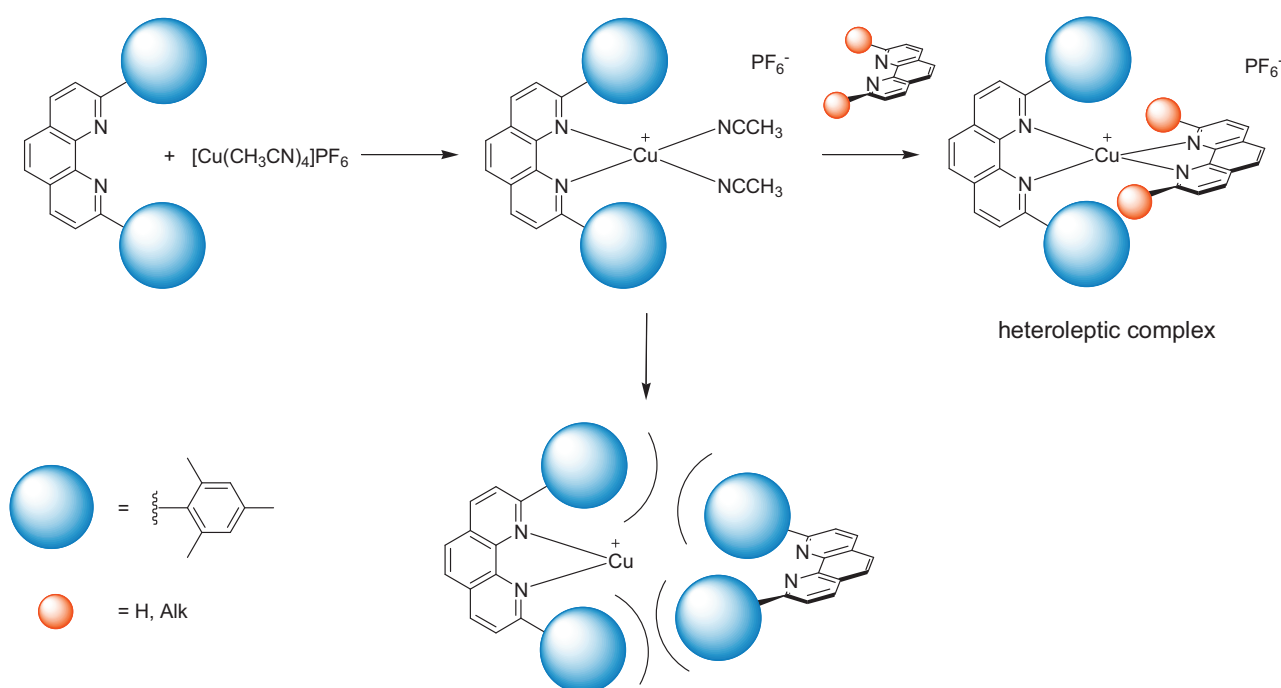
Fig. 1. 28. HETPHEN approach for the synthesis of heteroleptic copper(I) diimine complexes.

The bulky groups can be aromatic (like mesityl, 2,4,6-trimethylphenyl) or aliphatic (for example *tert*-butyl). The advantage in using aromatic rings is the stabilization of the resulting heteroleptic complex by π-stacking with the opposite phenanthroline ligand. The opposite ligand can be an unsubstituted phenanthroline or an alkyl-substituted one. The use of bulky diphosphine ligands (for example **DPEphos**) to build heteroleptic copper(I) complexes is based on the same kind of concept.

The synthesis is performed following a two-step protocol, which can be conducted in one pot without isolating the intermediate species. In order to obtain the pure heteroleptic compound, the Cu^I precursor is first reacted with a slight excess of the most hindered ligand. The formation of the sole 1:1 adduct at this stage is due to the extreme steric hindrance provided by the bulky groups, preventing the formation of the homoleptic 2:1 complex. The addition of the second ligand leads to the instantaneous formation of the heteroleptic complex, indicated by a sudden colour change of the solution due to the MLCT absorption of copper(I) bis-diimine.

The HETPHEN approach will used throughout this thesis in order to build the heteroleptic copper(I) complexes.

1.8. Copper(I) for solar energy conversion

In the last paragraphs, the structural, photophysical and electrochemical properties of copper(I) complexes were described. In light of the mentioned data, these compounds appear as a really interesting alternative to ruthenium(II) complexes in the field of solar energy conversion. They exhibit visible absorption thanks to an MCLT band in the blue region of the visible spectrum, have fairly long-lived excted state and are good photoreductants. Indeed, the fundamental studies reported above triggered some research work aimed at using copper(I) complexes as the light absorbers in order to achieve charge-separated states or to sensitize wide band gap semiconductors. The advancements in these domains will be described in greater detail in chapter 4 and 5, respectively. For example, a 2.5% efficiency was reached in DSSCs using a copper-based dye (see chapter 5).

In order to use copper(I) complexes as possible substitutes for ruthenium(II) complexes, however, some issues have to be dealt with, in particular the low absorption coefficient and the quite short excited-state lifetimes. This and the construction of molecular building blocks for the synthesis of elaborated heteroleptic structures will be the focus of chapters 2 and 3. In the last two chapters (4 and 5), copper(I) complexes will be used as chromophores to build photosensitive polyads and sensitizers for DSSCs.

References

1. Armaroli, N.; Balzani, V. *Angew. Chem. Int. Ed.* **2007**, *46*, 52-66.
2. Lewis, N. S.; Nocera, D. G. *Proc. Nat. Acad. Sci.* **2006**, *103*, 15729-15735.
3. Nocera, D. G. *ChemSusChem* **2009**, *2*, 387-390.
4. Magnuson, A.; Styring, S. *Aust. J. Chem.* **2012**, *65*, 564-572.
5. Nocera, D. G. *Inorg. Chem.* **2009**, *48*, 10001-10017.
6. Gust, D.; Moore, T. A.; Moore, A. L. *Faraday Discuss.* **2012**, *155*, 9-26.
7. Barber, J. *Chem. Soc. Rev.* **2009**, *38*, 185-196.
8. Pellegrin, Y.; Odobel, F. *Coord. Chem. Rev.* **2011**, *255*, 2578-2593.
9. Barber, J. *Bioelectrochemistry* **2002**, *55*, 135-138.
10. Umena, Y.; Kawakami, K.; Shen, J.-R.; Kamiya, N. *Nature* **2011**, *473*, 55-60.
11. Thorndike, E. H. *Energy and the Environment*; Pub Addison-Wesley, **1996**.
12. Dau, H.; Zaharieva, I. *Acc. Chem. Res.* **2009**, *42*, 1861-1870.
13. Moore, T. A.; Moore, A. L.; Gust, D. *Philos. Trans. R. Soc. London, B* **2002**, *357*, 1481-1498.
14. Balzani, V.; Campagna, S.; Denti, G.; Juris, A.; Serroni, S.; Venturi, M. *Acc. Chem. Res.* **1998**, *31*, 26-34.
15. Jones, W. E.; Baxter, S. M.; Strouse, G. F.; Meyer, T. J. *J. Am. Chem. Soc.* **1993**, *115*, 7363-7373.
16. Choi, M.-S.; Yamazaki, T.; Yamazaki, I.; Aida, T. *Angew. Chem. Int. Ed.* **2004**, *43*, 150-158.
17. Adronov, A.; Frechet, J. M. J. *Chem. Commun.* **2000**, 1701-1710.
18. Terazono, Y.; Kodis, G.; Liddell, P. A.; Garg, V.; Moore, T. A.; Moore, A. L.; Gust, D. *J. Phys. Chem. B* **2009**, *113*, 7147-7155.
19. Jullien, L.; Canceill, J.; Valeur, B.; Bardez, E.; Lefèvre, J.-P.; Lehn, J.-M.; Marchi-Artzner, V.; Pansu, R. *J. Am. Chem. Soc.* **1996**, *118*, 5432-5442.
20. Sauvage, J. P.; Collin, J. P.; Chambron, J. C.; Guillerez, S.; Coudret, C.; Balzani, V.; Barigelletti, F.; De Cola, L.; Flamigni, L. *Chem. Rev.* **1994**, *94*, 993-1019.
21. Gust, D.; Moore, T. A.; Moore, A. L.; Macpherson, A. N.; Lopez, A.; DeGraziano, J. M.; Gouni, I.; Bittersmann, E.; Seely, G. R. *J. Am. Chem. Soc.* **1993**, *115*, 11141-11152.
22. Gust, D.; Moore, T. A.; Moore, A. L. *Acc. Chem. Res.* **1993**, *26*, 198-205.
23. Wenger, O. *Coord. Chem. Rev.* **2009**, *253*, 1439-1457.
24. Treadway, J. A.; Chen, P.; Rutherford, T. J.; Keene, F. R.; Meyer, T. J. *J. Phys. Chem. A* **1997**, *101*, 6824-6826.
25. Kumar, R. J.; Karlsson, S.; Streich, D.; Rolandini Jensen, A.; Jäger, M.; Becker, H.-C.; Bergquist, J.; Johansson, O.; Hammarström, L. *Chem. Eur. J.* **2010**, *16*, 2830-2842.
26. Flamigni, L.; Baranoff, E.; Collin, J.-P.; Sauvage, J.-P. *Chem. Eur. J.* **2006**, *12*, 6592-6606.
27. Chakraborty, S.; Wadas, T. J.; Hester, H.; Schmehl, R.; Eisenberg, R. *Inorg. Chem.* **2005**, *44*, 6865-6878.
28. Holler, M.; Cardinali, F.; Mamlouk, H.; Nierengarten, J.-F.; Gisselbrecht, J.-P.; Gross, M.; Rio, Y.; Barigelletti, F.; Armaroli, N. *Tetrahedron* **2006**, *62*, 2060-2073.
29. Megiatto, J. D.; Li, K.; Schuster, D. I.; Palkar, A.; Herranz, M. A. n.; Echegoyen, L.; Abwandner, S.; de Miguel, G.; Guldi, D. M. *J. Phys. Chem. B* **2010**, *114*, 14408-14419.
30. Kuroda, Y.; Ito, M.; Sera, T.; Ogoshi, H. *J. Am. Chem. Soc.* **1993**, *115*, 7003-7004.
31. Torres, T.; Gouloumis, A.; Sanchez-Garcia, D.; Jayawickramarajah, J.; Seitz, W.; Guldi, D. M.; Sessler, J. L. *Chem. Commun.* **2007**, 292-294.
32. Hunter, C. A.; Sanders, J. K. M.; Beddard, G. S.; Evans, S. *Chem. Commun.* **1989**, 1765-1767.

33. Kercher, M.; König, B.; Zieg, H.; De Cola, L. *J. Am. Chem. Soc.* **2002**, *124*, 11541.

34. Hara, M.; Lean, J. T.; Mallouk, T. E. *Chem. Mater.* **2001**, *13*, 4668-4675.

35. Kanan, M. W.; Surendranath, Y.; Nocera, D. G. *Chem. Soc. Rev.* **2009**, *38*, 109-114.

36. Gersten, S. W.; Samuels, G. J.; Meyer, T. J. *J. Am. Chem. Soc.* **1982**, *104*, 4029-4030.

37. Polyansky, D. E.; Muckerman, J. T.; Rochford, J.; Zong, R.; Thummel, R. P.; Fujita, E. *J. Am. Chem. Soc.* **2011**, *133*, 14649-14665.

38. Zong, R.; Thummel, R. P. *J. Am. Chem. Soc.* **2005**, *127*, 12802-12803.

39. Duan, L.; Bozoglian, F.; Mandal, S.; Stewart, B.; Privalov, T.; Llobet, A.; Sun, L. *Nat. Chem.* **2012**, *4*, 418-423.

40. McDaniel, N. D.; Coughlin, F. J.; Tinker, L. L.; Bernhard, S. *J. Am. Chem. Soc.* **2007**, *130*, 210-217.

41. Yin, Q.; Tan, J. M.; Besson, C.; Geletii, Y. V.; Musaev, D. G.; Kuznetsov, A. E.; Luo, Z.; Hardcastle, K. I.; Hill, C. L. *Science* **2010**, *328*, 342-345.

42. Natali, M.; Orlandi, M.; Berardi, S.; Campagna, S.; Bonchio, M.; Sartorel, A.; Scandola, F. *Inorg. Chem.* **2012**, *51*, 7324-7331.

43. Wang, M.; Chen, L.; Li, X.; Sun, L. *Dalton Trans.* **2011**, *40*, 12793-12800.

44. Kaur-Ghumaan, S.; Schwartz, L.; Lomoth, R.; Stein, M.; Ott, S. *Angew. Chem. Int. Ed.* **2010**, *49*, 8033-8036.

45. Connolly, P.; Espenson, J. H. *Inorg. Chem.* **1986**, *25*, 2684-2688.

46. Dempsey, J. L.; Brunschwig, B. S.; Winkler, J. R.; Gray, H. B. *Acc. Chem. Res.* **2009**, *42*, 1995-2004.

47. Baffert, C.; Artero, V.; Fontecave, M. *Inorg. Chem.* **2007**, *46*, 1817-1824.

48. Appel, A. M.; DuBois, D. L.; Rakowski DuBois, M. *J. Am. Chem. Soc.* **2005**, *127*, 12717-12726.

49. Karunadasa, H. I.; Chang, C. J.; Long, J. R. *Nature* **2010**, *464*, 1329-1333.

50. Lehn, J. M.; Sauvage, J. P. *Nouv. J. Chim.* **1977**, *1*, 449-451.

51. Koriakin, B. V.; Dzhabiev, T. S.; Shilov, A. E. *Dokl. Bulg. Akad. Nauk* **1977**, *233*, 620.

52. Moradpour, A.; Amouyal, E.; Keller, P.; Kagan, H. *Nouv. J. Chim.* **1978**, *2*, 547.

53. Magnuson, A.; Anderlund, M.; Johansson, O.; Lindblad, P.; Lomoth, R.; Polivka, T.; Ott, S.; Stensjö, K.; Styring, S.; Sundström, V.; Hammarström, L. *Acc. Chem. Res.* **2009**, *42*, 1899-1909.

54. Eckenhoff, W. T.; Eisenberg, R. S. *Dalton Trans.* **2012**.

55. Borgström, M.; Shaikh, N.; Johansson, O.; Anderlund, M. F.; Styring, S.; Åkermark, B.; Magnuson, A.; Hammarström, L. *J. Am. Chem. Soc.* **2005**, *127*, 17504-17515.

56. Kaveevivitchai, N.; Chitta, R.; Zong, R.; El Ojaimi, M.; Thummel, R. P. *J. Am. Chem. Soc.* **2012**, *134*, 10721-10724.

57. Rangan, K.; Arachchige, S. M.; Brown, J. R.; Brewer, K. J. *Energ. Environ. Sci.* **2009**, *2*, 410-419.

58. Concepcion, J. J.; Jurss, J. W.; Brennaman, M. K.; Hoertz, P. G.; Patrocinio, A. O. v. T.; Murakami Iha, N. Y.; Templeton, J. L.; Meyer, T. J. *Acc. Chem. Res.* **2009**, *42*, 1954-1965.

59. Youngblood, W. J.; Lee, S.-H. A.; Kobayashi, Y.; Hernandez-Pagan, E. A.; Hoertz, P. G.; Moore, T. A.; Moore, A. L.; Gust, D.; Mallouk, T. E. *J. Am. Chem. Soc.* **2009**, *131*, 926-927.

60. Li, L.; Duan, L.; Wen, F.; Li, C.; Wang, M.; Hagfeldt, A.; Sun, L. *Chem. Commun.* **2012**, *48*, 988-990.

61. Marcus, R. A.; Sutin, N. *Biochim. Biophys. Acta-Rev. Bioen.* **1985**, *811*, 265-322.

62. Balzani, V. *Electron transfer in chemistry*; Wiley-VCH Verlag GmbH, **2008**.

63. Forster, T. *Discuss. Faraday Soc.* **1959**, *27*, 7-17.

64. Dexter, D. L. *J. Chem. Phys.* **1953**, *21*, 836-850.

65. Rehm, D.; Weller, A. *Isr. J. Chem.* **1970**, *8*, 259-271.

66. Marcus, R. A., Nobel lecture, **1992**.

67. Marcus, R. A. *J. Chem. Phys.* **1956**, *24*, 966-978.

68. Marcus, R. A. *Annu. Rev. Phys. Chem.* **1964**, *15*, 155-196.

69.   Miller, J. R.; Calcaterra, L. T.; Closs, G. L. *J. Am. Chem. Soc.* **1984**, *106*, 3047-3049.

70.   Armaroli, N.; Accorsi, G.; Cardinali, F.; Listorti, A. *Top. Curr. Chem.* **2007**, *280*, 69-115.

71.   Hammond, C. R. *The Elements, in Handbook of Chemistry and Physics 81st edition*; CRC press, **2004**.

72.   Pratesi, A.; Giuli, G.; Cicconi, M. R.; Della Longa, S.; Weng, T.-C.; Ginanneschi, M. *Inorg. Chem.* **2012**, *51*, 7969-7976.

73.   DuBois, J. L.; Mukherjee, P.; Stack, T. D. P.; Hedman, B.; Solomon, E. I.; Hodgson, K. O. *J. Am. Chem. Soc.* **2000**, *122*, 5775-5787.

74.   Gray, H. B.; Malmström, B. G.; Williams, R. J. P. *J. Biol. Inorg. Chem.* **2000**, *5*, 551-559.

75.   Magdesieva, T.; Dolganov, A.; Yakimanskii, A.; Goikhman, M.; Podeshvo, I.; Kudryavtsev, V. *Russ. J. Electrochem.* **2007**, *43*, 1133-1143.

76.   Blaskie, M. W.; McMillin, D. R. *Inorg. Chem.* **1980**, *19*, 3519-3522.

77.   Dietrich-Buchecker, C. O.; Marnot, P. A.; Sauvage, J.-P.; Kirchhoff, J. R.; McMillin, D. R. *Chem. Commun.* **1983**, 513-515.

78.   Lavie-Cambot, A.; Cantuel, M.; Leydet, Y.; Jonusauskas, G.; Bassani, D. M.; McClenaghan, N. D. *Coord. Chem. Rev.* **2008**, *252*, 2572-2584.

79.   Horváth, O. *Coord. Chem. Rev.* **1994**, *135–136*, 303-324.

80.   Goodwin, K. V.; McMillin, D. R.; Robinson, W. R. *Inorg. Chem.* **1986**, *25*, 2033-2036.

81.   Cunningham, C. T.; Moore, J. J.; Cunningham, K. L. H.; Fanwick, P. E.; McMillin, D. R. *Inorg. Chem.* **2000**, *39*, 3638-3644.

82.   Cesario, M.; Dietrich-Buchecker, C. O.; Guilhem, J.; Pascard, C.; Sauvage, J. P. *Chem. Commun.* **1985**, 244-247.

83.   McMillin, D. R.; Kirchhoff, J. R.; Goodwin, K. V. *Coord. Chem. Rev.* **1985**, *64*, 83-92.

84.   Armaroli, N. *Chem. Soc. Rev.* **2001**, *30*, 113-124.

85.   McGarvey, J. J.; Bell, S. E. J.; Bechara, J. N. *Inorg. Chem.* **1986**, *25*, 4325-4327.

86.   Gordon, K. C.; McGarvey, J. J. *Inorg. Chem.* **1991**, *30*, 2986-2989.

87.   Chen, L. X.; Shaw, G. B.; Novozhilova, I.; Liu, T.; Jennings, G.; Attenkofer, K.; Meyer, G. J.; Coppens, P. *J. Am. Chem. Soc.* **2003**, *125*, 7022-7034.

88.   Ichinaga, A. K.; Kirchhoff, J. R.; McMillin, D. R.; Dietrich-Buchecker, C. O.; Marnot, P. A.; Sauvage, J. P. *Inorg. Chem.* **1987**, *26*, 4290-4292.

89.   Iwamura, M.; Watanabe, H.; Ishii, K.; Takeuchi, S.; Tahara, T. *J. Am. Chem. Soc.* **2011**, *133*, 7728-7736.

90.   Gushurst, A. K. I.; McMillin, D. R.; Dietrich-Buchecker, C. O.; Sauvage, J. P. *Inorg. Chem.* **1989**, *28*, 4070-4072.

91.   Miller, M. T.; Gantzel, P. K.; Karpishin, T. B. *Inorg. Chem.* **1999**, *38*, 3414-3422.

92.   Cunningham, C. T.; Cunningham, K. L. H.; Michalec, J. F.; McMillin, D. R. *Inorg. Chem.* **1999**, *38*, 4388-4392.

93.   Everly, R. M.; McMillin, D. R. *Photochem. Photobiol.* **1989**, *50*, 711-716.

94.   Gothard, N. A.; Mara, M. W.; Huang, J.; Szarko, J. M.; Rolczynski, B.; Lockard, J. V.; Chen, L. X. *J. Phys. Chem. A* **2012**, *116*, 1984-1992.

95.   Miller, M. T.; Gantzel, P. K.; Karpishin, T. B. *Inorg. Chem.* **1998**, *37*, 2285-2290.

96.   Green, O.; Gandhi, B. A.; Burstyn, J. N. *Inorg. Chem.* **2009**, *48*, 5704-5714.

97.   Kirchhoff, J. R.; Gamache, R. E.; Blaskie, M. W.; Del Paggio, A. A.; Lengel, R. K.; McMillin, D. R. *Inorg. Chem.* **1983**, *22*, 2380-2384.

98.   Everly, R. M.; McMillin, D. R. *J. Phys. Chem.* **1991**, *95*, 9071-9075.

99.   Chen, L. X.; Jennings, G.; Liu, T.; Gosztola, D. J.; Hessler, J. P.; Scaltrito, D. V.; Meyer, G. J. *J. Am. Chem. Soc.* **2002**, *124*, 10861-10867.

100.   Smolentsev, G.; Soldatov, A. V.; Chen, L. X. *J. Phys. Chem. A* **2008**, *112*, 5363-5367.

101.   Iwamura, M.; Takeuchi, S.; Tahara, T. *J. Am. Chem. Soc.* **2007**, *129*, 5248-5256.

102.   Shaw, G. B.; Grant, C. D.; Shirota, H.; Castner, E. W.; Meyer, G. J.; Chen, L. X. *J. Am. Chem. Soc.* **2007**, *129*, 2147-2160.

103.   Masood, M. A.; Zacharias, P. S. *Dalton Trans.* **1991**, 111-114.
104.   Bard, A. J.; Faulkner, L. R. *Electrochemical Methods: Fundamentals and Applications*; 2nd ed.; Wiley, **2000**.
105.   Scaltrito, D. V.; Thompson, D. W.; O'Callaghan, J. A.; Meyer, G. J. *Coord. Chem. Rev.* **2000**, *208*, 243-266.
106.   Cunningham, K. L.; McMillin, D. R. *Inorg. Chem.* **1998**, *37*, 4114-4119.
107.   Miller, M. T.; Gantzel, P. K.; Karpishin, T. B. *Angew. Chem. Int. Ed.* **1998**, *37*, 1556-1558.
108.   Titze, C.; Kaim, W. *Z. Naturforsh. B* **1996**, *51*, 981-988.
109.   McMillin, D. R.; Buckner, M. T.; Ahn, B. T. *Inorg. Chem.* **1977**, *16*, 943-945.
110.   Ahn, B.-T.; McMillin, D. R. *Inorg. Chem.* **1978**, *17*, 2253-2258.
111.   Ahn, B.-T.; McMillin, D. R. *Inorg. Chem.* **1981**, *20*, 1427-1432.
112.   Koshino, N.; Kuchiyama, Y.; Ozaki, H.; Funahashi, S.; Takagi, H. D. *Inorg. Chem.* **1999**, *38*, 3352-3360.
113.   Ruthkosky, M.; Castellano, F. N.; Meyer, G. J. *Inorg. Chem.* **1996**, *35*, 6406-6412.
114.   Winkler, J. R.; Wittung-Stafshede, P.; Leckner, J.; Malmström, B. G.; Gray, H. B. *Proc. Nat. Acad. Sci.* **1997**, *94*, 4246-4249.
115.   Cuttell, D. G.; Kuang, S.-M.; Fanwick, P. E.; McMillin, D. R.; Walton, R. A. *J. Am. Chem. Soc.* **2002**, *124*, 6-7.
116.   Kuang, S.-M.; Cuttell, D. G.; McMillin, D. R.; Fanwick, P. E.; Walton, R. A. *Inorg. Chem.* **2002**, *41*, 3313-3322.
117.   Linfoot, C. L.; Richardson, P.; Hewat, T. E.; Moudam, O.; Forde, M. M.; Collins, A.; White, F.; Robertson, N. *Dalton Trans.* **2010**, *39*, 8945-8956.
118.   Yang, L.; Feng, J.-K.; Ren, A.-M.; Zhang, M.; Ma, Y.-G.; Liu, X.-D. *Eur. J. Inorg. Chem.* **2005**, *2005*, 1867-1879.
119.   Ge, H.; Wei, W.; Shuai, P.; Lei, G.; Qing, S. *J. Lumin.* **2011**, *131*, 238-243.
120.   Hsu, C.-W.; Lin, C.-C.; Chung, M.-W.; Chi, Y.; Lee, G.-H.; Chou, P.-T.; Chang, C.-H.; Chen, P.-Y. *J. Am. Chem. Soc.* **2011**, *133*, 12085-12099.
121.   Saito, K.; Tsukuda, T.; Tsubomura, T. *Bull. Chem. Soc. Jpn.* **2006**, *79*, 437-441.
122.   Moudam, O., Ph.D. Thesis, Université Paul Sabatier, Toulouse, **2007**.
123.   Moudam, O.; Kaeser, A.; Delavaux-Nicot, B.; Duhayon, C.; Holler, M.; Accorsi, G.; Armaroli, N.; Seguy, I.; Navarro, J.; Destruel, P.; Nierengarten, J.-F. *Chem. Commun.* **2007**, 3077-3079.
124.   Cain, M. F.; Reynolds, S. C.; Anderson, B. J.; Glueck, D. S.; Golen, J. A.; Moore, C. E.; Rheingold, A. L. *Inorg. Chim. Acta* **2011**, *369*, 55-61.
125.   Che, G.; Su, Z.; Li, W.; Chu, B.; Li, M.; Hu, Z.; Zhang, Z. *Appl. Phys. Lett.* **2006**, *89*, 103511-103513.
126.   Zhang, Q.; Zhou, Q.; Cheng, Y.; Wang, L.; Ma, D.; Jing, X.; Wang, F. *Adv. Mater.* **2004**, *16*, 432-436.
127.   Wada, A.; Zhang, Q.; Yasuda, T.; Takasu, I.; Enomoto, S.; Adachi, C. *Chem. Commun.* **2012**, *48*, 5340-5342.
128.   Czerwieniec, R.; Yu, J.; Yersin, H. *Inorg. Chem.* **2011**, *50*, 8293-8301.
129.   Crestani, M. G.; Manbeck, G. F.; Brennessel, W. W.; McCormick, T. M.; Eisenberg, R. *Inorg. Chem.* **2011**, *50*, 7172-7188.
130.   Armaroli, N.; Accorsi, G.; Holler, M.; Moudam, O.; Nierengarten, J. F.; Zhou, Z.; Wegh, R. T.; Welter, R. *Adv. Mater.* **2006**, *18*, 1313-1316.
131.   Shi, L.; Li, B.; Yue, S.; Fan, D. *Sensors and Actuators B: Chemical* **2009**, *137*, 386-392.
132.   Wang, L.-Y.; Xu, Y.; Lin, Z.; Zhao, N.; Xu, Y. *J. Lumin.* **2011**, *131*, 1277-1282.
133.   Ford, P. C.; Cariati, E.; Bourassa, J. *Chem. Rev.* **1999**, *99*, 3625-3648.
134.   Wing-Wah Yam, V.; Kam-Wing Lo, K. *Chem. Soc. Rev.* **1999**, *28*, 323-334.
135.   Zhang, C.; Song, Y.; Kuhn, F. E.; Wang, Y.; Fun, H.; Xin, X.; Herrmann, W. A. *New J. Chem.* **2002**, *26*, 58-65.

136.   Yam, V. W.-W.; Choi, S. W.-K.; Chan, C.-L.; Cheung, K.-K. *Chem. Commun.* **1996**, 2067-2068.

137.   Maini, L.; Braga, D.; Mazzeo, P. P.; Ventura, B. *Dalton Trans.* **2012**, *41*, 531-539.

138.   Perruchas, S.; Tard, C.; Le Goff, X. F.; Fargues, A.; Garcia, A.; Kahlal, S.; Saillard, J.-Y.; Gacoin, T.; Boilot, J.-P. *Inorg. Chem.* **2011**, *50*, 10682-10692.

139.   Stoddart, J. F. *Chem. Soc. Rev.* **2009**, *38*, 1521-1529.

140.   Beves, J. E.; Blight, B. A.; Campbell, C. J.; Leigh, D. A.; McBurney, R. T. *Angew. Chem. Int. Ed.* **2011**, *50*, 9260-9327.

141.   Collin, J.-P.; Dietrich-Buchecker, C.; Gaviña, P.; Jimenez-Molero, M. C.; Sauvage, J.-P. *Acc. Chem. Res.* **2001**, *34*, 477-487.

142.   Ruben, M.; Rojo, J.; Romero-Salguero, F. J.; Uppadine, L. H.; Lehn, J.-M. *Angew. Chem. Int. Ed.* **2004**, *43*, 3644-3662.

143.   Fan, J.; Bats, J. W.; Schmittel, M. *Inorg. Chem.* **2009**, *48*, 6338-6340.

144.   Kalsani, V., Ph.D. Thesis, University of Siegen, **2005**.

145.   Lehn, J. M.; Rigault, A.; Siegel, J.; Harrowfield, J.; Chevrier, B.; Moras, D. *Proc. Nat. Acad. Sci.* **1987**, *84*, 2565-2569.

146.   Hasenknopf, B.; Lehn, J.-M.; Kneisel, B. O.; Baum, G.; Fenske, D. *Angew. Chem. Int. Ed.* **1996**, *35*, 1838-1840.

147.   Schmittel, M.; Kalsani, V.; Michel, C.; Mal, P.; Ammon, H.; Jäckel, F.; Rabe, J. P. *Chem. Eur. J.* **2007**, *13*, 6223-6237.

148.   Schmittel, M.; Ganz, A. *Chem. Commun.* **1997**, 999-1000.

CHAPTER 2

A toolbox to build heteroleptic copper(I) complexes with phenanthroline ligands

2.1. Study of the coordination cage structure

As pointed out in the previous chapter, the coordination cage structure, and in particular the presence of encumbering groups in the positions 2 and 9 of the phenanthroline molecular skeleton, has major consequences on the photophysical and electrochemical properties of the resulting copper(I) complexes. It appears therefore fundamental to conduct a study about different substitution patterns on the phenanthroline ligands, as it has been previously done in literature for homoleptic copper(I) complexes,[1-4] in order to be aware of their influence on the properties of heteroleptic compounds. Having these results in mind, it will be possible to elaborate new structures with controlled properties to match the requirements for the different applications in solar energy conversion.

The heteroleptic structure is essential if one wants to fine tune the functionalities of copper(I) complexes as photosensitive chromophores. Indeed, the applications in photoinduced electron transfer and semiconductor sensitization require directionality of the charge transfer and thus the use of different ligands around Cu^I. The linear arrangement provided by the tetrahedral coordination is also useful for the construction of well-defined structures with a maximized and controlled distance between the different components.

The fundamental concept that should be kept in mind is that the synthesis of heteroleptic copper(I) complexes relies on the combination of an encumbered ligand, containing bulky groups in the 2 and 9 positions, with a less hindered one, containing small groups such as mere hydrogen atoms or alkyl chains (HETPHEN approach, see paragraph 1.7.3).[5] Furthermore, strong steric hindrance around copper is responsible for a dramatic increase of the emission lifetime,[6-8] and at the same time for an increase of the oxidation potential of the $Cu^{II/I}$ redox couple. The latter is caused by the different structural arrangement of the ligands around the Cu^I and the Cu^{II}.[4] Elevated excited state lifetimes are normally a basic requirement when an exploitation of the excited state energy is planned (photoinduced charge transfer, photosensitization of catalysts), however this is not always true (for example, in the case of TiO_2 sensitization, which will be treated more extensively in chapter 5). In general, in this thesis work, the aim of getting excited states as long-lived as possible

47

was pursued. An accurate balance has to be done in order to increase the steric hindrance around the copper ion (and prevent the flattening distortion in the excited state) without affecting the stability of the complex. Very hindered structures lead to impressive emission lifetimes, but at the expense of stability, as in the example of the $[Cu(\textbf{tbp})_2]^{+}$.[7] Indeed, this complex is not stable in presence of moisture and must be prepared in a glovebox, which represents a severe limitation for its practical use.

The aim of the research work presented in this chapter is first of all to put into shape the overall guidelines to prepare stable heteroleptic complexes which are compatible with solar energy conversion purposes. This necessitates a few important features, among which absorption in the visible domain of the solar spectrum, a positive enough oxidation potential (to provide significant driving forces for the photo-induced processes), and existence of a decently long-lived excited state. To achieve this task, we propose to study different coordination cages, with differently substituted phenanthroline ligands. In all cases, a mesityl bearing ligand will be used (bulky groups are a mandatory condition to obtain heteroleptic complexes) with a less sterically challenged phenanthroline derivative, such as unsubstituted phenanthroline or a phenanthroline bearing linear alkyl chains in α positions of the chelating nitrogen atoms. First of all a series of heteroleptic structures having different coordination spheres will be presented (**C1**-**C3**, Fig. 2. 1), followed by a second series based on the use of two original ligands with an extended phenanthroline core (**C4**-**C8**).

C1: R=nBu, R'=H
C2: R=nBu, R'=CH3
C3: R=Ph, R'=H

C4: R = H
C5: R = Me
C6: R = nBu

C7

C8
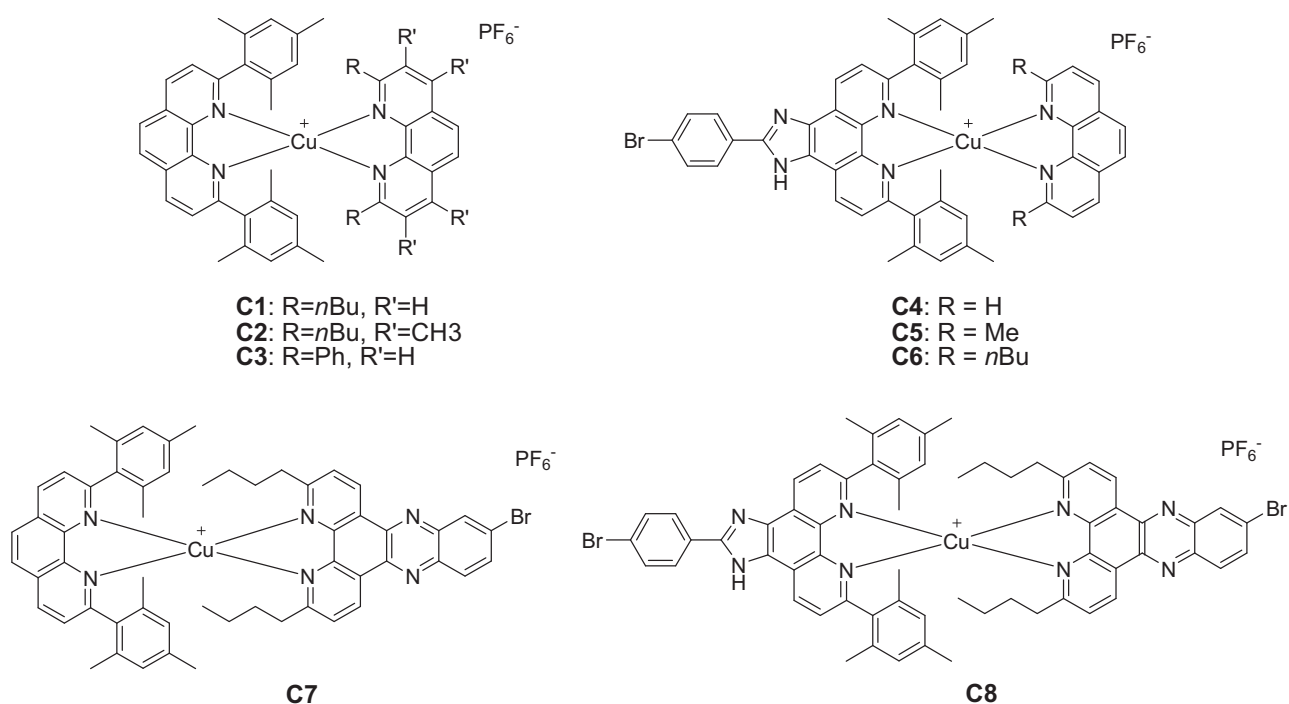
Fig. 2. 1. Structures of the complexes **C1**-**C8**.

2.1.1. Synthesis of the substituted 1,10-phenanthroline motif

1,10-phenanthroline is a very extensively used ligand:[9] it can coordinate various metal ions (Ru, Os, Rh, Ir, Cu, …) and be modified in a controlled way at different positions. It has a rigid and planar structure, with the two nitrogen atoms conveniently placed to interact with metal cations, which ensures a strong, entropically favoured, chelation. From an electronic point of view, it is an electron-poor heteroaromatic system: this characteristic makes it very suitable to stabilize metals in their low oxidation states, and provides low energy π^* orbitals. For this reason MLCT transitions in the visible region are often observed in phenanthroline-containing metal complexes, together with red-shifted emissions.
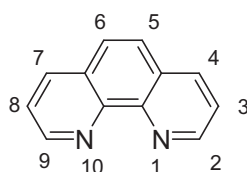
Fig. 2. 2. Structure of 1,10-phenanthroline and position numbering.

The modification of the phenanthroline core can be operated by different means, and each position can be selectively modified by various means, that will be briefly reviewed.

The Friedländer reaction allows to prepare 2-substituted phenanthrolines by the condensation of 8-amino-7-quinolinecarboxaldehyde with enolizable ketones in basic conditions.[10] This synthesis is however performed in harsh conditions, in particular high temperatures, and is therefore incompatible with the presence of certain fragile molecular functionalities.
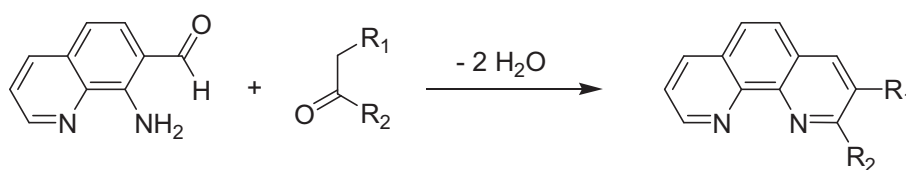
Scheme 2. 1. Friedländer synthesis.

The direct nucleophilic attack of aryl or alkyl-lithium compounds on the bare phenanthroline, followed by hydrolysis and rearomatization with manganese dioxide,[11] affords either 2,9-disubstituted or 2-monosubstituted cores, and therefore opens the way to the synthesis of asymmetrical ligands.[12] This method was first proposed by Sauvage and co-workers in 1982, and was used for the preparation of phenanthroline-based catenanes, rotaxanes and knots.[13] Despite the

good yields normally provided by this reaction,[1] there are cases of very poor yields reported in literature.[2]
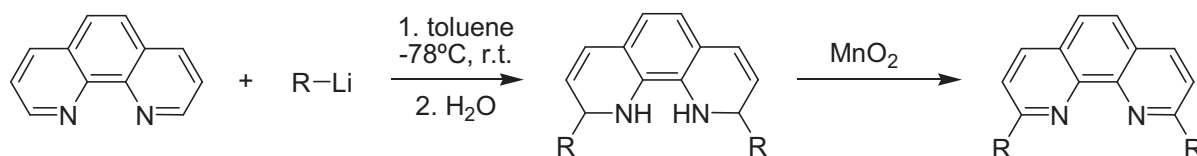
Scheme 2. 2. Phenanthroline modification by nucleophilic attack with organolithium compounds.

An interesting building block is 2,9-dichloro-1,10-phenanthroline, that can be obtained in three steps from phenanthroline.[14,15] This intermediate provides the access to a variety of products through cross-coupling reactions.[9]
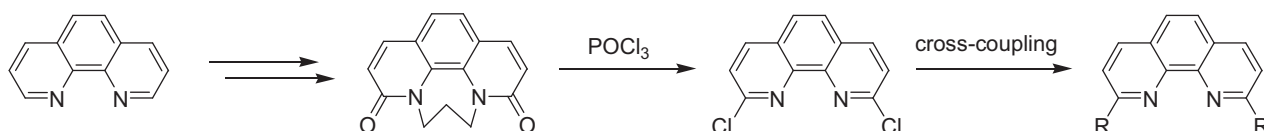
Scheme 2. 3. Synthesis of 2,9-dichloro-1,10-phenanthroline and its use in cross-coupling reactions.

Phenanthrolines functionalized on the 3, 4, 7 and 8 positions are synthesized starting from the halogenated precursors. The 3-bromo- and the 3,8-dibromophenanthroline are obtained by direct bromination of 1,10-phenanthroline.[16] The 4,7-halogenated compound is prepared starting from the dihydroxy derivative by reaction with PBr_3 in PBr_5.[17] Cross-coupling reactions afford then a variety of compounds like multitopic ligands or macrocyclic ligands with *exo*-coordinating sites.[9].

Finally, the central ring (positions 5 and 6, Fig. 2. 2) can be modified in different ways. The oxidation with commercial bleach under phase transfer conditions affords the 5,6-epoxide in good yields, and the attack with different nucleophiles allows to obtain many different 5-substituted compounds.[18] The 5 position, moreover, can be nitrated in a HNO_3/H_2SO_4 mixture and then reduced to amine, that opens the way to the formation of amide bonds or reaction with electrophiles. [19-21] The oxidation of the central double bond can be achieved with a mixture of HNO_3/H_2SO_4 in presence of KBr to provide the phenanthroline-5,6-dione,[15] that is a useful intermediate towards the synthesis of more extended polycycles as dppz (dipyrido[3,2-a:2',3'-c]phenazine, see Scheme 2. 4)[22-24] or phenanthroline-[a:b]imidazole or oxazole.[25,26] The oxidation can also be performed at room temperature by using $KBrO_3$ and 60% H_2SO_4 as oxidant.[27] This method uses much milder conditions, and considerably reduces compounds degradation by unselective oxidation.
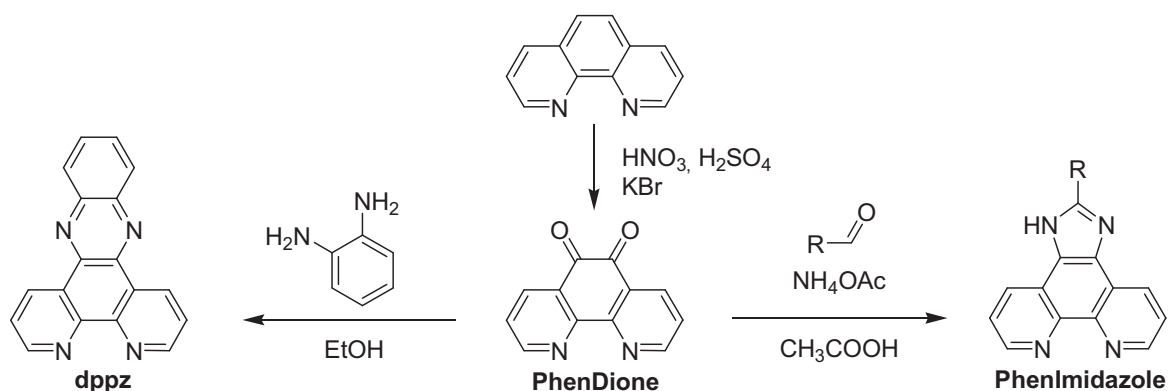
Scheme 2. 4. Synthesis of the 1,10-phenanthroline-5,6-dione, dppz and PhenImidazole.

Another important phenanthroline derivative functionalized on the 5 and 6 positions is 5,6-diamino-1,10-phenanthroline, which was extensively used to obtain homoditopic ligands like tetrapyridophenazine [28] or heteroditopic ligands by the formation of amide bonds.[29]
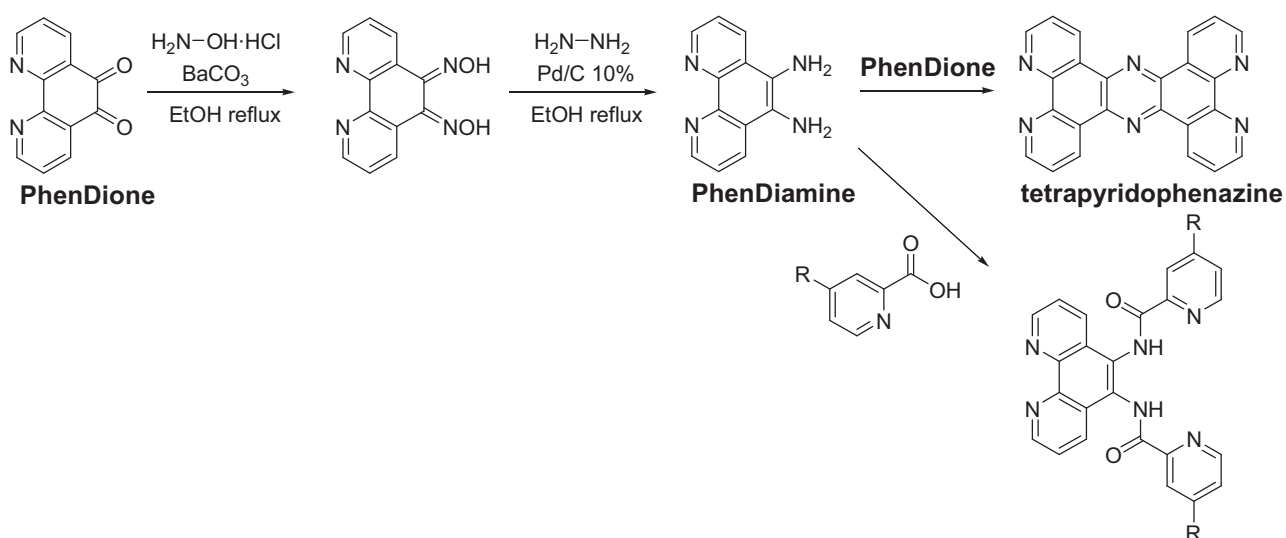
Scheme 2. 5. Synthesis of 5,6-diamino-1,10-phenanthroline (**PhenDiamine**),[30] **tetrapyridophenazine**[28] and an example of heteroditopic ligand containing amide bonds.[29]

2.1.2. Target structures

As described in chapter 1 (paragraph 1.4), many copper(I) diimine complexes have already been studied from an electrochemical and photophysical point of view, mostly homoleptic.

For our study on heteroleptic complexes, the first step was the selection of a convenient coordination cage to get satisfactory electrochemical and spectroscopic properties, coupled with a structure allowing further modifications with the minimal synthetic effort.

The general guideline for the elaboration of the new structures was the optimization of the emission lifetime of the complexes. For this purpose, the increase of the steric hindrance in the copper coordination cage was considered (by means of the introduction of bulky substituents at the 2 and 9 positions of the phenanthroline), together with the evaluation of the influence of methyl substitution at the 3 and 8 positions, which proved to dramatically increase the emission lifetime in the case of homoleptic complexes.[3] The selected structures are shown in Fig. 2. 3.
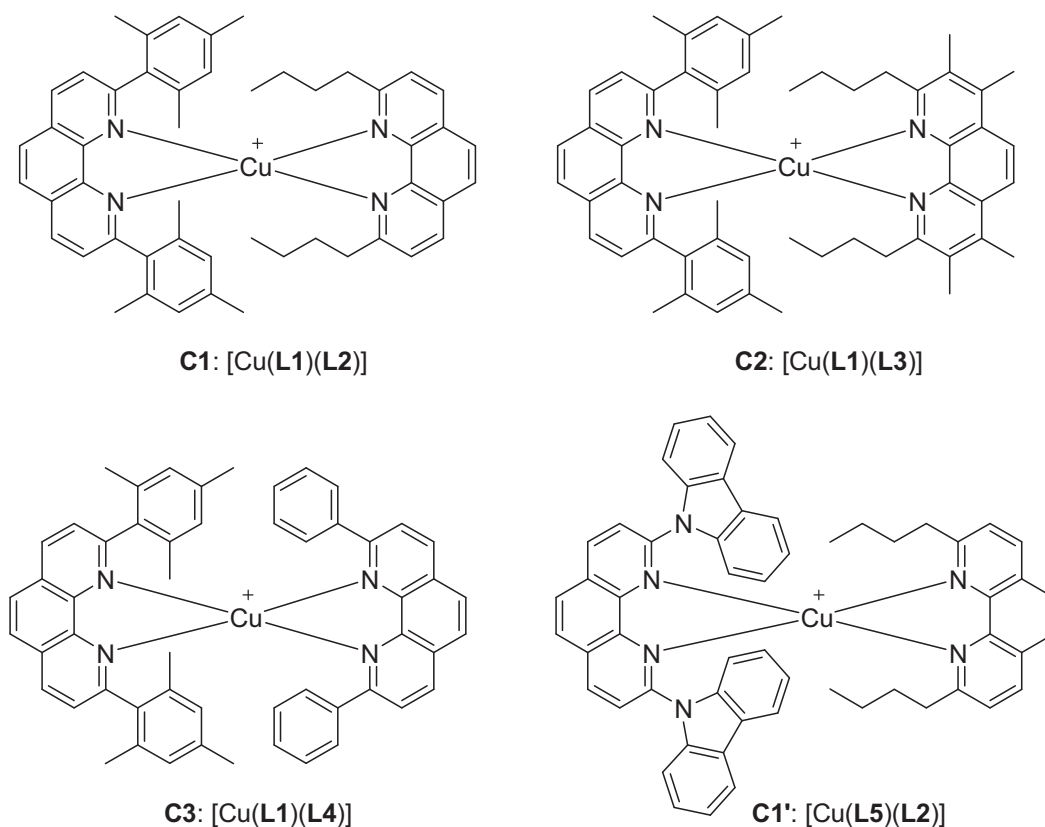
Fig. 2. 3. Structures of the complexes **C1**-**C3** and **C1'**.

The 2,9-dimesityl-1,10-phenanthroline was chosen as the most bulky ligand in nearly all cases because, besides allowing the synthesis of stable heteroleptic complexes, it stabilizes the final compounds by π-stacking interactions with the opposite phenanthroline. Carbazoles (**C1'**) were selected too as highly bulky substituents for the phenanthroline, and their electron-donor properties may increase the coordinating ability of the ligand, bringing further stability to the resulting complex.

As for the less hindered side, all the 2,9-disubstituted phenanthrolines that form homoleptic complexes can be chosen. **C1** was designed to get a better protection of the copper ion with respect to shorter chains (methyl for example), **C2** is a modification of the previous complex to evaluate the effect of the 3 and 8 methyl substitution on the photophysical properties.[3]

C3 seems an interesting structure to obtain a good shielding of the metal ion from the nucleophilic attack of the solvent molecules, responsible for the exciplex quenching of the excited state.[31] Moreover, four aryl groups are attached to the phenanthroline ligands, and an important stabilization by π-stacking can be imagined. Most importantly, the homoleptic complex displays one of the longest-lived excited states for a copper(I) bis(phenanthroline) complex (310 ns in dichloromethane).[8]

2.1.3. Synthesis of the ligands L1-L5

As none of the ligands used for the synthesis of these four complexes was commercially available, they were prepared using literature procedures.

2,9-dimesityl-1,10-phenanthroline synthesis is described in literature by nucleophilic attack of the mesityl-lithium on the 1,10-phenanthroline in dry diethyl ether.[32] The reaction, either performed in one or two steps, afforded only a very low yield of the pure compound in our hands, so the product was finally synthesized by Suzuki cross-coupling between 2,9-dichloro-1,10-phenanthroline and excess mesitylboronic acid in presence of $Ba(OH)_2$ and $Pd(PPh_3)_4$ as the catalyst, with a very satisfactory yield of 95%.
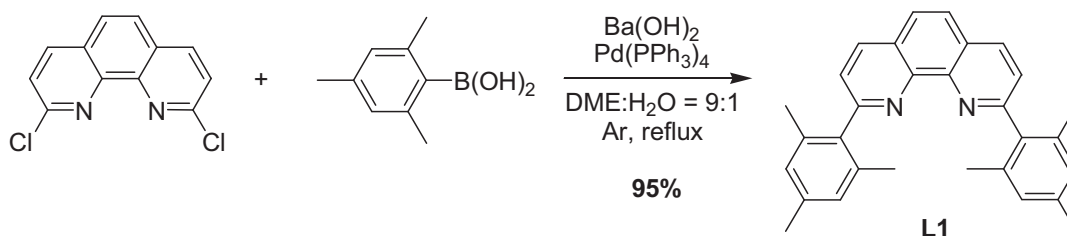
Scheme 2. 6. Synthesis of the 2,9-dimesityl-1,10-phenanthroline (**L1**) by Suzuki cross-coupling.

2,9-dibutyl-1,10-phenanthroline **L2** and 2,9-dibutyl-3,4,7,8-tetramethyl-1,10-phenanthroline **L3** were prepared by nucleophilic attack of an excess of *n*Bu-Li on 1,10-phenanthroline and 3,4,7,8-tetramethyl-1,10-phenathroline, respectively. After quenching the reaction with water, and rearomatization by oxidation with activated MnO_2 in dichloromethane, the ligands were obtained in 66% and 59% yields, respectively (Scheme 2. 7). **L4** was prepared in quantitative yield using phenyllithium, according to the same procedure used for **L2** and **L3**.
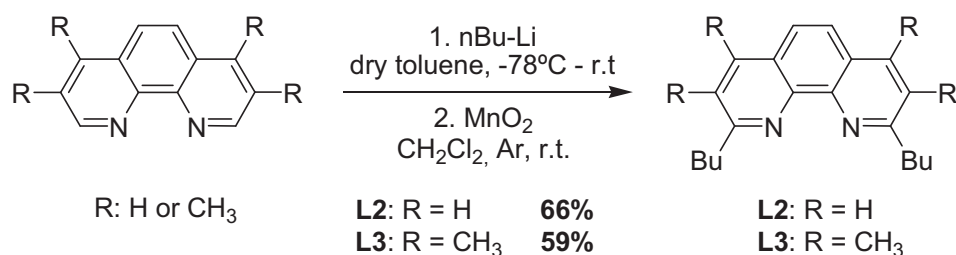
Scheme 2. 7. Synthesis of ligands **L2** and **L3**.

2,9-dicarbazole-1,10-phenanthroline was prepared by nucleophilic substitution of deprotonated carbazole on 2,9-dichloro-1,10-phenanthroline. The reaction was performed in presence of Cs_2CO_3 as the base, and afforded ligand **L5** in 49% yield. The high steric hindrance at the 2 and 9 positions can account for the moderate yield.
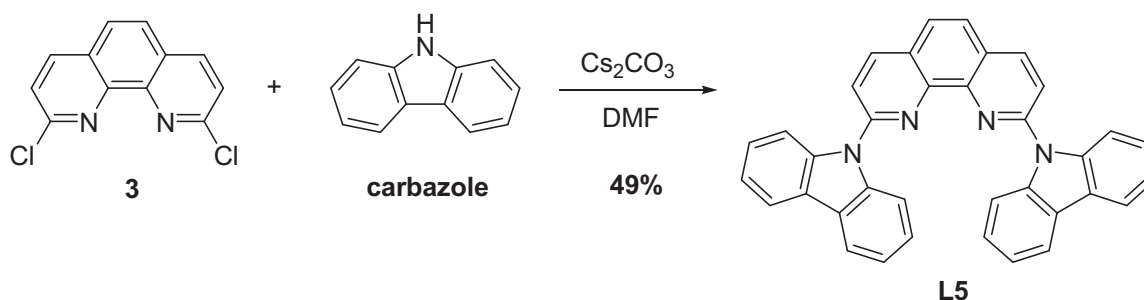
Scheme 2. 8. Synthesis of ligand **L5**.

All the ligands were characterized by ^{1}H and ^{13}C-NMR, and HR-MS. The ^{1}H-NMR spectra of the ligands **L1**, **L2**, **L4** and **L5**, performed in deuterated chloroform, show the typical pattern of the 2,9-substituted phenanthrolines, constituted by two doublets (J ~ 8.7 Hz, H^4 + H^7 and H^3 + H^8) and a singlet (H^5 + H^6). **L3** lacks the two doublets, that are substituted by additional peaks in the aliphatic zone. The position of the peaks is influenced by the groups at the 2 and 9 positions, as can be seen from the superposition of the aromatic part of the ^{1}H-NMR spectra shown below (Fig. 2. 4). In particular **L4** and **L5** have very deshielded H^3 and H^8 protons, probably due to anisotropic effects provoked by the rings.
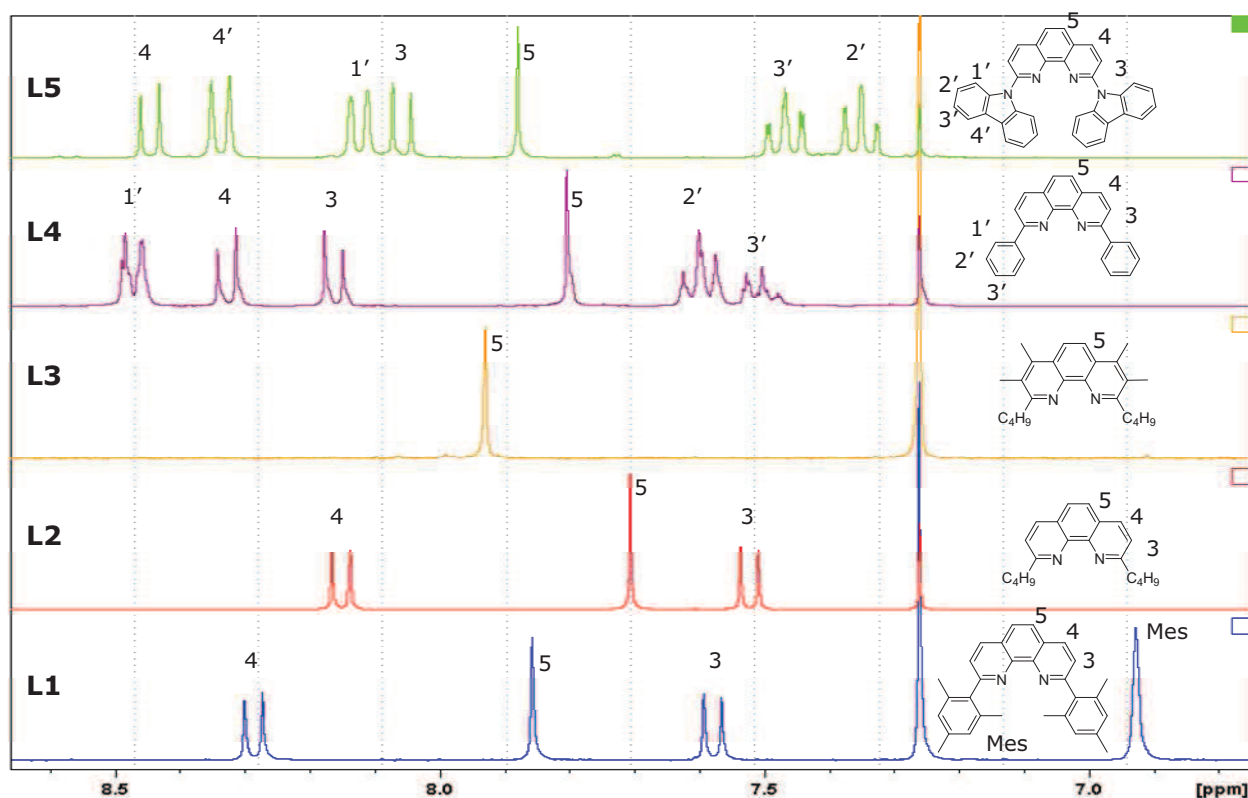
Fig. 2. 4. Superimposition of the aromatic portion of the NMR spectra of ligands **L1**-**L5**.

2.1.4. Synthesis of the complexes C1-C3

The heteroleptic copper(I) complexes were synthesized in a two-step synthesis performed one-pot under argon atmosphere in distilled dichloromethane. The most hindered ligand is first dissolved in a dichloromethane solution of tetrakis-acetonitrile copper(I) hexafluorophosphate ([Cu(CH$_3$CN)$_4$]PF$_6$), to form an intermediate solvato complex [Cu(**L1**)(NCCH$_3$)$_2$]$^+$, then the second ligand is added to form the heteroleptic species (Scheme 2. 9).
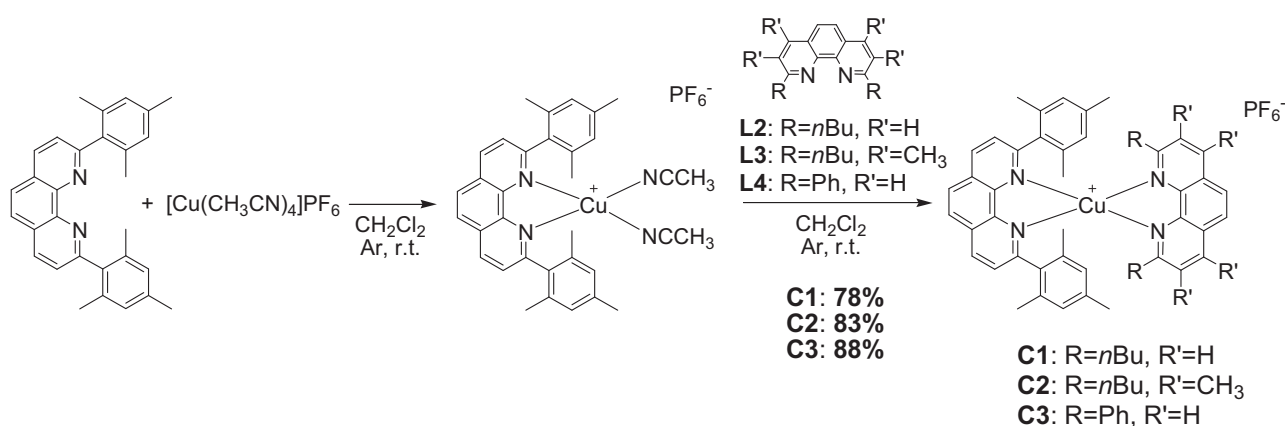
Scheme 2. 9. Synthesis of the complexes **C1**-**C3**. The same procedure is used for the other heteroleptic complexes.

The solvato complex is usually reported with two acetonitrile molecules coordinating the Cu^I, but some structures have been resolved where the metal ion is bound to only one solvent molecule.[33] The structure in solution, however, is probably a dynamic equilibrium between $[Cu(\mathbf{L})(NCCH_3)_2]^+$ and the tricoordinated $[Cu(\mathbf{L})(NCCH_3)]^+$.[34] Let us underline that the second, less hindered ligand, was systematically in default, with regards to copper(I) and mesityl bearing phen, in order to avoid the formation of the homoleptic complex.

The intermediate solvato complex formation is easily visible by the yellow colour of the solution, while, when the second ligand is coordinated, the presence of the MLCT band of the $[Cu(NN)_2]^+$ at around 450 nm leads to the instantaneous development of a red colour. The purification of the crude is performed by column chromatography on silica gel, eluted with dichloromethane with about 2% methanol. If necessary, a precipitation with petroleum ether from a dichloromethane solution of the complex was used to eliminate the last ligand traces.

All syntheses gave the desired product, except with ligand $\mathbf{L5}$, which was used as the hindered ligand (like $\mathbf{L1}$, it is expected not to form the homoleptic complex). In this case, the formation of the $[Cu(\mathbf{L5})]^+$ intermediate was not noticed (no colour changes). The second ligand addition ($\mathbf{L2}$) was however tried, but yielded only the homoleptic complex $[Cu(\mathbf{L2})_2]PF_6$. The formation of $[Cu(\mathbf{L5})]^+$ was probably prevented by the excessive steric hindrance provided by the carbazoles, and $\mathbf{L2}$, even if added in default, bound to uncoordinated copper(I) in solution, immediately forming the homoleptic species.

Complexes $\mathbf{C1}$, $\mathbf{C2}$ and $\mathbf{C3}$ were obtained in good yields of 78%, 83% and 88%, respectively.

The ^{1}H-NMR spectra of the complexes showed, as usual, the superposition of the two ligands signals. As a general rule, an upfield shift of the protons of the substituents is observed, as a result of the increased electron density due to the interaction with the opposite ligand. Conversely, the phenanthroline rings protons are deshielded because of the coordination of the metal ion, that pulls the electron density away from the ligand. This phenomenon can be clearly seen if the ^{1}H-NMR spectra of the complex is superposed to those of the ligands in Fig. 2. 5.
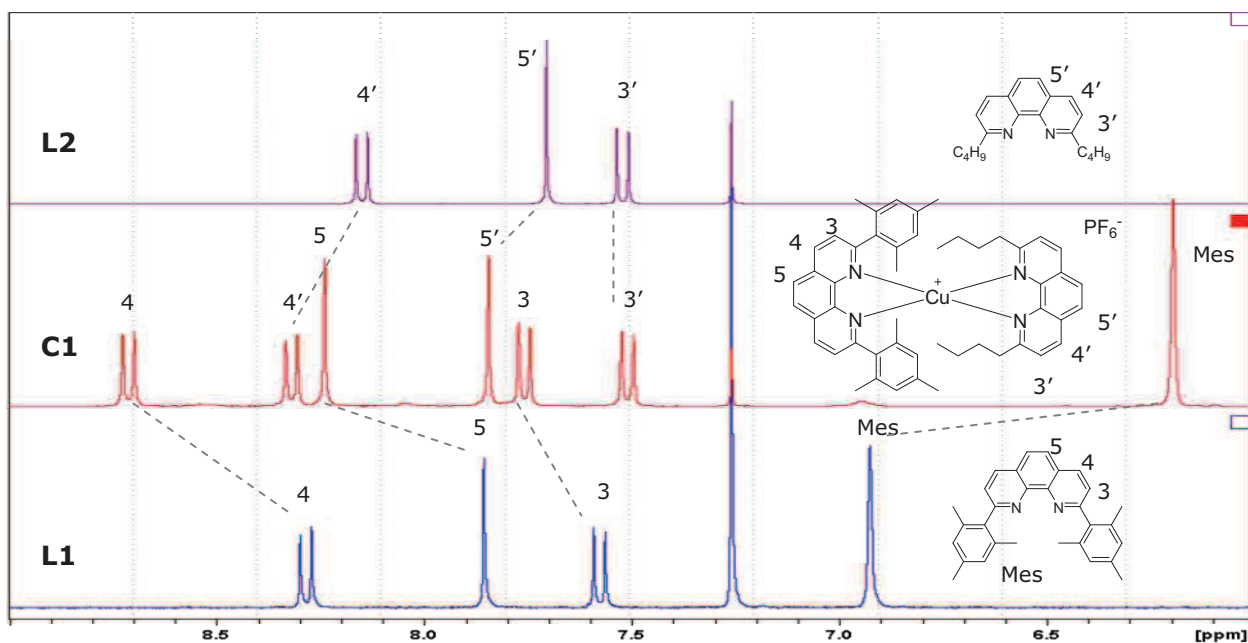
Fig. 2. 5. Superimposition of the aromatic part of the NMR spectra of **C1**, **L1** and **L2**. The changes in the chemical shifts of the ligands protons upon coordination are indicated by the dotted lines.

2.1.5. X-Ray structure of the complex C3

Slow vapour diffusion of petroleum ether into a dichloromethane solution of the compound afforded X-ray quality crystals for complex **C3**. The obtained structure is shown in Fig. 2. 6.
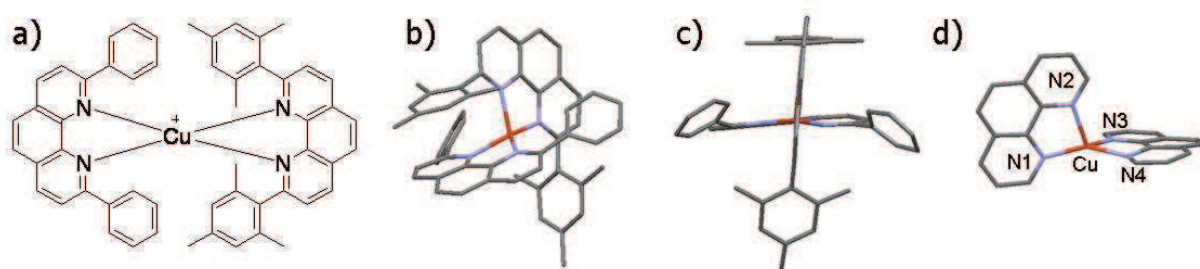
Fig. 2. 6. a) Structure of **C3**; **b)** complete X-ray structure of the compound **C3**, the H atoms have been removed for the sake of clarity. Cu: orange; N: blue; C: grey; **c)** side view of the complex; **d)** arrangement of the two phenanthroline ligands and coordination cage (diMesPhen **L1** on the left, diPhPhen **L4** on the right).

The complex crystallizes in an orthorhombic crystal lattice ($\alpha = \beta = \gamma = 90°$; a = 28.6055 Å; b = 54.1883 Å; c = 13.1165 Å; Fdd2 space group).

The first aspect one can notice is the distorted coordination cage of the complex. To better visualize this feature, the complex was represented in Fig. 2. 6 (d) without substituents on the phenanthrolines. The structure is not tetrahedral, as it is commonly assumed for copper(I)

57

complexes, but nearly pyramidal, with the metal that nearly lies in the plane formed by three of the coordinating nitrogens (N1, N3 and N4), and the N2 in an apical position. This arrangement is due to the π-stacking between one of the mesityl rings and the phenanthroline core of the second ligand, that lies on nearly parallel planes with a distance of about 3.5 Å. The four Cu-N distances are all different from each other: for **L1** (diMesPhen) Cu-N1 = 1.9770 Å and Cu-N2 = 2.1330 Å, while for **L4** (**dpp**) Cu-N3 = 2.0416 Å and Cu-N4 = 2.0843 Å. Evidently, the fact that **L1** is implied in π-stacking limits its freedom in the coordination cage and forces it to establish two very different bonds, while **L4** is free to dispose in a more symmetrical way. Interestingly, none of the phenyl rings participates to π-stacking interactions with ligand **L1**, as it can be seen from Fig. 2. 6 (c). The two aromatic rings are sloping with respect to both the phenanthroline cores of the ligands. This kind of distortion is not always found in homoleptic complexes containing aromatic groups in the 2 and 9 positions (like the parent compound [Cu(**dpp**)$_2$]$^+$), but appears for particularly strained structures such as [Cu(**dptmp**).[35] In these structures, the rotation of the phenyl rings around the C-C bond with phenanthroline is hindered by the presence of bulky groups in the 3 and 8 positions.

The distortion of the cage can be quantified by approximately measuring the angles for the flattening (~85º), rocking (~61º) and wagging (~84º). If the three values are taken into account using the equation 1.14[4] (Paragraph 1.4.1), a ξ value of 0.78 is obtained, compared to a unitary value which indicates a perfect tetrahedral symmetry.

2.1.6. Characterization of complexes C1-C3

The complexes were characterized by UV-Visible, emission spectroscopy and electrochemistry. The combination of these three methods is of a fundamental importance when aiming at applications in the field of light-molecules interaction, as they allow to assess the redox potentials of the ground and excited state (which are used to foresee if the charge transfer reactions are thermodynamically allowed or not), according to equations 1.1, 1.4 and 1.5 (see paragraph 1.2.1).[36]

2.1.6.a. Electrochemical properties

The electrochemical properties were studied in dichloromethane. All the potentials are referred to saturated calomel electrode (SCE) as a reference. The three complexes have reversible (quasi reversible, from a strictly electrochemical point of view) oxidation peaks, with a half-wave potential dependence on the steric hindrance of the coordination cage. The oxidation is attributed to the removal of an electron from the metal centred HOMO, thus leading to the Cu^{II} complex. The

most hindered **C3** has a more positive $E_{1/2}$ value due to the fact that the flattening deformation of the coordination cage upon oxidation is strongly prevented: the Cu^{II} form is therefore destabilized. For all the compounds, the ΔE between the forward and backward waves shows a dependence on the scan rate: this phenomenon is characteristic for species that have structurally different oxidized and reduced forms, and thus have an important kinetic barrier for the backward electron transfer.[37] For this reason, the peak separation is given for v_{scan}= 100 mV/s in all the tables. Cyclic voltammetry measurements performed on **C3** at different scan rates showed that for the slower rates ($v = 0.1$ and 0.05 V/S) there are even two backward peaks, indicating that the complex is likely to be unstable under the oxidized form in the electrochemical experiment timescale. This was also confirmed by electrochemical measurements in acetonitrile, where the peak was irreversible. The oxidized complex, where the copper has oxidation number II, tends to flatten, and also opens to the coordination of a fifth ligand. Acetonitrile being a nucleophilic solvent, it is likely to attack the metal centre and probably provoke ligand expulsion from this particularly hindered coordination cage. The redox potentials for the three complexes are summarized in Table 2. 1.

Complex	$E_{1/2}$ (V) vs.SCE [$\Delta E = E_{pa} - E_{pc}$ mV][a]
C1	0.99 [140]
C2	0.87 [110]
C3	1.06 [95[b]]

Table 2. 1. Electrochemical data for complexes **C1**-**C3**. The measurements are performed in distilled, argon purged CH$_2$Cl$_2$ at room temperature; supporting electrolyte: TBAPF$_6$; WE: Pt disk; RE: SCE; CE: Pt foil. [a] The peak separation for $v = 100$ mV is given. [b] The peak is not completely reversible.

One last remark can be made comparing **C1** to **C2**. In the second case, the presence of four methyl groups at the 3, 4, 7 and 8 positions of the phenanthroline accounts for a global electron enrichment of the molecule. Therefore, oxidation to copper(II) occurs at lower potentials (120 mV cathodic shift) since the copper(II) ion is stabilized by the electron donating ability of the methyl substituents.

At negative potentials, nothing different from the blank signal was found, indicating that the ligand-centred reduction steps occur outside of our operating potential window (< -1.5 V vs. SCE). Indeed, the oxidation of copper(I) diimine complexes (sometimes reported as Cu$^{I/0}$ but more likely to be localised on one ligand) is reported in literature between -1.5 and -1.7 V vs. SCE.[2]

2.1.6.b. Absorption

The UV-Visible absorption spectra, recorded in dichloromethane, show the classical features for Cu(I) diimine complexes. The UV region is dominated by intense ligand-centered π-π* transitions, with a molar extinction coefficient between 4 and $6 \cdot 10^4$ $M^{-1}cm^{-1}$, while the visible part is dominated by less intense MLCT band ($\varepsilon \sim 4 \cdot 10^3$ $M^{-1}cm^{-1}$), that covers the blue region of the spectrum. The band intensity of the three compounds is comparable. The spectra are shown in Fig. 2. 7, and the data are gathered in Table 2. 2.
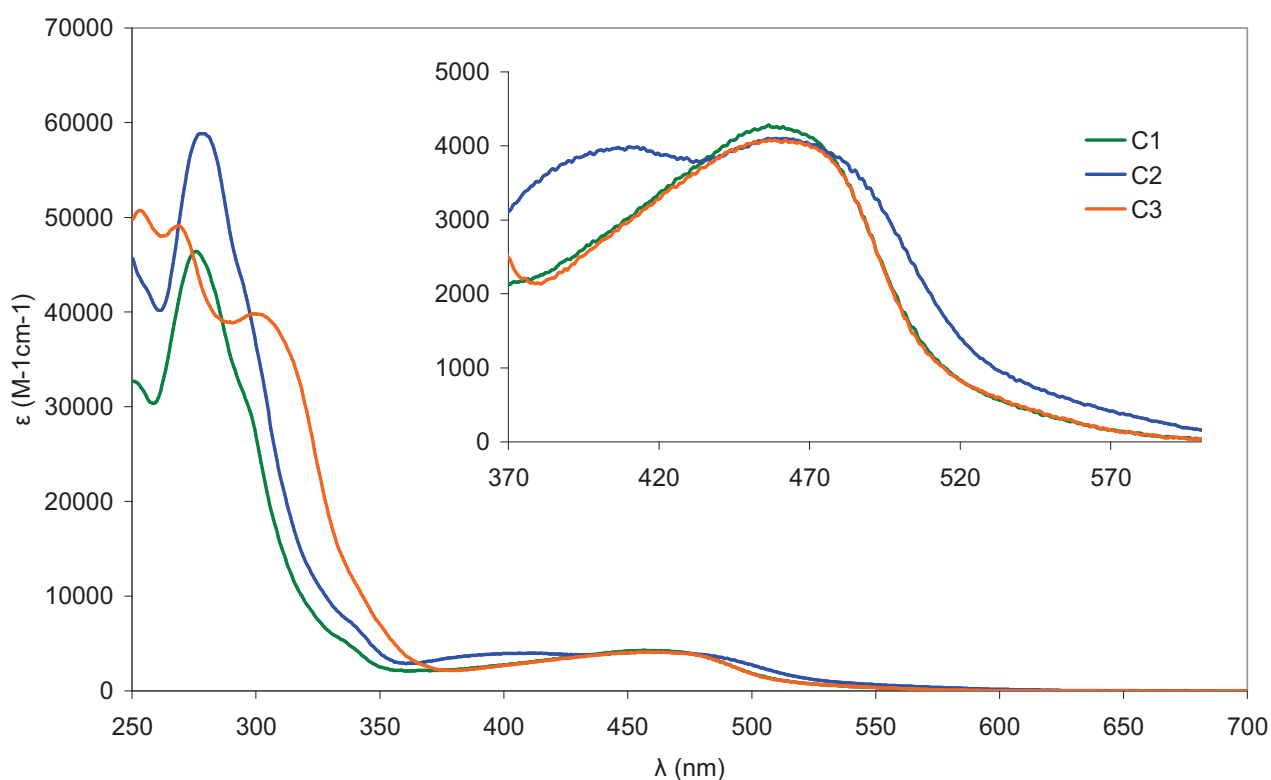
Fig. 2. 7. UV-Visible spectra of the complexes **C1**-**C3**, recorded in dichloromethane.

C1 and **C2** have very similar UV profiles, while the visible spectra present some differences: in **C2** the MLCT band at 458 nm is broader, and there is a second band at higher energies (410 nm) with a very similar molar extinction coefficient, also showing the broad profile of MLCT bands. Quantum mechanical calculations would be required in order to understand the exact nature of this second transition.

The spectrum of **C3** deserves a further comment. Its profile is in fact nearly superposed to the spectrum of **C1**, while in the homoleptic case the UV-Visible absorption of $[Cu(dpp)_2]^+$ presents an absorption at 440 nm and a broad shoulder extending until 600 nm,[8] attributed to the strong deformation of the homoleptic structure already in the ground state. Here, the structure is dictated

60

by the π-stacking between one mesityl ring and the opposite phenanthroline ligand, and therefore it can be assumed to be similar in the two cases (see Fig. 2. 6 for **C3** and Fig. 2. 12 for **C1**). The extinction coefficient is also very similar, while $[Cu(\mathbf{dpp})_2]^+$ is known to have an extremely poor ε of 3000 $M^{-1}cm^{-1}$.

	λ_{abs} (nm) [ε ($M^{-1}cm^{-1}$)]
C1	458 [$4.2 \cdot 10^3$]
	276 [$4.6 \cdot 10^4$]
C2	459 [$4.1 \cdot 10^3$]
	410 [$4.0 \cdot 10^3$]
	278 [$5.9 \cdot 10^4$]
C3	457 [$4.0 \cdot 10^3$]
	300 [$3.9 \cdot 10^4$]
	269 [$4.8 \cdot 10^4$]
	253 [$4.9 \cdot 10^4$]

Table 2. 2. UV-Vis absorption data for the complexes **C1**-**C3**, recorded in dichloromethane.

The calculated spectrum for **C1** was obtained by means of TD-DFT calculations (performed in the group of Dr. C. Daniel in Strasbourg), using B3LYP functional without solvent correction. The complex is characterized by an intense absorption at 271 nm, which results from a mixture of LLCT, IL and MLCT transitions. An intermediate peak calculated at 350 nm is a combination of IL and MLCT states. The low energy band, calculated around 490 nm, corresponds to an envelope of two MLCT states localized on the two ligands.

The spectra recorded in acetonitrile show a different profile for the MLCT, which also appears slightly blue-shifted. This behaviour is not unexpected, since a band with charge transfer character is strongly influenced by the solvent polarity. Negative solvatochromism indicates that the excited state is less polar than the ground state. This result is not unusual for copper(I) complexes,[38,39] but calculations of the distribution of the entire electron density would be required in order to know the dipolar moments of the ground and excited state.

2.1.6.c. Emission

The emission properties of the three compounds were investigated in dichloromethane and acetonitrile. A general result is a low emission quantum yield of about $1.5 \cdot 10^{-3}$ for **C1** ($[Ru(bpy)_3]^{2+}$ was taken as the reference value). The lifetime of ^{3}MLCT was determined using two different techniques, the classical single photon counting (SPC) experiments and nanosecond transient absorption (nanosecond flash photolysis). Indeed, as we will show later on, this low emission quantum yield is due to fast non radiative relaxation and not to a low quantum yield of the emissive excited state (^{3}MLCT) formation. Nanosecond flash photolysis leads to a strong signal which decays mono-exponentially, mainly equal to the longest time constant in SPT experiments. This justifies the fact that nanosecond flash photolysis results are considered as representative of the emission lifetime. Single photon counting experiments give in fact a multiexponential decay, with lifetime and contribution depending of the emission wavelength. The origin of the shorter time constants is assigned to singlet MLCT and non flattened triplet MLCT.

The complexes exhibit broad, red-shifted and moderately intense emission bands, according to what is reported in literature.[40] Complex **C1** emits at 730 nm with a lifetime of about 64 ns in degassed dichloromethane, while this value drops to 25 ns in degassed acetonitrile. This result is not surprising, since acetonitrile is a coordinating solvent and can easily interact with the copper ion in the excited state, to form an exciplex that rapidly relaxes to the ground state following non-radiative pathways (paragraph 1.4.3).

	λ_{em} (nm) [τ (ns)^a]		$\lambda_{em, homoleptic}$ (nm) [τ (ns)]
	CH_2Cl_2	CH_3CN	CH_2Cl_2^{b}
C1	730 [64 (75)]	735 [25 (30)]	725 [150] [38]
C2	700 [41 (44)]	680 [50 (270)]	670 [920] [3]
C3	694 [180 (260)]	740 [55 (100)]	675 [310] [8]

Table 2. 3. Emission properties of complexes **C1**-**C3**, recorded in dichloromethane and acetonitrile at room temperature. ^{a} The value in brackets is obtained in deoxygenated solution. ^{b} Deoxygenated solution.

Even if the solvent influence was reduced, the four additional methyl groups in positions 3,4, 7 and 8 on the 2,9-dibutyl-1,10-phenanthroline in complex **C2** do not contribute to a substantial increase of the emission lifetime (41 ns in degassed dichloromethane), unlike what is found for homoleptic complexes.[3] Therefore, this structure will not be considered for further studies.

The third compound **C3** shows a more intense luminescence in steady-state measurements. This was explained by the better shielding of the formally oxidized copper ion in the excited state, provided by the four bulky substituents on the two ligands. The complex has only limited possibilities for flattening, so the excited state is protected from the exciplex quenching by the solvent. Indeed, the measured emission lifetime of 180 ns is very interesting from the point of view of the possible applications.

The lifetime measurements were also performed in degassed solutions: the values only show a slight increase in deoxygenated solvents, indicating that the emissive state has a limited triplet character. This characteristic makes copper(I) complexes fundamentally different from ruthenium(II)-based systems, for which the emitting state is the ^{3}MLCT. This feature is related to the fact that for copper(I) complexes the ^{3}MLCT state is in thermal equilibrium with the more luminescent ^{1}MLCT [41] (see chapter 1 for a more detailed description).

If compared to the homoleptic compounds (Table 2. 3), the complexes **C1**-**C3** display emission in the same region of the spectrum, with impressive Stokes' shifts and a dependence on the steric properties of the ligands. However, the emission lifetimes are much shorter, most probably owing to the structural distortion imposed by the π-stacking between the mesityl ring and the opposite ligand. This leads to an intrinsically asymmetrical structure where one of the sides is less shielded than the other from the nucleophilic attack of the solvent (Fig. 2. 6).

2.1.7. Excited-state redox potentials

Three new heteroleptic copper(I) complexes with 2,9-dimesityl-1,10-phenanthroline and a less sterically challenged phenanthroline ligand were synthesized and characterized. The evaluation of the electrochemical and spectroscopic properties was used to prove that this class of compounds can be exploited with the aim of developing new copper(I)-based molecules for the conversion of solar energy. For this kind of applications, a particular attention should be devoted to the excited-state lifetime and the redox properties of the ground and excited state. Since the goal is to deal with photoinduced electron transfer (to and from catalysts, acceptors and donors in polyads, or semiconductors in dye-sensitized solar cells), the excited-state properties measure the possibility for the transfer while the ground-state ones indicate the feasibility of the regeneration or the secondary processes. A comparison with ruthenium(II) complexes can be useful to better understand the properties of this molecules, and to plan which applications could be more fruitful.

In the ground state, the lower oxidation potential of the Cu^I complexes indicates a higher energy HOMO with respect to polypyridyl Ru^{II} complexes. This means that, once oxidized, Cu will provide a lower driving force for the regeneration process than Ru. Nothing can be said about the

LUMO level for copper, because in our experimental conditions the reduction peak was not detectable, as it occurs at too negative a potential (below -1.5 V vs. SCE).

The E^{00} values, necessary to calculate the excited-state redox potentials, are deduced from the crossing point of the absorption and emission spectra. For the complexes **C1**-**C3**, only the oxidation side is considered, since the reduction potential is not known (for this reason the reduction is represented in grey in Fig. 2. 8). The ground and excited state properties can be summarized by using the graph below (see paragraph 1.4.5 for a comparison between $[Cu(dpp)_2]^{2+}$ and $[Ru(bpy)_3]^{2+}$).[42] The properties of the three complexes **C1**-**C3** are reported on the right side of Fig. 2. 8.

	$E_{S+/S}$ (V)	$E^{00 \ a}$ (eV)	$E_{S+/S*}$ (eV)
C1	0.99	2.16	-1.17
C2	0.87	2.16	-1.29
C3	1.06	2.16	-1.10
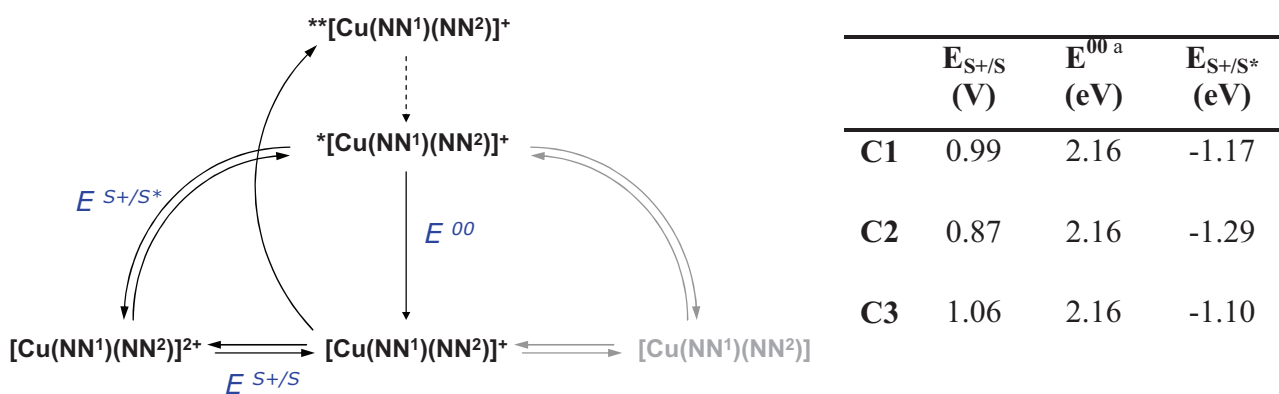
Fig. 2. 8. Left: Graphical representation of the photophysical and electrochemical properties of the complexes.[42] Two asterisks represent the excited state directly populated by excitation at the maximum absorption wavelength; one asterisk denotes the lowest energy, emitting MLCT state. **Right**: Excited-state oxidation potentials of the complexes **C1**-**C3**. [a] E^{00} is calculated from the crossing λ of the absorption and emission spectra.

The three complexes can be ranked according to the reducing power at the excited state:

$$\textbf{C2} > \textbf{C1} > \textbf{C3} > [Ru(bpy)_3]^{2+}$$
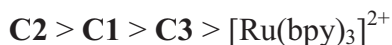
The $[Ru(bpy)_3]^{2+}$ oxidation potential is 1.3 V vs. SCE and $E_{S+/S*}$ = -0.85 V.[42] From the observation of the obtained values, it is possible to deduce that copper(I) heteroleptic complexes, like the previously studied homoleptic ones, are powerful reductants at the excited state, even more than ruthenium(II) tris-bipyridine. On the contrary, they do not exhibit very impressive oxidative properties.

Complex **C1** displays very interesting reductive properties at the excited state and a non negligible excited state lifetime, together with the possibility of synthetic modification of both ligands, which is required to tailor the structure of the complexes in view of further applications. Moreover, it has quite high oxidation potential (120 mV higher than **C2**), thus providing a good

driving force to regenerate the complex after a photoinduced oxidation processes. The study of a series of complexes based on this coordination cage will be detailed in the following paragraphs.

C2 is the most powerful photooxidant of the three complexes, thanks to the low ground-state oxidation potential. However, the excited-state lifetime is not improved with respect to **C1**, and so it will not be further investigated.

Complex **C3** has the longest excited state lifetime, and its properties seem worthy of further investigation in future work. The only issue raised by this compound is its slight instability upon oxidation, as shown by the double backward wave obtained in cyclic voltammetry at low scan rates. Nevertheless, the rates of photoinduced processes (fs-µs) are much faster than the timescale of cyclic voltammetry measurements (s) and the regeneration of the Cu^I species after the primary photoinduced event could be faster than the degradation.

From these results, we can anticipate that these molecules will be suited for applications in photoinduced electron transfer towards electron-acceptor groups and for the sensitization of n-type semiconductors. Homogeneous photocatalysis (where the sensitizer is coupled to a catalyst), requires however an optimization of the excited state lifetimes, as bimolecular oxidative quenching is required and can occur on timescales longer than those measured for these compounds.

2.1.8. Stability assessment for the complex C1

Dealing with labile complexes, which undergo fast ligand scrambling in solution (even at room temperature[5]), requires some knowledge about their stability, in order to avoid the formation of complex mixtures whose purification can be tedious. In particular, from the experimental work carried out on the Cu^I complexes, it is known that the homoleptic and heteroleptic complexes are often impossible to separate by chromatographic techniques.

Some NMR studies have already been done on the heteroleptic complexes synthesized by M. Schmittel and A. Ganz in 1997, leading to the observation that the homoleptic complex is more stable than the heteroleptic.[5] A study about our complexes stability was then conducted, using the complex **C1** as a model, to get a better insight in this system.

The experiments are based on the observation of the evolution in time of the ^{1}H-NMR spectrum of copper complex **C1** in the presence of the free **L2** ligand. The spectra were measured in deuterated chloroform, in which all the compounds exhibit a good solubility and well resolved signals. The quantification of the percentages of the different species was made by the integration of the characteristic peaks. In order to avoid as much as possible the integration errors due to the difference in proton relaxation times, all the signals in the spectra were assigned and an average value for the signals of the non-superimposed protons was taken for each species. The results were

finally formulated as percentage molar fractions, so that the experiments conducted at slightly different concentrations can be compared.

Three experiments were carried out. The first one consisted in mixing one equivalent of $[Cu(CH_3CN)_4]PF_6$ with two equivalents of each ligand (**L1** and **L2**). After 30 minutes stirring in dry dichloromethane under argon atmosphere, the NMR spectrum indicated the formation of **C1** and $[Cu(\textbf{L2})_2]PF_6$ in a ratio of about 2:1. The solution was then split into two portions and the solvent was substituted with a more polar and coordinating one. Acetonitrile and N,N-dimethylformamide were the selected solvents, and the mixture was treated at first at room temperature (CH_3CN, DMF) and then heated (CH_3CN). The solvent was then evaporated and the ^{1}H-NMR spectrum was recorded in $CDCl_3$. In the three cases the **C1**: $[Cu(\textbf{L2})_2]PF_6$ ratio decreased to nearly 1:2. The results seem to indicate that the heteroleptic complex is the kinetically favoured species, while the homoleptic one is more thermodynamically stable, and forms in presence of coordinating solvents such as acetonitrile and N,N-dimethylformamide, even at room temperature. Potentially coordinating solvents and high temperature are expected to increase the ligand scrambling of these labile complexes, and to favour the formation of the most thermodynamically stable compound.

The second experiment consisted in mixing one equivalent of **C1** and one equivalent of free **L2**. The solution, in deuterated chloroform, was kept at room temperature and its evolution was controlled by ^{1}H-NMR (concentration of **C1**, $[Cu(\textbf{L2})_2]PF_6$, **L1** and **L2**). In the graph that reports the concentration of the four species as a function of time (Fig. 2. 9, left), it is possible to see that there is $[Cu(\textbf{L2})_2]PF_6$ formation until reaching an equilibrium after about 10 hours, then the concentrations remain stable in time and are only slightly affected by heating the solution in chloroform or refluxing acetonitrile (conditions favouring ligand scrambling).

The experiment was then repeated, as a control test, by mixing one equivalent of $[Cu(\textbf{L2})_2]PF_6$ with one equivalent of **L1**. The concentrations of the four species (Fig. 2. 9, right) evolve in time until reaching the same situation obtained in the previous case.
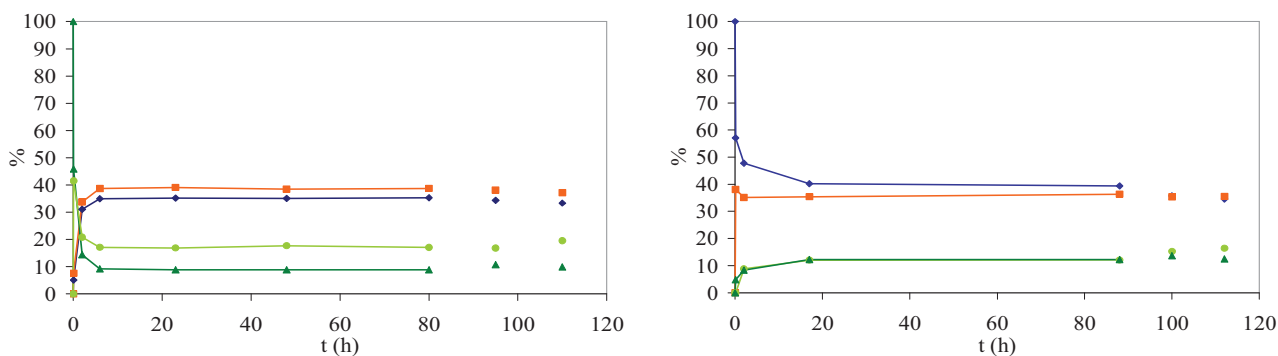
Fig. 2. 9. Left: experiment 2 (— $[Cu(\textbf{L2})_2]PF_6$; — **C1**; — **L1**; — **L2**). The initial concentration of $[Cu(\textbf{L2})_2]PF_6$ is 21mM. **Right**: experiment 3. The initial concentration of **C1** is 11mM. The last two points on the right refer to the mixture heated at reflux in dichloromethane and acetonitrile, respectively.

From the data obtained in the two experiments, the ratio of the two association constants K_{homo} and K_{hetero} can be calculated in the following way.

The association constant for the heteroleptic complex **C1** corresponds to the equilibrium:

$$\textbf{L1} + \textbf{L2} + [Cu(CH_3CN)_4]PF_6 \rightleftharpoons \textbf{C1}$$

$[Cu(\textbf{L1})(CH_3CN)_2]^+$ and $[Cu(\textbf{L2})(CH_3CN)_2]^+$ were neglected, as their contribution was assumed to be very low in presence of an excess of ligands.

The thermodynamic constant of the complexation reaction can be written as

$$K_{hetero} = \frac{[C1]}{[L1]\cdot[L2]\cdot[Cu^1]} \qquad\qquad \text{Eq. 2.1}$$

In an analogous way

$$K_{homo} = \frac{[[Cu(L2)_2]PF_6]}{[L2]^2\cdot[Cu^1]} \qquad\qquad \text{Eq. 2.2}$$

The ratio of the two constants is therefore

$$\frac{K_{homo}}{K_{hetero}} = \frac{[[Cu(L2)_2]PF_6]\cdot[L1]}{[C1]\cdot[L2]} \qquad\qquad \text{Eq. 2.3}$$

The concentration of the different compounds can be obtained from the molar fraction of the species in the ^{1}H-NMR spectra.

In stability experiment 2:

	$[Cu(\textbf{L2})_2]PF_6$	**L1**	**L2**	**C1**
t = 0	1 eq.	1 eq.	0	0
Equilibrium	1-x	1-x	x	x

therefore

$$\frac{K_{homo}}{K_{hetero}} = \frac{[[Cu(L2)_2]PF_6]\cdot[L1]}{[C1]\cdot[L2]} = \frac{(1-x)^2}{x^2} \approx 8 \qquad\qquad \text{Eq. 2.4}$$

with x = 0.26 (molar faction = x/2, Fig. 2. 9, left).

In stability experiment 3:

	C1	**L2**	**L1**	$[Cu(\mathbf{L2})_2]PF_6$
t = 0	1 eq.	1 eq.	0	0
Equilibrium	1-x	1-x	x	x

therefore

$$\frac{K_{homo}}{K_{hetero}} = \frac{[[Cu(L2)_2]PF_6]\cdot[L1]}{[Cl]\cdot[L2]} = \frac{x^2}{(1-x)^2} \approx 7 \qquad \text{Eq. 2.5}$$

with x = 0.73 (molar faction = x/2, Fig. 2. 9, right).

These data confirm literature results stating that the heteroleptic compounds are less thermodynamically stable than the homoleptic ones,[5] and must be taken into account while working with heteroleptic complexes. The complexes can be isolated in their pure form and are stable towards light, moisture and oxygen, but an excess of the less hindered ligand must be carefully avoided since the ligand exchange rapidly leads to a mixture of compounds that are seldom differentiated by chromatography. Interestingly, the π-stacking stabilization provided by one of the mesityl rings is not strong enough to make the heteroleptic complex more stable than the homoleptic. The reason for this difference in stability is believed to be the stronger σ-donating ability of the 2,9-dibutyl-1,10-phenanthroline (**L2**) with respect to the mesityl-substituted ligand, together with the reduced steric hindrance of the homoleptic complex.

The information collected about the model compounds **C1**-**C3** provides an important basis to prepare and characterize a series of 5 heteroleptic copper(I) complexes bearing more elaborated ligands, described in the following paragraphs, that open the way to the construction of photosensitive arrays for the conversion of solar energy.

A more rigorous approach could involve the measurement of the association constants of the homoleptic and heteroleptic complexes in order to determine their ratio.

2.2. Synthesis of original dipyridophenazine or imidazole fused phenanthroline ligands

In order to tune the properties of the complexes, to match the requirements needed for the different kinds of application in solar energy conversion, it is important to functionalize the ligands to obtain more complex structures that possess additional functionalities such as electron withdrawing, electron donor or anchoring groups.

In this paragraph, the synthesis and characterization of two new phenanthroline-based ligands and of the relative copper(I) complexes is described. The molecular structures of the two ligands **L6** and **L7** are inspired by the well known structures phen-imidazole (2-phenylimidazo[4,5-*f*][1,10]phenanthroline) and dppz (dipyrido[3,2-*a*:2',3'-*c*]phenazine), surrounded by a dotted line in Fig. 2. 10.
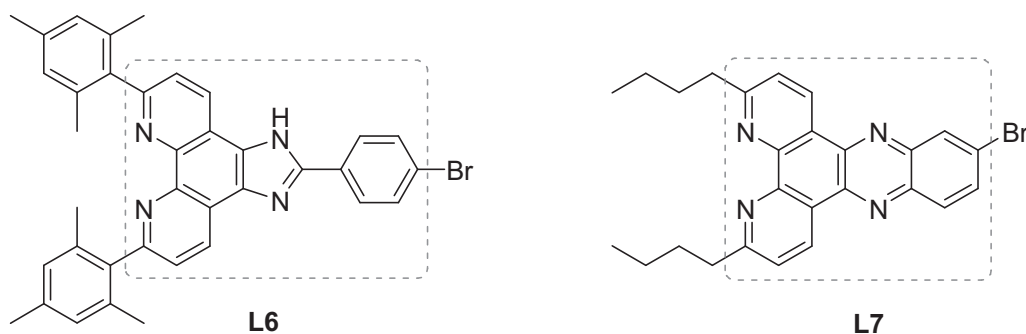
Fig. 2. 10. Structure of the ligands **L6** and **L7**, the phen-imidazole (left) and dppz (right) structures are surrounded by a dotted line.

These two ligands are widely used in coordination chemistry, and possess well-established electronic properties. Phen-imidazole is donating in nature, and has a labile proton. It has been conveniently used as a connecting moiety to bind metal complexes (thanks to it chelating ability) with other functionalities as for example catalysts, electroactive groups[25] or peptides chains.[26] Dppz, on the contrary, has electron acceptor properties and has been widely used in the design of photosensitive polyads[22,23] and for the conception of DNA intercalating agents.[24] Its planar geometry is in fact very adapted to set up π-stacking interactions with the nitrogenous bases.

The ligands **L6** and **L7** were specially designed for the synthesis of heteroleptic Cu[I] complexes: the very encumbering mesityl groups on the 2 and 9 position of **L6** allow it to play the role of the most hindered ligand, while **L7** is equipped with *n*-butyl chains, which are mildly encumbering, that means enough to provide photophysical properties to the final scaffold. Additionally, both molecules bear a bromo unit, which is particularly interesting from a synthetic

point of view since it can be involved in catalyzed cross-coupling reactions[43] thus opening the way to further structural modifications.

2.2.1. Synthesis of the ligands L6 and L7

The synthesis of the ligands **L6** and **L7** requires the use of two very similar building blocks: 2,9-dimesityl- (**7**) and 2,9-dibutyl-1,10-phenanthroline-5,6-dione (**8**), shown in Scheme 2. 11 and Scheme 2. 12.[44]

The oxidation of the 5 and 6 positions of phenanthroline requires harsh conditions (concentrated sulphuric and nitric acids and sodium bromide), and an accurate control of the temperature conditions during the step of acids addition to avoid the degradation of the molecule. This protocol could not be used for the oxidation of 2,9-dimesityl-1,10-phenanthroline (**L1**), which was irremediably damaged during the reaction, and did not lead to any detectable quantity of **8**. For this reason, another approach, proposed by Sauvage and co-workers,[15] was chosen. This method relies on the synthesis of the 2,9-dichloro-1,10-phenanthroline-5,6-dione **4**, obtained in 4 steps starting from commercial 1,10-phenanthroline (Scheme 2. 10), followed by the introduction of the aromatic rings at the 2 and 9 positions by palladium-catalysed Suzuki cross-coupling. The $K_3Fe(CN)_6$ oxidation of the 2 and 9 positions of **1** requires a particularly careful temperature control, and leads to a very low yield of **2**, of about 30%. Fortunately, the key intermediate **4** can be prepared on the gram scale.
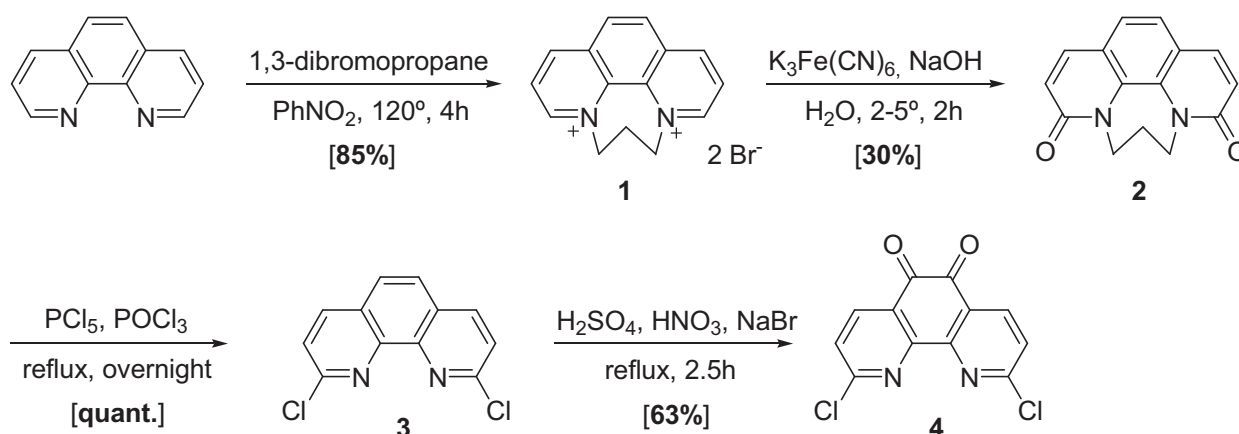
Scheme 2. 10. Synthesis of the 2,9-dichloro-1,10-phenanthroline-5,6-dione (**4**).

As the basic conditions used for the coupling reaction can degrade the dione, leading to the formation of the fluorenone derivative,[45] it was necessary to protect it as a ketal by reaction with the 2-nitropropane in basic water/acetonitrile solution. The obtained intermediate **5** was then reacted

with mesitylboronic acid in presence of tetrakis triphenylphosphine palladium(0) and barium hydroxide. The deprotection of the ketal in TFA/CH$_2$Cl$_2$ afforded the dione **7** in 87% yield, which was subsequently reacted with 4-bromobenzaldehyde in the presence of excess ammonium acetate giving **L6** in 62% yield.
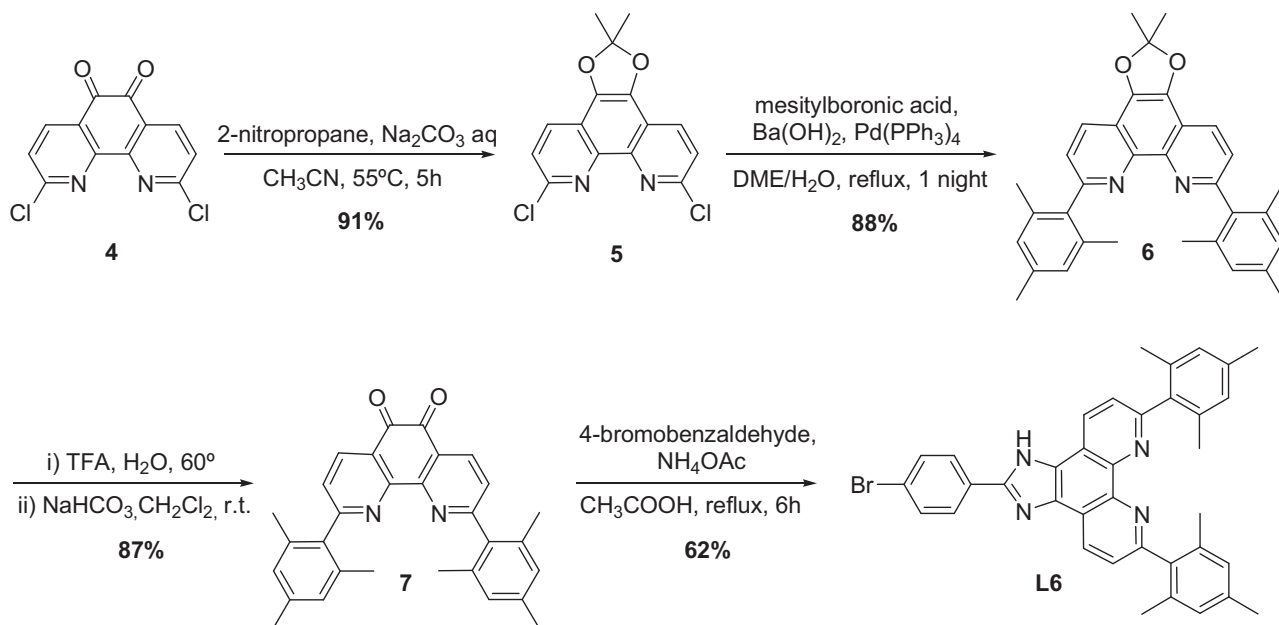
Scheme 2. 11. Synthesis of the ligand **L6**.

The synthesis of 2,9-dibutyl-1,10-phenanthroline-5,6-dione consists in an oxidation of **L2** in a mixture of concentrated sulphuric and nitric acid with sodium bromide.
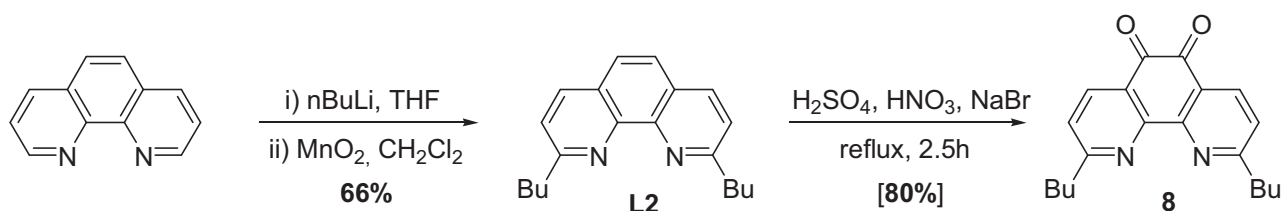
Scheme 2. 12. Synthesis of the 2,9-dibutyl-1,10-phenanthroline-5,6-dione **8**.

The dione **8** is then reacted with 1,2-diamino-4-bromobenzene to give ligand **L7** in one step (62% yield).
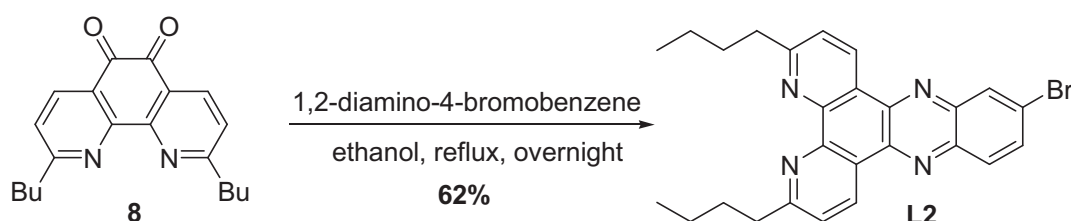
Scheme 2. 13. Synthesis of ligand **L7**.

71

The two ligands structures were confirmed by the ^{1}H-NMR spectra. In particular, the spectrum of **L6** in DMSO-d_6 presents a broad and very unshielded singlet at 13.81 ppm corresponding to the slightly acidic proton on the imidazole ring. The four hydrogens on the phenanthroline ring are not chemically equivalent, and this translates in the presence of two different doublets corresponding to H^3 and H^8. The difference is not so marked for H^4 and H^7, which are displayed as a single doublet. This behaviour was explained by considering the imidazole asymmetry: indeed, if a strong acid (trifluoroacetic acid) or a base (triethylamine) are added, the two doublets merge to give the spectrum of a symmetrical C_2 molecule. Indeed, both the completely protonated imidazole and the deprotonated heterocycle have a C_2 axe.

The aromatic mesityl protons appear as a singlet at 6.95 ppm, while the methyl signals appear as two singlets at 2.29 (6H) and 2.03 ppm (12H). These three signals constitute a characteristic fingerprint of mesityl-containing molecules.
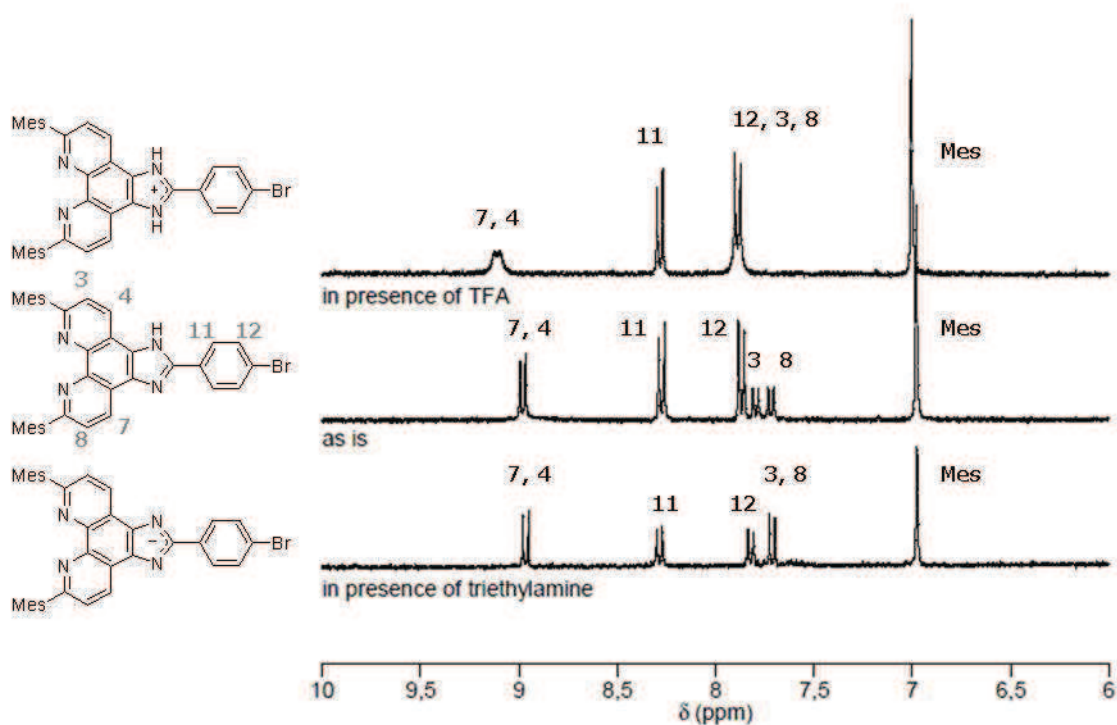
Fig. 2. 11. Expansion of the aromatic portion of the ^{1}H-NMR spectrum of **L6**, recorded in DMSO-d_6.

2.2.2. Synthesis of the ligand L6'

The presence of the acidic imidazole proton in ligand **L6** can provoke a change in the spectroscopic properties depending on the environment's pH. Indeed, the presence of a labile proton, whose exchange in solution is very fast, can interfere with photoinduced processes and particularly with those associated with charge transfer.[46] For this reason, ligand **L6'**, where the

imidazole is alkylated by an hexyl chain, was synthesized. The alkyl chain is also expected to improve the solubility properties of the ligand and complexes, even if Cu^I diimine complexes already exhibit a very good solubility in dichloromethane.

The heterocycle was deprotonated by Cs_2CO_3, and the resulting anion was reacted with *n*-hexyl iodide to give ligand **L6'** in good yield (75%).
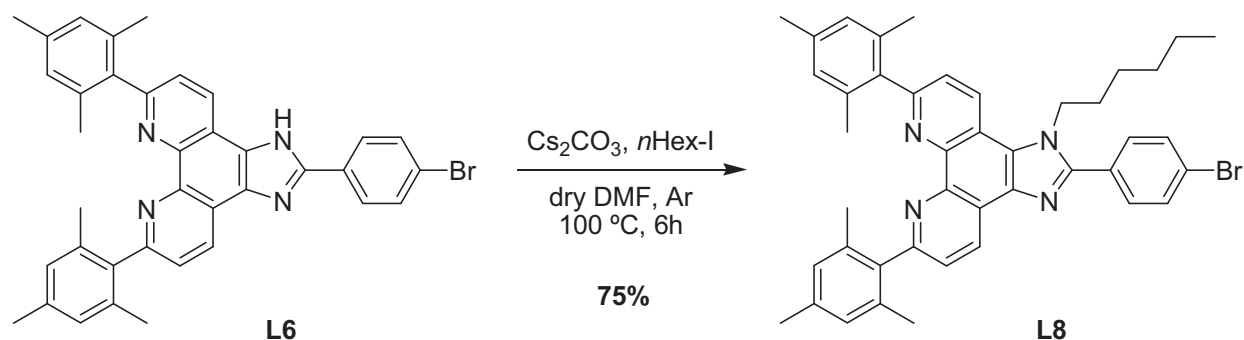
Scheme 2. 14. Synthesis of ligand **L6'**.

The NMR spectrum was recorded in deuterated chloroform, and unlike for **L6** the signals of **L6'** were well resolved in this solvent. The hexyl chain is characterized by a typical pattern in the aliphatic region, with a characteristic broad triplet at 4.64 ppm corresponding to the methylene directly bound to the imidazole nitrogen. The other aliphatic protons are displayed as two separate multiplets ($CH_2 + 3CH_2$) and a triplet (CH_3). This sequence of signals can be found even for longer chains, like octyl.

Finally, the asymmetry induced by the introduction of a chain on the imidazole is visible through the splitting of all the mesityl signals (aromatic and aliphatic), indicating that the two rings have different environments.

2.3. Synthesis and characterization of heteroleptic copper(I) complexes with ligands L6, L7 and L6'

2.3.1. Synthesis of the complexes C4-C8

The ligands **L6** and **L7** were used to prepare a series of complexes. The bulky ligand **L6** was opposed to bare 1,10-phenanthroline (R = H) and two different alkyl substituted phenanthrolines, neocuproine (R = Me) and dibutylphenanthroline (R = *n*Bu), to further explore the influence of the steric hindrance in the coordination sphere on the complexes properties. **L7**, bearing butyl chains, was used in combination with ligand **L1**. Finally, the two ligands were used together to synthesize **C8**.
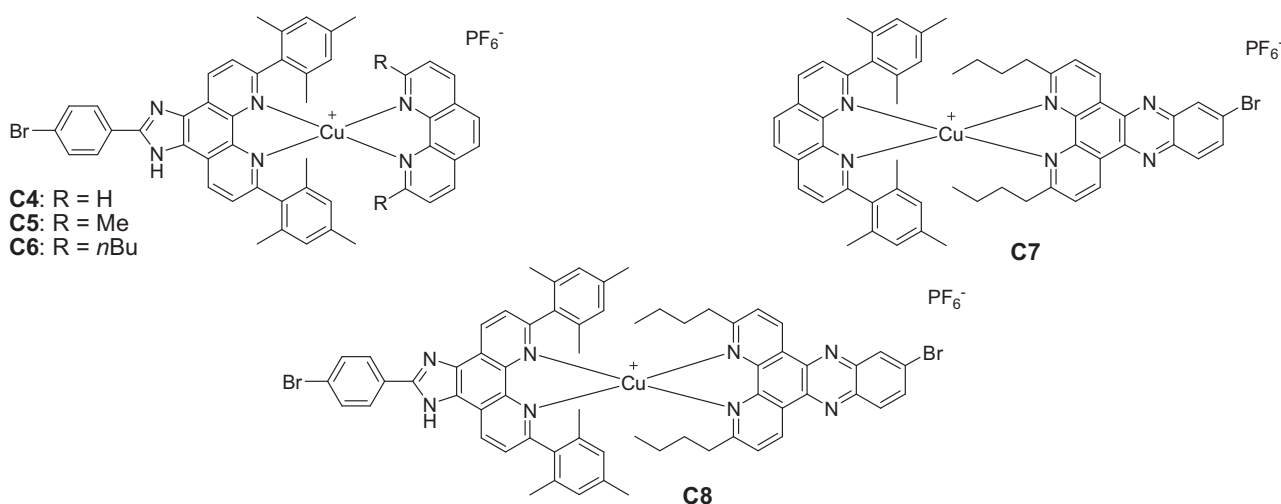
Fig. 2. 12. Structures of the complexes **C4**-**C8**.

The five Cu^I complexes were synthesized in distilled, argon purged dichloromethane. As described previously, the idea is to place a bulky ligand opposite to a less hindered one, in presence of copper(I). The molecules were purified by chromatography on silica gel, and characterized by NMR, mass spectrometry and elemental analysis proving the formation of pure heteroleptic complexes.

The ^{1}H-NMR spectra are composed by the superimposition of the signals of the two ligands, with an overall downfield shift due to copper(I) coordination, and an upfield shift of the mesityl protons which are shielded by the electron density of the opposite phenanthroline. Interestingly, in the spectra of **C4**-**C7** the aromatic mesityl signals are split, indicating a difference in the environment of the two rings, very likely to be caused by the π-stacking interaction of one ring with the opposite phenanthroline.

In general, the asymmetry induced by the imidazole proton is observed in all the spectra as a difference between the protons H^3 and H^8, and H^4 and H^7. In presence of deuterated water, the signals of symmetrical molecules are obtained, supporting once more that H^{imi} plays a crucial role in the determination of molecular symmetry.

2.3.2. Chemistry on the complexes

The HETPHEN concept allows to obtain many elaborated molecular structures.[47,48] After having proved that the synthesis of heteroleptic copper(I) complexes bearing a bromo function was possible, it was our interest to investigate the complexes reactivity: in particular, the possibility of carrying out cross-coupling reactions which involve the halogen function on the ligands **L6** and **L7** was studied. This kind of chemistry is already known in the case of inert complexes of Ru^{II}, Os^{II} or Ir^{III}.[49-53] However, copper(I) coordination compounds are kinetically labile, so their use as building blocks looks more challenging, but some encouraging examples of the application of pre-formed complexes as reactants in synthetic chemistry are already known. For example, a square-shaped nanogrid was prepared by Glazer oxidative homocoupling[54] and a rotaxane was obtained in good yield by the use of click chemistry to perform a stoppering reaction on a Cu^I complex functionalized with azide groups.[55]

Suzuki cross-coupling was chosen as a test reaction to verify the possibility of a further structural modification directly on the synthesized structures **C6** and **C7**. The two complexes are the most sterically hindered of the series, and therefore the most shielded against any external nucleophilic attack. Nevertheless, the Suzuki cross-coupling conditions are quite challenging for a labile complex: in the chosen protocol, water and 1,2-dimethoxyethane (potentially coordinating solvents) are used at reflux temperature and the reaction is performed in presence of a nucleophilic base (barium hydroxyde). Moreover, the catalyst is a metal different from copper, exhibiting a certain affinity for phenanthroline coordination cages, and in ligand scrambling conditions (high temperature, coordinating solvents) could favour the formation of a very complex reaction mixture.

As a proof of concept, the two bromo-terminated molecules were engaged in a $Pd(PPh_3)_4$ catalysed reaction with p-methoxy phenyl boronic acid, which is highly reactive thanks to the methoxy donating group, and polar, so that the separation of the homoleptic complex from the heteroleptic one is expected to be easier. The products, **C9** and **C10**, were isolated in 34 and 84% yield, respectively. These very different results (confirmed by the repetition of the reaction) can be rationalized by the greater activation of the C-Br bond in the latter case, given the electron withdrawing character of phenazine. A considerable quantity of unreacted **C9** was found after purification, further supporting this hypothesis.

Interestingly, only a small quantity of homoleptic complex was formed during the reaction (about 5% of the final product by estimation from ^{1}H-NMR spectra). The complexes are then stable enough to withstand the simultaneous presence of a oxygenated bases and solvents at high temperatures. Unfortunately, the retention factor of the homoleptic and heteroleptic complexes on silica gel was very similar in the case of **C9** and prevented from getting satisfactory microanalysis.
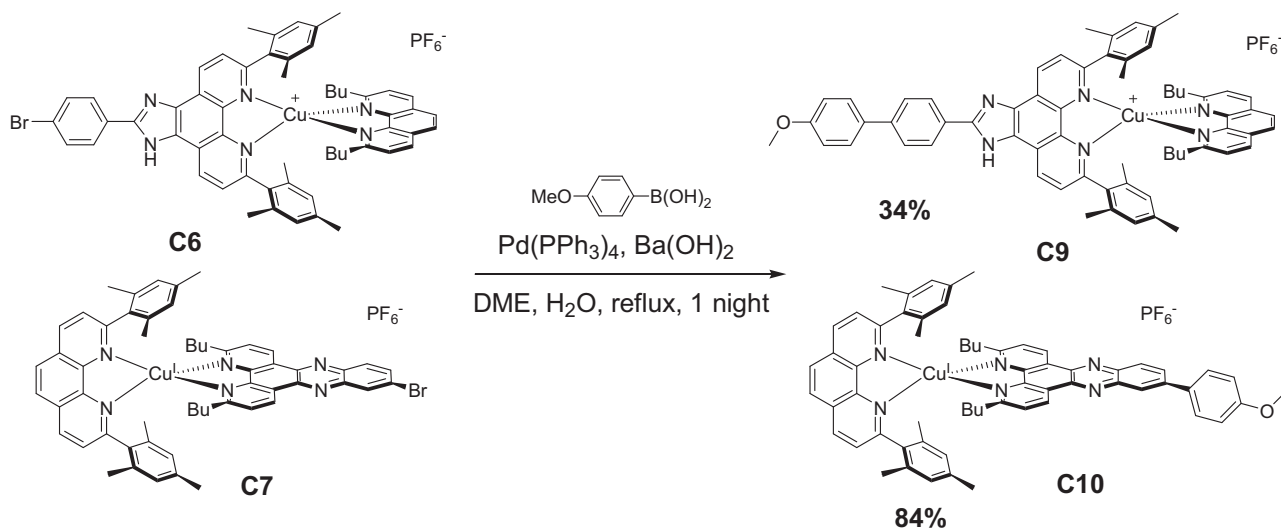
Scheme 2. 15. Suzuki cross-coupling on complexes **C6** and **C7**.

In conclusion, it was proven that it is possible to chemically modify the structure of preformed complexes to obtain more elaborated systems. This, besides proving the stability of our systems, offers an extreme synthetic versatility and paves the way towards the conception of complex arrays.

2.3.3. X-Ray structure of C7 and computated structures of C4-C8

Slow diffusion of cyclohexane into a solution of **C7** afforded good quality crystals, suitable for a structure resolution by X-Ray diffraction at 100 K. The obtained structure (Fig. 2. 13) confirmed the hypothesized geometry for the metal centre: a very distorted symmetry (with flattening, rocking and wagging distortions), where the copper(I) ion is surrounded by the four nitrogen atoms of the ligands, forming a distorted trigonal pyramid. The mesityl ring B is parallel to the dppz ligand, with a distance of about 3.5 Å.

The complex crystallizes in a triclinic crystal lattice (α = 73.945°; β = 83.606°; γ = 85.364°; a = 13.6027 Å; b = 14.2161 Å; c = 15.44 Å; P1 space group). In the crystal, the molecules are disposed in a sort of head-to-tail arrangement with the planes of all the dppz ligands which are parallel to each other, as those of the phenanthrolines of **L1**. The cell also contains the PF$_6^-$

counterion and one dichloromethane molecule. The distortion is quantified by the three angles $\theta_{flattening} \approx 69°$, $\theta_{rocking} \approx 61°$ and $\theta_{wagging} \approx 66°$, leading to an overall ξ of about 0.64. The two mesityl rings form an angle of 64.11° (ring A) and 72.97° (ring B) with the phenanthroline core of **L1**.
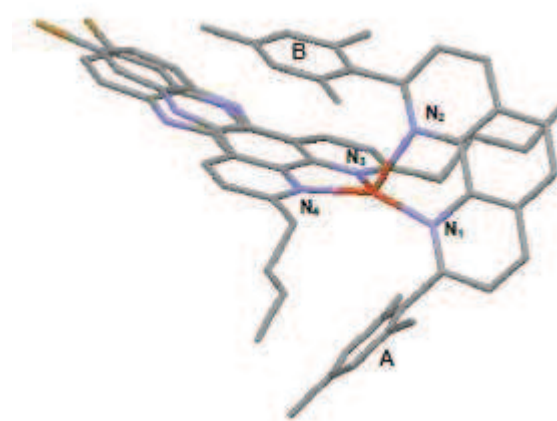
Fig. 2. 13. X-Ray structure of complex **C7**. Hydrogen atoms, PF_6^- and solvent molecules have been removed for clarity. Cu: orange; N: blue; C: grey; Br: brown.

The Cu(I) ion is bound to the ligands through four non equivalent bonds (see Table 2. 4) and each ligand establishes a longer and a shorter bond, of about 2.10 and 2.01 Å respectively.

The most puzzling feature of this structure is that the bromo unit seems to give two signals for each molecule. Indeed, while the copper coordination sphere is very well defined, the **L7** moiety is subjected to a very disordered environment. As there was no doubt about the structure of the complex, which had been confirmed by all the analytical techniques, the explanation was found in the fact that the bromo substitution on the dppz entails the existence of two possible regioisomers that crystallize almost in the same way. It was however possible to fit the complex diffraction pattern by considering a ratio of 3:7 between the two isomers, whose superimposition is shown in Fig. 2. 13, with a very satisfying R factor. This quite peculiar phenomenon had already been observed for the complex [ReCl(CO)(dppzBr)], where dppzBr is equivalent to **L7** but devoid of *n*butyl chains.[23]

The structures of the complexes **C4**-**C8** were also optimized using density functional theory (DFT/PBE-D/TZP) in the Daniel group at the University of Strasbourg. Selected theoretical bond lengths and angles are reported in Table 2. 4, together with the corresponding experimental data for the complex **C7**, for comparison. The optimized structures are represented in Fig. 2. 14. The optimized geometries compare rather well with the X-Ray data, even if the Cu-N bond length appears slightly underestimated. Interestingly, the calculated structures foresee π-stacking interactions for all the complexes except **C4** and **C5**, which do not possess the bulky *n*-butyl chains.

77

These two compounds have a more symmetrical structure, with very close Cu-N bond distances and N_1-Cu-N_4 angles. These differences may be attributed to the steric hindrance of *n*Bu groups, and to π-stacking between one mesityl group and the opposite phenanthroline.

Geometrical parameters		C1	C4	C5	C6	C7[a]	C8
Cu-N$_{PhenA}$	**Cu-N$_4$**	2.011	1.996	2.003	2.005	2.003 *2.009*	1.999
	Cu-N$_3$	2.075	2.025	2.028	2.060	2.075 *2.115*	2.072
Cu-N$_{PhenB}$	**Cu-N$_1$**	2.017	2.006	2.020	2.014	2.008 *2.004*	1.999
	Cu-N$_2$	2.071	2.023	2.031	2.057	2.075 *2.124*	2.068
N$_{PhenB}$-Cu-N$_{PhenB}$	**N$_3$-Cu-N$_4$**	82.36	83.27	83.35	82.65	82.15 *81.45*	82.24
N$_{PhenA}$-Cu-N$_{PhenA}$	**N$_1$-Cu-N$_2$**	81.96	82.12	81.88	82.32	82.26 *81.98*	82.49
N$_{PhenB}$-Cu-N$_{PhenA}$	**N$_3$-Cu-N$_1$**	124.32	133.08	131.84	124.87	124.55 *123.38*	124.52
	N$_2$-Cu-N$_3$	98.68	109.35	109.10	100.42	97.31 *95.53*	96.75
	N$_1$-Cu-N$_4$	143.09	123.85	127.58	142.04	144.47 *147.18*	144.67
	N$_2$-Cu-N$_4$	122.21	131.24	127.58	121.34	120.47 *119.68*	120.10

Table 2. 4. Selected bond lengths (in Å) and bond angles (in deg) of complexes **C1** and **C4-C8**. The numbering of the atoms is in accord with the structures depicted in Fig. 2. 14. Phen[A] and Phen[B] refer respectively to mesityl and non-mesityl derivatized ligands. [a] The values in italics are the experimental values measured from the X-Ray structure.

It is important to note that the choice of the functional has dramatic consequences on the obtained structures: the first optimization, made with B3LYP functional, had produced symmetrical molecules, without the least trace of π-stacking. Finally, PBE proved to afford much more reliable results, in good agreement with the experimental data.[56]
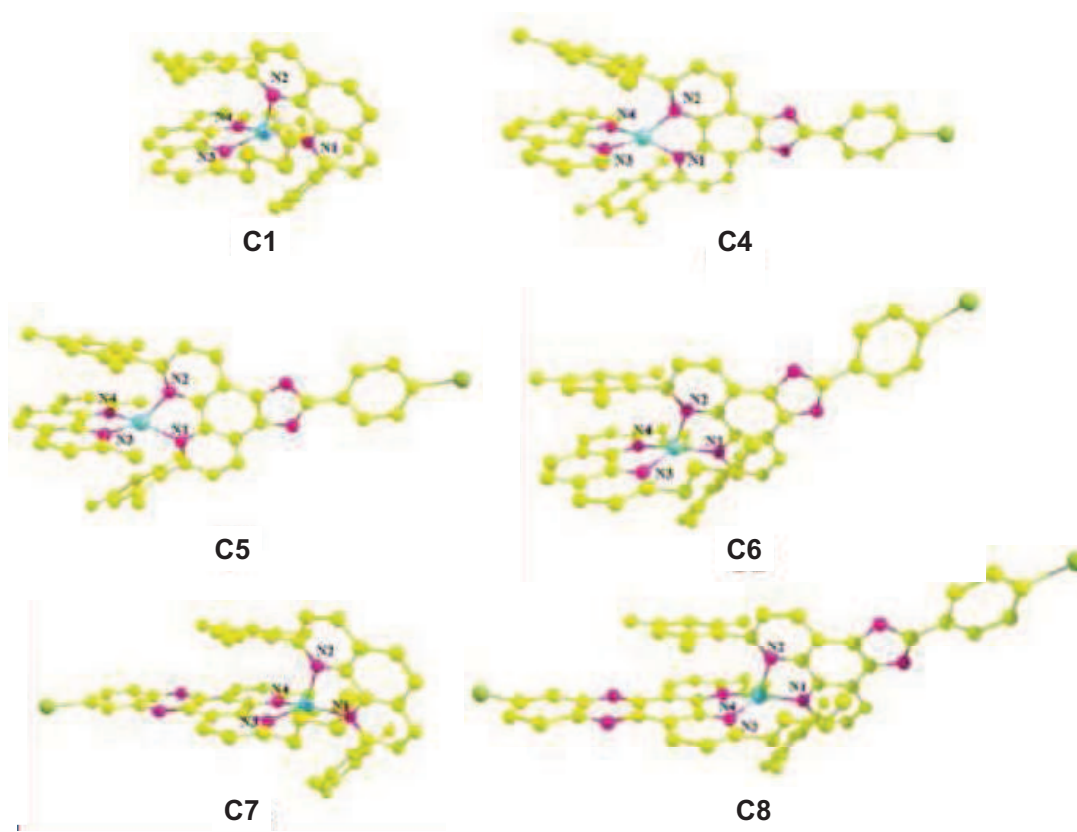
Fig. 2. 14. Calculated structures of the complexes **C1** and **C4-C8** (DFT/PBE-D/TZP).

2.3.4. UV-Visible absorption and calculated spectra for the complexes C4-C8

The electronic absorption spectra of complexes **C1** (model) and **C4-C8** are shown in Fig. 2. 15, and the corresponding data are collected in Table 2. 5.

All the complexes exhibit very intense UV bands below 360 nm, that were assigned to ligand-centred π-π* transitions. The quantum mechanical calculations confirmed their mixed nature, with IL, LLCT and MLCT components. The complexes containing the dppz-based **L7** have an additional vibrationally resolved band with two peaks at about 386 and 366 nm, typical of aromatic systems with fused rings.

The visible region of the spectrum is dominated by the classical copper(I) diimine complexes MLCT broad band, around 460 nm. The corresponding transition consists in the displacement of the electron density from the copper-centred HOMO to the ligand-centred LUMO, yielding a final charge separated state that can be described as Cu^{II}-Phen$^{\cdot-}$. The energy of the band is only slightly affected by the complexes structure, except for **C4** that absorbs at a notably higher wavelength (476 nm). The reason lies in the steric hindrance of the coordination cage: as reported in literature, bulkier substituents prevent the flattening of the complex in the excited state and make the formal oxidation of the Cu centre more difficult, raising the energy of the MLCT state.[2,38] Indeed, **C4**, with

a mere phenanthroline opposite to the ligand **L6**, has the most flexible coordination sphere among this series. The complex **C5** has an intermediate absorption wavelength between **C4** and the other compounds, owing to the presence of the methyl groups of **dmp**.
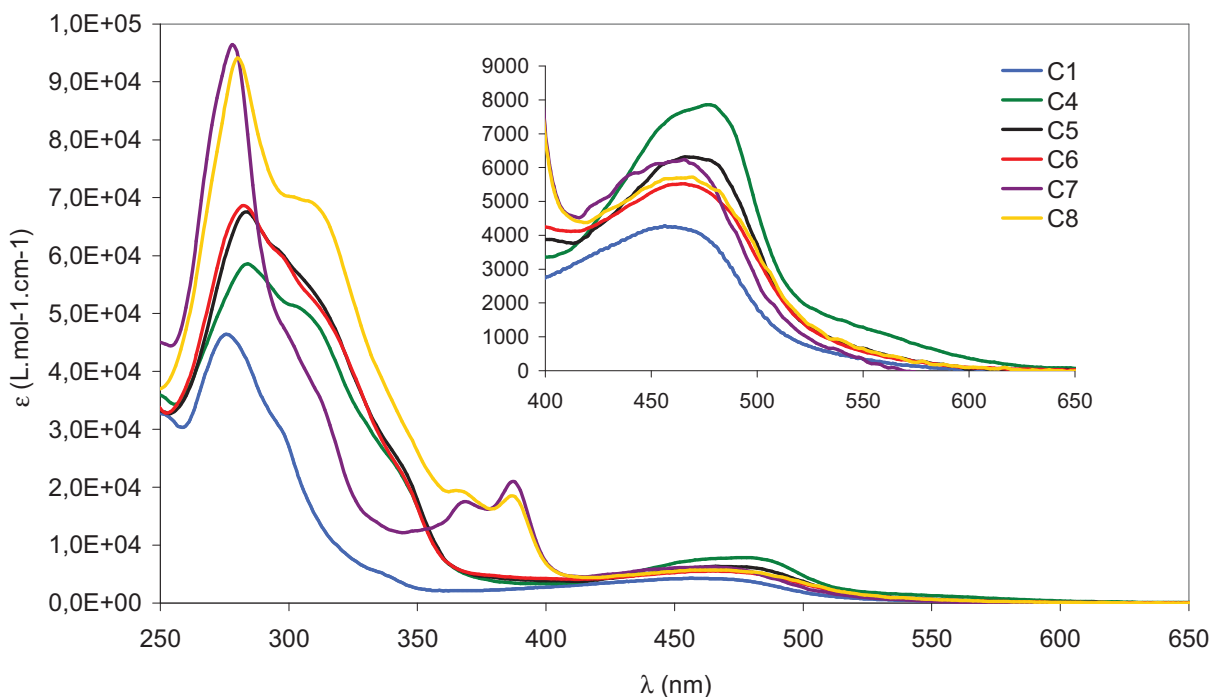
Fig. 2. 15. UV-Visible absorption spectra of the complexes **C1** and **C4**-**C8**, recorded in dichloromethane. Inset: magnification of the 400-600 nm domain.

Another interesting feature is the broad shoulder at around 550 nm in **C4** spectrum. This characteristic is diagnostic for a D_2 deformation of the complex, that breaks the symmetry of the structure and allows the $S_1 \leftarrow S_0$ transition.[57] The transition which is responsible for this shoulder, however, is much weaker than in complexes built on phenyl substituted phenanthrolines, like [Cu(**dpp**)$_2$]PF$_6$ (**dpp** = 2,9-diphenyl-1,10-phenanthroline). In those compounds, the strong deformation is due to π-stacking interactions between the phenyl rings and the opposite phenanthroline.

The energy of the MLCT band of **C1** is slightly blue shifted compared to the other compounds, and interestingly it is very similar to that of [Cu(neocuproine)$_2$]$^+$. The coordination cage of **C1** and **C6**-**C8** is practically the same, and thus cannot be invoked to explain this experimental data. On the other hand, the extended conjugation in **L6** and **L7** is certainly responsible for a stabilization of the MLCT state, however quite weak. Moreover, the existence of a dipole in heteroleptic complexes could be held responsible for an MLCT state stabilization. In **C1** the dipole is less pronounced, and the absorption wavelength is thus a little shorter.

	λ_{abs} (nm) [ε (M^{-1}cm^{-1})]
C4	476 [7.9·10^3]; 284 [5.9·10^4]
C5	468 [6.3·10^3]; 284 [6.8·10^4]
C6	463 [5.5·10^3]; 282 [6.9·10^4]
C7	465 [6.3·10^3]; 388 [2.1·10^4]; 368 [1.7·10^4]; 278 [9.6·10^4]
C8	467 [5.7·10^3]; 386 [1.8·10^4]; 366 [1.9·10^4]; 280 [9.4·10^4]

Table 2. 5. Absorption data for the complexes **C4**-**C8** recorded in dichloromethane.

The molar extinction coefficients, from 5.5 to 7.9·10^3 M^{-1}cm^{-1}, are in good agreement with published data on copper(I) bisphenanthroline complexes.[6,58] The sterically challenging mesityl groups are twisted with respect to the phenanthroline (about 65-75º), and this dramatically reduces the conjugation of the system. For this reason, the electronic spectra of **L6** and its unsubstituted homologue (2-*p*-bromophenylimidazo[4,5-*f*][1,10]phenanthroline) have similar features. The remarkable difference between the intensity of the MLCT band for **C1** and **C4**-**C8** can probably be explained by considering the significant electron delocalization on the π systems of **L6** and **L7**, yielding higher dipolar moments.

The spectra of dichloromethane or acetonitrile solutions of these compounds remain unchanged in time even if exposed to atmospheric oxygen and moisture, indicating that the complexes are stable and do not undergo oxidation to copper(II), or ligand loss.

The theoretical absorption spectra of **C1** and **C7** were calculated in vacuum, and are helpful to confirm the nature of electronic transitions. The low energy MLCT band is composed by charge transfer transitions towards the two phenanthroline ligands, while the higher energy bands (UV absorption) are characterized by a mixture of intra-ligand, ligand-to-ligand and metal-to-ligand charge transfer transitions.

2.3.5. Electrochemical properties

The electrochemical properties of the five complexes were investigated in distilled, argon purged dichloromethane, and are here compared to those of **C1**, which acts as a model compound sharing the same coordination cage than **C6**, **C7** and **C8**. The data are gathered in Table 2. 6.

All the compounds show a quasi reversible[37] oxidation wave, which corresponds to the removal of an electron from the metal-centred HOMO and thus the oxidation of Cu^{I} to Cu^{II}.

The $E_{1/2}$ value is strongly dependent on the coordination sphere steric hindrance, and follows this order:

C4 < C5 < C6 < C1 < C7 ≈ C8

When the copper(I) complexes are oxidized, they undergo a shift from a pseudo-tetrahedral to a flattened geometry, the most stable for $[Cu^{II}(Phen^A)(Phen^B)]^{2+}$. If such a deformation is prevented by the presence of bulky groups at the 2 and 9 positions of the phenanthrolines, the oxidized form is destabilized and the oxidation potential shifts anodically. So, as a general rule, the most hindered the coordination cage, the higher the oxidation potential (when the rest of the structure is equivalent).

Indeed, in the case of **C4**, a mere phenanthroline is opposed to **L6** and the complex is therefore more prone to a flattening distortion upon formal oxidation of Cu(I) to Cu(II), thus more easily oxidized. The coordination sphere of **C5** is composed of dimethylphenanthroline and dimesitylphenanthroline, and has therefore an intermediate steric hindrance between **C4** and **C6**, resulting in an intermediate oxidation potential. The simultaneous presence of butyl chains and mesityl rings in the coordination cage considerably increases the value of $E_{1/2}$ for **C1**, **C6**, **C7** and **C8**. The value is slightly lower for **C6**, probably because of the mild donating properties of the imidazole ring. *Vice versa*, the electron withdrawing properties of the dppz moiety in **L7** could account for the higher oxidation potential of **C7** and **C8**, that share the same coordination cage as **C1** and **C6** but are less prone to oxidation.

	$E_{1/2}$ (V) vs.SCE [$\Delta E = E_{pa} - E_{pc}$ mV][a]
C1	0.99 [110]
C4	0.71 [95]
C5	0.87 [95]
C6	0.94 [105]
C7	-1.09 [95], 1.06 [85]
C8	-1.03 [80], 1.05 [140]

Table 2. 6. Oxidation and reduction potential of the complexes **C1** and **C4-C8**, recorded in distilled, argon purged dichloromethane. WE: Pt disc; RE: SCE; CE: Pt foil; supporting electrolyte: TBAPF$_6$ 0.1 M. [a] The ΔE values are reported for a 100 mV/s scan rate.

The cathodic behaviour of the complexes was investigated as well, in the limits imposed by the solvent and our experimental setup. No reduction wave was observed for **C1**, **C4**, **C5** or **C6**,

confirming the literature data[2] according to which the phenanthroline based reduction occurs at more cathodic potentials than -1.5 V vs. SCE (limit of our operating window). On the contrary, **C7** and **C8** show well-defined, reversible reduction waves at $E_{1/2}$ = -1.09 and -1.03 V vs. SCE, respectively. Based on the comparison with literature data for complexes containing the same dppz motif, on the shape of the wave and on the apparent insensitivity to the complementary ligands, these were assigned to the addition of one electron to the phenazine moiety.

To further prove this assumption, cathodic spectroelectrochemistry was performed on **C7**. Several spectral changes were observed upon electrolysis (Fig. 2. 16): the growth of a broad shoulder around 560 nm and the decline of the **L7** centred bands at 275 and 380 nm. These features are characteristic of metal-bound dppz[.-] radical anion formation.[59] The spectrum is moreover characterized by the presence of isosbestic points, proving the formation of only one species. Interestingly, the position and intensity of the MLCT band remain nearly unchanged, confirming the weak electronic coupling between the phenazine and the $[Cu(Phen)_2]^+$ core, another feature shared with Ru-dppz complexes.
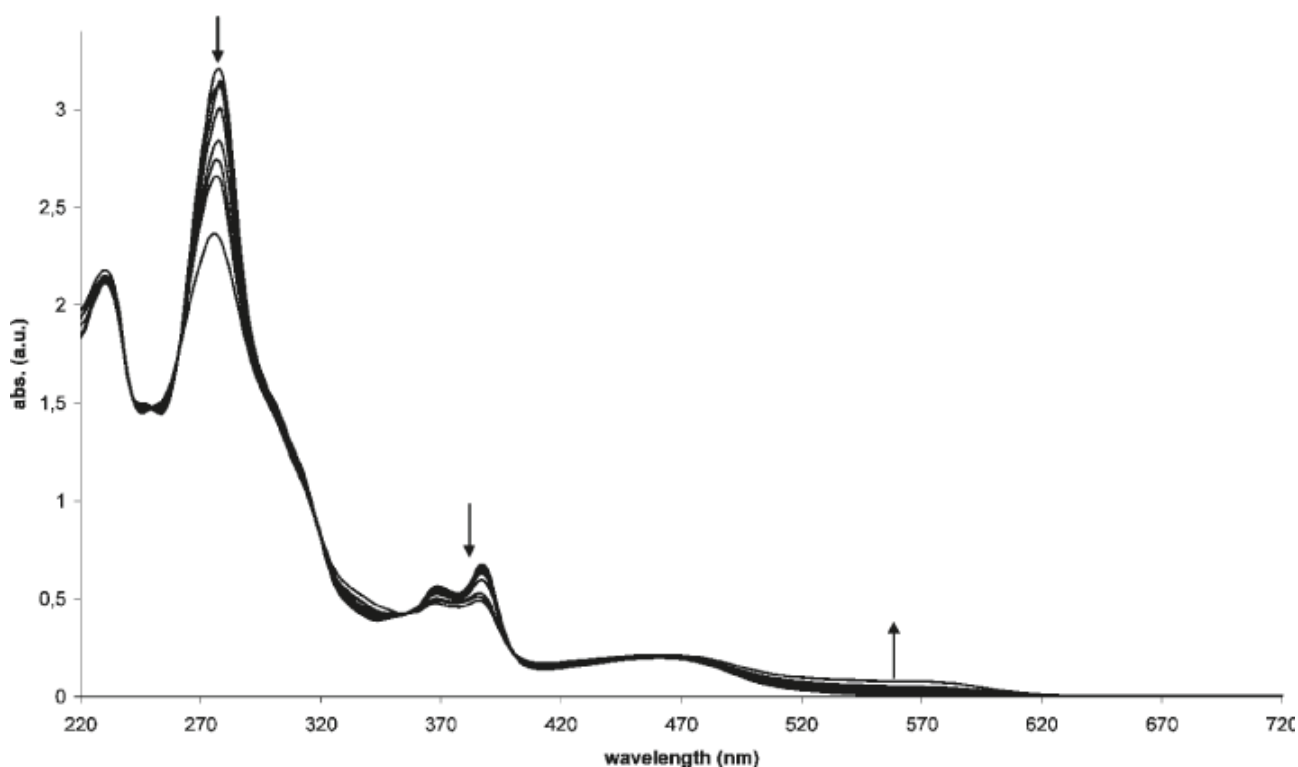
Fig. 2. 16. Evolution of the absorption spectrum of **C7** upon cathodic electrolysis. The experiment was performed in dichloromethane, with TBAPF$_6$ as a supporting electrolyte and a platinum grid as the working electrode.

2.3.6. Luminescence

The photoluminescence of the five synthesized complexes was studied in dichloromethane and acetonitrile. **C1** was used as a first tool to assess the ligand mobility in the coordination sphere. As already mentioned, the challenge for increasing the emission of copper(I) diimine complexes consists in preventing the flattening distortion in the excited state and consequent "exciplex quenching".[41] The emission spectra and the decay of the emissive excited states (nanosecond flash photolysis) are shown in Fig. 2. 17, and the luminescence data are collected in Table 2. 7.
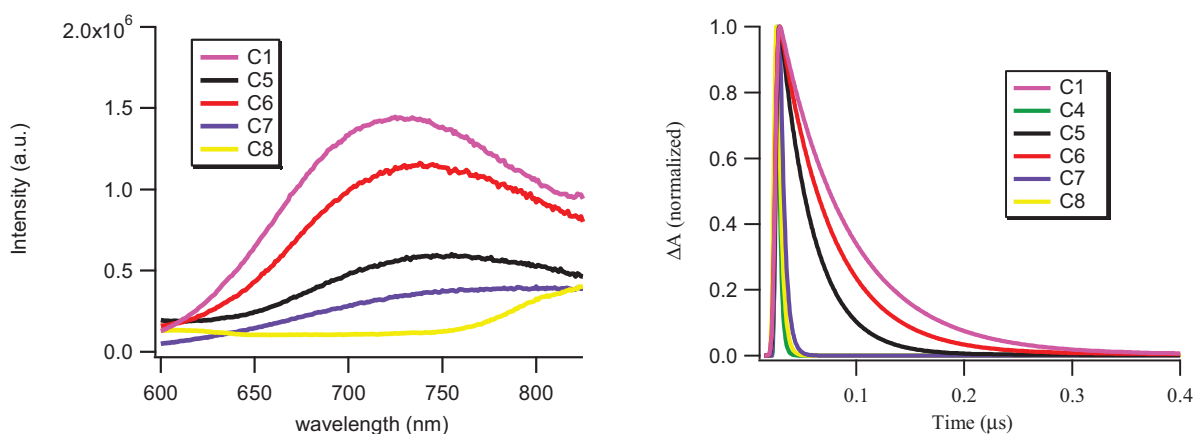
Fig. 2. 17. Emission spectra and excited-state decays for complexes **C1** and **C4-C8**, recorded in degassed dichloromethane. The absorbance value at the excitation wavelength and the slits opening are the same for all the compounds.

	CH$_2$Cl$_2$	CH$_3$CN
	λ_{em}(nm) [τ^a (ns)]	
C1	730 [64]	738 [25]
C4	nd [≤4]	nd [≤4]
C5	754 [31]	753 [21]
C6	740 [52]	743 [30]
C7	~ 800 [5]	~ 730 [≤4]
C8	> 800 [≤4]	> 800 [≤4]
C6'	735 [48]	~735 [24]

Table 2. 7. Emission wavelength and excited-state lifetimes of complexes **C1** and **C4-C8**, recorded in degassed dichloromethane or acetonitrile. [a] Lifetime determined by nanosecond flash photolysis.

The emission spectra consist in very broad and red-shifted bands. This feature is characteristic of MLCT luminescence,[40] and the large Stokes' shift (8000-9000 cm^{-1}) indicates that

the excited state undergoes an important geometrical change before relaxing to the ground state. The comparison of the spectra recorded in dichloromethane and acetonitrile evidences a very slight bathochromic shift and a remarkable decrease of the excited-state lifetime (Table 2. 7) in the latter. Indeed, acetonitrile is more coordinating than dichloromethane and for this reason efficiently quenches the emissive state by exciplex formation (pentacoordinated Cu^{II}).

The measurements in dichloromethane deserve some further comments. The influence of the extent of the steric hindrance of the coordination sphere, already observed for homoleptic complexes, is well represented by the three complexes **C4**, **C5** and **C6**, sharing the ligand **L6**. While **C4** is completely non emissive, **C6** has nearly the same emission intensity as **C1**, indicating that the fused imidazole ring does not impact, to a significant extent, the luminescence properties. **C5** has an intermediate value, due to the presence of the moderately bulky methyl groups in the coordination sphere. The comparison is done by recording all the emission spectra in the same conditions (matching absorbance at the excitation wavelength as well as slits opening) and comparing the luminescence intensities.

Another interesting aspect is the absence of luminescence of **C7** and **C8**. These two complexes are barely emissive, displaying extremely broad and shallow emission bands, an effect due to the ligand **L7**. The dppz unit is known, from previous studies on Ru^{II} complexes, to behave like a weakly coupled dyad, where the two units (dipyrido and phenazine) behave nearly independently.[59] The luminescence quenching is therefore assumed to be due to a fast electron transfer to the phenazine unit. This hypothesis was further confirmed by nanosecond transient absorption spectroscopy (see following paragraphs), which was used to follow the relaxation of the triplet MLCT state of **C7**. The transient trace is red shifted with respect to the other complexes of the series, and shows a resemblance with the copper-bound dppz$^{\cdot-}$ signal obtained from the spectroelectrochemical data. The quenching was then explained by a fast electron transfer from the Cu^{I} to the dppz moiety to form a short lived charge separated state, followed by charge recombination on the nanosecond timescale.

The emission properties of **C6'** are very similar to those of **C6**, indicating that the alkyl chain, and the lack of the labile proton on the imidazole, have a negligible influence on the photoinduced processes.

2.4. Time-resolved photophysical characterization of the complexes

The use of molecules in solar energy conversion requires the knowledge of different parameters, as those derived from electrochemistry, absorption and steady-state emission in order to assess the thermodynamic aspects for each process.

Optical time-resolved spectroscopy is a useful tool to study the dynamic processes of a system using spectroscopic techniques. Among these pump-probe techniques, UV-visible transient absorption allows to follow the evolution of the molecules after an instantaneous pulse excitation. This is done by measuring the variation of the electronic absorption spectrum from femtosecond to millisecond timescale. This part of the project was carried out in the *LAboratoire de Spectrochimie Infrarouge et Raman* (LASIR) in Lille by Dr. Michel Sliwa, Dr. Mateusz Rebarz and Dr. Olivier Poizat (chapters 2, 3 and 4).

UV-visible transient absorption consists of an intense monochromatic excitation laser pulse ("pump beam"), exciting the analyte (about 10%), and a weak white light beam which "probes", the excited molecules generated by the pump pulse. This technique is widely used for the study of photoactive systems, and in particular in this thesis it will appear in chapter 2 and 3 for the investigation of the relaxation dynamics of copper(I) complexes and in chapter 4, for the study of photoinduced charge transfer processes. In this paragraph, the technique and the results obtained on the previously described compounds will be reviewed.

2.4.1. Transient absorption: principles and experimental setup

The transient absorption signal is given by the difference between the absorption signal of the excited sample after the pump pulse, and the absorption of the solution without pump. It is a non dimensional number and is expressed as ΔA. This treatment is necessary because the pump pulse usually only excites a relatively small fraction of the sample molecules, and the spectral changes would be more delicate to observe and dependent on the probe light intensity.[60]

$$\Delta A = A_{pump} - A_{GS}$$

where GS is the ground state.

The global result obtained after a complete experiment is a surface that describes the ΔA evolution as a function of λ and τ, i.e. $\Delta A(\lambda,\tau)$.[61] The section of this surface at a fixed wavelength gives information about the kinetics of the decay, while if the time τ is kept constant the spectrum of the transient species present at that time is obtained.

The main contributions to the transient absorption spectrum are:

- *ground state bleach*: due to the depopulation of the ground state, it appears as a negative peak at the ground state absorption wavelength (the weak probe light does not influence the excited population);

- *excited state absorption*: this contribution corresponds to the optically allowed transitions of the molecules in the excited state, and therefore is represented by positive bands in the transient absorption spectrum. As in the previous case, the excited state population is not noticeably lowered;

- *photoproducts absorption*: if the studied system evolves to give products, isomers or charge-separated states, their absorption will give rise to positive bands in the spectrum.

- *stimulated emission*: as the Einstein coefficients for ground state absorption (A_{12}) and stimulated emission (A_{21}), for a two-level system, have the same value, the population of the excited state results in the emission of photons in the same direction as the probe pulse. These photons provoke an increase of the light intensity collected by the detector and therefore contribute as negative signals, with a profile in the region of the fluorescence spectrum.

An electronic detector can follow variation of few hundred picoseconds and thus the experimental setup will be different for femtosecond (femtosecond to nanosecond) and nanosecond (nanosecond to millisecond) transient absorption techniques. The two experimental setups used for nanosecond and femtosecond scale transient absorption experiments will be briefly described before presenting the results.

2.4.1.a. Nanosecond transient absorption

The nanosecond transient absorption setup is constituted by two independent light sources. The pump beam is a nanosecond laser pulse whereas the probe beam is a white light delivered from a stationary Xenon lamp.

The pump beam is generated by a 10Hz, 1064 nm, 4 ns Nd:YAG laser (Continuum Surelite II) , tripled at 355 nm and coupled to an Optical Parametric Oscillator (Continuum Panther EX OPO) and SH05 shutter (Thorlabs). The pump wavelength can thus be selected from 355 nm to 2550 nm. The white light (probe) is generated by a Xe arc lamp, and hits the sample cuvette at 90º with respect to the pump. The output signal is then selected through a monochromator and recorded by means of a photomultiplier tube. To increase the signal-to-noise ratio the Xenon pulse and transient signal are measured during a 400 microsecond plateau (Fig. 2. 18, inset). The recorded traces for one wavelength are averaged for several pulses and repeated for different wavelengths to

reconstruct the spectra afterwards. The instrument has a 4 ns time resolution. Samples were contained in a quartz cell (10×10 mm^2) and the concentration was adjusted ($\sim 10^{-4}$ mol dm^{-3}) to get an absorption value of about 0.5 at the pump excitation wavelength.
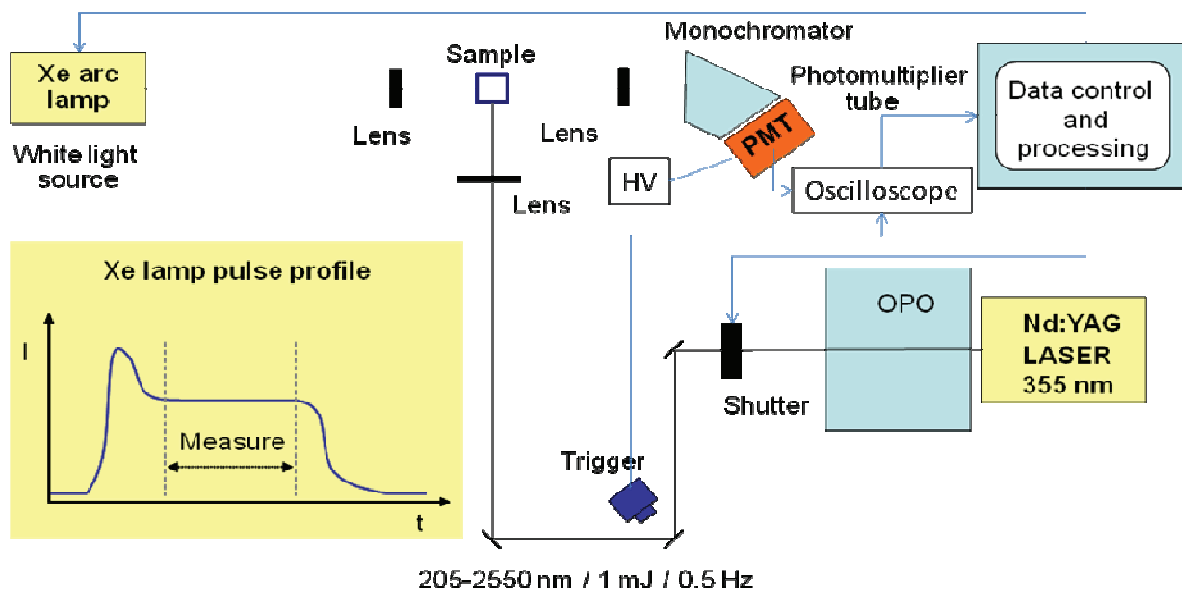
Fig. 2. 18. Scheme of the nanosecond transient absorption experimental setup.

2.4.1.b. Femtosecond transient absorption

The main aspect that distinguishes femtosecond from nanosecond transient absorption is the shorter timescale. This makes that the electronics are not fast enough to follow the decay of the signal any more. For this reason, the researchers had to elaborate a special setup, different from the one previously described: two femtosecond pulses (pump and probe) are used and the probe beam takes a picture (time resolution is within the pulse width) after a certain delay time after the excitation.[62]

The most widely used laser source is a Ti:sapphire laser system, that delivers pulses of about 1 mJ with a pulse duration of 80 fs. The fundamental beam is in a spectral range of 780 to 820 nm. The pump and probe beams are obtained by the beam-split technique: the monochromatic laser beam is split into two contributions, each of which is sent through a different optical path. The delay of the probe beam is obtained by a "delay line", which allows to tune the Δt between the pump and the probe pulses by mechanically moving the mirrors. A 15 μm displacement results in a 30 μm delay after the excitation, i.e. a Δt of approximately 100 fs. The continuum (white) light is generated through the use of an oscillating CaF$_2$ crystal and is further split in order to obtain the reference and the sample beam. The transient absorption measurement covers the 350–700 nm spectral range and the 0–2 ns time range. The instrumental response function is about 200

femtoseconds. The detector is a CCD camera, whose channels are split into two sets, one dedicated to the reference beam (that signal of the ground state sample) and the other to the sample (excited state sample, after the pump pulse). The sample cuvette path length is 1 mm. The studied compounds were diluted in the solvent at a concentration corresponding of OD=1 at the pump wavelength. The stability of the sample was checked after each experiment.
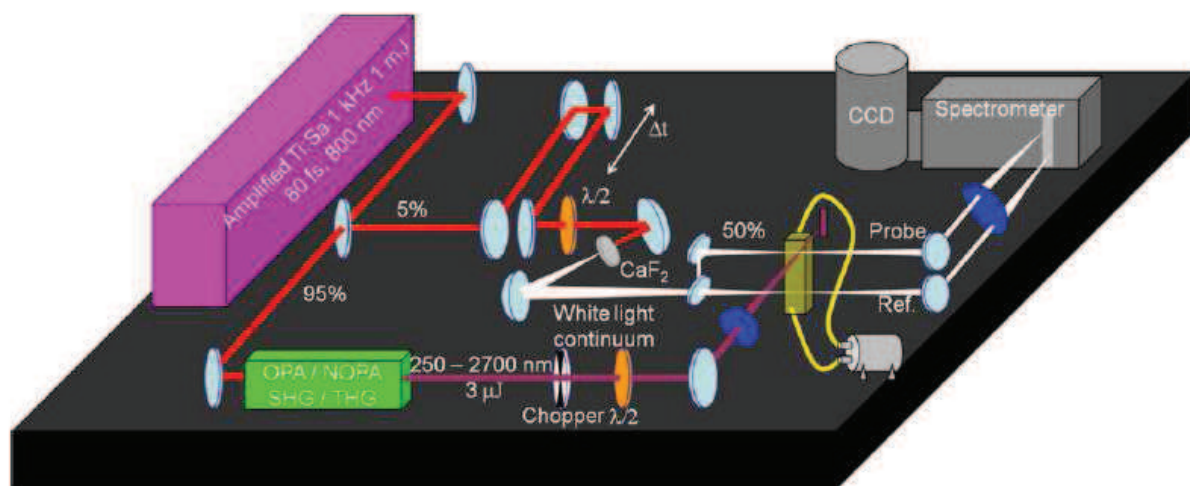
Fig. 2. 19. Scheme of the femtosecond transient absorption experimental setup.[63]

89

2.4.2. Photophysical study of the complexes C1, C6, C7 and C8

Heteroleptic complexes with and without imidazole and phenazine units (**C1**, **C6**, **C7**, **C8**) described previously were studied by transient absorption spectroscopy, in order to get insights into the evolution of the excited states.

The interpretation of nanosecond transient absorption spectra is quite straightforward. Fig. 2. 20 shows the evolution of transient absorption spectra after 460 nm excitation in dichloromethane in the nanosecond timescale for the heteroleptic complexes studied in this chapter. **C4** and **C8** have a ^{3}MLCT lifetime shorter than the instrument time resolution (4 ns).

>310, 390, 530, 570 nm   310, 350, 530, 570 nm   >350, 390, 530, 550, 590 nm

360, 400, 540 nm   360, 390, 550 nm   350, 400, 630 nm
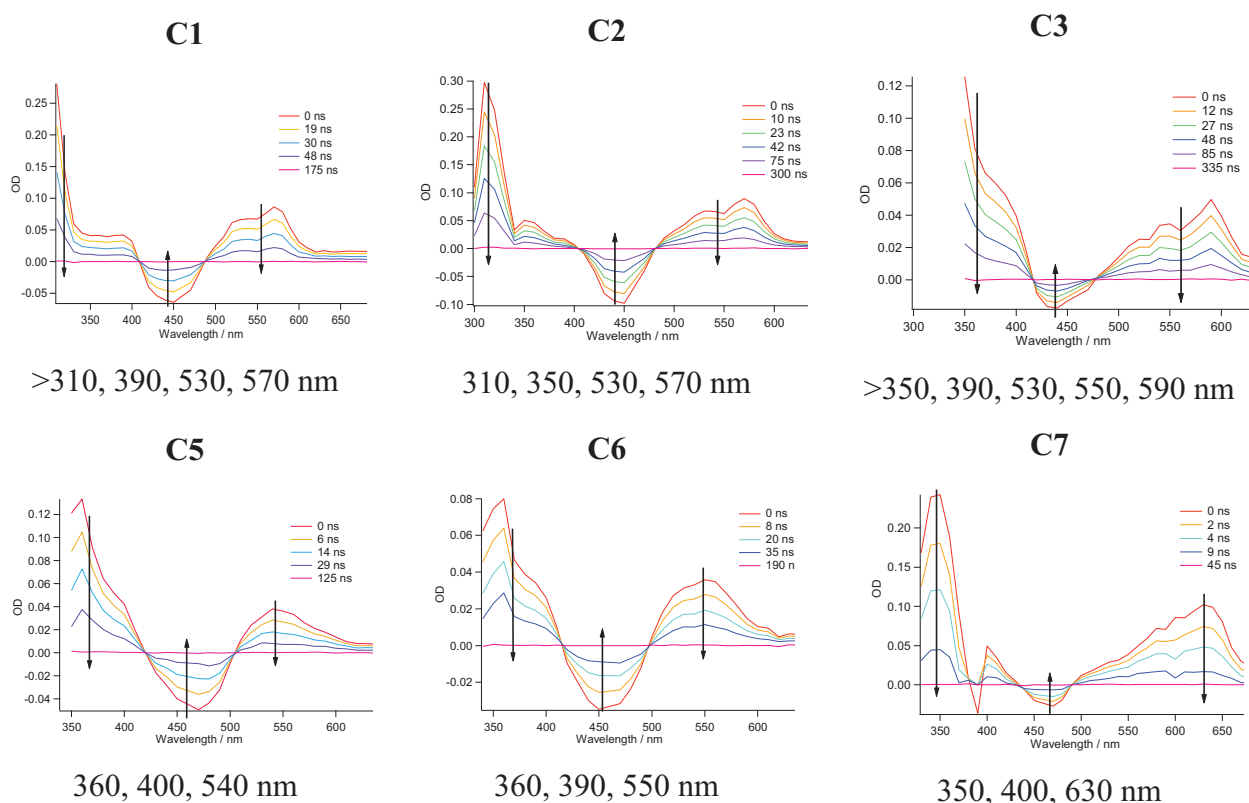
Fig. 2. 20. Nanosecond transient differential spectra at different time delays for heteroleptic complexes after 460 nm excitation in dichloromethane.

Two broad positive bands, 300 nm to 400 nm and 480 to 700 nm were observed, with a negative band between 400 to 480 nm assigned to the ground state depopulation signal of the MLCT. The ground state depopulation band and positive bands decay monoexponentially with the same time constant. As it was discussed before, this decay is equal to the longest luminescence decay. The positive bands are thus assigned to the excited emissive triplet MLCT state similarly to what is reported in the literature.[64] From Fig. 2. 20 we can see that **C1** and **C2** have similar spectra for the MLCT emissive state, with two maxima around 530 and 570 nm. **C3** has also similar

positive spectrum, however it is red-shifted of about 20 nm. This bathochromic shift for the triplet MLCT state can be explained by a slightly increased conjugation degree induced by the phenyl substituents. The effect is even stronger for dppz and leads to an absorption maximum at 630 nm. Furthermore, complexes **C5**, **C6** and **C7** display only one maximum in the visible part. This absence of vibrational structure could be assigned to a less rigid structure and explains the lower lifetime combined to higher efficiency for the excimer formation with coordinating solvent. Finally, one can see a second negative contribution at 390 nm for **C7**, which is due to the absorption of dppz in the ground state.

Femtosecond experiments and data analysis are quite time consuming, that is why we decided to focus only on the four complexes **C1**, **C6**, **C7** and **C8** which are quite representative of the series.

2.4.2.a. Complex C1

Femtosecond transient absorption spectra recorded within the first picosecond after 400 nm excitation pulse in acetonitrile (Fig. 2. 21, left) show the rise of three main bands: a broad absorption band covering the 320–430 nm domain with a maximum at 360 nm, a negative band in the 430–500 nm domain with a maximum at 460 nm (ground state depopulation), and a featureless broad absorption band covering the 500 to 650 nm domain. The latter undergoes a red-shift while growing. Both positive bands evolve then in a few tens of picoseconds: the high energy band decays while the broad band in the visible evolves by narrowing and blue-shifting, until reaching the final transient spectrum with two peaks at 533 and 574 nm which is the same spectrum obtained with nanosecond TA. There are three clear isosbestic points at 390 nm, 550 nm and 580 nm, which are characteristic of the evolution from A to B species. By comparison with the literature data obtained for homoleptic complexes,[64] the first process, occurring in about 0.2 ps, was attributed to the flattening of the Franck-Condon state directly formed after excitation. The slower one, occurring on a timescale of 10 ps, is instead due to the intersystem crossing to the flattened triplet state (T_1). Interestingly, the intensity of the negative band, a bleaching due to ground state depopulation, does not evolve during the ISC, suggesting quantitative formation of the triplet state. The rate constants of these early processes are not strongly influenced neither by the solvent nor by the excitation wavelength, as observed for homoleptic complexes.

Fig. 2. 21. Femtosecond transient absorption spectra of **C1** and **C6** in acetonitrile obtained for different time delays after 400 nm excitation (3 mJ.cm^2).

2.4.2.b. Complex C6

In acetonitrile, time evolution and transient spectra observed for **C6** (Fig. 2. 21, right) were similar to those of **C1**. It starts with a flattening in about 130 femtoseconds, followed by an intersystem crossing in about 12 ps. No change of the spectra is observed after 50 ps until 1 ns and the spectra corresponds to the one obtained by nanosecond transient absorption experiments, leading to the formation of triplet MLCT excited state about 100% (no decay of ground-state bleaching band). The only slight difference is that neither clear maxima nor isosbestic points were observed during the ISC step and only a decrease of the red part the spectra has occurred. As mentioned for nanosecond transient absorption spectra, **C6** has more vibrational degrees compared to **C1**, explaining this difference. Another hypothesis is that there is no clear difference between singlet and triplet MLCT, the lowest MLCT state has not a strong triplet character (its lifetime is quite oxygen insensitive) and the ISC is thus mainly only a vibrational cooling after flattening. This should be confirmed by theoretical calculations. To conclude, the time-resolved spectra of **C6** show an evolution very similar to that of **C1**, indicating, in line with the luminescence lifetime data, that the imidazole moiety does not have a strong influence on the formation and decay of the flattened triplet excited state.

2.4.2.c. Complexes C7 and C8

Fig. 2. 22 shows femtosecond transient spectra for **C7** and **C8** in acetonitrile after 400 nm excitation. They exhibit different features with respect to the previously described compounds, which can be attributed to the presence of the dppz moiety.

Concerning the rise of the transient absorption signals, the flattening time constant is shorter and a two-step process can be seen: at first, the rise of a band at 500 nm, then, a blue-shift to give the final positive band at 625 nm within 0.5 ps with an isosbestic point about 550 nm. The same experiments in dichloromethane show that this second step occurs within about 1 ps. The spectro-electrochemical study has shown that dppz radical anion has a broad absorption in the same region. Accordingly, the formation of 625 nm band can be assigned to an electron transfer from copper(I) to dppz moiety and could explain the difference of behaviour with respect to complexes **C1** and **C6**. The ISC step is also much faster (around 1.5 ps) and mainly characterized by a decrease of the red part and a blue-shift, like for **C1**. The reasons for the faster intersystem crossing are still unclear, but a lower energy gap between the flattened singlet and triplet states can be hypothesized. Moreover, the ISC is now involving dppz radical anion and the bromine atom could favour the triplet formation. Eventually, the final state decays in about 900 ps for both **C7** and **C8**. The lower energy gap between the excited and the ground state may induce a fast back electron transfer and a non radiative relaxation. Theoretical calculations on the different triplet / singlet / flattened / non flattened state are still in progress to get a deeper understanding of the behaviour of these complexes.
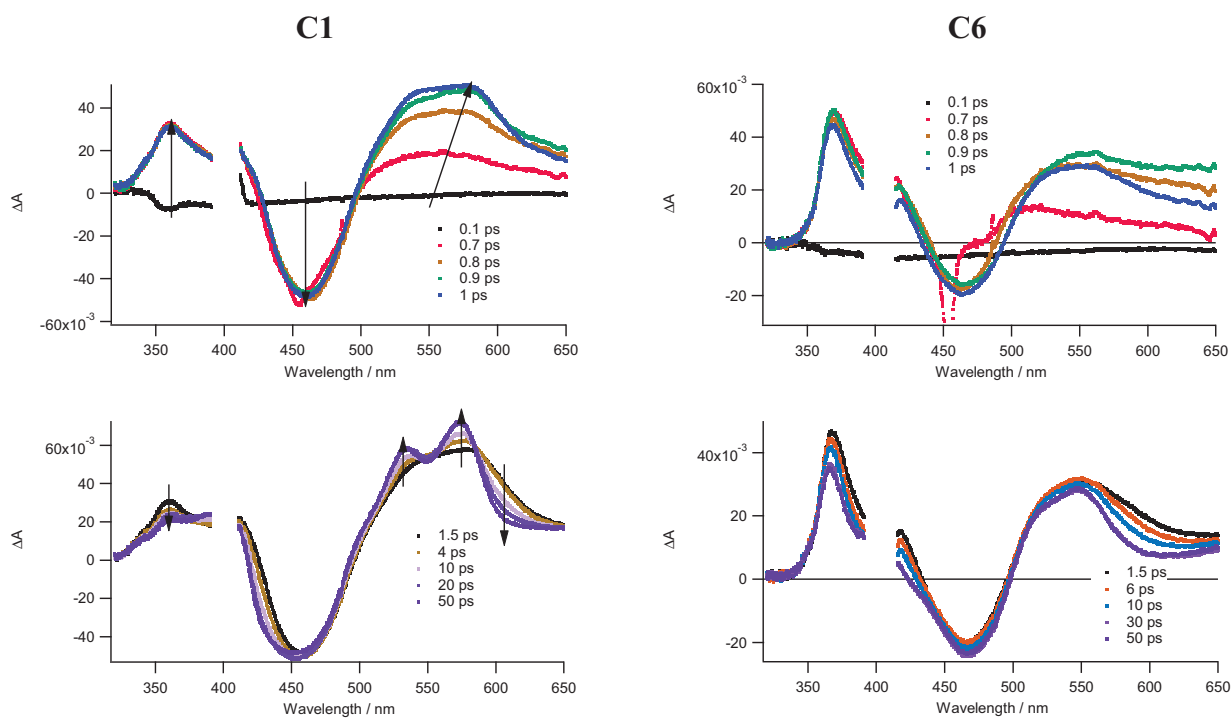
C7   **C8**
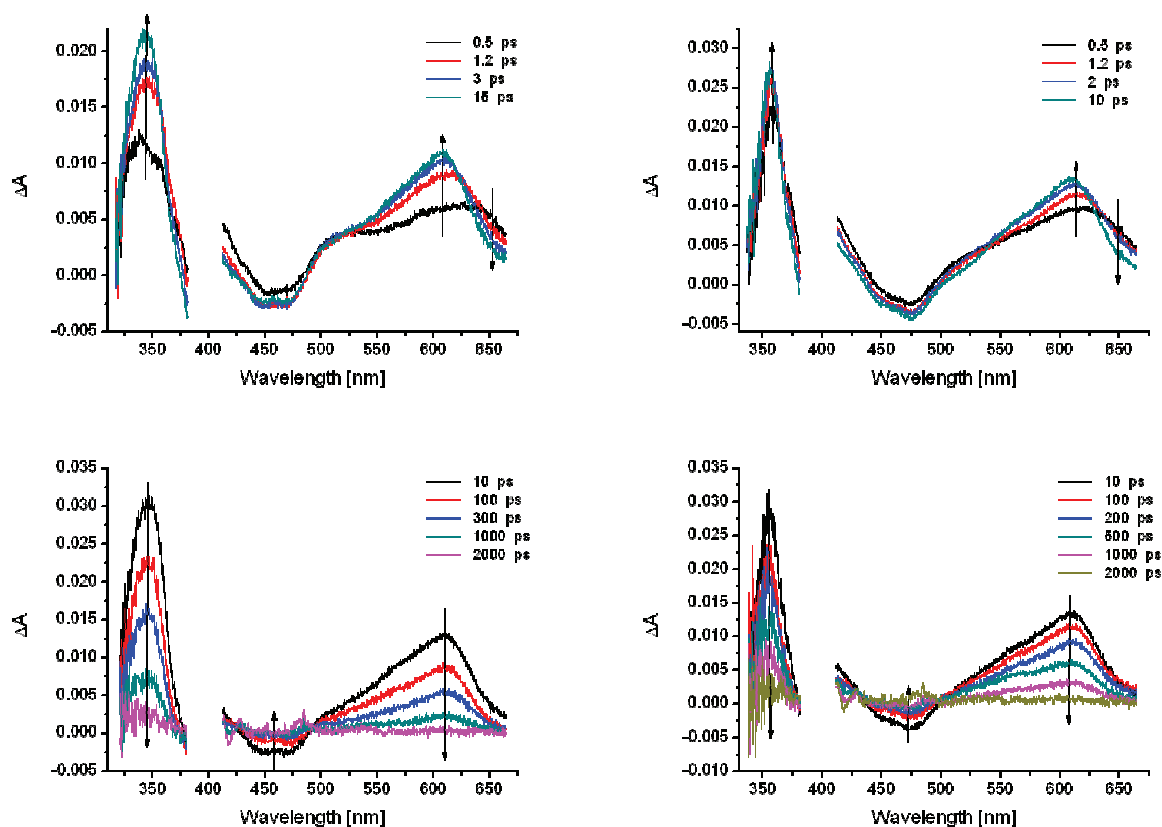
Fig. 2. 22. Femtosecond transient absorption spectra of **C7** and **C8** in acetonitrile obtained for different time delays after 400 nm excitation (3 mJ.cm^2).
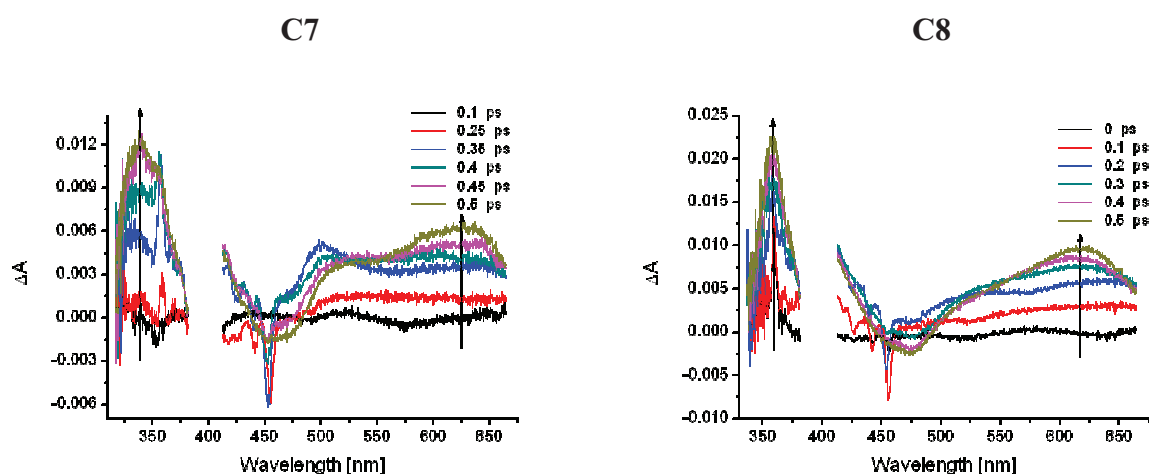
2.5. Conclusions

The HETPHEN synthetic approach was used to prepare different heteroleptic copper(I) complexes with an hindered coordination sphere in order to set-up the synthetic strategy and to elucidate the electro- and photochemical properties of this type of heteroleptic copper(I) diimine complexes. The photophysical and electrochemical characterization evidenced interesting properties. As their homopletic counterparts, the heteroleptic complexes **C1**-**C3** are good photoreductants but poor photooxidants. Moreover, the molecules are extremely stable in solution and are not degraded in presence of oxygen and atmospheric moisture. However, as evidenced by the stability tests, the contact with an excess of less hindered ligand must be avoided, since it leads to the formation of a mixture containing the homoleptic complex by fast ligand scrambling.

The second series of complexes presented in this chapter (**C4-C8**) is based on the use of two new ligands, **L6** and **L7**. Both ligands bear bulky groups at the 2 and 9 positions of the phenanthroline core, and allow the construction of stable heteroleptic copper(I) complexes using appropriate complementary ligands. The electrochemical and photophysical properties were found to depend on the steric hindrance of the coordination cage and the nature of the ligands. In

94

particular the electron withdrawing dppz ligand **L7** was observed to drastically quench the luminescence of the complexes, while the phenanthroline-imidazole moiety does not have a strong influence on it.

The complexes **C6** and **C7** were furthermore engaged in palladium-catalysed cross-coupling reactions with the anisylboronic acid, indicating that the complexes are stable even in quite hard temperature conditions and in presence of coordinating molecules. This opens the way to the increase of the structural complexity in quite a simple and rapid way.

The time-resolved photophysical studies indicate that the evolution of the excited states of these compounds is similar to that of the widely studied homoleptic copper(I) complexes, being characterized by a rapid flattening of the structure upon formation of the singlet MLCT state, followed by an intersystem crossing to the triplet MLCT and final decay to the ground state.

References

1. Pallenberg, A. J.; Koenig, K. S.; Barnhart, D. M. *Inorg. Chem.* **1995**, *34*, 2833-2840.
2. Miller, M. T.; Gantzel, P. K.; Karpishin, T. B. *Inorg. Chem.* **1999**, *38*, 3414-3422.
3. Cunningham, C. T.; Cunningham, K. L. H.; Michalec, J. F.; McMillin, D. R. *Inorg. Chem.* **1999**, *38*, 4388-4392.
4. Lavie-Cambot, A.; Cantuel, M.; Leydet, Y.; Jonusauskas, G.; Bassani, D. M.; McClenaghan, N. D. *Coord. Chem. Rev.* **2008**, *252*, 2572-2584.
5. Schmittel, M.; Ganz, A. *Chem. Commun.* **1997**, 999-1000.
6. Felder, D.; Nierengarten, J.-F.; Barigelletti, F.; Ventura, B.; Armaroli, N. *J. Am. Chem. Soc.* **2001**, *123*, 6291-6299.
7. Green, O.; Gandhi, B. A.; Burstyn, J. N. *Inorg. Chem.* **2009**, *48*, 5704-5714.
8. Dietrich-Buchecker, C. O.; Marnot, P. A.; Sauvage, J.-P.; Kirchhoff, J. R.; McMillin, D. R. *Chem. Commun.* **1983**, 513-515.
9. Bencini, A.; Lippolis, V. *Coord. Chem. Rev.* **2010**, *254*, 2096-2180.
10. Riesgo, E. C.; Jin, X.; Thummel, R. P. *J. Org. Chem.* **1996**, *61*, 3017-3022.
11. Dietrick-Buchecker, C. O.; Marnot, P. A.; Sauvage, J. P. *Tetrahedron Lett.* **1982**, *23*, 5291-5294.
12. Klein Gebbink, R. J. M.; Watanabe, M.; Pratt, R. C.; Stack, T. D. P. *Chem. Commun.* **2003**, 630-631.
13. Beves, J. E.; Blight, B. A.; Campbell, C. J.; Leigh, D. A.; McBurney, R. T. *Angew. Chem. Int. Ed.* **2011**, *50*, 9260-9327.
14. Yamada, M.; Nakamura, Y.; Kuroda, S.; Shimao, I. *Bull. Chem. Soc. Jpn.* **1990**, *63*, 2710-2712.
15. Frey, J.; Kraus, T.; Heitz, V.; Sauvage, J.-P. *Chem. Eur. J.* **2007**, *13*, 7584-7594.
16. Tzalis, D.; Tor, Y.; Salvatorre, F.; Jay Siegel, S. *Tetrahedron Lett.* **1995**, *36*, 3489-3490.
17. Schmittel, M.; Ganz, A. *Synlett* **1997**, *1997*, 710,712.
18. Shen, Y.; Sullivan, B. P. *Inorg. Chem.* **1995**, *34*, 6235-6236.
19. Lee, S. J.; Lee, S. S.; Lah, M. S.; Hong, J.-M.; Jung, J. H. *Chem. Commun.* **2006**, 4539-4541.
20. Deroo, S.; Defrancq, E.; Moucheron, C.; Kirsch-De Mesmaeker, A.; Dumy, P. *Tetrahedron Lett.* **2003**, *44*, 8379-8382.
21. Sazanovich, I. V.; Alamiry, M. A. H.; Best, J.; Bennett, R. D.; Bouganov, O. V.; Davies, E. S.; Grivin, V. P.; Meijer, A. J. H. M.; Plyusnin, V. F.; Ronayne, K. L.; Shelton, A. H.; Tikhomirov, S. A.; Towrie, M.; Weinstein, J. A. *Inorg. Chem.* **2008**, *47*, 10432-10445.
22. Konduri, R.; Ye, H.; MacDonnell, F. M.; Serroni, S.; Campagna, S.; Rajeshwar, K. *Angew. Chem. Int. Ed.* **2002**, *41*, 3185-3187.
23. Lundin, N. J.; Walsh, P. J.; Howell, S. L.; McGarvey, J. J.; Blackman, A. G.; Gordon, K. C. *Inorg. Chem.* **2005**, *44*, 3551-3560.
24. Zeglis, B. M.; Pierre, V. C.; Barton, J. K. *Chem. Commun.* **2007**, 4565-4579.
25. Fan, S.-H.; Zhang, A.-G.; Ju, C.-C.; Gao, L.-H.; Wang, K.-Z. *Inorg. Chem.* **2010**, *49*, 3752-3763.
26. Neugebauer, U.; Pellegrin, Y.; Devocelle, M.; Forster, R. J.; Signac, W.; Moran, N.; Keyes, T. E. *Chem. Commun.* **2008**, 5307-5309.
27. Zheng, R. H.; Guo, H. C.; Jiang, H. J.; Xu, K. H.; Liu, B. B.; Sun, W. L.; Shen, Z. Q. *Chin. Chem. Lett.* **2010**, *21*, 1270-1272.
28. Bolger, J.; Gourdon, A.; Ishow, E.; Launay, J.-P. *Chem. Commun.* **1995**, 1799-1800.
29. Comba, P.; Krämer, R.; Mokhir, A.; Naing, K.; Schatz, E. *Eur. J. Inorg. Chem.* **2006**, *2006*, 4442-4448.

30. Bodige, S.; MacDonnell, F. M. *Tetrahedron Lett.* **1997**, *38*, 8159-8160.
31. Miller, M. T.; Gantzel, P. K.; Karpishin, T. B. *Inorg. Chem.* **1998**, *37*, 2285-2290.
32. Schmittel, M.; Lüning, U.; Meder, M.; Ganz, A.; Michel, C.; Herderich, M. In *Heterocycl. Commun.* 1997; Vol. 3, p 493.
33. Munakata, M.; Maekawa, M.; Kitagawa, S.; Matsuyama, S.; Masuda, H. *Inorg. Chem.* **1989**, *28*, 4300-4302.
34. J. Blake, A.; Hubberstey, P.; Li, W.-S.; J. Quinlan, D.; E. Russell, C.; L. Sampson, C. *Dalton Trans.* **1999**, 4261-4268.
35. Cunningham, C. T.; Moore, J. J.; Cunningham, K. L. H.; Fanwick, P. E.; McMillin, D. R. *Inorg. Chem.* **2000**, *39*, 3638-3644.
36. Juris, A.; Balzani, V.; Barigelletti, F.; Campagna, S.; Belser, P.; von Zelewsky, A. *Coord. Chem. Rev.* **1988**, *84*, 85-277.
37. Bard, A. J.; Faulkner, L. R. *Electrochemical Methods: Fundamentals and Applications*; 2nd ed.; Wiley, **2000**.
38. Eggleston, M. K.; McMillin, D. R.; Koenig, K. S.; Pallenberg, A. J. *Inorg. Chem.* **1997**, *36*, 172-176.
39. Kuang, S.-M.; Cuttell, D. G.; McMillin, D. R.; Fanwick, P. E.; Walton, R. A. *Inorg. Chem.* **2002**, *41*, 3313-3322.
40. Blaskie, M. W.; McMillin, D. R. *Inorg. Chem.* **1980**, *19*, 3519-3522.
41. McMillin, D. R.; Kirchhoff, J. R.; Goodwin, K. V. *Coord. Chem. Rev.* **1985**, *64*, 83-92.
42. Armaroli, N. *Chem. Soc. Rev.* **2001**, *30*, 113-124.
43. Suzuki, A., *Nobel Lecture,* Stockholm, **2010**
44. Ott, S.; Faust, R. *Synthesis* **2005**, *2005*, 3135,3139.
45. Inglett, G. E.; Smith, G. F. *J. Am. Chem. Soc.* **1950**, *72*, 842-844.
46. Huynh, M. H. V.; Meyer, T. J. *Chem. Rev.* **2007**, *107*, 5004-5064.
47. Schmittel, M.; Kalsani, V.; Michel, C.; Mal, P.; Ammon, H.; Jäckel, F.; Rabe, J. P. *Chem. Eur. J.* **2007**, *13*, 6223-6237.
48. Fan, J.; Bats, J. W.; Schmittel, M. *Inorg. Chem.* **2009**, *48*, 6338-6340.
49. Connors, P. J.; Tzalis, D.; Dunnick, A. L.; Tor, Y. *Inorg. Chem.* **1998**, *37*, 1121-1123.
50. Aspley, C. J.; Gareth Williams, J. A. *New J. Chem.* **2001**, *25*, 1136-1147.
51. Fang, Y.-Q.; Polson, M. I. J.; Hanan, G. S. *Inorg. Chem.* **2002**, *42*, 5-7.
52. Griffiths, P. M.; Loiseau, F.; Puntoriero, F.; Serroni, S.; Campagna, S. *Chem. Commun.* **2000**, 2297-2298.
53. Arm, K. J.; Williams, J. A. G. *Chem. Commun.* **2005**, 230-232.
54. Schmittel, M.; Kalsani, V.; Bats, J. W. *Inorg. Chem.* **2005**, *44*, 4115-4117.
55. Durot, S.; Mobian, P.; Collin, J.-P.; Sauvage, J.-P. *Tetrahedron* **2008**, *64*, 8496-8503.
56. Kayanuma, M.; Bera, N.; Sandroni, M.; Pellegrin, Y.; Blart, E.; Odobel, F.; Daniel, C. *C. R. Chim.* **2012**, *15*, 255-266.
57. Ichinaga, A. K.; Kirchhoff, J. R.; McMillin, D. R.; Dietrich-Buchecker, C. O.; Marnot, P. A.; Sauvage, J. P. *Inorg. Chem.* **1987**, *26*, 4290-4292.
58. Gushurst, A. K. I.; McMillin, D. R.; Dietrich-Buchecker, C. O.; Sauvage, J. P. *Inorg. Chem.* **1989**, *28*, 4070-4072.
59. Fees, J.; Kaim, W.; Moscherosch, M.; Matheis, W.; Klima, J.; Krejcik, M.; Zalis, S. *Inorg. Chem.* **1993**, *32*, 166-174.
60. Karlsson, S., Ph.D. Thesis, Uppsala Universitet, **2010**.
61. Berera, R.; VanGrondelle, R.; Kennis, J. T. M. *Photosynth. Res.* **2009**, *101*, 105-118.
62. Foggi, P.; Bussotti, L.; Neuwahl, F. V. R. *Int. J. Photoen.* **2001**, *3*, 103-109.
63. Ruckebusch, C.; Sliwa, M.; Pernot, P.; de Juan, A.; Tauler, R. *J. Photochem. Photobiol. C* **2012**, *13*, 1-27.
64. Iwamura, M.; Watanabe, H.; Ishii, K.; Takeuchi, S.; Tahara, T. *J. Am. Chem. Soc.* **2011**, *133*, 7728-7736.

CHAPTER 3

Heteroleptic copper complexes displaying transitions in the visible with large extinction coefficients

3.1. Introduction

Solar energy conversion is an impressively wide field, where many subthemes can be identified, experiencing an extensive investigation by researchers from all over the world. As stated in chapter 1, the sun provides us with an enormous amount of energy, but it is an intrinsically discontinuous source and therefore needs storage systems to be efficiently used. Moreover, light cannot be used as such but needs to be converted into another form, like electricity, heat or chemical energy.[1]

Academic and industrial researches are currently focussing extensively on the production of fuels or electricity stemming from the conversion of solar energy.[2-4] All these applications are based on light absorption, triggering charge transfer processes. A fundamental element in this field is therefore played by the light absorber, or photosensitizer. This compound has to fulfil a number of requirements, among which photochemical and electrochemical stability, efficient absorption of the solar spectrum (intense bands and wide spectral coverage), long-lived excited-state lifetime (depending on the kind of application) and redox potentials of the ground and excited states well matched with those of the other components of the system, in order to thermodynamically favour the desired photochemical processes.

At the present time, the most widely studied compounds for solar energy conversion are Ru^{II} polypyridine complexes.[5] Besides the characteristics listed above, they have the undeniable advantage of an easy synthetic accessibility, since their very stable and quite inert nature allows to synthesize a great variety of structures in a controlled and selective way. Moreover, the frontier orbitals of this kind of molecules are tunable, by acting on the nature of the ligands. Other metallic complexes present such characteristics, like polypyridine Ir^{III}, Os^{II}, Pt^{II} and Re^{I} coordination complexes [6-9] but they all are expensive owing to their poor availability, and toxic, like ruthenium.

In this chapter, the attention will be focussed on the improvement of the light absorption properties of heteroleptic Cu^{I} complexes. Indeed, we gave strong evidence in the previous chapter that heteroleptic copper(I)-diimine complexes are serious alternatives to ruthenium polypyridine systems, paving the way towards a cheaper, less toxic copper-based photochemistry. Numerous

issues yet remain to be solved. In particular, the absorption coefficient of copper(I) diimine complexes in the visible region of the spectrum typically ranges from 3 to $8 \cdot 10^3$ M^{-1} cm^{-1}, being a serious limitation to their application in fields like semiconductors or photocatalysts sensitization.

One of the possible application domains is the use of light absorbing molecules (called dyes or sensitizers) to foster catalytic reactions. The concept, which has been already mentioned in chapter 1 is that the excited sensitizer (having increased oxidation and reduction potentials with respect to the ground state molecule) is quenched by charge transfer to a catalyst, and the latter is then able to perform oxidation or reduction reactions without the use of other energy sources. The efficiency of these molecular arrays is therefore connected with the light absorption properties of the photosensitizer, with the redox potentials of the ground and excited states of the sensitizer and catalyst(s), and with the kinetics of the forward and side processes.

3.2. Aim of the study

As introduced in the previous paragraph, the absorption properties of the sensitizer have to be optimized in order to obtain an efficient harvesting of solar energy. Visible absorption, in Cu^I diimine complexes, is due to a metal-to-ligand charge transfer transition from a metal-centred HOMO to a ligand-centred LUMO, located on the π conjugated system.[10] This transition is responsible for an absorption in the blue part of the solar spectrum, resulting in the red colour of the complexes, in the form of a broad band peaking around 450-460 nm. The intensity of this transition is not very intense, since the molar extinction coefficient ranges from 3 to $8 \cdot 10^3$ $M^{-1}cm^{-1}$ (for a comparison, Ru^{II} tris(bipyridine) complexes absorb roughly in the same zone with an ε around $1.5 \cdot 10^4$ $M^{-1}cm^{-1}$). Ideally, a good photosensitizer should absorb on a wide range of wavelengths and with an elevated extinction coefficient, so that as many solar photons as possible, a mandatory condition to observe efficient overall light conversion into a useful form of energy.

The aim of this part of the work is to conceive new copper(I)-based molecular structures with efficient light absorption. Their use in photocatalytic systems, in couple with a catalyst for proton reduction, could then be planned in case of satisfactory results from the point of view of absorption and emission lifetime.

The structures designed to improve the visible absorption of Cu^I complexes are shown in Fig. 3. 1.
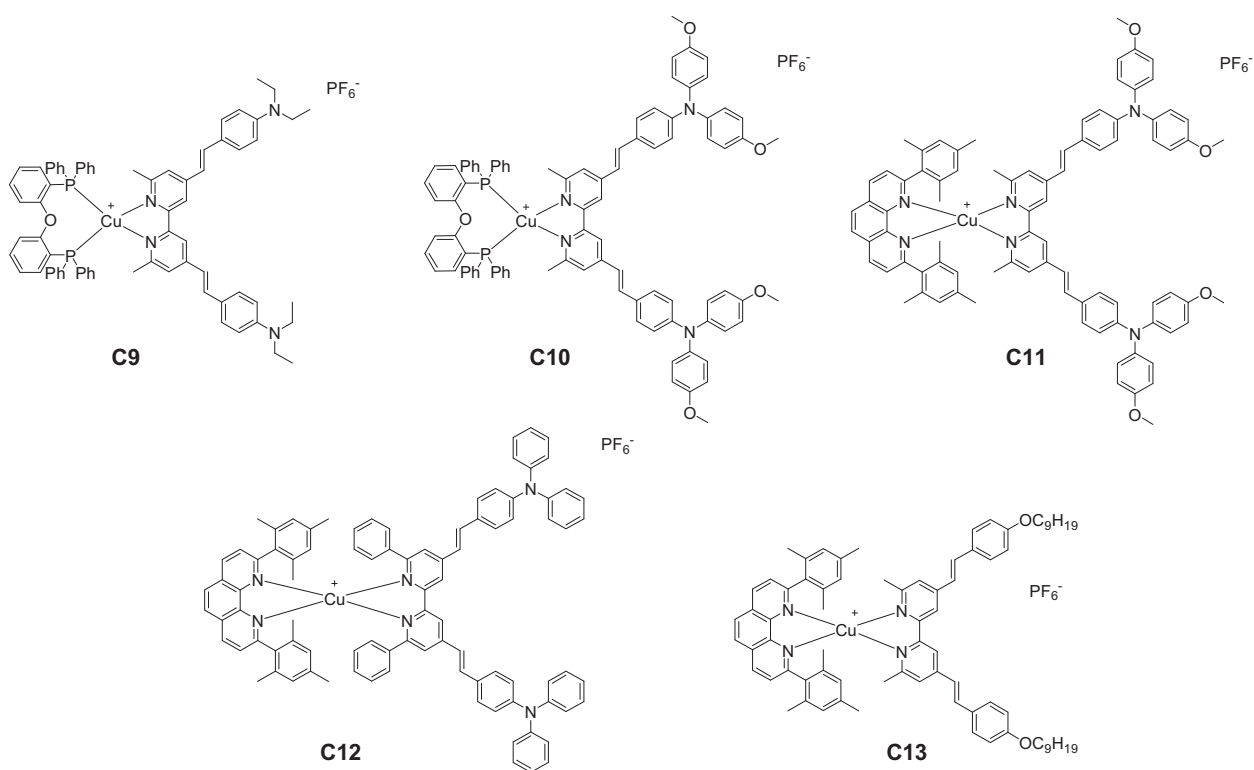
Fig. 3. 1. Structures of the complexes **C9-C13** with styrylbipyridine ligands.

The design of the heteroleptic molecular structures relies on the HETPHEN approach proposed by Schmittel, and π-conjugated styrylbipyridines will be used to improve the light harvesting properties of the complexes. These chromogenic ligands present an extended conjugation with electron donor groups attached to the styryl moiety; therefore, it can be anticipated that they will result in intense ligand-centred absorption bands. Moreover, the extended conjugation could stabilize the orbitals located on the bipyridine π system, and red-shift the MLCT band. Indeed, it was already proven in the case of ruthenium complexes designed for TiO_2 sensitization that the use of conjugated push-pull ligands considerably increases the overall light harvesting properties.[11,12] The improvement of the absorption efficiency is obtained on one hand through the appearance of ligand-centred ILCT bands, red-shifted with respect to the free ligand thanks to the coordination of the metallic ion,[13] and on the other hand through the extension of the ligand π conjugation, that red-shifts the MCLT band.[12]

Furthermore, the influence of different electron donor groups on the styryl moiety will be assessed, as they can be foreseen to play an important role in determining the shape and energy of the frontier orbitals. The intra-ligand charge-transfer transitions characteristic of these ligands, in fact, correspond to a displacement of the electron density from the donor group to the bipyridine

moiety.[13] A change in the donor strength of the ligands substituents is therefore expected to act directly on the properties of the higher occupied molecular orbitals

On the other hand, the influence of the complementary hindered ligand will be evaluated. This aspect is known to play a fundamental role in the determination of the photophysical properties of Cu^I complexes, as bulky substituents around the copper atom prevent exciplex quenching of the excited state. Two bulky ligands were selected for this study: ligand **L1**, diMesPhen, and **DPEphos**. The former has been already used in the previous chapter and will allow a direct comparison of the styryl-derivatized systems with regards to plain copper(I)-diimine complexes. The latter, as explained in greater detail in chapter 1, was at the core of a breakthrough in the field of copper(I) complexes photochemistry.[14] This highly bulky ligand allowed to isolate stable heteroleptic complexes while effectively shielding the metal ion and giving very luminescent complexes, with long excited-state lifetimes (τ = 14.3 µs for [Cu(**DPEphos**)(**dmp**)]BF$_4$) and high luminescence quantum yields (Φ = 0.15), way above those displayed by ruthenium(II) complexes, which is quite unusual for copper(I) diimine complexes.[10] However, these complexes are light yellow at best, barely absorbing in the visible, with a limited use for solar light conversion and storage. The presence of a styrlyl ligand, as introduced before, could considerably increase their visible absorption properties.

The synthesis and characterization of the ligands and complexes will be described in the following paragraphs. The compounds were characterized by ^{1}H and ^{13}C-NMR, HR-MS, elemental analysis, UV-Visible absorption, steady-state emission and electrochemistry. Furthermore, time-resolved spectroscopy allowed the characterization of the excited states temporal evolution.

3.3. Synthesis of ligands L8-L11

3.3.1. Introduction

The ligands used for the synthesis of this series of complexes were synthesized by Dr. Huriye Akdas-Kilig on the occasion of a collaboration with the group of Dr. Hubert Le Bozec at the University of Rennes, and are shown in figure Fig. 3. 2.

The styrylbipyridine ligands have already been used for the synthesis of copper(I) homoleptic complexes in the field of nonlinear optics, because of their push-pull structure and intense ILCT absorption bands.[15-17] Their extended π-conjugated system makes these molecules extremely suitable for the conception of highly absorbing supramolecular structures. The structure,

besides, offers many ways to tune the absorption properties by acting on the donor groups (amines, alkoxy groups) or the conjugated bridge nature (styryl, thiophene, diazo, imino).[16]

Due to the moderately hindering groups present in α of the coordinating nitrogen atoms, these ligands are well adapted to form homoleptic copper(I) complexes and therefore will be used in combination with ligands possessing highly bulky groups beside the coordinating atoms.
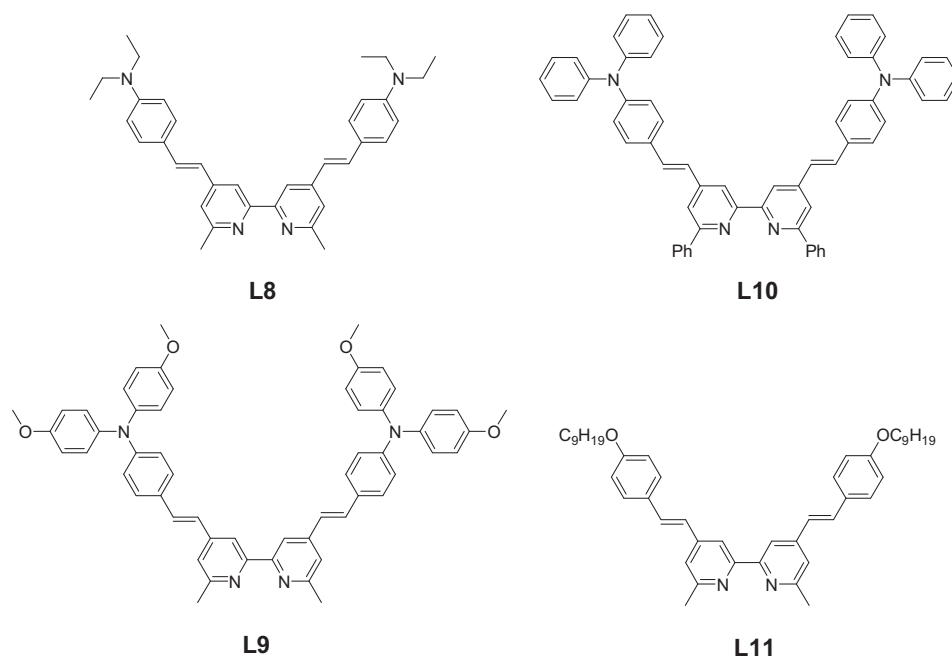
Fig. 3. 2. Structures of the styrylbipyridine ligands **L8**-**L11** used for the synthesis of complexes **C9**-**C13**.

3.3.2. Synthesis of the ligands L8-L11

The ligands **L8** and **L11** were synthesized according to a Knoevenagel reaction. The 4,4',6,6'-tetramethyl-2,2'-bipyridine was dilithiated on the 4 and 4' positions with lithium diisopropylamine (LDA) followed by the addition of two equivalents of the corresponding aldehyde. The obtained dialcohol was dehydrated in presence of an acid (PPTS, pyridinium *p*-toluenesulfonate).[15]
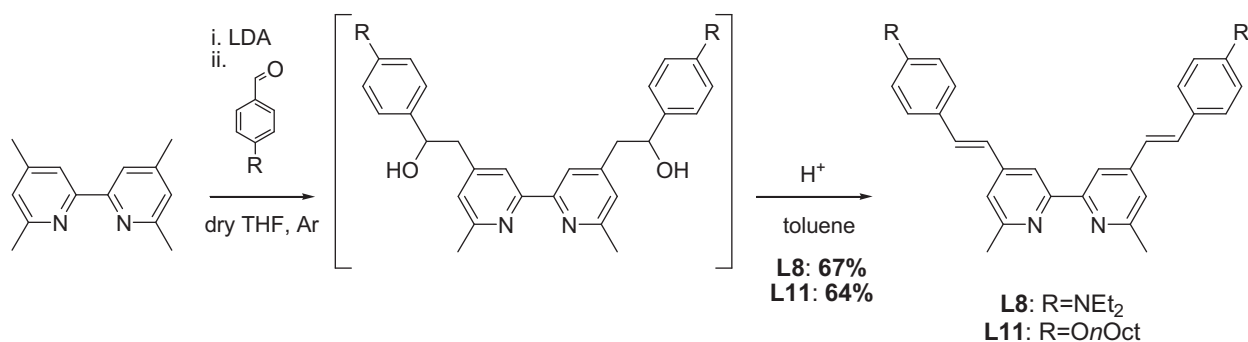
Scheme 3. 1. Synthesis of ligand **L8** and **L11** by Knoevenagel reaction.

Usually, the Knoevenagel condensation is performed starting from an active hydrogen compound, which is easily deprotonated by a base, like LDA. Here, this role is played by the 4,4',6,6'-tetramethyl-2,2'-bipyridine, whose methylic hydrogen atoms are slightly more acidic than diisopropylamine and can therefore be deprotonated. The selectivity between the methyl in 4 and 6 positions is achieved owing to the higher acidity of the former.[18]

Ligand **L10**[19] was also prepared in Knoevenagel conditions, but tBuOK was used as a base to deprotonate 4,4'-dimethyl-6,6'-diphenyl-2,2'-bipyridine (Scheme 3. 2). The ligand was obtained in 62% yield after purification.
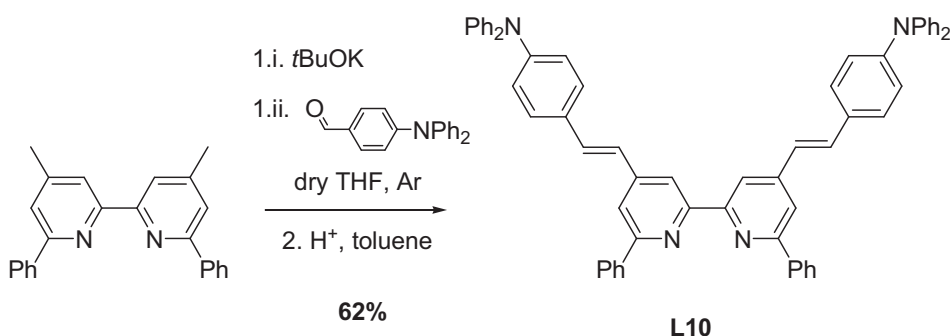
Scheme 3. 2. Synthesis of ligand **L10**.

The ligand **L9** was prepared according to a Horner-Wadsworth-Emmons reaction between the 4,4'-methylphosphonate ethyl ester-6,6'-dimethyl-2,2'-bipyridine **11** and the aldehyde **13**. The 4,4'-methylphosphonate ethyl ester-6,6'-dimethyl-2,2'-bipyridine **11** was obtained in three steps from 4,4',6,6'-tetramethyl-2,2'-bipyridine. Deprotonation with LDA was followed by quenching by chlorotrimethylsilane, to provide **9** in 97% yield. The silyl groups of **9** were then displaced by chlorine to give the dichloro derivative **10**, which was converted into the phosphonate ester according to an Arbuzov reaction with triethylphosphite to afford **11** in 85 % overall yield.[20,21]
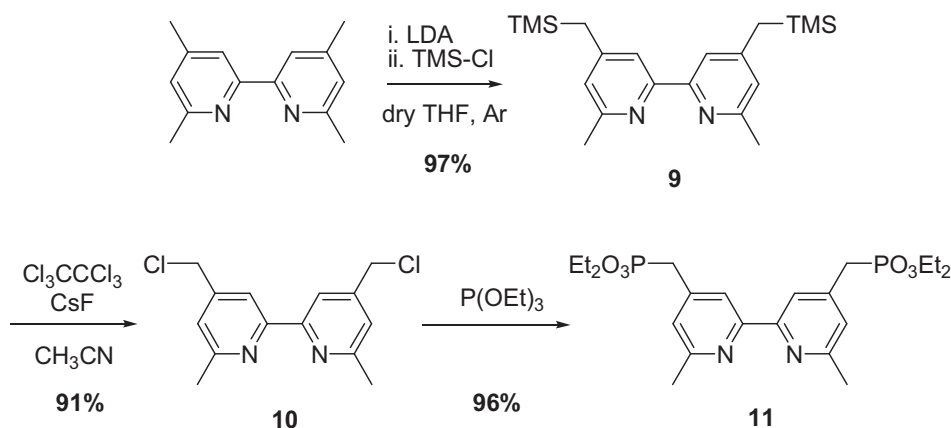
Scheme 3. 3. Synthesis of the intermediate **11**.

The Horner-Wadsworth-Emmons reaction is a modification of the Wittig reaction that employs phosphonate-stabilized carbanions.[22,23] The use of phosphonate carbanions instead of phosphorous ylides is dictated by their more nucleophilic nature, and results in the possibility of using milder reaction conditions. The Horner-Wadsworth-Emmons reaction has a good E selectivity,[24] leading in most cases to only trace amounts of the Z isomer of the double bond. The reaction proceeds through a series of equilibriums and, since the intermediate leading to the E isomer is the most stable, only this product is obtained after the final dehydration step.

It is interesting to note that the deprotonation of **11** is not perfectly selective. A fraction of the product is also deprotonated on the methyl substituent in the 6 position of the bipyridine, leading to the trifunctionalized product (detected by mass spectrometry in the crude reaction product) and lowering the reaction yield.
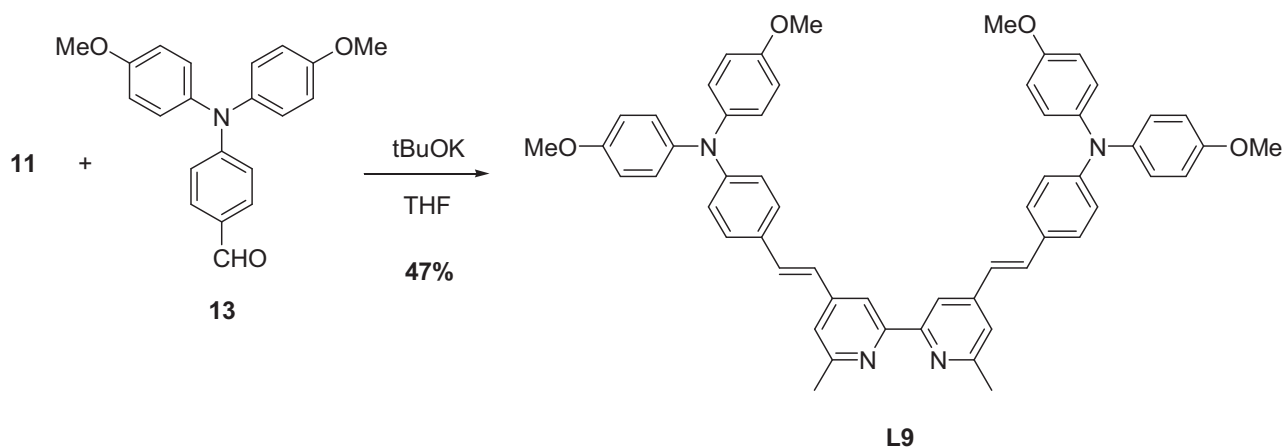
Scheme 3. 4. Synthesis of ligand **L9**.

The ligands were characterized by ^{1}H-NMR and mass spectrometry, which confirmed the structures. The ^{1}H-NMR spectra are characteristic of symmetric molecules, with an inversion centre in the middle of the C^2-$C^{2'}$ bond. In particular, the two doublets of the protons of the E double bond, H^7 and H^8, are observed at about 7.4 and 6.9 ppm (depending on the ligands) with a high coupling constant of 16 Hz, typical of *trans* protons. The two singlets situated at 8.2 and 7.2 ppm correspond to the H^5 and H^3 protons, and are nearly not affected by the different donor groups on the *para* position of the phenyl ring. Only **L10** shows a downfield shift of H^5, which is found at nearly 8.7 ppm. The *p*-substituted phenyl gives two doublets with a coupling constant around 8 Hz (H^9 and H^{10}). The numbering of the ligand protons is shown in Fig. 3. 3.
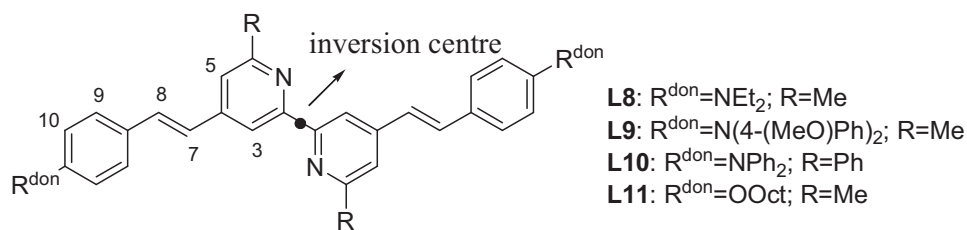
Fig. 3. 3. General structure of the ligands **L8**-**L11**, with position numbering. R^{don}: donor group.

3.4. Heteroleptic copper(I) complexes C9-C13

The complexes described in this chapter are represented in Fig. 3. 1. In order to exploit the HETPHEN approach for the synthesis of the molecules, complementary ligands with bulky groups have to be used. By an analysis of literature data, it resulted that the bis-phosphine ligand **DPEphos** gives extremely luminescent and long-lived copper(I) complexes,[10,14] thus providing stable excited states that are particularly appealing in the field of catalysts sensitization towards light. Their limited absorption in the visible domain raises however important issues, being limited to a tail in the blue region.
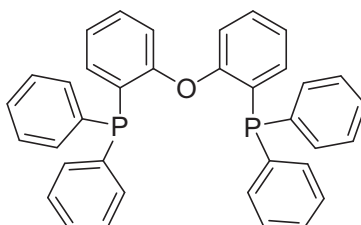
Fig. 3. 4. Structure of **DPEphos**.

The five complexes prepared will allow us to examine the influence of different factors on the properties, in particular from the point of view of the extinction coefficient of the transitions arising in the visible, by keeping one ligand constant and varying the complementary one. Two parameters are essentially taken into account: the influence of the steric hindrance around copper(I) and the strength of the electron donor groups R^{don} (Fig. 3. 3). The first one was examined at first by comparing complexes **C10**, **C11** and **C12**: with **DPEphos** and **L1** (**C10** vs. **C11**), then another coordination cage was introduced, containing a dimesitylphenanthroline (**L1**) and a diphenylbipyridine (**L10**). Electron releasing susbtituents of different strength on the styryl bipyridine ligand were used to tune the energy of the frontier molecular orbitals of the ligand and to assess their impact on the photophysical properties of the complexes **C9** and **C10**, **C11** and **C13**.

In this chapter, the synthesis of new highly absorbing copper(I) complexes are reported, and their absorption and emission properties will be analyzed in detail through electronic spectroscopy and DFT calculations.

3.4.1. Synthesis of the complexes C9-C13

The five complexes **C9-C13** were synthesized in degassed dichloromethane following the HETPHEN approach,[25] which allows the synthesis of stable heteroleptic structures despite the known lability of copper(I) complexes, normally leading to a fast ligand scrambling in solution. In this case, the role of the bulky ligand is played by **DPEPhos** or 2,9-dimesityl-1,10-phenanthroline (**L1**), both known to form heteroleptic complexes with copper(I).[14,25] The less hindered one is a styryl bipyridine structure with 6,6'-dimethyl-2,2'-bipyridine or 6,6'-diphenyl-2,2'-bipyridine as the coordinating units (**L8-L11**, Fig. 3. 2).

In the first step, a 1:1 complex is obtained by stirring the metallic precursor $[Cu(MeCN)_4]PF_6$ with **DPEPhos** or **L1**, the formation of the 2:1 homoleptic adduct being prevented at this stage by the steric hindrance around the copper(I) ion. A first difference between the two ligands can already be remarked at this early complexation stage: while 1:1 adducts between diimines and copper(I) display a slight visible absorption (yellow colour), the one with **DPEphos** is completely colourless, indicating that all the electronic transitions occur in the ultraviolet. This feature is characteristic of the Cu^I-**DPEphos** complexes, that exhibit very limited absorption in the visible spectrum due to the electron withdrawing properties of this ligand stabilizing the HOMO.

The second step, the addition of the less hindered species (**L8-L11**), provides the heteroleptic complexes in moderate to good yield. A degassed solution of the ligand was injected into the stirring solution containing the 1:1 adduct and the coordination reaction was instantaneous. Nevertheless, the solution was allowed to stir for about 30 minutes at room temperature. Remarkably, the addition of the second ligand immediately provoked an intense colour change, which could be seen by naked eye: the solution passed from colourless (or light yellow when **L1** was used) to deep orange or deep red, depending on the ligands. This fact is unusual for Cu^I-**DPEphos** complexes, whose absorption in the visible is normally limited to a tail and are consequently only slightly coloured (λ_{max}< 400 nm). For copper diimine complexes, on the other hand, the MLCT band belongs to the visible region (λ_{max} ~ 450 nm) but the typical absorption coefficients are quite low and the solutions are not intensely coloured.

The products were purified by column chromatography on silica gel.
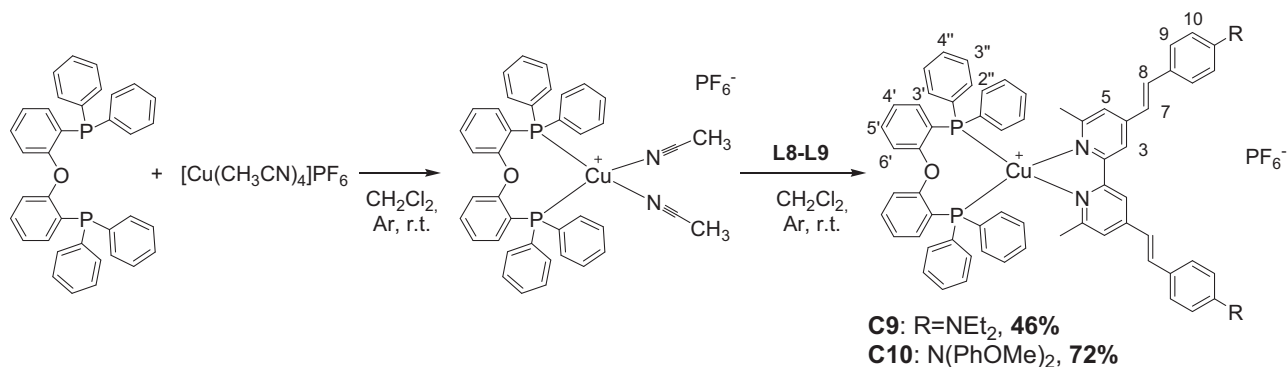
Scheme 3. 5. Synthesis of complexes **C9** and **C10** with ligand **DPEphos**.

C11: R=N(PhOMe)$_2$; R'=Me, **68%**
C12: R=NPh$_2$; R'=Ph, **87%**
C13: R=OnOct; R'=Me, **83%**
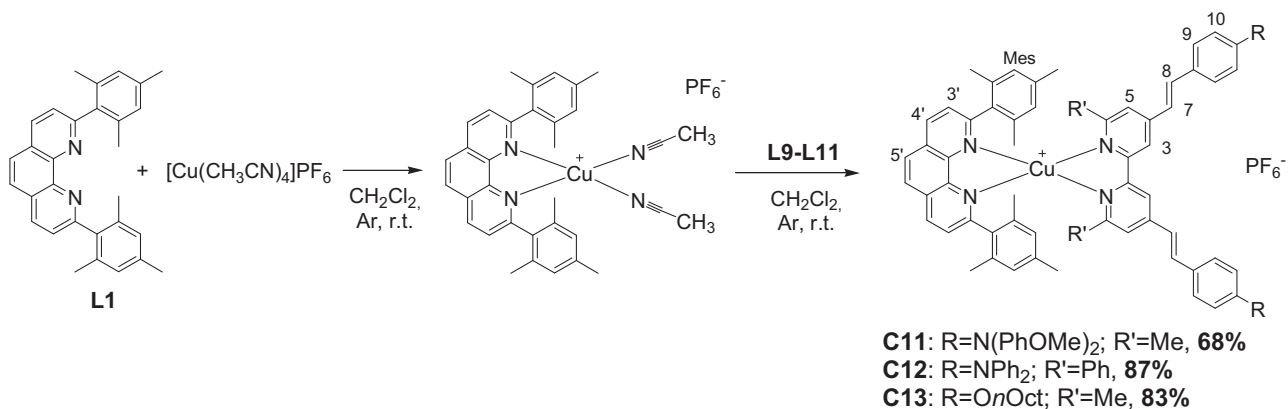
Scheme 3. 6. Synthesis of complexes **C11-C13** with ligand **L1**.

The five copper(I) heteroleptic complexes are stable in the solid state and in solution and can be conserved under normal atmospheric conditions without degradation.

Interestingly, even the phenyl substituents on the bipyridine **L10** enable the formation of a stable copper(I) complex with the bulky **L1**, possessing a hindered coordination cage. However, a partial dissociation of complex **C12** was observed on silica gel thin layer chromatography (TLC), probably due to the high steric hindrance introduced by the phenyl groups on the 6 and 6' positions of the bipyridine, which prevents a close approach of the nitrogen to the copper(I) cation giving weaker bonds. On the other hand, the steric strains imposed by ligand **L10** are not compatible with the formation of a copper complex with the very encumbered **DPEphos** ligand. The synthesis of [Cu(**DPEphos**)(**L10**)]PF$_6$ was attempted, but the complex proved to be highly unstable during the purification: degradation was observed by TLC, with release of the highly luminescent **L10**. Analogous behaviour was previously reported in literature, where the attempt to prepare [Cu(**DPEphos**)(**L4**)]BF$_4$ failed, giving only [Cu(**L4**)$_2$] BF$_4$ (**L4**: 2,9-diphenyl-1,10-phenanthroline).

The synthesis of the complex [Cu(**DPEphos**)(**L11**)]PF$_6$ (Fig. 3. 5) was attempted as well, but the product seems to degrade in time. The crude product was initially slightly yellow, as

expected for a bisphosphine complex without strong donor groups on the complementary ligand, but as soon as the excess **DPEphos** was removed, a red colour was observed. This and some signals arising in the NMR spectrum led us to the conclusion that the product is not stable and tends to form the homoleptic complex [Cu(**L11**)$_2$]PF$_6$. It was however possible to obtain a high resolution mass spectrum, and to identify the signals of the complex in the ^{1}H-NMR. Because of this instability, whose causes are still unknown, however, the photophysical properties of this compound were not studied.
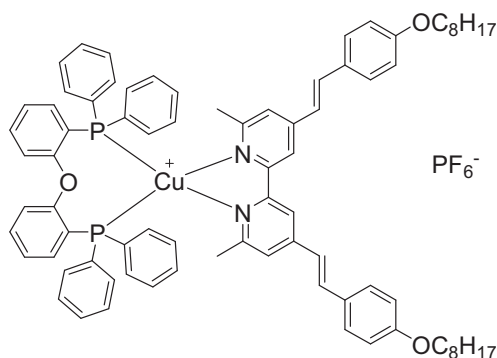
Fig. 3. 5. Structure of the complex [Cu(**DPEphos**)(**L11**)]PF$_6$.

The products were characterized by satisfying ^{1}H-NMR, ^{13}C-NMR, HR-MS and elemental analysis. It was observed that the ^{1}H-NMR spectra in deuterated chloroform are not very well resolved, with a remarkable signal broadening and a superimposition of all the aromatic protons (which constitutes a problem in dealing with this kind of molecules). The use of acetone-d$_6$ allowed a much better resolution of the aromatic signals, and induced a sharpening of the styrylbipyridine ligands peaks.

As usual, the ^{1}H-NMR spectra of the complexes are composed of the signals of the two ligands. In particular, the ligands **L8**-**L11** can be easily recognised by the characteristic doublets with a high coupling constant (J ~ 16 Hz), attributed to the protons H[7] and H[8] on the *E* double bond. These signals are slightly downfield-shifted after coordination to the copper(I) ion. The bipyridine protons H[3] and H[5] are displayed as quite broad singlets (or doublets with J ~ 1 Hz) and are more unshielded after coordination, with an increase in the chemical shift value of about 0.2 ppm.

Concerning mass spectrometry, the high resolution mass spectra of all the ligands and complexes could be obtained. The complexes are seen in positive mode as the [CuL$_A$L$_B$]$^+$ cation. However, not all the ionization sources are adapted for this kind of molecules: the complexes containing **L1** as the bulky ligand can be studied using MALDI+, while complexes with **DPEphos** are detected only by means of electrospray ionization (ESI).

3.5. Characterization of the ligands and complexes

3.5.1. Calculated structures

For this series of compounds, it was not possible to obtain crystals suitable for X-Ray diffraction. However, the structures were calculated by DFT in the Daniel group in Strasbourg. The geometry optimization was done in vacuum using PBE functional, which reproduces well the π-stacking interactions (as observed also for the complexes studied in chapter 2). However, this functional tends to bend large ligands, so a constraint of planarity for ligands **L8**-**L11** was added, even though the calculations were done under C_1 symmetry.

Some distances and angles from the calculated structures are reported in Table 3. 1. It can be observed that in general the complexes bearing the bulky **DPEphos** ligand (**C9** and **C10**) exhibit slightly longer Cu-N distances for the complementary ligand, which also has a lower bite angle if compared to complexes **C11**-**C13**.

The bond distances and bite angles for **C9** and **C10** are in line with those obtained in literature by X-ray diffraction on complexes having a [Cu(**DPEphos**)(**bpy**)]$^+$ structure.[26] The Cu-P distances are, as usual, higher than Cu-N.

The two complexes containing **DPEphos** are characterized by a higher θ_x with respect to complexes **C11**-**C13**, which can be explained with an increased steric hindrance around the copper(I) ion that prevents the flattening distortion. A bending between the two branches of styrylbipyridine ligands is however observed, going from 6.5º in **C9** to 26.1º in **C10** (and with intermediate values for **C11**-**C13**). In the complexes **C11**-**C13**, bearing ligand **L1**, a π-stacking interaction is observed between one of the mesityl rings and one pyridine ring of the complementary ligand.

	Cu-N$_1$ (Å)	Cu-N$_2$ (Å)	Cu-P$_1$ (Å)	Cu-P$_2$ (Å)	N$_1$-Cu-N$_2$	P$_1$-Cu-P$_2$	θ_x	Cu-O (Å)
C9	2.090	2.085	2.251	2.231	79.59	116.86	89.92	3.258
C10	2.091	2.089	2.250	2.226	79.52	118.31	86.48	3.237
	Cu-N$_1$ (Å)	Cu-N$_2$ (Å)	Cu-N$_3$ (Å)	Cu-N$_4$ (Å)	N$_1$-Cu-N$_2$	N$_3$-Cu-N$_4$	θ_x	
C11	2.016	2.012	2.063	2.018	83.29	82.12	83.44	
C12	2.023	2.013	2.112	1.985	84.45	82.43	82.46	
C13	2.005	2.000	2.045	2.005	83.63	82.90	82.02	

Table 3. 1. Selected bond distances and angles from the calculated structures of the complexes **C9**-**C13**. N$_1$ and N$_2$ belong to the less hindered ligand (**L8**-**L11**), while N$_3$ and N$_4$ belong to **L1**. θ_x is the flattening angle in degrees, calculated as the angle between the N$_1$-Cu-N$_2$ and the P$_1$-Cu-P$_2$ (or N$_3$-Cu-N$_4$) planes.

3.5.2. Absorption spectroscopy

3.5.2.a. Ligands L8-L11

The UV-Visible spectra of the four ligands (Fig. 3. 6, Table 3. 2) are characterized by a strong absorption in the near UV with an extinction coefficient between 4 and $6 \cdot 10^4$ $M^{-1}cm^{-1}$. Given the ligands conjugated structure, this band can be assigned to an intra-ligand charge transfer (ILCT) transition from the donor amines or alkoxy groups to the bipyridine core.[16,17]
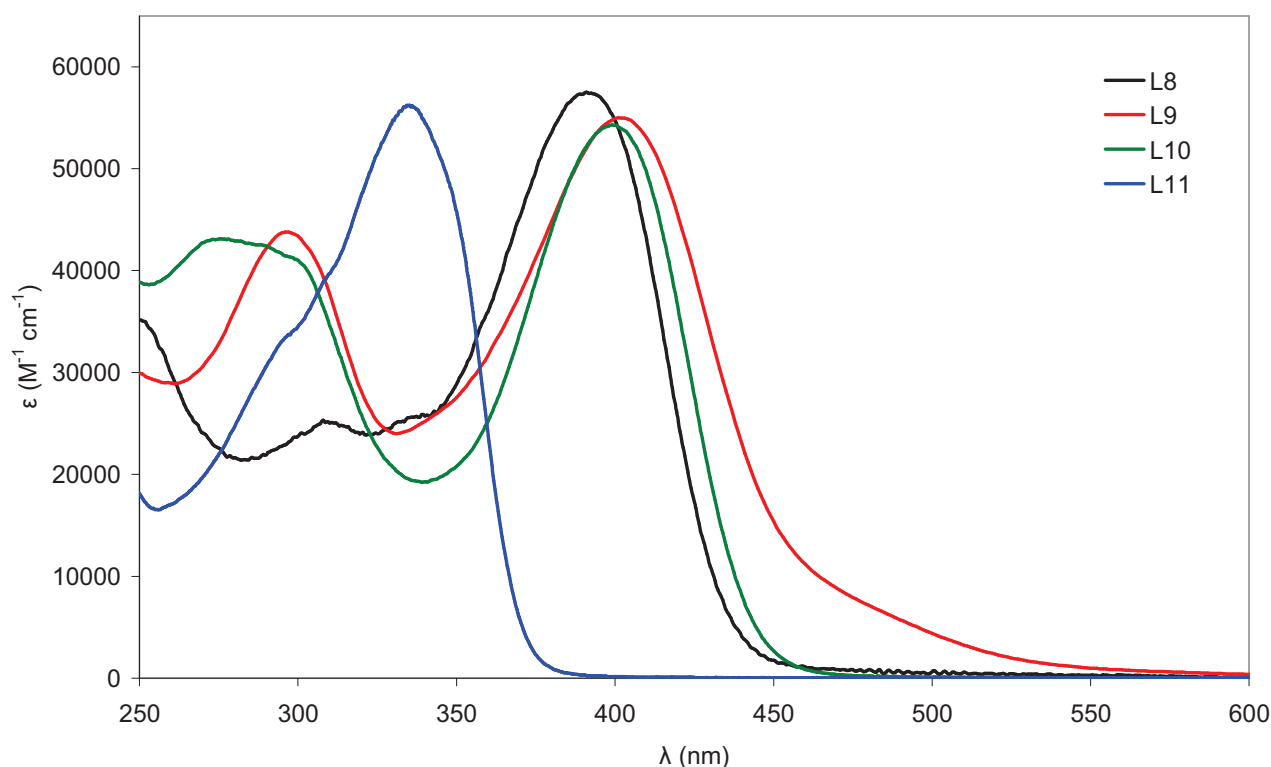
Fig. 3. 6. UV-Visible absorption spectra of the ligands **L8**-**L11**, recorded in dichloromethane.

The influence of the donor groups on the optical properties is well demonstrated in comparing **L8** and **L9** to **L11**. The first two ligands appear as yellow to orange powders and have an absorption maximum around 390 nm, with a tail in the visible responsible for their colour; on the contrary, **L11** is perfectly white and absorbs at 334 nm. The octyloxy group is definitely a weaker donor than the amino group, and therefore destabilizes less the HOMO which is centred on the styryl-donor portion of the molecule. The same behaviour was observed in literature for ligands having a similar structure but lacking the methyl groups at the 6 and 6' positions of the bipyridine.[16]

Measurements of the λ_{max} in different solvents indicate that the four ligands show a slight positive solvatochromic effect, meaning that the excited state is more polar than the ground state.[16,27]

111

	λ (nm) [ε (M^{-1}cm^{-1})]	λ (nm)
	CH$_2$Cl$_2$	CH$_3$CN
L8	393 [5.8·10^4]	393
	310 [2.4·10^4]	
L9	401 [5.5·10^4]	397
	296 [4.4·10^4]	
L10	399 [5.4·10^3]	393
	272 [3.9·10^4]	
L11	334 [6.1·10^4]	333

Table 3. 2. Absorption data for ligands **L8**-**L11**.

3.5.2.b. UV-Visible absorption and calculated spectra for the complexes C9-C13

The UV-Vis absorption spectra of the complexes **C9**-**C13**, recorded in dichloromethane, are shown in Fig. 3. 7 and the corresponding data are gathered in Table 3. 3. The spectra are characterized by two main contributions: a broad absorption band in the visible region and a ligand-centred band in the UV.

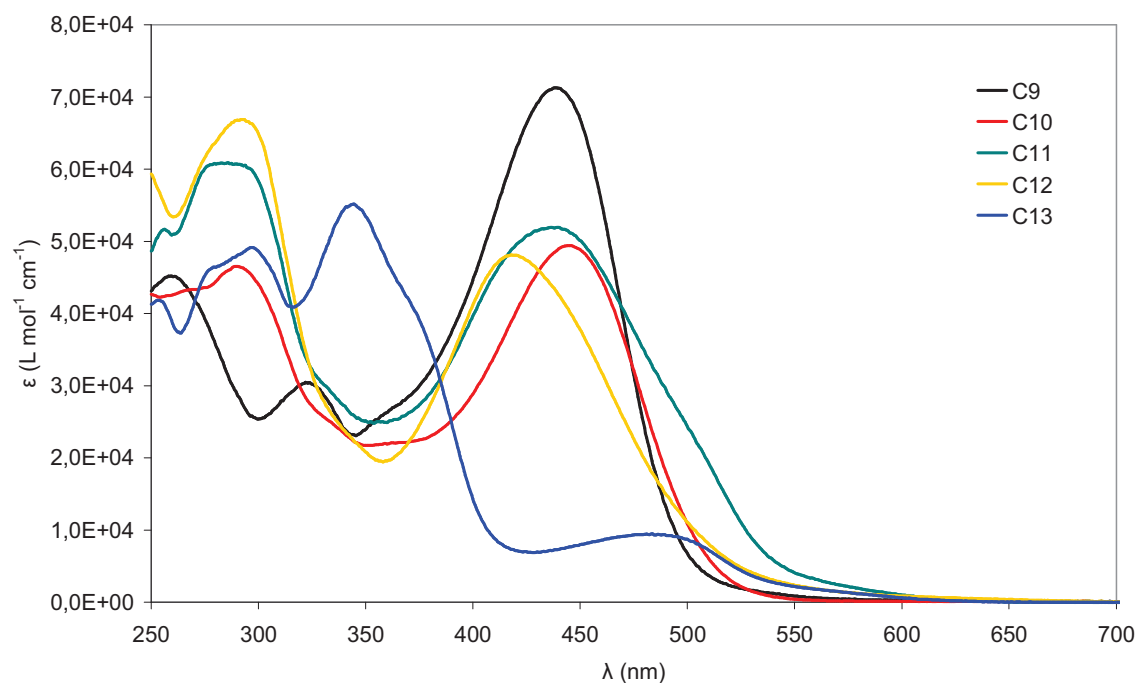**Fig. 3. 7.** UV-Vis absorption spectra of the complexes **C9**-**C13**, recorded in dichloromethane.

The complexes show very intense transitions with absorption maxima ranging from 418 nm to 445 nm, which provide a deep orange to red colour to the solutions. It is important to underline the fact that intense visible absorption is very unusual for **DPEphos**-containing copper(I) complexes, whose absorption over 400 nm is normally limited to a tail. The molar extinction coefficient values of the visible band ($\sim 5 \cdot 10^4$ L mol^{-1} cm^{-1}) also constitute a marked improvement of the light absorbing properties of Cu^I complexes: indeed, the molar extinction coefficients of **C9-C13** represent almost one order of magnitude increase over that of copper(I) diimine complexes, for example [Cu(**neocuproine**)$_2$]$^+$ ($\varepsilon = 8 \cdot 10^3$ L mol^{-1} cm^{-1}) and this constitutes a considerable gain in the absorption cross-section. The visible absorption band is a superposition of several transitions corresponding to a mixture of metal to ligand charge transfers (MLCTs) and intraligand charge transfer (ILCT, see below). The contribution of the intense styrylbipyridine ligand-centred transitions is responsible for this impressive ε value, as the metal ion acts as an inductive acceptor by stabilizing the bipyridine-centred LUMO and provoking the red-shift of the band with respect to the free ligands.

An interesting comparison can be made between the spectra of the series **C9-C12**, containing strongly donating tertiary amines, and the spectrum of **C13,** which bears *n*-octyloxy groups on the styrylbipyridine. The latter immediately shows a different behaviour: it has a less intense absorption band in the visible region, with a shape and intensity which are characteristic of MLCT transitions, while the intense and thinner ligand-centered transitions can be found in the UV. This can be explained by considering the lower donating power of the *n*-octyloxy substituents (**C13**) compared to the amines (**C9-C12**), which changes the nature of the low energy transition. The contributions of the various transitions to the spectra of the complexes will be commented further on in the text.

The absorption spectrum of **C9** was also recorded in various solvents (DCM, toluene, ACN, DMF), in order to elucidate the polarity of the excited-state in comparison with that of the ground-state. A negative solvatochromic effect was observed, indicating an excited-state less polar than the ground state, in agreement with a strong charge transfer transition from the periphery to the core of the complex.
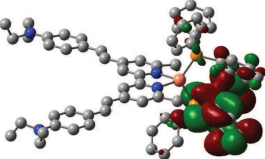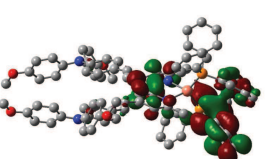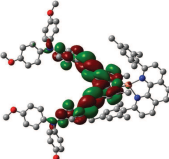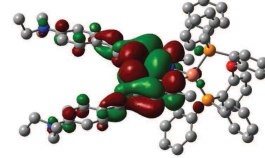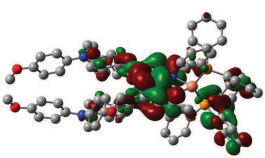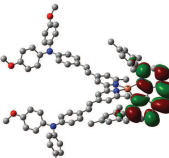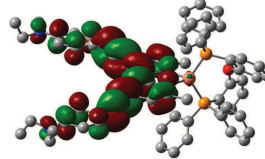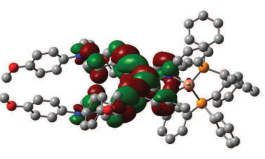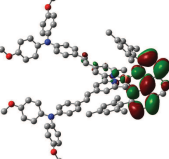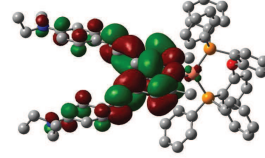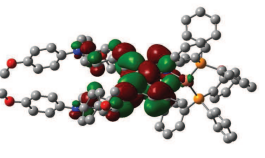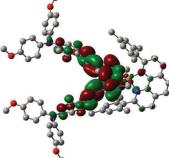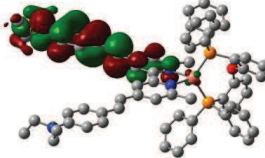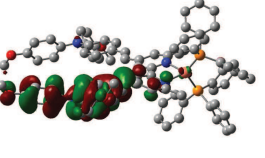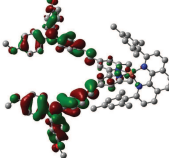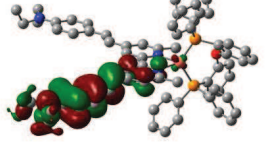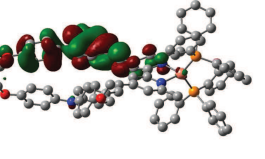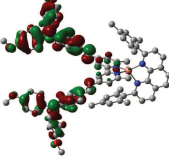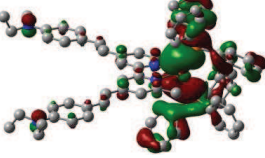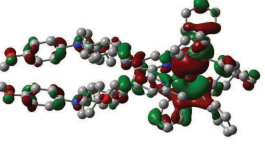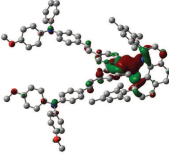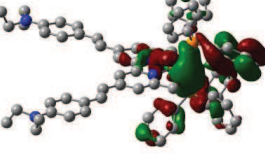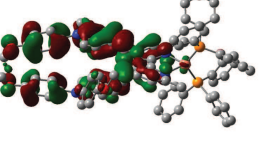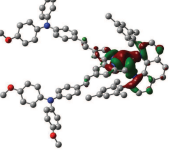
	λ (nm) [ε (L mol^{-1} cm^{-1})]	λ (nm)
	CH$_2$Cl$_2$	CH$_3$CN
C9	439 [6.8 10^4]	393
	323 [2.8 10^4]	
	259 [4.3 10^4]	
C10	445 [4.9 10^4]	397
	290 [4.6 10^4]	
C11	438 [5.1 10^4]	397
	285 [5.9 10^4]	
	256 [5.0 10^4]	
C12	418 [4.8 10^4]	393
	291 [6.5 10^4]	
C13	484 [1.1 10^4]	484
	344 [5.9 10^4]	333
	297 [5.1 10^4]	
	253 [4.0 10^4]	

Table 3. 3. Data for the UV-Vis absorption of complexes **C9**-**C13**, recorded in dichloromethane.

3.5.3. Calculated spectra

To get a better understanding of the absorption properties of these series of complexes and to determine the nature of the electronic transitions implied in the visible absorption band, Time-Dependent Density Functional Theory (TD-DFT) calculations were undertaken (Dr. Kayanuma, University of Strasbourg). The electronic density distribution of the frontier orbitals (from HOMO-3 to LUMO+3) is represented in Table 3. 4 and the dipole-allowed vertical absorption wavelength (λ, in nm) with their oscillator strengths (*f*) are listed in Appendix A. To better visualize the energy of the frontier orbitals, they are reported in Fig. 3. 8.

A qualitative analysis of the main contributions to the molecular orbitals, coupled with the data from the dipole-allowed transitions, provides useful information about the nature of the bands. The HOMO and HOMO-1 orbitals are mainly localised on the donor groups of the styryl ligand for all the complexes. In **C9-C12** these orbitals are nearly degenerate, and correspond to an electron density localized on the two styryl-R^{don} branches of the ligands **L8-L10**. The HOMO of **C13**, on the contrary, additionally contains a strong contribution of copper, and lies at lower energy (Fig. 3. 8). This is clearly an effect of the reduced electron donating character of the *n*-octyloxy group with respect to aliphatic and aromatic amines, and corroborates the above observations. The HOMO-2 and HOMO-3 have different characters depending on the nature of the bulky ligand. They are essentially metal-based orbitals with some contribution of styryl ligand for diimine complexes (**C11**, **C12** and **C13**), whereas they are delocalized over metal and phosphines for complexes with **DPEphos** (**C9** and **C10**), in agreement with literature data.[28-30] Besides, the energy spacing between HOMO-1 and HOMO-2 is larger for bisphosphine complexes while it is weaker in diimine complexes. On the other hand, the LUMO and LUMO+1 are localized on the pyridyl units of styryl bipyridine for mixed [Cu(PP)(NN)]PF$_6$ complexes, while in diimine complexes the LUMO+1 already shifts to **L1** and it is close in energy to the LUMO, which is on the styryl bipyridine. These differences in the localization of the molecular orbital translate into the nature of the transitions occurring in the visible region (Table 3. 4).

L+3			
	-0.00979	-0.01001	-0.03758
L+2			
	-0.01152	-0.01105	-0.04061
L+1			
	-0.03380	-0.04086	-0.04642
L			
	-0.05723	-0.05797	-0.05599
H			
	-0.23755	-0.23574	-0.23040
H-1			
	-0.23817	-0.23681	-0.23088
H-2			
	-0.27335	-0.27065	-0.25817
H-3			
	-0.29572	-0.28123	-0.26584
	C9	**C10**	**C11**
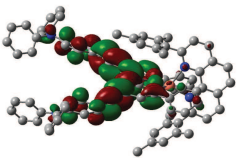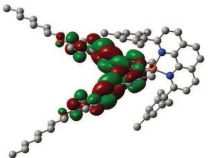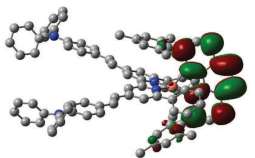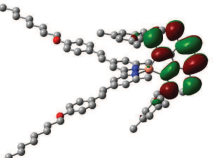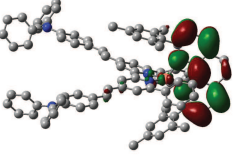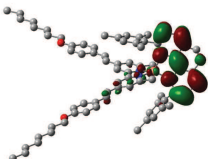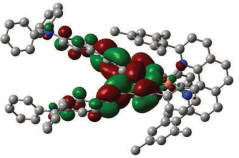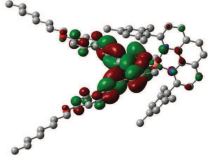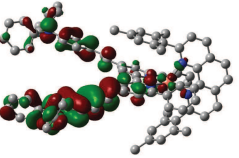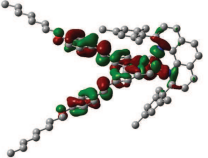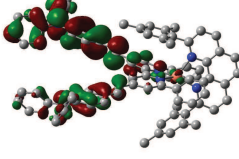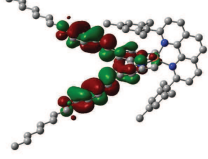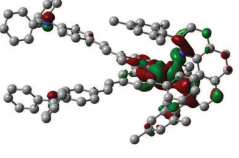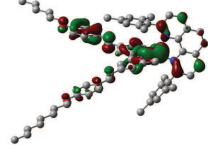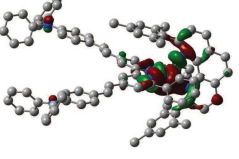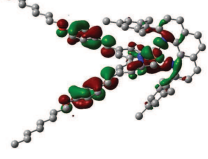
	C12	C13
L+3	-0.04014	-0.03600
L+2	-0.04278	-0.04174
L+1	-0.04698	-0.04666
L	-0.05974	-0.05588
H	-0.24019	-0.25183
H-1	-0.24117	-0.26121
H-2	-25886	-0.26425
H-3	-0.26957	-0.27341

Table 3. 4. Optimized structure and frontier molecular orbitals of the Cu[I] complexes **C9-C13** calculated using CAM-B3LYP functional, considering the solvent effect of dichloromethane. The energies are expressed in atomic units.
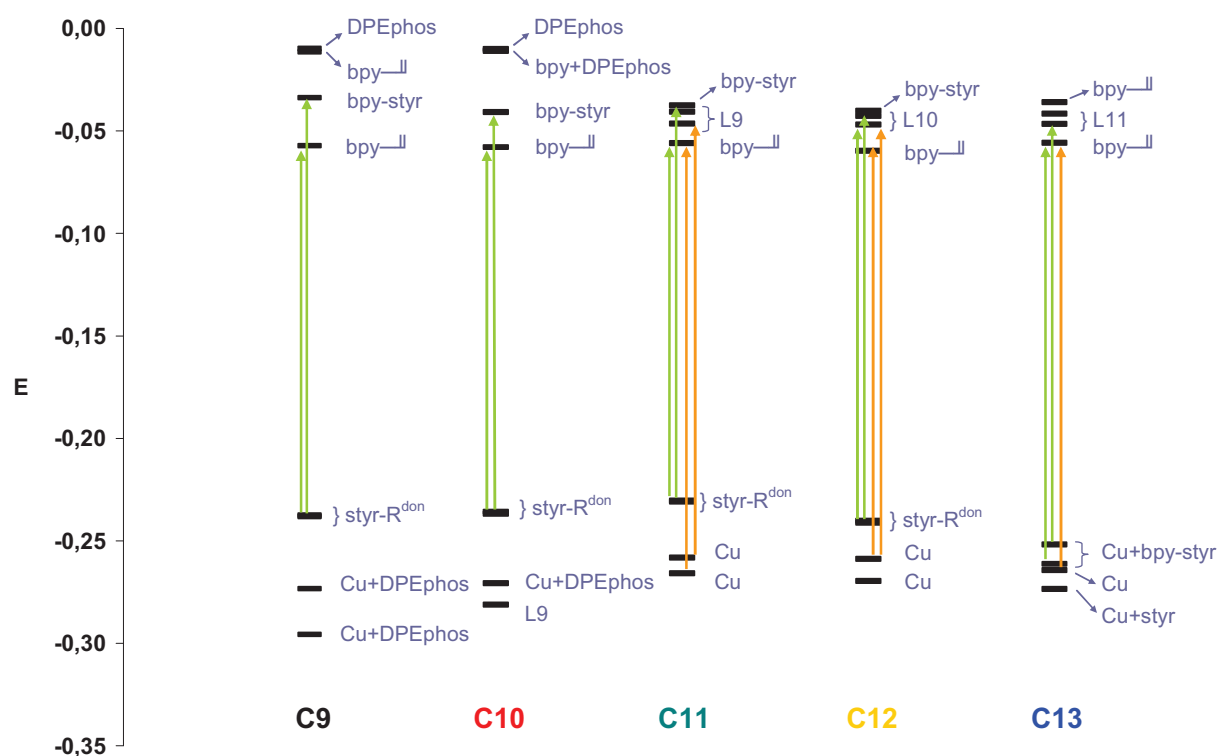
Fig. 3. 8. Energy diagram representing the frontier orbitals of the complexes **C9**-**C13**. The main contributions to the electronic density are reported besides each orbital. The arrows indicate the electronic transitions responsible for the visible absorption: ILCTs (intra-ligand charge transfer) are represented in green and MLCTs (metal-to-ligand charge transfer) in orange. Bpy—⊥ indicates the bipyridine plus the double bond of the styryl group.

In the complexes with the **DPEphos** ligand (**C9** and **C10**), the absorption band around 440 nm is a mixture of pure ILCT transitions corresponding to a displacement of the electron density on the styryl bipyridine ligand from the donor group R to the bipyridyl, electron poor subunit. The lowest MLCT absorption bands are calculated in the near UV with weak oscillator strength, and assigned to a mixed MLCT/ILCT state with more than 70% of MLCT character (see Appendix A for the detail of transition wavelengths and oscillator strengths). This is the consequence of the low lying position of the filled copper orbital (HOMO-3) which is due to the lower σ-donating strength of the phosphine compared to the diimine ligand. The interest in using conjugated styryl-bipyridine ligands is evidenced by the fact that the LUMOs are centred on the bipyridine core plus the double bond or the entire styryl moiety. The extended conjugation of the π system, compared to simple bipyridine or alkyl-bipyridine ligands, contributes to the red-shift of the absorption bands.

In heteroleptic bis-dimine complexes (**C11**, **C12** and **C13**), the absorption band in the visible is an envelope of distinct transitions containing both MLCTs and ILCT excitations calculated between ~ 440 nm and ~ 370 nm with significant oscillator strengths. Interestingly, there are two main MLCTs transitions: the main one involves the diMesPhen (**L1**) and its oscillator strength is

118

twice as intense as that involving the styryl bipyridine (Appendix A). However, the high energy side of the visible band is dominated by an intense ILCT transition, which is certainly mostly responsible for the high extinction coefficient of the complexes in this region. The strongest calculated peak locates around 400 nm for **C11** and **C12** while around 360 nm for **C13**. Logically, the intensity of this transition is proportional to the strength of the electron releasing group on the styryl moiety and naturally decreases in the following order $N(Et)_2 > N(Anysyl)_2 \approx N(Ph)_2 >>$ OOctyl. In the spectrum of **C13**, even the low energy bands formally assigned to ILCT transitions contain the contribution of copper(I) to the electron density of the departure orbital, thus having a partial MLCT character.

Another distinction of the spectra of the diimine complexes is the presence of a small absorption tail above 430 nm, attributed to band I according to the nomenclature of Ichinaga and co-workers[31] and which is typical of a flattened complex. The flattening is caused by the π-stacking interactions of the mesytyl groups with the bipyridine and this raises the energy of the d_{yz} upon bending of **L1** in the xz plane (Fig. 3. 9).
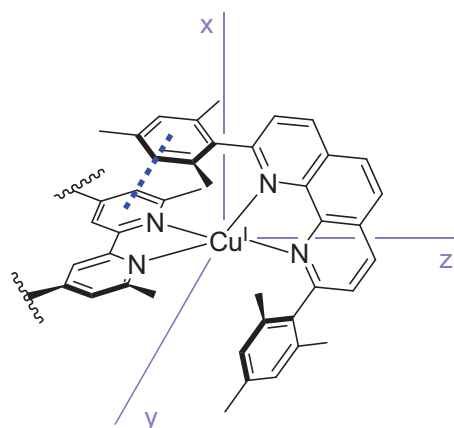
Fig. 3. 9. Bending of **L1** in the xz plane due to π-stacking interactions with bipyridine.

In conclusion, the light harvesting properties of copper(I) diimine and bisphosphine complexes were considerably improved, reaching ε values as high as $7 \cdot 10^4$ $M^{-1}cm^{-1}$ for **C9**, thanks to the use of highly conjugated styrylbipyridine ligands possessing donor terminal groups. The analysis of the main contributions to the absorption in the visible region of the spectrum unveils that intra-ligand charge transfer transitions play a major role. This fact could cause important consequences on the emission properties, as all the considerations made until now on the luminescence properties of copper(I) complexes are based on emission from MLCT states. The emission of the complexes **C9**-**C13** will be examined in paragraph 3.5.4.

3.5.4. Electrochemical properties

The electrochemical properties of the ligands in dichloromethane were assessed in order to have a complete understanding of the complexes behaviour. The analysis was conducted on 1 mM solutions of the complexes in dichloromethane, using TBAPF$_6$ 0.1 M as the supporting electrolyte, on a platinum electrode. All the potentials are referred to SCE reference electrode. Nothing different from the blank was found during the cathodic scan, indicating that the bipyridine-based reduction step occurs at potentials outside our experimental window. The irreversible wave around 0.64 V vs. SCE was attributed to the oxidation of the amines in **L8**. **L10** displays an irreversible oxidation at 0.90 V, followed by two less intense waves at 1.00 and 1.17 V. The first oxidation was attributed to the removal of an electron from the amine-centred HOMO. The process is not reversible, probably because, in the absence of a *para* substitution, a reactive hole can form on one of the phenyl rings and start radical reactions. The oxidation of **L9**, having donating methoxy groups in the para position, is reversible and occurs at 0.87 V. The E$_{ox}$ value is considerably higher than that recorded for **L8**, accounting for the less electron rich nature of the diphenylamine with respect to diethylamine. No oxidation waves were recorded for **L11**, confirming that the less donating nature of the alkyloxy groups has a great influence on the ligand properties (important differences in the absorption and emission behaviour have already been described). Indeed, in this case the donor group bound to the styryl moiety does not participate to the HOMO electron density, as discussed in the section about the calculated frontier orbitals.

	E(amine$^+$/amine) (V vs. SCE)	E(Cu^{II}/Cu^{I}) (V vs. SCE)
L8	0.64 [a]	—
L9	0.87	—
L10	0.90 [a]	—
L11	—	—
C9	0.73 [a]	1.32 [a]
C10	0.70	1.34
C11	0.71	0.87
C12	0.96 [b]	1.03 [b]
C13	—	0.80

Table 3. 5. Electrochemical data for the complexes **C9**-**C13** measured by square wave voltammetry in argon purged dichloromethane. Working electrode: Pt disc; Reference electrode: SCE; Counter-electrode: Pt foil; Supporting electrolyte: TBAPF$_6$ 0.1 M. [a] Irreversible process. [b] Superimposed waves.

The electrochemical properties of the complexes **C9-C13** were also investigated. The cyclic voltammograms were recorded in argon purged dichloromethane on a platinum working electrode and the redox potential values, measured by square wave voltammetry, are listed in Table 3. 5. The superposition of the SW voltammograms is shown in Fig. 3. 10. The choice to report square wave E values and not the $E_{1/2}$ is dictated by the fact that in some cases the waves superimpose, so the cyclic voltammetry (CV) data are difficult to analyse.
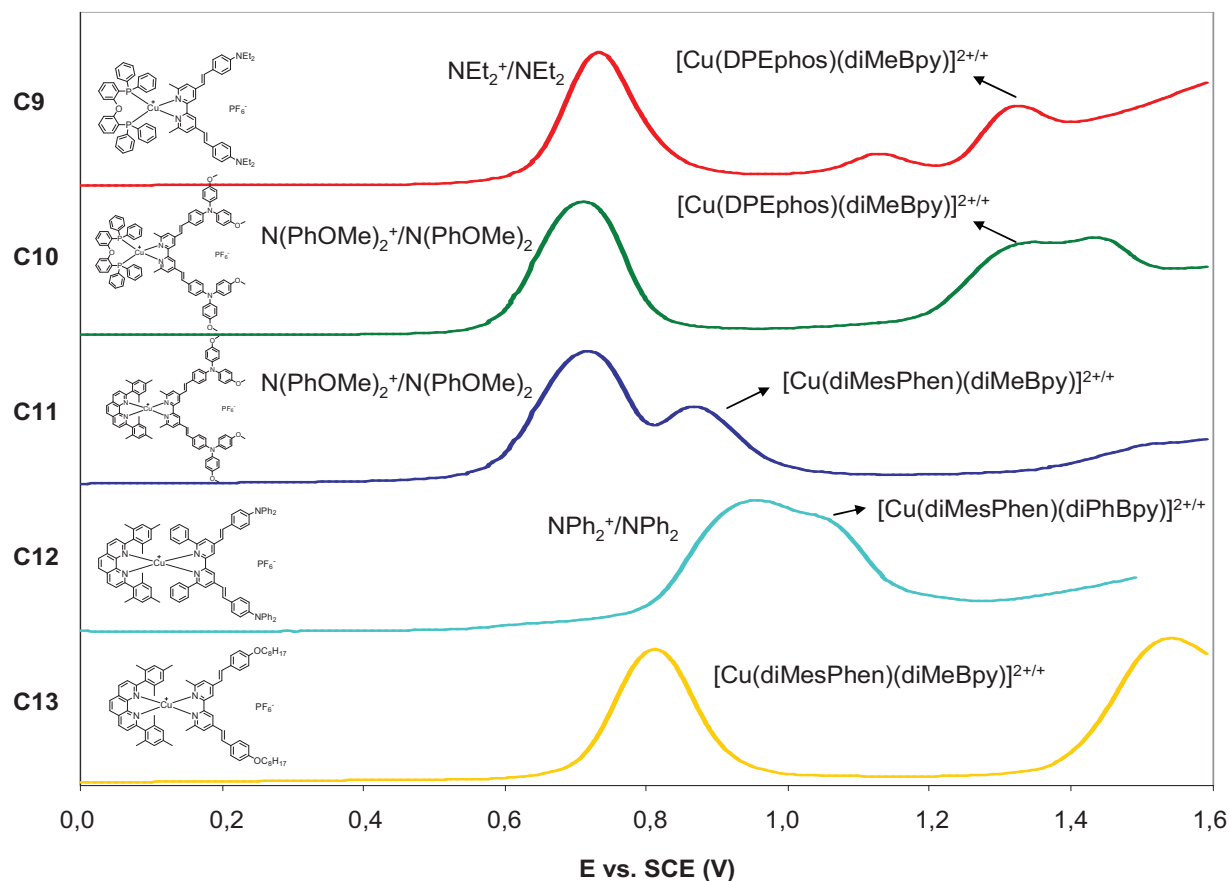
Fig. 3. 10. Square wave voltammetries of the complexes **C9**-**C13**. The peak attribution is reported on the figure; for the $Cu^{II/I}$ couples, the composition of the coordination sphere is reported, in order to evidence its role in determining the potential of the metal-centred oxidation.

The first complex, **C9**, shows a two-electron irreversible process assigned to oxidation of the diethylaminophenyl units, which is consistent with the well-known oxidative decomposition of aliphatic amines upon β-elimination.[27]

Complexes **C10-C12**, containing the aromatic tertiary amines, display a reversible two-electron oxidation wave around 0.7 V assigned to electron removal on the nitrogen of the amine substituents of the styryl moieties. This assignment is in agreement with the localization of the

HOMO orbitals on these moieties (see paragraph 3.4.3). The oxidation of simple triphenylamine in **C12** is anodically shifted (0.96 V vs. SCE), in agreement to that observed for the ligands. The amine oxidation potential is anodically shifted with respect to free ligands, which can be explained by a global stabilization of the electron density on the ligands upon coordination of the metal cation.

A second one-electron oxidation reaction, attributed to the Cu^{II}/Cu^{I} couple, is then observed. Interestingly, the sterically more constrained coordination sphere of complex **C12** pushes anodically the oxidation potential of Cu^{II}/Cu^{I} because the four aryl rings hinder the flattening of the diimine ligands and destabilize the Cu^{II} state, which prefers a tetragonal environment, with possibility of coordinating a fifth ligand.

The **DPEPhos** ligand induces an important anodic shift of the oxidation potential of Cu^{II}/Cu^{I} couple (see **C10** *versus* **C11**), because of the larger steric hindrance around the metal, together with its lower electron-donating effect compared to that of **L1**. [11,12,26,32]

The cathodic behaviour was also investigated, but nothing significantly different from the blank was observed until a potential of -1.5 V vs. SCE, which was the onset of solvent electroactivity in our conditions. This indicates that the first reduction processes (localized on the bipyridine portion of the diimine ligand according to TD-DFT calculations) occur at a more negative potential than -1.5 V vs. SCE.

3.5.5. Photoluminescence

The ligands **L8**-**L11** show an intense emission (Table 3. 6), that can be seen by the naked eye, in the blue-green region, due to fluorescence from the first singlet excited state.[27] The emission quantum yield is dependent on the solvent and on the ligand. The steady-state emission measurements show that there is an important Stokes shift in polar solvents such as acetonitrile.

The steady-state emission properties of the complexes **C9**-**C13** were recorded in dichloromethane and acetonitrile at room temperature and they are shown in Fig. 3. 11. The five complexes exhibit very different emission behaviour in terms of both maximum emission wavelength and emission quantum yield. The luminescence spectra of **C11** and **C13** appear in the low energy region and are remarkably less intense than the other complexes. In acetonitrile, the emissions are slightly blue-shifted and much closer to those of the ligands.

It is important to indicate that the emission intensities for the complexes **C9** and **C10** are much higher than those of the copper(I) diimine complexes studied previously (chapter 2). This fact was initially attributed to the effect of the bulky and rigid **DPEphos** ligand. The emission of complex **C12** is also very intense but, as it is superimposable to that of the free **L10** ligand, we strongly

suspect that it comes from the ligand because this very hindered complex can dissociate in solution at low concentration.
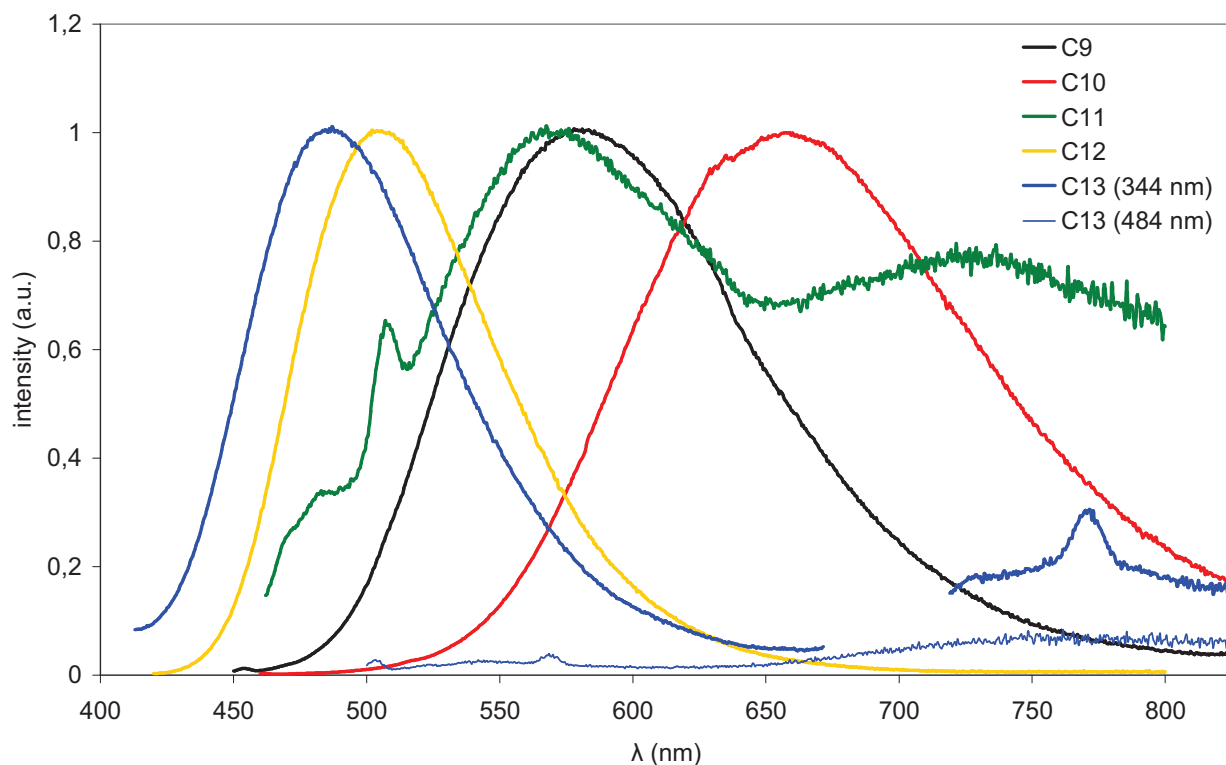
Fig. 3. 11. Normalized emission spectra of the complexes **C9**- **C13** recorded in CH$_2$Cl$_2$. The complexes are excited at the lowest energy maximum wavelength. **C13** was excited at 344 nm (the spectrum was recorded in two different parts, before and after the second harmonic) and at 484 nm, in the two lowest energy absorption bands. The two spectra were recorded using the same experimental conditions and the relative intensities are maintained in the figure.

The maximum emission wavelengths, quantum yields and lifetimes were recorded in two solvents and the results are gathered in Table 3. 6. This table contains kinetic data obtained using different techniques: single photon counting, nanosecond and femtosecond transient absorption. The technique used is indicated beside each lifetime value, and the results will be discussed in the following paragraphs, dedicated to time-resolved spectroscopy.

The lifetimes for all the complexes do not exceed 1 ns, even for **C9** and **C10** which are the most emissive complexes. These very short decays and the position of the emission band are reminiscent of a ligand-centred fluorescence, already observed for some rhenium(I) complexes containing alkylaminostyryl bipyridine ligands.[27]

	CH₂Cl₂		CH₃CN			
	λ_{em} (nm)	ϕ_{em} (%)	λ_{em} (nm)	τ_{em} (ns)	process	ϕ_{em} (%)
L8	486	10.6	518	0.344[a]	[1]ILCT em	10.3
L9	567	53.3	606	0.305[a]	[1]ILCT em	4.5
L10	502	67.6	532	n.d.		57.8
L11	406	0.1	423	n.d.		1.1
C9	562	1.2	518	0.340[c]	[1]ILCT em	9.2
				1500	[3]MLCT nr	
C10	652	7.1	606	0.301[a]	[1]ILCT em	4.5
				1700	[3]MLCT nr	
C11	567 (exc 436)	< 0.1	606	0.540[a]	[1]ILCT em	3.8
	752 (exc 515)	< 0.01		19[b]	[3]MLCT nr	
C12	502	50	530	n.d.		51
	> 800 nm	< 0.01		< 4 ns[b]		
C13	500 (exc 344)	< 0.1	423	n.d.		0.9
	751 (exc 483)	<0.01		20[b]	[3]MLCT nr	

Table 3. 6. Emission and excited-state data of the ligands **L8**-**L11** and complexes **C9**-**C13**, recorded in dichloromethane and acetonitrile at room temperature. [a] Excited-state lifetime measured by femtosecond transient absorption. [b] Excited-state lifetime measured by nanosecond transient absorption. [c] Emission lifetime measured by single photon counting. Processes: [1]ILCT em: emission from the ligand-centred singlet ILCT state; [3]MLCT nr: non radiative relaxation of the triplet MLCT state.

3.6. Nanosecond and femtosecond transient absorption of complexes C9-C13

Given the short emission lifetimes measured for this series of complexes, nanosecond and femtosecond transient absorption measurements were performed on **C9**, **C10** and **C11**. Complexes **C9** and **C10** share the same **DPEphos** ligand with different donor styrilbipyridine group, while **C10** and **C11** share the same styrylbipyridine group and bear different bulky ligands.

Nanosecond TA shows a negative band (depopulation of the ground state) for all the complexes and the formation of a broad positive band after 500 nm, characteristic of the triplet MLCT excited state (as observed in the complexes of the previous chapter). The decay analysis of the transient band provides the excited-state lifetime for these species (Table 3. 6). Interestingly, the decay of the MLCT triplet for **C9** and **C10** was extremely slow (respectively 1.5 and 1.7 μs in CH₃CN). For complexes **C11**-**C13** two luminescence bands were found, the first one around 550 nm and the second one around 750 nm. The former was assigned to ILCT fluorescence, with

hundred picoseconds lifetime and the latter was attributed to triplet MLCT state with a lifetime of about 20 ns (as observed in the previous chapter). The excited-state lifetimes were measured by means of transient absorption. The transient spectra for **C12** and **C11** (in acetonitrile) are covered by the strong fluorescence from the ligand.

Femtosecond transient absorption was thus carried out, to study more precisely the evolution of the excited state on a shorter timescale after excitation. Let us first compare **L8** and **C9**. For **L8** (Fig. 3. 12, left), after excitation, two main bands rise within the first 0.5 ps: a depopulation band ($\Delta A < 0$) around 400 nm and the broad absorption between 450 and 700 nm, corresponding to the Franck-Condon electronic and vibrational excited state. Afterwards, within 1 ps, the FC state relaxes to the emissive ILCT singlet state with a blue-shift of the positive band and formation of a negative contribution at 530 nm, corresponding to the stimulated emission. The bands decay with two time constants, 3 ps and 344 ps. The 3 ps component was thus assigned to the relaxation of hot vibrational state and the 340 ps was assigned to the lifetime of the ILCT fluorescent state.

The spectral evolution of **C9** (Fig. 3. 12, right) is quite similar to **L8** during the first picoseconds: formation and fast relaxation of the Franck-Condon state. A new, positive contribution can however be noticed at 350 nm. After 1 ps, the rise of a broad band at 525-700 nm occurs with a maximum at 550 nm, with a 10 ps time constant. The 350 and the 475 bands decay biexponentially with a few picoseconds time constant and 340 ps time constant, similar to the time constant observed for **L8**. The few picoseconds time constant is difficult to assign and to determine because it occurs at the same time as the rise of band at 550 nm. The absorption band recorded at longer times has a maximum at 590 nm which is similar to that obtained on the nanosecond timescale.
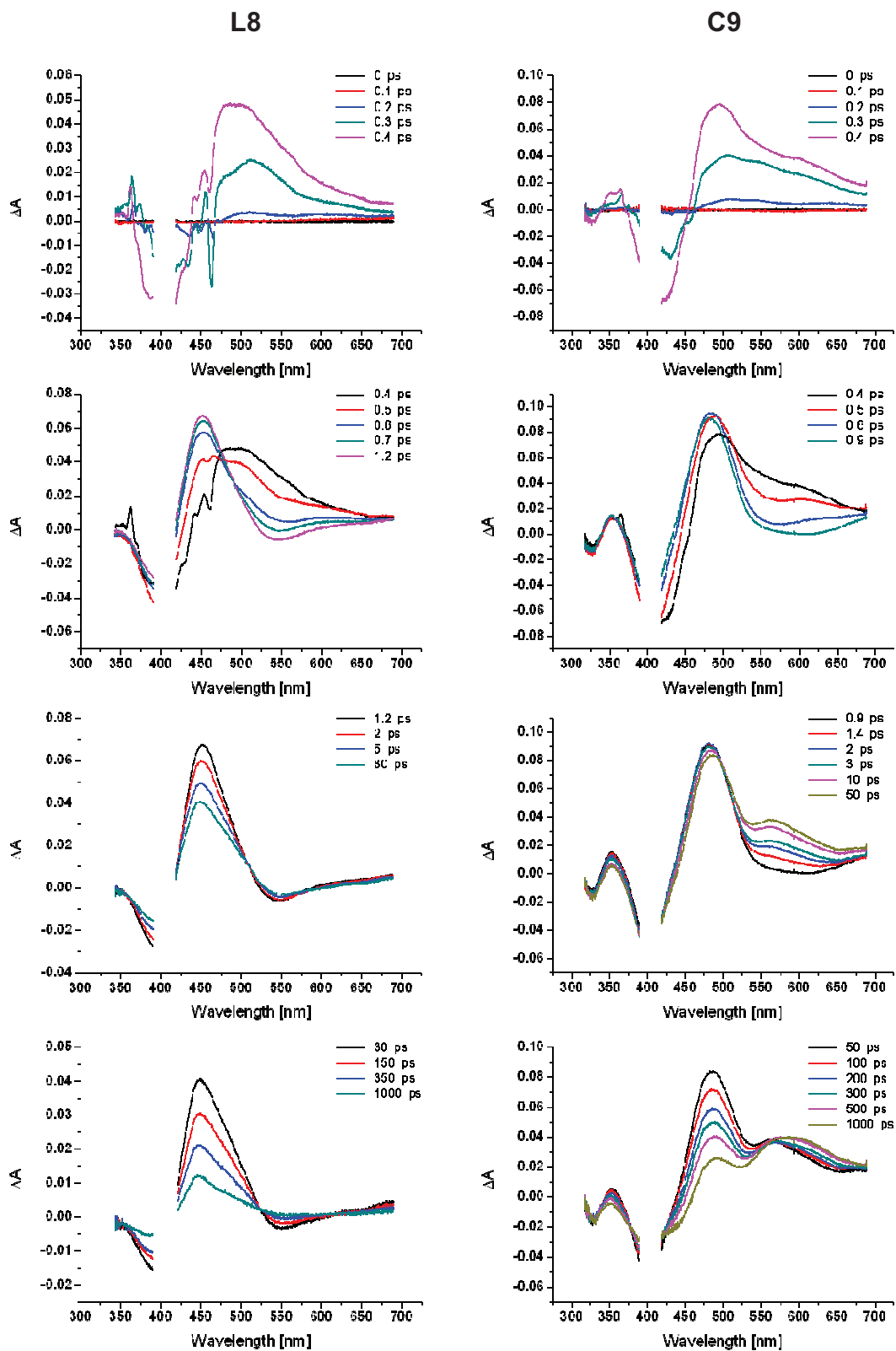
Fig. 3. 12. Femtosecond transient absorption spectra obtained for **L8** (left) and **C9** (right) in acetonitrile after 400 nm excitation.

126

Given the previous knowledge accumulated on heteroleptic copper(I) complexes (see chapters 1 and 2), the following interpretation is proposed. The excitation at 400 nm gives rise to two different populations: an ILCT state, which follows the same fate as that of the ligand **L8**, and a MLCT state. For the latter, the flattening step was not observed because this complex is quite rigid, due to the presence of the **DPEphos** ligand, which prevents the ligands to move around the copper cation. Since the depopulation band recovers at 75% within 300 ps, it can be assumed that the major population of excited states is a ligand-centred state (75%) which stands along a MLCT state (25%). This is also confirmed by the quantum mechanical calculations, showing that the main visible absorption band has an important ILCT character.
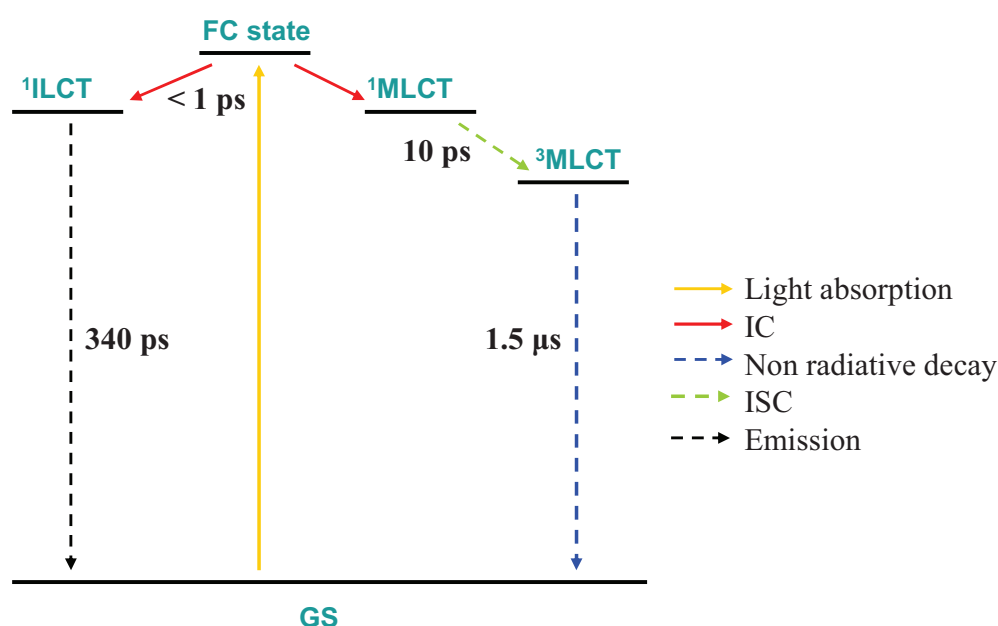
Fig. 3. 13. Schematic representation of the evolution of the excited states for complex **C9**.

L9 and **C10** behave very similarly to **L8** and **C9**, with only slightly different time constants (25 ps for the ISC and 300 ps for the ^{1}ILCT decay). The population partition between the ILCT and the MLCT state for **C10** is 90% and 10%, respectively.

For **C11**, the evolution is similar but the MLCT state is populated at 90% starting from the Franck-Condon state. The ISC to the triplet MLCT occurs in 10 ps, as observed for the heretoleptic copper(I) diimine complexes studied in chapter 2.

3.7. Conclusions

In this chapter, a series of heteroleptic copper(I) complexes was designed with the aim of improving the visible absorption properties of this class of compounds, which are, at the present time, one of the limitations for their use in solar energy conversion.

To reach this goal, chromophoric styrylbipyridine ligands were introduced in the coordination sphere. Indeed, these push-pull ligands have already proven to effectively increase the molar absorption coefficient of Ru^{II} complexes.[33] Bulky **L1** and **DPEphos** were chosen as complementary ligands.

This series of complexes exhibits indeed very intense absorption bands (5-7·10^4 M^{-1}cm^{-1}) in the visible. The analysis of the position, intensity and band shape indicates a strong contribution of an intra-ligand charge-transfer transition centred on the styrylbipyridine ligand. This assignment was also confirmed by TD-DFT calculations.

The complexes **C9**-**C13** showed surprisingly short emission lifetimes, which do not exceed 1 ns. This was unexpected, in particular for **C9** and **C10** that bear the **DPEphos** ligand, usually providing exceptionally strong and long-lived luminescence in copper(I) complexes.[14] Transient absorption spectroscopy was then used to investigate the evolution of the excited states. A very fast radiative relaxation of the ligand-centred state, responsible for the intense but short-lived luminescence, was observed. The MLCT state was longer-lived but not emissive. Interestingly, the two states seem to be strongly decoupled, and the population of the ILCT does not result in a relaxation to the MLCT, when the latter lies at lower energy.

References

1. Crabtree, G. W.; Lewis, N. S. *Phys. Today* **2007**, *60*, 37-42.
2. Magnuson, A.; Styring, S. *Aust. J. Chem.* **2012**, *65*, 564-572.
3. Barber, J. *Chem. Soc. Rev.* **2009**, *38*, 185-196.
4. Grätzel, M. *Acc. Chem. Res.* **2009**, *42*, 1788-1798.
5. Campagna, S.; Puntoriero, F.; Nastasi, F.; Bergamini, G.; Balzani, V. *Top. Curr. Chem.* **2007**, *280*, 117-214.
6. Flamigni, L.; Barbieri, A.; Sabatini, C.; Ventura, B.; Barigelletti, F. *Top. Curr. Chem.* **2007**, *281*, 143-203.
7. Kumaresan, D.; Shankar, K.; Vaidya, S.; Schmehl, R. *Top. Curr. Chem.* **2007**, *281*, 101-142.
8. Williams, J. *Top. Curr. Chem.* **2007**, *281*, 205-268.
9. Kirgan, R.; Sullivan, B.; Rillema, D. *Top. Curr. Chem.* **2007**, *281*, 45-100.
10. Armaroli, N.; Accorsi, G.; Cardinali, F.; Listorti, A. *Top. Curr. Chem.* **2007**, *280*, 69-115.
11. Lee, C.; Yum, J.-H.; Choi, H.; Ook Kang, S.; Ko, J.; Humphry-Baker, R.; Grätzel, M.; Nazeeruddin, M. K. *Inorg. Chem.* **2007**, *47*, 2267-2273.
12. Jiang, K.-J.; Xia, J.-b.; Masaki, N.; Noda, S.; Yanagida, S. *Inorg. Chim. Acta* **2008**, *361*, 783-785.
13. Feuvrie, C.; Maury, O.; Le Bozec, H.; Ledoux, I.; Morrall, J. P.; Dalton, G. T.; Samoc, M.; Humphrey, M. G. *J. Phys. Chem. A* **2007**, *111*, 8980-8985.
14. Cuttell, D. G.; Kuang, S.-M.; Fanwick, P. E.; McMillin, D. R.; Walton, R. A. *J. Am. Chem. Soc.* **2002**, *124*, 6-7.
15. Renouard, T.; Le Bozec, H.; Brasselet, S.; Ledoux, I.; Zyss, J. *Chem. Commun.* **1999**, 871-872.
16. Maury, O.; Guegan, J.-P.; Renouard, T.; Hilton, A.; Dupau, P.; Sandon, N.; Toupet, L.; Bozec, H. L. *New J. Chem.* **2001**, *25*, 1553-1566.
17. Maury, O.; Viau, L.; Sénéchal, K.; Corre, B.; Guégan, J.-P.; Renouard, T.; Ledoux, I.; Zyss, J.; Le Bozec, H. *Chem. Eur. J.* **2004**, *10*, 4454-4466.
18. Zoltewicz, J. A.; Helmick, L. S. *J. Org. Chem.* **1973**, *38*, 658-662.
19. Akdas-Kilig, H.; Malval, J.-P.; Morlet-Savary, F.; Singh, A.; Toupet, L.; Ledoux-Rak, I.; Zyss, J.; Le Bozec, H. *Dyes Pigm.* **2012**, *92*, 681-688.
20. Smith, A. P.; Lamba, J. J. S.; Fraser, C. L. *Org. Synth.* **2002**, *78*, 82-87.
21. Hutchison, A. J.; Williams, M.; Angst, C.; De Jesus, R.; Blanchard, L.; Jackson, R. H.; Wilusz, E. J.; Murphy, D. E.; Bernard, P. S. *J. Med. Chem.* **1989**, *32*, 2171-2178.
22. Horner, L.; Hoffmann, H.; Wippel, H. G. *Chem. Ber.* **1958**, *91*, 61-63.
23. Wadsworth, W. S.; Emmons, W. D. *J. Am. Chem. Soc.* **1961**, *83*, 1733-1738.
24. Wadsworth, D. H.; Schupp, O. E.; Seus, E. J.; Ford, J. A. *J. Org. Chem.* **1965**, *30*, 680-685.
25. Schmittel, M.; Ganz, A. *Chem. Commun.* **1997**, 999-1000.
26. Linfoot, C. L.; Richardson, P.; Hewat, T. E.; Moudam, O.; Forde, M. M.; Collins, A.; White, F.; Robertson, N. *Dalton Trans.* **2010**, *39*, 8945-8956.
27. Ziessel, R.; Juris, A.; Venturi, M. *Inorg. Chem.* **1998**, *37*, 5061-5069.
28. Yang, L.; Feng, J.-K.; Ren, A.-M.; Zhang, M.; Ma, Y.-G.; Liu, X.-D. *Eur. J. Inorg. Chem.* **2005**, *2005*, 1867-1879.
29. Wang, L.-Y.; Xu, Y.; Lin, Z.; Zhao, N.; Xu, Y. *J. Lumin.* **2011**, *131*, 1277-1282.
30. Wen, C.; Tao, G.; Xu, X.; Feng, X.; Luo, R. *Spectrochim. Acta, Part A* **2011**, *79*, 1345-1351.
31. Ichinaga, A. K.; Kirchhoff, J. R.; McMillin, D. R.; Dietrich-Buchecker, C. O.; Marnot, P. A.; Sauvage, J. P. *Inorg. Chem.* **1987**, *26*, 4290-4292.

32.   Moudam, O.; Kaeser, A.; Delavaux-Nicot, B.; Duhayon, C.; Holler, M.; Accorsi, G.; Armaroli, N.; Seguy, I.; Navarro, J.; Destruel, P.; Nierengarten, J.-F. *Chem. Commun.* **2007**, 3077-3079.

33.   Wang, P.; Klein, C.; Humphry-Baker, R.; Zakeeruddin, S. M.; Grätzel, M. *J. Am. Chem. Soc.* **2004**, *127*, 808-809.

CHAPTER 4

Photoinduced charge transfer with heteroleptic copper(I) diimine complexes

4.1. Photoinduced charge transfer with coordination compounds

A brief overview of the different approaches to artificial photosynthesis was given in the first paragraphs of chapter 1. The reproduction of the entire photosynthetic apparatus is an extremely complicated task, therefore the research community concentrates on the study of the various elements that constitute the complete system. The theme which is probably the most extensively investigated is photoinduced electron transfer within molecular arrays containing a photosensitizer connected through a molecular bridge to an electron donor and/or an electron acceptor.[1,2] These systems allow to investigate the parameters which govern the efficiency of the photoinduced electron transfer. Indeed, the charge separation over long distances, achieved by a sequence of rapid short-distance electron transfers in photosystems I or II, is the key strategy to generate long-lived charge-separated states required to perform catalytic reactions (see chapter 1). In artificial systems, this goal is pursued by linking several electroactive groups to the photosensitizer, in order to form polyads. The spatial arrangement is obtained in the natural photosynthetic apparatus by embedding the electron transport chain in a protein environment, while in artificial systems it is achieved by means of chemical bonds (of different type). The simplest molecular array in which the final charge-separated state (CSS) is achieved by two successive electron transfers is a triad. The processes leading to the photoinduced CSS are detailed in chapter 1 (paragraph 1.1.2.b), and can be resumed in a first photoinduced charge transfer that quenches the excited state of the sensitizer, followed by a hole or electron shift reaction leading to the final state D^+-S-A^-. In the final charge-separated state, the two charges are very distant from each other, and the back recombination reaction yielding the ground state is slowed down by a weak electronic coupling between the donor and the acceptor (low V_{DA} value in Eq. 1.6). Furthermore, the ΔG^o for the charge recombination is usually quite high, which locates this reaction in the Marcus inverted region ($-\Delta G^o > \lambda$, see paragraph 1.2.1).

Given the very different structures found in literature concerning the formation of charge-separated states triggered by light, a selection of some relevant examples from the point of view of this thesis project will be presented. A great deal of works has been published in literature about

systems composed of organic sensitizers.[3] In particular, free base or metallated porphyrins were widely used as photosensitizers to trigger charge separation processes in multi-component arrays, linked by covalent[4-7] or coordination bonds.[8,9] Nevertheless, these systems will not be considered here because the structures and properties are quite different from the compounds prepared in this thesis.

This introduction will focus on some polyads grounded in coordination complexes involving heavy metal ions (such as iridium, platinum and of course ruthenium). Furthermore, the approach based on coordination compounds allows building the final arrays in a "modular" way, which is convenient from a synthetic point of view because it enables to screen different combinations of donors and acceptors in a rather simple way.

4.1.1. Ruthenium complexes

Among the structures having a coordination complex as photosensitizer, those based on ruthenium(II) complexes are certainly the most widely investigated.[10] This stems from the suitable photophysical properties of these compounds, combined with their stability and the easy accessibility of stable heteroleptic structures.

The archetype $[Ru(bpy)_3]^{2+}$ complex can be used to design a large variety of triads by appending donor and acceptor units to two different bipyridine ligands. However, this approach suffers from the unavoidable formation of different isomers leading to uncontrolled donor-acceptor distances.[11] In the **PTZ-Ru-MV^{2+}** triad prepared by Meyer and colleagues (Fig. 4. 1), this was indeed the case, but the four isomers could be isolated.[12] The phenothiazine (**PTZ**) and the methylviologen (**MV^{2+}**) can therefore be at a distance ranging from 7.0 to 16.5 Å.
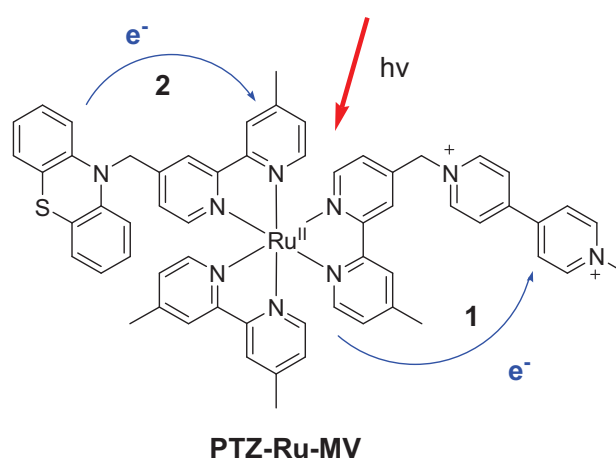
PTZ-Ru-MV

Fig. 4. 1. Structure of one of the possible isomers of the triad **PTZ-Ru-MV** published by Meyer and colleagues.[12]

Upon excitation of the $[Ru(bpy)_3]^{2+}$ unit, the charge-separated state $PTZ^{\bullet+}-Ru-MV^+$ was obtained and characterized by transient absorption spectroscopy. The four positional isomers showed excited-state lifetimes ranging from 115 to 220 ns, reflecting different distances between the electroactive units. However, in all cases the charge-separated lifetime was remarkably enhanced with respect to the $Ru-MV^{2+}$ dyad ($\tau_{CR} \sim 25$ ps).

To overcome the problem of isomer formation and separation, different strategies were elaborated. In all cases the target was to find rigid linear structures providing a fixed donor-acceptor distance. The first choice was based on the use of a $[Ru(tpy)_2]^{2+}$ core (tpy = 2,2';6,2''-terpyridine), allowing the construction of triads with the appended groups pointing in diametrically opposite directions.[13,14] The intrinsic problem of this kind of structure, however, is the short lifetime of the ^{3}MLCT excited state (in the ns timescale, due to the weak ligand field imparted by the poor bite angle of 158º of the terpyridine ligands) that leads to a rapid nonradiative decay through the contribution of d-d states,[15] and therefore to inefficient electron-transfer quenching. However, many systems based on the $[Ru(tpy)_2]^{2+}$ core can be found in literature.[13,15]

Recently, two strategies were proposed to obtain linear Ru^{II}-based triads. The first one consists in the use of a 5,5'-disubstituted bipyridine ligand, bearing the donor group (**TAA**, trisarylamine) on one side and the acceptor group (**AQ**, anthraquinone) on the opposite direction (Fig. 4. 2, left).[16] Upon excitation in the MLCT band of the ruthenium(II) complex, the charge-separated state $TAA^{\bullet+}-Ru-AQ^{\bullet-}$ is attained by reductive quenching of the ^{3}MLCT state followed by an electron transfer from the reduced ruthenium complex to the anthraquinone moiety. The CSS is obtained with a quantum yield exceeding 64%, and has lifetime around 1.3 μs in acetonitrile (about 2 orders of magnitude longer than that of the corresponding **TAA-Ru** dyad).
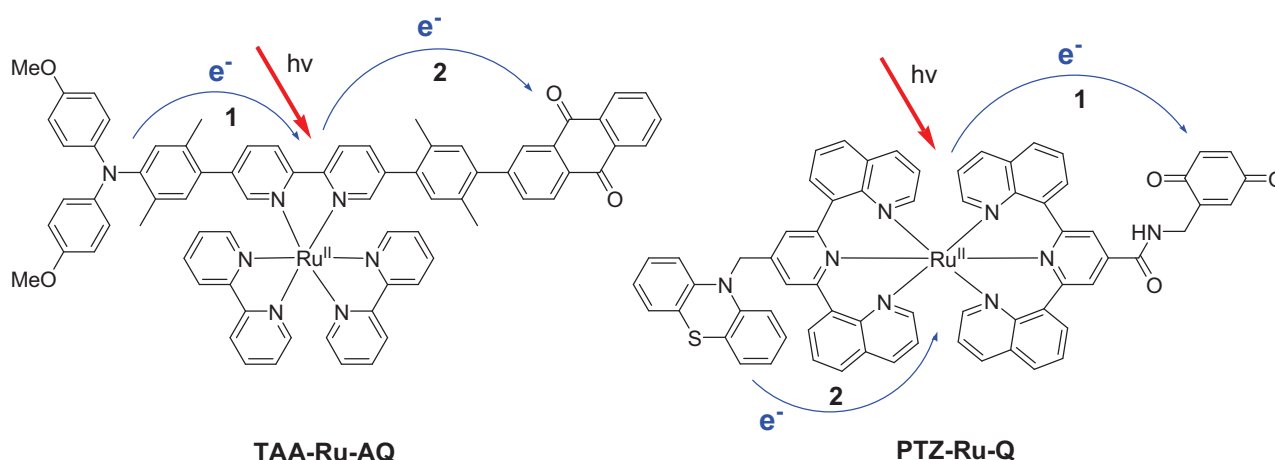
Fig. 4. 2. Structure of the linear triads **TAA-Ru-AQ** [16] and **PTZ-Ru-Q**.[17]

The second strategy is based on the use of a new terdentate ligand, bis(diquinolinyl)pyridine (bqp), having an increased bite angle with respect to terpyridine.[18] Thanks to the nearly perfect octahedral coordination geometry creating a strong ligand field, the ^{3}MLCT state has a microsecond timescale lifetime. This property, joint to the linear arrangement of the appended electroactive groups, led to the elaboration to the **PTZ-Ru-Q** triad (Fig. 4. 2, right).[17] The excited state of the Ru^{II} complex, obtained upon visible excitation, undergoes oxidative quenching by electron transfer to the quinone group, followed by a very fast hole shift to the phenothiazine moiety, to yield **PTZ$^{\bullet+}$-Ru-Q$^{\bullet-}$** with a 95% yield ($\tau_{CR} \sim 200$ ns). It is important to note that the corresponding **Ru-Q** dyad did not show any **Q$^{\bullet-}$** signal in transient absorption, due to inverted kinetics ($k_{BET} > k_{ET}$). The secondary electron transfer from the **PTZ** moiety was able to compete with the back electron transfer, indicating the pertinence of constructing a triad.

Another interesting triad was the **Mn$_2^{II,II}$-Ru^{II}-NDI$_2$** triad studied by Hammarström and co-workers, where the charge-separated state **Mn$_2^{III,II}$-Ru^{II}-NDI$^{\bullet-}$NDI** exhibited an impressive lifetime of 600 μs.[19] This system has been already mentioned in chapter 1, in the section concerning the photosensitization of water splitting catalysts (paragraph 1.2.2.d).

4.1.2. Iridium complexes

Iridium(III) terpyridine complexes, due to the linear arrangement of the electroactive units provided by the terdentate ligands, appear as another very interesting possibility. The higher energy content of the excited state and its much longer lifetime with respect to Ru^{II} or Os^{II} analogues represent valuable properties.

An interesting structure was published by Sauvage and co-workers in 2006 (Fig. 4. 3).[20] The Ir^{III} terpyridine core (**Ir**) allows to build a linear triad containing a trisarylamine (**TAA**) as the electron donor and a naphthalene diimide as the electron acceptor (**NDI**). The three units are connected by amide bonds, providing a very small electronic coupling as confirmed by the electrochemical and spectroscopic measurements. Excitation of the Ir^{III} terpyridine core results in a reductive quenching of the excited state by hole shift to the amine group, yielding the first charge-separated state **TAA$^{\bullet+}$-Ir$^{\bullet-}$-NDI** after less than 20 ps. The charge recombination at this stage is quite rapid ($\tau \sim 70$ ps), but a second electron transfer from the reduced complex to the NDI group can operate, to give the fully charge-separated state **TAA$^{\bullet+}$-Ir-NDI$^{\bullet-}$**. The latter is obtained with a quantum yield of 10% (due to the fast charge recombination after the first photoinduced electron transfer) but has a very interesting lifetime of 120 μs. The long τ_{CR} is attributed to the long distance attained between the opposite charges (5 nm) and proves the relevance to design linear polyads.
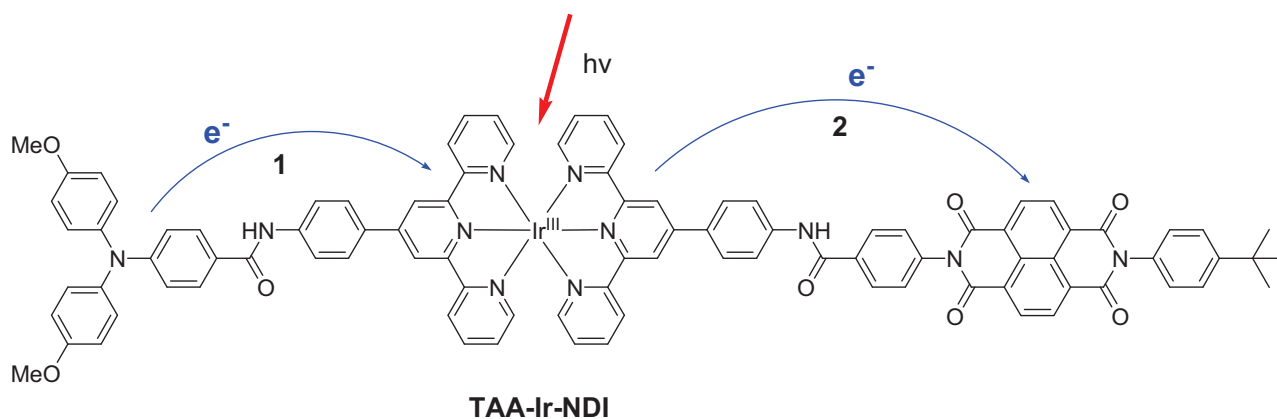
Fig. 4. 3. Structure of the triad **TAA-Ir-NDI** of Sauvage and co-workers.[20]

4.1.3. Platinum complexes

Platinum(II) complexes containing diimine or terpyridine ligands show interesting features both from photophysical and structural points of view. They display long-lived ^{3}MLCT excited states that can undergo reductive or oxidative quenching[21] if connected with electron donors or acceptors, however these complexes being not very stable upon oxidation, oxidative quenching should be avoided. Some examples studied in the Eisenberg group are reported below.[21-23]

The first example **(PTZ)$_2$-Pt-PhNO$_2$**, is based on a Pt^{II} diimine bis-acetylide chromophore (Fig. 4. 4).[22] Upon excitation of the MLCT band at 405 nm, the characteristic features of the **PTZ$^{\bullet+}$** and **PhNO$_2^{\bullet-}$** species were observed by transient absorption spectroscopy. The charge-separated state transiently stores 1.67 eV, and decays with a time constant of 70 ns. However, in this kind of structure, the distance between the donor and the acceptor moieties is not maximized.
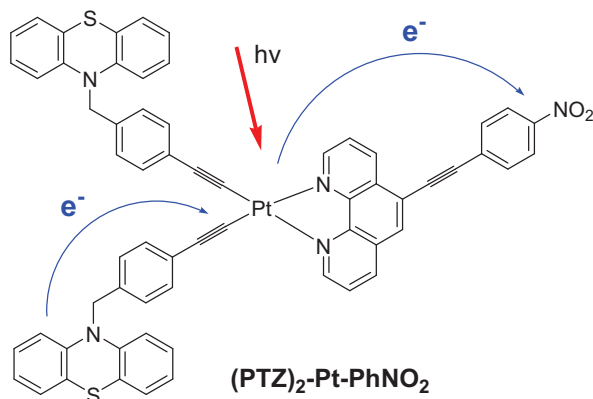
Fig. 4. 4. Structure of the **(PTZ)$_2$-Pt-PhNO$_2$** triad published by Eisenberg and co-workers.[22]

Other platinum(II) bis-acetylide systems were also published by Weinstein and colleagues. In one case, the structure is very similar to that reported by Eisenberg, except that a naphthalene

diimide acceptor was directly linked to the phenanthroline ligand. The corresponding **Pt-NDI** dyad did not exhibit a charge-separated state due to an ultrafast ISC of the excited platinum(II) complex, leading to nonradiative decay.[24] The triad with the secondary **PTZ** donor, conversely, underwent charge separation, recombining is 65 ns.

Alternatively, terpyridine allows the preparation of linear structures in which the maximal separation between the donor and the acceptor is achieved. In the **TMB-Pt-Py$^+$** system,[23] the Pt^{II} complex is connected to a trimethoxybenzene (**TMB**) *via* an amide linker, and to a pyridinium (**Py$^+$**) acceptor through a methylene spacer (Fig. 4. 5). In this case, the first charge-separated state **TMB$^{\bullet+}$-Pt$^{\bullet-}$-Py$^+$** is formed, but the second electron transfer to obtain the fully charge-separated state **TMB$^{\bullet+}$-Pt-Py** does not occur. This underlines the importance of the choice of both the electroactive groups and the linkers in order to control the photophysical properties.

On the contrary, in triad **PTZ-Pt-PhNO$_2$**,[21] the charge-separated state **PTZ$^{\bullet+}$-Pt-PhNO$_2$$^{\bullet-}$** is obtained with 20-30% quantum yield and a lifetime of about 230 ns. Interestingly, despite the fact that reductive quenching is the most thermodynamically and kinetically favoured process for the primary electron transfer ($\Delta G \sim 0.4$ eV, $\tau < 10$ ns), the charge recombination of the corresponding **PTZ$^{\bullet+}$-Pt$^{\bullet-}$-PhNO$_2$** state is very rapid and gives the ground state in about 30 ns. The fully charge-separated state is achieved after oxidative quenching to form the intermediate **PTZ-Pt$^{\bullet+}$-PhNO$_2$$^{\bullet-}$** ($\Delta E \sim 0.1$ V, $\tau \sim 30$ ns), which undergoes the second electron transfer in about 30 ns.
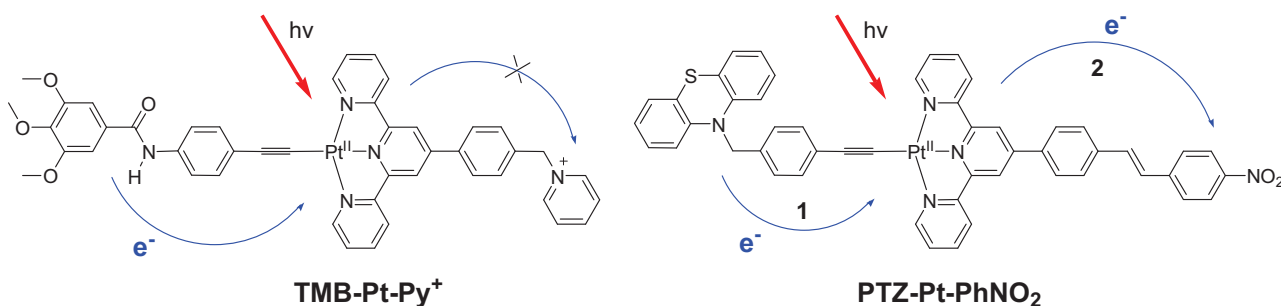
Fig. 4. 5. Structure of the triads **TMB-Pt-Py$^+$** [23] and **PTZ-Pt-PhNO$_2$**.[21]

4.1.4. Copper complexes

The use of copper(I) complexes as sensitizers for photoinduced electron transfer being the central topic of this chapter, the literature in this area will be reviewed in greater detail. The studies concerning electron transfer to molecular quenchers in solution were mentioned in chapter 1. Despite some examples of reductive quenching of *[Cu(NN)$_2$]$^+$,[25] the excited states of copper(I) complexes are essentially good reductants (with $E(Cu^{II}/Cu^{I}*) \sim -1.1$ eV vs. SCE). For this reason the majority of the published systems concentrate on Cu^I-electron acceptor systems.

The first studies on covalently-bound Cu^I-acceptor dyads were undertaken by the group of G. J. Meyer.[26,27] An heteroleptic copper(I) complex coordinated by a bipyridine and two triphenylphosphine ligands was bound to a methylviologen *via* a butyl chain (Fig. 4. 6). In this dyad, emission was found to be efficiently quenched by comparison to the reference compound $[Cu(dmb)(PPh_3)_2]PF_6$ (dmb = 4,4'-dimethyl-2,2'-bipyridine). Transient absorption spectroscopy attributes this phenomenon to a photoinduced electron transfer to the MV^{2+} moiety. The charge-recombination lifetime (comprised between 20 ns in dichloroethane and 1.8 µs in DMSO), was found to be strongly solvent-dependent, underlining the influence of the structure of the complex and of the coordination character of the solvent on the charge-transfer dynamics. The proposed explanation is that solvent molecules can coordinate the oxidized Cu^{II} ion, and add a kinetic barrier for the charge recombination reaction.
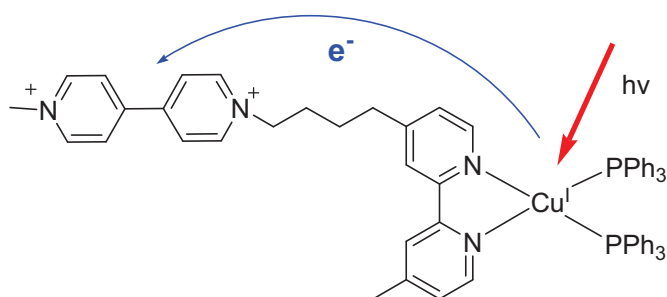
Fig. 4. 6. Structure of the **Cu-MV^{2+}** dyad synthesized by Meyer's group.[26,27]

Other systems were elaborated, in which the copper(I) diimine core is connected to metal-containing groups. Structurally interesting arrays were formed by connecting a copper(I) bis-bipyridine complex to four Ru^{II} porphyrins by means of axial coordination.[28] This structure can be used to study energy transfer processes in spatially assembled porphyrins, but the photophysical studies for the Cu^I complex were not reported in the paper.

The connection of Cu^I complexes to other coordination compounds was also explored by the construction of mechanically interlocked molecules. In the [2]-catenate bound to a $[Ru(tpy)_2]$, shown in Fig. 4. 7 (top), energy transfer was evidenced between the two weakly coupled units. At 77 K, the Ru^{II}-centred MLCT emission was strongly quenched, but electron transfer from Cu^I to the excited Ru^{II} complex moiety was ruled out by the small ΔG° value of this process.[29] Similar energy transfer quenching of $[Ir(tpy)_2]$ excited state was observed in the Ir^{III}-Cu^I pseudo-rotaxane shown in **Fig. 4. 7** (bottom).[30]
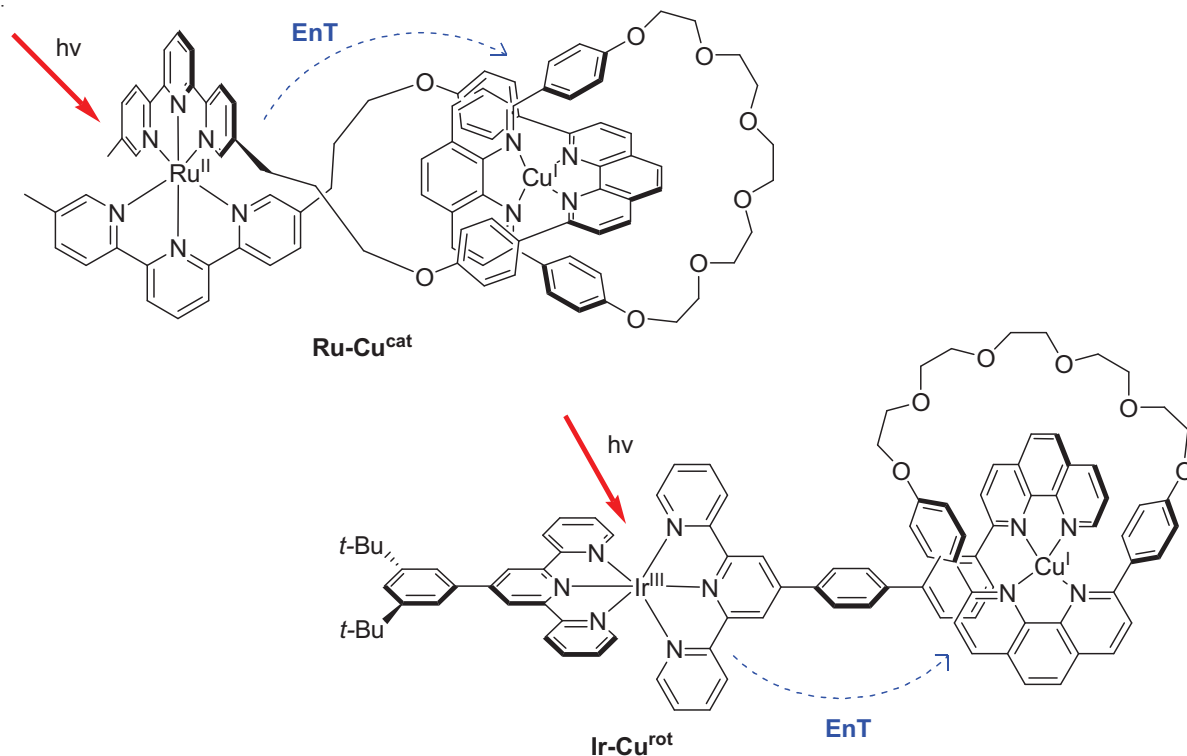
Fig. 4. 7. Structure of two mechanically interlocked structures where copper(I) diimine is covalently bound to $[Ru(tpy)_2]^{2+}$ or $[Ir(tpy)_2]^{3+}$ units.[29,30] EnT: energy transfer.

Another important family of compounds, developed by Nierengarten and Armaroli, is composed of copper(I) complexes connected to fullerene. The latter is a good electron acceptor and has characteristic singlet and triplet transient absorption features.[31,32] Moreover, it displays low energy $\pi\pi^*$ states (good energy acceptor). In the sandwich structure C_{60}-Cu^I-C_{60} presented in Fig. 4. 8,[33] electronic absorption and electrochemical data reveal a certain degree of electronic communication between the electroactive units. Complete quenching of the copper(I) diimine-centred MLCT state was observed, while the C_{60} unit deactivated like the model fullerene compound upon excitation. This phenomenon was explained by a photoinduced electron transfer from excited copper(I) diimine to the fullerene moiety, favoured by the formation of a Cu^{II}-phen$^{\bullet-}$ (MLCT state) that deactivates by transferring an electron to the C_{60} acceptor. The formation of the flattened Cu^{II} species during the excitation step, in fact, contributes to lowering the kinetic barrier for the charge transfer reaction by reducing the inner and outer-sphere reorganization energies.

Further studies on fullerohelicates containing bismethanofullerene and methanofullerene (Fig. 4. 8, right) evidenced the fundamental difference imparted by the number of binding sites on the C_{60} group.[34] As in the previous case, quenching of the MLCT emission of $[Cu(NN)_2]^+$ was observed for the two compounds. However, quenching of the fullerene-centred emission was observed only for the methanofullerene adduct. This difference was explained by a smaller reorganization energy and

slightly less negative reduction potential of methanofullerenes, that are thus more prone to undergo electron transfer. In copper(I)-assembled rotaxanes containing methanofullerenes stoppers (not shown),[32] the same quenching of both the photoactive units was observed. However, the charge-separated state could not be observed by transient absorption, probably due to ultrafast charge recombination.
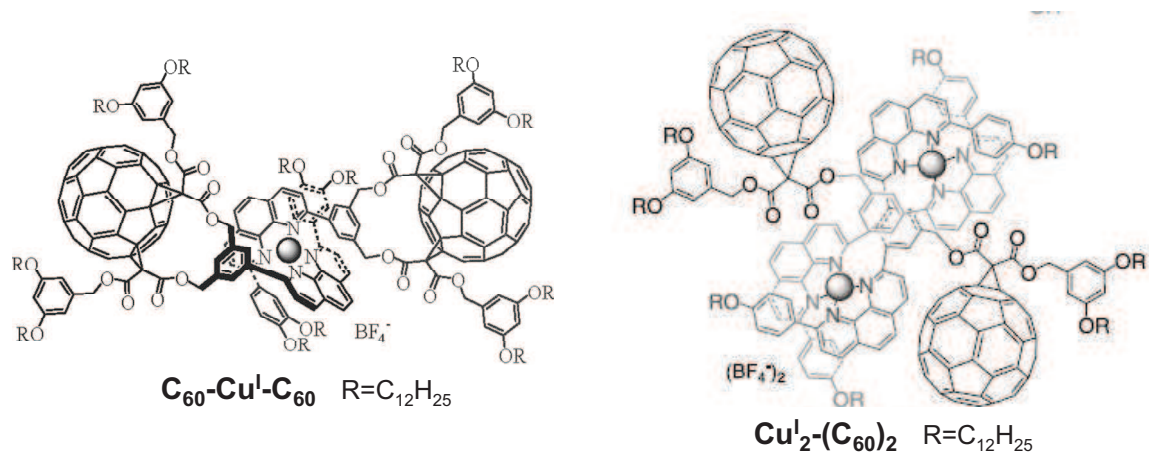
Fig. 4. 8. Sandwich structure of C_{60}-Cu^I-C_{60} (left) [33] and fullerohelicate containing methanofullerene (right).[34]

Cu^I bisphosphine complexes, which are generally strongly emissive, were also used to build Cu^I-C_{60} systems.[35] Two bisphosphine ligands were investigated: **DPEphos** (already used in the previous chapter) and **dppf** (diphenylphosphinoferrocene), and both complexes were connected to methanofullerene (Fig. 4. 9). In the first case, electron transfer to C_{60}, followed by relaxation to the Cu^I-$^3C_{60}$* state (energy sink) were observed. In the ferrocene-containing system, the **Fc** moiety acts as energy acceptor quenching all the excited states.
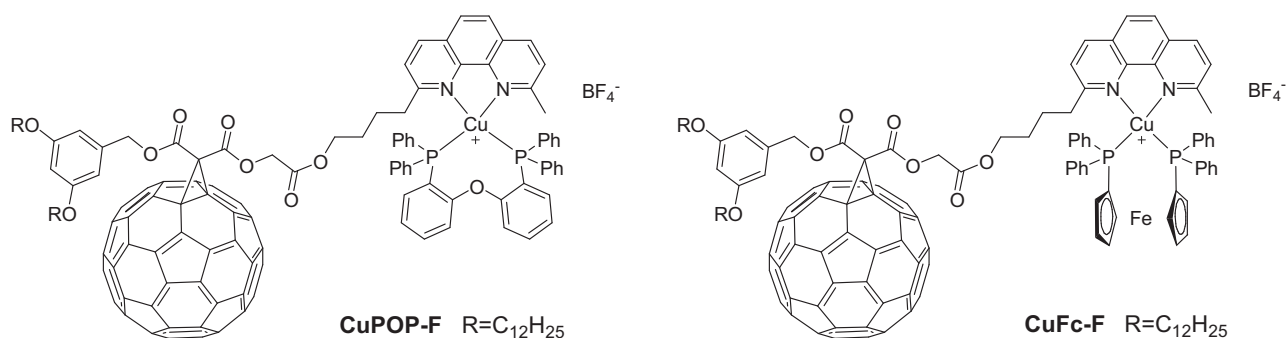
Fig. 4. 9. Structure of the complexes **CuPOP-F** and **CuFc-F**.[35]

A last and very elegant example of copper(I) based complex used for photoinduced charge-separation was reported in 2010 by Schuster and colleagues (Fig. 4. 10).[36] The molecules are rotaxanes, assembled around a Cu^I diimine complex, with a C_{60} sphere connected to the macrocycle

(through one or two bonds) and two **Fc** units as stoppers, at each end of the thread. The formation of the **Fc-Cu^{II}-C$_{60}$$^{\cdot-}$** state is followed by transient absorption spectroscopy, but no evidence of the second electron transfer to give the fully charge-separated state **Fc$^{\cdot+}$-Cu^{I}-C$_{60}$$^{\cdot-}$** is seen (the model **Cu^{I}-C$_{60}$** and the triads show the same charge-separated-state lifetime). This fact was attributed to a lack of electronic coupling between the Fc and the oxidized copper complex.

Fc-Cu^{I}-C$_{60}$ R = ferrocene (Fc)
ZnP-Cu^{I}-C$_{60}$ R = zinc porphyrin (ZnP)
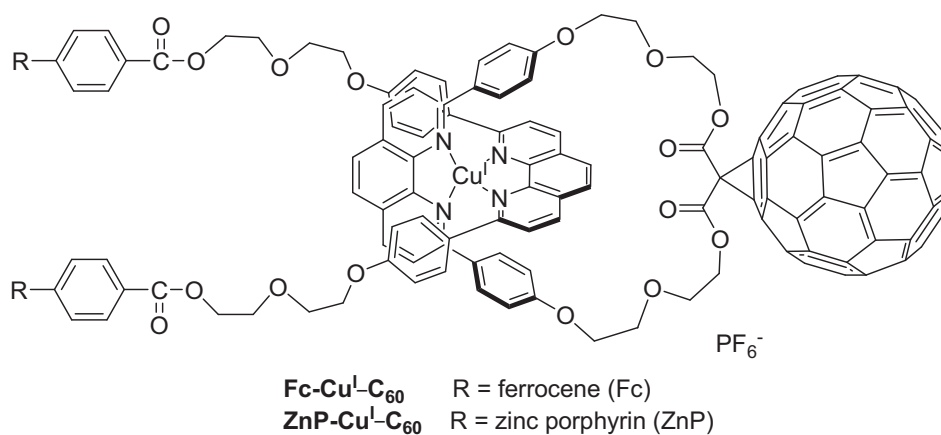
Fig. 4. 10. Structure of the **Fc-Cu^{I}-C$_{60}$** triad published by Schuster and colleagues.[36]

Catenate and rotaxane triads bearing porphyrins instead of ferrocenes as electron donors were also prepared very recently by the same group, and the charge-separated state **ZnP$^{\cdot+}$-Cu^{I}-C$_{60}$$^{\cdot-}$** was observed by nanosecond transient absorption upon excitation at 355 nm. The charge recombination occurs in 240 ns.[37]

Copper(I) bis-phenanthroline complexes were also abundantly used to assemble photoactive units such as porphyrins,[38-40] but this aspect is beyond the scope of this work as the copper complex was not the main photoactive unit to trigger the photoinduced process.

4.2. Synthesis and characterization of copper(I)-based dyads for photoinduced charge transfer

The aim of this part of the work is to show that a heteroleptic copper(I) diimine complex can be used as central unit to prepare dyads and linear triads to perform photoinduced electron transfer. Taking into account the impressive reductive properties of the excited state, the first task was to synthesize and characterize a dyad where the copper(I) diimine core is connected to an electron acceptor. Then, a donor group will be added to form a Donor-Sensitizer-Acceptor (**D-S-A**) triad, in order to contemplate the possibility to extend the lifetime of the charge-separated state.

The structures designed to conduct this study are presented in Fig. 4. 11.
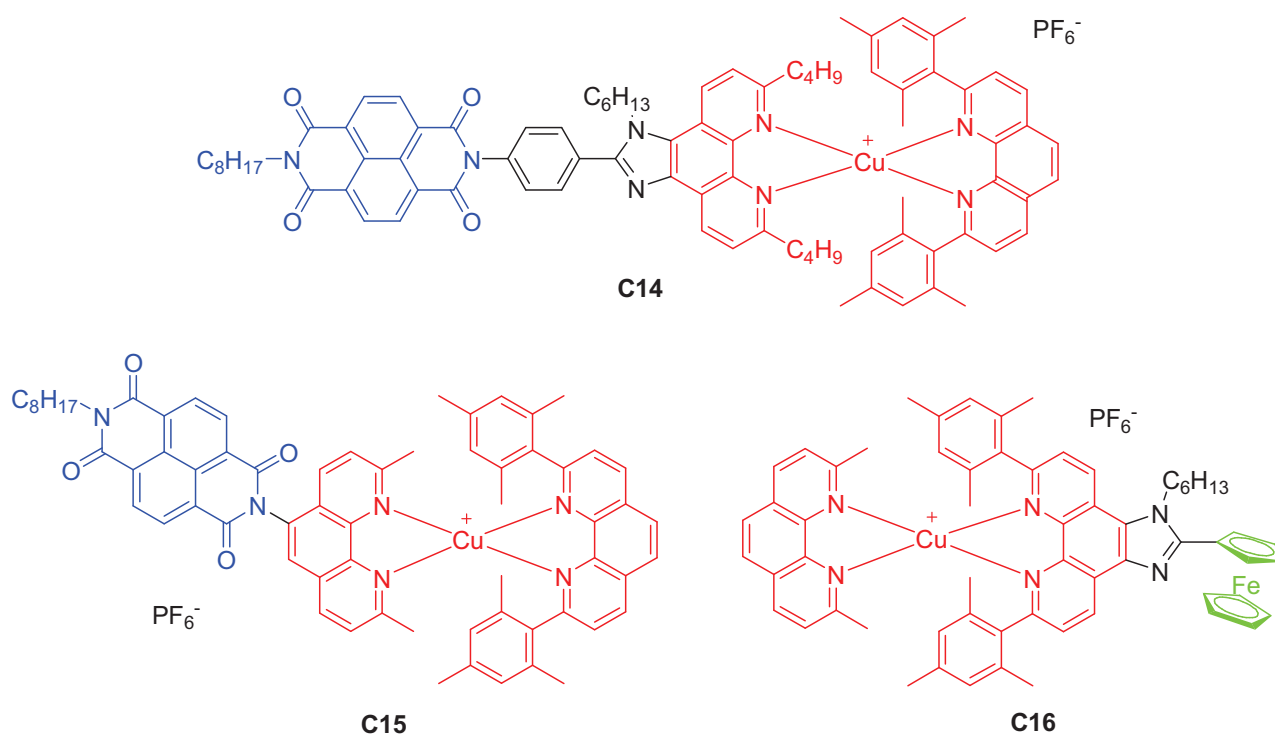
Fig. 4. 11. Structures of the copper-based dyads for photoinduced electron transfer. ▬ Sensitizer (**Cu^I diimine**); ▬ Donor group (**NDI**); ▬ Acceptor group (**Fc**).

The electron acceptor selected for this purpose was naphthalene diimide, **NDI**. This molecule was used for the construction of an impressive number of donor-acceptor arrays,[14,41,42] and displays extremely useful features, such as relatively anodic reduction potential (around -0.6 V vs. SCE) implying that electron transfer from excited copper(I)-diimine complexes ($E_{Cu(II)/Cu(I)^*} \sim$ -1.1 eV vs. SCE) should be thermodynamically possible. It is also known that the HOMO and LUMO orbitals of naphthalene diimide display nodes on the nitrogen atom of the imide group, that break the electronic interaction with the rest of the molecule.[43] In addition to this, the excited singlet,

triplet states of NDI, along with the reduced radical, display characteristic spectral signatures,[44] facilitating the detection of the charge-separated state by transient absorption spectroscopy.

Two dyads bearing the NDI moiety were synthesized (**C14** and **C15**), differing by the nature and length of the linker between the electron acceptor and the phenanthroline ligand. The first one results from the connection of the Cu^I diimine complex to the NDI moiety through a phenyl-imidazole spacer, while NDI is directly attached to the phenanthroline in the second case. Both structures are rigid, and will allow us to investigate the effect of the spacer between the copper-based photosensitizer and the NDI electron acceptor.

Ligand **L12** (see Fig. 4. 12) enables the construction of a linear rigid structure **C14** and to control the distance between the electroactive groups. A similar structure, devoid of butyl chains and bearing a donor polyamine group, has been previously reported for the study of accumulative photoinduced electron transfer.[45] In this case, the phenanthroline core is modified with bulky groups in order to obtain a Cu^I complex with an excited-state lifetime compatible with charge transfer processes. The *n*-hexyl chain bound to the imidazole spacer has the role of increasing the solubility of the ligand in organic solvents; an important issue when dealing with NDI-containing molecules, which are very prone to aggregation.[46] Moreover, as already pointed out, the presence of a labile proton on the imidazole makes the photophysical studies more complicated, due to the possible occurrence of proton coupled electron transfers.[47]

A second ligand bearing the NDI group was also designed (**L13**, Scheme 4. 9), where the naphthalene diimide is directly connected to the phenanthroline through a simple C-N bond. The corresponding Cu-NDI dyad (**C15**) allows studying the effect of the spacer on the behaviour of these electronically decoupled systems.

In order to build a triad, another ligand containing an electron donor group was prepared. Ferrocene was selected because of its reversible electrochemical behaviour and low oxidation potential (around 0.5 V vs. SCE), which provides a sufficient free energy for electron transfer to the oxidized copper(II) complex ($E_{Cu(II)/Cu(I)} \sim 0.9$ V vs. SCE).[48] Moreover, ferrocene displays a high synthetic versatility and a low reorganization energy. The corresponding Fc-Cu dyad (**C16**) was synthesized to provide the donor-sensitizer block. However, given the excited state reduction potential of our complexes ($E_{Cu(I)*/"Cu(0)"} < 0.4$ V vs. SCE, as $E^{00} \sim 2.0$ eV and $E_{Cu(I)/"Cu(0)"} < -1.6$ V vs. SCE) we do not expect reductive quenching. A rather short spacer between the coordinating phenanthroline and the ferrocene moiety was chosen, in order to favour a fast hole shift. To obtain a pure heteroleptic complex by applying the HETPHEN synthetic strategy, two hindering mesityl rings were placed in position 2 and 9 of phenanthroline. The synthesis of the different ligands and complexes will be now presented.

4.2.1. Synthesis of the NDI-containing ligands L12^Imi and L12^Oxa

The ligand **L12^Imi** can be roughly divided into three portions: 2,9-di-*n*-butyl-1,10-phenanthroline-5,6-dione (**A**), the central phenyl ring (**B**) and the terminal naphthalene diimide (**C**), as shown in Fig. 4. 12. The synthesis of such a structure can be performed using two strategies: either C is connected to AB, or A is connected to BC. In all cases, NDI is connected to the rest of the molecule by reacting the corresponding monoanhydride on an aromatic amine.
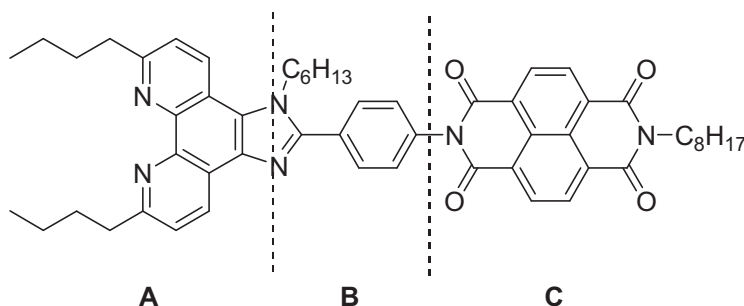
Fig. 4. 12. Structure of the ligand **L12^Imi** and identification of the three blocks **A**, **B** and **C**.

4.2.1.a. Strategy 1: (AB)+C.

The first strategy consisted in the sequential addition of the three blocks. 2,9-di-*n*-butyl-1,10-phenanthroline-5,6-dione **8** was prepared by oxidation of the 2,9-di-*n*-butyl-1,10-phenanthroline by a mixture of sulphuric and nitric acid with sodium bromide according to an earlier reported procedure,[49] as described in chapter 2. The harsh operating conditions (concentrated and strongly oxidizing acid mixture, high temperature) and the careful temperature control needed during the addition of the reactants led to quite variable yields, ranging from 40% to 95%, owing to the possibility of unselective oxidation of the molecule. Therefore, another protocol was attempted, in which diluted sulphuric acid was used with potassium bromate as the oxidant, at room temperature.[50] These milder conditions gave a high, reproducible reaction yield (93%), and could be performed on large reactant quantities.
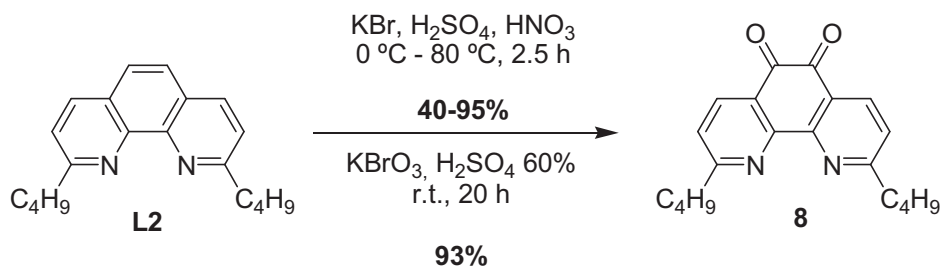
Scheme 4. 1. Oxidation of **L2**.

Condensation of the dione **8** with 4-nitrobenzaldehyde in presence of ammonium acetate afforded 4'-nitrophenylimidazo[4,5-*f*][1,10]phenanthroline **14**. The subsequent alkylation reaction was performed directly on the crude of **14** due to purification difficulties (the polar product tends to stick on silica gel and alumina). The imidazole ring was deprotonated with caesium carbonate in dry DMF and then alkylated with hexyl iodide to afford **15** in 30% yield (2 steps). The low yield can be attributed to the formation of the oxazole derivative, in the imidazole synthesis step, which however was not isolated during purification.

The formation of the oxazole derivative during the Steck and Day synthesis is not unusual, but the factors leading to the formation of imidazole or oxazole are not completely unravelled. However, the reaction conditions (temperature, reaction time) seem to play an important role, as well as the aldehyde nature.[51] Moreover, the two pathways leading to the formation of the two heterocycles, share a common intermediate. The imidazole pathway is taken upon attack of ammonia on this intermediate,[52] so it is probable that the excess ammonium acetate favours the formation of the imidazole ring.
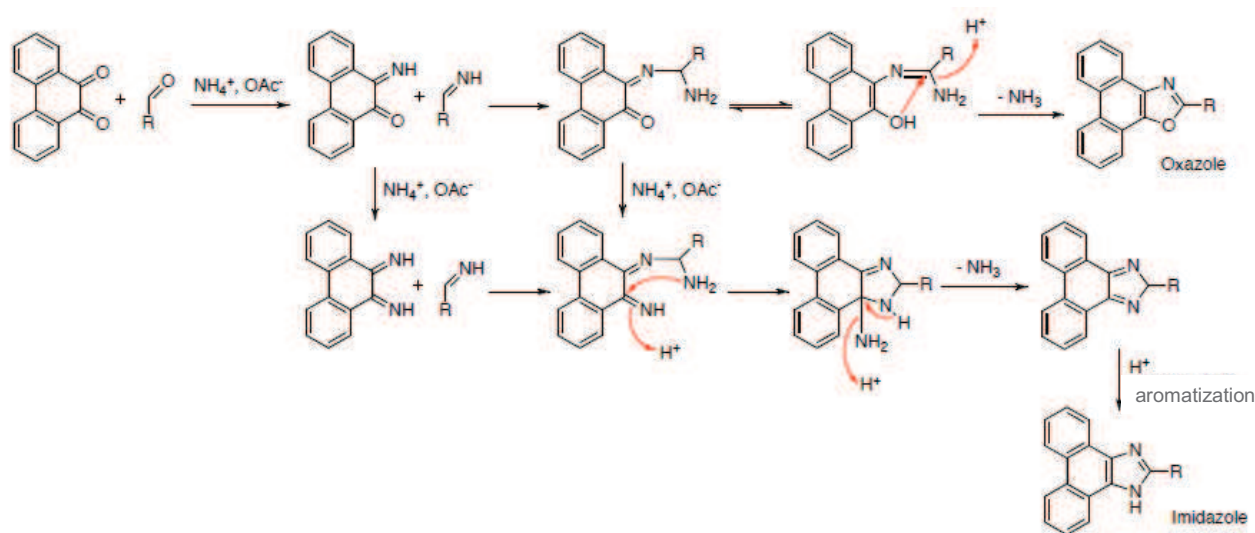
Scheme 4. 2. Mechanism for the imidazole and oxazole formation during Steck and Day reaction.[52]

The alkylation of the nitrogenated heterocycle avoids dealing with a mixture of different species in solution since the imidazole proton is quite acidic and therefore easily prone to deprotonation. Additionally, the long alkyl chain imparts an increased solubility in organic solvents. The nitro group was then reduced with hydrazine in presence of palladium on charcoal, to yield the desired aromatic amine. The reaction proceeded smoothly with a quantitative yield.
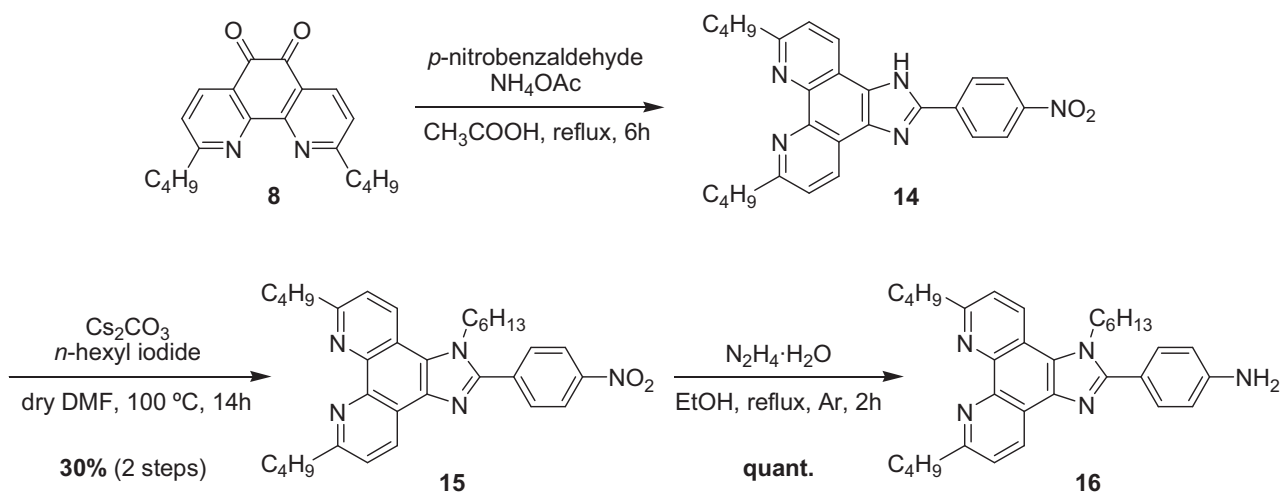
Scheme 4. 3. Synthesis of **16**.

The amino group was finally reacted under microwave activation with naphthalene imide mono anhydride **17**[53] to give ligand **L12^Imi**. However, the purification of the molecule was tedious, probably because of the presence of excess **17** interacting by strong π-stacking with the product, making the separation by column chromatography very tricky. For this reason, size exclusion chromatography was chosen (Sephadex LH20 swollen in CH_2Cl_2: CH_3OH = 60: 40).
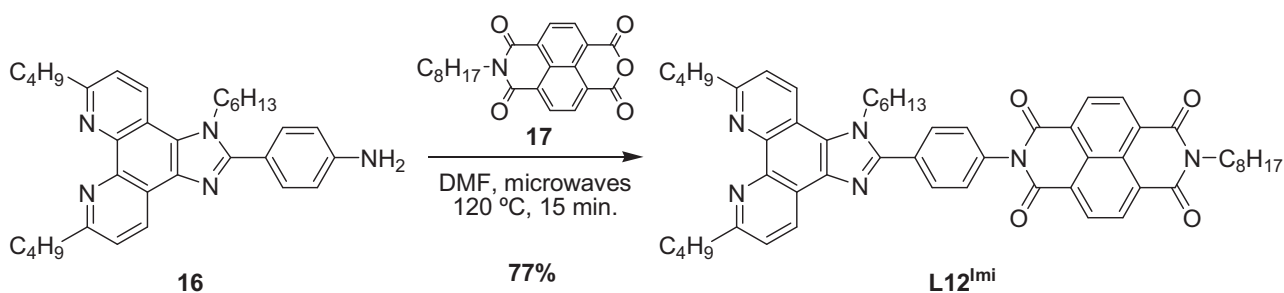
Scheme 4. 4. Synthesis of **L12^Imi**.

Even if the ligand could be obtained in a satisfactory yield, the purification after the last step proved to be complicated, and it was difficult to obtain an extremely pure compound. For this reason, another synthetic pathway was elaborated.

4.2.1.b. Strategy 2: A+(BC)

This convergent approach is based on the synthesis of a NDI-substituted benzaldehyde, which is coupled with the dione **8** in the last reaction step providing the desired structure.

The first block, **B**, was obtained by protecting 4-nitrobenzaldehyde as an acetal, and then reducing it to amine under hydrogen pressure in presence of palladium on charcoal as a catalyst.[54] It should be

noted that the amine **19** proved not to be very stable, as it tended to degrade in presence of even slightly acidic solvents (the formation of a bright yellow compound was observed in the NMR tube containing deuterated chloroform as the solvent, probably a polymer).
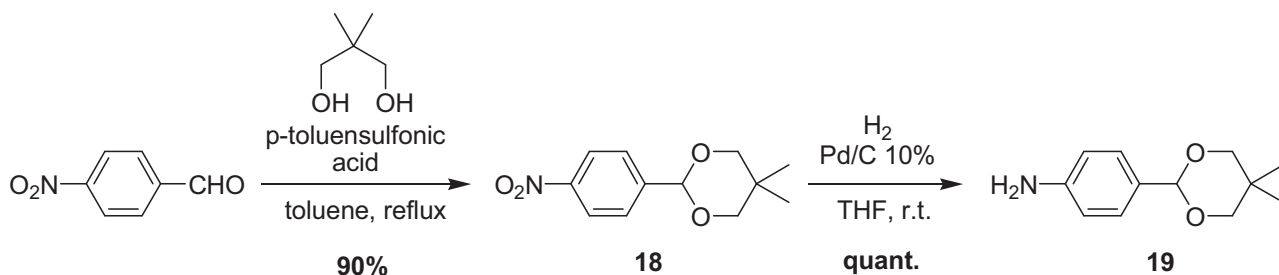
Scheme 4. 5. Synthesis of the block **B**.

The obtained aniline derivative was reacted with naphthalene monoimide **17** in presence of a stoichiometric quantity of Zn(OAc)$_2$, using molten imidazole as solvent. These conditions had previously been used for the synthesis of similar compounds.[55] In this case, the product was obtained in quite a modest yield of 46%, that is not unusual for this kind of reaction.[14] After purification, the aldehyde was deprotected in acidic conditions by using trifluoroacetic acid in chloroform.
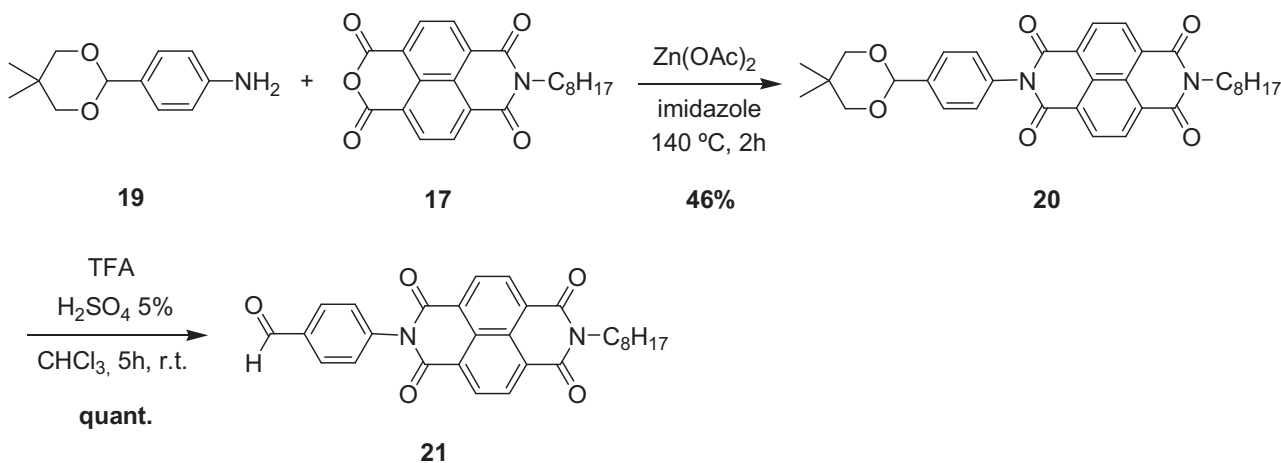
Scheme 4. 6. Synthesis of the block **BC**.

The two final steps to get ligand **L12** are the imidazole formation and the alkylation of the heterocycle. The first reaction was performed using a modification of the Steck and Day protocol,[56] using milder conditions and provides higher yield and purer product.[57] This method uses chloroform, instead of acetic acid, as the solvent and therefore the temperature is lower (61 ºC instead of 120 °C). Surprisingly, the main product obtained after purification was the oxazole

derivative (**L12**[**Oxa**]), instead of the imidazole (**L12**[**Imi**]). The imidazole/oxazole proportion depends on the water content of the reaction mixture; the higher the latter, the larger the amount of oxazole vs. imidazole. Even if the molecule was not the one initially planned, the synthesis of the corresponding Cu[I]-NDI dyad can be interesting to compare the effect of the linker on the electron transfer efficiency. Indeed, this aspect has already proven to play an important role in ruthenium dyads for the study of accumulative photoinduced electron transfer.[45]
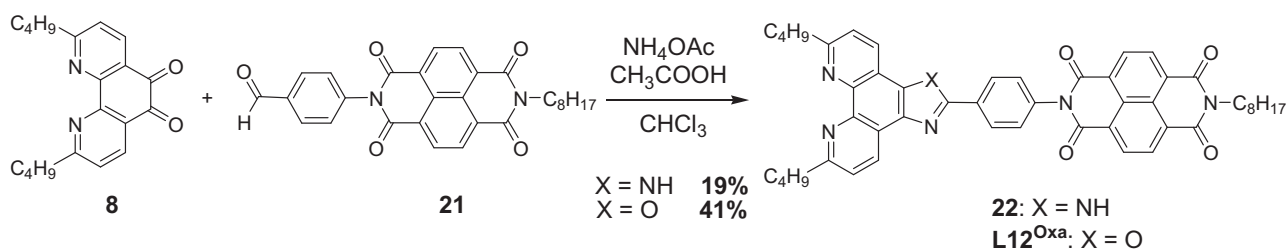
Scheme 4. 7. Synthesis of **22** and **L12**[**Oxa**].

The reaction conditions were then optimized to get a higher imidazole proportion: all the solvents were distilled and the ammonium acetate was sublimated before use, in order to have a water content as low as possible in the reaction medium. Lowering the water content, which is quite high in both acetic acid and ammonium acetate, helps preventing hydrolysis of the many imine intermediates in the synthesis (Scheme 4. 2). The strategy proved to be successful, as **22** was obtained as the major product. Since the imidazole derivative is very polar, and tends to stack on silica gel, the crude **22** was engaged in the following step without further purifications. Ligand **L12**[**Imi**], was obtained by alkylation of the heterocycle, and was separated from the oxazole impurities by repeated column chromatographies on silica gel.
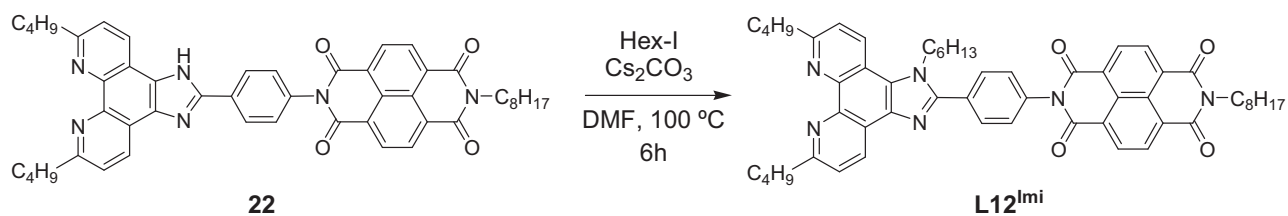
Scheme 4. 8. Synthesis of **L12**[**Imi**].

This strategy led to a global yield (imidazole formation and alkylation) of 29%. The low yield can be certainly ascribed to the formation of a minority but non negligible percentage of the oxazole derivative, and to the several purification steps required to separate the two molecules.

The two ligands were characterized by ^{1}H and ^{13}C-NMR, and high-resolution mass spectrometry confirmed the hypothesized structures. The NMR spectrum of **L12^{Imi}** (Fig. 4. 13), recorded in deuterated chloroform, shows the typical pattern of asymmetrical 2,9-disubstituted phenanthroline ligands, with two different doublets corresponding to the protons H^4 and H^7. H^3 and H^8 are displayed as a single doublet (2H). The NDI moiety is displayed as an intense signal at 8.82 ppm, composed of a doublet with a very low coupling constant (0.8 Hz) with one very low peak on each side. Interestingly, in the spectrum of **17** the four protons H^{NDI} originate a singlet. In the aliphatic part, **L12^{Imi}** is characterized by the signals of the different linear chains; in particular, the two triplets of the nitrogen-bound methylenes are found at 4.67 (N-CH$_2^{nHex}$) and 4.22 ppm (N-CH$_2^{nOct}$) and constitute a good fingerprint of the molecule, together with the multiplet of the phenanthroline-bound butyls at 3.24 ppm. **L12^{Oxa}** has very similar features but lacks the hexyl chain signals around 4.7 ppm.
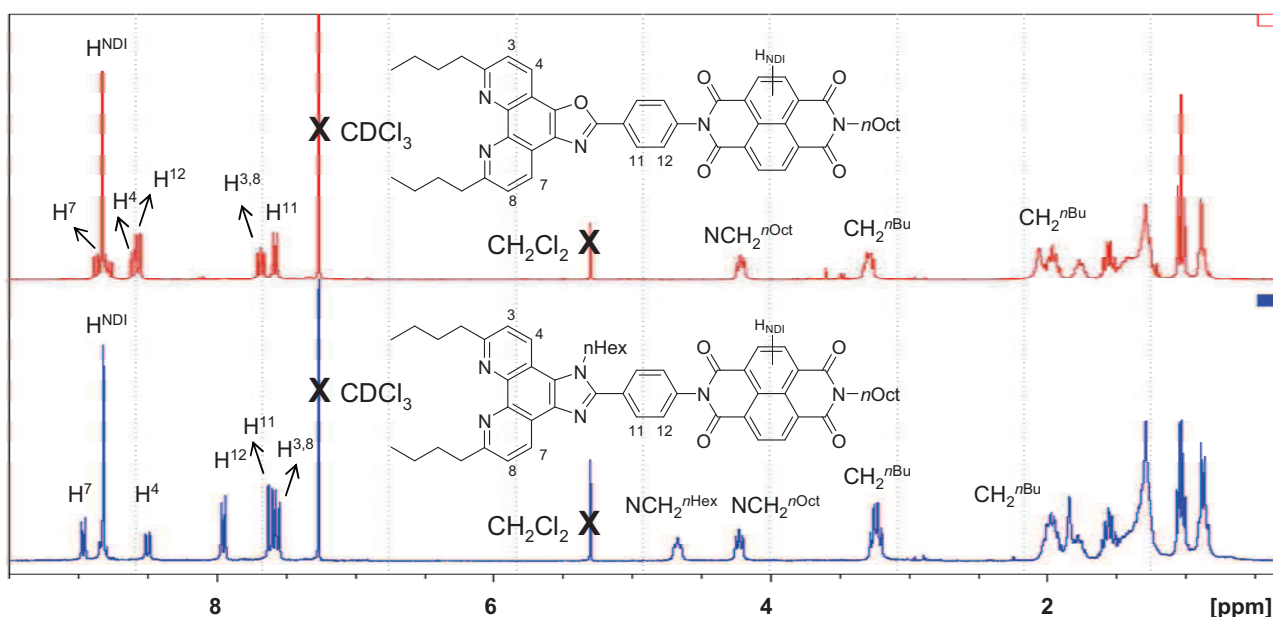
Fig. 4. 13. ^{1}H-NMR spectra of the ligands **L12^{Imi}** and **L12^{Oxa}**, recorded in CDCl$_3$.

Interestingly, the two ligands have very different solubility properties: **L12^{Oxa}** is quite insoluble in dichloromethane while **L12^{Imi}** displays a good solubility, proving that the alkyl chain on the central heteroatomic ring plays an important role.

4.2.2. Synthesis of the NDI-containing ligand L13

Ligand **L13** has a structure which is very similar to a previously reported ligand used for the synthesis of a Pt^{II}-based dyad.[24] In our case, two methyl groups at the 2 and 9 positions of the

phenanthroline ring are added to increase the excited state lifetime of the Cu^I complex, leaving therefore more time for the photoinduced charge transfer processes to occur.

The synthesis of ligand **L13** was carried out in three steps starting from commercial neocuproine (2,9-dimethyl-1,10-phenanthroline). The central ring underwent nitration in a mixture of nitric and sulphuric acid,[58] and the nitro group was subsequently reduced with hydrazine using palladium 10% on charcoal as catalyst.[24] It is important to note that all the attempts to prepare 5-amino-2,9-di-*n*-butyl-1,10-phenanthroline failed. The nitration conditions led to irremediable degradation of **L2** (only a few mg of 5-amino-2,9-di-*n*-butyl-1,10-phenanthroline were isolated) and no results were obtained by the alkylation of 5-nitro or 5-amino-1,10-phenanthroline.

24 was then reacted with naphthalene imide mono anhydride **17** to obtain ligand **L13**. Attempts to increase the yield by using different reaction conditions (microwave activation, use of molten imidazole as the solvent) did not lead to substantial improvement. The best yield (23%) was obtained by heating the amine **24** in presence of excess **17** in dry N,N-dimethylformamide for 14 hours. It should be noted, however, that this amine is particularly hindered, and deactivated by the electron withdrawing capacity of the phenanthroline core. These facts could account for the low nucleophilicity of the amine.
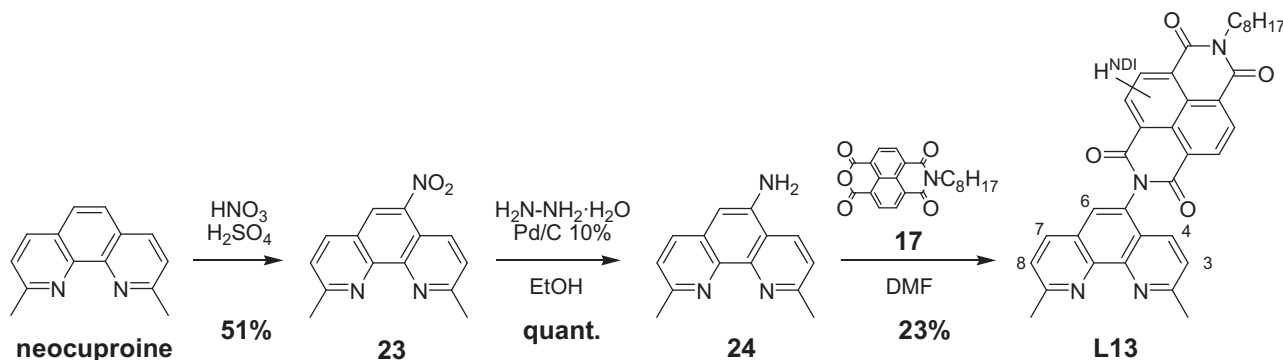
Scheme 4. 9. Synthesis of the ligand **L13**.

The ^{1}H-NMR spectrum was recorded in deuterated chloroform. It shows the expected pattern for a 5-substituted neocuproine derivative: the signals of H^3, H^4, H^7 and H^8 appear as four distinct doublets because of the asymmetry of the molecule, while H^6 is displayed as a singlet. H^{NDI} originates the typical intense peak at 8.84 ppm, already described for **L12^{Imi}**. Even the two methyl groups appear as two close singlets at 2.99 and 2.95 ppm. The characteristic broad triplet of the N-CH$_2$^{nOct} is found at 4.23 ppm.

4.2.3. Synthesis of the ferrocene-containing ligand L14

The ligand **L14** is composed of a 2,9-dimesityl-1,10-phenanthroline unit connected to a ferrocene moiety through an imidazole linker. Like in the previous cases, the imidazole ring is alkylated with a hexyl chain. The choice of a short linker, an imidazole, was motivated by the need of insuring a rapid hole transfer from the photo-oxidized copper(II) cation.

The synthesis of this ligand was performed in two steps starting from 2,9-dimesityl-1,10-phenanthroline-5,6-dione **7**. At first, the imidazole was formed by reacting **7** with ferrocene carboxaldehyde. For this step, a modified Steck and Day protocol was used, which was found in literature for the synthesis of a very similar phenanthroline ligand lacking mesityl substituents in the 2 and 9 positions.[57] The reaction is described as proceeding with quantitative yield, after simple precipitation, but in our case many successive purifications by column chromatography were needed to obtain high purity of **25** (the mesityl groups have probably altered the solubility properties of the final compound, precluding precipitation/crystallization as described in the aforementioned article) and this led to a mediocre yield of 37%. The alkylation step was performed using the protocol described before, and afforded **L14** as a beige-yellow solid in 83% yield.
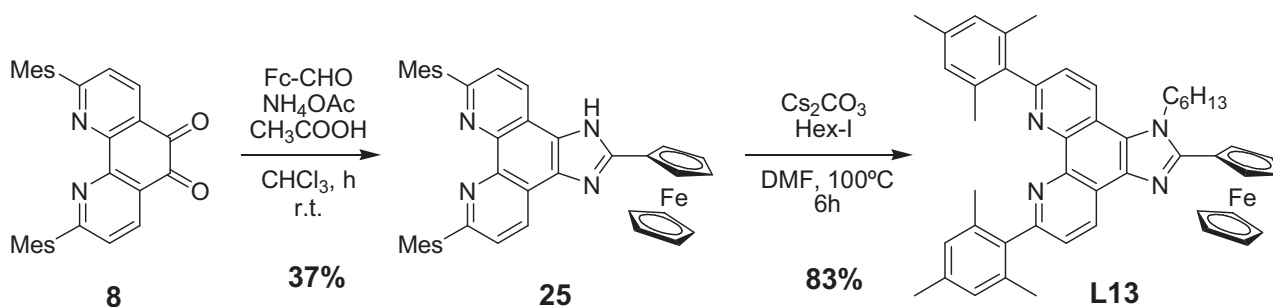
Scheme 4. 10. Synthesis of ligand **L14**.

The ^{1}H-NMR of the ligand was recorded in deuterated chloroform and displays the characteristics of unsymmetrical 2,9-disubstituted phenanthrolines owing to the presence of the *n*-hexyl chain on the imidazole. The three ferrocene peaks can be found in the region between 4 and 5 ppm.

4.2.4. Synthesis of the Cu-NDI dyads C14^{Imi} and C14^{Oxa}

The copper(I)-naphthalene diimide dyads **C14^{Imi}** and **C14^{Oxa}** were synthesized according to the HETPHEN protocol already described in chapters 2. The syntheses were performed in dry degassed dichloromethane at room temperature. Ligand 2,9-dimesity-1,10-phenanthroline **L1**,

containing the bulky mesityl rings, was chosen as the complementary ligand. Interestingly, a mixture of compounds formed for both the molecules after the synthesis, probably containing a non negligible quantity of homoleptic complex, despite the excess of **L1** used. The problem was observed through the NMR spectrum of the crude product. To solve this problem, the lability of Cu^I complexes was exploited: an excess of **L1** was added and the obtained mixture was purified by repeated column chromatography. Finally, the best conditions were obtained through the use of preparative TLC on silica gel, with dichloromethane and 4% methanol as the eluent. Pure **C14^{Imi}** was thus obtained in 29% yield. However, it was not possible to completely purify **C14^{Oxa}**, and this prevented us from studying the photophysical behaviour of this compound. The cause of the formation of the homoleptic complex is not clear yet, though probably in the case of **C14^{Oxa}** it can be ascribed to the highly diluted conditions imposed by the low solubility of the ligand **L12^{Oxa}** in dichloromethane. The complexes were obtained as orange solids.
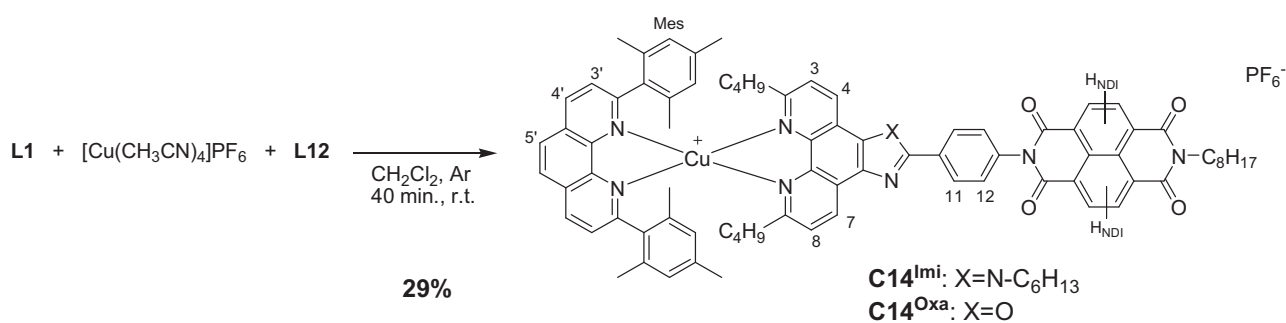
Scheme 4. 11. Synthesis of the complexes **C14^{Imi}** and **C14^{Oxa}**.

The aromatic region of the ^{1}H-NMR spectrum of **C14^{Imi}**, recorded in deuterated chloroform, is shown in Fig. 4. 14.
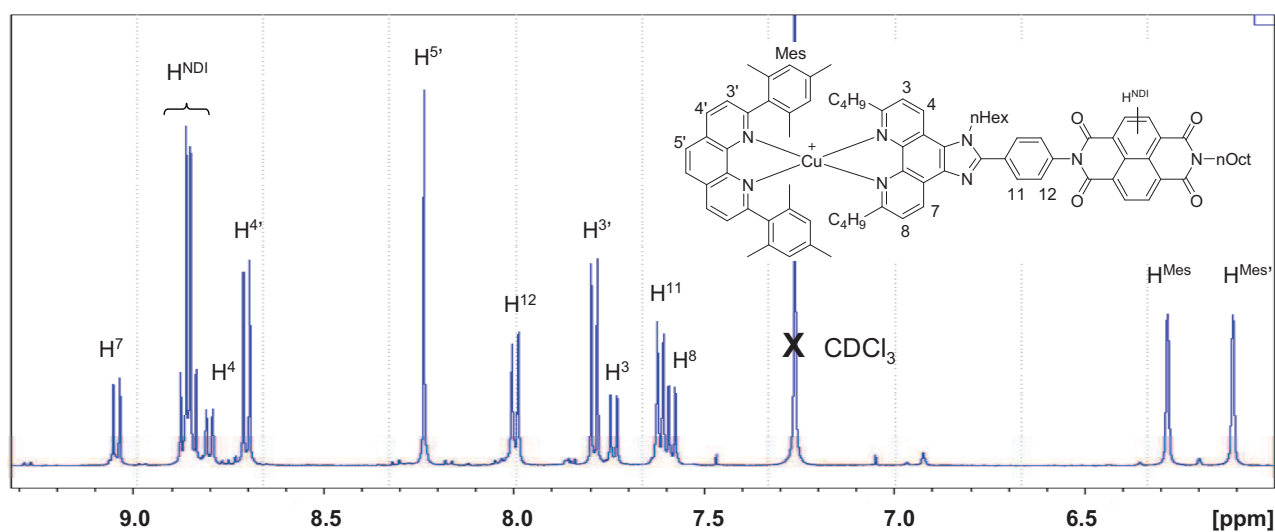
Fig. 4. 14. Enlargement of the aromatic part of the ^{1}H-NMR spectrum of **C14^{Imi}**, recorded in CDCl$_3$.

Similarly to the other complexes, it is composed by the superimposition of the signals of the two ligands, with some changes in the chemical shift values due to the coordination of the metal cation on one hand (downfield shift of the protons on the phenanthrolines) and to the shielding imposed by the phenanthroline cores to the substituents in α of the nitrogens on the other hand (upfield shift of the signals of protons H^{Mes}, due to ring-current effects). It is important to note that the H^{NDI} signal is split into a characteristic multiplet (see Fig. 4. 14), as already observed in the ligand $L12^{Imi}$.

4.2.5. Synthesis of the Cu-NDI dyad C15

The Cu-NDI dyad **C15** differs from the two previous ones by the nature of the linker between the copper-diimine sensitizer S and the NDI acceptor moiety A, which is directly bound to the phenanthroline ligand through a C-N imide bond. Another difference with the previously described structures is the coordination cage, which is slightly less encumbered owing to the presence of the methyl groups on the acceptor ligand, instead of the butyl chains found in $L12^{Imi}$. The synthesis scheme is represented below, **C15** was obtained in 55% yield after purification.
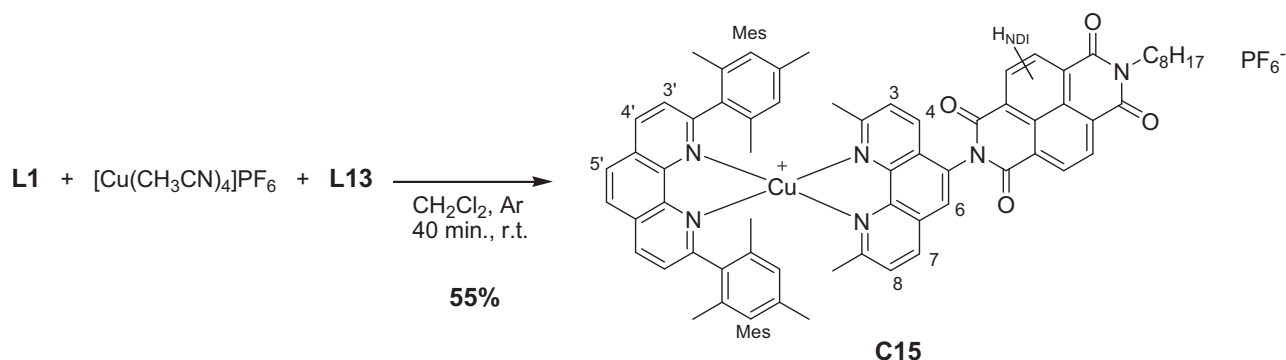
Scheme 4. 12. Synthesis of the complex **C15**.

The ^{1}H-NMR spectrum, recorded in deuterated chloroform, shows the usual superposition of the ligands signals with downfield shift of the peaks relative to the phenanthroline protons and upfield shift of those attributed to the substituents in the 2 and 9 positions of the two chelating ligands.

4.2.6. Synthesis of the Cu-Fc dyad C16

As mentioned earlier in this chapter, copper(I)-diimine sensitizers are poor photooxidants and electron transfer from Fc to the excited sensitizer is highly improbable for thermodynamic reasons. However, the study of the dyad **C16** is just as mandatory as the study of **C14** and **C15** in

order to anticipate and analyse the behaviour of the future triads. The synthesis of dyad **C16** was performed like the previous ones, but **L14** was used in excess, and **dmp** was used as the complementary ligand so that **C15** and **C16** bear the same coordination cage. The product was repeatedly purified by column chromatography on silica gel and size exclusion chromatography, and was obtained as a red solid in 49% yield.
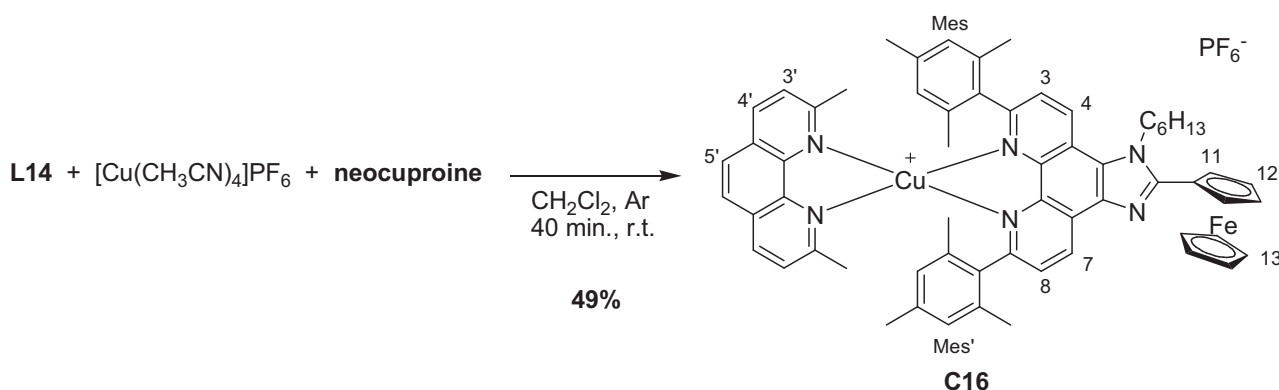
Scheme 4. 13. Synthesis of the complex **C16**.

Unlike what was found for the other compounds, the NMR spectrum of complex **C16** presented very broad peaks in deuterated chloroform. In particular, the signals of the ligand **L14** were poorly resolved. However, the mass spectrometry showed the sole presence of the expected product, and no impurities were detected.

4.2.7. Reference compounds

The choice of the reference compounds has an important role because it allows to study the behaviour of each component of the molecular scaffolds independently, and to have a term of comparison to help identify the charge transfer processes.

A special attention has to be paid to the copper complexes. As seen before, the coordination cage plays a major role in determining the photophysical and electrochemical properties of the molecules. For this reason, complex **C1** can conveniently act as a good model for **C14^{Imi}**, while **C18** (Fig. 4. 15) was synthesized as a model for **C15** and **C16**.

C14^{Imi}, however, presents a more complex structure, comprising an imidazo-phenyl spacer between the copper(I)-diimine complex and the acceptor naphthalene diimide. For this reason, the use of **C6'** was initially planned. The use of this compound as a reference, though, raises some issues about the possibility of an increased intersystem crossing rate due to the heavy atom effect provided by bromine. As a consequence, the possibility of using this compound as a reference for time-resolved

photophysical measurements was put aside. However, it can be useful in order to compare other properties like ground-state absorption. The complexes were synthesized with the usual protocols and were fully characterized by NMR and mass spectrometry (see experimental part).
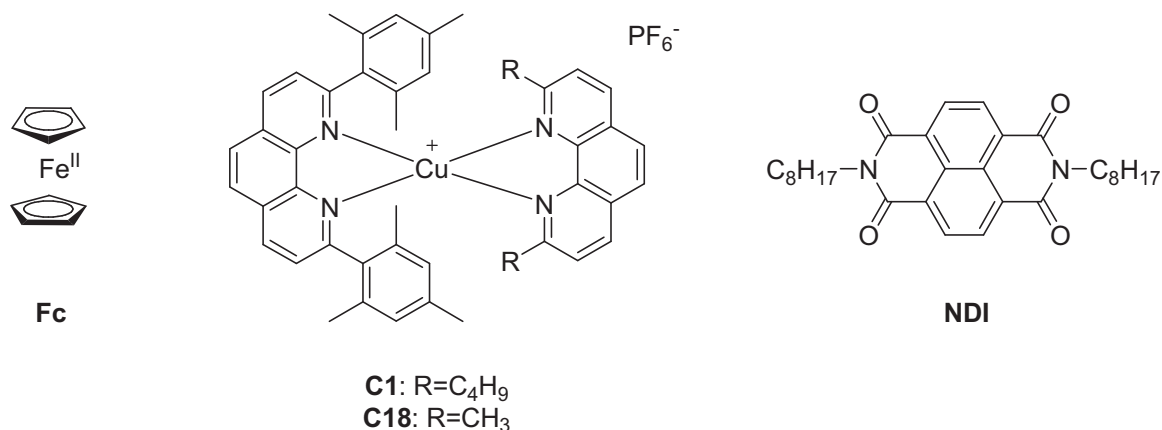
Fig. 4. 15. Structure of the reference compounds **Fc**, **C1**, **C18** and **NDI**.

4.3. Characterization of the dyads

In this paragraph, the characterization of the ligands and dyads will be described, and the properties will be related to those of the reference compounds in order to first evaluate the possibility of photoinduced electron transfer. The time-resolved photophysical measurements will be commented afterwards.

4.3.1. Absorption spectroscopy

The absorption spectra of all the complexes along with the corresponding references recorded in dichloromethane are presented in Fig. 4. 16, while the data are collected in Table 4. 1.

The three ligands containing the naphthalene diimide moiety are easily recognised by the characteristic vibrationally resolved bands peaking at 338, 359 and 379 nm. These bands originate from the $S_1 \leftarrow S_0$ transition.[24,44,59] Ligand **L13**, lacking the spacer between phenanthroline and NDI, has a very low absorption below 340 nm, while **L12^{Imi}** and **L12^{Oxa}** display intense bands in that region. Such bands have already been observed in the spectrum of ligand **L6** and are attributed to π-π* transitions centred on the phenanthroline fused with the adjacent heterocycle (imidazole or oxazole). The spectrum of the simple **NDI** model bis-*n*-octyl naphthalene diimide (Fig. 4. 15) reveals the structured spectrum with maxima at 340, 357 and 378 nm attributed to the π-π* transitions as reported in the literature. The spectral features of NDI are virtually not altered by the

154

presence of phenanthroline and imidazole moieties, revealing the lack of electronic communication between these units.

L14 displays another important feature: the low shoulder at 438 nm ($\varepsilon = 850$ M^{-1}cm^{-1}) due to the d-d transitions centred on the ferrocene moiety. These transitions are responsible for the orange colour of the ferrocene-based compounds. The presence of such low lying d-d states is not innocent towards the charge transfer phenomena that we aim to study, since it can be involved in energy transfer processes.[35,48] In particular, the MLCT excited state of copper(I) complexes can potentially be quenched by energy transfer to ferrocene. This aspect will be discussed further on in the paragraphs dedicated to emission properties and photophysical studies. The UV part of the spectrum is dominated by the strong π-π* absorptions, with two absorption bands at 263 and 297 nm.

	λ (nm) [ε (M^{-1}cm^{-1})]
L12^{Imi}	380 [3.2·10^4]; 359 [2.9·10^4]; 340 [2.3·10^4]; 289 [4.0·10^4]; 277 [4.2·10^4]
L12^{Oxa}	380 [3.8·10^4]; 359 [4.2·10^4]; 339 [3.4·10^4]; 280 [3.7·10^4]
L13	427 [9.6·10^3]; 407 [9.7·10^3]; 378 [2.1·10^4]; 358 [1.8·10^4]; 339 [1.3·10^4]
L14	438 [850]; 297 [4.6·10^4]; 263 [4.6·10^4]
NDI	378 [2.9·10^4]; 357 [2.3·10^4]; 340 [1.4·10^4]
C18	461 [5.5·10^3]; 275 [4.8·10^4]
C1	458 [4.2·10^3]; 276 [4.6·10^4]
C6'	465 [5.0·10^3]; 394 [4.2·10^3]; 278 [7.5·10^4]
C14^{Imi}	462 [4.9·10^3]; 377 [3.4·10^4]; 357 [3.2·10^4]; 275 [8.7·10^4]
C15	466 [5.1·10^3]; 380 [2.8·10^4]; 360 [2.4·10^4]; 342 [1.7·10^4]; 275 [4.8·10^4]
C16	475 [6.9·10^3]; 284 [5.0·10^4]; 263 [5.2·10^4]

Table 4. 1. UV-Visible absorption data for the ligands and the complexes described in the previous paragraphs, recorded in dichloromethane.

C1 and **C6'** were chosen as the reference compounds for **C14^{Imi}**. The former reproduces the structure of **C14^{Imi}** lacking the naphthalene diimide moiety, but has a bromine atom which could influence the intersystem crossing process thanks to the heavy atom effect, while the latter has a simpler structure that accounts for the coordination cage. The reference compounds show two characteristic bands: the lower energy, weaker band at around 460 nm is the classical copper(I) diimine MLCT absorption and the more intense one, located below 300 nm, is assigned to the phenanthroline ligand-centred π-π* transitions. The higher extinction coefficient of **C6'** is ascribed to the presence of the spacer, which absorbs in the same region.

Absorption spectrum of dyad **C14^{Imi}** exhibits the independent features of both the Cu^I diimine and the NDI moieties and the characteristic bands are only slightly modified compared to parent compounds. This indicates that the electronic interaction of the phenanthroline moiety with the appended NDI or fused imidazole is relatively weak in the ground state. This was much expected since there are orbital nodes on the nitrogen atoms of the NDI, weakening electronic communication between the latter and any nitrogen-connected moiety.[43]
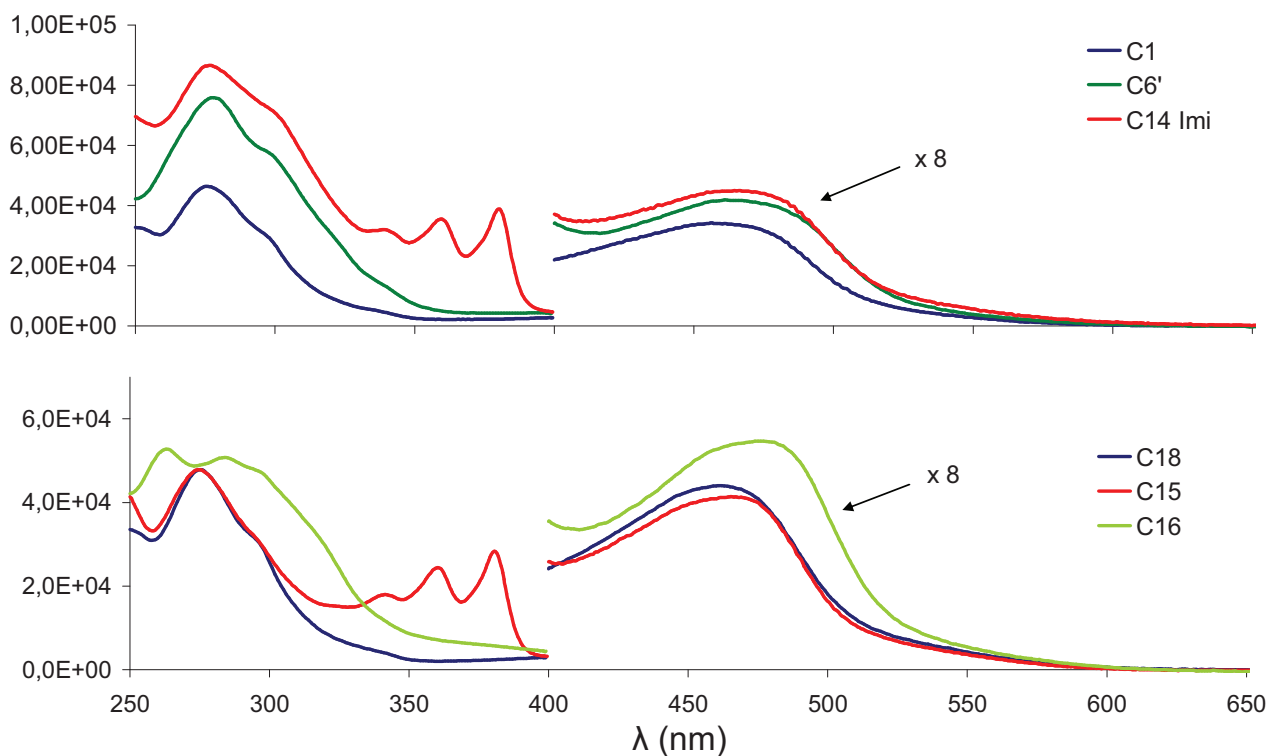
Fig. 4. 16. UV-Visible absorption spectra of the dyads along with the reference complexes. The most hindered species, having a [Cu(**L1**)(**L2**)]$^+$ coordination cage, are shown in the upper part of the figure, while those having a [Cu(**L1**)(**dmp**)]$^+$ sphere are shown in the lower part.

The same comparison can be done for **C18** and **C15**. The spectra superimpose well in the areas of MLCT and phenanthroline-centred π-π* bands, while the contribution of the NDI transitions is clearly visible in the 340-380 nm region. Even with a much shorter linker between the two components, they continue to behave as independent elements, without significant electronic communication in the ground state. It should be pointed out that the intensity of the UV band at 275 nm is much weaker than for the previous series: this can be ascribed to the lack of the phenyl-imidazole linker in these molecules and can be observed even when comparing the ε of the ligands at these wavelengths. **L13** has a very weak absorption in the 250-300 nm region, and all the

contributions come from the opposite ligand **L1**, while in **C14^{Imi}** both ligands (**L1** and **L12^{Imi}**) contribute to the overall absorption.

In the spectrum of **C16**, the MLCT band of copper complex is slightly more intense than in the other dyads owing to the superimposition of the ferrocene d-d transitions which occurs in the same region. Moreover, the presence of two intense UV bands observed at 284 and 263 nm are likely to be the signature of $\pi-\pi*$ ligand-centred transitions as **L14** presents the same bands.

4.3.2. Emission

The steady-state emission properties of the dyads were measured in dichloromethane and acetonitrile, in order to evaluate the possibility of a charge transfer from the excited state of Cu^I diimine complex towards the electron acceptor, naphthalene diimide. For a Cu^I-acceptor dyad, given the highly reductive properties of excited copper(I)-diimine complexes, an efficient photoinduced electron transfer should quench the MLCT luminescence.

Complexes **C1** and **C18** exhibit relatively weak ($\Phi \sim 10^{-4}$ in CH_3CN) but easily detectable ^{3}MLCT emission in the 700-800 nm region. It was shown in literature that these charge transfer states are characterized by a whole charge transfer from copper(I) to phenanthroline ligand.[60] The dyad **C14^{Imi}** has nearly identical features when it is excited at 460 nm, but no emission was observed in the same region upon 355 nm irradiation, unravelling that a non radiative photoinduced process is most certainly taking place. Interestingly, for **C15** the MLCT emission is strongly quenched, regardless the excitation region. Transient absorption experiments will help to characterize the non radiative processes which quench the luminescence of the MLCT excited state.

Complex **C16**, when excited in the MLCT band, barely showed luminescence, indicating an efficient quenching. As the excited state of copper(I) diimine complexes is a quite poor oxidant, it seems unlikely to have a reductive quenching by electron transfer from the ferrocene to the excited Cu^I moiety. On the other hand, ferrocene possesses low-lying d-d states (as shown by the low intensity band in the absorption spectrum of **L14**) which can act as an efficient energy acceptor from the MLCT state of the complex.[48] This quenching can constitute a problem when aiming at using this kind of compound as an electron donor in a triad, because it could compete with the electron transfer towards the acceptor. Therefore, a thorough study of the kinetics of the decay is needed in order to assess if electron transfer can compete with the energy transfer. We will comment more precisely on this aspect in the section devoted to the time-resolved photophysical measurements.

The excited-state lifetimes of the different complexes were obtained by measuring the decay of the transient absorption spectra upon excitation of the complexes, and are reported in paragraph 4.4, concerning time-resolved spectroscopy.

4.3.3. Electrochemistry

The electrochemical properties of the ligands and complexes were recorded in dichloromethane. A superposition of the cyclic voltammogramms obtained at a scan rate of 100 mV/s is shown in Fig. 4. 17, and the data are gathered in Table 4. 2.

	$E_{1/2}$ (NDI$^{0/-}$) [ΔE (mV)]	$E_{1/2}$ (Fc$^{+/0}$) [ΔE (mV)]	$E_{1/2}$ (Cu$^{II/I}$) [ΔE (mV)]
L12^{Imi}	- 0.60 [113]	—	—
L12^{Oxa}	-0.58 [70]	—	—
L13	-0.60^a	—	—
L14	—	0.59 [91]	—
C18	—	—	0.90 [89]
C1	—	—	0.99 [140]
C14^{Imi}	-0.59 [99]	—	0.99 [99]
C15	-0.55 [150]	—	0.97 [170]
C16	—	0.62 [87]	0.90 [89]

Table 4. 2. Electrochemical properties of the ligands and complexes for photoinduced electron transfer, recorded in dry degassed dichloromethane. WE: Pt disc; RE: SCE; CE: Pt foil; supporting electrolyte: TBAPF$_6$ 0.1 M. ^{a} Due to weak solubility in dichloromethane of the ligand, the peak was not reversible and the peak potential was assessed by square wave voltammetry.

These molecules contain three electroactive elements: NDI, Cu^I bisphenanthroline and Fc, exhibiting well-separated reversible or quasi-reversible redox processes.

However, the three ligands **L12^{Imi}**, **L12^{Oxa}** and **L14** present an irreversible oxidation process at high potentials, ranging from 1.25 V for **L12^{Oxa}** to 1.4 V for **L14**. This wave was tentatively ascribed to the imidazole or oxazole ring oxidation. This hypothesis is also supported by the electrochemical analyses conducted on ligand **L6'** (bearing no reversible electroactive groups) in acetonitrile, which allows to explore the electrochemical behaviour at higher potentials. The ligand is oxidized irreversibly around 1.5 V vs. SCE in acetonitrile, so the wave observed for the three ligands bearing NDI or Fc bound to the phenanthroline through an heterocyclic linker is probably due to the latter oxidation.

The naphthalene diimide one-electron reduction occurs, for ligands and complexes, between -0.55 V and -0.60 V vs. SCE. Once again, the lack of electronic communication between the NDI unit and the rest of the molecule is evidenced by the constancy of the half-wave potential, monitored for the couple NDI/NDI$^{\bullet-}$.

In the complexes, the first oxidation corresponds to the reversible removal of an electron from the copper(I) ion from a t_2 orbital which has an antibonding character. This potential is anodically shifted in complexes containing the bulkier butyl substituents on the phenanthroline (**C1** and **C14^{Imi}**) compared to those with methyl substituents (**C15**-**C18**) owing to the restricted flattening of the former complexes upon copper(II) formation, which destabilizes the square based pyramidal geometry preferred by the metal ion in its higher oxidation state. However, in the dyad **C15** the oxidation occurs at 0.97 V, which is quite a high potential considering the coordination cage (the same as **C18**). This could result from the electron poor character of the NDI unit, directly connected to the phenanthroline moiety through a diimide bond, indicating a slight interaction between the two moieties.

The oxidation of ferrocene occurs between 0.58 and 0.62 V, at higher potentials than those recorded for the unsubstituted ferrocene (0.47 V vs.SCE in our conditions). The electron withdrawing character of phenanthroline based ligands may manifest itself through these measurements.

In general, the slight variations of the oxidation potential observed for the electroactive groups are an indication of the weak electronic coupling between the components of the system. This is in good agreement with the conclusions from the electronic absorption. This fact is highlighted in Fig. 4. 17, where the redox processes occurring for the three electroactive groups are indicated by different colours: NDI reduction in blue, ferrocene oxidation in green and copper(I) complexes oxidation in red.
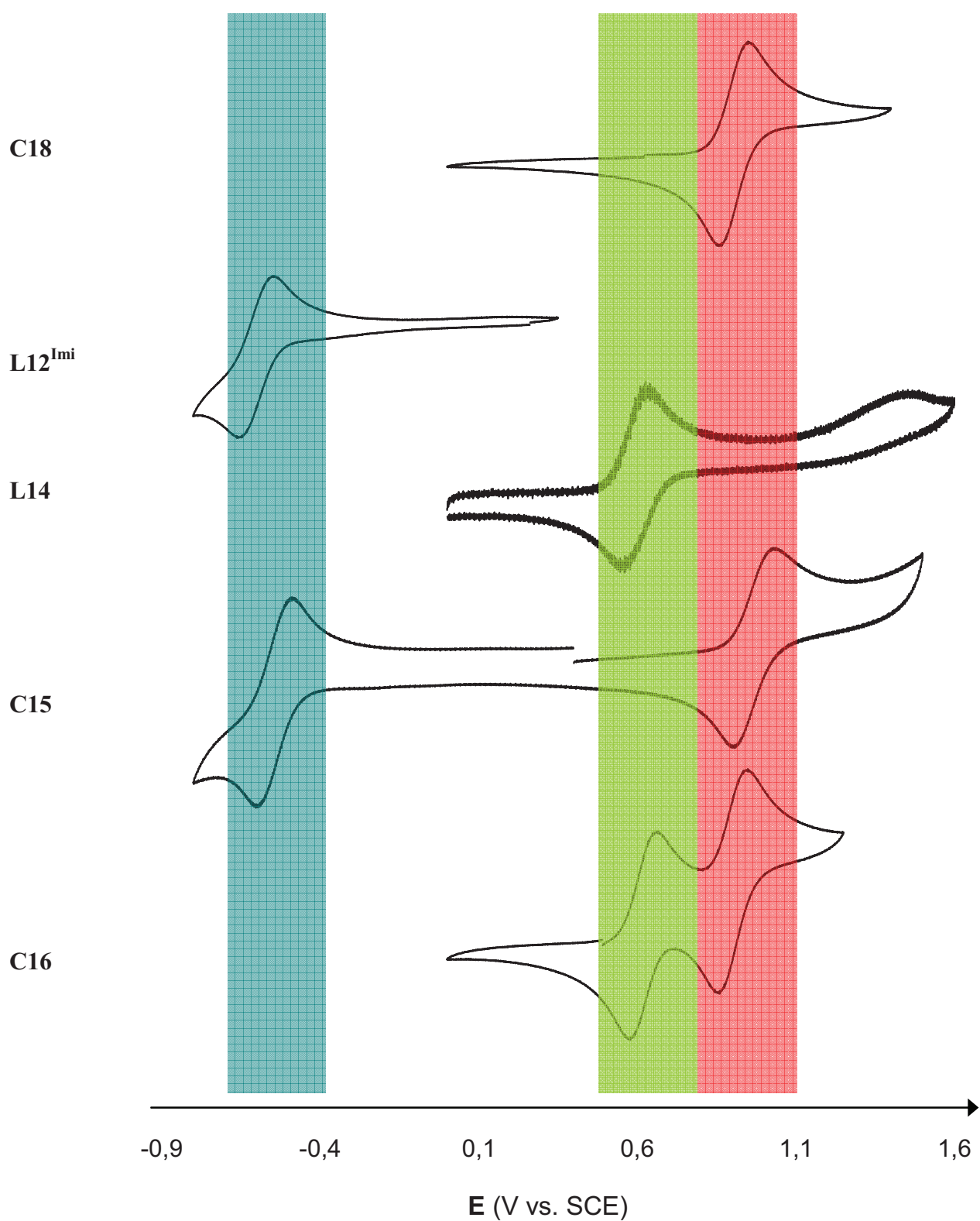
Fig. 4. 17. Superimposition of the cyclic voltammograms of selected ligands and complexes for photoinduced charge transfer. The CV of **L12^{Oxa}**, **L13**, **C1**, **C14^{Imi}** and **C14^{Oxa}** were removed for clarity, since they are very similar to **L12^{Imi}** (**L12^{Oxa}** and **L13**), **C18** (**C1**) and **C15** (**C14^{Imi}**). The NDI reduction is highlighted in blue, the Fc oxidation in orange and the Cu oxidation in red.

160

4.3.4. Driving forces for photoinduced charge transfer

Taking into account the data from absorption and emission spectroscopy, and electrochemistry, a first picture of the possible charge transfer processes between the three electroactive groups can be drawn. The oxidation and reduction potentials for the copper(I) sensitizer are obtained from equations 4.1 and 4.2, already used in chapter 2 and reported again below for clarity.

$$E_{S+/S*} = E_{S+/S} - E^{00} \qquad\qquad \text{Eq. 4.1}$$

$$E_{S*/S-} = E_{S/S-} + E^{00} \qquad\qquad \text{Eq. 4.2}$$

Let us begin by considering the photoinduced electron transfer in Cu^I diimine-NDI dyads. The complexes $C14^{Imi}$ and $C15$ are oxidized at 0.99 and 0.97 V vs. SCE ($E_{S+/S}$), respectively, depending on the coordination cage steric hindrance, and the E^{00} can be estimated around 1.9/2.0 eV (the normalized absorption and emission spectra of $C14^{Imi}$ and of the reference compounds cross around 600 nm). From these data, an excited state oxidation potential $E_{S+/S*} \sim -1.0$ V vs. SCE is calculated for the copper(I) complexes. This value proves that in both cases the photo-induced electron transfer towards the electron acceptor is thermodynamically allowed, as the reduction potential for the NDI group is found around -0.60 V vs. SCE, providing a 0.4 eV driving force for the React. 4.1 (if the coulombic work term is neglected). Moreover, even the excitation of NDI moiety would provide an excited state capable of transferring a hole to the complex, with a driving force of around 1.6 eV (React 4.2).

$$[Cu^I]*\text{---}NDI \;\rightarrow\; [Cu^{II}]\text{---}NDI^{\bullet-} \qquad\qquad \text{React. 4.1}$$

$$[Cu^I]\text{---}NDI* \;\rightarrow\; [Cu^{II}]\text{---}NDI^{\bullet-} \qquad\qquad \text{React. 4.2}$$

Conversely, in the copper(I) complex – ferrocene dyad $C16$ no photoinduced charge transfer processes is expected. In fact, the excited state reduction potential of the copper(I) photosensitizer is below 0.4 V vs. SCE (since the phenanthroline-centred reduction is known to occur below -1.5 V vs. SCE[61]). For this reason, the emission quenching found for this dyad is ascribed to energy transfer from the excited copper(I) complex to ferrocene, which has already been reported for compounds with absorption bands around 450 nm.[15,48]

4.4. Time-resolved photophysical characterization of the dyads

The time-resolved measurements on the previously described compounds were realized by Dr. Mateusz Rebarz in the LASIR laboratory in Lille. The details of the techniques used to perform nanosecond and femtosecond transient absorption spectroscopy are given in chapter 2.

Transient absorption experiments were performed using two different excitation wavelengths. As it can be observed in the electronic absorption spectra of the dyads, the MLCT band centred on the copper(I) diimine moiety and the NDI π-π* band are well separated, so that the two units can be excited nearly selectively (the copper(I) complex accounts for a minority absorption when the NDI is excited). Excitation of the MLCT band was achieved at the maximum absorption, by using a 460 nm LASER, for nanosecond transient absorption spectroscopy; for the femtosecond TA, excitation was performed at 400 nm, where the copper(I) complex is still the main absorber, due to technical reasons. NDI is excited at 355 nm in both experimental setups.

Two different solvents (acetonitrile and toluene), having different polarity and coordinating ability, were used.

4.4.1. Copper(I)-NDI dyads

The transient absorption experiments for dyads **C14**[Imi] and **C15** were compared with the reference copper(I) compounds **C1**, **C6'** and **C18**. The transient absorption data are gathered in Table 4. 3 and the obtained spectra are given in Fig. 4. 18.

	Transient absorption spectra[c]	Transient absorption kinetics[d]	
	λ_{max} / nm (species)	τ / ns	process
C1	530, 570[a] (^{3}MLCT)	27[a]	^{3}MLCT decay
C6'	550[b] (^{3}MLCT)	24[b]	^{3}MLCT decay
C18	530, 570[b] (^{3}MLCT)	21[b]	^{3}MLCT decay
C14[Imi]	530, 570[b] (^{3}MLCT)	31[b]	^{3}MLCT decay
	475, 605[a] (NDI$^{\bullet-}$)	9 (85%), 280 (15%)[a] [44 (80%), 276 (20%)][a,e]	B.E.T., ^{3}NDI
C15	475, 605[b] (NDI$^{\bullet-}$)	1-4[b]	B.E.T.
C16	550[b] (^{3}MLCT)	10[b]	^{3}MLCT decay
NDI	450, 480[a] (^{3}NDI)	318[a]	^{3}NDI

Table 4. 3. Transient absorption data obtained in CH$_3$CN for the compounds described. [a] λ_{ex}=355 nm, [b] λ_{ex}=460 nm, [c] error ~ +/- 5nm, [d] measured under air at room temperature with error ~ +/- 4ns, [e] measured in toluene.
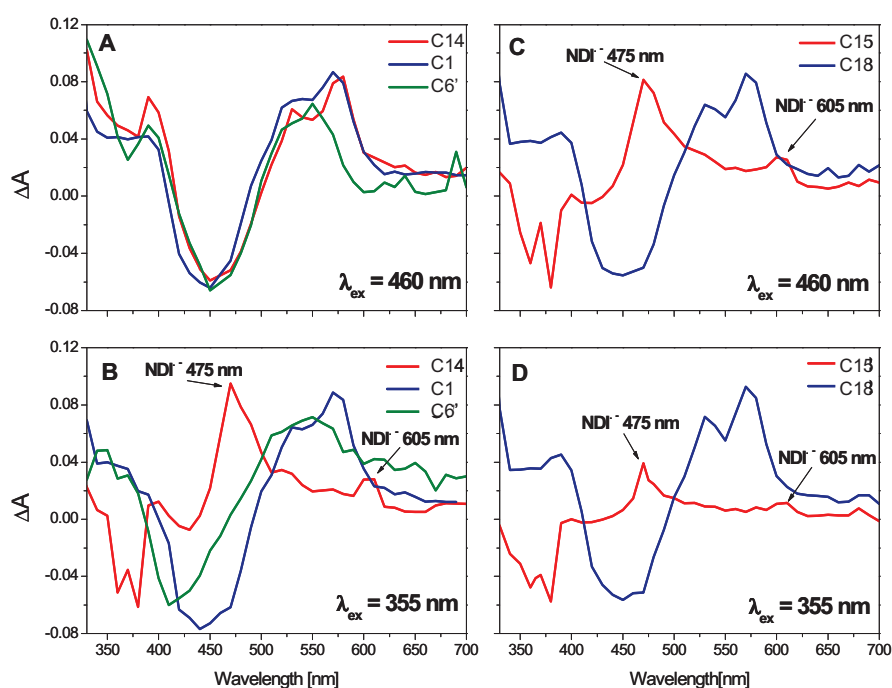
Fig. 4. 18. Transient absorption spectra obtained with nanosecond laser flash photolysis of **C14^Imi**, **C1** and **C6'** (A,B, resp.) and **C15**, **C18** (C,D, resp.) in CH₃CN for different excitation wavelengths. Spectra were recorded immediately after the laser pulse (OD=0.5 at λ_exc).

4.4.1.a. Time-resolved spectroscopy of C14^Imi

Photo-excitation of dyad **C14^Imi** by a 460 nm laser pulse (Fig. 4. 18 A) gives the transient spectrum which features the typical characteristics of the ³MLCT excited-state and decays homogenously in the whole examined spectral range. At no time was observed the spectroscopic signature of radical anion NDI⁻. This indicates that the intrinsic decay of the excited copper chromophore takes place *via* the usual radiative pathway, regardless of the presence of the electron acceptor NDI. This is consistent with the steady-state MLCT emission observed for **C14^Imi** when excited at 460 nm. The shape of the spectrum and the rate constant of the decay (Table 4. 3) are quite similar to those of the reference complexes **C1** and **C6'**, bringing further support to the fact that no photoinduced electron transfer takes place within **C14^Imi** upon excitation in the MLCT band, in spite of its significant driving force (~ 0.4 eV). The long distance between the copper centre and the NDI, as well as the weak electronic coupling between these two units, due to the absence of conjugation through the imide group, certainly explain the slow rate of the electron transfer.

Interestingly, upon irradiation of **C14^Imi** in the UV region, where the NDI unit is the main chromophore, the transient absorption spectrum reveals the formation of the NDI radical anion.

This is clearly visible in Fig. 4. 18 B where the spectrum of the dyad has a strong band around 470 nm, and the absorption extends up to 700 nm with a second distinct band at 605 nm. This pattern is characteristic for the well-known NDI radical anion generated by electrochemical reduction, which is described in the literature.[62,63] Therefore, we conclude that a photoinduced hole transfer takes place when the NDI chromophore is photoexcited, whereas no charge transfer is observed upon irradiation in the MLCT band (Fig. 4. 19). It should be noticed that the copper unit has a non zero absorption at 355 nm, so both partners in dyad **C14^{Imi}** are excited. We suppose that the initially excited Cu(I)-NDI* state is deactivated by a combination of two mechanisms. The first one is the formation of a charge separated state, corresponding formally to Cu^{II}-NDI$^{\bullet-}$, followed by charge recombination with a time constant of 9 ns in acetonitrile and 44 ns in toluene. The second process, competitive to the direct NDI reduction, is intersystem crossing to Cu(I)-^{3}NDI state, decaying back to the ground state with a time constant of 276 ns and with oxygen sensitive kinetics.

The higher driving force for reaction 4.2 (~1.6 eV) compared to reaction 4.1 (~0.4 eV, see paragraph 4.3.4) accounts for the occurrence of the photo-induced hole transfer upon excitation in the UV. Additionally, the phenyl-imidazole spacer is rather electron rich and favours in principle a hole vs. an electron transfer. The supposedly large outer sphere reorganization energy that accompanies the electron transfer, due to the structure rearrangement of the copper complex after oxidation of the metal from Cu^I to Cu^{II}, contributes to the activation barrier for the electron transfer and can explain the slow electron transfer rate, according to Marcus theory.

If the data recorded in the two solvents are compared, it is possible to note that the kinetics of the electron transfer reaction (both forward and backward) are faster in acetonitrile. Usually, polar solvents do stabilize the charge separated states, entailing faster charge recombination.

In order to assess the role of the spacer in the charge transfer mechanism, femtosecond transient absorption spectra of the free ligand were recorded. Three different processes are observed after excitation: 1) the fast formation of the ^{1}NDI* (S$_1$ state) characterized by two bands at 480 and 605 nm (already observed after the excitation of the **NDI** model); 2) the formation of NDI$^{\bullet-}$, with intensification of the 480 nm band and decrease of the one at 605 nm ($\tau \sim 0.4$ ps); 3) decay of the NDI$^{\bullet-}$ signal due to back electron transfer ($\tau \sim 5$ ps). The formation of the NDI$^{\bullet-}$ is likely due to a fast electron transfer from the phenyl-imidazole spacer. Indeed, Ganesan et al. showed that the presence of a phenyl substituent on the imide nitrogen of NDI resulted in very fast ($\tau = 0.5$ ps) electron transfer from the phenyl ring to the NDI moiety, which further supports our interpretation.[64] This shows that the spacer plays a non negligible role in the electron transfer from excited copper(I) to the NDI group.

However, the much faster decay of the NDI$^{\bullet-}$ observed in the free ligand provides a piece of evidence that the process taking place upon photoexcitation of **C14^{Imi}** is not merely due to electron transfer from the phenyl-imidazole spacer to the acceptor. Most probably, the spacer mediates the hole transfer from excited NDI to copper(I) diimine, and the longer distance between the separated charges attained in the dyad accounts for the longer charge separated lifetime of 9 ns in acetonitrile (Table 4. 3).

The information gathered by means of the different transient absorption experiments allow us to trace a scheme summarizing the different photoinduced processes occurring in the dyad **C14^{Imi}**.
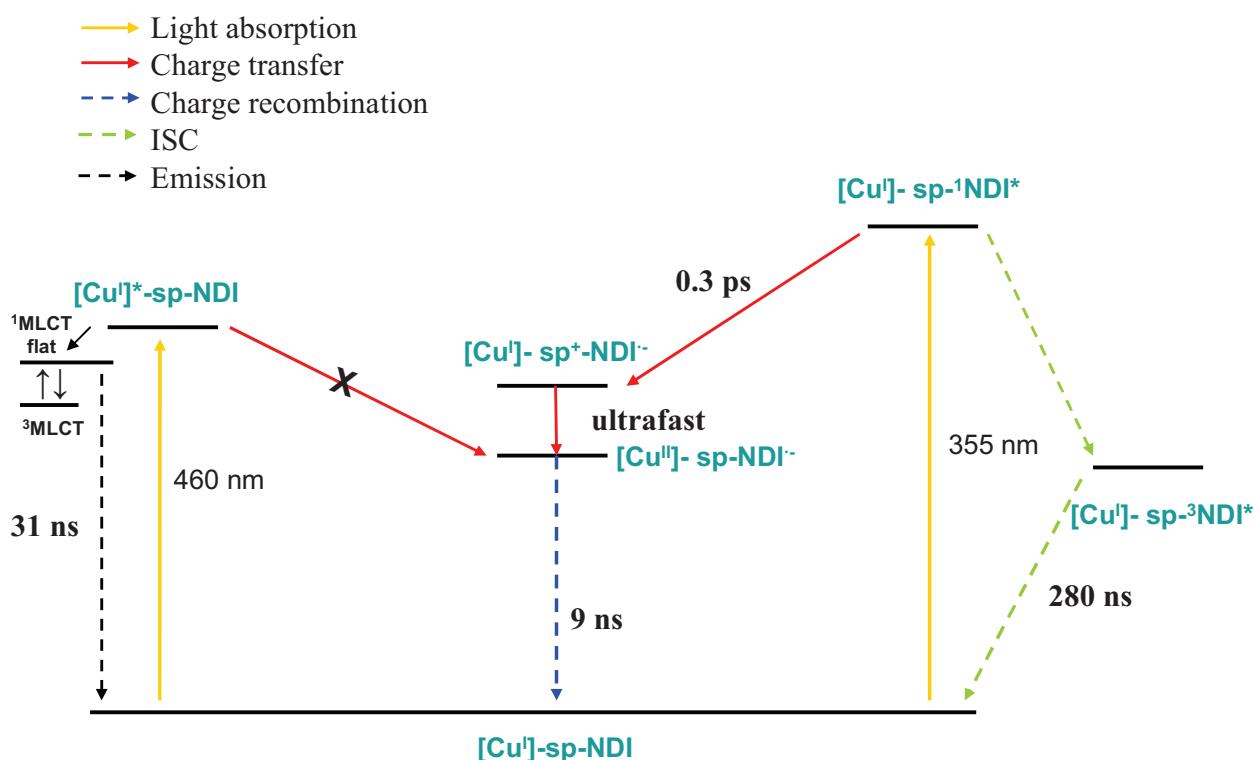
Fig. 4. 19. Proposed scheme for the photoinduced processes occurring upon photoexcitation of **C14^{Imi}**, in acetonitrile. The states relative to the classical excited Cu^{I} decay (left part of the scheme) are not explained in detail.

The photophysical study helped determining the operation of the dyad **C14^{Imi}**. If no PET occurred upon excitation in the MLCT, a photoinduced hole transfer from NDI to copper(I) could be triggered by selective excitation of the NDI unit. The rationale relies on both thermodynamics and kinetics: the long distance between the sensitizer and the electron acceptor claims a very large driving force in order to observe a charge shift upon light exposure.

4.4.1.b. Time-resolved spectroscopy of C15

Nanosecond time-resolved measurements were undertaken on **C15** in acetonitrile at the two pump wavelengths. Satisfyingly, this dyad, unlike **C14^{Imi}**, exhibits the formation of the NDI radical anion upon excitation within the MLCT absorption band, which means that the charge-separated state can be achieved by oxidative quenching of the excited copper(I) photosensitizer. This is presented in Fig. 4. 18 C and D, where the transients, formed immediately after the nanosecond laser pulse, exhibit the typical NDI radical anion spectral features described in the previous paragraph. In both cases, the intensity of the radical spectral signature disappears homogeneously according to a decay curve corresponding to the instrument response function, indicating that back electron transfer is shorter than the laser pulse ($\tau < 4$ ns).

This rapid reaction was too fast to be followed on nanosecond experiment and consequently femtosecond pump-probe measurements were performed. Upon excitation at 400 nm (where the main contribution is MLCT absorption) below 1 ps, we observed a very broad, structureless band with maximum at 550 nm and a bleaching around 450 nm that corresponds to the depletion of the ground state. Nevertheless, 1 ps after excitation, the characteristic features of NDI radical anion appear already, as two peaks at 470 and 605 nm. The absorption of this species increases with a time constant of 155 ps and this process can be ascribed to the forward electron transfer from the copper(I) ion to the NDI partner. Above 500 ps, the bands of NDI$^{\bullet-}$ start decreasing because of the back electron transfer. Unfortunately, the experimental conditions used in this study allowed recording only the beginning of this process and the real time constant associated to the latter lies in our experimental gap. We can only estimate this value as longer than 1 ns and shorter than 4 ns. This value is shorter than the lifetime obtained for the charge-separated state in **C14^{Imi}**, because of the shorter distance between the photosensitizer and the acceptor group in **C15**, favouring the back electron transfer. The information acquired about the photoinduced processes in **C15** are summarized in Fig. 4. 20.
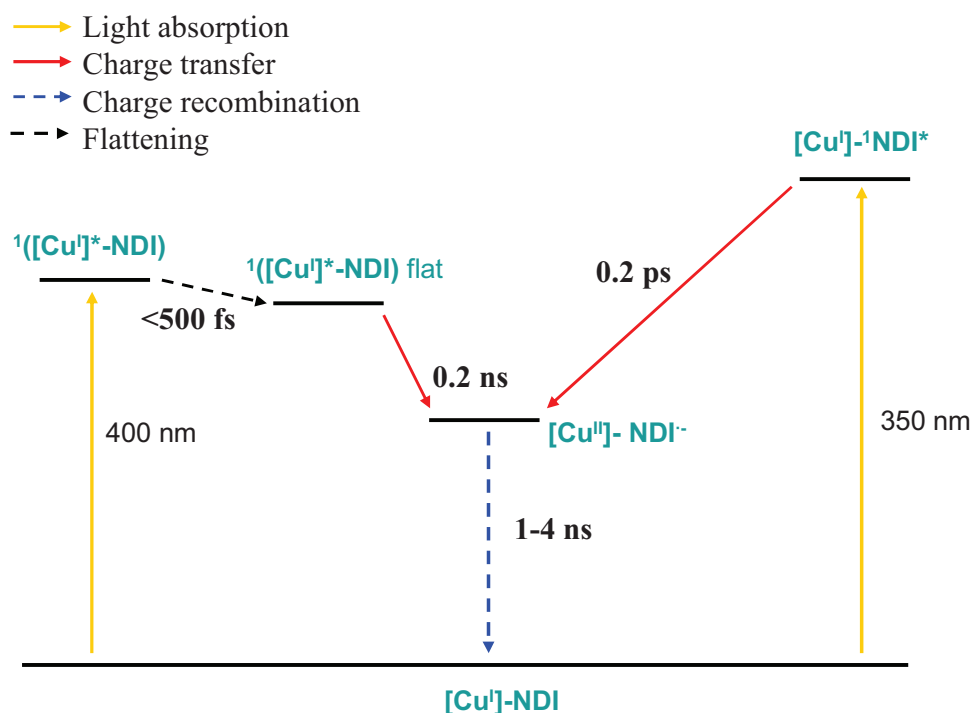
Fig. 4. 20. Proposed scheme for the photoinduced processes occurring upon photoexcitation of **C15**, in acetonitrile.

4.4.2. Copper(I)-Fc dyad C16

The deactivation process of the MLCT excited state in dyad **C16** was studied in order to understand if the kinetics of energy transfer to the ferrocene d-d states could be slow enough to allow an electron transfer to the NDI acceptor, and so if the synthesis of a Fc-Cu-NDI triad could be appropriate to obtain a long-distance charge-separated state. As said previously, copper(I) diimine complexes are strong reductants but quite mild oxidants in the excited state, so the first process that is expected in a D-[Cu]-A triad (D: donor; A: acceptor) is the electron transfer to the acceptor, followed by a hole shift from the oxidized copper sensitizer to the donor.

The study was performed by measuring the MLCT luminescence decay of the Cu-Fc dyad **C16**, and the lifetime of the emission in acetonitrile was found to be around 10 ns. Therefore, it is reasonable to assume that the energy transfer step from the excited copper(I)-diimine moiety to the ferrocene fragment occurs within 10 ns.[15,48]

4.5. Synthesis and characterization of the triad C17

From the previously described study about the kinetics of electron transfer to NDI in the dyad **C15**, it appears that the charge-separated state is formed within 0.2 ns. For this reason, it seemed pertinent to synthesize the Fc-Cu-NDI triad **C17** (Fig. 4. 21), since the photo-induced electron transfer could in principle outcompete the deleterious energy transfer step to Fc. The short linker between copper(I) and the acceptor was chosen because, unlike the long one present in **C14^{Imi}**, it allows electron transfer using visible light, which is more relevant to solar energy conversion. However, the short distance between the sensitizer and the electron acceptor also accounts for a short charge-separated state lifetime, which is estimated to be between 1 and 4 ns. This motivated the choice of directly binding the ferrocene on the imidazole linker, without adding an extra phenyl spacer.

The operation principle expected for such a **D-S-A** array, considering the data obtained for the reference dyads **C15** and **C16**, consists of a first photoinduced electron transfer from the excited copper(I) complex to the NDI, followed by a hole shift from the resulting copper(II) species to ferrocene.

C17
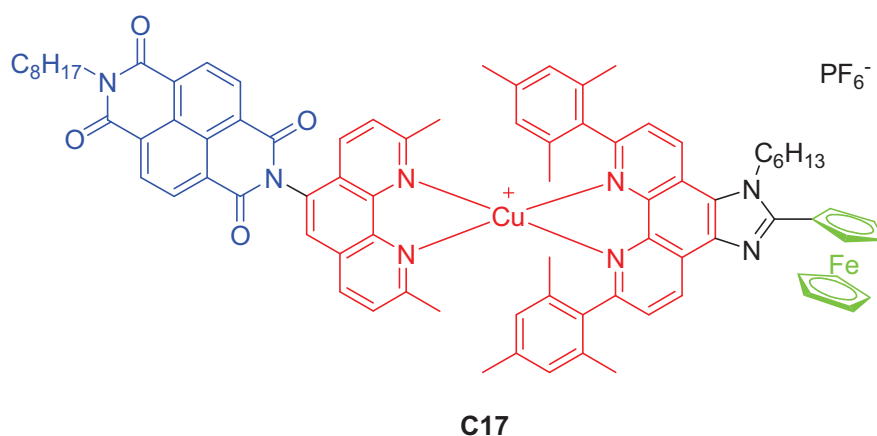
Fig. 4. 21. Structure of the triad **C17**.

It has to be pointed out that the use of a coordination complex as the chromophore is particularly interesting, because it offers a "modular" approach, in which the donor and the acceptor groups are assembled at the end of the synthesis. This potentially provides the possibility of screening different combination of donor and acceptor groups with a minimal synthetic effort. The final coordination step has thus the double role of forming the chromophore and bringing together the donor and acceptor groups.

4.5.1. Synthesis of the Fc-Cu-NDI triad C17

The triad **C17** was prepared in dichloromethane at room temperature by using an excess of hindered ligand **L14**. The product was purified by chromatography on silica gel, size exclusion chromatography and preparative thin layer chromatography, until the pure **C17** was obtained as a red solid (30% yield).
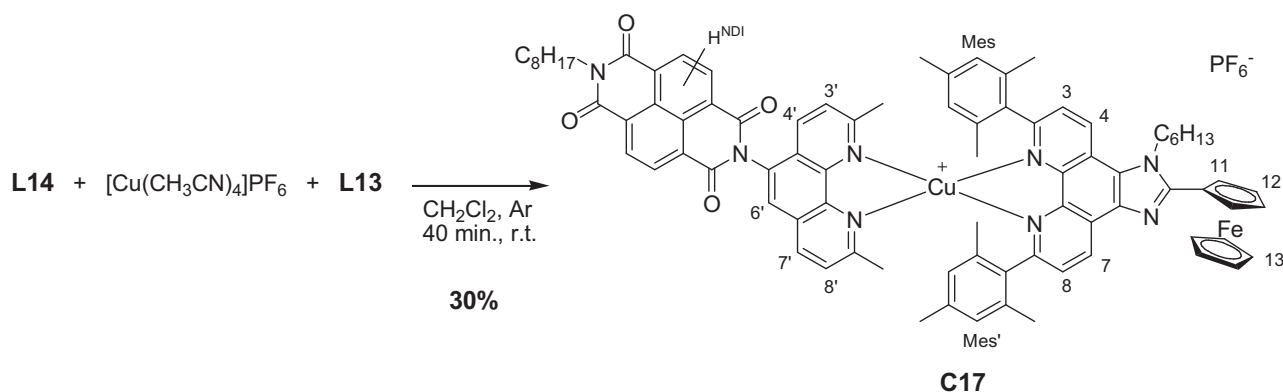
Scheme 4. 14. Synthesis of the Fc-Cu-NDI triad **C17**.

The NMR spectrum was recorded in deuterated chloroform (Fig. 4. 22).

Fig. 4. 22. ^{1}H-NMR spectrum of triad **C17**, recorded in CDCl$_3$.
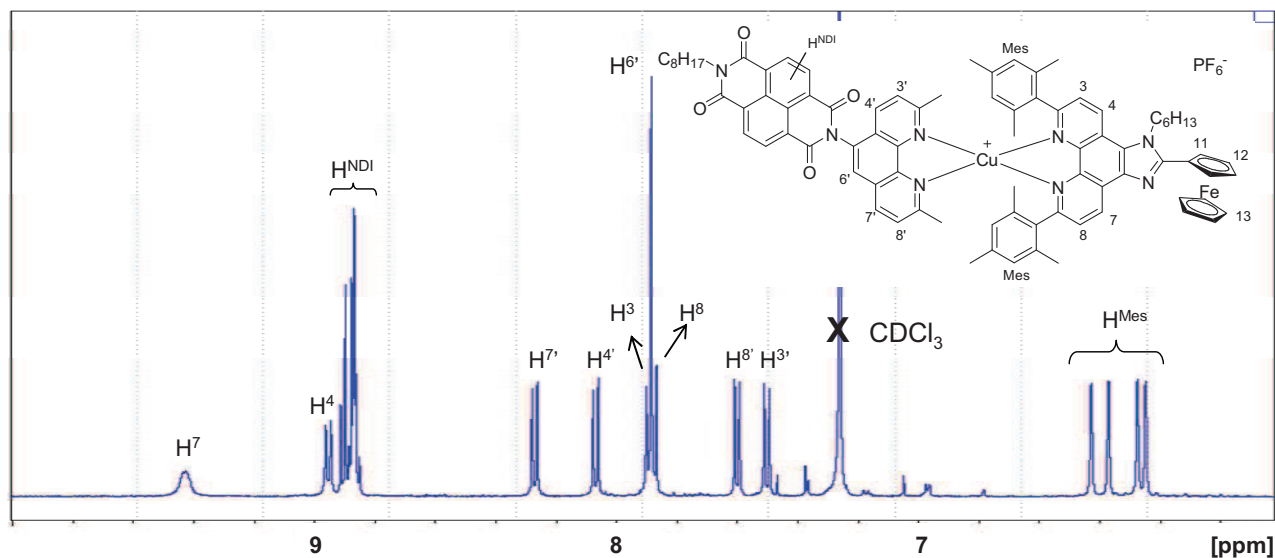
Besides the well-known effect of the coordination of the copper(I) ion on the chemical shifts of the ligands protons, we observed that the four aromatic protons H^{Mes} are magnetically non-equivalent and appear therefore as four distinct singlets. Probably the π-stacking between one of the mesityl rings of **L14** and the phenanthroline core of **L13** is strong enough to create quite a rigid structure in

solution, and the asymmetry of **L13** contributes to differentiate the two protons of each mesityl ring. The same effect can be remarked on the aliphatic mesityl protons.

4.5.2. Absorption and emission spectroscopy

The UV-Visible spectrum of the triad **C17**, recorded in dichloromethane, is shown in Fig. 4. 23 (with references **C15**, **C16** and **C18** for direct comparison) and displays all the features previously described for the reference dyads: a broad MLCT band in the blue region of the visible spectrum, the vibrationally structured band of the NDI in the near UV and phenanthroline ligand-centred π-π* between 250 and 340 nm. In the UV region it shows a double peak (at 290 and 263 nm), that is also observed in **L14** spectrum. The intensity of the UV bands, around $4.5 \cdot 10^4$ M^{-1}cm^{-1}, confirms what said before about the complexes lacking the long phenyl-imidazole spacer, having a less intense absorption in the UV. The MLCT band is red shifted of about 10 nm with respect to the **C18** and **C15**, as was observed in the spectrum of the ferrocene-copper(I) dyad **C16**. The electronic absorption data are gathered in Table 4. 4.
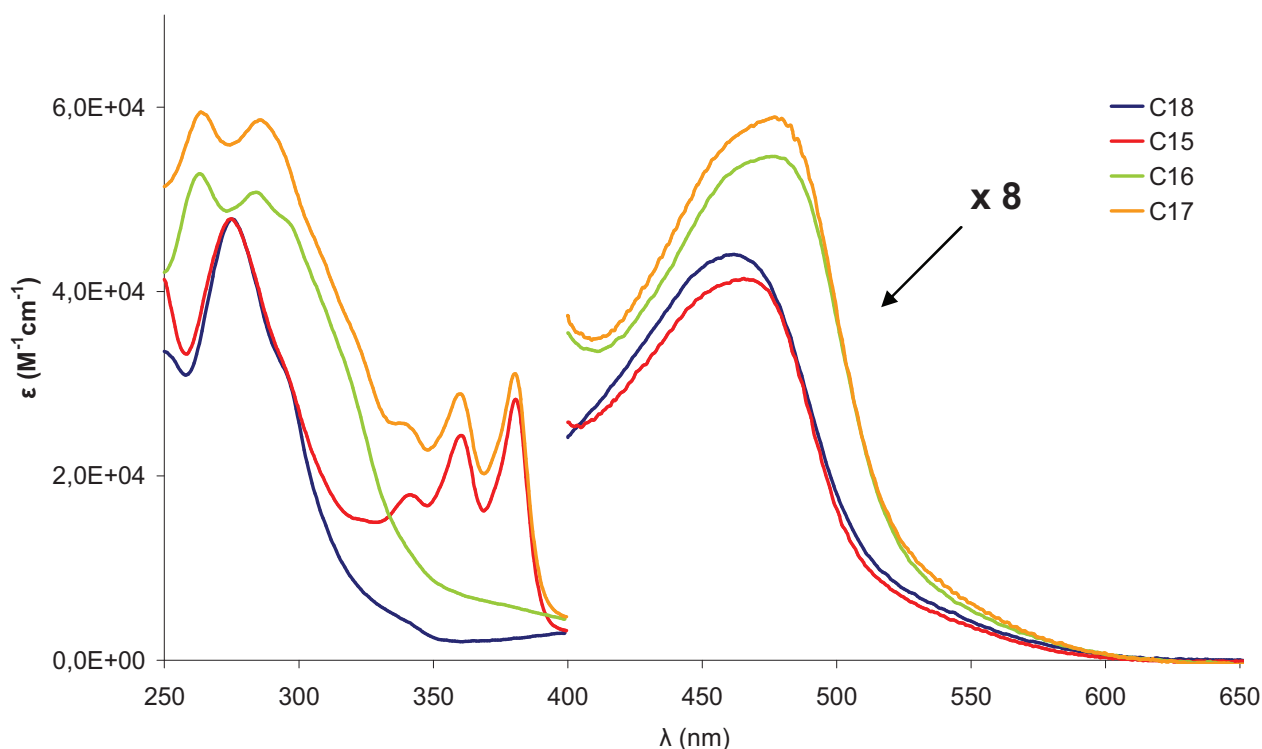
Fig. 4. 23. Electronic absorption spectra of the triad **C17**, recorded in dichloromethane. The reference **C18** and the reference dyads **C15** and **C16** are shown for direct comparison.

170

	λ (nm) [ε (M-1cm-1)]
C17	263 [5.9·10^4]
	286 [5.9·10^4]
	339 [2.6·10^4]
	360 [2.9·10^4]
	380 [3.1·10^4]
	477 [7.4·10^3]

Table 4. 4. UV-Visible absorption data for triad **C17**, recorded in dichloromethane.

As expected, the emission from the MLCT state of the copper(I) complex is quenched.

4.5.3. Electrochemistry

The electrochemical data for the triad **C17**, recorded in dichloromethane, are reported in Table 4. 5. The voltammogram evidences the presence of the three electroactive groups, and the minor shifts displayed with respect to the reference compounds and the dyads (see Table 4. 2) confirm the weak electronic communication at the ground state.

	E$_{1/2}$ (NDI$^{0/-}$) [ΔE (mV)]	E$_{1/2}$ (Fc$^{+/0}$) [ΔE (mV)]	E$_{1/2}$ (Cu$^{II/I}$) [ΔE (mV)]
C17	-0.55 [90]	0.60 [89]	0.93 [89]

Table 4. 5. Electrochemical properties of the triad **C17**, recorded in dry degassed dichloromethane. WE: Pt disc; RE: SCE; CE: Pt foil; supporting electrolyte: TBAPF$_6$ 0.1 M.

4.5.4. Driving forces for photoinduced charge separation

In the triad **C17**, the two processes leading to the formation of the charge-separated state **Fc$^+$---[Cu^I]---NDI$^{•-}$** are thermodynamically allowed. The first electron transfer from the excited complex to the NDI (React. 4.3) is allowed, as explained previously for the Cu^I-NDI dyads, as well as the second transfer from ferrocene to the oxidized copper(II) (React 4.4). In this compound, however, there is a competition between the forward process and the energy transfer to the ferrocene moiety (React. 4.5), observed for the dyad **C16**.

$$Fc\text{---}[Cu^I]^*\text{---}NDI \rightarrow Fc\text{---}[Cu^{II}]\text{---}NDI^{•-} \qquad \text{React. 4.3}$$

$$Fc\text{---}[Cu^{II}]\text{---}NDI^{•-} \rightarrow Fc^+\text{---}[Cu^I]\text{---}NDI^{•-} \qquad \text{React. 4.4}$$
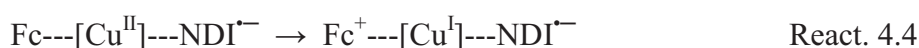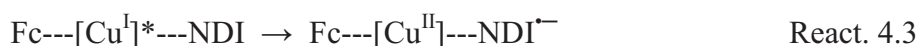
$$Fc\text{---}[Cu^I]^*\text{---}NDI \ \rightarrow \ Fc^*\text{---}[Cu^I]\text{---}NDI \qquad\qquad \text{React. 4.5}$$

The photoinduced processes in **C17** were studied by means of time-resolved spectroscopic techniques and are discussed in the following paragraph.

4.5.5. Time-resolved spectroscopy of the Fc-Copper(I)-NDI triad C17

The photophysical behaviour of the triad **C17** was assessed in acetonitrile and toluene. The nanosecond absorption spectroscopy measurements indicated that, upon excitation at 355 nm, the NDI$^{\bullet-}$ spectral features formed in about 150 ps, similarly to the reference dyad **C15** (135 ps). Satisfyingly, the signal decay was found to be significantly slower than in dyad **C15**, the lifetime value being around 30 ns (vs. 1-4 ns in dyad **C15**, see Fig. 4. 24). All the kinetic data are obtained by observing the rise or decay of the NDI$^{\bullet-}$ signal. It is difficult to observe Fc$^+$ spectral features by UV-Vis transient spectroscopy because ferrocenium displays low intensity absorption bands. Undisputable evidence for ferrocenium ion formation can be brought by transient infrared absorption,[65] but our instrumental facilities does not allow such an experiment. Nevertheless, the marked increase of the lifetime for the charge-separated state is in strong agreement with a larger distance between the two photogenerated charges, due to hole shift from formal copper(II)-diimine to Fc.
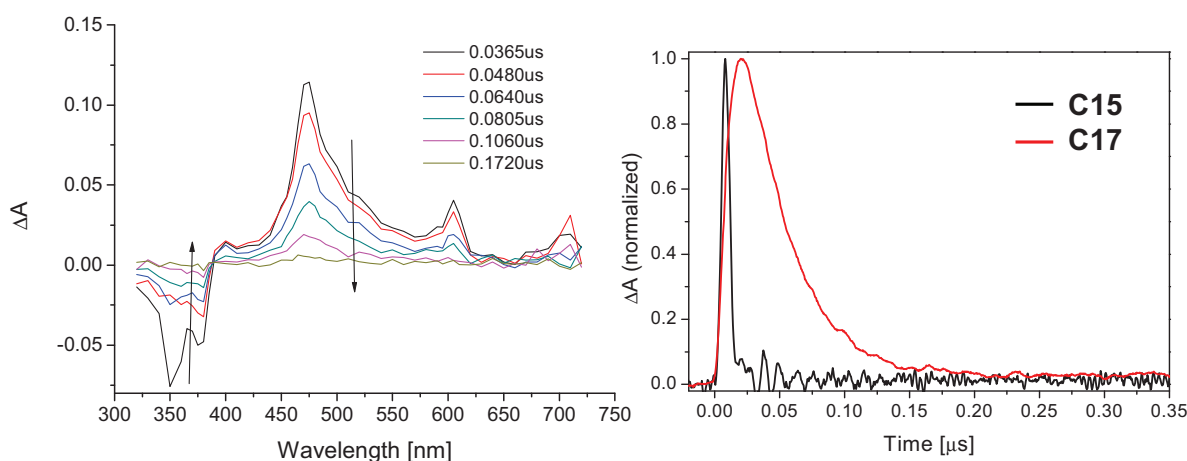
Fig. 4. 24. Decay of the NDI$^{\bullet-}$ signal observed by nanosecond transient absorption spectroscopy, in ACN upon excitation of **C17** at 355 nm. Right: comparison between the decay rates of **C15** and **C17**.

Transient absorption measurements carried out by exciting the MLCT band centred on the copper(I) diimine moiety also confirm that NDI radical anion is formed. This is a particularly encouraging result, since in this triad there is a competition between the electron transfer from the excited

copper(I) complex to the NDI and the energy transfer towards the ferrocene, as indicated by the steady-state emission data (paragraph 4.4.2).

Measurements conducted in solvents of different polarity confirm the results obtained for dyad **C15**, i.e. no major changes in the kinetics are observed.

The above reported data globally indicate that our approach for improving the charge-separated lifetime was successful. Further pump/probe experiments will be conducted, namely by excitation of the copper(I) complex, to investigate deeper the photophysical properties of this triad.

4.6. Conclusions and perspectives

To sum up, two new Cu^I diimine−NDI dyads were synthesized and characterized by standard techniques and by nanosecond and femtosecond transient absorption. The time-resolved measurements evidenced different behaviour for the dyads, depending on the spacer between the copper(I) diimine complex, the electron donor, and the naphthalene diimide, the electron acceptor. The dyad **C14^{Imi}**, having a long phenyl-imidazole linker, led to a charge-separated state only upon excitation of the NDI moiety at 355 nm, while for **C15,** the signal of the $NDI^{•−}$ could be observed regardless of the pump wavelength (355 or 400 nm).

These results were very encouraging, so we decided to explore the possibility of further increasing the charge-separated state lifetime by building a triad to increase the distance between the photogenerated charges. The rationalisation of the behaviour of the triad is made easier when all protagonists can be studied separately. Hence, a dyad where the copper(I) diimine complex is bound to a ferrocene donor was prepared. Despite the quenching of the MLCT excited state by energy transfer, it was observed that the lifetime of the MLCT excited state (10 ns) was still much longer than the time for the forward electron transfer from excited copper(I) complex to NDI in **C15** (~ 0.2 ns).

C17 is a triad where copper(I) diimine is connected to a ferrocene (electron donor) and a NDI (electron acceptor). It was prepared in order to improve the charge-separated state lifetime of **C15** by moving the charges farther away from each other. In fact, the copper(II) complex is sufficiently oxidizing to transfer a hole to ferrocene, therefore leading to a $Fc^{+}−[Cu^I]−NDI^{•−}$ state. The molecule was studied by absorption spectroscopy and electrochemistry, which indicated a negligible electronic coupling between the three moieties (as observed for the three dyads). Transient absorption spectroscopy measurements indicate the formation of a charge-separated state upon visible excitation of the Cu^I diimine MLCT band. Rewardingly, the charge-separated lifetime

was improved by a factor of at least 10 by the addition of the secondary electron donor, providing a copper(I)-based triad where the full charge-separated state is characterized.

Further studies will be carried out to isolate the pure **C14^{Oxa}**, and characterize its photophysical behaviour. **C12^{Imi}** and **C12^{Oxa}** could furthermore be used for the synthesis of linear triads with a longer charge-separated distance. In these systems, however, the charge-separated state is obtained only upon excitation in the UV.

Finally, research on alternative electron donor groups is under way, in order to increase the CSS lifetime. The aim is to suppress the side reaction of energy transfer from the excited chromophore to the low-lying states of the donor evidenced with ferrocene. Possible candidates could be tetrathiafulvalene,[66] *N,N,N'N'*-tetramethyl-2,5-diaminobenzene,[67] and trisarylamines.[45]

References

1. Gust, D.; Moore, T. A.; Moore, A. L. *Acc. Chem. Res.* **2009**, *42*, 1890-1898.
2. Kalyanasundaram, K.; Graetzel, M. *Curr. Opin. Biotechnol.* **2010**, *21*, 298-310.
3. Wasielewski, M. R. *J. Org. Chem.* **2006**, *71*, 5051-5066.
4. Wasielewski, M. R.; Niemczyk, M. P.; Svec, W. A.; Pewitt, E. B. *J. Am. Chem. Soc.* **1985**, *107*, 5562-5563.
5. Liddell, P. A.; Kuciauskas, D.; Sumida, J. P.; Nash, B.; Nguyen, D.; Moore, A. L.; Moore, T. A.; Gust, D. *J. Am. Chem. Soc.* **1997**, *119*, 1400-1405.
6. Gust, D.; Moore, T. A.; Moore, A. L.; Macpherson, A. N.; Lopez, A.; DeGraziano, J. M.; Gouni, I.; Bittersmann, E.; Seely, G. R. *J. Am. Chem. Soc.* **1993**, *115*, 11141-11152.
7. Heiler, D.; McLendon, G.; Rogalskyj, P. *J. Am. Chem. Soc.* **1987**, *109*, 604-606.
8. D'Souza, F.; Ito, O. *Coord. Chem. Rev.* **2005**, *249*, 1410-1422.
9. Trabolsi, A.; Elhabiri, M.; Urbani, M.; Delgado de la Cruz, J. L.; Ajamaa, F.; Solladie, N.; Albrecht-Gary, A.-M.; Nierengarten, J.-F. *Chem. Commun.* **2005**, 5736-5738.
10. Campagna, S.; Puntoriero, F.; Nastasi, F.; Bergamini, G.; Balzani, V. *Top. Curr. Chem.* **2007**, *280*, 117-214.
11. Opperman, K. A.; Mecklenburg, S. L.; Meyer, T. J. *Inorg. Chem.* **1994**, *33*, 5295-5301.
12. Treadway, J. A.; Chen, P.; Rutherford, T. J.; Keene, F. R.; Meyer, T. J. *J. Phys. Chem. A* **1997**, *101*, 6824-6826.
13. Collin, J. P.; Guillerez, S.; Sauvage, J. P.; Barigelletti, F.; De Cola, L.; Flamigni, L.; Balzani, V. *Inorg. Chem.* **1991**, *30*, 4230-4238.
14. Johansson, O.; Borgström, M.; Lomoth, R.; Palmblad, M.; Bergquist, J.; Hammarström, L.; Sun, L.; Åkermark, B. *Inorg. Chem.* **2003**, *42*, 2908-2918.
15. Sauvage, J. P.; Collin, J. P.; Chambron, J. C.; Guillerez, S.; Coudret, C.; Balzani, V.; Barigelletti, F.; De Cola, L.; Flamigni, L. *Chem. Rev.* **1994**, *94*, 993-1019.
16. Hankache, J.; Wenger, O. S. *Chem. Commun.* **2011**, *47*, 10145-10147.
17. Kumar, R. J.; Karlsson, S.; Streich, D.; Rolandini Jensen, A.; Jäger, M.; Becker, H.-C.; Bergquist, J.; Johansson, O.; Hammarström, L. *Chem. Eur. J.* **2010**, *16*, 2830-2842.
18. Abrahamsson, M.; Jäger, M.; Österman, T.; Eriksson, L.; Persson, P.; Becker, H.-C.; Johansson, O.; Hammarström, L. *J. Am. Chem. Soc.* **2006**, *128*, 12616-12617.
19. Borgström, M.; Shaikh, N.; Johansson, O.; Anderlund, M. F.; Styring, S.; Åkermark, B.; Magnuson, A.; Hammarström, L. *J. Am. Chem. Soc.* **2005**, *127*, 17504-17515.
20. Flamigni, L.; Baranoff, E.; Collin, J.-P.; Sauvage, J.-P. *Chem. Eur. J.* **2006**, *12*, 6592-6606.
21. Chakraborty, S.; Wadas, T. J.; Hester, H.; Schmehl, R.; Eisenberg, R. *Inorg. Chem.* **2005**, *44*, 6865-6878.
22. McGarrah, J. E.; Kim, Y.-J.; Hissler, M.; Eisenberg, R. *Inorg. Chem.* **2001**, *40*, 4510-4511.
23. Chakraborty, S.; Wadas, T. J.; Hester, H.; Flaschenreim, C.; Schmehl, R.; Eisenberg, R. *Inorg. Chem.* **2005**, *44*, 6284-6293.
24. Sazanovich, I. V.; Alamiry, M. A. H.; Best, J.; Bennett, R. D.; Bouganov, O. V.; Davies, E. S.; Grivin, V. P.; Meijer, A. J. H. M.; Plyusnin, V. F.; Ronayne, K. L.; Shelton, A. H.; Tikhomirov, S. A.; Towrie, M.; Weinstein, J. A. *Inorg. Chem.* **2008**, *47*, 10432-10445.
25. Cunningham, K. L.; McMillin, D. R. *Inorg. Chem.* **1998**, *37*, 4114-4119.
26. Ruthkosky, M.; Kelly, C. A.; Zaros, M. C.; Meyer, G. J. *J. Am. Chem. Soc.* **1997**, *119*, 12004-12005.
27. Scaltrito, D. V.; Kelly, C. A.; Ruthkosky, M.; Zaros, M. C.; Meyer, G. J. *Inorg. Chem.* **2000**, *39*, 3765-3770.
28. Fabrizi de Biani, F.; Grigiotti, E.; Laschi, F.; Zanello, P.; Juris, A.; Prodi, L.; Chichak, K. S.; Branda, N. R. *Inorg. Chem.* **2008**, *47*, 5425-5440.

29. Cárdenas, D. J.; Collin, J.-P.; Gaviña, P.; Sauvage, J.-P.; Cian, A. D.; Fischer, J.; Armaroli, N.; Flamigni, L.; Vicinelli, V.; Balzani, V. *J. Am. Chem. Soc.* **1999**, *121*, 5481-5488.

30. Baranoff, E.; Griffiths, K.; Collin, J.-P.; Sauvage, J.-P.; Ventura, B.; Flamigni, L. *New J. Chem.* **2004**, *28*, 1091-1095.

31. Clifford, J. N.; Accorsi, G.; Cardinali, F.; Nierengarten, J.-F.; Armaroli, N. *C. R. Chim.* **2006**, *9*, 1005-1013.

32. Armaroli, N.; Diederich, F.; Dietrich-Buchecker, C. O.; Flamigni, L.; Marconi, G.; Nierengarten, J.-F.; Sauvage, J.-P. *Chem. Eur. J.* **1998**, *4*, 406-416.

33. Rio, Y.; Enderlin, G.; Bourgogne, C.; Nierengarten, J.-F.; Gisselbrecht, J.-P.; Gross, M.; Accorsi, G.; Armaroli, N. *Inorg. Chem.* **2003**, *42*, 8783-8793.

34. Holler, M.; Cardinali, F.; Mamlouk, H.; Nierengarten, J.-F.; Gisselbrecht, J.-P.; Gross, M.; Rio, Y.; Barigelletti, F.; Armaroli, N. *Tetrahedron* **2006**, *62*, 2060-2073.

35. Listorti, A.; Accorsi, G.; Rio, Y.; Armaroli, N.; Moudam, O.; Gégout, A.; Delavaux-Nicot, B. a.; Holler, M.; Nierengarten, J.-F. o. *Inorg. Chem.* **2008**, *47*, 6254-6261.

36. Megiatto, J. D.; Li, K.; Schuster, D. I.; Palkar, A.; Herranz, M. A. n.; Echegoyen, L.; Abwandner, S.; de Miguel, G.; Guldi, D. M. *J. Phys. Chem. B* **2010**, *114*, 14408-14419.

37. Megiatto, J. D.; Schuster, D. I.; de Miguel, G.; Wolfrum, S.; Guldi, D. M. *Chem. Mater.* **2012**, *24*, 2472-2485.

38. Chambron, J. C.; Harriman, A.; Heitz, V.; Sauvage, J. P. *J. Am. Chem. Soc.* **1993**, *115*, 6109-6114.

39. Faiz, J. A.; Heitz, V.; Sauvage, J.-P. *Chem. Soc. Rev.* **2009**, *38*, 422-442.

40. Vannelli, T. A.; Karpishin, T. B. *Inorg. Chem.* **1999**, *38*, 2246-2247.

41. Baron, A.; Herrero, C.; Quaranta, A.; Charlot, M.-F.; Leibl, W.; Vauzeilles, B.; Aukauloo, A. *Chem. Commun.* **2011**, *47*, 11011-11013.

42. Chaignon, F.; Falkenstrom, M.; Karlsson, S.; Blart, E.; Odobel, F.; Hammarstrom, L. *Chem. Commun.* **2007**, 64-66.

43. Würthner, F.; Ahmed, S.; Thalacker, C.; Debaerdemaeker, T. *Chem. Eur. J.* **2002**, *8*, 4742-4750.

44. Bhosale, S. V.; Jani, C. H.; Langford, S. J. *Chem. Soc. Rev.* **2008**, *37*, 331-342.

45. Karlsson, S.; Boixel, J.; Pellegrin, Y.; Blart, E.; Becker, H.-C.; Odobel, F.; Hammarström, L. *J. Am. Chem. Soc.* **2010**, *132*, 17977-17979.

46. Erten, Ş.; Posokhov, Y.; Alp, S.; İçli, S. *Dyes Pigm.* **2005**, *64*, 171-178.

47. Lachaud, F.; Quaranta, A.; Pellegrin, Y.; Dorlet, P.; Charlot, M.-F.; Un, S.; Leibl, W.; Aukauloo, A. *Angew. Chem. Int. Ed.* **2005**, *44*, 1536-1540.

48. Fery-Forgues, S.; Delavaux-Nicot, B. *J. Photochem. Photobiol. A* **2000**, *132*, 137-159.

49. Ott, S.; Faust, R. *Synthesis* **2005**, *2005*, 3135,3139.

50. Zheng, R. H.; Guo, H. C.; Jiang, H. J.; Xu, K. H.; Liu, B. B.; Sun, W. L.; Shen, Z. Q. *Chin. Chem. Lett.* **2010**, *21*, 1270-1272.

51. Kreps, S. I.; Day, A. R. *J. Org. Chem.* **1941**, *06*, 140-156.

52. Boixel, J., Ph.D. Thesis, University of Nantes, **2009**.

53. Hayes, R. T.; Wasielewski, M. R.; Gosztola, D. *J. Am. Chem. Soc.* **2000**, *122*, 5563-5567.

54. Imahori, H.; Azuma, T.; Ajavakom, A.; Norieda, H.; Yamada, H.; Sakata, Y. *J. Phys. Chem. B* **1999**, *103*, 7233-7237.

55. Le Pleux, L., Ph.D. Thesis, University of Nantes, **2010**

56. Steck, E. A.; Day, A. R. *J. Am. Chem. Soc.* **1943**, *65*, 452-456.

57. Zapata, F.; Caballero, A.; Espinosa, A.; Tárraga, A.; Molina, P. *J. Org. Chem.* **2008**, *73*, 4034-4044.

58. Blake, R. C.; Pavlov, A. R.; Khosraviani, M.; Ensley, H. E.; Kiefer, G. E.; Yu, H.; Li, X.; Blake, D. A. *Bioconjugate Chem.* **2004**, *15*, 1125-1136.

59. Rogers, J. E.; Kelly, L. A. *J. Am. Chem. Soc.* **1999**, *121*, 3854-3861.

60. Armaroli, N.; Accorsi, G.; Cardinali, F.; Listorti, A. *Top. Curr. Chem.* **2007**, *280*, 69-115.

61. Miller, M. T.; Gantzel, P. K.; Karpishin, T. B. *Inorg. Chem.* **1999**, *38*, 3414-3422.

62. Gosztola, D.; Niemczyk, M. P.; Svec, W.; Lukas, A. S.; Wasielewski, M. R. *J. Phys. Chem. A* **2000**, *104*, 6545-6551.

63. Green, S.; Fox, M. A. *J. Phys. Chem.* **1995**, *99*, 14752-14757.

64. Ganesan, P.; Baggerman, J.; Zhang, H.; Sudhölter, E. J. R.; Zuilhof, H. *J. Phys. Chem. A* **2007**, *111*, 6151-6156.

65. Bullock, J. P.; Boyd, D. C.; Mann, K. R. *Inorg. Chem.* **1987**, *26*, 3084-3086.

66. Canevet, D.; Salle, M.; Zhang, G.; Zhang, D.; Zhu, D. *Chem. Commun.* **2009**, 2245-2269.

67. Kercher, M.; König, B.; Zieg, H.; De Cola, L. *J. Am. Chem. Soc.* **2002**, *124*, 11541-11551.

CHAPTER 5

Heteroleptic copper(I) complexes for Dye-Sensitized Solar Cells

5.1. Dye-Sensitized Solar Cells (DSSCs)

In a world where the energy demand is continuously growing, a special attention should be paid to the electricity production. There are several methods to produce electricity, many of them use heat engines where a turbine is operated by a moving fluid. The most extensively used energy carrier is steam, generated by heating a mass of water. The energy required to drive such machines is obtained by different sources, that can be non renewable (combustion of fossil fuels, accounting for about 80% of the world electricity supply, or nuclear fission) or renewable (biomass combustion, solar thermal energy, geothermal energy). Other fluids can be used, as flowing water (hydroelectric energy) or wind (windpower).[1]

Other methods are known, but account for the moment for a minority percentage of the global energy production, among them the conversion of chemical potential energy (batteries, fuel cells) and the photovoltaic effect. The latter is particularly appealing because solar energy is abundant, available for several billions of years and well distributed on Earth, unlike fossil fuel reserves.

The photovoltaic effect was discovered in 1839 by Becquerel,[2] who observed the emergence of an electric voltage when two electrodes were connected through a solid or liquid junction and exposed to light. The phenomenon was then studied theoretically by Einstein. This observation led to the development of photovoltaic cells based on p-n junctions in the Bell laboratories in 1954.[3] Two layers of semiconductor are put in close contact, one doped with electron rich elements (n-type) and the other with electron poor elements (p-type). The contact between an n-type and a p-type semiconductor results in an initial flow of electrons from the former to the latter, with formation of a depletion layer having low concentration of charge carriers. The uneven charge distribution is responsible for the development of a potential difference. Upon exposure to light, some electrons are excited from the valence to the conduction band and can therefore move in the material under the influence of this potential difference, creating an electric current that is collected in an external circuit.[4]

The most extensively used semiconductor in this field is silicon, doped either with group 13 (p-type) or group 15 (n-type) elements. Originally conceived for aerospace applications,

monocrystalline silicon solar cells reached very impressive performances (25% record efficiency in laboratory)[5] but rely on expensive and energy consuming technologies. Polycrystalline and amorphous silicon cells provide lower performances (20% and 15%, respectively), but are more moderately priced and therefore largely diffused.

Even if silicon is the second element on the Earth crust (nearly 28%), it is usually found under an oxidized form, like silica and silicates.[6] Solar cells technology requires high purity elemental silicon (99.999%), which is commonly obtained as a by-product of the electronic industry. The lowering availability of this resource, and above all the extremely expensive purification processes, challenge the researchers to develop new technologies based on readily available and less expensive materials. There are several new technologies which are thought to be serious alternatives to silicon based photovoltaic cells. The very competitive CIGS systems rely, like silicon cells, on thin semi-conductor layers in close contact.[7] Organic photovoltaic cells are based on heterogeneous blends of organic hole and electron transporting materials (usually a polymer like P3HT and fullerene derivatives like PCBM, respectively). These systems have now reached very satisfying yields (around 10%)[8] and present several advantages among which the low price, lightweight and easy industrial processability (roll to roll printing allowing to prepare meters of flexible photovoltaic panels in only a few steps). Grätzel cells, based on the use of nanoparticles of semiconductor, stand for another very promising technology. They are also called dye-sensitized solar cells, because their operation principle relies on the sensitization of a mesoporous inorganic semi-conductor material by a molecular chromophore. These cells, which are more precisely photoelectrochemical cells as they are not based on the photovoltaic effect, display very promising yields of above 12% in laboratory.[9]

The history of semiconductors sensitization began with the studies on the photographic process, in the first half of the nineteenth century.[10,11] Moser obtained in 1887 the first sensitization of an electrical current.[12] Titanium dioxide was first sensitized by a ruthenium-based dye by Dare-Edwards and co-workers in 1980,[13] and Ru-coated polycrystalline anatase films were reported in 1988 to produce a 12% efficient bromide to bromine light induced oxidation.[14] It is only with the high efficiency photovoltaic device published in 1991 by O'Regan and Grätzel,[9] however, that this technology was recognized as a real potential competitor to the silicon-based solar cells.

TiO_2 is a wide band gap n type semiconductor, therefore absorbing only UV light. A large band gap is the key for a high stability towards photocorrosion. In visible light absorbing materials, in fact, irradiation results in the formation of highly reactive hole-electron couples, that can react with the electrolyte with consequent degradation of the surface. However, UV light accounts for only 4% of the solar irradiance spectrum. In order to obtain an efficient conversion of solar energy into electricity, it is thus fundamental to get a sub-band gap response from the semiconductor. A

device was elaborated, in which the functions of light absorption and charge transport are separated, unlike what happens in classical silicon solar cells, but noticeably similar to the natural photosynthesis process: the dye-sensitized solar cell (DSSC).

One of the main merits of DSSCs is the use of a cheap, readily available and non toxic semiconductor, TiO_2. The lower purity and lower technological efforts required for the cells elaboration, moreover, reduce considerably the cost of the final device, making them potentially very competitive from an economic point of view.

5.1.1. Composition and principles of operation

A dye-sensitized solar cell (DSSC) is composed of two parallel electrodes. The photoanode is a highly conductive transparent fluorine doped tin oxide (FTO) substrate coated with a layer of mesoporous titanium dioxide, on which a monolayer of dye molecules is chemisorbed (Fig. 5. 1). The cathode, or the counter-electrode, is an FTO plate covered with a catalyst, generally platinum nanoparticles. A frame of insulating hotmelt polymer is used as a spacer between the two electrodes. The gap between the two plates is filled by an electrolyte, containing the redox mediator (usually the iodide/triiodide couple, I^-/I_3^-). The electrodes are connected to an external circuit.
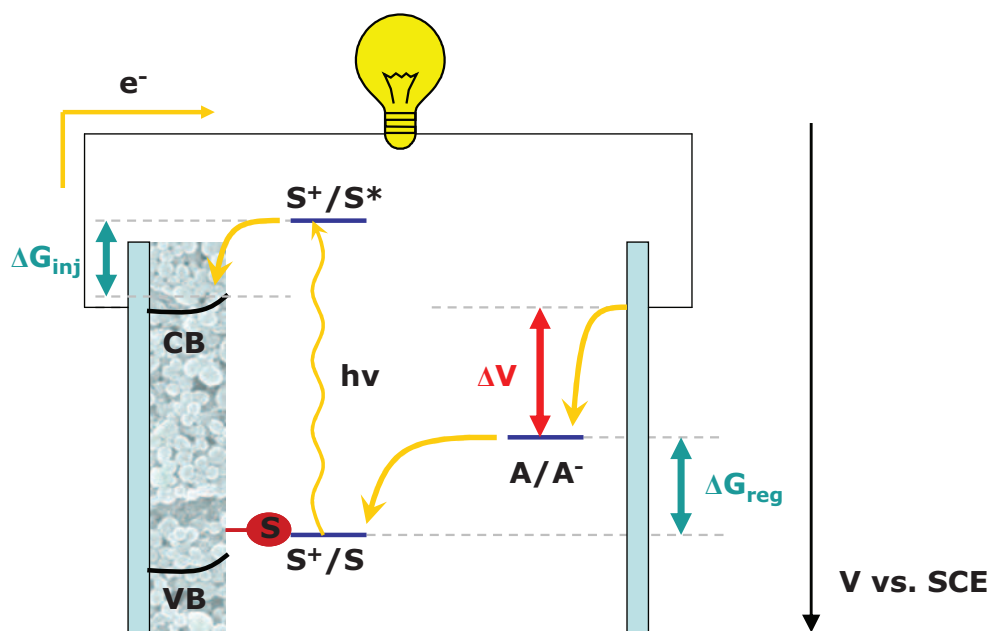
Fig. 5. 1. Structure and operation principle of a DSSC. S / S$^+$ / S*: ground / oxidized / excited states of the sensitizer; A/A$^-$: redox mediator couple.[15]

181

The cell operates as follows. Light absorption leads the sensitizer to an electronically excited state (React. 5. 1), with a decreased oxidation potential (Eq. 1. 4), that undergoes oxidative quenching by injecting an electron into the conduction band of titanium dioxide (React. 5. 2). Charge percolation through the semiconductor nanostructure allows the electron to be collected in the external circuit (React. 5. 4). The oxidized dye is then regenerated by electron transfer from the reduced form of the redox mediator, normally the I_3^-/I^- couple (React. 5. 3). The latter is in turn efficiently reduced back to I_3^- at the counter-electrode, thanks to the presence of the platinum catalyst (React. 5. 5). Thus, a current flow is produced, without overall consumption of any chemicals.

$S + h\nu \rightarrow S^*$	excitation of the sensitizer	React. 5. 1
$S^* \rightarrow S^+ + e^-_{TiO2}$	electron injection into the TiO_2	React. 5. 2
$2S^+ + 3I^- \rightarrow 2S + I_3^-$	sensitizer regeneration by the electrolyte	React. 5. 3
$e^-_{TiO2} \rightarrow e^-_{FTO}$	charge transport	React. 5. 4
$I_3^- + 2e^-_{Pt} \rightarrow 3I^-$	electrolyte regeneration at the cathode	React. 5. 5
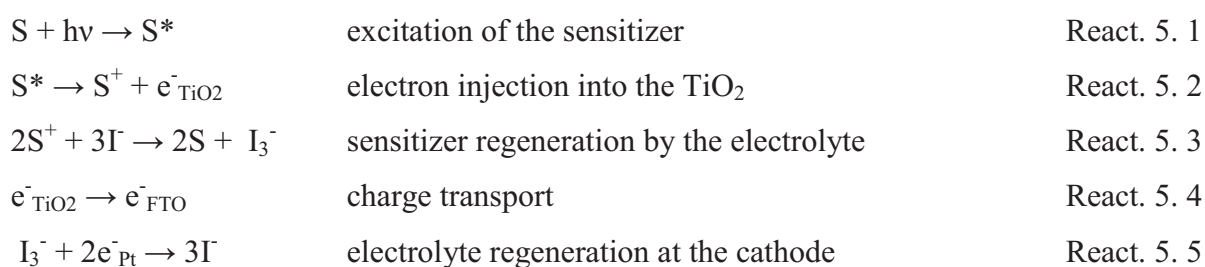
The processes indicated above describe the proper operation of a solar cell, but there are some competing processes lowering its efficiency (React. 5. 6-5. 9). The electrons injected in the TiO_2 conduction band can recombine with the oxidized sensitizer, or with the redox mediator, giving rise to back-electron transfer or dark current. Besides, if the electron injection is extremely sluggish, the excited state of the dye can be quenched by electron (or energy) transfer to the redox mediator, a phenomenon known as charge interception, or relax to its ground state by radiative or non-radiative deactivation.[16]

$S^+ + e^-_{TiO2} \rightarrow S$	geminate recombination or back electron transfer	React. 5. 6
$2e^-_{TiO2} + I_3^- \rightarrow 3I^-$	charge recombination (also called dark current)	React. 5. 7
$2S^* + I_3^- \rightarrow S + 3I^-$	charge interception	React. 5. 8
$S^* \rightarrow S (+ h\nu)$	relaxation of the excited dye	React. 5. 9
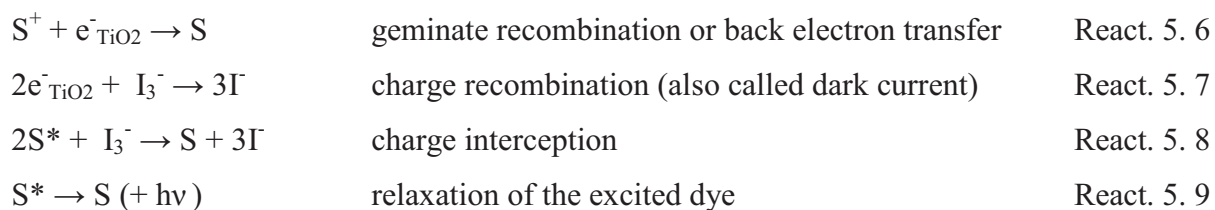
The operation efficiency of a dye-sensitized solar cell is based on a kinetic competition between the forward (Eq. 5. 1-5. 5) and reverse processes (Eq. 5. 6-5. 9).[16] Electron injection usually occurs on very short timescales, from femto- to nanoseconds.[17] The rate of the sensitizer regeneration by the redox mediator (nanoseconds/tenths of nanoseconds) has a crucial importance, as it moves the hole away from the proximity of the semiconductor surface before geminate recombination (occurring on μs to ms timescales). On the cathodic side of the device, a fast redox

mediator reduction pulls the electrons from the external circuit and cooperates to the efficient kinetic balance. Electron transport through the TiO_2 nanostructured network and interfacial recombination processes (e^-_{TiO2} with S^+ or I_3^-) occur on a longer, millisecond timescale. This is the main reason explaining the successful operation of the dye sensitized solar cell: the counter-productive steps are kinetically outperformed by the productive ones.

5.1.2. Dyes

In the field of dye-sensitized solar cells, a capital attention has been paid to the improvement of the dyes properties in order to better satisfy the requirements for a good cell performance. The ideal sensitizer[17] must fulfil several requirements:

- efficiently absorb all the photons below the threshold wavelength of 920 nm (panchromatic dye);
- possess anchoring groups, such as carboxylate or phosphonate, which allow strong grafting to the semi-conductor surface and provide a strong electronic coupling with the conduction band of the semiconductor;
- once excited, inject an electron into the conduction band of the semiconductor with a quantum yield of unity, thanks to a good electronic coupling between the LUMO and the semiconductor conduction band;
- have an excited state energy such as the thermodynamics of injection are favourable and provide an adequate ΔG_{inj} but with minimal energy losses (React. 5. 2). The latter is the difference between the conduction band potential of TiO_2 and the oxidation potential of the excited state S*, $E_{S+/S*}$ (Fig. 5. 1);
- have a redox potential positive enough to allow the efficient regeneration of the dye by the electrolyte or the hole conductor in general (React. 5. 3);
- be thermally, optically and electrochemically stable, so that it can undergo 10^8 turnover cycles under illumination (corresponding to 20 years of operation under natural light) without degradation.

The first and most extensively studied dyes for TiO_2 sensitization are ruthenium(II) polypyridyl complexes.[18] These systems were selected because of their outstanding photoredox properties, in particular they display MLCT transitions located in the visible region. Their synthesis is relatively easy, they have a good stability and ligands can be designed in order to finely tune the electronic properties of the complexes, and introduced in a controlled way. Moreover, their photophysical and electrochemical properties are well known and can be tuned in predictable ways. The HOMO is

centred on the t_{2g} Ru orbital and can thus be destabilized by adding strongly donor ligands. The energy of the LUMO, located on the π^* ligand orbital, is controlled by varying the substituents on the bipyridines. The optimal spectral and electrochemical properties must provide rapid electron injection and dye regeneration in the solar cell, so the redox potential of the excited state has to be at least -0.9 V vs. SCE and the oxidation potential of the ground state should be around 0.5 V vs. SCE, if one considers that the redox mediator is still I^-/I_3^-. These values are derived from the evaluation of the thermodynamics that control electron injection and dye regeneration. In order to have negative ΔG_{inj} and ΔG_{reg} (see Fig. 5. 1), the excited state of the sensitizer must be more negative that the potential of the TiO_2 conduction band ($\sim$ -0.8 V vs. SCE), while its oxidation potential in the ground state must be higher than $E(I^-/I_3^-)$ ($\sim$ 0.1 V vs. SCE).

[Ru(2,2'-bipyridine-4,4'-dicarboxylic acid)$_3$]$^{2+}$ was first considered for TiO_2 sensitization.[14] However, the substitution of one of the three bipyridines by two electron rich thiocyanato ligands and the optimization of the protonation degree of the carboxylic acids proved to give much better performances.[19] The donor ligands rise the HOMO level, decreasing the HOMO-LUMO energy gap, which results in a bathochromic shift of the MLCT band and in an increased harvesting efficiency of the solar spectrum. The protonation degree of the carboxylic acids is instead responsible for the tuning of the TiO_2 conduction band energy (see paragraph 5.1.3), which has an influence on the open circuit voltage delivered by the solar cell (paragraph 5.1.5). These modifications led to **N3**[19] and **N719**[20] (Fig. 5. 2), which are widely used as reference dyes for the test of the experimental conditions, and provide overall efficiencies of about 10%. The use of a tri-carboxylic-terpyridine and three thiocyanate ligands resulted in an even more efficient absorption, virtually covering the whole solar spectrum, and giving the so-called "**black dye**"[21] (Fig. 5. 2), which collects photons until 900 nm.
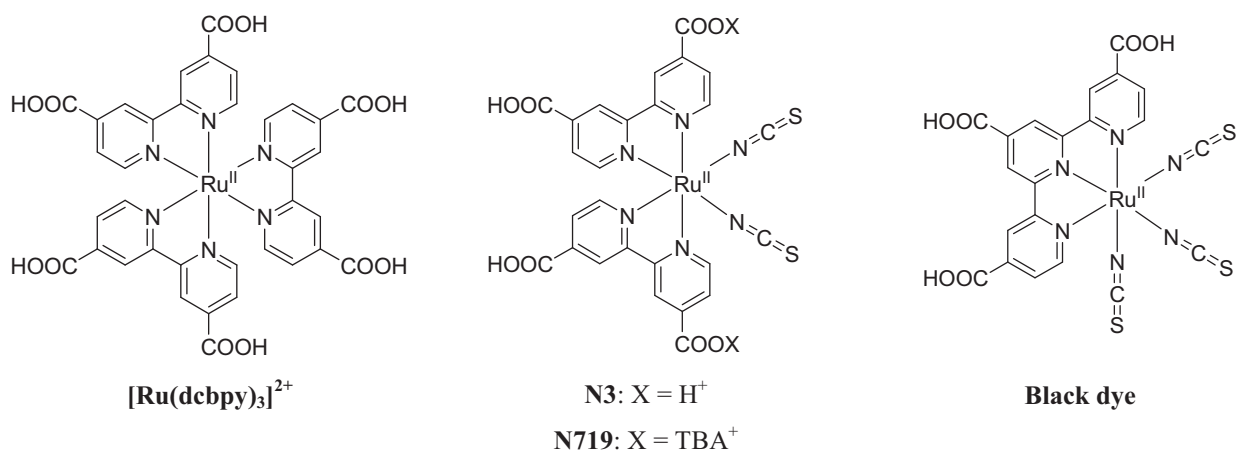
Fig. 5. 2. Structures of four widely used ruthenium(II)-based dyes.

Further improvements of the dyes properties were achieved by adding long hydrophobic chains on one of the bipyridine ligands:[22] this approach afforded on one hand increased stability towards water desorption, and on the other hand a considerable reduction of the dark current due to the limited access of the redox mediator (and water) to the semiconductor surface.

An interesting approach consists in stabilizing the *trans* form of the complex, known to have a red-shifted absorption with respect to the *cis* isomer, by using a tetradentate hybrid ligand bearing both donor (*tert*-butylpyridine) and acceptor ligands (pyridine carboxylic acid).[23] In this way, a panchromatic absorption in the visible is obtained. However, the relatively low absorption coefficient and an unfavourable alignment with the TiO_2 conduction band lead to lower performances with respect to the reference **N719**.

One of the major drawbacks of ruthenium dyes **N3** and **N719** is however the relatively low molar extinction coefficient. To solve this problem, new complexes bearing alkoxy styrylbipyridine ligands were synthesized,[24] with a remarkable improvement of the light harvesting and conversion efficiencies of the devices (**K-19**, Fig. 5. 3). These species have a *push-pull* character, due to the donor properties of the alkoxy groups. The hydrophobic chains also act as a protective layer, according to the principle described above, accounting for a higher stability of the cells. Thiophene-bearing heteroleptic ruthenium dye **CYC-B11** also showed considerably high absorption properties, leading to very impressive photovoltaic performances (η = 11.5% under AM 1.5G simulated sunlight).[25] The rather donor character of the conjugated ligand also allows a localization of the positive charge away from the TiO_2 surface after electron injection, reducing charge recombination.
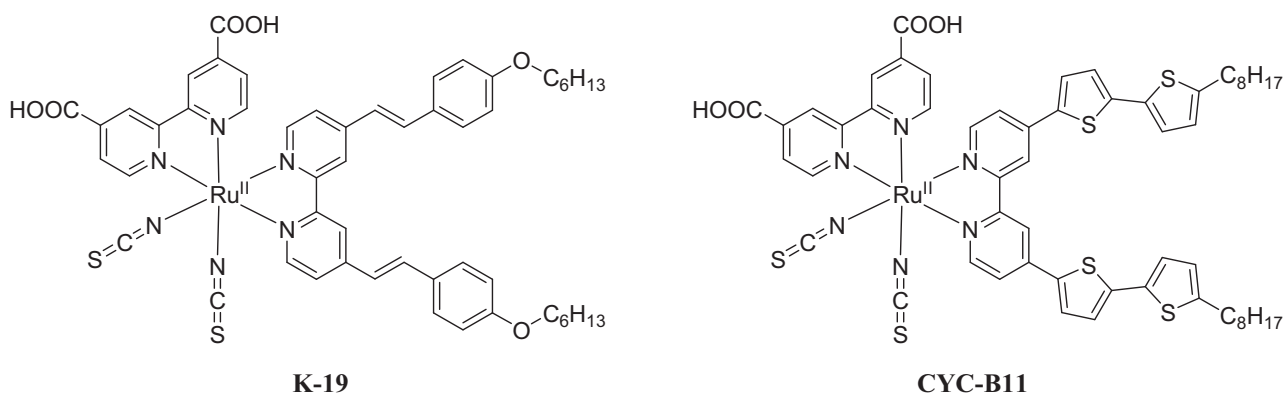
Fig. 5. 3. Structure of the highly absorbing ruthenium dyes **K-19**[24] and **CYC-B11**.[25]

Other metal complexes can be used for the conception of sensitizers for DSSCs, like osmium,[26] iridium[27] or copper (that will be examined later on, in paragraph 5.2)

Besides the coordination complexes, an active research is currently going on to develop completely organic dyes,[28] that can provide very intense and tuneable absorption bands.[29] The cost

of these sensitizers is expected to be cheaper than for the Ru(II) based dyes, as the raw material is less expensive and more readily available.

5.1.3. Semiconductor: TiO$_2$

The titanium dioxide, or titania, plays a fundamental role in the dye-sensitized solar cell, where it performs a double function of electron transporter to the conducting FTO glass and high surface support for the grafting of the sensitizer. This semiconductor presents many advantages: it is abundant, cheap and has a low toxicity. Its weak absorption in the visible region of the solar spectrum increases the resistance against photocorrosion, but at the same time makes it necessary to couple it with a photosensitizer able to absorb the visible photons and subsequently inject electrons into the conduction band. Of the three more abundant polymorphs of TiO$_2$ (anatase, rutile and brookite), the anatase exhibits the most suitable characteristics for an application in DSSC. It has a band gap of 3.2 eV, while rutile exhibits a gap of only 3.0 eV. A small value should be avoided, since excitation within the band gap produces highly oxidizing holes that lower the stability of the cell.[15] Moreover, the conductivity, the electronic structure and the crystalline surface, well suited for adsorption of acidic functions, make anatase the most suitable choice for the construction of DSSCs.

The morphological properties of the TiO$_2$ film are of primary importance for the performances of DSSCs. The first factor to take into account is the surface area, which has to be maximized in order to obtain an efficient collection of the incident light. In fact, as the area occupied by a dye on a flat surface is much larger than its cross-section, a monolayer of sensitizer would absorb only a few percents of the incident light. Another important feature is the porosity of the film. The oxidized dye is regenerated by an electrolyte which must be able to penetrate the film and reach all the dye molecules. For this reason the size of the particles and of the pores has to be accurately controlled.

Since a large concentration of cations in the electrolyte screens the charge of the electrons injected in the titanium dioxide, the charge movement in the semiconductor can be approximately described as diffusive.[30] The diffusion length depends on the diffusion coefficient and on the electron lifetime according to the law:

$$L = \sqrt{D \cdot \tau}$$
<div align="right">Eq. 5. 1</div>

The nanoparticle synthesis is performed by hydrothermal technique. Often, additional titanium dioxide layers are added in order to improve the performances by increasing light scattering (diffusive layer)[31] and reducing charge recombination at the FTO-TiO$_2$ junction (dense blocking layer).[32]

5.1.4. Electrolyte and additives

The electrolyte has the role of regenerating the oxidized sensitizer after the electron injection into the titanium dioxide layer, and transporting the holes to the Pt counter-electrode. In order to have a good device efficiency, it must fulfil several requirements: good electrochemical reversibility and stability under both the oxidized and reduced forms, negligible light absorption, fast electron transfer kinetics, good ability to penetrate the mesoporous TiO_2 layer and redox potential well matched to the S^+/S couple so that the dye regeneration has a sufficient driving force but with minimum potential losses.[15] In addition to this, the potential of the redox mediator couple imposes the Fermi level of the counter-electrode, following Nernst formalism. Therefore, the redox mediator has a major influence on the output potential, since the latter is equal to the difference between the Fermi levels of each electrode, under illumination.

The most widely used redox couple in DSSCs is the iodide/triiodide couple, where triiodide is an adduct formed by iodine and iodide in organic solvents. Its efficiency is mainly due to the kinetic constants of the different competing processes: the dye regeneration and the iodine reduction at the counter-electrode are much faster than the recombination between the injected electrons and the triiodide, or the direct oxidative quenching of the excited sensitizer by the iodine. Moreover, the triiodide reduction reaction, generating iodide, is bielectronic and is therefore not efficient in the absence of a catalyst, such as the platinum particles deposited on the cathode surface.[33] The redox chemistry of the iodide/triiodide couple is rather complex. Recent studies evidenced the importance of considering the intermediate one-electron reactions involved in the iodide oxidation.[34] The iodide ion is not oxidized to free $I^{\bullet-}$ (for thermodynamic reasons) but forms with iodine the $I_2^{\bullet-}$ radical, which then disproportionates to I^- and I_3^-. The authors suggest thus that the potential of the $I_2^{\bullet-}/I^-$ couple (0.79 V vs. NHE, 0.55 V vs. SCE) should be used to calculate ΔG_{reg}. In the paragraphs dedicated to the photovoltaic performances of the dyes, thus, the redox potentials of the two couples will be used.

The I^-/I_3^- couple has nevertheless some major drawbacks: absorption in the blue part of the visible spectrum which can compete with the sensitizing dye, and corrosive properties. Moreover its low oxidation potential (0.35 V vs. NHE, 0.1 V vs. SCE) provokes important potential losses in the devices (a lower ΔG_{reg} would be large enough). For example, **N719** (Fig. 5. 2) has an oxidation potential of about 1.0 V vs. NHE, that leads to a ΔG_{reg} of 0.65 eV, which is obviously excessive and constitutes a waste of energy.[35]

To overcome the problems described previously, some other redox couples[36] were proposed: Br^-/Br_3^-,[37] pseudohalogens [38] as $SCN^-/(SCN)_3^-$ and $SeCN^-/(SeCN)_3^-$ are some examples which are based on the same operating principles as I^-/I_3^-. For what concerns the one-electron couples,

Co(II),[39] Ni(III)[40,41] and Cu(I)[42-44] coordination complexes were also studied. The use of the TEMPO radical[45] and other small molecules was also investigated.[46-48]

The solvent also deserves a few words. The viscosity of the solution has an important influence on the diffusion of the redox mediator, and therefore on the regeneration of the oxidized dye, the lower the viscosity, the faster the mediator diffusion. Unfortunately, low viscosity solvents as acetonitrile also have a low boiling point, and can easily evaporate at the quite high temperatures reached under operating conditions. This reduces considerably the stability of the cells and induces sealing problems. The use of higher boiling point solvents, like valeronitrile or propylene carbonate,[49] was therefore proposed. Ionic liquids are another interesting alternative.[50,51] An active research also concerns the development of gel or solid hole conductors to overcome the issues raised by the use of volatile, corrosive and non-renewable organic solvents.[52]

Another important aspect of the electrolyte composition is the use of additives that modify the conduction band potential of titanium dioxide. The presence of cationic species, such as Li^+ or H^+ ions, adsorbed on the TiO_2 surface shifts the conduction band edge away from the vacuum level, favouring the electron injection by increasing the driving force for the reaction.[31] This usually translates into a higher short circuit current, but lower V_{OC}. Vice versa, the addition of electron rich molecules, like *tert*-butyl pyridine (tBuPy),[53] decreases the energy of the CB and contributes therefore to improving the open circuit potential of the cell (see paragraph 5.1.5), to the expense of the output current. Indeed, the band bending generated by tBuPy can dramatically decrease the injection thermodynamics. The concentration of these additives must be carefully tuned in order to provide and equilibrium between all the electron transfer processes and reach the optimum performance.

Finally, the interfacial charge recombination can be limited by the co-adsorption of saturated hydrocarbons that can bind to the surface between the dye molecules, preventing the direct electron transfer from the reduced titania to the redox mediator. The most widely used is chenodeoxycholic acid (Fig. 5. 4),[15,54] whose planar structure is also very effective in suppressing dye aggregation. The latter is very counter-productive because it leads to a premature quenching of the excited state, before interfacial photochemistry can happen, and consequently lowers the injection yield.
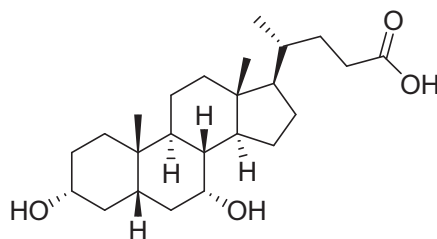
Fig. 5. 4. Structure of chenodeoxycholic acid.

5.1.5. Figures of merit

The performances of a dye-sensitized solar cell are quantified by measuring the current density J produced in an external circuit under illumination, as a function of the applied voltage V. The result is a J/V curve (J vs. V), an example is shown in Fig. 5. 5.
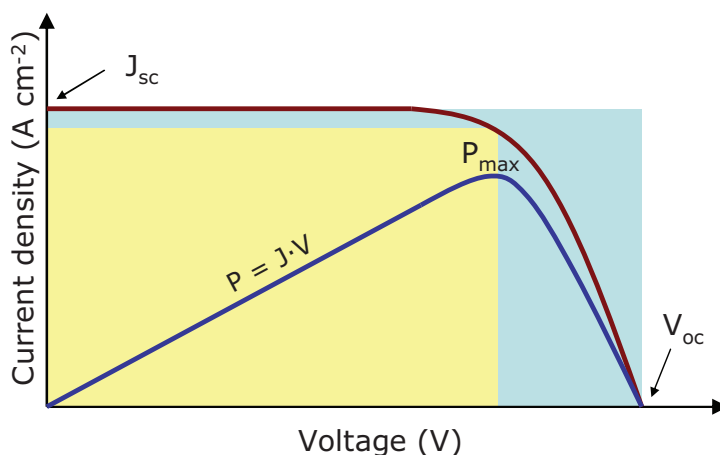
Fig. 5. 5. Representation of a model J/V curve. J_{sc}: short circuit photocurrent; V_{oc}: open circuit voltage; P: power density.

The open circuit potential (V_{oc}) is the potential developed by the cell under irradiation when no current flows in the external circuit. Its maximum thermodynamic value is given by the difference from the TiO_2 Fermi level under illumination and the Nernst potential of the redox mediator;[18] it is strongly influenced by the interfacial charge recombination rate (React. 5. 6-9). The short circuit photocurrent density (J_{sc}) is the current density obtained in the circuit under illumination when a zero potential is applied. The third parameter is the fill factor (ff), which represents the ratio between the area of the yellow and the blue rectangles in Fig. 5. 5 and accounts for the deviation of the cell from the ideal characteristics.

The overall efficiency of the device (η) is obtained using the following formula:[19]

$$\eta = \frac{Jsc \cdot Voc \cdot ff}{I}$$

Eq. 5. 2

where J_{SC}, V_{OC} and ff were defined previously, and I is the intensity of the incident light. The latter is provided by a solar simulator which displays a 100 mW/cm^2 irradiance, with a spectrum closely matching terrestrial solar light (the conventional AM 1.5 conditions).

The IPCE (Incident Photon to Current Efficiency) is the ratio between the number of electrons generated in the external circuit and the number of photons reaching the cell surface. It is

189

measured as a percentage value in function of the incident wavelength, and provides a spectrum of the dye sensitization efficiency.

L = 4,4'-COOH-2,2'-bipyridine
L' = 4,4',4"-COOH-2,2':6',2"-terpyridine
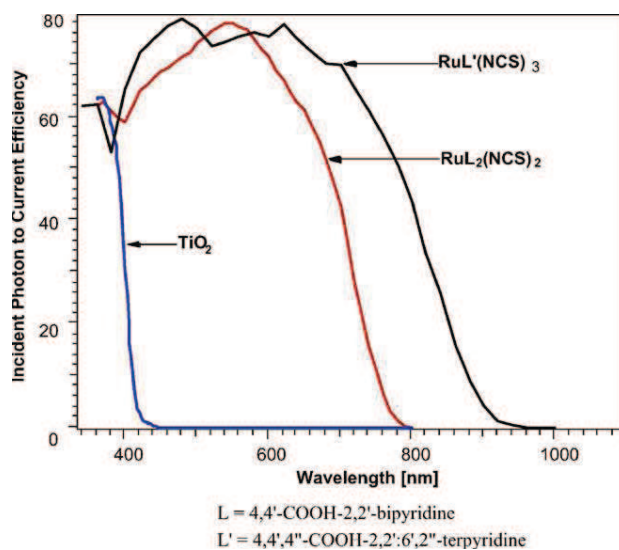
Fig. 5. 6. IPCE spectra obtained with the **N3** complex (ligand L) and the **black dye** (ligand L'). The structures of the dyes are shown in Fig. 5. 2. [55]

The IPCE value, for each wavelength, is given by:[56]

$$IPCE = \frac{1.24 \cdot 10^3 \cdot J_{sc}}{\lambda \cdot \phi}$$

Eq. 5. 3

where λ is the wavelength and Φ is the photon flux (W.m^{-2}). The IPCE is also equal to the product

$$IPCE = LHE \cdot \phi_{inj} \cdot \eta_{cc}$$

Eq. 5. 4

where LHE is the light harvesting efficiency of the sensitizer, ϕ_{inj} is the quantum efficiency of the electron injection process from the sensitizer into the conduction band, and η_{cc} is the quantum efficiency of the charge collection in the semi-conductor TiO$_2$. The J/V characteristic and IPCE measurement are essential tools to evaluate both the performances of a DSSC, and their weaknesses. This analysis is of course mandatory to improve the overall device and, in our particular case, the properties of the sensitizer.

5.2. Copper in TiO₂ sensitization

Compared to the mastodontic research effort devoted to ruthenium sensitizers, the investigation about copper complexes has been much less developed. As said before, copper(I) has several advantages over ruthenium(II) and impressive results could probably be obtained if the same attention was put in improving the molecular structures to match the requirements for DSSC dyes. Due to the well-known lability of copper(I) complexes, the existing work essentially concerns homoleptic species.[57-63] Some examples are shown in Fig. 5. 7.
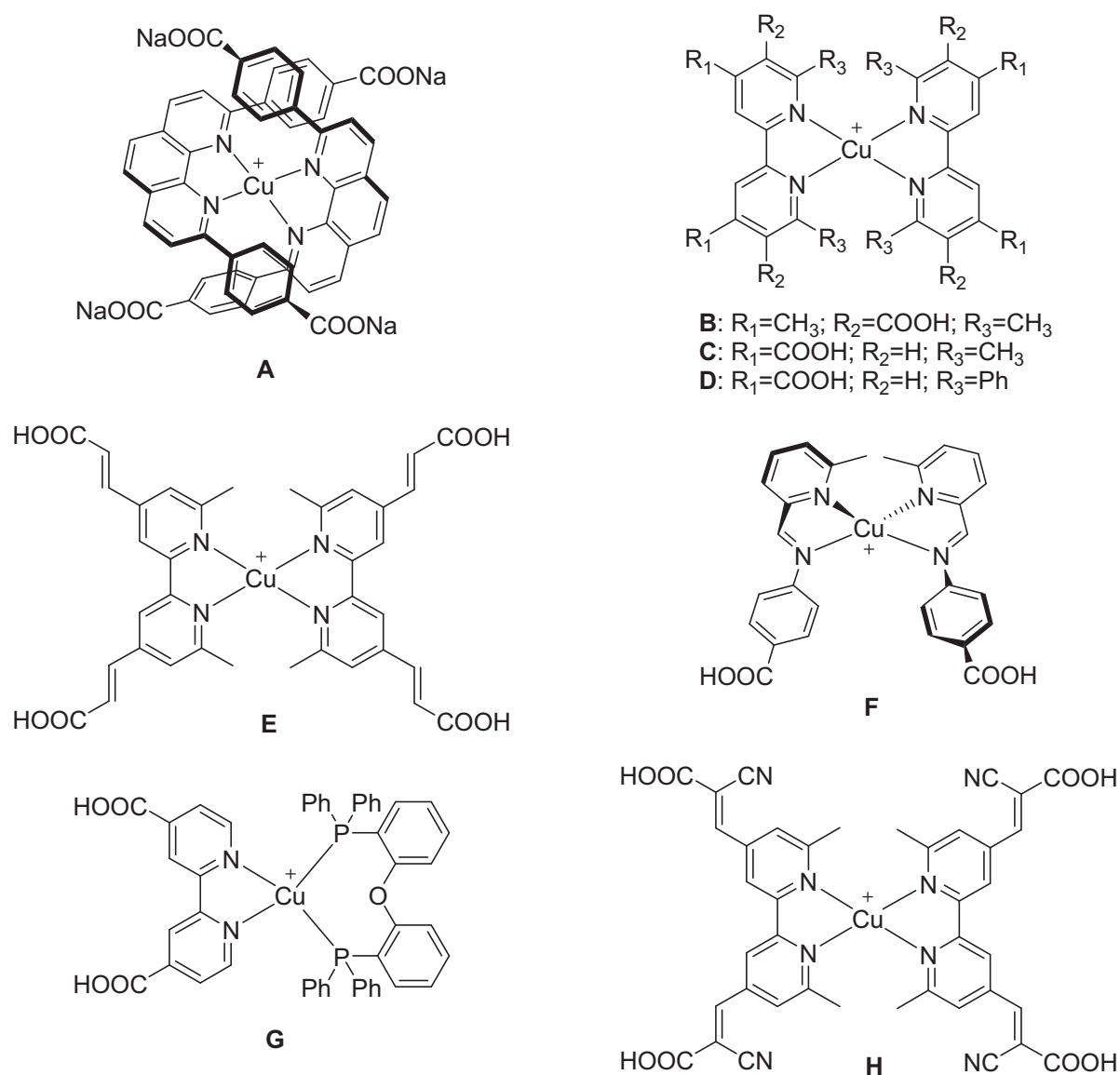
Fig. 5. 7. Structures of some copper(I) complexes for TiO₂ sensitization: **A-F** and **H** are homoleptic while **G** is heteroleptic. The corresponding references are indicated in Table 5. 1.

These compounds have most of the times a Cu^I diimine structure, where the diimines are phenanthrolines, bipyridines or pyridinyl-methanimines possessing carboxylic groups disposed in

various ways. The visible light is absorbed in all cases by an MLCT band, corresponding to an electron density movement from the copper (or in general a copper-centred orbital) to the anchoring ligand. The drawback of this kind of molecules is the relatively low intensity of the visible absorption bands ($\varepsilon \sim 5 \cdot 10^3$ $M^{-1}cm^{-1}$), that intrinsically lowers the device efficiency (low LHE). Moreover, the homoleptic nature of the complexes prevents the directionality of the charge shift upon light absorption, a particularly relevant feature, carefully addressed with ruthenium based sensitizers.

The only undoubtedly formed heteroleptic complex reported for applications in DSSCs contains a bis-phosphine ligand (DPEphos, or bis(2-diphenylphosphinophenyl)ether) opposed to the bipyridine bearing the carboxylic functions (**G**, Fig. 5. 7).[64] The DPEphos ligand provides the steric hindrance necessary to synthesize and isolate the pure heteroleptic compound but, because of its electron-accepting properties, dramatically shifts the absorption spectrum to the ultraviolet region. For this reason, the complex is only slightly coloured, and harvests inefficiently the sunlight, yielding a very low J_{sc} and therefore an overall weak photovoltaic yield.

The photovoltaic data for some copper-based sensitizers are gathered in Table 5. 1. The most remarkable feature, if the values are compared with those of reference ruthenium dyes ($J_{sc} \sim 17$ mA cm^{-2}; $V_{oc} \sim 800$ mV; ff ~ 0.75; $\eta \sim 10\%$), is the very low current density value, due to the inefficient harvesting of visible light.

Dye	J_{sc} (mA cm^{-2})	V_{oc} (mV)	ff	η (%)	η_{N719} (%)	% N719
A[58]	~ 0.60	~ 600	0.60	0.07[a]	–	–
B[63]	3.9	630		2.5	–	–
C[60]	1.15	530	0.68	0.41	5.0	8.2
D[60]	0.69	484	0.63	0.21	5.0	4.2
E[59]	5.9	556	0.70	2.3	9.7	23.7
F[61]	0.84	442	0.61	0.23	4.60	5.0
G[64]	0.23	347	0.65	0.053	3.05	1.7
H[62]	4.69	570	0.79	2.2	7.8	28.2

Table 5. 1. Photovoltaic properties of some copper-based sensitizers, **N719** is used as a reference (the different efficiency values are due to the different preparation conditions of the cells). In the last column, the conversion efficiency of the dye is represented as a percentage value of η_{N719} to facilitate the comparison. [a] Calculated considering the 300 mW cm^{-2} lamp power.

The low V_{oc} values also have important consequences on the overall efficiency of the devices. They probably partly stem from the inefficient electron injection, but a low surface coverage could also

play a role. In fact, all these complexes are positively charged, and therefore prone to electrostatic repulsion which prevents close approach to one another, while the most efficient Ru^{II} sensitizers are neutral species.

From Table 5. 1, it appears that complex B,[63] E[59] and H[62] display the best photovoltaic performances (2.2-2.5%). Indeed, they have a relatively high J_{SC}, which for E and H is most probably due to the extension of the electronic delocalization of the LUMO on the double bonds of the ligands.

The synthesis of heteroleptic complexes *in situ* on the semiconductor was also attempted (Fig. 5. 8).[65] The naked anchoring ligand L was first adsorbed on the surface, and then the TiO$_2$ plate was dipped into a solution containing the homoleptic complex [CuL'$_2$]PF$_6$, in order to form [CuLL']PF$_6$ directly on the surface. Unfortunately, comparison with the spectrum of the homoleptic species [CuL$_2$]PF$_6$ shows that the latter is the only species that forms on the semiconductor surface. Subsequent works reported efficient formation of heteroleptic species on the TiO$_2$ surface, with conversion efficiencies until 1.45% (η_{N719} = 4.50%).[66]
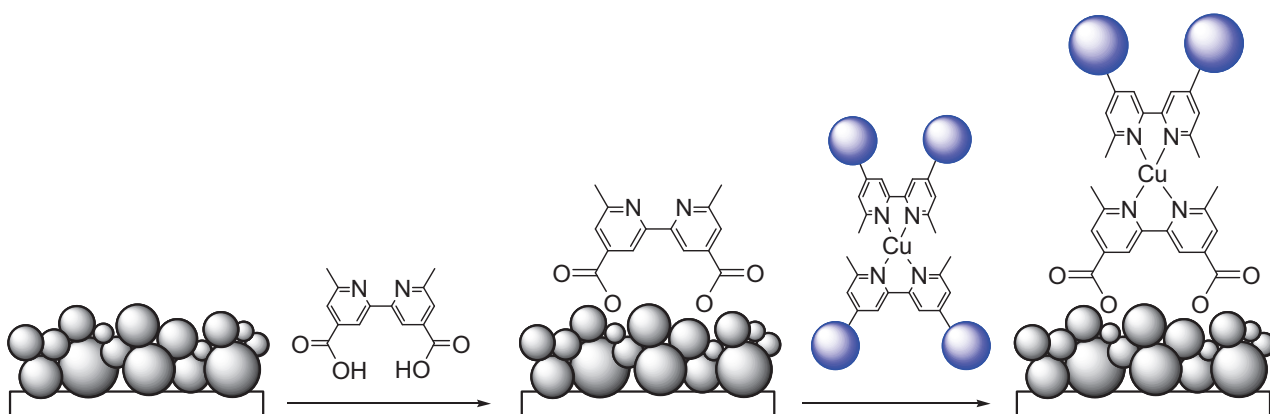
Fig. 5. 8. Schematic representation of the technique used for the *in situ* synthesis of heteroleptic complexes.[65]

Theoretical studies about the use of copper(I) complexes in Dye-Sensitized Solar Cells[67] considered different aspects in the structural design of the dyes, comparing several homoleptic and heteroleptic complexes to N3 and to the record dye CYC-B11 (Fig. 5. 3).[25] The effect of the extension of the π conjugated system (either by a double bond between the bpy ligand and the carboxylic function, or by a bithiophene moiety; see Fig. 5. 9) was evaluated, and it was found to shift bathochromically the absorption spectrum, as expected. The main visible absorption bands of I-M in Fig. 5. 9 display an MLCT character with some minority LLCT contribution, with a 50 nm shift for the latter two complexes. N-P show a bathochromic and hyperchromic shift of the low energy band and the presence of intense bands in the region of 400-500 nm. Globally, the absorption cross-section of these copper(I) complexes exceed those of N3 and even of CYC-B11,

underlining the interest in developing new copper(I) based sensitizers with increased conjugation (lower HOMO-LUMO gap) and chromophoric ligands (higher oscillator strength). It should however be pinpointed that the heteroleptic species presented in this study cannot be obtained pure, because they would give a complicated mixture of three compounds in solution owing to fast ligand scrambling.

I: R$_1$=H; R$_2$=COOH
J: R$_1$=CH$_3$; R$_2$=COOH
K: R$_1$=CH$_3$; R$_2$=COOCH$_3$
L: R$_1$=CH$_3$; R$_2$=C$_2$H$_2$COOH
M: R$_1$=CH$_3$; R$_2$=C$_2$H$_2$COOCH$_3$

N: R$_3$=O
O: R$_3$=S
P: R$_3$=Se
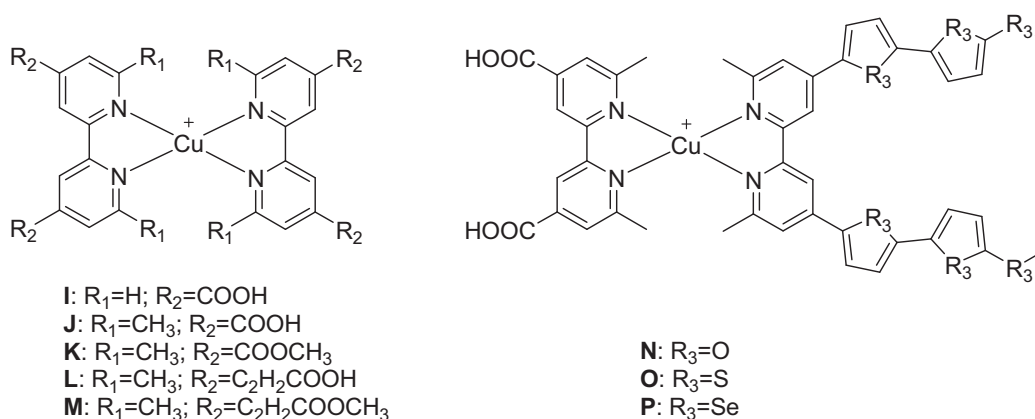
Fig. 5. 9. Structure of the complexes **I-P** studied by Lu and co-workers.[67]

Considering the literature data reported above, it appears relevant to put some efforts towards the synthesis of heteroleptic copper(I) complexes for TiO$_2$ sensitization. These compounds could be very suitable to this kind of application, but some major problems have to be addressed and in particular the low extinction coefficient. The heteroleptic nature, moreover, could bring the directionality of the electron displacement upon light absorption, favouring electron injection in the cell work. In this chapter, the synthesis and characterization of two new series of copper-based sensitizers for Dye-Sensitized Solar Cells will be presented, as well as the photovoltaic performances. The first series is devoted to proving the advantages of heteroleptic complexes to design efficient sensitizers for DSSC. The second series of complexes follows two rationales: using the advantages of the heteroleptic nature of our copper complexes, while improving their extinction coefficients.

5.3. Complexes based on 2,2'-biquinoline-4,4'-dicarboxylic acid: synthesis

2,2'-biquinoline is a bidentate ligand with the same structure than 2,2'-bipyridine, having fused phenyl rings that confer steric hindrance around the chelating nitrogen atoms. We focused our attention on this ligand because its carboxylated equivalent (2,2'-biquinoline-4,4'-dicarboxylic acid, **biQuiH2**, shown in Fig. 5. 10) is commercially available as a di-potassium salt (**biQuiK2**, Fig. 5.

10). In presence if copper(I) and a di-mesityl diimine ligand, the heteroleptic complex is therefore accessible and stable. With respect to 2,2'-bipyridine-4,4'-dicarboxylic acid, commonly used to synthesize Ru^{II} sensitizers, the extended conjugation in **biQuiH2** could stabilize the heteroleptic species by interaction with the mesityl groups of the opposite ligand. The higher steric hindrance provides a protection against an excessive deformation of the coordination cage in the excited state. Furthermore, the higher electron acceptor character of **biQuiH2** is expected to significantly red-shift the MLCT by stabilizing the ligand-centred LUMO, entailing a better harvesting of photons over a wider wavelength frame than typical diimine copper(I) complexes. Additionally, the stronger electron withdrawing character of **biQuiH2** induces a marked vectorialization of the electronic transition. This strategy was actually already employed with ruthenium dyes, to extend the broad MLCT towards the near IR domain.[68,69]
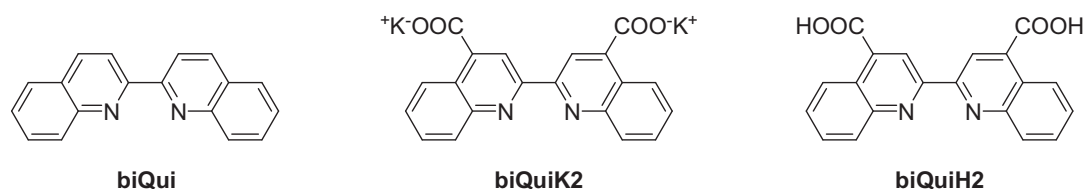
Fig. 5. 10. Structure of the ligands **biQui**, **biQuiK2** and **biQuiH2**.

Copper complexes with 2,2'-biquinoline can be found in the literature, where they have been used for various purposes. The carboxylic group allows the functionalization of the ligand to obtain complex arrays such as copper-based dendrimers [70] and macrocycles with peripheral binding sites.[71] The same structure, incorporated into polymer chains, was used for the preparation of modified electrodes containing copper catalytic sites able to oxidize molecular oxygen and to perform hydroquinones and alcohol oxidation to carbonyl compounds.[72]

One of the possible side processes that can lower the performances of dye-sensitized solar cells is the charge recombination between the oxidized dye and the electron in the conduction band of titanium dioxide. Given the electronic structure of titanium dioxide and the kinetics of interfacial recombination, this phenomenon becomes important when the dye regeneration by the electrolyte is rather sluggish. In this case it is then necessary to increase as much as possible the lifetime of the interfacial charge-separated state, in order to make it survive long enough to allow the slow dye regeneration to operate. An elegant technique to achieve this goal is the use of dyads, composed of a sensitizer grafted to TiO$_2$ and a secondary electron donor (Fig. 5. 11). The hole on the oxidized dye can be rapidly transferred to the donor group, and a final state, where the two charges are separated by a longer distance is attained.[73] The requirements for this approach are a fast electron

transfer from the donor group to the oxidized sensitizer and a well suited oxidation potential of the donor group. Its value must be comprised between $E_{S+/S}$ and $E_{I3-/I-}$ in order to ensure on one hand electron transfer to the oxidized dye ($\Delta G_{ET} < 0$, Eq. 5. 5), and on the other hand a negative ΔG_{reg} (Eq. 5. 6), respectively.
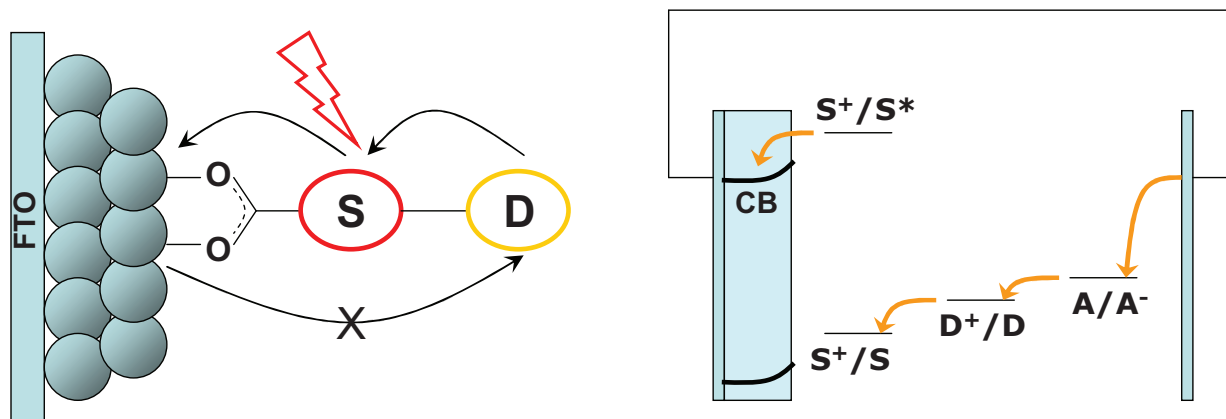
Fig. 5. 11. Schematic representation of a dyad bound to TiO_2 surface, and the strategy to reduce back electron transfer. S: sensitizer; D: donor group; A: redox mediator; → electron transfer.

$$\Delta G_{ET} = E(D^+/D) - E(Cu^{II/I})$$

Eq. 5. 5

$$\Delta G_{reg} = E(I_3^-/I^-) - E(D^+/D)$$

Eq. 5. 6

A rather similar strategy employs dye molecules with a very marked push-pull character. In this case, the "pull" side of the sensitizer is close to the TiO_2 surface, and the "push" side is located away from the semi-conductor surface. Upon excitation, the push-pull nature of the dye favours the injection of an electron in the conduction band of TiO_2, and the resulting hole, being located on the "push" moiety remote from the surface, is less likely to recombine with e^-_{TiO2}. Moreover, an increased push-pull character of the molecule provides a higher value of the molar extinction coefficient, thanks to an increase of the transition moment and improves the light harvesting efficiency of the dye.

The use of **biQuiH2** to synthesize heteroleptic copper(I) complexes for DSSCs will be explored by preparing heteroleptic structures containing a donor group: a tertiary aromatic amine or a ferrocene (shown in Fig. 5. 12). Such structures are expected to reduce the interfacial charge recombination by assisting electron injection through vectorialization of the photo-induced electron transfer step (the positive charge on the oxidized dye is in fact localized far away from the semiconductor surface).
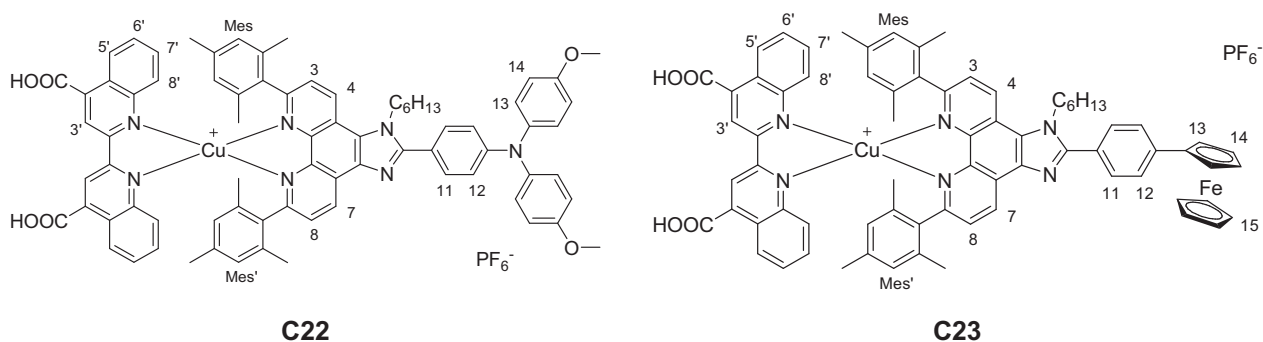
Fig. 5. 12. Structure of the two sensitizers with **biQuiH2** ligand and donor groups, **C22** and **C23**.

Since the complex comprising **biQui** and **L1** (dimesitylphenanthroline) was not known in literature, the model complex **C19** ([Cu(**L1**)(**biQui**)]PF$_6$) was first synthesized as a reference compound in order to study the influence of **biQui** on the photophysical and electrochemical properties of heteroleptic species (Scheme 5. 3). Indeed, it has a higher flexibility compared to phenanthroline but an extended conjugation if compared to 2,2'-bipyridine, two properties that are known to play a major role in defining the properties of copper(I) diimine complexes. The model complex containing the carboxylic anchoring functions was also prepared, under the protonated (**C20**) and deprotonated (**C21**) form in order to study the effect of the protonation grade on the photovoltaic performances of the dye. Finally, the two complexes **C22** and **C23** were synthesized (Fig. 5. 12). The compounds were then characterized and tested as sensitizers in photovoltaic devices.

5.3.1. Synthesis of the ligands L15 and L16 containing electron donor groups

For this study, two different donors were chosen: a dianisyl phenylamine and a ferrocene, which were connected to the **C20** through a fused imidazo bridge. Both are well-known reversible electron donors, with oxidation potentials of about 0.70 V[74] and 0.45 V[75] vs. SCE respectively. As the redox potential of the Cu^{II}/Cu^{I} couple is usually around 0.9 V vs. SCE, and that of the iodide/triiodide couple is 0.10 V vs. SCE, it appears immediately that the triaryl amine seems well suited to ensure a better regeneration by the cell electrolyte, while ferrocene provides a higher ΔG for the electron transfer to the oxidized copper complex (see Eq. 5. 5 and 5. 6) but a moderate regeneration driving force.

The synthesis of the ligand **L15** was performed from dianisylamine and p-bromobenzaldehyde protected as a cyclic acetal, which were coupled with a Buchwald-Hartwig type cross-coupling reaction (Scheme 5. 1). The aldehyde group was then deprotected in acidic conditions and reacted with 2,9-dimesityl-1,10-phenanthroline-5,6-dione **7** (prepared as described in

chapter 2) following the classical Steck and Day protocol,[76] to obtain the imidazole, which was finally alkylated to give **L15** in 42% yield (based on the dione as the limiting reactant).
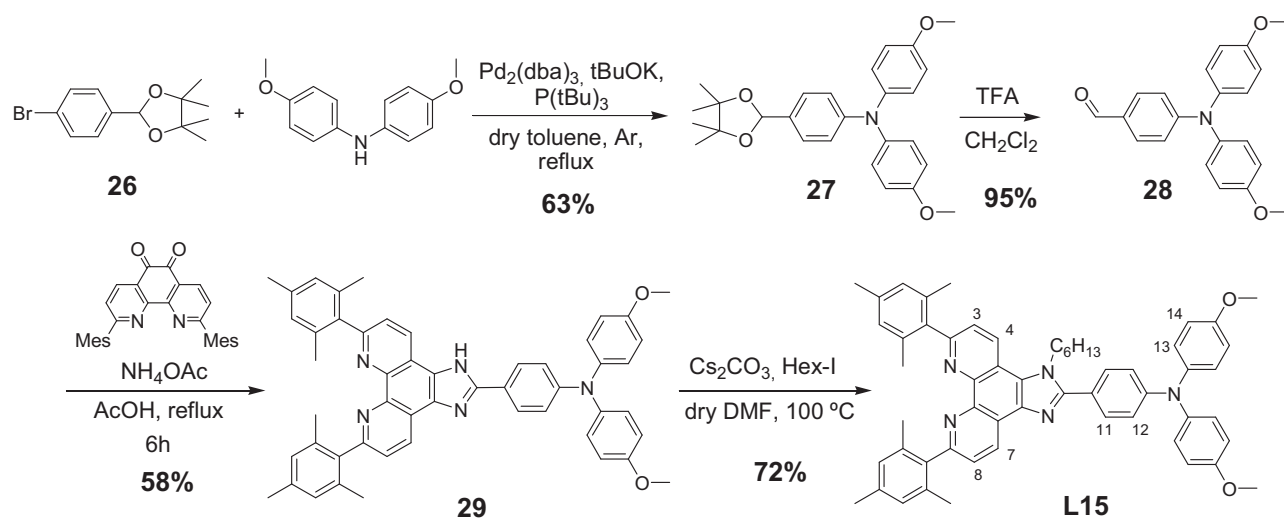
Scheme 5. 1. Synthesis of the ligand **L15**.

The ^{1}H-NMR spectrum clearly shows that the phenanthroline has become asymmetrical due to the alkyl chain on the imidazole, with a 0.5 ppm difference between the signals of H^4 and H^7 and split mesityl signals both in the aromatic and the aliphatic region. The characteristic broad triplet of the NCH_2^{nHex} is found at 4.69 ppm.

The ligand **L16** was synthesized by Suzuki cross-coupling from **L6'** and ferrocene-boronic acid, which provided the final product in 54% yield (Scheme 5. 2). The aromatic portion of ^{1}H-NMR shows the pattern of asymmetrically substituted phenanthroline (non equivalent signals of H^7 and H^8, and split signal of H^{Mes}). Interestingly, the H^{11} and H^{12} are displayed as a singlet, instead of two doublets. The characteristic signals of the ferrocene are observed at 4.77, 4.42 and 4.10 ppm as two triplets (2H) and one singlet (5H) respectively.
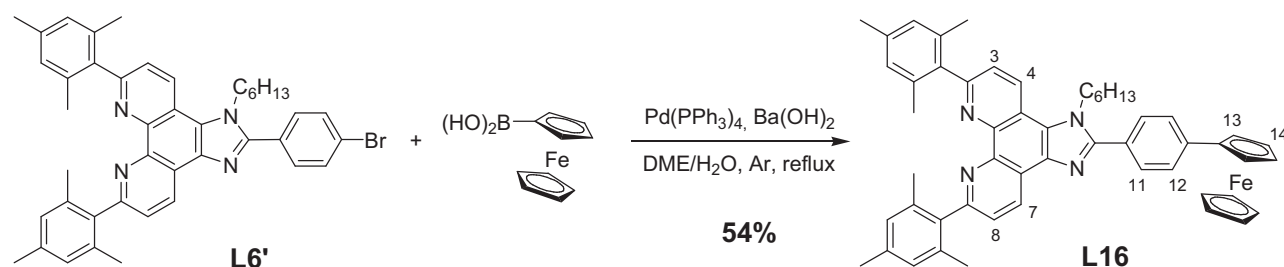
Scheme 5. 2. Synthesis of the ligand **L16**.

5.3.2. Synthesis of [Cu(diMesPhen)(biQui)]PF₆: a model complex

As the heteroleptic coordination cage containing 2,9-dimesityl-1,10-phenanthroline and 2,2'-biquinoline was not known in literature, it appeared necessary to synthesize the model complex **C19** (Scheme 5. 3). In this complex, the Cu[I] ion is surrounded by a rigid and encumbering ligand, the dimesitylphenanthroline **L1**, and by a smaller one, **biQui**, where nonetheless the chelating nitrogen atoms are sterically hindered.

The complex was prepared using the classical HETPHEN protocol in dichloromethane, and purified by column chromatography on silica gel, then crystallized from a dichloromethane solution by diffusion of petroleum ether vapours to obtain the pure **C19** in 54% yield, as a violet solid. The molecule is stable as a solid and in solution, even when exposed to atmospheric oxygen.
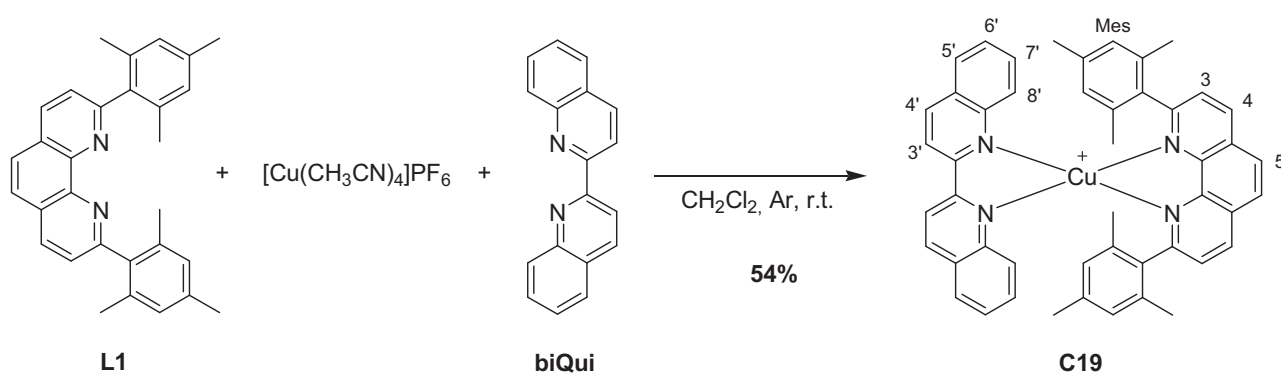
Scheme 5. 3. Synthesis and structure of the complex **C19**.

The ^{1}H-NMR spectrum is composed of a superimposition of the spectra of the two ligands, with shifts due to the coordination of the metal ion. The protons of the phenanthroline core are downfield shifted upon coordination, because of the electron withdrawing effect of the copper ion coordinated to the nitrogen atoms. On the contrary, the mesityl protons are characterised by an upfield shift (H^{Mes}) and appear as a singlet at 5.85 ppm. The shielding effect is due to the electron density of the biquinoline ligand. A comparison between the ^{1}H-NMR spectra of the coordinated and free **biQui** shows an important upfield shift of H$^{8'}$ (from 8.24 ppm in the free ligand to 7.54 ppm in the complex), and a general slight upfield shift of the other protons too. This effect is due to the shielding provided by the mesityl rings, which is interestingly high enough to overcome the unshielding effect of the coordination of copper(I).

The successful preparation of complex **C19** proved the stability of this new kind of heteroleptic coordination cage, paving the way to the synthesis of a series of copper based dyes containing the 2,2'-biquinoline-4,4'-dicarboxylic acid as the anchoring ligand.

5.3.3. Synthesis of [Cu(diMesPhen)(biQuiCOOH)]PF₆: a reference compound for TiO₂ sensitization

Once taken for granted that copper complexes comprising 2,9-dimesityl-1,10-phenanthroline (**L1**) and 2,2'-biquinoline (**biQui**) are stable and can be prepared by the classical HETPHEN synthetic approach, the synthesis of the parent complexes containing COOH anchoring groups was performed, with the commercially available potassium salt of 2,2'-biquinoline-4,4-dicarboxylate. The protonation state of a sensitizer can dramatically affect the performances of the corresponding DSSC (as witnessed by the comparison between **N3** and **N719**).[19,20]

Due to the insolubility of the ligand in dichloromethane, the reaction was performed in dry degassed N,N-dimethylformamide. Once again, to avoid the undesired formation of homoleptic complexes, excess mesityl phen and tetrakis acetonitrile copper(I) were used. The product was then purified by size exclusion chromatography on Sephadex LH20, swollen in a mixture of methanol and dichloromethane, a commonly used method when dealing with molecules possessing anchoring functions. Complex **C20** was obtained as a dark violet solid in 65% yield. FTIR spectra exhibited the characteristic peak of PF₆⁻ at 848 cm⁻¹, confirming that the obtained complex was associated with this counter-anion. However, the latter showed surprisingly poor solubility in commonly used solvents, which complicated the NMR study. We therefore synthesized in parallel the fully deprotonated complex as dicarboxylate tetrabutylammonium salt (**biQuiTBA2**) to insure a decent solubility in organic medium. The subsequent synthesis of the complex, **C21**, was performed in similar conditions than **C20**, albeit distilled methanol was used as solvent. The product was obtained in 60% yield.
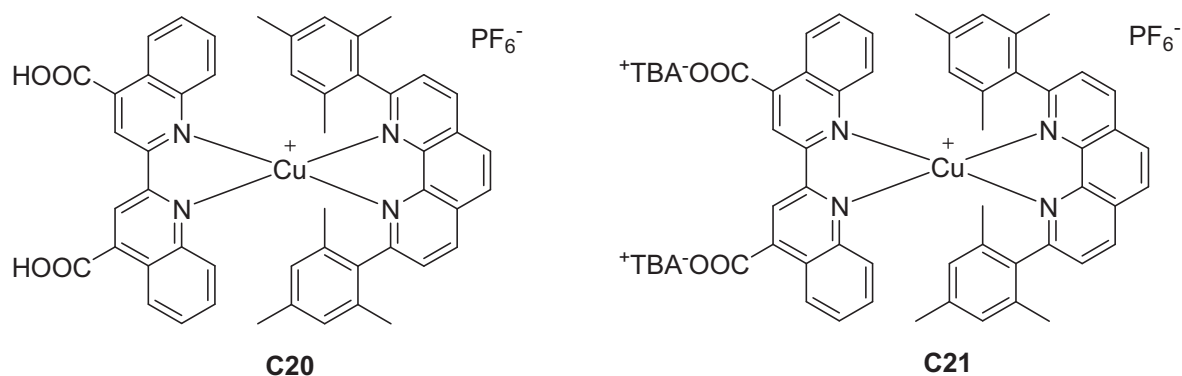
Fig. 5. 13. Structure of the complexes **C20** and **C21**, containing carboxylic anchoring functions.

Complex **C21** proved to be highly soluble in methanol, and the corresponding NMR spectrum in MeOD is well-resolved. The usual signals of both **L1** and **biQuiTBA2** were monitored, with a significant downfield shift due to the presence of electropositive copper(I) in the

coordinating cavities. As usual, the singlet assigned to the aromatic hydrogen nuclei borne by mesityl groups experienced an upfield shift, due to the shielding effect of the vicinal aromatic rings of biquinoline. Multiplets in the aliphatic part of the spectrum were assigned to the alkyl chains of tetrabutylammonium counterions. Interestingly, the integration of these signals revealed the presence of two cations, while the FTIR spectrum clearly displayed the characteristic vibration band of PF_6 ions. Gathering up all these data, we propose the following structure for **C21**: $[Cu^I(\mathbf{L1})(\mathbf{biQuiTBA2})]^+(PF_6^-)$ (represented in Fig. 5. 13).

5.3.4. Synthesis of complexes C22 and C23: heteroleptic complexes with donor groups

The complexes **C22** and **C23** (Fig. 5. 12) were prepared in dry degassed N,N-dimethylformamide by reacting 1.15 equivalents of the hindered ligands, **L15** and **L16** with 1 eq. of tetrakis acetonitrile copper(I) hexafluorophosphate and 0.9 equivalents of **biQuiH2**. The purification of the dyes was carried out by size exclusion chromatography using a dichloromethane/methanol eluent, and the complexes **C22** and **C23** were obtained respectively in quantitative and 78% yield.

The ^{1}H-NMR spectra were recorded in a mixture of CDCl$_3$: MeOD = 4: 1 and present an important peak broadening, which is typical of anchoring functions containing complexes, because of additional protonation-deprotonation equilibriums in solution. However, the signals belonging to the two ligands can be distinguished, and an upfield shift of all the mesityl centred signals (in ligands **L15** and **L16**) was observed as a general trend due to the shielding provided by the biquinoleine ligand. On the contrary, the peaks of the phenanthroline protons were slightly downfield shifted due to the coordination of the copper(I) ion, as described for the other complexes.

5.4. Characterizations of the complexes based on 2,2'-biquinoline-4,4'-dicarboxylic acid

5.4.1. Absorption spectroscopy of the ligands C15 and C16 and complexes C19-C23

The UV-Visible absorption properties of the complexes **C19**-**C23** were studied in dichloromethane, methanol or ethanol solution. The absorption data for the four complexes are gathered in Table 5. 2, and the spectra are shown in Fig. 5. 14.

	λ_{base} [ε]	λ (nm) [ε ($M^{-1}cm^{-1}$)]	λ_{acid} [ε]
C19	-	265 [5.3 10^4]	-
		342 [1.6 10^4]	
		357 [1.7 10^4]	
		536 [3.1 10^3]	
C20/C21	530[a] [3.6 10^3]	544 [3.3 10^3]	558[b] [3.2 10^3]
C22	534 [5.1 10^3]		562 [4.4 10^3]
C23	537 [4.0 10^3]	555 [3.2 10^3]	576 [3.5 10^3]

Table 5. 2. Absorption data for complexes **C19**-**C23**, recorded in dichloromethane (**C19**), methanol (**C22**, **C23**) or ethanol (**C20/C21**). λ_{acid} and λ_{base} were recorded in presence of TFA and Et_3N, respectively. [a] **C21**. [b] **C20**.

The UV-Vis absorption spectra of the biquinoline-containing complexes immediately show major differences when compared to those of the bis-phenanthroline complexes (see complexes **C4**-**C8** in chapter 2). Let us start by describing the characteristics of the model complex **C19** recorded in dichloromethane. The UV part is dominated by ligand-centred transitions: the contributions at 356 and 340 nm are attributed to biquinoline by comparison with the spectrum of the free ligand. The absorption in the visible is very broad and the MLCT band maximum is located at 530 nm, with a low intensity tail extending until 700 nm. This represents a remarkable bathochromic shift with respect to the classical position of the MLCT band in Cu[I] complexes (around 450 nm), leading to an improvement of the light harvesting efficiency. Interestingly, the spectrum is quite similar to that of **N3** (Fig. 5. 2), one of the best performing sensitizers in the field of DSSCs, but it must be pointed out that the ε values of **C19** are much lower ($\sim 3 \cdot 10^3$ $M^{-1}cm^{-1}$, compared to the $\sim 1.5 \cdot 10^4$ $M^{-1}cm^{-1}$ of **N3**). The red-shift of the MLCT is due to the LUMO stabilization caused by the extended π-conjugation of the quinolines. Moreover, the MLCT transition involves the formal oxidation of the copper(I) centre into copper(II), which is favoured in flexible coordination cages that can flatten towards a tetragonal symmetry.[77]

Complex **C20** has a UV-Vis spectrum very similar to **C19**, consisting of a broad visible absorption, ascribed to an MLCT transition, and a series of ligand-centred bands in the UV. The visible band extends from 470 to 650 nm (λ_{max}= 558 nm, ε = 3.2·10^3 M^{-1}cm^{-1}) and is attributed to a MLCT transition from the copper(I) centre to the anchoring ligand, by comparison with the DFT calculated spectrum. The second, lower contribution in the visible region, extending until 370 nm, also has an MLCT character but with some contribution of the 2,9-dimesityl-1,10-phenanthroline. In the UV portion, the main contributions come from IL and LLCT with some MLCT character, particular in the low energy region, vibrationally resolved band peaking at 357 and 340 nm can be ascribed to the biquinoline core by comparison to the spectrum of the free ligand.
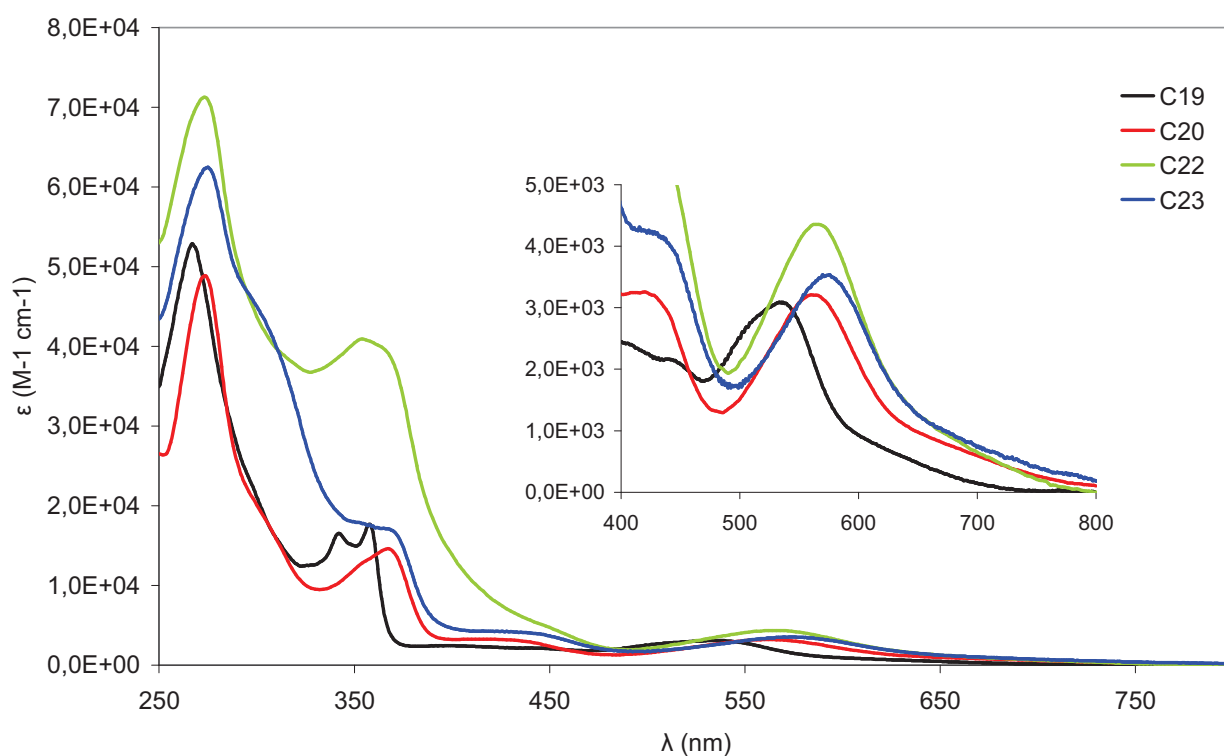
Fig. 5. 14. UV-Vis spectra of **C19**, **C20**, **C22** and **C23**. For the complexes containing carboxylic functions, the spectra are recorded in presence of a slight excess of trifluoroacetic acid, in order to have the completely protonated complexes. Inset: magnification of the visible region.

DFT calculations (Dr. Kayanuma, University of Strasbourg) performed with CAM-B3LYP functional, well adapted to simulate charge-transfer states,[78] confirmed the interest of such kind of structure. The visible bands of the spectrum were proved to have a metal-to-ligand charge transfer character, with the LUMO localized on the **biQuiH2** ligand, containing the anchoring functions. The HOMO and LUMO profiles are shown in Fig. 5. 15.
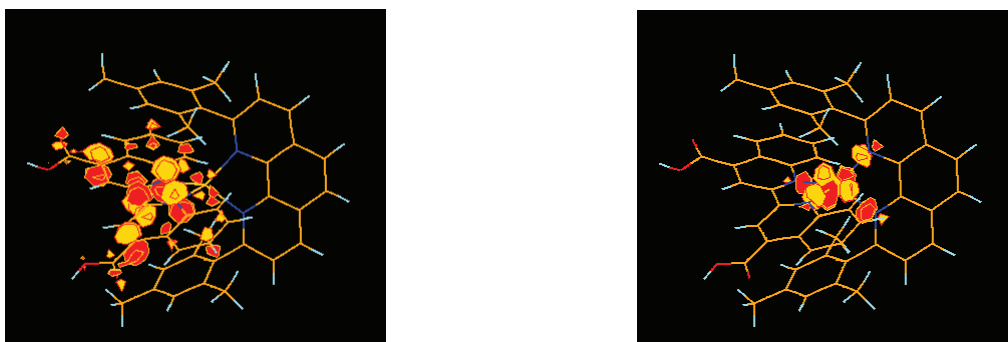
Fig. 5. 15. LUMO (left) and HOMO (right) electronic distributions of the complex **C20**.

The protonation state of the ligand **biQuiH2** can have a significant influence on the absorption spectrum, thus a systematic study of the electronic spectrum was undertaken. To do so, the complex **C21**, completely deprotonated, was dissolved in ethanol and titrated by adding controlled aliquots of a diluted solution of HPF$_6$ (Fig. 5. 16).
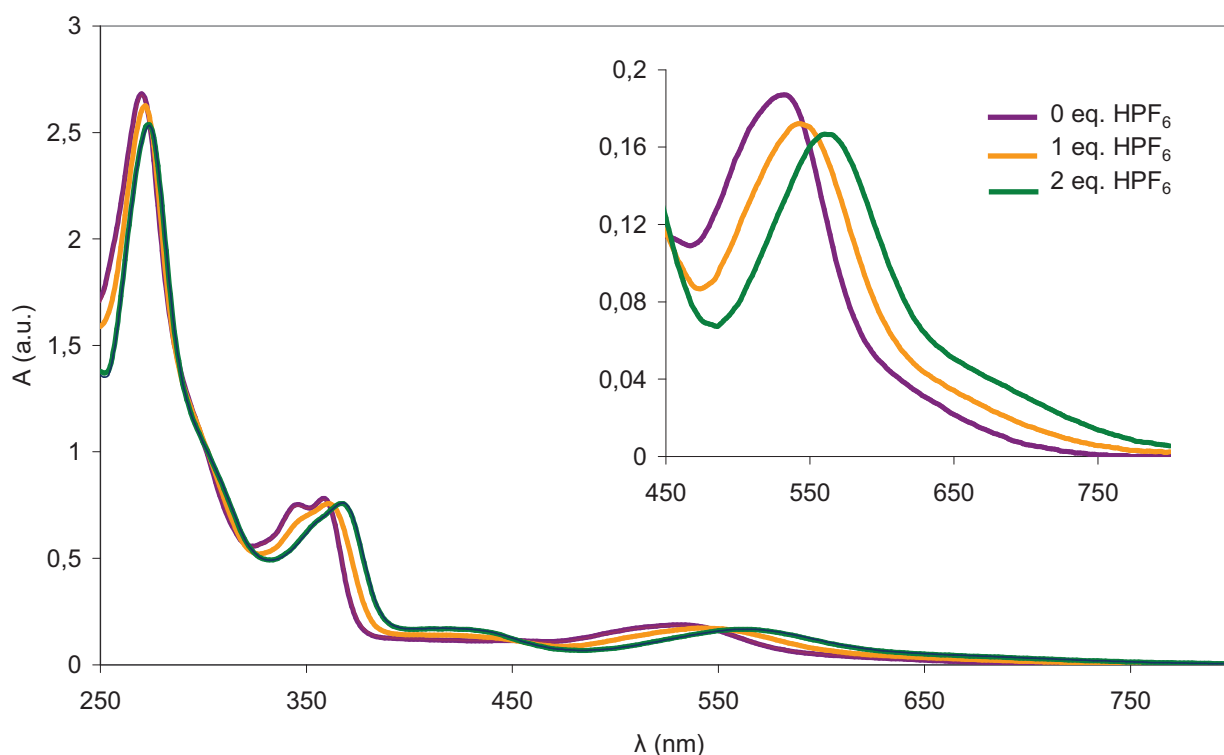
Fig. 5. 16. Evolution of the UV-Vis spectrum of **C21** (violet line) in ethanol upon the addition of HPF$_6$. The protonated complex, obtained after addition of two equivalents of acid, is **C20**.

The spectra show a 30 nm bathochromic shift of the MLCT band when passing from **C21** to **C20**, (λ_{max} = 530 and 560 nm, respectively) while the monoprotonated species has an intermediate

λ_{max} value (544 nm). This can be rationalized by the electron rich character of carboxylate, which is likely to destabilize the ligand-centred vacant frontier orbitals, therefore leading to an overall blue shift of the MLCT upon deprotonation. The well separated bands allow the use of UV-Vis spectra as a diagnostic tool to identify the degree of protonation of the complex in solution.

The same behaviour was observed in literature for complex [Cu(**biQuiH2**)(**biQuiH⁻**)]. Its spectral properties were assessed in water, showing that it possesses a broad band at 560 nm. Moreover, it was observed that the spectrum of the free ligand is bathochromically shifted upon protonation (pH< 6).[79]

Before studying the complexes **C22** and **C23**, the spectroscopic properties of the two ligands were recorded in dichloromethane. Both ligands display intense transitions in the UV part of the spectrum ($\varepsilon \sim 4.5 \cdot 10^4$ M^{-1}cm^{-1}), assigned to π-π* transitions of the conjugated structure. **L16** shows a very weak and broad absorption at 446 nm ($\varepsilon \sim 800$ M^{-1}cm^{-1}), due to the forbidden d-d transitions of the ferrocene moiety.

The two sensitizers **C22** and **C23** were studied in methanol solution. The assignment of the absorption bands is done by comparison with the previously analysed reference complex **C20**. The broad band around 550 nm corresponds to the MLCT arising from an electron displacement from the Cu(I) towards the anchoring ligand, the shoulder around 430 nm (less pronounced for **C22**) is attributed to a MLCT to the dimesityl ligand. In the UV, the biquinoline-centred $\pi-\pi$* transitions are around 350 nm and the band at 270 nm is centred on **L15/L16**. The band at 350 nm, however, is not resolved and nearly appears as a shoulder, due to the presence of another contribution at 300 nm, which was lacking in the spectrum of **C20**. The latter is probably due to a transition centred on the **L15/L16** ligand.

Interestingly, the maximum absorption wavelength of both complexes underwent a blue-shift upon dilution, which is likely due to a gradual deprotonation of the acid groups in methanol. Complementary experiments confirmed that the λ_{max} of the MLCT band of **C23** shifted from 536 nm to 575 nm when the solution passed from basic (excess NEt$_3$) to acid (excess TFA). The same dependence on the protonation state had previously been observed for **C20**/**C21**. This translates in a reversible colour change from violet-pink in basic solvent to dark green in acid conditions, which incidentally indicates that the complex is stable under these experimental conditions.

The only difference concerning **C22** is that the spectrum of the deprotonated (and of the TiO$_2$ grafted) form can be attained upon simple dilution. This might be an effect of the amine group, which act as a base to help deprotonation of the carboxylic groups.

DFT calculations for the complex **C22**, using CAM-B3LYP functional, confirmed that the calculated HOMO orbital is localized on the amine donor, while the LUMO is on the anchoring

ligand (Fig. 5. 17). The localization of the HOMO on the amine group is also deduced from the electrochemical study (see following paragraph). However, the lowest energy absorption, corresponding to the broad band around 550 nm, is attributed to a MLCT transition from a copper(I)-centred orbital to the **BiQuiH2** ligand and not to a LLCT (from amine to **biQuiCOOH**). Furthermore, the absorption maximum is not extremely red-shifted with respect to the model complex **C20**, as it would be if the electronic communication between the amine and the phenanthroline was large. For this reason, it can be hypothesized that **C22** behaves more like two independent units (dyad) than a push-pull system. This means that the charge injection into the TiO$_2$ and the hole shift towards the donor group are likely to be two separate steps.
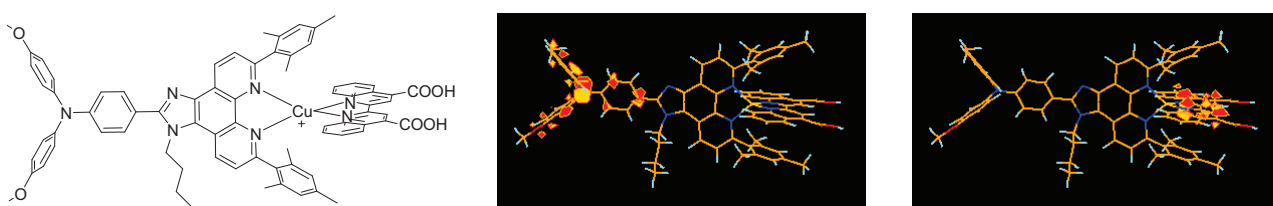
Fig. 5. 17. Structure (left) and frontier orbitals, HOMO (centre) and LUMO (right), of the complex **C22**.

5.4.2. Emission properties of L15 and L16 and complexes C19-C23

The ligands are luminescent upon excitation in the UV, **L15** emits at 487 nm and **L16** at 411 nm, as usual for phenanthroline-based ligands.

However, all these new complexes with biquinoline ligand are not luminescent in dichloromethane at room temperature. This is a consequence of the excited state flattening distortion, which stabilizes the Cu^{II}-L$^-$ state and makes the nonradiative deactivation pathways like exciplex quenching very efficient. The biquinoline, despite the presence of the fused phenyl rings, is not a very hindering ligand, and therefore opposes a limited resistance to the distortions of the coordination cage.

5.4.3. Electrochemistry of L15 and L16 and complexes C19-C23

The electrochemical properties of the ligands **L15** and **L16**, and of the complexes **C19-C23** were recorded in dichloromethane. They are particularly interesting both from a fundamental and applied point of view, because they can provide information about the rigidity of the coordination cage, and they can above all be used to calculate the thermodynamics of dye regeneration and electron injection when coupled to spectroscopic data. Half-wave potentials are gathered in Table 5. 3, while cyclic voltammograms of **C22** and **C23** are presented in Fig. 5. 18.

Ligands **L1** and **biQui** are electrochemically silent within the electrochemical window explored in this study. However, the amine and ferrocene bearing ligands display the expected reversible oxidations. The measured oxidation potentials of the ligands were 0.77 V (**L15**) and 0.52 V (**L16**), and correspond to the abstraction of one electron from the anisylamine and the ferrocene moiety respectively. The potentials are quite similar to those obtained for plain ferrocene or trisarylamine, indicating a rather weak electronic coupling between the phenimidazole and the electron donor moieties.

All complexes exhibit a quasi-reversible oxidation wave between 0.8 and 1.0 V vs. SCE, corresponding to the formal oxidation of the copper(I) ion into copper(II). The presence of amine or ferrocene in complexes **C22** and **C23** is confirmed by the apparition of an additional wave at 0.79 V and 0.52 V vs. SCE, respectively. The oxidation potentials of the two electroactive donor groups in the ligands also show a very slight dependence upon complexation of the copper(I) ion, indicating that there is little or no electronic communication between the donors and the complex.

For what concerns the Cu^I moiety, a shift towards anodic potentials is observed upon complexation with biquinoline carboxylic acid, with respect to the value obtained for **C19**. This is provoked by the presence of the electron withdrawing carboxylic groups and the coulombic repulsion with the positive charge already formed on the donor moiety (ferrocene or arylamine). All the oxidation processes assessed were reversible, with no loss in current intensity during the backward scan.

	$E_{1/2}$ ($Cu^{II/I}$) [ΔE (mV)]	$E_{1/2}$ ($Fc^{+/0}$) [ΔE (mV)]	$E_{1/2}$ ($NR_3^{+/0}$) [ΔE (mV)]
L15	—	—	0.77 [90]
L16	—	0.52 [88]	—
C19	0.84 [110]	—	—
C20	0.87 [87]	—	—
C22	1.02 [83]	—	0.79 [83]
C23	0.98 [100]	0.52 [60]	—

Table 5. 3. Electrochemical data for **L15**, **L16** and complexes **C19**-**C23**, recorded in dichloromethane. WE: Pt disc; RE: SCE; CE: Pt foil; supporting electrolyte: $TBAPF_6$ 0.1 M.
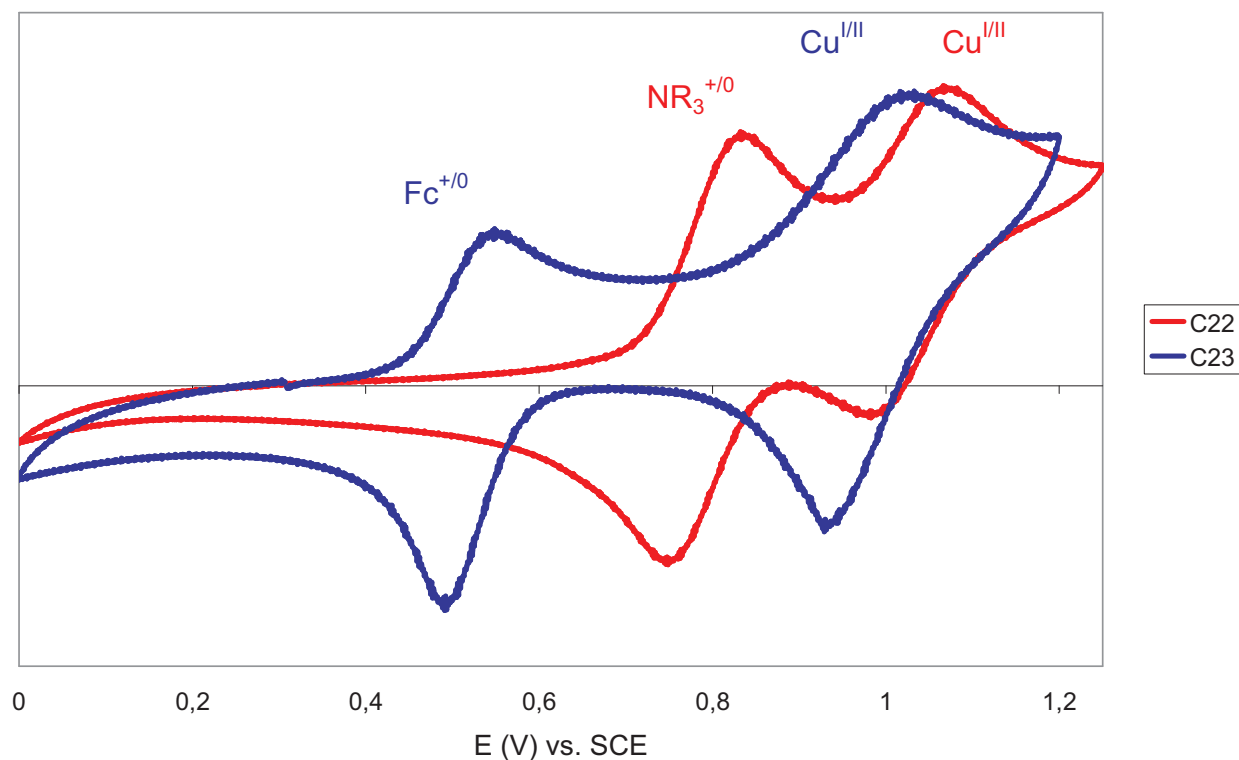
Fig. 5. 18. Cyclic voltammetries of **C22** and **C23**, recorded in dichloromethane at 100 mV/s. The intensities are normalized.

5.4.4. Thermodynamic considerations

The excited-state oxidation potential of the sensitizers can be calculated from the photophysical and electrochemical data described in the previous paragraphs. This value, together with the edge of the TiO_2 conduction band and the redox potential of the mediator, allows to estimate the Gibbs free energy for the injection and regeneration in a DSSC (represented in Fig. 5. 1). These complexes being not emissive, it was impossible to obtain the wavelength corresponding to the 00 transition from the crossing point of the absorption and emission spectra. The E_{00} was therefore calculated from the λ at which the compounds have an absorption corresponding to 10% of the maximum value. ΔG_{inj} and ΔG_{reg} were calculated using the following formulae:

$$\Delta G_{inj} = E(Cu^{II}/*Cu^{I}) - E_{CB, TiO2} \qquad \text{Eq. 5. 7}$$

$$\Delta G_{reg} = E^0(I_3^-/I^-) - E_{ox} \qquad \text{Eq. 5. 8}$$

In Eq. 5. 8, E_{ox} corresponds to the lowest potential oxidation of the complex, which is centred on copper(I) diimine for **C20** and on the donor group (respectively amine or ferrocene) for **C22** and

208

C23. As explained previously, the ΔG_{reg} will be also estimated by using the potential of the $I_2^{\bullet-}/I^-$ couple. The ΔG values were calculated by considering a dyad behaviour of **C22** and **C23**, i.e. electron injection into the TiO$_2$ from the MLCT state followed by intramolecular electron transfer from the donor and regeneration of the oxidized donor by the redox mediator.

	$\lambda_{10\%}$	E_{00} (eV)	$E(Cu^{II}/{*}Cu^I)$ (V)	ΔG_{inj} (eV)	ΔG_{reg} (eV) $[I_3^-/I^-]$	ΔG_{reg} (eV) $[I_2^{\bullet-}/I^-]$
C20	704	1.76	-0.89	-0.19	-0.77	- 0.32
C22	662	1.87	-0.85	-0.15	-0.69	-0.24
C23	714	1.73	-0.75	-0.05	-0.42	+0.03

Table 5. 4. Estimated $E(Cu^{II}/{*}Cu^I)$, ΔG_{inj} and ΔG_{reg} values for the complexes **C20**, **C22** and **C23**. $E_{CB,TiO2}$ = -0.7 V vs. SCE; $E^0(I_3^-/I^-)$ = 0.10 V vs. SCE; $E^0(I_2^{\bullet-}/I^-)$ = 0.55 V vs. SCE.

The results evidence negative ΔG values for injection and regeneration for the three complexes. However, the low ΔG_{inj} values, in particular for **C23** and **C22**, give a first hint of the fact that the electron injection into the TiO$_2$ conduction band will be rather sluggish. Therefore it is possible to anticipate that the photovoltaic properties of this series of dyes will be modest, due to both poor light harvesting and weak charge injection driving force. For **C23**, even ΔG_{reg} is quite low (slightly positive, if the the $I_2^{\bullet-}/I^-$ couple is considered), so the regeneration step too is expected to be difficult, further lowering the efficiency of the cell.

Considering these thermodynamic data, the main interest of this series of complexes will be to assess the stability of heteroleptic complexes, known to be extremely labile, in the DSSC devices. Indeed, the presence of the electrolyte and additives could lead to the complexes degradation in time.

5.5. Photovoltaic performances of the complexes C20-C23

5.5.1. Cell preparation

The photovoltaic performances of the complexes containing anchoring groups were measured in TiO$_2$-based DSSCs. The devices assembly and the measurements were performed by Dr. Yann Pellegrin (CEISAM, University of Nantes). The electrodes were prepared by screen printing using TiO$_2$ nanoparticles (Dyesol) on an FTO conducting glass support (Pilkinton TEC 8). The mesoporous titanium dioxide layer had a 12 μm thickness, and the active cell surface was 5x5 mm. A light scattering layer, of 4 μm thickness, was deposited on top of the nanoparticles. The dye was chemisorbed by dipping the electrodes, still hot, in a solution containing ~ 0.5 mM complex

dissolved in an appropriate solvent (distilled methanol, ethanol or THF). The counter-electrode was an FTO plate covered with platinum nanoparticles and the two electrodes were sealed together by means of a Surlyn® tape mask (60 or 25 μm). The electrolyte was introduced into the cavity by vacuum backfilling and the cell was then permanently sealed. This method eliminates the problem of solvent evaporation during the measurements (the device heats considerably under artificial illumination) and providing the possibility to perform ageing tests without having to add fresh electrolyte.

Two electrolytes, both prepared in acetonitrile, were used:

- A: I_2, (0.05 M), LiI (0.1 M), 2-methyl-N-methyl-N-butylimidazolium iodide (0.6 M)
- B: I_2 (0.03 M), LiI (0.1 M), guanidinium thiocyanate (0.1 M), 2-methyl-N-methyl-N-butylimidazolium iodide (0.6 M).

In electrolyte B, the guanidinium cation (Fig. 5. 19) is able to adsorb on the TiO_2 surface, lowering the Fermi level of the semiconductor and inducing a band bending and thus favouring electron injection from the excited dye. Moreover, it "passivates" the surface and prevents the approach of the oxidized form of the redox mediator, reducing thus the interfacial charge recombination with I_3^-, which has a beneficial effect on J_{sc} and the V_{oc}. The concentration of I_2, which was slightly lower than that habitually used (0.05 M), also reduces the charge recombination.
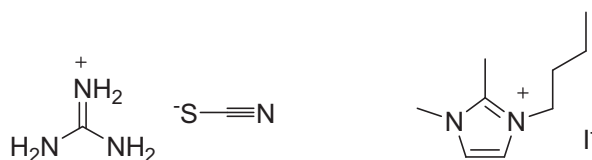
Fig. 5. 19. Structure of guanidinium thiocyanate (left) and 2-methyl-N-methyl-N-butylimidazolium iodide (right).

5.5.2. Complexes C20-C23 with 2,2'-biquinoline-4,4'-dicarboxylic acid

A series of tests was conducted on the model **C20** to investigate the influence of different parameters on the photovoltaic performances. The results are gathered in Table 5. 5. As explained previously, the protonation state of the molecules can be assessed by recording the absorption spectrum of the dying solution. By slow dissolution of the complex in methanol, the neutral monodeprotonated species was obtained. Although unexpected, this spontaneous deprotonation appeared to be a positive boon. Charged species are indeed subjected to coulombic repulsion, resulting in a lower dye coverage on the semiconductor surface. Additionally, protons are potential determining ions, namely they influence the potential of the conduction band edge, shifting the

latter away from the vacuum level. It is therefore particularly important to control the protonation state of the sensitizers since it can strongly affect the thermodynamics of the electron injection process.

Conditions	V_{oc} (mV)	J_{sc} (mA cm^{-2})	ff	η (%)
Electr. A	435	0.67	64.50	0.19
Electr. B	495	1.04	65.73	0.34
Electr. A + *t*BuPy	485	0.64	58.56	0.18
Electr. B + *t*BuPy	515	0.64	67.65	0.22
Electr. B + Surlyn 25 µm	475	2.17	68.72	0.71

Table 5. 5. Photovoltaic performances recorded with monodeprotonated **C20** in different conditions. The dye loading on TiO$_2$ film was carried out in distilled methanol.

First of all, the effect of the electrolyte was checked by comparing two different compositions (A and B) in acetonitrile. With electrolyte A, a V_{OC} of 435 mV and a J_{SC} of 0.67 mA cm^{-2} were measured. These results, leading to an overall photovoltaic conversion efficiency of 0.19%, can be explained by an inefficient electron injection, which reflects in the short circuit current density value. Indeed, the photovoltaic performances were remarkably increased using electrolyte B, with an improvement of both the V_{OC} (almost 500 mV) and the J_{SC} values (~ 1 mA/cm^2), yielding an overall conversion efficiency of 0.34%. This was attributed to a lower iodine concentration (reducing recombination at the semiconductor surface) and to the effect of guanidinium thiocyanate. The latter plays two roles: passivation of the surface and TiO$_2$ band bending. The Gibbs free energy for the electron injection is increased and the latter process is thermodynamically favoured. Consequently, the short circuit current will increase. On the other hand, the output potential will decrease, being limited by the conduction band edge potential.

The analysis of the current/potential characteristics recorded in the dark indicates that the passivation of TiO$_2$ surface is not the main factor at the origin of the impressive increase of the J_{sc}. The J/V plots recorded in the dark indicate the onset potential of the electrolyte electroactivity: a good coverage of the TiO$_2$ electrode can be monitored as higher values for this potential. As shown in Fig. 5. 20, there is a slight but significant difference between the curves obtained with the two electrolytes A and B. Accordingly, we conclude that the improvement is mainly due to the better electron injection into the TiO$_2$ conduction band upon band bending, with a small contribution of the passivation.
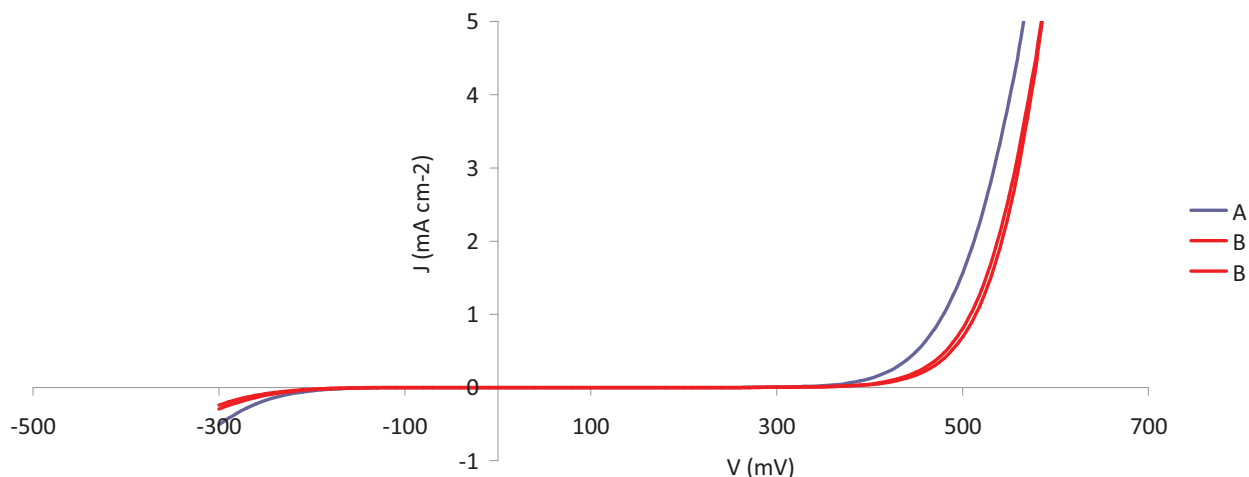
Fig. 5. 20. J/V plots recorded in the dark with electrolytes A and B.

The addition of *tert*-butylpyridine (*t*BuPy) to the electrolytes A and B increased V_{oc} but decreased J_{sc}. However, these variations roughly compensated each other and the overall photoconversion efficiencies of the cells were not improved. It is known that *t*BuPy (being an electron rich molecule) has an opposite band bending effect than lithium and guanidinium cations explaining the increase of V_{oc}.

Interestingly, the performances of the cells were improved in all cases upon ageing, even in the presence of the potentially coordinating *t*BuPy. This is not an unusual phenomenon for DSSCs and can be ascribed to a better organization of the dye molecules on the semiconductor surface. It also proves a large stability of the complexes in presence of the electrolyte. A further increase of the performances was obtained by reducing the thickness of the Surlyn® tape from 60 to 25 μm, because of a decrease in the resistance associated to the diffusion of the redox mediator from one electrode to the other. The best conditions were: electrolyte B, 2 days impregnation and ageing of the cell with 25 μm Surlyn hotmelt spacer giving an overall efficiency of 0.71%, mainly due to an impressive value of J_{sc}= 2.17 mA cm^{-2}. Overall, the performances of complex **C20** are quite low when compared to those of the ruthenium complex **N719**. This is due to both low values of J_{sc} and V_{oc} that stem from an inefficient electron injection and probably to a low dipolar moment of the copper(I) complex which bends the CB of TiO$_2$. The sluggish electron injection can be due to its low driving force and the short-lived MLCT, which decays to the ground-state extremely quickly before injecting electrons.

The complexes **C22** and **C23** were then tested, in the protonated and monodeprotonated form. The monodeprotonated species were isolated by treating the complexes with a sub-stoichiometric quantity (0.93 eq.) of triethylamine followed by purification with size exclusion

chromatography. The pink fraction was identified as the monodeprotonated complex by analysis of the electronic absorption spectrum. The green fraction represents instead the protonated complex. The performances of these two new dyads are inferior to those measured with the reference **C20**, with a η value around 0.19% for **C22** and 0.10% for **C23**. The change of the protonation state and the addition of chenodeoxycholic acid did not improve the performances.

Complex	Conditions	V_{oc} (mV)	J_{sc} (mA cm^{-2})	ff	η (%)
C22	Protonated	395	0.72	65.00	0.19
	Monodeprotonated	425	0.74	60.21	0.19
C23	Protonated	375	0.49	54.49	0.10
	Monodeprotonated	375	0.37	52.71	0.07

Table 5. 6. Photovoltaic performances recorded with **C22** and **C23**. Dye loading on TiO$_2$ in distilled methanol.

It must be considered that the values of the ΔG are only estimations as the exact energy level of the MLCT could be not determined from luminescence spectra. However, **C20** has a higher ΔG_{inj} than the other complexes **C22** and **C23**, which is likely to be the cause of the better performances of the former. **C23** has a remarkably low ΔG_{reg}, explaining that this compound affords the poorest conversion yields.

Overall, the observed performances are weak mostly because of a low short circuit current. The latter has been explained in terms of a feeble injection driving force, but it is worth mentioning that the light harvesting efficiency of the electrodes is weak too, due to the small extinction coefficients displayed by **C20**, **C22** and **C23**. Further transient absorption spectroscopic studies could be undertaken to validate these explanations, namely by determining the injection and regeneration rates.

To conclude, let us notice that these complexes are plagued by very low extinction coefficients and injection Gibbs free energy values. The latter experimental fact is due to high potential of the couple Cu$^{II/I}$ coupled to a feeble E$_{00}$ value. This could be due in part to ligand **biQuiCOOH**. The same low injection features were as a matter of fact observed for a ruthenium(II) thiocyanato complex bearing the same ligand.[69] It is therefore of a primal importance to change and carefully tune the coordination cage around the copper(I) ion, in order to design a more efficient sensitizer for TiO$_2$.

5.6. Complexes based on 6,6'-dimesityl-2,2'-bipyridine-4,4'-dicarboxylic acid: synthesis

As mentioned above, **biQuiH2** is likely to entail a rather poor injection yield, and it is therefore mandatory to fish out a better anchoring ligand to improve the properties of the copper-based dyes. Thanks to the impressive work realized on ruthenium-polypyridine dyes, a huge catalogue of diimine ligands, either bipyridine or phenanthroline, is now available.[80,81] The anchoring ligands **L17** (6,6'-dimesityl-2,2'-bipyridine-4,4'-dicarboxylic acid) and **L17'** were designed in order to have a versatile building block compatible with a wide variety of complementary ligands, since simple bis alkyl substituted bipyridine or phenanthroline could form stable heteroleptic complexes with the latter (Fig. 5. 21). In particular, the possibility to use chromogenic ligands to improve the light harvesting efficiency of the resulting complexes is very appealing, given the fact that copper(I)-diimine complexes are poor absorbers in the visible.
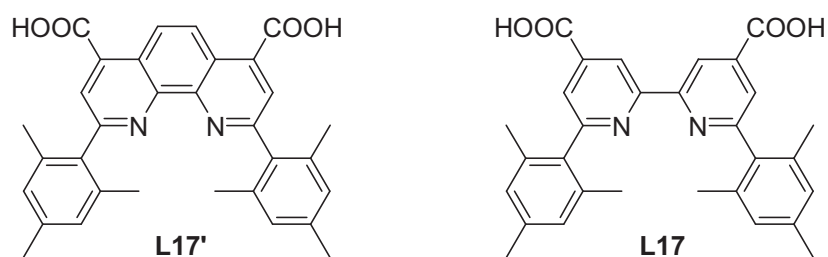
Fig. 5. 21. Structures of the anchoring ligands originally designed for the synthesis of new Cu^I-based dyes for DSSCs.

The 2,9-dimesityl-1,10-phenanthroline-4,7-dicarboxylic acid **L17'** was the natural choice stemming from our previous works on heteroleptic copper complexes, which are based on the application of the HETPHEN approach.[82] We tried to prepare **L17'** from several synthetic strategies but they all failed. An appealing one relies on the synthesis of the intermediate 2,4,7,9-tetrachloro-1,10-phenanthroline.[83,84] However, in our hands the synthesis gave very poor yields and this target molecule was put aside.

The synthesis of ligand **L17**, on the contrary, was much more successful. Compared to **L17'**, the bipyridine ligand **L17** is expected to have similar coordination properties, but the lack of the central fused aromatic ring entails some flexibility and therefore a potentially lower stability of the complex.

Three styrylbipyridine ligands were selected as complementary ligands (**L8**, **L11** and **L19** in Fig. 5. 22), bearing three different electron donating groups, with increasing donor strength: octyl-oxy, diphenylamine and diethylamine. These ligands were provided by the team of Dr. Le Bozec

and their synthesis is described in chapter 3. The role of these chromogenic ligands is twofold. First of all, the extended π-conjugation of these molecules coupled to their push-pull character is expected to dramatically enhance the absorption properties of the final complexes. Second, the donor groups may assist the photo-induced electron injection into the conduction band of TiO_2, by vectorializing the injection, and possibly decreasing the geminate charge recombination rate, by localizing the photogenerated hole away from the surface. Conceptually, it is interesting to compare the effects of these three different donating groups on the electronic properties of the associated complexes and, above all, on the performances of the resulting DSSCs.

Ligand **L11** reminds the extended conjugation ligand that was used for the synthesis of the heteroleptic ruthenium(II) complex **K-19** (Fig. 5. 3).[24] This sensitizer had both an increased efficiency and an increased stability with respect to the bench-marking **N719**: the hydrophobic alkyl chains prevented the iodide/triiodide couple from approaching the semiconductor surface and the interfacial charge recombination was considerably suppressed.

5.6.1. Synthesis of methyl 6,6'-dimesityl-2,2'-bipyridine-4,4'-dicarboxylate (L17) and 6,6'-dimesityl-4,4'-dicarboxylic acid (L18)

Two possible synthetic routes that lead to the synthesis of the ligand **L17** are shown in the retrosynthetic scheme below (Scheme 5. 4).
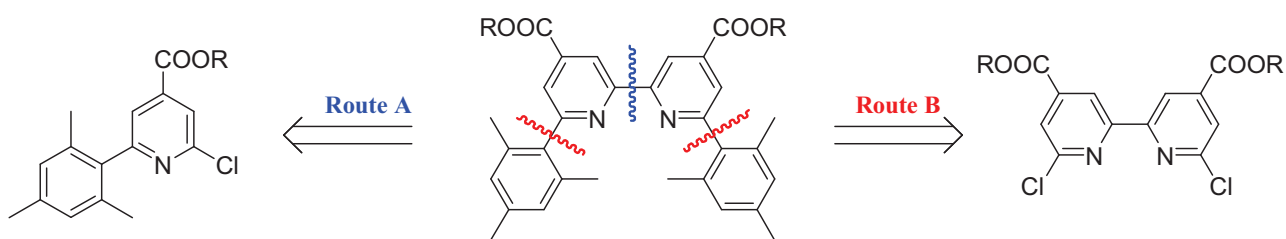
Scheme 5. 4. Retrosynthetic paths to obtain **L17**.

Route A was the first was attempted strategy, consisting in the synthesis of an asymmetric pyridine building block bearing a chloro substituent (Scheme 5.5). The asymmetric intermediate **30** was obtained by Suzuki cross-coupling from 4-carboxy-2,6-dichloropyridine ethyl ester and mesitylboronic acid. The synthesis of **L17** was performed by Stille coupling between the aryl chloride **30** and the corresponding *in situ* generated organotin derivative (Scheme 5. 5). Compound **30** was reacted with 0.5 equivalents of Sn_2Bu_6 in presence of tetrakis (triphenylphosphine)palladium(0) in dry N,N-dimethylformamide. The same catalytic system was

then used for the Stille cross-coupling with the complementary aryl chloride. Despite the encouraging results of the crude product, as judged from the ^{1}H-NMR spectrum, only a small quantity of the pure compound was isolated after column chromatography (12%), and this strategy was abandoned.
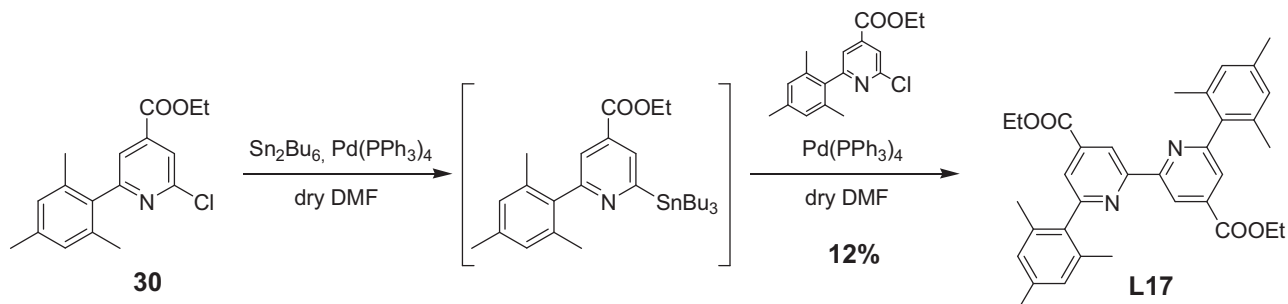
Scheme 5. 5. Synthesis of the ligand **L17** by Stille cross-coupling reaction.

Route B is based on the already preformed bis-chloro-bipyridine ligand previously reported in the literature (Scheme 5.6).[23] The key precursor methyl 6,6'-dichloro-2,2'-bipyridine-4,4'-dicarboxylate was synthesized in three steps starting from 2,2'-bipyridine-4,4'-dicarboxylic acid.
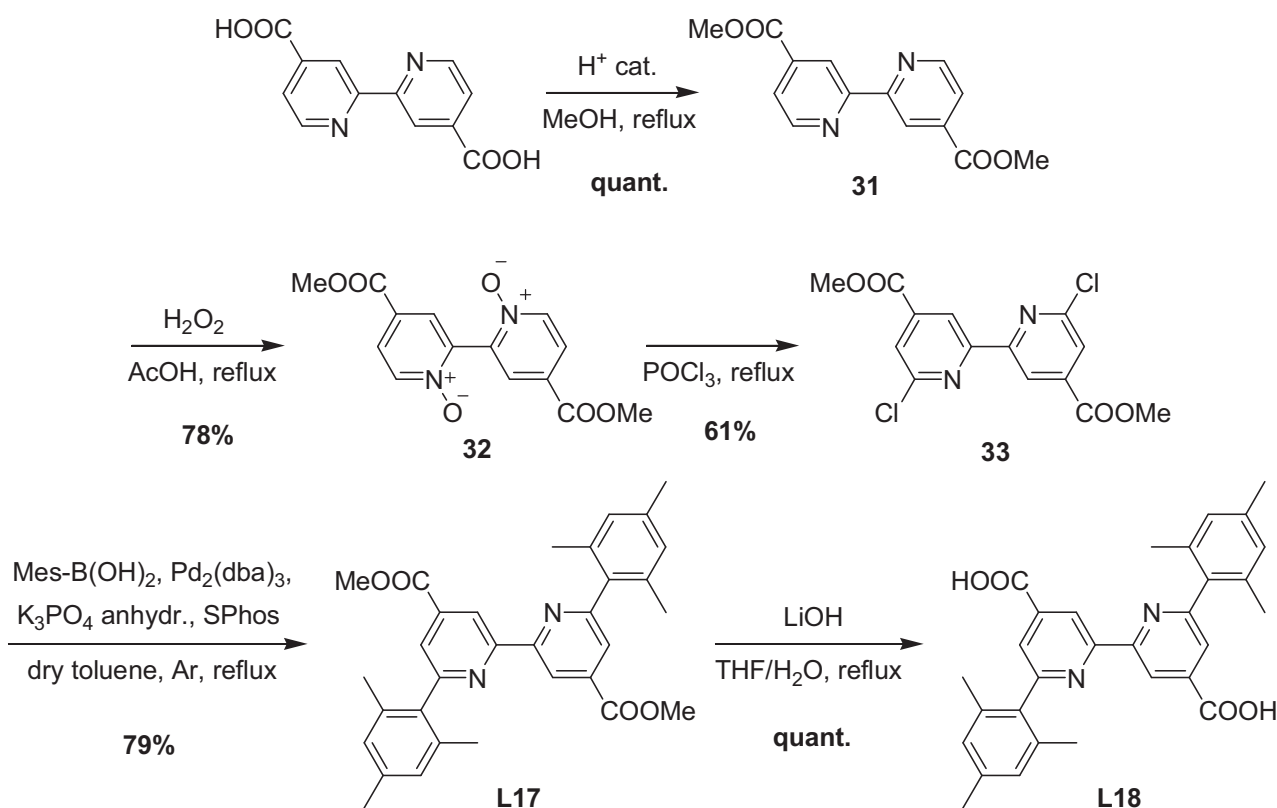
Scheme 5. 6. Synthesis of the ligands **L17** and **L18**.

First, an esterification of the carboxylic groups by methanol was performed and then the pyridine rings were activated as N-oxides by oxidation with hydrogen peroxide in acetic acid (**32**) in order to be subsequently chlorinated by $POCl_3$. The electron-withdrawing character of pyridine increases the reactivity of the chloro substituent which makes it a suitable leaving group in Suzuki cross-coupling reaction to afford ligand **L17** in a good yield. The cross-coupling reaction between **33** and the mesitylboronic acid must be carried out under anhydrous conditions, as the presence of hydroxyl ions is incompatible with the ester functions and their hydrolysis makes the purification and characterization far more difficult. The selected protocol used $Pd_2(dba)_3$ as a catalyst, in combination with the phosphine ligand SPhos, and anhydrous K_3PO_4 in dry toluene.[85] The product was obtained in 79% yield after purification, consisting in washing with methanol followed by a column chromatography on silica gel prepared and eluted in dichloromethane. The hydrolysis of the ester functions was very straightforward and was performed in basic conditions by refluxing a solution of **L17** in THF/H_2O in presence of 20 equivalents of lithium hydroxide. **L18** was obtained by precipitation from an acidic aqueous solution.

5.6.2. Synthesis of complexes C24-C27

With an anchoring ligand possessing strongly hindering groups in α position of the nitrogen atoms in hand, a wide range of tetrahedral copper(I) complexes are available. The reference complex **C24** was also synthesized in order to assess the influence of the extended conjugation on the photovoltaic performances.
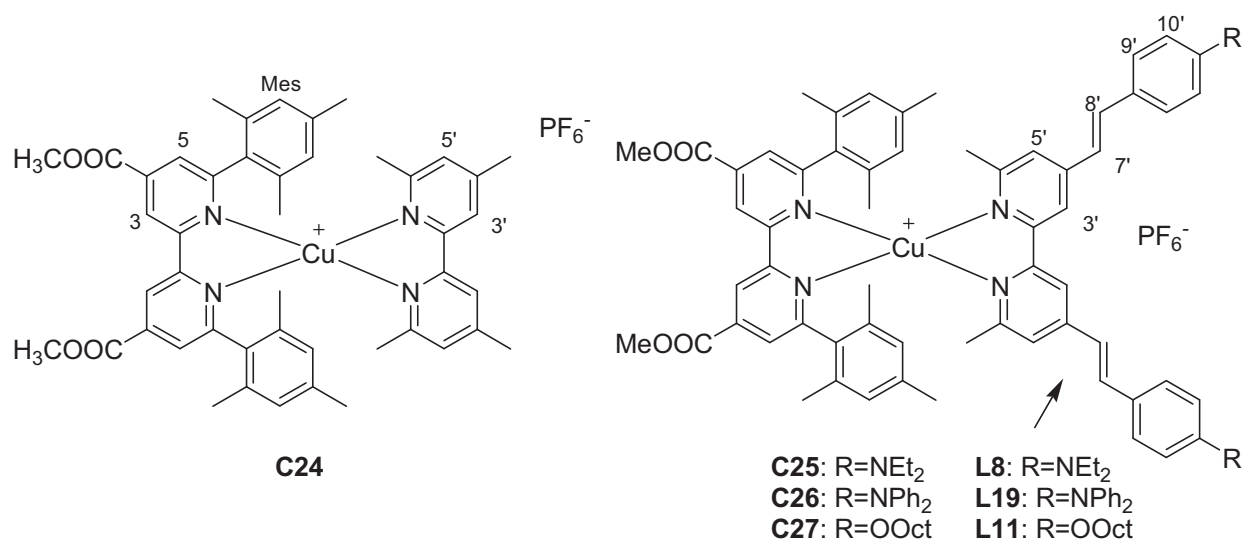
Fig. 5. 22. Structure of the ligands **L8**, **L11** and **L19** and of the complexes **C24**-**C27**.

217

The synthesis of the heteroleptic complexes was first attempted starting from the anchoring ligand **L18** having free carboxylic acid groups, but the crude product was a mixture of compounds which were not separable by size exclusion chromatography (BioBeads X1, swollen in THF). The peak of the expected complex was, however, found in the mass spectrum of the crude product (ESI+). This behaviour can be ascribed to the chelating properties of the free carboxylic acids, that can interact with the metal ion to form many different complexes already in the first synthetic step (formation of the 1:1 adduct between the copper and the hindered ligand). The synthesis of the complex was then attempted with ligand **L17**, bearing the ester instead of the free carboxylic acids.

The synthesis followed the classical two-step procedure. Starting with the preparation of the $[Cu(\mathbf{L17})(CH_3CN)_2]^+$ adduct in dry degassed dichloromethane, a solution containing a slight default of 6,6'-dimethyl-2,2'-bipyridine ligand was added, and the solution was stirred under inert atmosphere at room temperature. In comparison to $[Cu(\mathbf{L1})(CH_3CN)_2]^+$, $[Cu(\mathbf{L17})(CH_3CN)_2]^+$ has an extended absorption in the visible (resulting in a dark orange solution instead of yellow), probably stemming from the acceptor properties of **L17** that lower the energy of the electronic transition inducing a bathochromic shift of the corresponding band in the UV-Visible spectrum.

All the four complexes (**C24-C27**) were obtained in good yields (77-97%) after purification by column chromatography on silica gel (CH_2Cl_2: $CH_3OH = 98: 2$). The ^{1}H-NMR spectra, recorded in acetone-d_6 ($CDCl_3$ gives larger and less resolved signals) show a superposition of the signals of the two ligands, which are shifted with respect to the free ligands (Fig. 5. 23). The signals of ligand **L17** show very well the shielding of the mesityl protons after coordination of the Cu^I ion, together with an important downfield shift of the bipyridine protons.
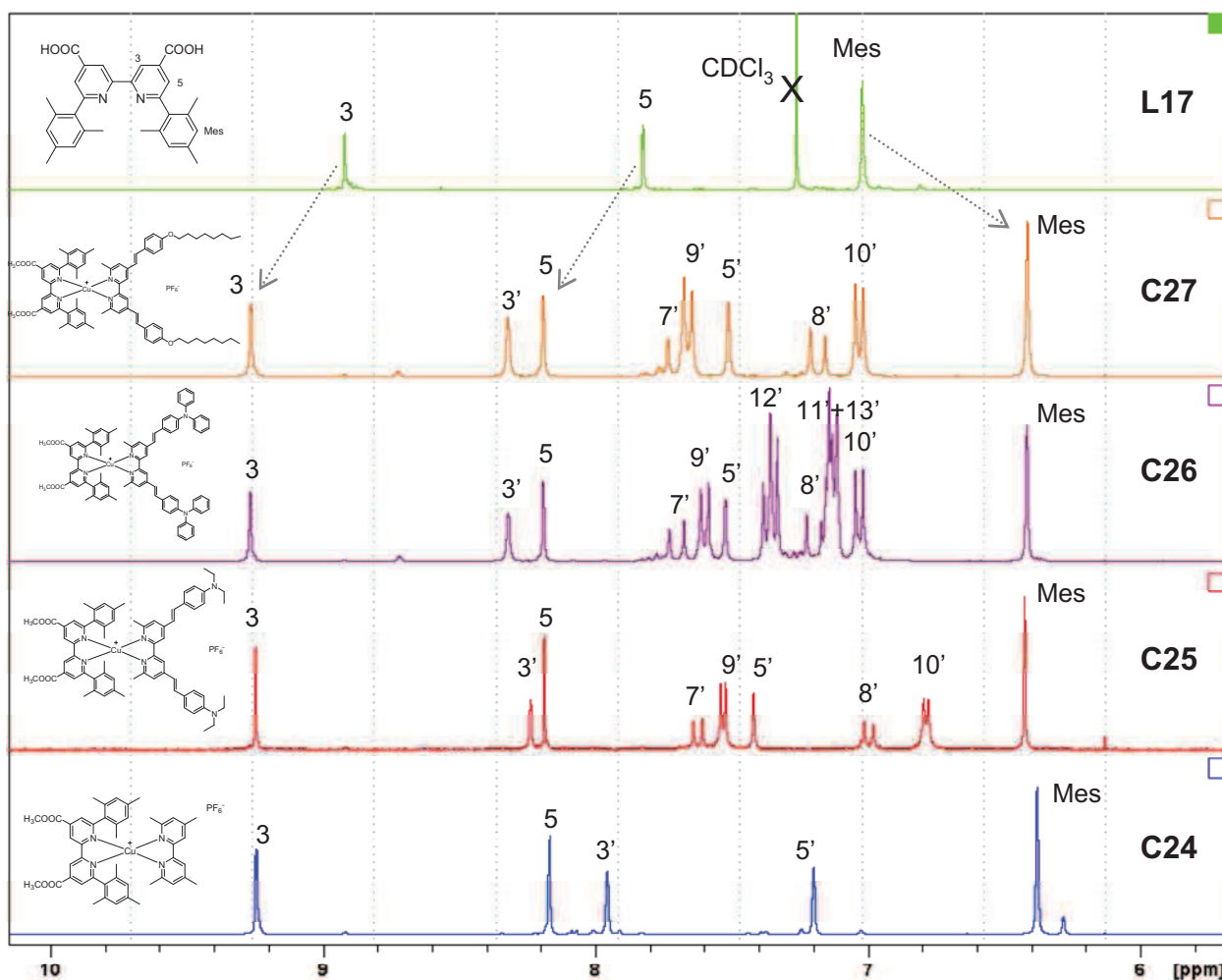
Fig. 5. 23. ^{1}H-NMR spectra of complexes **C24-C27** (acetone-d$_6$) and ligand **L17** (CDCl$_3$). For H numbering please refer to Fig. 5. 22 (in complex **C26** H$^{11'}$, H$^{12'}$ and H$^{13'}$ are the phenyl protons).

5.6.3. Synthesis of complexes C24'-C27'

The hydrolysis of the ester groups was performed at room temperature in basic conditions (LiOH) using THF/H$_2$O as a solvent. The product formation was followed by TLC on silica gel. The carboxylate groups stick to the solid phase and the hydrolysed complex has a R$_f \approx 0$. Once the reaction was complete, the solvents were removed and the crude reaction mixture was dissolved in methanol. A slight excess trifluoroacetic acid was added (dissolved in methanol) to protonate the two carboxylic groups. The product became extremely soluble in dichloromethane. The complexes were finally purified by size exclusion chromatography on BioBeads, using THF as the eluent.

The purity of the compounds was checked by ^{1}H-NMR and mass spectrometry. The NMR signals, as usual, undergo a marked broadening and it was very difficult to obtain well-resolved signals. The presence of low intensity signals in the ^{1}H NMR spectra and in the mass spectra, however, evidenced the presence of the monoester and diester complexes. The attempts to eliminate

these complexes by adding a large excess of LiOH or increasing the reaction time (one night) always failed, since this led to complete degradation of the complexes even under inert atmosphere. Accordingly, the complexes were studied with a small contamination with partially hydrolysed complexes, but they will most certainly not bind to the TiO$_2$ surface and therefore not affect the overall photovoltaic study.

5.7. Characterizations of complexes based on 6,6'-dimesityl-2,2'-bipyridine-4,4'-dicarboxylic acid

5.7.1. X-Ray structure of L17

X-Ray quality crystals of **L17** were grown from a chloroform solution of the ligand by slow evaporation of the solvent.

The molecule crystallizes in a triclinic crystal lattice (α = 73.58º; β = 78.68º; γ = 84.38º; a = 7.3774 Å; b = 9.1258 Å; c = 10.7977 Å; P1 space group). The unit cell contains one ligand molecule.

The bipyridine is in *trans*-coplanar conformation, with the ester groups lying in the same plane as the two heterocycles. The mesityl groups are twisted with respect to the molecular plane, with an angle of about 62º (dihedral angle between the least squares plane of the mesityl ring and of the bipyridine). In the crystal all the bipyridines lie on parallel planes, as the mesityl rings. As expected, the COO groups and the pyridine rings are coplanar, insuring a significant electronic communication between the ester and the pyridine (and, one may anticipate, between the complex and TiO$_2$).
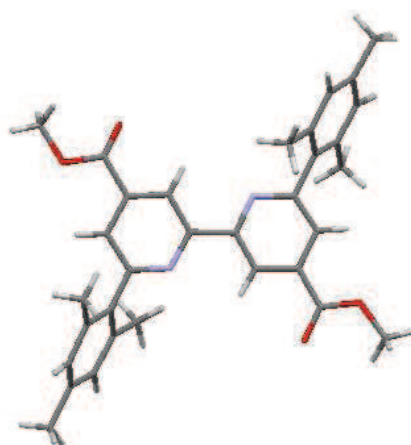
Fig. 5. 24. X-Ray structure of the ligand **L17**. C: grey; H: white; N: light blue; O: red.

5.7.2. X-Ray structure of C24

Quite thick, needle-like X-Ray quality crystals of **C24** were grown by diffusion of diethyl ether vapours in a chloroform solution of the complex.

The complex crystallizes in a monoclinic crystal lattice ($\alpha = 90°$; $\beta = 94.78°$; $\gamma = 90°$; $a = 23.952$ Å; $b = 12.15$ Å; $c = 16.417$ Å; cell volume = 4761.01 Å^3; P2$_1$/n space group). The unit cell contains four molecules.

The copper(I) atom is surrounded by the four coordinating nitrogens, forming a distorted pyramid. While **L17** forms two nearly equivalent bonds (Cu-N1 = 2.034 Å and Cu-N2 = 2.039 Å), the 4,4',6,6'-tetramethyl-2,2'-bipyridine ligand is involved in a less symmetrical chelation and forms a longer and a shorter bond (Cu-N3 = 2.062 Å and Cu-N4 = 1.995 Å). The bite angles are 80.2° (N1-Cu-N2) and 83.1° (N3-Cu-N4). The bipyridine ligands are not completely planar, with the two pyridyl rings forming angles of 9.3° (tetramethylbipyridine) and 13.6° (**L17**). In **L17**, the two ester functions are slightly twisted with respect to the planes of the respective pyridyl rings, unlike what was found for the free **L17**.

The most interesting feature is probably the distortion of **L17** structure. The two mesityl rings form angles of 75.3° (A) and 75.8° (B) with the respective pyridyl rings. In an undistorted molecule, we would expect an angle between the two ring planes approaching 60°, while in this case the angle between the mean square planes (calculated from the average of the 6 ring carbons) is only 31°. The aromatic groups tighten to staple one of the rings of the opposite tetramethylpyridine ligand (the pyridine containing N4), owing to some sort of π-stacking interactions. The latter forms an angle of 22.0° with ring B and 9.7° with ring A. This "pincer" effect can be remarked also in the two N-Cu-C$_{Mesityl}$ angles, that are around 115°, and is likely to be the origin of the distorted chelation of the tetramethylbipyridine ligand, pulling one of the pyridyl rings towards the Cu^I atom and pushing away the other causing the shortening of the Cu-N4 bond and the lengthening of Cu-N3 (which belongs to the pyridine "pushed away" from the copper(I) atom).
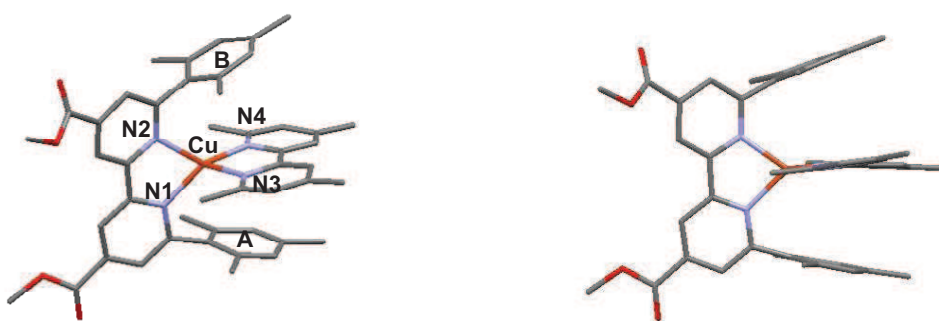
Fig. 5. 25. Structure of **C24** with atom numbering (left) and "pincer" effect (right). C: grey; H: white; N: light blue; O: red; Cu: orange.

221

5.7.3. Absorption spectroscopy

The UV-Visible spectra of the four complexes are shown in Fig. 5. 26, and the maximum absorption wavelengths and the molar coefficients are gathered in Table 5. 7. The reference complex **C24** displays a broad MLCT band but as weak in intensity as the usual copper diimine complexes. Conversely, the complexes **C25-C27** show a broad MLCT (500-600 nm) of relatively high intensity ($\varepsilon > 10^4$ $M^{-1}cm^{-1}$) for copper(I) diimine complexes. Let us first notice that the wavelength at maximum absorbance of the MLCT is strongly red-shifted (by 60 nm at least) relative to bisphenanthroline-based complexes (ca. 460 nm). This feature may be grounded on the extended electronic delocalization provided by the styryl substituents and the electron withdrawing ability of the ester groups, which are well conjugated with the bipyridine core as proven by the X-Ray structure. Moreover, the flexibility of the coordination sphere provided by bipyridine is enhanced compared to phenanthroline: a more important flattening distortion in the excited state is expected, thus stabilizing the formal Cu^{II} nucleus and subsequently decreasing the energy of the MLCT state.
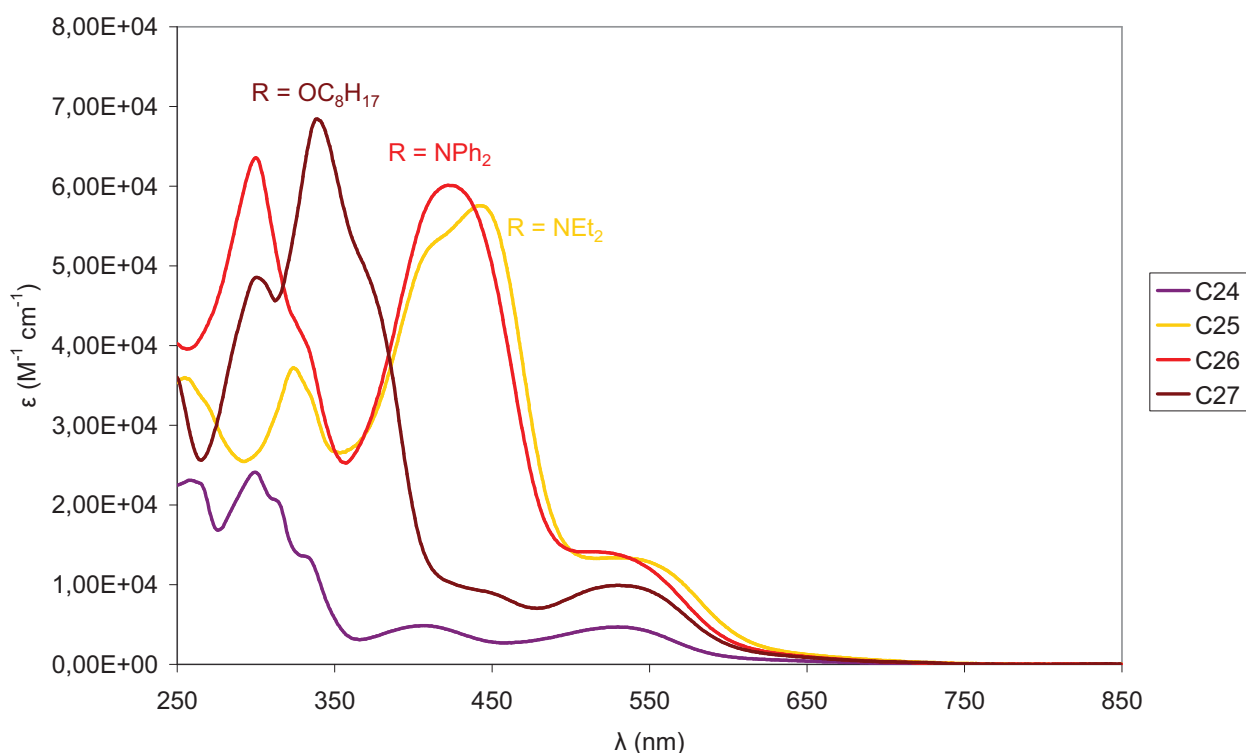
Fig. 5. 26. UV-Vis spectra of the complexes **C24-C27** recorded in dichloromethane.

222

	C24	C25	C26	C27
	Absorption: λ (nm) [ε (M^{-1}cm^{-1})]			
	530 [$4.7 \cdot 10^3$]	528 [$1.3 \cdot 10^4$]	510^a [$1.4 \cdot 10^4$]	532 [$9.8 \cdot 10^3$]
	407 [$4.9 \cdot 10^3$]	442 [$5.8 \cdot 10^4$]	423 [$6.0 \cdot 10^4$]	
	299 [$2.4 \cdot 10^4$]	324 [$3.7 \cdot 10^4$]	300 [$6.4 \cdot 10^4$]	340 [$6.7 \cdot 10^4$]
	258 [$2.3 \cdot 10^4$]	255 [$3.5 \cdot 10^4$]		300 [$4.7 \cdot 10^4$]
	Emission: λ_{em} (nm) [λ_{exc} (nm)]			
	− [530]	− [528]	620 (low) [510]	− [532]
	− [406]	617 [442]	620 [423]	485 [370]

Table 5. 7. Absorption and emission data for complexes **C24**-**C27**, recorded in dichloromethane. ^{a} Shoulder

The spectra of the complexes **C25**-**C27** show additional bands in the visible due to the intense absorption of the styrylbipyridine ligands. As already noticed for complexes bearing the same kind of ligands in chapter 3, the strong ligand-centred bands are due to intra-ligand charge transfer transitions, and are red-shifted upon coordination to copper(I). In the free ligand spectrum they are situated in the near UV with a tail in the visible, but upon coordination to the metallic ion they shift to longer wavelengths, as the electron density on the bipyridine is decreased, conferring an intense red colour to the two complexes. The ligand centred transition in **C27** is blue-shifted with respect to the amine bearing ligands, probably because of the weaker electron donor strength of octyloxy compared to phenyl- or alkyl-amines. Complexes **C25** and **C26** exhibit very similar spectroscopic features corresponding to intense visible bands around 420-440 nm nearly superimposable, except for **C26** which features a slight hypsochromic shift. The intense band at 300 nm, absent in **C25** is probably centred on the phenyl groups of the diphenylamine substituent.

The absorption spectra of **C24'**-**C27'** were recorded in order to have a qualitative idea of the band displacement after the hydrolysis, but since the complexes are a mixture of compounds no quantitative data can be obtained. In general, the complexes undergo an hypsochromic shift after hydrolysis, but they **C24'** and **C27'** continue to harvest photons until 550 nm and **C25'** and **C26'** until 600 nm. The shape of the spectra are similar to those for the ester complexes **C24**-**C27**.

5.7.4. Emission

The emission properties of complexes **C24**-**C27** were also investigated in dichloromethane. The model complex **C24** was not emissive neither upon excitation at 530 nor at 407 nm, at room temperature. This is not very surprising because the increased possibility of flattening in the excited state can result in efficient non radiative relaxation deactivation to the ground state.

Complexes **C25**, **C26** and **C27** showed a very particular behaviour. They are completely not emissive when excited in the low energy band MLCT band, but luminescent when excited in the ILCT band located at higher energy. Complex **C27** even emits at a shorter wavelength than the MLCT band, if excited in the UV (Table 5. 7).

This phenomenon is quite unexpected, as the higher excited state is supposed to rapidly relax to the lower energy excited state according to Kasha's rule.[86] Dual emission is an exceptionally rare property in molecular systems, and is difficult to be unambiguously rationalized. First of all, the possibility of contamination of the complex solutions by emissive species had to be assessed. Several experimental facts have to be considered, to support the assumption that the recorded emission signals are indeed generated by the complex itself.

- contamination by the highly fluorescent free ligands can be excluded because the styrylbipyridine ligands were used in default during the synthesis and the ^{1}H NMR spectra do not show the characteristic signals of these species, whose signals cannot be missed as they are shielded relative to those in the complexes. Moreover, the emission band from the free ligands occurs at higher energies than those recorded in our case;
- the excitation spectrum recorded at the emission wavelength features the ILCT band in the absorption spectrum of the complex but not the MLCT;

Another factor that has to be assessed in order to support the hypothesis of a dual emission is the possible contamination by the homoleptic complex. This can be checked by preparing the homoleptic complex (ex. [Cu(**L8**)$_2$]PF$_6$ compared to **C25**) and recording the luminescence spectrum. Indeed, the emission of the homoleptic species ([Cu(**L8**)$_2$]PF$_6$) occurs at the same energy as that of **C25**, but the high intensity of the emission band suggests an important degree of contamination by the homoleptic species, which was not evidenced by the proton NMR spectrum. However, before giving any final conclusion, complementary data about the emission quantum yields have to be collected for both compounds (which are under way).

Furthermore, new measurements will be performed in order to check the stability of the ligands and complexes after irradiation, to exclude degradation during the analyses (for example isomerisation of the double bond).
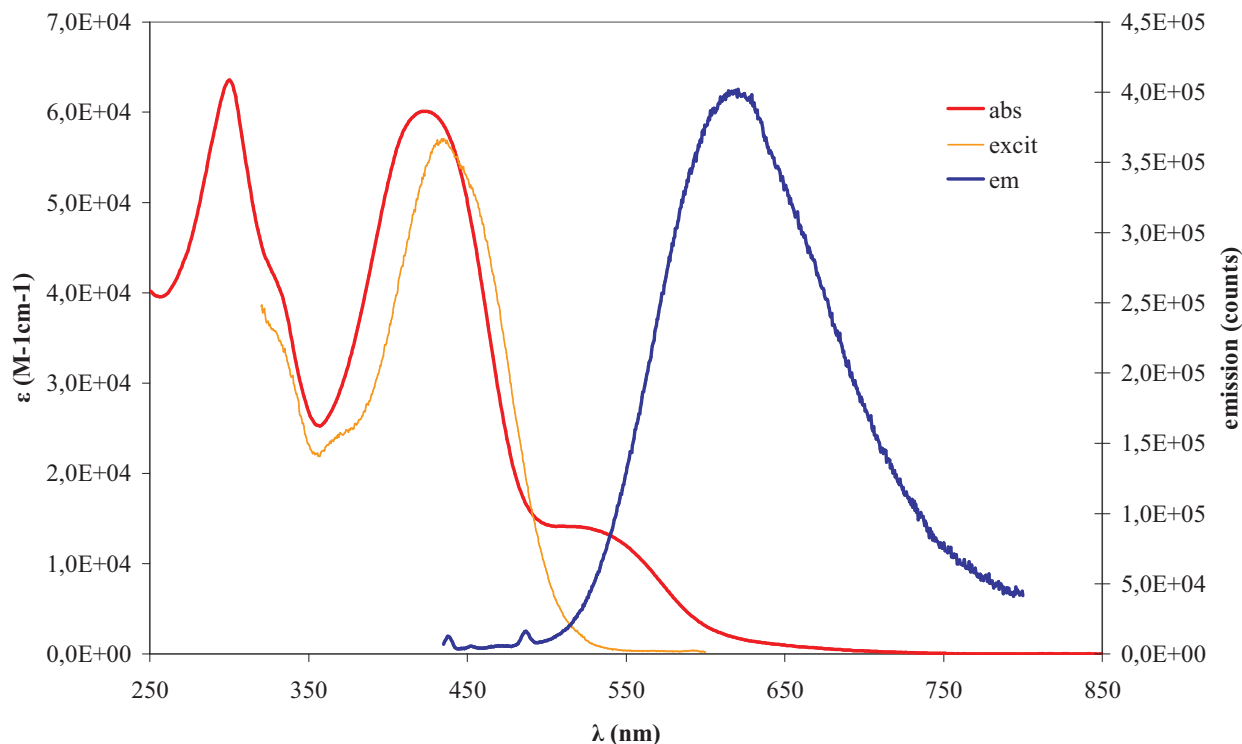
Fig. 5. 27. Absorption, emission and excitation spectra (λ_{em} = 620 nm) of **C26** recorded in dichloromethane.

This "dual" emission phenomenon is very rare, and can only be found in a few examples in literature. Among the coordination compounds that present such a behaviour, it seems particularly interesting to observe:

- heteroleptic Ru(II) complexes with MLCT transitions to different ligands, which bring to excited states which are separated by an energetic barrier that prevents interconversion between the two states; [87,88]

- Ru(II) and Cu(I) complexes with emissive states characterized by different geometrical structures, as MLCT and intra-ligand states; [89,90]

- Re(I) complexes with dual $^1\pi$-π^* and $^3\pi$-π^* ligand-centred emission, where the former is observed because of the high decay rates of the free ligands and the latter is obtained after an intersystem crossing due to the heavy atom effect. [91]

In this case, it seems quite likely that the ILCT state has a very rapid emissive decay, that could compete with the relaxation to the lower energy MLCT excited state. Indeed, in the complexes described in chapter 3 we already observed a very intense but short-lived luminescence due to the decay of the ligand-centred excited state, while the long-lived triplet MLCT relaxed following a non

radiative pathway. Time-resolved spectroscopy and quantum mechanical calculations will be used to shed more light on the peculiar emission behaviour observed of these new complexes.

5.7.5. Electrochemistry

The electrochemical properties of the compounds were recorded in dry degassed dichloromethane, using a platinum disc as working electrode. The values are reported versus SCE reference electrode and are gathered in Table 5. 8.

	$E_{1/2}$ ($Cu^{II/I}$) [ΔE (mV)]	$E_{1/2}$ ($NR_3^{+/0}$) [ΔE (mV)]
C24	0.94 [96]	—
C25	1.08[a] [-]	0.80[a] [-]
C26	1.03[b] [-]	0.95[b] [-]
C27	0.91 [96]	—

Table 5. 8. Oxidation potentials of the complexes **C24-C27**, recorded in dichloromethane. WE: Pt disc; RE: SCE; CE: Pt foil; supporting electrolyte: TBAPF$_6$ 0.1 M. [a] E_a, irreversible wave. [b] As the two waves merge, the square wave voltammetry value is given.

All the complexes show a copper(I)-centred oxidation, around 0.9-1.1 V vs. SCE, and additional oxidation waves for amine bearing complexes. The cyclic-voltammogram of the amine-containing complexes **C25** and **C26** displays two anodic waves. This first one is assigned to the removal of an electron from the amine substituents and the second one to the copper(I) cation. The rather high potential of the latter relative to that in **C24**, despite the stabilizing electron donating effect of the amine substituents, is probably due to electrostatic stringent interactions between copper(II) and the electrogenerated hole on the amine substituents. Only one broad oxidation wave was monitored for **C26**; however, square wave voltammogram clearly featured two distinct oxidation peaks, indicating that two anodic processes were occurring. On the other hand, the oxidation process is slightly less anodic for **C27** than for **C24**, a feature tentatively assigned to the electron donating effect of the alkoxy groups, which are not oxidized prior to the copper centre. The oxidation potential of an aromatic amine being more positive than the one of alkylamine, both arylamine and copper(I) oxidation steps occur at close potentials, which cannot be separated by cyclic voltammetry in our conditions. The different nature of the amine group (aliphatic in ligand **L8** and aromatic in ligand **L19**) has an influence on the reversibility of the oxidation wave, which is irreversible in the former case and reversible in the latter due to the efficient degradation pathways that can be observed upon oxidation of aliphatic amines.[92] No reduction processes were observed

for complexes **C24-C27** until a potential of -1.5 V vs. SCE in our conditions. This is not surprising since the first ligand based reduction is reported to occur below -1.6 V vs. SCE.[64]

5.7.6. Thermodynamic considerations

As done for the previous series of complexes, the Gibbs free energy values for the complexes **C24'-C27'** are now calculated. The injection occurs from the MLCT state of the copper(I) complex, so the ΔG_{inj} is calculated as the difference between $E_{CB,TiO2}$ and $E(Cu^{II/I})$ according to Fig. 5. 1. Since the electrochemical data for **C24'-C27'** were not recorded (the products were not pure), the thermodynamic considerations reported below are based on the oxidation potential of the corresponding ester complexes. The regeneration free energy is calculated using the less anodic oxidation potential (oxidation of the copper(I) diimine core for **C24** and **C27** and of the amines for **C25** and **C26**, Eq. 5. 6).

	$\lambda_{10\%}$	E_{00}	$E(Cu^{II}/{}^*Cu^{I})$	ΔG_{inj}	$\Delta G_{reg}\,[I_3^-/I^-]$	$\Delta G_{reg}\,[I_2^{\bullet-}/I^-]$
C24'	643	1.93	-0.99	-0.29	-0.84	-0.39
C25'	647	1.92	-0.84	-0.14	-0.70	-0.25
C26'	628	1.97	-0.94	-0.24	-0.85	-0.40
C27'	643	1.93	-1.02	-0.32	-0.81	-0.36

Table 5. 9. Estimated $E(Cu^{II}/{}^*Cu^{I})$, ΔG_{inj} and ΔG_{reg} values for the complexes **C24'-C27'**. $E_{CB,TiO2}$ = -0.7 V vs. SCE; $E^0(I_3^-/I^-)$ = 0.10 V vs. SCE; $E^0(I_2^{\bullet-}/I^-)$ = 0.55 V vs. SCE.

The calculated values indicate a high regeneration free energy for all the complexes, slightly less favoured for **C25'** because of the low oxidation potential of the aliphatic amines. Even if the $I_2^{\bullet-}/I^-$ couple is considered, these values remain quite high. Concerning the ΔG_{inj}, however, important differences are observed within the series. **C27'** and **C24'** display the highest injection driving force, followed by the two complexes containing the donor amine groups (**C25'** and **C26'**). This can be explained by a higher oxidation potential of the copper(I) core in the latter two dyes. For **C25'**, the lower energy content of the MLCT band (compared to **C26'**) also contributes to anodically shift the excited-state redox potential, making this sensitizer the worst photoreductant of the series. This complex displays the worst ΔG_{inj} and ΔG_{reg} values.

.

5.8. Photovoltaic properties of complexes C24'-C27' with 6,6'-dimesityl-2,2'-bipyridine-4,4'-dicarboxylic acid

Preliminary photovoltaic measurements were undertaken with the complexes **C24'-C27'** using the same procedure as that described for the previous series **C20-C23**. The complexes were not completely pure as they contain traces of complexes having not fully hydrolysed carboxylic ester groups. However, these measurements probably give an estimation of the potentials of these complexes in DSSCs with probably underestimated power photo-conversion efficiencies. Besides, the performances of the complexes were not optimized since these measurements were carried out once just before the writing of the thesis. The tests were conducted using electrolyte A (described in paragraph 5.5.1) and the complexes were used in the fully protonated form. The photovoltaic characteristics of the solar cells recording under AM1.5 are collected in Table 5. 10.

	Conditions	V_{oc} (mV)	J_{sc} (mA cm^{-2})	ff	η (%)
C24'	**Electr. A**	515	2.89	71.63	1.07
	+ CDCA	535	4.60	71.83	1.77
	+ *t*BuPy	565	0.93	66.50	0.35
C25'	**Electr. A**	515	1.27	68.94	0.45
	+ CDCA	495	2.19	67.86	0.74
C26'	**Electr. A**	585	3.11	68.53	1.25
	+ CDCA	635	2.75	70.90	1.24
	+ *t*BuPy	665	1.93	72.10	0.93
C27'	**Electr. A**	585	5.25	74.07	2.27
	CDCA	635	5.15	72.43	2.37

Table 5. 10. Photovoltaic performances obtained with **C24'-C27'** in different conditions. The adsorption was carried out in MeOH: THF = 1: 1. CDCA (0.1 M in ethanol) was spin coated on the cells after the adsorption of the dyes. *t*BuPy was present in the electrolyte at a 0.5 M concentration.

The tests conducted in the absence of additives in the electrolyte evidenced that **C27'** gives much better photovoltaic performances than the other complexes, owing to both better V_{oc} and J_{sc}. In particular, a significant J_{sc} value superior to 5 mA cm^{-2} could be attained, together with a 585 mV V_{oc} value leading to an overall efficiency of 2.27%, which is quite satisfactory for a copper-based dye.[60,62,63]

The IPCE values match the trend deduced from the photocurrent-photovoltage measurements. It is particularly interesting to compare the IPCE with the LHE (light harvesting

efficiency) obtained from the electronic spectra of the dyes adsorbed onto the semiconductor), the curves are shown in Fig. 5. 28. There is a striking difference between the behaviour of **C24'** and **C27'** (whose visible absorption is due to MLCT transitions) and **C25'** and **C26'** (that have a strong ILCT component in the visible absorption bands). For the former complexes, the IPCE curves match quite well the profile of the LHE spectra, indicating that the band is active in the photoproduction of electricity. Conversely, for the latter two dyes, the blue part of the visible absorption band seems to be less effective for TiO_2 sensitization. This is visible in the curves of **C26'**, and supports the hypothesis that the ILCT and MLCT states are strongly decoupled. The very low IPCE values obtained for **C25'** are caused by the low driving forces for electron injection and dye regeneration (see paragraph 5.7.6).
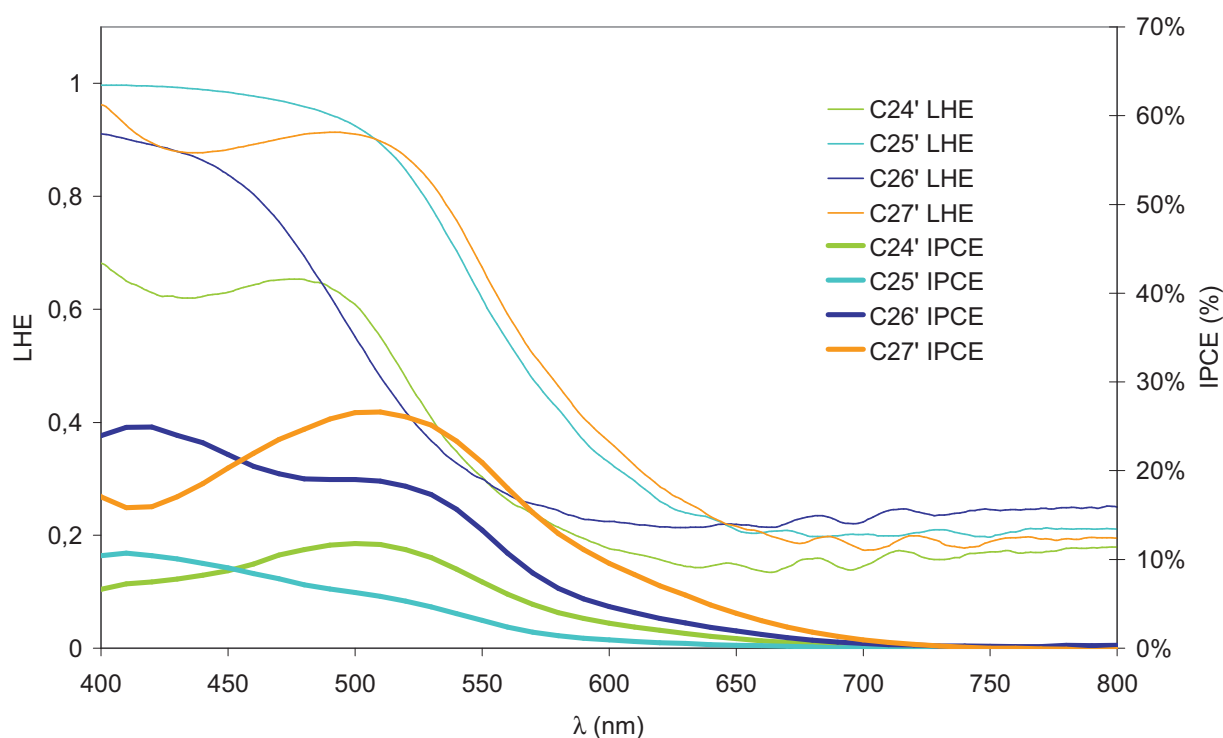
Fig. 5. 28. LHE and IPCE curves for the complexes **C24'-C27'**. For the LHE measurements, the complexes are adsorbed on a 4 μm TiO_2 electrode. The results are then normalized for an electrode thickness of 12 μm and the LHE is calculated by means of the following formula: LHE = $1-10^{-A}$ (A: absorbance of the complex on the 12 μm electrode).

If we analyse more carefully the J_{SC} data, it is possible to go deeper into the behaviour of the different sensitizers. The short circuit current density values obtained in the absence of additives decrease in the following order:

C27' > C26' ~ C24' > C25'

The best performance of **C27'** is due to high light harvesting efficiency ($\varepsilon \sim 10^4$ M^{-1} cm^{-1} at the maximum of the absorption bands) along with to the high ΔG_{inj}. Conversely, the two complexes exhibiting the most impressive absorption properties (**C25'** and **C26'**) generate relatively low current densities under illumination. This fact is certainly partially due to the weak injection driving force, suggesting that the absorbed light is to a certain extent "wasted". The J_{SC} value obtained for **C24'** takes into account two opposite effects: the modest light harvesting efficiency (due to the low molar extinction coefficient of the complex) but which is somehow compensated by a quite singificant injection driving force.

The V_{OC} data are mainly controlled by the recombination reaction between the electrons in the TiO$_2$ conduction band and the redox mediator, occurring at the naked semiconductor surface. **C24'** is the smallest complex of the series, and for this reason the less efficient in shielding the surface from the electrolyte approach. This aspect is well supported by the J/V plots recorded in the absence of light (Fig. 5. 29), indicating that the onset of the electrolyte electroactivity on the sensitized semiconductor surface is at lower potentials than for the other dyes. Complexes **C25'**-**C27'**, which are bulkier, provide a better protection of the TiO$_2$ surface as shown by similar curves in Fig. 5. 29. The poor V_{OC} value obtained for **C25'** still cannot be explained in the light of these considerations. All these compounds being cationic, moreover, electrostatic repulsion is probably also responsible for a general poor coverage of the TiO$_2$ surface.
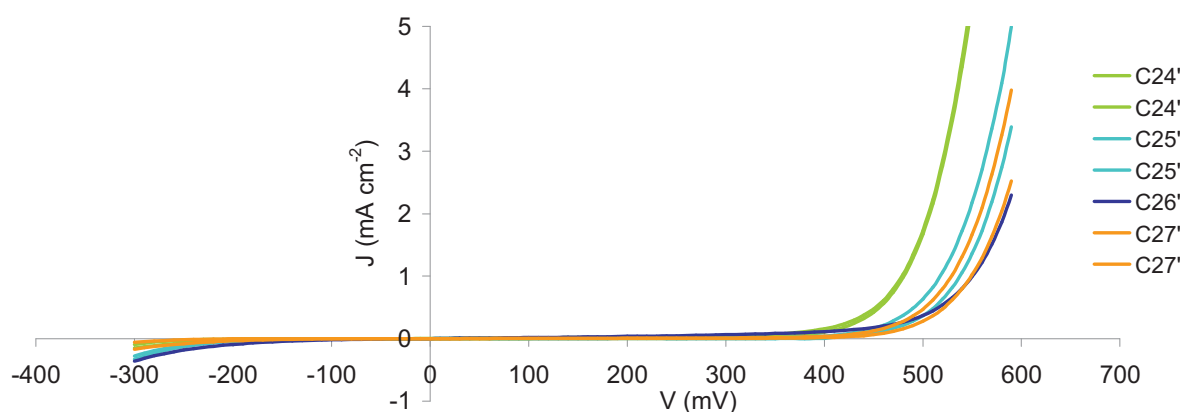
Fig. 5. 29. J/V plots recorded for **C24'**-**C27'** recorded in the absence of light.

The addition of *tert*-butylpyridine (for **C24'** and **C27'**) increased V_{oc} but decreased J_{sc}, leading to stable or decreased overall photo-conversion efficiency (Table 5. 10).

The effect of the addition of chenodeoxycholic acid was then assessed. The first test was carried out by spin-coating a 0.1 M CDCA solution (in ethanol) on the cells already covered by the sensitizer. This additive is expected to improve the performances because it can fill the spaces

between the dye molecules on the semiconductor surface, thus reducing the extent of the recombination between the injected electrons and the electrolyte. These voids are expected to be large herein, since the complexes are positively charged and they can undergo electrostatic repulsion preventing a close packing of the dye on the TiO_2 surface.

The overall efficiency was improved in all cases (except for **C26'** which remains unaltered), but the improvement for **C24'** was remarkable, with a more than two-fold η increase. The reason is probably that, the latter being the smallest complex of the series, the loading density was higher and the penetration of chenodeoxycholic acid (CDCA) to reach the TiO_2 surface was easier.

Further studies have to be carried out for example by co-adsorbing CDCA directly during coating of the TiO_2 film with the copper sensitizer, as is usually done. One can note that the 2.37 % efficiency obtained with **C27'** stands among the best photovoltaic performances measured with copper-based dyes.[60,62,63]

The photovoltaic performances proved to be stable in time, undergoing very slight variations after an ageing period of 2 days. This is particularly appealing since the lability of copper(I) complexes, which could have put a premature end to this project, does not seem to lead to any deleterious process like decomplexation of the ancillary ligand, even in the presence of *tert*-butylpyridine and iodide in the electrolyte. The most important parameter that will be optimized in the future is the electrolyte composition, and in particular the use of guanidinium thiocyanate and the reduction of iodine concentration (electrolyte B, previously described). The use of a cobalt redox mediator will be also investigated with these complexes as it may boost the Voc and the overall performances. Another factor playing a non negligible role is the thickness of the Surlyn tape.

However, given the absorption spectra and the electrochemical properties of these complexes, higher photovoltaic performances could have been expected. This aspect still needs to be rationalised by means of new measurements (electronic impedance and transient absorption spectroscopy) and quantum mechanical calculations, but a hypothesis can be already made. As stated in the paragraph 5.7.4, the MLCT and ILCT transitions in the UV-Vis spectrum (the latter being the most important contribution to the absorption of visible light) seem to be strongly decoupled, *i.e.* the ligand-centred higher energy state does not relax to the lower energy MLCT excited state. In this case, light absorbed in the ILCT band would poorly participate to charge injection because the electron density is sent to the pyridyl units of the ancillary ligand and not to the anchoring one.

5.9. Conclusions and perspectives

Two series of heteroleptic copper(I) dyes for the sensitization of titanium dioxide were presented in this chapter.

The first one is based on the combination of the commercially available **biQuiCOOH** and dimesitylphenanthroline ligands. A first model compound, **C20**, was prepared along with two dyads bearing a secondary electron donor group (an aromatic amine or a ferrocene) connected to the copper(I) complex through a phenyl-imidazole spacer. The three complexes display rather low molar extinction coefficients limiting the light harvesting efficiency. The three sensitizers revealed modest photovoltaic performances which were somewhat expected given the low absorbance and low driving force for electron injection reaction. The optimization work conducted by screening different electrolytes and additives, however, evidenced the major importance of the choice of the protonation state of the anchoring group. An overall efficiency of 0.71% could be nevertheless obtained for **C20** (in the monodeprotonated form), which stands among the usual performances of many copper diimine complexes (reported in paragraph 5.2).

Complexes **C22** and **C23** gave poorer photovoltaic performances, which were rationalised by an extremely weak electron injection driving force (even for the dye regeneration in the case of **C23**). Further studies will be carried out in order to give a deeper understanding of the photovoltaic results and to optimize the device fabrication.

A second series of sensitizers was prepared using a novel anchoring ligand: 6,6'-dimesityl-2,2'-bipyridine-4,4'-dicarboxylic acid. This ligand appears as a promising building block for the construction of heteroleptic copper(I) sensitizers, since it allows to use a large variety of bipyridines as the complementary ligands enabling the preparation of a great number of heteroleptic sensitizers. Herein, we chose to use styryl-bipyridine as ancillary ligands in order to increase the molar extinction coefficient of the sensitizers. Indeed, the complexes **C24-C27** displayed very large absorption cross-section, comparable to those achieved with highly performing ruthenium(II) complexes. The dyes for TiO_2 sensitization were obtained by hydrolysis of the ester functions, performed on the complexes. The reaction conditions still have to be optimized, since a mixture containing partially hydrolysed complexes was obtained. Longer reaction times lead to degradation, probably due to copper(I) oxidation, which occurs despite the inert atmosphere. The use of reducing molecules, like ascorbic acid or hydroquinone, will be tried in the future in order to limit the degradation and obtain the pure hydrolysed dyes.

With respect to the first series, the efficiency was improved thanks to both higher V_{oc} and J_{sc}. The highest efficiency was obtained with complex **C27'**, followed by **C24'**. The use of chenodeoxycholic acid, to passivate the surface free from the dye after the adsorption step, enabled

to increase the performances of the cells (while the effect of *t*BuPy was negligible) and provided a 2.37 % efficiency for **C27'**, which is among the highest photo-conversion efficiency measured with copper-based dyes. This rewarding result indicates the pertinence of heteroleptic copper-based complexes, and that the anchoring ligand **L18** has some potential in the development of new copper-based sensitizers.

However, the presence of ligand-centred excited states, strongly decoupled from the MLCT states, in these molecules likely decrease the photovoltaic performances of these copper-based dyes, which are still inferior to those of ruthenium(II) complexes. Further studies will be carried out in order to elucidate this aspect and to elaborate new and more efficient, copper(I)-based sensitizers. New complexes containing an anion ligand will be developed in order to obtained neutral dyes allowing dense and closely packed monolayer on the TiO$_2$ surface.

References

1. *Key World Energy Statistics*; International Energy Agency, **2011**.
2. Becquerel, A. E. *C. Rendus* **1839**, *9*, 561-567.
3. Chapin, D. M.; Fuller, C. S.; Pearson, G. L. *J. Appl. Phys.* **1954**, *25*, 676-677.
4. Martinuzzi, S. *Reflets Phys.* **2007**, 8-12.
5. Green, M. A.; Emery, K.; Hishikawa, Y.; Warta, W. *Prog. Photovoltaics* **2010**, *18*, 144-150.
6. Exley, C. *J. Inorg. Biochem.* **1998**, *69*, 139-144.
7. Schock, H.-W.; Noufi, R. *Prog. Photovoltaics* **2000**, *8*, 151-160.
8. http://www.heliatek.com/ 2012.
9. O'Regan, B.; Gratzel, M. *Nature* **1991**, *353*, 737-740.
10. Gurney, R. W.; Mott, N. F. *Proc. Roy. Soc. A* **1938**, *164*, 151-167.
11. W.West *Proc. Vogel Cent. Symp., Photog. Sci. Eng.* **1974**, *18*.
12. Moser, J. *Monatsh. Chem.* **1887**, *8*, 373-373.
13. Dare-Edwards, M. P.; Goodenough, J. B.; Hamnett, A.; Seddon, K. R.; Wright, R. D. *Faraday Discuss. Chem. Soc.* **1980**, *70*, 285-298.
14. Vlachopoulos, N.; Liska, P.; Augustynski, J.; Graetzel, M. *J. Am. Chem. Soc.* **1988**, *110*, 1216-1220.
15. Kalyanasundaram, K.; Grätzel, M. *Coord. Chem. Rev.* **1998**, *177*, 347-414.
16. Martinson, A. B. F.; Hamann, T. W.; Pellin, M. J.; Hupp, J. T. *Chem. Eur. J.* **2008**, *14*, 4458-4467.
17. Grätzel, M. *J. Photochem. Photobiol. A* **2004**, *164*, 3-14.
18. Nazeeruddin, M.; Grätzel, M.; Yam, V., Ed.; Springer Berlin / Heidelberg: **2007**; Vol. 123, p 113-175.
19. Nazeeruddin, M. K.; Kay, A.; Rodicio, I.; Humphry-Baker, R.; Mueller, E.; Liska, P.; Vlachopoulos, N.; Graetzel, M. *J. Am. Chem. Soc.* **1993**, *115*, 6382-6390.
20. Nazeeruddin, M. K.; De Angelis, F.; Fantacci, S.; Selloni, A.; Viscardi, G.; Liska, P.; Ito, S.; Takeru, B.; Grätzel, M. *J. Am. Chem. Soc.* **2005**, *127*, 16835-16847.
21. K. Nazeeruddin, M.; Pechy, P.; Gratzel, M. *Chem. Commun.* **1997**, 1705-1706.
22. Wang, P.; Zakeeruddin, S. M.; Moser, J. E.; Nazeeruddin, M. K.; Sekiguchi, T.; Gratzel, M. *Nat. Mater.* **2003**, *2*, 402-407.
23. Barolo, C.; Nazeeruddin, M. K.; Fantacci, S.; Di Censo, D.; Comte, P.; Liska, P.; Viscardi, G.; Quagliotto, P.; De Angelis, F.; Ito, S.; Grätzel, M. *Inorg. Chem.* **2006**, *45*, 4642-4653.
24. Wang, P.; Klein, C.; Humphry-Baker, R.; Zakeeruddin, S. M.; Grätzel, M. *J. Am. Chem. Soc.* **2004**, *127*, 808-809.
25. Chen, C.-Y.; Wang, M.; Li, J.-Y.; Pootrakulchote, N.; Alibabaei, L.; Ngoc-le, C.-h.; Decoppet, J.-D.; Tsai, J.-H.; Grätzel, C.; Wu, C.-G.; Zakeeruddin, S. M.; Grätzel, M. *ACS Nano* **2009**, *3*, 3103-3109.
26. Zabri, H.; Odobel, F.; Altobello, S.; Caramori, S.; Bignozzi, C. A. *J. Photochem. Photobiol. A* **2004**, *166*, 99-106.
27. Baranoff, E.; Yum, J.-H.; Graetzel, M.; Nazeeruddin, M. K. *J. Organomet. Chem.* **2009**, *694*, 2661-2670.
28. Mishra, A.; Fischer, M. K. R.; Bäuerle, P. *Angew. Chem. Int. Ed.* **2009**, *48*, 2474-2499.
29. Yella, A.; Lee, H.-W.; Tsao, H. N.; Yi, C.; Chandiran, A. K.; Nazeeruddin, M. K.; Diau, E. W.-G.; Yeh, C.-Y.; Zakeeruddin, S. M.; Grätzel, M. *Science* **2011**, *334*, 629-634.
30. Yanagida, S. *C. R. Chim.* **2006**, *9*, 597-604.
31. Wang, Z.-S.; Kawauchi, H.; Kashima, T.; Arakawa, H. *Coord. Chem. Rev.* **2004**, *248*, 1381-1389.
32. Hart, J. N.; Menzies, D.; Cheng, Y.-B.; Simon, G. P.; Spiccia, L. *C. R. Chim.* **2006**, *9*, 622-626.

33. Boschloo, G.; Hagfeldt, A. *Acc. Chem. Res.* **2009**, *42*, 1819-1826.
34. Boschloo, G.; Gibson, E. A.; Hagfeldt, A. *J. Phys. Chem. Lett.* **2011**, *2*, 3016-3020.
35. Grätzel, M. *Acc. Chem. Res.* **2009**, *42*, 1788-1798.
36. Hamann, T. W.; Ondersma, J. W. *Energ. Environ. Sci.* **2011**, *4*, 370-381.
37. Ferrere, S.; Zaban, A.; Gregg, B. A. *J. Phys. Chem. B* **1997**, *101*, 4490-4493.
38. Oskam, G.; Bergeron, B. V.; Meyer, G. J.; Searson, P. C. *J. Phys. Chem. B* **2001**, *105*, 6867-6873.
39. Nusbaumer, H.; Moser, J.-E.; Zakeeruddin, S. M.; Nazeeruddin, M. K.; Grätzel, M. *J. Phys. Chem. B* **2001**, *105*, 10461-10464.
40. Li, T. C.; Spokoyny, A. M.; She, C.; Farha, O. K.; Mirkin, C. A.; Marks, T. J.; Hupp, J. T. *J. Am. Chem. Soc.* **2010**, *132*, 4580-4582.
41. Spokoyny, A. M.; Li, T. C.; Farha, O. K.; Machan, C. W.; She, C.; Stern, C. L.; Marks, T. J.; Hupp, J. T.; Mirkin, C. A. *Angew. Chem. Int. Ed.* **2010**, *49*, 5339-5343.
42. Hattori, S.; Wada, Y.; Yanagida, S.; Fukuzumi, S. *J. Am. Chem. Soc.* **2005**, *127*, 9648-9654.
43. Bai, Y.; Yu, Q.; Cai, N.; Wang, Y.; Zhang, M.; Wang, P. *Chem. Commun.* **2011**, *47*, 4376-4378.
44. Brugnati, M.; Caramori, S.; Cazzanti, S.; Marchini, L.; Argazzi, R.; Bignozzi, C. A. *Int. J. Photoen.* **2007**, *2007*.
45. Zhang, Z.; Chen, P.; Murakami, T. N.; Zakeeruddin, S. M.; Grätzel, M. *Adv. Funct. Mater.* **2008**, *18*, 341-346.
46. Wang, M.; Chamberland, N.; Breau, L.; Moser, J.-E.; Humphry-Baker, R.; Marsan, B.; Zakeeruddin, S. M.; Grätzel, M. *Nat. Chem.* **2010**, *2*, 385-389.
47. Snaith, H. J.; Zakeeruddin, S. M.; Wang, Q.; Péchy, P.; Grätzel, M. *Nano Lett.* **2006**, *6*, 2000-2003.
48. Tian, H.; Gabrielsson, E.; Yu, Z.; Hagfeldt, A.; Kloo, L.; Sun, L. *Chem. Commun.* **2011**, *47*, 10124-10126.
49. Yu, Z.; Vlachopoulos, N.; Gorlov, M.; Kloo, L. *Dalton Trans.* **2011**, *40*, 10289-10303.
50. Wang, P.; Zakeeruddin, S. M.; Moser, J.-E.; Humphry-Baker, R.; Grätzel, M. *J. Am. Chem. Soc.* **2004**, *126*, 7164-7165.
51. Gorlov, M.; Kloo, L. *Dalton Trans.* **2008**, 2655-2666.
52. Cai, N.; Moon, S.-J.; Cevey-Ha, L.; Moehl, T.; Humphry-Baker, R.; Wang, P.; Zakeeruddin, S. M.; Grätzel, M. *Nano Lett.* **2011**, *11*, 1452-1456.
53. Boschloo, G.; Häggman, L.; Hagfeldt, A. *J. Phys. Chem. B* **2006**, *110*, 13144-13150.
54. Yum, J.-H.; Jang, S.-r.; Humphry-Baker, R.; Grätzel, M.; Cid, J.-J.; Torres, T.; Nazeeruddin, M. K. *Langmuir* **2008**, *24*, 5636-5640.
55. Pelet, S.; Moser, J.-E.; Grätzel, M. *J. Phys. Chem. B* **2000**, *104*, 1791-1795.
56. Hagfeldt, A.; Graetzel, M. *Chem. Rev.* **1995**, *95*, 49-68.
57. Alonso-Vante, N.; Ern, V.; Chartier, P.; Dietrich-Buchecker, C. O.; McMillin, D. R.; Marnot, P. A.; Sauvage, J. P. *Nouv. J. Chim.* **1983**, *7*, 3-5.
58. Alonso-Vante, N.; Nierengarten, J.-F.; Sauvage, J.-P. *Dalton Trans.* **1994**, 1649-1654.
59. Bessho, T.; Constable, E. C.; Graetzel, M.; Hernandez Redondo, A.; Housecroft, C. E.; Kylberg, W.; Nazeeruddin, M. K.; Neuburger, M.; Schaffner, S. *Chem. Commun.* **2008**, 3717-3719.
60. Constable, E. C.; Redondo, A. H.; Housecroft, C. E.; Neuburger, M.; Schaffner, S. *Dalton Trans.* **2009**, 6634-6644.
61. Bozic-Weber, B.; Constable, E. C.; Housecroft, C. E.; Neuburger, M.; Price, J. R. *Dalton Trans.* **2010**, *39*, 3585-3594.
62. Yuan, Y.-J.; Yu, Z.-T.; Zhang, J.-Y.; Zou, Z.-G. *Dalton Trans.* **2012**, *41*, 9594-9597.
63. Sakaki, S.; Kuroki, T.; Hamada, T. *Dalton Trans.* **2002**, 840-842.
64. Linfoot, C. L.; Richardson, P.; Hewat, T. E.; Moudam, O.; Forde, M. M.; Collins, A.; White, F.; Robertson, N. *Dalton Trans.* **2010**, *39*, 8945-8956.

65.   Hernández-Redondo, A., Ph.D. Thesis, University of Basel, **2009**.

66.   Bozic-Weber, B.; Constable, E. C.; Housecroft, C. E.; Kopecky, P.; Neuburger, M.; Zampese, J. A. *Dalton Trans.* **2011**, *40*, 12584-12594.

67.   Lu, X.; Wei, S.; Wu, C.-M. L.; Li, S.; Guo, W. *J. Phys. Chem. C* **2011**, *115*, 3753-3761.

68.   K. Nazeeruddin, M.; Muller, E.; Humphry-Baker, R.; Vlachopoulos, N.; Gratzel, M. *Dalton Trans.* **1997**, 4571-4578.

69.   Johansson, P. G.; Rowley, J. G.; Taheri, A.; Meyer, G. J.; Singh, S. P.; Islam, A.; Han, L. *Langmuir* **2011**, *27*, 14522-14531.

70.   Patri, A.; Moorefield, C. N.; Newkome, G. R. *Heterocycles* **2012**, *84*, 1023-1032.

71.   Li, X.-y.; Illigen, J.; Nieger, M.; Michel, S.; Schalley, C. A. *Chem. Eur. J.* **2003**, *9*, 1332-1347.

72.   Magdesieva, T. V.; Dolganov, A. V.; Yakimansky, A. V.; Goikhman, M. Y.; Podeshvo, I. V.; Kudryavtsev, V. V. *Electrochim. Acta* **2008**, *53*, 3960-3972.

73.   Haque, S. A.; Handa, S.; Peter, K.; Palomares, E.; Thelakkat, M.; Durrant, J. R. *Angew. Chem. Int. Ed.* **2005**, *44*, 5740-5744.

74.   Boixel, J., Ph.D. Thesis, University of Nantes, **2009**.

75.   Fery-Forgues, S.; Delavaux-Nicot, B. *J. Photochem. Photobiol. A* **2000**, *132*, 137-159.

76.   Steck, E. A.; Day, A. R. *J. Am. Chem. Soc.* **1943**, *65*, 452-456.

77.   Cunningham, C. T.; Moore, J. J.; Cunningham, K. L. H.; Fanwick, P. E.; McMillin, D. R. *Inorg. Chem.* **2000**, *39*, 3638-3644.

78.   Kobayashi, R.; Amos, R. D. *Chem. Phys. Lett.* **2006**, *420*, 106-109.

79.   Bucci, R.; Carunchio, V.; Magri', A. D.; Magri', A. L. *Ann. Chim. (It.)* **1994**, *84*, 509-520.

80.   Qin, Y.; Peng, Q. *Int. J. Photoen.* **2012**, *2012*.

81.   Hagfeldt, A.; Boschloo, G.; Sun, L.; Kloo, L.; Pettersson, H. *Chem. Rev.* **2010**, *110*, 6595-6663.

82.   Schmittel, M.; Ganz, A. *Chem. Commun.* **1997**, 999-1000.

83.   Mohamed, E. A.; Tawfik, A. M.; Morsy, J. M. *J. Indian Chem. Soc.* **1995**, *72*, 93-97.

84.   Mohamed, E. A.; Ibrahim, S. S.; Abdel-Halim, A. M.; Morsy, J. M. *Pak. J. Sci. Ind. Res.* **1994**, *37*, 171-174.

85.   Jäger, M.; Eriksson, L.; Bergquist, J.; Johansson, O. *J. Org. Chem.* **2007**, *72*, 10227-10230.

86.   Kasha, M. *Discuss. Faraday Soc.* **1950**, *9*, 14-19.

87.   Chen, Y.; Zhou, X.; Wei, X.-H.; Yu, B.-L.; Chao, H.; Ji, L.-N. *Inorg. Chem. Commun.* **2010**, *13*, 1018-1020.

88.   E. Keyes, T.; O'Connor, C.; Vos, J. G. *Chem. Commun.* **1998**, 889-890.

89.   Blakley, R. L.; Myrick, M. L.; DeArmond, M. K. *J. Am. Chem. Soc.* **1986**, *108*, 7843-7844.

90.   Casadonte, D. J.; McMillin, D. R. *Inorg. Chem.* **1987**, *26*, 3950-3952.

91.   Salassa, L.; Garino, C.; Albertino, A.; Volpi, G.; Nervi, C.; Gobetto, R.; Hardcastle, K. I. *Organometallics* **2008**, *27*, 1427-1435.

92.   Ziessel, R.; Juris, A.; Venturi, M. *Inorg. Chem.* **1998**, *37*, 5061-5069.

Conclusions

The aim of this thesis was to explore the possibilities offered by heteroleptic copper(I) complexes in the field of solar energy conversion. This objective was pursued starting from some model complexes with ligands spanning different substituent patterns in 2,9- positions on the phenanthroline ligand. The improvement of the molar absorption coefficient was then addressed. Finally, the use diimine heteroleptic copper(I) complexes for two different applications was investigated, first as chromophore to perform photoinduced charge separation in rod-like multicomponent arrays and then as photosensitizers for dye-sensitized solar cells.

In chapter 2, the HETPHEN approach, developed by Schmittel and co-workers, was used to synthesize a series of model complexes (**C1**-**C3**), which exhibit good stability and interesting photophysical properties. Like their homoleptic counterparts, they are good photoreductants but poor photooxidants. Excited-state lifetimes between 40 and 180 ns were measured in degassed dichloromethane, and the excited-state redox potentials were around -1.1 eV vs. SCE. A second series of complexes, containing an extended phenanthroline ligand either with a dipyrido[3,2-a:2',3'-c]phenazine, (dppz) or with phenyl-imidazole structure (**C4**-**C8**) was then prepared. The photophysical characterization evidenced that the phenyl-imidazole does not affect significantly the excited-state properties, while the electron withdrawing dppz acts as a strong luminescence quencher. The "chemistry on the complex" performed on **C6** and **C7** indicates that the heteroleptic copper(I) complexes are stable during Suzuki cross-coupling reaction and can be used as building blocks to synthesize more elaborated structures.

An improvement of the visible absorption properties was achieved with chromophoric push-pull styrylbipyridine ligands (chapter 3). This strategy led to a new series of complexes with high absorption coefficients ranging from 4 to $7 \cdot 10^4$ $M^{-1}cm^{-1}$ between 400 and 460 nm. The visible absorption bands of the mixed diphosphine diimine complexes are essentially composed of an ILCT transition, while the MLCT is the major component for the bis diimine complexes **C11**-**C13.** This difference has a strong influence on the emission properties. The **DPEphos**-containing complexes **C9** and **C10** display an intense but short-lived luminescence (τ < 1 ns), attributed to the prompt fluorescence from the singlet ILCT state. The MLCT state decay is slower ($\tau \sim 1.5$ μs) but is non radiative. For the diimine complexe **C11**, the MCLT state is populated at 90% upon excitation at 400 nm, and results in a weak and short-lived luminescence. Interestingly, the ILCT and MCLT states appear to be strongly decoupled.

In the last two chapters, the knowledge accumulated on heteroleptic copper(I) complexes was used to develop molecular arrays for photoinduced electron transfer and to engineer sensitizers for dye-sensitized solar cells (DSSCs).

Photoinduced electron transfer was approached at first by synthesizing two copper(I) acceptor dyads with naphthalene diimide (NDI) as electron acceptor, taking advantage of the good photoreducing properties of copper(I) diimine complexes. The two dyads differ by the spacer between the two electro- (and photo-)active units. In both the systems, excitation of the NDI moiety at 355 nm led to a charge separated state. The recombination rate depends on the spacer, being 9 ns in acetonitrile for **C14^{Imi}** (with the longer phenyl-imidazole spacer) and between 1 and 4 ns for **C15**. In the second dyad, the electron transfer was achieved also by excitation of the MLCT band centred on copper(I) complex, with visible light. The construction of the triad **C17**, bearing a secondary ferrocene electron donor, led to an increase of the excited-state lifetime (30 ns in acetonitrile) which is explained with a higher distance between the two photogenerated charges.

The last chapter is devoted to the synthesis and characterization of heteroleptic copper complexes for dye-sensitized solar cells. Two series were prepared. The first one, based on **biQuiCOOH** as anchoring ligand (**C20-C23**), provided lower photo-conversion efficiencies, mainly due to a low molar extinction coefficient of the dyes and low electron injection driving force. The latter is a consequence of the feeble E_{00} induced by the biquinoline ligand. The second series is based on a new anchoring ligand: the 4,4'-dicarboxylic acid-6,6'-bis mesityl bipyridine **L18**. Ancillary styrylbipyridines ligands enhance the light absorption efficiency of the complexes. As observed in chapter 3, the ILCT states responsible for absorption and the MLCT states responsible for injection into the TiO$_2$ appear to be strongly decoupled. Preliminary photovoltaic measurements indicate interesting conversion efficiencies (2.4% under 1000 W/m^2), which rank some of these complexes among the best performing copper(I) complexes in DSCs.

In conclusion, it can be stated that heteroleptic copper(I) complexes exhibit rich photochemistry, and the possibility to finely tune their photo- and electro-chemical properties with two different ligands around the copper(I) cation make them valuable new dyes for solar energy conversion schemes.

Experimental part

General methods

NMR:

^{1}H and ^{13}C-NMR spectra were recorded on a Bruker ARX 300 MHz or AMX 400 MHz Brucker spectrometer. AVANCE III 500 Bruker. Chemical shifts for ^{1}H-NMR spectra are referenced relative to residual protium in the deuterated solvent (CDCl$_3$ ™ = 7.26 ppm).

Mass spectrometry:

Mass spectra were recorded on a EIMS HP 5989A spectrometer or on a JMS-700 (JEOL LTD, Akishima, Tokyo, Japan) double focusing mass spectrometer of reversed geometry equipped with electrospray ionization (ESI) source. Electrospray ionization mass spectroscopy (ESI) analyses were performed on a ThermoFinnigan LCQ Advantage spectrometer. MALDI-TOF analyses were performed on a BRUKER Ultraflex III, micrOTOF Q spectrometer in positive linear mode at 20 kV acceleration voltage with 2,5-dihydroxybenzoic acid (DHB) or dithranol as matrix.

Spectroscopy:

UV-Visible absorption spectra were recorded on a UV-2401PC Shimadzu spectrophotometer, using optically matched quartz cuvettes with a 1 cm path length for the reference and the sample.
Steady-state luminescence spectra were recorded using a FluoroMax3 (Jobin Yvon Horiba), and emission was corrected for the spectral sensitivity of the instrument.

Electrochemistry:

The electrochemical measurements were performed with an Autolab PGSTAT 302N potentiostat controlled by GPES software using a conventional single-compartment three-electrode cell. The working electrode was a Pt disc, the counterelectrode was a Pt foil and the reference electrode was the saturated potassium chloride calomel electrode (SCE). The supporting electrolyte was 0.1 M Bu$_4$NPF$_6$ in freshly distilled dichloromethane and the solutions were purged with argon before the measurements. All potentials are quoted relative to SCE. The CV experiments were performed at different scan rates, and the results are reported for v = 100 mV/s. The frequency was 25 Hz for square wave and differential pulse voltammetry.

Spectroelectrochemistry:

Spectroelectrochemical spectra were recorded with the system described above for the UV-Vis spectra, with a quartz UV-Visible cell (0.5 mm) surmounted with an electrochemical cell. The working electrode was a platinum roast and the operating conditions are the same as for electrochemistry.

Transient absorption:

Nanosecond transient absorption experiments were performed using a laser flash photolysis apparatus. Excitation pulses at 460 nm (4 ns, 1 mJ) were provided by a 10-Hz Nd:YAG laser coupled to an OPO (Continuum Panther EXOPO pumped by a Surelite II). The probe light was provided by a pulsed Xe lamp (XBO 150W/CR OFR, OSRAM). Samples were contained in a quartz cell (10 x 10 mm section) at an adjusted concentration (~10^{-4} mol dm^3) to get an OD value of about 1.0 at the pump excitation wavelength. The transmitted light was dispersed by a monochromator (Horiba Jobin-Yvon, iHR320) and analyzed with a photomultiplier (R1477-06, Hamamatsu) coupled to a digital oscilloscope (LeCroy 454, 500 MHz). The experiment was

repeated for different wavelengths of the monochromator, and transient spectra were afterward reconstructed.

Femtosecond transient absorption measurements were performed with an apparatus based on a 1-kHz Ti:sapphire laser system (Coherent, BM Industries) delivering 100 fs (0.8 mJ) pulses at 800 nm. The 400 nm excitation pulses were obtained from the second harmonic of the amplifier output. White light continuum probe pulses were generated by focusing a few microjoules of the fundamental onto a 1 mm CaF_2 rotating plate. The pump-probe polarization configuration was set at the magic angle (54.7°) and the probe pulse is delayed in time relative to the pump pulse using an optical delay line (Microcontrol, precision: 0.1 μm). The white light was split into two beams using a 50% beam splitter to yield the probe and the reference beam recording on two different channels of a multichannel spectrograph equipped with a CCD camera (Princeton Instrument). The sample cuvette path length was 1 mm. The studied compounds were diluted in acetonitrile at a concentration corresponding OD=1 at the pump wavelength.

Solar cells preparation:

FTO conductive glass substrates (F-doped SnO_2) were purchased from Solems (5Ω/square). The plates were cleaned by successive sonication in acetone, distilled water and ethanol for 10 minutes, then dried by an air flow. A paste of TiO_2 nanoparticles (Dyesol) was then spread on FTO substrate by screen printing (three layers were deposited). The electrodes were then sintered at 450º for 30 minutes, and 12 μm electrodes were obtained. The thickness of the TiO_2 electrodes was determined with a Dektak 8 profilometer and the data analysis was done with Dektak software v. 8.34.

The grafting was obtained by dipping the electrodes, still hot, in a solution containing ~ 0.5 mM complex dissolved in an appropriate solvent, usually distilled methanol or ethanol. The electrodes were kept in the dark and then extracted from the dye solution, washed with ethanol and allowed to dry.

The counterelectrode was constituted by an FTO plate coated with Pt nanoparticles.

The two electrodes are separated by a hotmelt Surlyn® tape mask (25 or 60 μm) and the electrolyte was introduced into the cavity by vacuum backfilling. The cell was then permanently sealed with a cover glass.
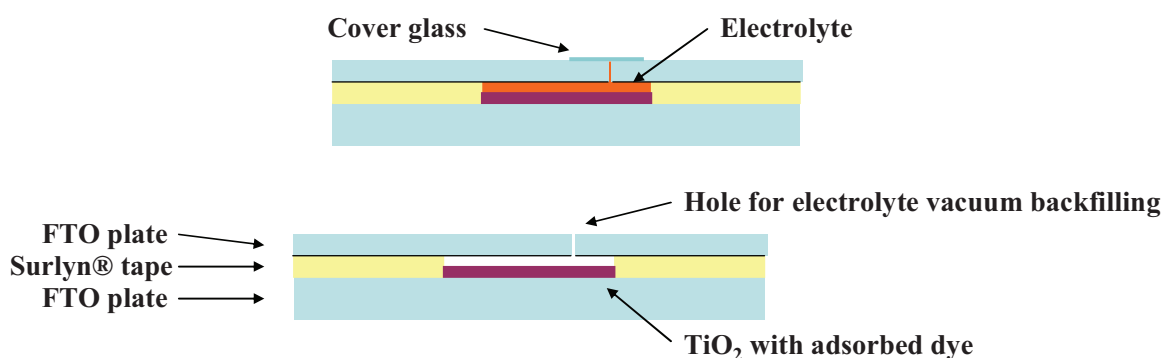
Air sensitive reactions:

Air sensitive reactions were carried out under argon atmosphere in dry solvents and glassware.

Chromatography:

Thin-layer chromatography (TLC) was performed on aluminium sheets precoated with Merck 5735 Kieselgel 60F254. Column chromatography was carried out either with Merck 5735 Kieselgel 60F (0.040-0.063 mm mesh) or with SDS neutral alumina (0.05-0.2 mm mesh). Preparative thin-layer chromatography (preparative TLC) was performed with a Merk Kieselgel 60PF254.

Chapter 2 – A toolbox to build heteroleptic copper(I) complexes with phenanthroline ligands

2,9-Di-*n*-butyl-1,10-phenanthroline (**L2**),[1] 2,9-di-*n*-butyl-3,4,7,8-tetramethyl-1,10-phenanthroline (**L3**),[2] 2,9-diphenyl-1,10-phenanthroline (**L4**),[1] 2,9-dichloro-1,10-phenanthroline (**3**),[3] 2,9-dichloro-1,10-phenanthroline-5,6-dione (**4**),[4] 2,9-dichloro-1,10-phenanthroline-5,6-dioxolane (**5**),[4] 2,9-di-*n*-butyl-1,10-phenanthroline-5,6-dione (**8**)[5] and [Cu(MeCN)₄]PF₆ [6] were prepared according to literature procedures. The other reagents were purchased by Sigma Aldrich or Acros Organics and used as received, without further purification.

2,9-dimesityl-3,4,7,8-tetramethyl-1,10-phenanthroline (L1)
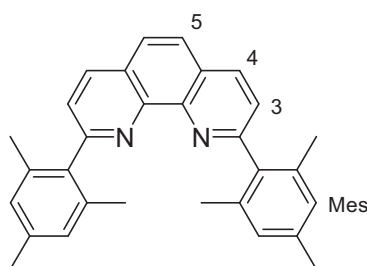

The synthesis of this ligand is already known in literature,[7] but the protocol was modified.

2,9-Dichloro-1,10-phenanthroline **3** (502 mg, 2.01 mmol), mesitylboronic acid (690 mg, 4.21 mmol) and Ba(OH)₂ (1.322 g, 7.72 mmol) were put in a Schlenk tube with 35 mL of 1,2-dimethoxyethane and 4 mL of water. The mixture was degassed thoroughly and Pd(PPh₃)₄ (118 mg, 0.10 mmol) was added quickly. It was then heated to reflux under Ar atmosphere for 3 hours, and allowed to cool to room temperature. Water was added and DME was removed under reduced pressure. The white precipitate was collected by filtration, washed with water and dissolved in dichloromethane. The solution was dried on MgSO₄ and the solvent was removed. The crude product was purified by column chromatography on aluminium oxide (eluent CH₂Cl₂: petroleum ether = 50: 50) to obtain **L1** as a white powder (794 mg, 95%).

¹H-NMR (300 MHz, CDCl₃, 25°C): δ = 8.29 (d, 2H, J = 8.4 Hz, H⁴), 7.86 (s, 2H, H⁵), 7.58 (d, 2H, J = 8.4 Hz, H³), 6.93 (s, 4H, H^Mes), 2.31 (s, 6H, CH₃^Mes), 2.13 (s, 12H, 2 CH₃^Mes) ppm.

MS (ESI+): m/z = 416.2, calculated for [M + H]⁺= 416.6.

2,9-dicarbazole-1,10-phenanthroline (L5)
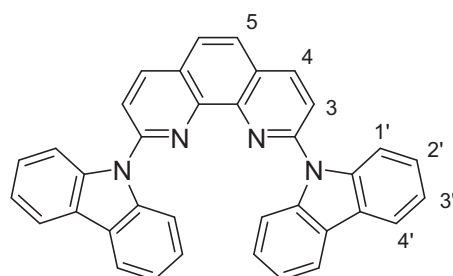
2,9-dichloro-1,10-phenanthroline **3** (91 mg, 0.36 mmol), carbazole (182 mg, 1.09 mmol) and Cs₂CO₃ (694 mg, 2.13 mmol) were dissolved in 10 mL of dry DMSO in a round-bottomed flask. The dark red-brown mixture was heated at 170 ºC under Ar for one night, then allowed to cool to

room temperature. Water was added and the light brown suspension was extracted three times with dichloromethane. After drying and removal of the solvent, the product was precipitated again from the remaining DMSO by adding water, and collected by filtration. The crude compound was purified by column chromatography on alumina (CH_2Cl_2) to obtain pure **L5** (90 mg, 49%).

^{1}H-NMR (300 MHz, $CDCl_3$, 25°C): δ = 8.45 (d, 2H, J = 8.7 Hz, H^4), 8.34 (d, 4H, J = 8.1 Hz, $H^{4'}$), 8.12 (d, 4H, 7.2 Hz, $H^{1'}$), 8.06 (d, 2H, J = 8.4 Hz, H^3), 7.88 (s, 2H, H^5), 7.47 (m, 4H, J^3 = 8.4 Hz, $H^{3'}$), 7.35 (m, 4H, $H^{2'}$) ppm.

^{13}C-NMR (75 MHz, $CDCl_3$, 25°C): δ = 151.23, 145.33, 139.59, 138.47, 126.85, 126.46, 125.42, 124.73, 121.26, 120.06, 118.74, 111.87 ppm.

**HR-MS** (MALDI+) m/z = 511.1923, calculated for $[MH]^+$ = 511.1917.

[Cu(L1)(L2)]PF$_6$ (C1)
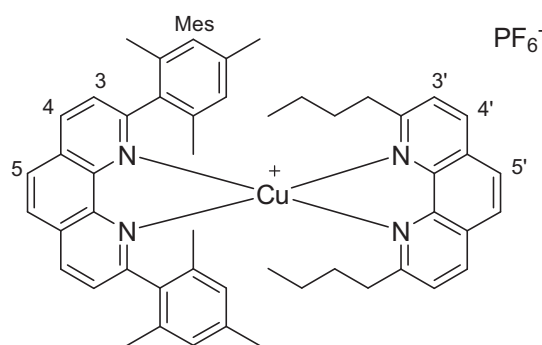
[Cu(CH$_3$CN)$_4$]PF$_6$ (50 mg, 0.13 mmol) and **L1** (61 mg, 0.15 mmol) were put under Ar in a dry round-bottomed flask. 12 mL of distilled and degassed dichloromethane were injected and the yellow solution was stirred at room temperature. **L2** (38 mg, 0.13 mmol) was dissolved in 4 mL of dry dichloromethane and the solution was degassed for 5 minutes by argon bubbling, then injected into the flask: the colour immediately turned to red. The solution was stirred at room temperature for 30 minutes and the removal of the solvent afforded the crude **C1**, which was purified by column chromatography on silica gel (CH_2Cl_2: CH_3OH = 98: 2). Pure **C1** was obtained as a red powder (93 mg, 78%).

^{1}H-NMR (300 MHz, $CDCl_3$, 25°C): δ = 8.70 (d, 2H, H^4), 8.31 (d, 2H, $H^{4'}$), 8.24 (s, 2H, H^5), 7.85 (s, 2H, $H^{5'}$), 7.76 (d, 2H, H^3), 7.51 (d, 2H, $H^{3'}$), 6.20 (s, 4H, H^{Mes}), 2.31 (m, 4H, CH_2^{nBu}), 1.91 (s, 6H, CH_3^{Mes}), 1.54 (s, 12H, CH_3^{Mes}), 1.16 (m, 4H, CH_2^{nBu}), 0.81 (m, 4H, CH_2^{nBu}), 0.67 (m, 6H, CH_3^{nBu}) ppm.

HR-MS (MALDI): m/z = 771.3489, calculated for $[M-PF_6]^+$ = 771.3483.

Elemental analysis for **C1·CH$_3$OH·H$_2$O**. Found (%): C, 63.31; H, 6.08; N, 5.44. Calcd.: C, 63.31; H, 6.04; N, 5.79.

[Cu(L1)(L3)]PF₆ (C2)
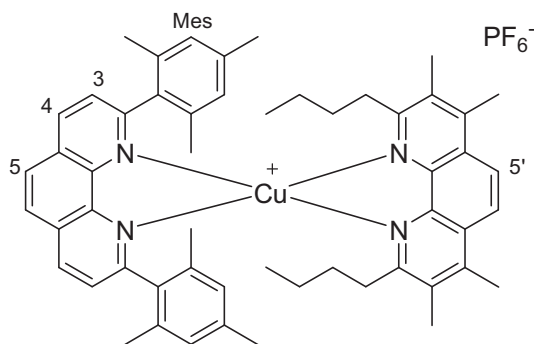
[Cu(CH₃CN)₄]PF₆ (29 mg, 7.9·10⁻² mmol) and **L1** (41 mg, 9.8·10⁻² mmol) were put under Ar in a dry round-bottomed flask. 7 mL of distilled and degassed dichloromethane were injected and the yellow solution was stirred at room temperature for 15 minutes. **L3** (27 mg, 7.8·10⁻² mmol) was dissolved in 3 mL of dry dichloromethane and the solution was degassed for 5 minutes by argon bubbling, then injected into the flask: the colour immediately turned to deep red. The solution was stirred at room temperature for 30 minutes and the removal of the solvent afforded crude **C2**, which was purified by column chromatography on silica gel (CH₂Cl₂: CH₃OH = 98: 2). The main red fraction was collected, and the product was precipitated by dichloromethane / petroleum ether, to give pure **C2** as a red powder (63 mg, 83%).

^{1}H-NMR (300 MHz, CDCl₃, 25°C): δ = 8.70 (d, 2H, J = 8.1 Hz, H^4), 8.24 (s, 2H, H^5), 8.05 (s, 2H, H$^{5'}$), 7.73 (d, 2H, J = 8.1 Hz, H^3), 6.26 (s, 4H, H^{Mes}), 2.70 (s, 6H, CH₃), 2.45 (m, 4H, CH₂^{nBu}), 2.34 (s, 6H, CH₃), 1.96 (s, 6H, CH₃^{Mes}), 1.51 (s, 12H, 2 CH₃^{Mes}), 0.89-0.82 (m, 4H, CH₂^{nBu}) 0.60 (s broad, 10H, CH₂^{nBu} and CH₃^{nBu}) ppm.

^{13}C-NMR (75 MHz, CDCl₃, 25ºC): δ = 159.92, 159.48, 144.39, 143.48, 141.22, 137.84, 137.67, 136.24, 134.62, 130.68, 128.45, 127.56, 127.38, 127.22, 126.32, 121.77, 40.19, 30.05, 22.87, 20.85, 20.06, 16.17, 15.37, 13.52 ppm.

HR-MS (MALDI+): m/z = 827.4138, calculated for [M-PF₆]$^+$ = 827.4109.

[Cu(L1)(L4)]PF₆ (C3)
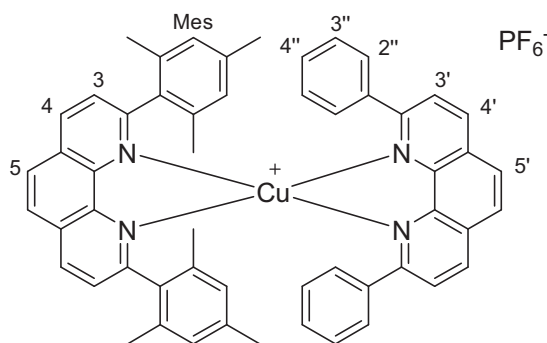
L1 (40 mg, 9.6·10⁻² mmol) and [Cu(CH₃CN)₄]PF₆ (35 mg, 9.4·10⁻² mmol) were dissolved in 5 mL of dry degassed dichloromethane under Ar, and the yellow solution was stirred at room temperature. **L4** (26 mg, 7.7·10⁻² mmol) was dissolved in 3 mL of dry dichloromethane and the solution was degassed for 5 minutes by Ar bubbling, then injected into the flask. The solution immediately turned red. After removal of the solvent, the crude product was purified by column chromatography on silica gel (CH₂Cl₂: CH₃OH = 98: 2) and then by crystallization from dichloromethane/petroleum ether to yield **C3** as red crystals (65 mg, 88%).

¹H-NMR (300 MHz, CDCl₃, 25°C): δ = 8.65 (d, 2H, J = 8.1 Hz, H⁴), 8.55 (d, 2H, J = 8.4, H⁴'), 8.30 (s, 2H, H⁵), 8.01 (s, 2H, H⁵'), 7.98 (d, 2H, J = 8.4 Hz, H³), 7.61 (d, 2H, J = 8.1 Hz, H³'), 7.56 (dd, 4H, J³ = 8.4 Hz, J⁴ = 0.9 Hz, H³''), 7.04 (t, 2H, J = 7.4 Hz, H⁴''), 6.65 (t, 4H, J = 7.8 Hz, H²''), 6.01 (s, 4H, H^Mes), 1.83 (s, 6H, CH₃^Mes), 1.08 (s, 12H, 2 CH₃^Mes) ppm.

¹³C-NMR (75 MHz, CDCl₃, 25ºC): δ = 160.19, 157.08, 144.36, 144.02, 138.91, 137.91, 137.77, 136.00, 134.79, 129.66, 128.90, 128.70, 128.54, 127.91, 127.58, 127.50, 127.27, 127.03, 125.98, 20.90, 19.75 ppm.

HR-MS (MALDI+): m/z = 811.2880, calculated for [M-PF₆]⁺ = 811.2857.

Elemental analysis for **C3**. Found (%): C, 67.84; H, 4.52; N, 5.81. Calcd.: C, 67.74; H, 4.63; N, 5.85.

*2,9-dimesityl-1,10-phenanthroline-5,6-dioxolane* **(6)**
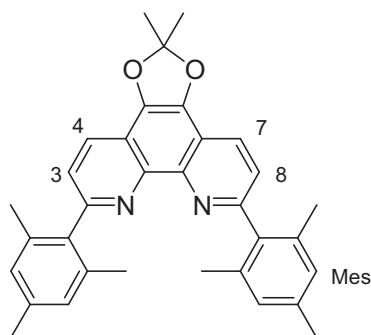
In a schlenk tube fitted with a water condenser, **5** (47 mg, 0.15 mmol), mesitylboronic acid (60 mg, 0.37 mmol) and barium hydroxide (94 mg, 0.55 mmol) were suspended in 5 mL of a 9:1 (v:v) mixture of 1,2-dimethoxyethane (DME) and water, respectively. The setup was thoroughly degassed with argon, and palladium tetrakis-triphenylphosphine (20 mg, 0.02 mmol) was quickly added. The mixture was heated to 115°C and stirred for 16 hours, under argon. It was then allowed to cool down to room temperature and water was added; the suspension was extracted four times with dichloromethane. The organic layers were gathered, dried on sodium sulphate, and evaporated under reduced pressure to afford a brown oil. The latter was purified by chromatography on silica gel, prepared in a 1:1 mixture of hexanes and dichloromethane. The second, bright orange fraction was collected and the solvents were removed by rotary evaporation, yielding **6** (63 mg, 88%).

¹H-NMR (300 MHz, CDCl₃, 25°C): δ = 8.31 (d, 2H, H₄ and H₇), 7.55 (d, 2H, H₃ and H₈), 6.92 (s, 4H, H_Mes), 2.31 (s, 6H, CH₃, Mes), 2.12 (s, 12H, CH₃, Mes), 1.92 (s, 6H, CH₃, dioxolane) ppm.

MS (ESI+): m/z = 489.2 [M + H]⁺.

Elemental analysis for **6·1/2DME·1/2CH₂Cl₂**. Found (%): C, 74.01; H, 6.38; N, 4.61. Calcd.: C, 74.01; H, 6.65; N, 4.86.

2,9-dimesityl-1,10-phenanthroline-5,6-dione (7)
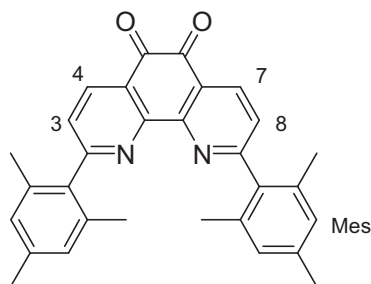
6 (163 mg, 0.33 mmol) was suspended in distilled water (5 mL). TFA (10 mL) was then added dropwise, at room temperature, and the yellow suspension eventually turned bright red. The mixture was then heated at 60°C for 5 hours. The solvents were evaporated and the brown residue was dissolved in 10 mL of dichloromethane, on top of which was added 10 mL of aqueous sodium hydrogen carbonate (1.0 mol L^{-1}). After 2 hours of vigorous stirring, the mixture has turned into a turbid, green-yellow emulsion. The latter was extracted four times with dichloromethane. The organic layers were gathered, washed with brine, dried on sodium sulphate and evaporated under reduced pressure. The resulting yellow oil was further dried on a vacuum line at room temperature, until a powder eventually appeared (130 mg, 87%).

^{1}H-NMR (300 MHz, CDCl$_3$, 25°C): δ = 8.53 (d, 2H, H$_4$ and H$_7$), 7.49 (d, 2H, H$_3$ and H$_8$), 6.92 (s, 4H, H$_{Mes}$), 2.30 (s, 6H, CH$_{3, Mes}$), 2.14 (s, 12H, CH$_{3, Mes}$) ppm.

HR-MS (m/z) 893.4067 [2M + H]$^+$.

## 2,9-dimesityl-1,10-phenanthroline-[a:b]imidazo-(4'-bromophenyl) (L6)
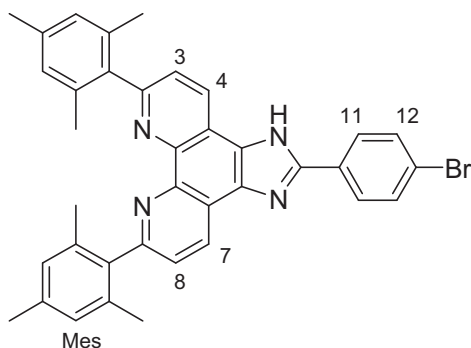
7 (50 mg, 0.10 mmol), *p*-bromobenzaldehyde (20 mg, 0.11 mmol) and ammonium acetate (170 mg, 2.2 mmol) were dissolved in glacial acetic acid (5 mL) and the mixture was refluxed overnight. After concentration under reduced pressure, water was added to precipitate a beige solid. The latter was subjected to column chromatography on silica, eluting with a gradient of methanol in dichloromethane (0 to 1%). The main yellow fraction was collected and the solvent was removed by rotary evaporation, to afford **L6** as an off white powder (42 mg, 62%).

^{1}H-NMR (300 MHz, [D$_6$] DMSO, 25°C): δ = 13.81 (s, broad, 1H, H^{imidazole}), 8.97 (d, 2H, H^4 and H^7), 8.27 (d, 2H, H^{11}), 7.82 (d, 2H, H^{12}), 7.74 (d, 1H, H^3), 7.68 (d, 1H, H^8), 6.95 (s, 4H, H^{Mes}), 2.29 (s, 6H, CH$_3^{Mes}$), 2.03 (s, 12H, CH$_3^{Mes}$) ppm.

HR-MS (m/z) 611.1810 [M+H]$^+$.

Elemental analysis for **L6**· 0.5 CH$_3$COOH. Found (%): C, 71.57; H, 5.31; N, 8.38. Calcd.: C, 71.14; H, 5.18; N, 8.73.

### *2,9-bis-nbutyl-3'-bromo-dipyrido[3,2-a:2',3'-c]phenazine* (L7)
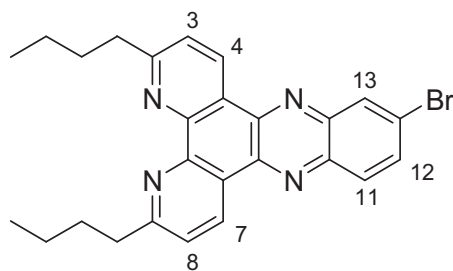
2,9-bibutyl-1,10-phenanthroline-5,6-dione **8** (91 mg, 0.28 mmol) and 4-bromo-1,2-diaminobenzene (53 mg, 0.28 mmol) were dissolved in 30 mL ethanol. The mixture was refluxed overnight. After concentration under reduced pressure, addition of water yielded a brown powder, which was chromatographed on silica, with dichloromethane as eluent to obtain pure **L7** (56 mg, 62%).

^{1}H-NMR (300 MHz, CDCl$_3$, 25°C): δ = 9.50 (m, 2H, H$_4$ and H$_7$), 8.53 (d, 1H, H$_{13}$), 8.20 (d, 1H, H$_{11}$), 7.95 (dd, 1H, H$_{12}$), 7.68 (d, 2H, H$_3$ and H$_8$), 3.28 (m, 4H, CH$_{2, butyl}$), 1.95 (m, 4H, CH$_{2, butyl}$), 1.55 (m, 4H, CH$_{2, butyl}$), 1.06 (t, 6H, CH$_{3, butyl}$).

HR-MS (m/z) 473.1351 [M]$^+$.

Elemental analysis **L7**·1/2H$_2$O. Found (%): C, 64.72; H, 5.38; N, 11.35. Calcd.: C, 64.73; H, 5.43; N, 11.61.

### *N-hexyl-2,9-dimesityl-1,10-phenanthroline-[a:b]imidazo-(4'-bromophenyl)* (L6')
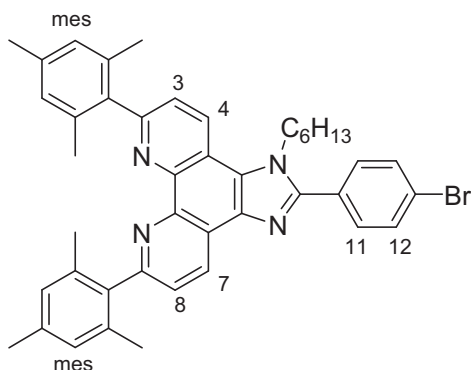
L6 (170 mg, 0.28 mmol) and Cs$_2$CO$_3$ (580 mg, 1.78 mmol)were degassed and dissolved in 8 mL of dry DMF under Ar atmosphere, then heated to 100 ºC under stirring. After 30 minutes 1-iodohexane (0.14 mL, 0.95 mmol) was injected, and the dark orange solution was stirred at 100 ºC for 6 hours. The solution was allowed to cool to room temperature and water was added; the precipitate was collected by filtration, washed with more water and dried. The crude product was then dissolved in dichloromethane and washed with water. The organic phase was then dried on MgSO$_4$ before removing the solvent. Pure **L6'** (147 mg, 75%) was obtained as an off-white solid after precipitation with petroleum ether from a dichloromethane solution.

^{1}H-NMR (300 MHz, CDCl$_3$): δ = 9.08 (d, 1H, J = 8.1 Hz, H^7), 8.60 (d, 1H, J = 8.7 Hz, H^4), 7.75 (d, 2H, J = 8.4 Hz, H^{12}), 7.65 (d, 4H, J = 8.4 Hz, H^{11}, H^3 and H^8), 6.94 (s, 2H, H^{mes}), 6.92 (s, 2H, H^{mes}), 4.64 (t, 2H, J = 6.9 Hz, NCH$_2$), 2.31 (s, 3H, CH$_3^{mes}$), 2.30 (s, 3H, CH$_3^{mes}$), 2.18 (s, 6H, 2 CH$_3^{mes}$), 2.15 (s, 6H, 2CH$_3^{mes}$), 1.99 (m, 2H, CH$_2^{Hex}$), 1.34-1.22 (m, 6H, 3 CH$_2^{Hex}$), 0.83 (t broad, 3H, CH$_3^{mes}$) ppm.

^{13}C-NMR (75 MHz, CDCl$_3$): δ = 158.53, 157.31, 152.48, 144.71, 144.09, 138.09, 137.57, 137.42, 137.15, 136.85, 136.27, 136.21, 132.08, 131.37, 129.91, 129.53, 128.51, 128.41, 127.71, 125.39, 125.08, 124.36, 124.25, 122.20, 118.10, 46.81, 30.94, 30.19, 25.93, 22.35, 21.06, 20.66, 13.81 ppm.

HR-MS (MALDI+): m/z = 695.2711, calculated for MH$^+$ m/z = 695.2744.

[Cu(Phen)(L6)]PF$_6$ (C4)
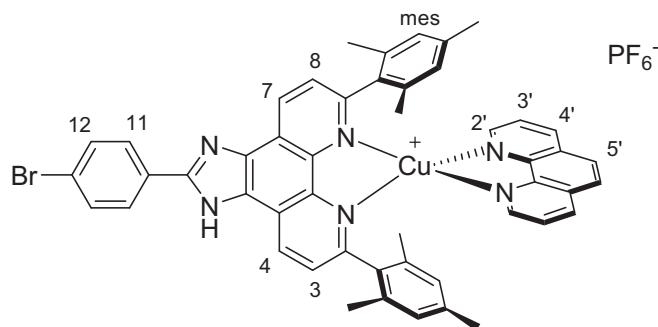
General procedure for the synthesis of the complexes **C4-C8**:

Cu(CH$_3$CN)$_4$PF$_6$ was dissolved in distilled dichloromethane, and thoroughly degassed by a few vacuum/argon cycles. An argon purged solution of mesityl bearing ligand **L1** or **L6** (1.0 equivalent) in dichloromethane was then syringed into the former solution, and the solution was stirred at room temperature. After 5 minutes, an argon purged solution of the less hindered ligand **X** (0.8 equivalents, **X** = **phen**, **dmp**, **L2** or **L7**) in dichloromethane was syringed into the yellow solution. The latter immediately turned deep red, and was left to stir for 30 minutes at room temperature. The solvent was then removed by rotary evaporation. The red residue was eventually purified by chromatography on silica gel. Yields were all between 75 and 85%.

^{1}H-NMR (300 MHz, CDCl$_3$, 25°C): δ = 9.36 (d, 2H, H^4 and H^7), 8.50 (d, 2H, H$^{2'}$), 8.39 (d, 2H, H$^{4'}$), 8.32 (d, 2H, H^{11}), 7.86 (s, 2H, H$^{5'}$), 7.82 (d, 2H, H^{12}), 7.70 (m, 4H, H^3, H^8, H$^{3'}$), 5.88 (s, 4H, H^{mes}), 1.70 (s, 12H, CH$_3^{mes}$), 1.53 (s, 6H, CH$_3^{mes}$) ppm.

HR-MS (m/z) 853.1721, calculated for [M-PF$_6$]$^+$= 853.1710.

Elemental analysis: **C4**.CH$_3$OH. Found (%): C, 58.15; H, 4.17; N, 7.84. Calcd.: C, 58.17; H, 4.20; N, 8.14.

[Cu(dmp)(L6)]PF$_6$ (C5)
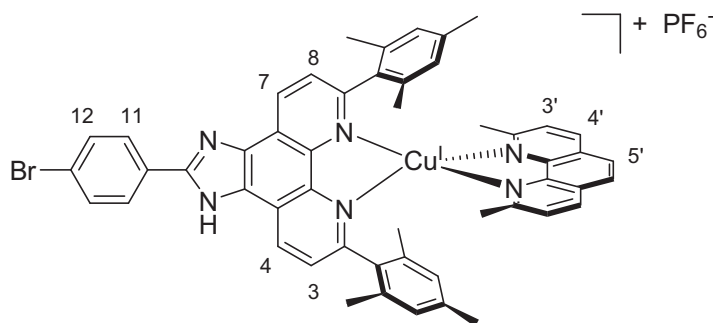
^{1}H-NMR (300 MHz, CDCl$_3$, 25°C): δ = 11.92 (s, 1H, H^{imidazole}), 9.45 (d, 1H, H^4 or H^7), 9.36 (d, 1H, H^7 or H^4), 8.34 (d, 2H, H^{11}), 8.22 (d, 2H, H$^{4'}$), 7.82 (d, 2H, H^{12}), 7.79 (s, 2H, H$^{5'}$), 7.72 (d, 2H, H^3 and H^8), 7.49 (d, 2H, H$^{3'}$), 6.11 (s, 2H, H^{mes}), 6.02 (s, 2H, H^{mes}), 2.21 (s, 6H, CH$_3^{methyl}$), 1.76 (s, 3H, CH$_3^{mes}$), 1.73 (s, 3H, CH$_3^{mes}$), 1.63 (s, 6H, CH$_3^{mes}$), 1.56 (s, 6H, CH$_3^{mes}$) ppm.

HR-MS (m/z) 881.2021, calculated for [M-PF$_6$]$^+$= 881.2023.

Elemental analysis: **C5**·CH$_3$OH. Found (%): C, 58.73; H, 4.28; N, 7.91. Calcd.: C, 58.90; H, 4.47; N, 7.93.

[Cu(L2)(L6)]PF$_6$ (C6)
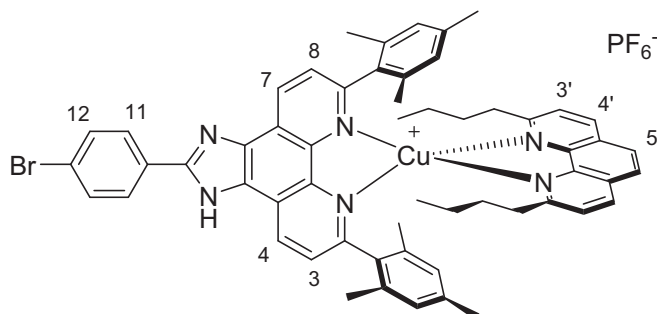
¹H-NMR (300 MHz, CDCl$_3$, 25°C): δ = 11.97 (s, 1H, H^{imidazole}),9.37 (m, 2H, H^4 and H^7), 8.31 (d, 2H, H^{11}), 8.27 (d, 2H, H$^{4'}$), 7.83 (s, 2H, H$^{5'}$), 7.78 (d, 2H, H^{12}), 7.65 (d, 2H, H^3 and H^8), 7.48 (d, 2H, H$^{3'}$), 6.22 (s, 2H, H^{mes}), 6.11 (s, 2H, H^{mes}), 2.33 (m, 4H, CH$_2^{butyl}$), 1.91 (s, 3H, CH$_3^{mes}$), 1.85 (s, 3H, CH$_3^{mes}$), 1.58 (s, 6H, CH$_3^{mes}$), 1.49 (s, 6H, CH$_3^{mes}$), 1.18 (m, 4H, CH$_2^{butyl}$), 0.80 (m, 4H, CH$_2^{butyl}$), 0.61 (t, 6H, CH$_3^{butyl}$) ppm.

HR-MS (m/z) 965.2970, calculated for [M-PF$_6$]$^+$= 965.2962.

Elemental analysis: **C6**·1/2CH$_3$OH. Found (%): C, 61.21; H, 4.85; N, 7.28. Calcd.: C, 61.20; H, 5.09; N, 7.26.

[Cu(L7)(L1)]PF$_6$ (C7)
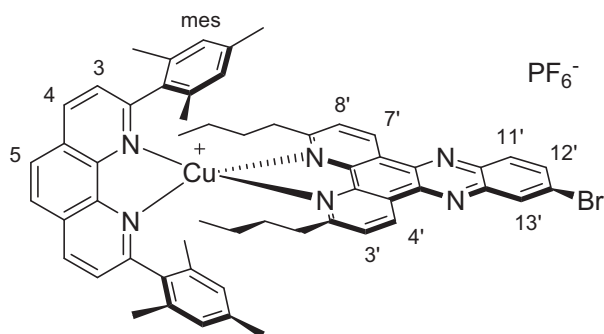
¹H-NMR (300 MHz, CDCl$_3$, 25°C): δ = 9.56 (m, 2H, H$^{4'}$ and H$^{7'}$), 8.76 (d, 2H, H^4), 8.60 (d, 1H, H$^{13'}$), 8.28 (m, 3H, H^5 and H$^{11'}$), 8.04 (dd, 1H, H$^{12'}$), 7.79 (d, 2H, H^3), 7.71 (m, 2H, H$^{3'}$ and H$^{8'}$), 6.19 (s, 2H, H^{mes}), 6.17 (s, 2H, H^{mes}), 2.38 (m, 4H, CH$_2^{butyl}$), 1.72 (s, 6H, CH$_3^{mes}$), 1.62 (s, 6H, CH$_3^{mes}$), 1.60 (s, 6H, CH$_3^{mes}$), 1.24 (m, 4H, CH$_2^{butyl}$), 0.84 (m, 4H, CH$_2^{butyl}$), 0.70 (m, 6H, CH$_3^{butyl}$) ppm.

HR-MS (m/z) 953.2801, calculated for [M-PF$_6$]$^+$= 953.2791.

Elemental analysis: **C7**·CH$_3$OH. Found (%): C, 60.63; H, 4.86; N, 7.34. Calcd.: C, 60.56; H, 5.08; N, 7.43.

[Cu(L6)(L7)]PF₆ (C8)

[Cu(L6)(L7)]PF₆ (C8)
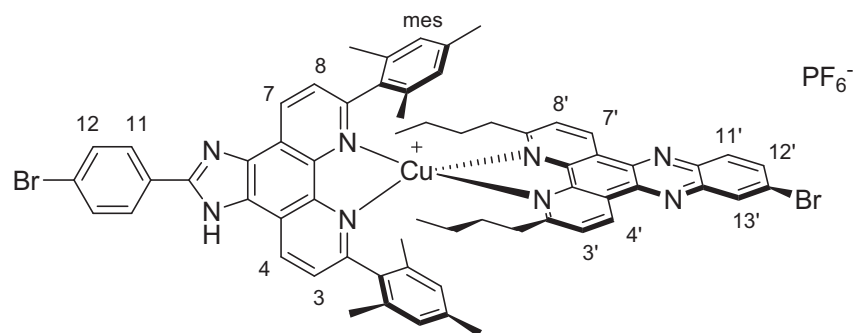
¹H-NMR (300 MHz, CDCl₃, 25°C): δ = 9.57 (d, 1H, H⁴' or H⁷'), 9.55 (d, 1H, H⁷' or H⁴'), 9.45 (d, 2H, H⁴ and H⁷), 8.64 (d, 1H, H¹³'), 8.38 (d, 2H, H¹¹), 8.31 (d, 1H, H¹¹'), 8.08 (dd, 1H, H¹²'), 7.82 (d, 2H, H³ and H⁸), 7.74 (d, 2H, H¹²), 7.65 (m, 2H, H³' and H⁸'), 6.17 (s, 2H, Hᵐᵉˢ), 6.15 (s, 2H, Hᵐᵉˢ), 2.40 (m, 4H, CH₂ᵇᵘᵗʸˡ), 1.72 (s, 6H, CH₃ᵐᵉˢ), 1.62 (s, 6H, CH₃ᵐᵉˢ), 1.60 (s, 6H, CH₃ᵐᵉˢ), 1.25 (m, 4H, CH₂ᵇᵘᵗʸˡ), 0.84 (m, 4H, CH₂ᵇᵘᵗʸˡ), 0.64 (m, 6H, CH₃ᵇᵘᵗʸˡ) ppm.

HR-MS (m/z) 1145.2266, calculated for [**C4**-PF₆]⁺= 1145.2285.

Elemental analysis: **C8**·3C₂H₅OH. Found (%): C, 58.18; H, 5.07; N, 7.46. Calcd.: C, 57.89; H, 5.21; N, 7.83.

[Cu(2,9-dibutyl-1,10-phenanthroline)(L3)]PF₆ (C6')

[Cu(2,9-dibutyl-1,10-phenanthroline)(L3)]PF₆ (C6')
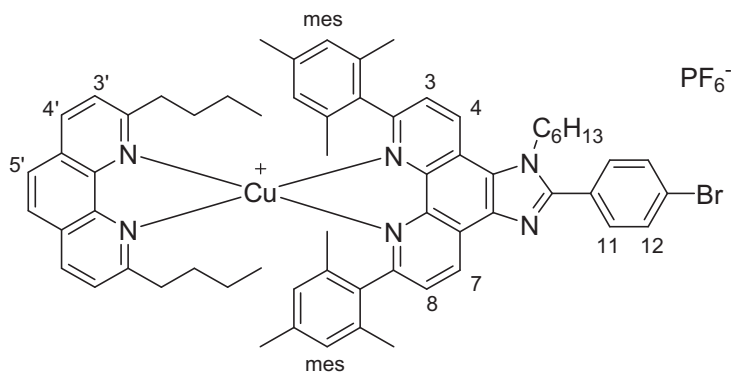
L6' (46 mg, 6.6 10⁻² mmol) and [Cu(CH₃CN)₄]PF₆ (21 mg, 5.6 10⁻² mmol) were degassed in a round-bottomed flask and 5 mL of freshly distilled CH₂Cl₂ were injected under Ar. The yellow solution was stirred at room temperature for 15 minutes, until complete dissolution of the solids. **L2** (15 mg, 5.1 10⁻² mmol) was dissolved in 2.2 mL of distilled CH₂Cl₂ and degassed for 5 minutes by Ar bubbling, then injected dropwise into the stirring solution, that immediately turned to red. After 20 minutes the solvent was removed. The crude product was purified by column chromatography on SiO₂ (eluant CH₂Cl₂: CH₃OH = 98: 2), then precipitated with petroleum ether from a dichloromethane solution to afford pure **C6'** as a red solid (50 mg, 82%).

¹H-NMR (300 MHz, CDCl₃): δ = 9.35 (d, 1H, J = 8.4 Hz, H⁷), 9.11 (d, 1H, J = 8.7 Hz, H⁴), 8.31 (d, 2H, J = 8.4 Hz, H⁴'), 7.94 (d, 1H, J = 8.4 Hz, H⁸), 7.85 (s, 2H, H⁵'), 7.81-7.77 (m, 3H, H¹² and H³), 7.72 (d, 2H, J = 8.4 Hz, H¹¹), 7.49 (d, 2H, J = 8.4 Hz, H³'), 6.20 (s, 2H, Hᵐᵉˢ), 6.13 (s, 2H, Hᵐᵉˢ), 4.88 (t broad, 2H, NCH₂), 2.34-2.28 (m, 4H, 2 CH₂ⁿᴮᵘ), 2.02-1.96 (m, 2H, CH₂ⁿᴴᵉˣ), 1.89 (s, 3H, CH₃ᵐᵉˢ), 1.86 (s, 3H, CH₃ᵐᵉˢ), 1.55 (s, 6H, 2 CH₃ᵐᵉˢ), 1.52 (s, 6H, 2 CH₃ᵐᵉˢ), 1.22-1.15 (m, 10H, 2 CH₂ⁿᴮᵘ and 3 CH₂ⁿᴴᵉˣ), 0.83-0.75 (m, 7H, 2 CH₂ⁿᴮᵘ and CH₃ⁿᴴᵉˣ), 0.62 (t, 6H, J = 7.2 Hz, 2 CH₃ⁿᴮᵘ) ppm.

**¹³C-NMR** (75 MHz, CDCl₃): δ = 160.89, 157.98, 157.30, 154.59, 142.86, 142.54, 142.34, 137.91, 137.84, 136.94, 136.79, 136.55, 134.78, 132.46, 132.04, 131.65, 130.87, 129.04, 127.47, 127.36, 127.23, 125.85, 125.61, 124.95, 123.88, 123.23, 120.06, 47.09, 39.32, 31.12, 30.41, 30.24, 25.94, 22.86, 22.55, 20.90, 20.04, 13.98, 13.85 ppm.

HR-MS (MALDI+): m/z = 1049.3898, calculated for (M-PF$_6$)$^+$ m/z = 1049.3901.

Chapter 3 – Heteroleptic copper complexes displaying transitions in the visible with large extinction coefficients

Ligands **L10**,[8] 4,4',6,6'-tetramethyl-2,2'-bipyridine,[9] 4,4'-methylphosphonateethyl ester-6,6'-dimethyl-2,2'-bipyridine,[10,11] 4-di(4'-methoxyphenyl) aminobenzaldehyde[12] and ligand **L8**[13] were prepared according to literature procedures.

4,4'-dianisylaminostyryl-6,6'-dimethyl-2,2'-bipyridine (L9)
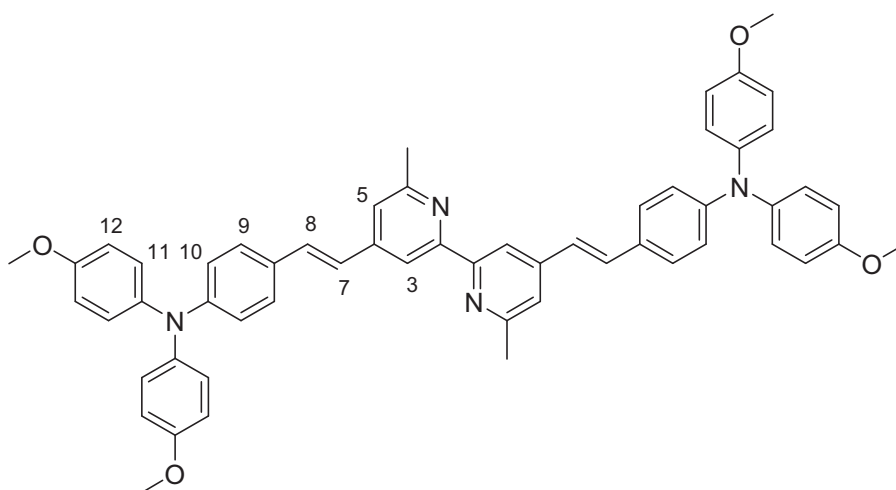

In a Schlenk flask, 4,4'-methylphosphonateethyl ester-6,6'-dimethyl-2,2'-bipyridine **11** (300 mg, $6.22.10^{-4}$ mol) and 4-dianisylaminobenzaldehyde **13** (517 mg, 1.55 mmol, 2.5 equiv.) were dissolved in THF (10 mL) and tBuOK (348 mg, 3.11 mmol) was slowly added at room temperature. The solution, which immediately turned brown, was then stirred for 3 h. Addition of water led to the formation of a pale precipitate, which was filtered. The crude solid was purified by column chromatography on silica gel (eluant CH_2Cl_2: AcOEt = 90:10 → 85: 15) to afford pure **L9** (227 mg, 43%).

^{1}H-NMR (300 MHz, CDCl$_3$, 25 ºC): δ = 8.24 (s, 2H, H^3), 7.38-7.32 (m, 6H, H^7 and H^9), 7.22 (s, 2H, H^5), 7.09 (d, 8H, J = 8.7 Hz, H^{11}), 6.89-6.95 (m, 6H, H^8 and H^{10}), 6.85 (d, 8H, J = 9 Hz, H^{12}), 3.81 (s, 12H, OCH$_3$), 2.66 (s, 6H, CH$_3$) ppm.

^{13}C-NMR (75 MHz, CDCl$_3$, 25 ºC): δ = 158.23, 156.52, 156.29, 149.24, 146.41, 140.53, 132.60, 128.47, 127.94, 127.07, 123.66, 120.04, 119.95, 115.74, 114.89, 55.63, 24.85 ppm.

HR-MS (MALDI): m/z = 843.3900, calculated for [M-H]$^+$= 843.3905.

4,4'- p-octyloxystyryl-6,6'-dimethyl-2,2'-bipyridine **(L11)**
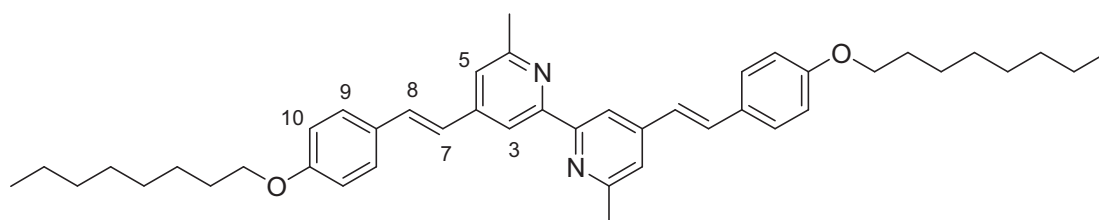
By the same procedure as described for **L9**, compound **L11** was isolated from 4,4' methylphosphonate ethyl ester-6,6'-dimethyl-2,2'-bipyridine **11** (200 mg, $4.13.10^{-4}$ mol), 4-octyloxybenzaldehyde (387 mg, 1.65 mmol, 4 equiv.) and tBuOK (185 mg, 1.65 mmol) in THF (10ml) as a creamy solid (170 mg, 64 %).

^{1}H-NMR (400 MHz, CDCl$_3$, 25 ºC): δ = 8.30 (s, 2H, H^3), 7.50 (d, J = 8.5 Hz, 4H, H^9), 7.38 (d, J = 16.3 Hz, 2H, H^7), 7.24 (s, 2H, H^5), 6.98 (d, J = 16.3 Hz, 2H, H^8), 6.92 (d, J = 8.5 Hz, 4H, H^{10}), 3.99 (t, J = 6.5 Hz, 4H, OCH$_2$^{nOct}), 2.68 (s, 6H, CH$_3$), 1.81 (m, 4H, CH$_2$^{nOct}), 1.48 (m, 4H, CH$_2$^{nOct}), 1.31 (m, 16H, 4 CH$_2$^{nOct}), 0.90 (m, 6H, CH$_3$^{nOct}) ppm.

^{13}C-NMR (100 MHz, CDCl$_3$, 25 ºC): δ = 159.63, 158.18, 156.43, 146.14, 132.40, 129.11, 128.32, 124.28, 120.06, 115.65, 114.82, 68.14, 31.84, 29.39, 29.27, 26.07, 24.73, 22.69, 14.13 ppm.

HR-MS (MALDI): m/z = 645.4438, calculated for [M-H]$^+$= 645.4415.

Elemental analysis: Calculated for C$_{44}$H$_{56}$N$_2$O$_2$: C, 81.94; H, 8.75; N, 4.34. Found: C, 81.79; H, 8.76; N, 4.41.

[Cu(DPEPhos)(L8)]PF$_6$ **(C9)**
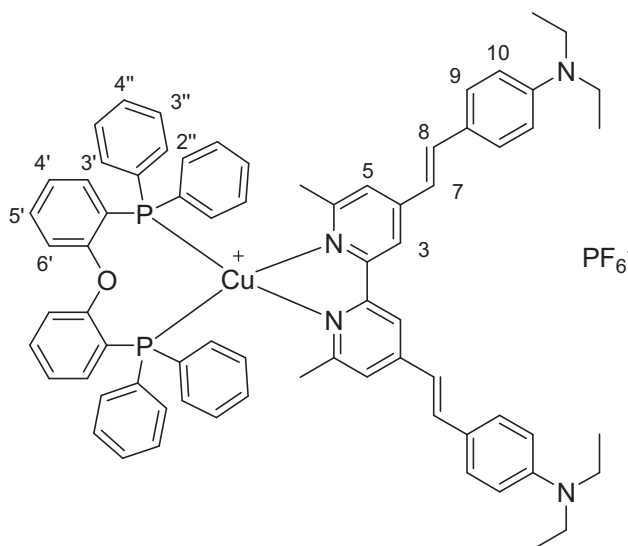
[Cu(MeCN)$_4$]PF$_6$ (45 mg, 0.12 mmol) and **DPEphos** (65 mg, 0.12 mmol) were stirred in 5 mL of distilled dichloromethane at room temperature for 10 minutes under Ar atmosphere, then 4 mL of a degassed solution of **L8** (57 mg, 0.11 mmol) in dichloromethane were injected under Ar and the resulting deep red solution was stirred for further 30 minutes at room temperature. The solvent was removed under reduced pressure and the resulting dark red solid was purified by column chromatography on silica gel (CH$_2$Cl$_2$: CH$_3$OH = 100: 0 → 92: 8, medium pressure chromatography) to afford 65 mg (46%) of pure **C9**.

^{1}H-NMR (500 MHz, acetone-d$_6$, 25 ºC): δ = 8.39 (d, 2H, J = 1 Hz, H^3), 7.64 (d, 2H, J = 16.5 Hz, H^7), 7.54 (d, 4H, J = 8.5 Hz, H^9), 7.47 (d, 2H, J = 1.5 Hz, H^5), 7.44 (m, 2H, H$^{5'}$), 7.36 (tm, 4H, H$^{4''}$), 7.29 (tm, 2H, H$^{4'}$), 7.27-7.22 (m, 10H, H$^{3''}$ and H$^{6'}$), 7.19-7.14 (m, 8H, H$^{2''}$), 7.03 (dm, 2H, H$^{3'}$),

7.02 (d, 2H, J = 16.5 Hz, H^8), 6.79 (d, 4H, J = 9.0 Hz, H^{10}), 3.46 (q, 8H, J = 6.9 Hz), 2.26 (s, 6H), 1.18 (t, 12H, J = 6.9 Hz) ppm.

^{13}C-NMR (125 MHz, acetone-d$_6$, 25 ºC): δ = 159.05, 153.99, 149.69, 136.94, 134.47, 134.13, 134.04, 133.94, 132.98, 132.77, 130.77, 130.01, 129.55, 126.45, 126.27, 126.09, 123.88, 122.73, 120.99, 120.12, 119.66, 117.43, 112.42, 44.96, 26.79, 12.89 ppm.

HR-MS (ESI+): m/z =1131.4266, calculated for [M-PF$_6$]$^+$=1131.4315.

Elemental analysis: Calculated for C$_{72}$H$_{70}$CuF$_6$N$_4$OP$_3$ ·0.75 CH$_2$Cl$_2$: C, 65.13; H, 5.37; N, 4.18. Found: C, 64.93; H, 5.19; N, 4.18.

[Cu(DPEPhos)(L9)]PF$_6$ (C10)
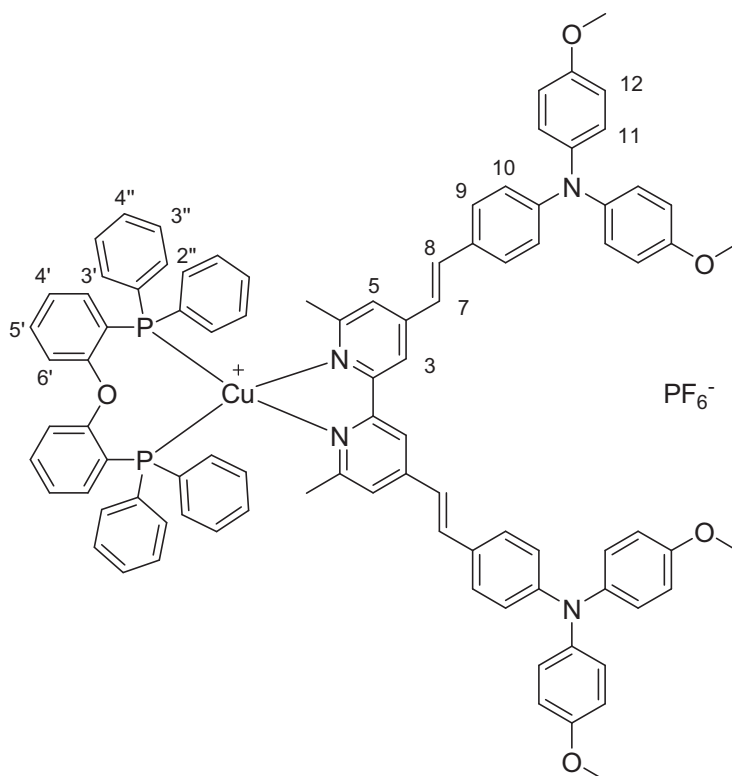
[Cu(MeCN)$_4$]PF$_6$ (9.3 mg, 0.025 mmol) and **DPEphos** (17 mg, 0.031 mmol) were stirred in 5 mL of distilled dichloromethane at room temperature for 15 minutes under Ar atmosphere, then 2 mL of a degassed solution of **L9** (21 mg, 0.024 mmol) in dichloromethane were injected under Ar and the resulting orange solution was stirred for further 30 minutes at room temperature. The solvent was removed under reduced pressure and the resulting orange solid was purified first by column chromatography on alumina (CH$_2$Cl$_2$) and then by size exclusion chromatography on Sephadex LH20 (acetone) to afford 28 mg (72%) of pure **C10**.

^{1}H-NMR (400 MHz, acetone-d$_6$, 25 ºC): δ = 8.40 (s, 2H, H^3), 7.64 (d, 2H, J = 16.4 Hz, H^7), 7.51 (s, 2H, H^5), 7.49 (d, 4H, J = 8.8 Hz, H^9), 7.42 (m, 2H, H$^{5'}$), 7.34 (tb, 4H, J = 7.2 Hz, H$^{4''}$), 7.30-7.20 (m, 12H, H$^{2''}$, H$^{4'}$ and H$^{6'}$), 7.17-7.08 (m, 18H, H^8, H^{12} and H$^{3''}$), 7.10 (dm, 2H, H$^{3'}$), 6.95 (d, 8H, J = 9.2 Hz, H^{11}), 6.84 (d, 4H, J = 8.8 Hz, H^{10}), 3.81(s, 12H, OCH$_3$), 2.29 (s, 6H, CH$_3$) ppm.

^{13}C-NMR (100 MHz, acetone-d$_6$, 25 ºC): δ = 159.30, 159.05, 157.87, 154.04, 151.01, 149.26, 140.82, 136.26, 134.52, 134.13, 134.05, 133.97, 133.18, 133.11, 132.96, 132.80, 130.81, 129.58, 129.31, 128.37, 126.40, 126.13, 123.14, 122.20, 120.99, 119.51, 117.89, 115.84, 55.81, 26.81 ppm.

HR-MS (ESI+): m/z =1443.47375, calculated for [M-PF$_6$]$^+$=1443.47380.

Elemental analysis: Calculated for $C_{92}H_{78}CuF_6N_4O_5P_3 \cdot 0.90\ CH_2Cl_2 \cdot 0.15\ H_2O$: C, 66.85; H, 4.84; N, 3.36. Found: C, 66.95; H, 4.95; N, 3.24.

[Cu(L1)(L9)]PF₆ (C11)
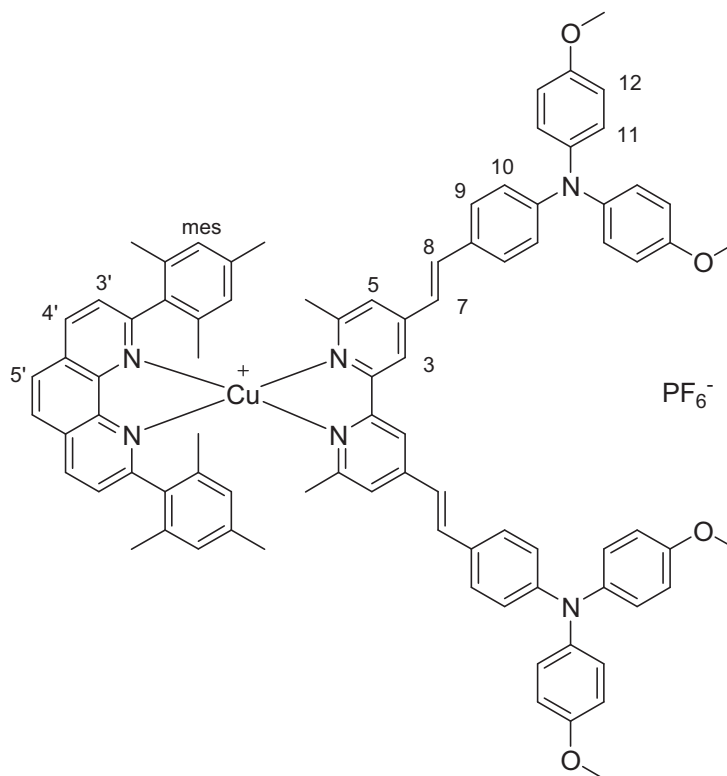
[Cu(MeCN)₄]PF₆ (10 mg, 0.027 mmol) and **L1** (13 mg, 0.032 mmol) were stirred in 8 mL of dry and degassed dichloromethane at room temperature for 15 minutes, then 5 mL of a degassed solution of **L9** (22 mg, 0.026 mmol) in dichloromethane were injected under Ar and the resulting deep red solution was stirred for further 30 minutes at room temperature. The solvent was removed under reduced pressure and the resulting red solid was purified by column chromatography on silica gel (CH₂Cl₂: CH₃OH = 98: 2 → 96: 4) to afford 26 mg (68%) of pure **C11**.

¹H-NMR (300 MHz, CDCl₃, 25 °C): δ = 8.67 (d, 2H, J = 8.4 Hz, H⁴'), 8.20 (s, 2H, H³'), 7.81 (d, 2H, J = 8.1 Hz, H⁵'), 7.78 (sb, 2H, H³), 7.44 (d, 4H, J = 9.0 Hz, H⁹), 7.38 (d, 2H, J = 16.2 Hz, H⁷), 7.22 (sb, 2H, H⁵), 7.10 (d, 8H, J = 9.0 Hz, H¹²), 6.97 (d, 2H, J = 16.2 Hz, H⁸), 6.92 (d, 4H, J = 8.7 Hz, H¹⁰), 6.86 (d, 8H, J = 9.0 Hz, H¹¹), 6.41 (s, 4H, H^Mes), 3.82 (s, 12H, OCH₃), 1.99 (s, 6H, CH₃), 1.91 (s, 6H, CH₃^Mes), 1.69 (s, 12H, CH₃^Mes) ppm.

HR-MS (MALDI): m/z = 1321.5351, calculated for [M-PF₆]⁺ =1321.5375.

Elemental analysis: Calculated for $C_{86}H_{78}CuF_6N_6O_4P \cdot 0.75\ CH_2Cl_2 \cdot 0.05\ H_2O$: C, 67.98; H, 5.23; N, 5.48. Found: C, 67.98; H, 5.21; N, 5.49.

***[Cu(L1)(L10)]PF₆* (C12)**
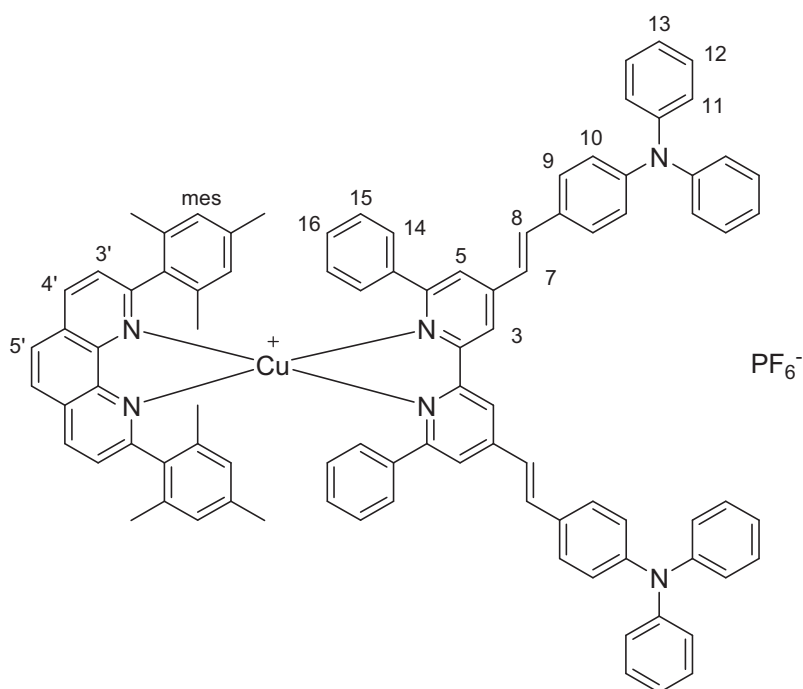
[Cu(MeCN)₄]PF₆ (8 mg, 0.021 mmol) and **L1** (11 mg, 0.026 mmol) were stirred in 5 mL of distilled dichloromethane at room temperature for 15 minutes under Ar atmosphere, then 3 mL of a degassed solution of **L10** (17 mg, 0.020 mmol) in dichloromethane were injected under Ar and the resulting red solution was stirred for further 30 minutes at room temperature. The solvent was removed under reduced pressure and the resulting red-orange solid was purified by size exclusion chromatography on Sephadex LH20 (acetone) to afford 26 mg (87%) of pure **C12**. Use of silica gel was avoided because the complex seemed to degrade on TLC with release of ligand **L10**.

¹H-NMR (300 MHz, acetone-d₆, 25 ºC): δ = 8.80 (d, 2H, J = 8.4 Hz, H$^{4'}$), 8.55 (s, 2H, H^3), 8.28 (s, 2H, H$^{5'}$), 7.89 (d, 2H, J = 16.5 Hz, H^7), 7.82 (m, 4H, H$^{3'}$ and H^5), 7.64 (d, 4H, J = 8.4 Hz, H^9), 7.40-7.32 (m, 14H, H^8, H^{12} and H^{14}), 7.15-7.12 (m, 12H, H^{11} and H^{15}), 7.04 (db, 6H, H^{10} and H^{16}), 6.77 (t, 4H, J = 7.8 Hz, H^{13}), 6.49 (s, 4H, H^{Mes}), 2.09 (s, 6H partially superposed to the solvent peak, CH₃^{Mes}), 1.42 (s, 12H, CH₃^{Mes}) ppm.

¹³C-NMR (75 MHz, acetone-d₆, 25 ºC): δ = 160.60, 158.67, 155.61, 149.80, 148.30, 148.08, 145.07, 139.55, 138.84, 138.69, 137.40, 135.98, 135.83, 130.67, 130.46, 129.64, 129.39, 129.07, 128.50, 128.18, 125.97, 124.78, 123.65, 123.50, 122.95, 120.07, 21.15, 20.42 ppm.

HR-MS (MALDI): m/z = 1325.4243, calculated for [M-PF₆]$^+$ = 1325.5265.

Elemental analysis: calculated for C₉₂H₇₄CuF₆N₆P ·0.55 CH₂Cl₂ ·0.05 H₂O: C, 73.14 ; H, 5.02 ; N, 5.53. Found: C, 73.06; H, 5.02; N, 5.62.

[Cu(L1)(L11)]PF₆ (C13)
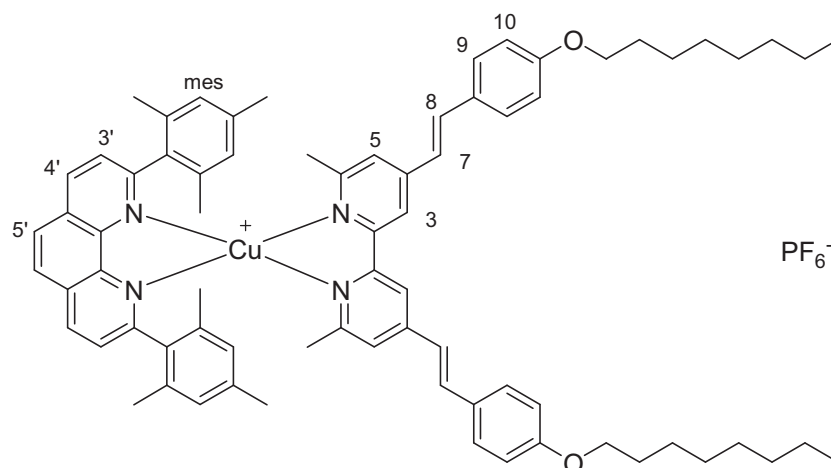
[Cu(MeCN)₄]PF₆ (17 mg, 0.045 mmol) and **L1** (21 mg, 0.051 mmol) were stirred in 4 mL of dry and degassed dichloromethane at room temperature for 15 minutes, then 4 mL of a degassed solution of **L11** (25 mg, 0.040 mmol) in dichloromethane were injected under Ar and the resulting deep red solution was stirred for further 30 minutes at room temperature. The solvent was removed under reduced pressure and the resulting red solid was purified by column chromatography on silica gel (CH₂Cl₂: CH₃OH = 98: 2) to afford 42 mg (83%) of pure **C13**.

^{1}H-NMR (300 MHz, acetone-d_6, 25 ºC): δ = 8.97 (d, 2H, J = 8.2 Hz, $H^{4'}$), 8.41 (s, 2H, $H^{5'}$), 8.28 (sb, 2H, H^3), 8.04 (d, 2H, J = 8.2 Hz, $H^{3'}$), 7.72-7.64 (m, 6H, H^7 and H^9), 7.50 (s, 2H, H^5), 7.18 (d, 2H, J = 16.3 Hz, H^8), 7.03 (d, 4H, J = 8.6 Hz, H^{10}), 6.48 (s, 4H, H^{Mes}), 4.07 (t, 4H, J = 6.5 Hz, OCH_2), 1.99 (s, 6H, CH_3^{Mes}), 1.85-1.73 (m, 16H, CH_3^{Mes} and CH_2^{nOct}), 1.53-1.45 (m, 4H, CH_2^{nOct}), 1.41-1.28 (m, 16H, 4 CH_2^{nOct}), 0.89 (t, 6H, J = 6.9 Hz, CH_3^{nOct}) ppm.

^{13}C-NMR (75 MHz, acetone-d_6, 25 ºC): δ = 161.18, 160.35, 157.44, 153.16, 147.86, 144.83, 138.89, 138.61, 137.88, 135.65, 135.40, 129.73, 129.65, 129.27, 128.45, 128.19, 127.93, 123.67, 122.72, 116.98, 115.87, 68.82, 32.57, 26.77, 25.92, 23.31, 21.08, 20.29, 14.34 ppm.

HR-MS (MALDI): m/z = 1123.5914, calculated for [M-PF₆]⁺=1123.5885.

Elemental analysis: Calculated for $C_{74}H_{84}CuF_6N_4O_2P \cdot 1.9\ H_2O$: C, 68.15; H, 6.79; N, 4.30. Found: C, 67.83; H, 6.45; N, 4.25.

Chapter 4 – Photoinduced charge transfer with heteroleptic copper(I) diimine complexes

Phen (1,10-phenanthroline) and **dmp** (2,9-dimethyl-1,10-phenanthroline or neocuproine) were purchased by Aldrich and used without further purification. N-octyl-1,4,5,8-naphthalenetetracarboxylic monoanhydride **17**,[14] 2,9-dimethyl-5-nitro-1,10-phenanthroline **23**,[15] 2,9-dimethyl-5-amino-1,10-phenanthroline **24**,[16] 2-(4-nitrophenyl)-5,5-dimethyl-1,3-dioxane (**18**),[17] 2-(4-aminophenyl)-5,5-dimethyl-1,3-dioxane (**19**),[17] N,N-dioctylnaphthalene-1,4,5,8-tetracarboxylic acid bisimide **NDI**[18] were prepared as described previously.

### 2,9-dibutyl-1,10-phenanthroline-[a:b]imidazo-(4'-nitrophenyl) (14)
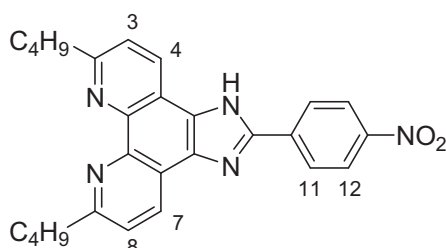
8 (242 mg, 0.75 mmol), 4-nitrobenzaldehyde (130 mg, 0.86 mmol) and NH_4OAc (1.227 g, 15.9 mmol) were dissolved in 25 mL of glacial acetic acid, and the solution was refluxed for 6 hours. After cooling to room temperature, water was added and the brown precipitate was collected by filtration, washed with water and allowed to dry (252 mg, 74% yield of crude product).

Due to difficulty in the purification, the crude product was used for the following step.

^{1}H-NMR (300 MHz, DMSO-d_6): δ = 13.94 (s, 1H, NH^{Imi}), 8.77 (d broad, 1H, H^7), 8.53-8.31 (m, 5H, H^4, H^{11} and H^{12}), 7.78-7.65 (m, 2H, H^3 and H^8), 3.04 (t broad, 4H, CH$_2^{nBu}$), 1.81 (m, 4H, CH$_2^{nBu}$), 1.45 (m, 4H, CH$_2^{nBu}$), 0.96 (t, 6H, J = 8 Hz, CH$_3^{nBu}$) ppm.

MS (CI, NH$_3$): 454 (MH$^+$)

N-hexyl-2,9-dibutyl-1,10-phenanthroline-[a:b]imidazo-(4'-nitrophenyl) (15)
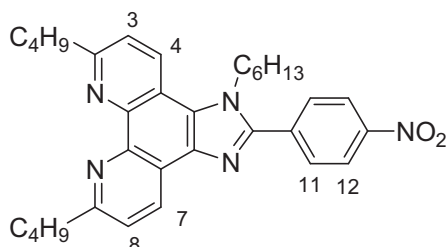
Crude **14** (250 mg, ~0.55 mmol) and Cs_2CO_3 (1.089 g, 3.34 mmol) were added to 20 mL of dry N,N-dimethylformamide in dry glassware, and the mixture was heated to 100 ºC for 40 minutes. 1-iodohexane (0.25 mL, 1.69 mmol) was injected and the mixture was stirred at 100 ºC for 14 hours under Ar atmosphere. The solution was then allowed to cool to room temperature and 100 mL of water were added. The precipitate was collected by filtration and washed with water, then dissolved in dichloromethane and dried over $MgSO_4$. The solvent was removed under reduced pressure and the crude product was purified by column chromatography on neutral alumina (eluant CH_2Cl_2: petroleum ether = 70: 30) to afford 99 mg (30% yield on the two steps) of pure product.

¹H-NMR (300 MHz, CDCl$_3$): δ = 8.95 (d, 1H, J = 8.1 Hz, H^7), 8.50-8.44 (m, 3H, H^4 and H^{12}), 7.97 (d, 2H, J = 8.7 Hz, H^{11}), 7.65-7.61 (m, 2H, H^3 and H^8), 4.61 (t broad, 2H, J = 7.2 Hz, CH$_2$^{nHex}), 3.26 (t broad, 4H, CH$_2$^{nBu}), 1.97-1.91 (m, 6H, CH$_2$^{nHex} + CH$_2$^{nBu}), 1.60-1.52 (m, 4H, CH$_2$^{nBu}), 1.25-1.20 (m, 6H, 3 CH$_2$^{nHex}), 1.06-1.00 (m, 6H, CH$_3$^{nBu}), 0.81 (t, 3H, J = 6.8 Hz, CH$_3$^{nHex}) ppm.

¹³C-NMR (75 MHz, CDCl$_3$): δ = 162.27, 161.28, 150.88, 148.52, 137.09, 136.94, 130.95, 128.66, 125.55, 124.18, 123.21, 122.25, 122.15, 118.00, 47.26, 39.11, 38.96, 32.01, 31.93, 31.88, 31.13, 30.35, 26.14, 23.03, 22.51, 14.20, 13.93 ppm.

HR-MS (ESI+): m/z = 538.3157, calculated for MH$^+$ m/z = 538.3177.

### *N-hexyl-2,9-dibutyl-1,10-phenanthroline-[a:b]imidazo-(4'-aminophenyl)* (16)
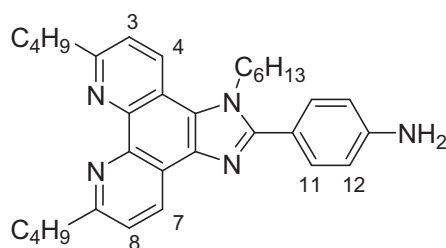
15 (60 mg, 0.11 mmol) was suspended in 9 mL of ethanol and the mixture was degassed and heated to reflux. Pd/C 10% (15 mg) was added and the mixture was stirred for 1h before injecting 0.11 mL of hydrazine hydrate (2.2 mmol). After 2 hours the reactant had disappeared, the heating was removed and the mixture was filtered on Celite to remove Pd/C. The solvent was removed and the obtained solid was dissolved in CH$_2$Cl$_2$ and washed with water, then dried on MgSO$_4$. Removal of the solvent afforded pure **16** (58 mg, quantitative) as a yellow solid.

¹H-NMR (300 MHz, CDCl$_3$): δ = 8.96 (d, 1H, J = 8.4 Hz, H$_7$), 8.44 (d, 1H, J = 8.4 Hz, H$_4$), 7.59-7.53 (m, 2H, H$_3$ and H$_8$), 7.47 (d, 2H, J = 8.1 Hz, H$_{11}$), 6.80 (d, 2H, J = 8.4 Hz, H$_{12}$), 4.52 (t, 2H, J = 7.2 Hz, N-CH$_2$), 3.22-3.17 (m, 4H, 2 CH$_{2, nBu}$), 2.00-1.82 (m, 6H, 2 CH$_{2, nBu}$, CH$_{2, nHex}$), 1.55-1.47 (m, 4H, 2 CH$_{2, nBu}$), 1.28-1.17 (m, 6H, 3 CH$_{2, nHex}$), 1.02-0.96 (m, 6H, 2 CH$_{3, nBu}$), 0.82 (m, 3H, CH$_{3, nHex}$) ppm.

¹³C-NMR (75 MHz, CDCl$_3$): δ = 161.61, 160.40, 154.12, 147.99, 136.10, 131.21, 130.97, 130.63, 128.48, 124.52, 122.91, 122.30, 121.88, 120.15, 118.23, 115.03, 114.88, 46.85, 39.07, 32.01, 31.17, 30.29, 29.82, 26.16, 23.05, 22.82, 22.56, 14.21, 13.99 ppm.

HR-MS (MALDI+): m/z = 508.3451, calculated for MH$^+$ m/z = 508.3435.

N-octyl-N'-(4'-dioxolanephenyl)naphthalene-1,4,5,8-tetracarboxylic acid diimide (20)
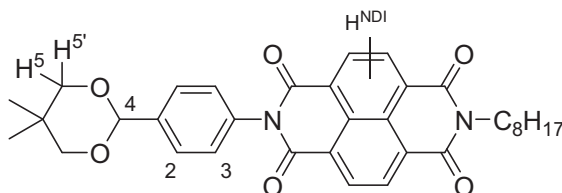
19 (164 mg, 0.79 mmol), N-octylnaphthalene diimide **17** (136 mg, 0.36 mmol), imidazole (2.57 g) and Zn(OAc)$_2$ (22 mg, 0.10 mmol) were heated to 140 ºC under stirring, then allowed to cool to room temperature and dissolved in dichloromethane. The solution was washed twice with HCl 1M, then with water and brine, dried on MgSO$_4$ and evaporated. The crude product was chromatographied on neutral alumina (eluted with dichloromethane) to obtain **20** as a pale pink powder (79 mg, 39%).

^{1}H-NMR (300 MHz, CDCl$_3$): δ = 8.75 (s, 4H, H^{NDI}), 7.69 (d, 2H, J = 8.4 Hz, H^2), 7.32 (d, 2H, J = 8.4 Hz, H^3), 5.48 (s, 1H, H^4), 4.18 (t broad, 2H, J = 7.6 Hz, NCH$_2$^{nOct}), 3.80 (d, 2H, J = 11.1 Hz, H^5), 3.68 (d, 2H, J = 10.9 Hz, H$^{5'}$), 1.73 (m, 2H, CH$_2$^{nOct}), 1.45-1.22 (m, 13H, 5 CH$_2$^{nOct} and CH$_3$), 0.87 (t, 3H, J = 7.0 Hz, CH$_3$^{nOct}), 0.82 (s, 3H, CH$_3$) ppm.

^{13}C-NMR (75 MHz, CDCl$_3$): δ = 162.92, 162.81, 139.51, 134.96, 131.37, 131.06, 128.47, 127.46, 127.05, 126.91, 126.76, 100.97, 77.73, 41.11, 31.88, 30.36, 29.37, 29.28, 28.16, 27.18, 23.15, 22.73, 22.00, 14.20 ppm.

HR-MS (ESI+): m/z = 569.26544, calculated for MH$^+$ m/z = 569.26461.

N-octyl-N'-(4'-formylphenyl)naphthalene-1,4,5,8-tetracarboxylic acid diimide (21)
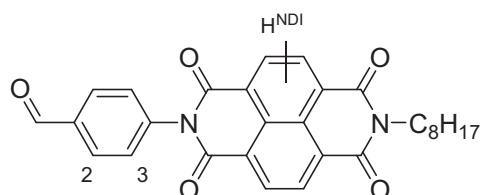

20 was dissolved in 5 mL CHCl$_3$, and 2.5 mL of trifluoroacetic acid were added. After 1 hour stirring at room temperature, 1 mL of H$_2$SO$_4$ 20% was added and the mixture was further stirred for 4 hours. Water was added and the solvents were evaporated under reduced pressure. The suspension was then extracted three times with dichloromethane; the organic phase was washed with NaHCO$_3$, dried on MgSO$_4$, filtered and evaporated to give pure **21** (70 mg, quantitative).

^{1}H-NMR (300 MHz, CDCl$_3$): δ = 10.14 (s, 1H, CHO), 8.82 (s, 4H, H^{NDI}), 8.11 (d, 2H, J = 8.5 Hz, H^2), 7.54 (d, 2H, J = 8.3 Hz, H^3), 4.22 (t broad, 2H, J = 7.3 Hz, NCH$_2$^{nOct}), 1.76 (m, 2H, CH$_2$^{nOct}), 1.48-1.25 (m, 13H, 5 CH$_2$^{nOct}), 0.88 (t, 3H, J = 6.9 Hz, CH$_3$^{nOct}) ppm.

^{13}C-NMR (75 MHz, CDCl$_3$): δ = 191.30, 162.88, 162.79, 140.06, 136.77, 131.70, 131.20, 130.88, 129.78, 127.39, 127.23, 127.01, 126.45, 41.27, 31.94, 29.42, 29.33, 28.23, 27.23, 22.78, 14.23 ppm.

HR-MS (ESI+): m/z = 483.19208, calculated for MH$^+$ m/z = 483.19145.

2,9-dibutyl-1,10-phenanthroline-[a:b]imidazo-(4'-(N-octylnaphthalenediimide)phenyl) (22)
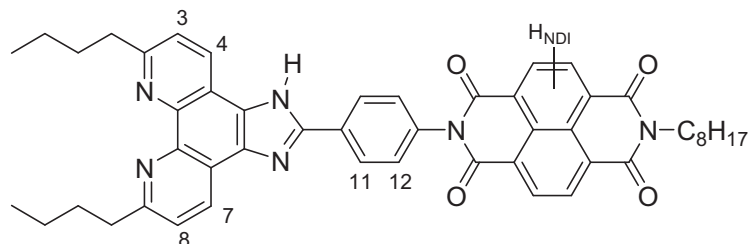
The reaction was performed in anhydrous conditions to avoid the formation of the oxazole. **21** (128 mg, 0.27 mmol), 2,9-dibutyl-1,10-phenanthroline-5,6-dione **8** (85 mg, 0.27 mmol) and NH$_4$OAc (451 mg, 5.85 mmol) sublimated before use were dissolved in 8 mL of distilled chloroform under Ar, and 1.5 mL of distilled acetic acid were injected. The solution was refluxed for 4 hours under Ar, then allowed to cool to room temperature. Water was added and the layers were separated, the organic phase was washed twice with water and then with brine, dried on Na$_2$SO$_4$, filtered and evaporated to give crude **22** (168 mg) which was directly engaged in the following step without further purification.

MS (CI-): m/z = 784.80, calculated for M$^{•-}$ m/z = 784.94.

N-hexyl-2,9-dibutyl-1,10-phenanthroline-[a:b]imidazo-(4'-(N-octylnaphthalenebisimide)phenyl) (L12^{Imi})
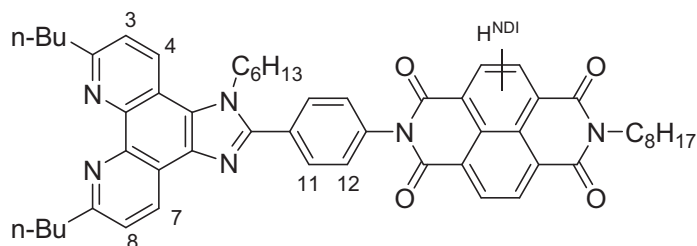
Method 1: **16** (21 mg, 4.04 10^{-2} mmol) and **17** (78 mg, 0.21 mmol) were put in a MW tube and 2 mL of dry DMF are added. The mixture was sonicated and degassed by Ar bubbling for 5 min, then heated to 120 ºC by microwave irradiation for 15 min (maximum power: 300 W). The suspension was diluted with CH$_2$Cl$_2$ and washed twice with water, then the organic solvent was removed and the obtained brown solid purified by Sephadex LH20 in CH$_2$Cl$_2$: CH$_3$OH = 60: 40. **L14^{Imi}** was obtained as a brown solid (27 mg, 77%).

Method 2: **22** (168 mg, 0.21 mmol) was dissolved in 14 mL of dry N,N-dimethylformamide and injected under Ar into a dry flask containing Cs$_2$CO$_3$ (323 mg, 0.90 mmol). The mixture was heated to 100 ºC and after 1 hour hexyl iodide (0.25 mL, 1.69 mmol) was added. The mixture was stirred for 3 hours at 100 ºC, then allowed to cool to room temperature. The solvent was removed under reduced pressure and the crude product was purified several times by column chromatography on silica gel (eluant CH$_2$Cl$_2$: CH$_3$OH = 99.5: 0.5) to obtain pure **L14^{Imi}** (63 mg, 29% on the two steps of imidazole formation and alkylation).

^{1}H-NMR (400 MHz, CDCl$_3$): δ = 8.95 (d, 1H, J = 8.3 Hz, H^7), 8.84-8.79 (m, 4H, H^{NDI}), 8.49 (d, J = 8.7 Hz, 1H, H^4), 7.95 (d, 2H, J = 8.5 Hz, H^{12}), 7.61 (d, 2H, J = 8.4 Hz, H^3 and H^8), 7.56 (d, 2H, J = 8.4 Hz, H^{11}), 4.67 (t broad, 2H, J = 6.9 Hz, N-CH$_2$^{nHex}), 4.22 (t broad, 2H, J = 7.6 Hz, N-CH$_2$^{nOct}), 3.24 (m, 4H, CH$_2$^{nBu}), 2.03-1.90 (m, 6H, CH$_2$^{nBu} and CH$_2$^{nHex}), 1.81-1.72 (m, 2H, CH$_2$^{nOct}), 1.70-1.25 (m, nH, CH$_2$^{nBu}, 3 CH$_2$^{nHex} and 5 CH$_2$^{nOct}), 1.07-1.00 (m, 6H, 2 CH$_3$^{nBu}), 0.88-0.84 (m, 6H, CH$_3$^{nHex} and CH$_3$^{nOct}) ppm.

^{13}C-NMR (100 MHz, CDCl$_3$): δ = 186.86, 163.03, 162.86, 161.95, 160.82, 152.39, 144.38, 143.58, 136.72, 136.05, 131.74, 131.58, 131.17, 131.06, 130.69, 129.46, 128.52, 127.29, 127.25, 127.04, 126.70, 125.06, 122.99, 122.39, 121.86, 118.20, 47.16, 41.27, 39.30, 39.07, 31.99, 31.96, 31.89, 31.27, 30.49, 29.44, 29.34, 28.26, 27.26, 26.22, 23.10, 22.78, 22.59, 14.24, 14.00 ppm.

HR-MS (MALDI+): m/z = 869.4767, calculated for MH$^+$ m/z = 869.4749.

N-hexyl-2,9-dibutyl-1,10-phenanthroline-[a:b]oxazo-(4'-(N-octylnaphthalenebisimide)phenyl) (L12^{Oxa})
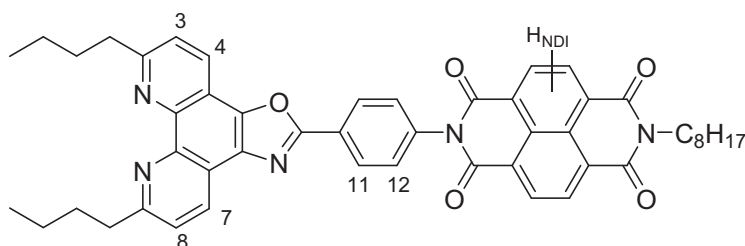
8 (40 mg, 0.13 mmol), **21** (60 mg, 0.13 mmol) and NH$_4$OAc (194 mg, 2.52 mmol) were dissolved in 5 mL CHCl$_3$ and 0.2 mL of acetic acid were added. The solution was stirred at reflux for 4 ½ hours. After cooling to room temperature, water was added and the mixture was extracted three times with CH$_2$Cl$_2$. The organic phase was washed with water and brine, and the solvent was

removed under reduced pressure. The crude product was purified on alumina gel (CH_2Cl_2) and **L12^{Oxa}** (40 mg, 41%) was obtained as the majoritary product, with some **22** (19 mg, 19%) in lower yield.

^{1}H-NMR (500 MHz, CDCl$_3$): δ = 8.86 (d, 1H, J = 8.3 Hz, H^7), 8.85-8.82 (m, 4H, H^{NDI}), 8.61 (d, 1H, J = 8.3 Hz, H^4), 8.57 (d, 2H, J = 8.6 Hz, H^{12}), 7.66 (t, 2H, J = 8.2 Hz, H^3 and H^8, two merged doublets), 7.56 (d, 2H, J = 8.6 Hz, H^{11}), 4.23 (t broad, 2H, J = 7.6 Hz, NCH$_2$^{nOct}), 3.28-3.24 (m, 4H, 2 CH$_2$^{nBu}), 1.97 (m, 4H, 2 CH$_2$^{nBu}), 1.78 (m, 2H, CH$_2$^{nOct}), 1.55 (m, 4H, 2 CH$_2$^{nOct}), 1.49-1.43 (m, 2H, CH$_2$^{nOct}), 1.42-1.35 (m, 2H, CH$_2$^{nOct}), 1.34-1.25 (m, 6H, 3 CH$_2$^{nOct}), 1.04 (t, 6H, J = 7.4 Hz, 2 CH$_3$^{nBu}), 0.89 (t, 3H, J = 7.0 Hz, CH$_3$^{nOct}) ppm.

^{13}C-NMR (125 MHz, CDCl$_3$): 163.20, 163.06, 162.87, 162.34, 144.50, 144.43, 143.73, 137.19, 134.57, 131.69, 131.22, 131.07, 129.61, 128.97, 128.46, 128.30, 127.38, 127.29, 127.08, 126.67, 123.05, 122.82, 121.23, 116.21, 53.56, 41.29, 39.50, 39.43, 32.00, 31.96, 29.45, 29.35, 28.27, 27.26, 23.07, 23.06, 22.79, 14.23 ppm.

HR-MS (MALDI+): m/z = 785.3526, calculated for M$^+$ m/z = 785.3572.

### *2,9-dimethyl-5-(N-octylnaphthalenediimide)-1,10-phenanthroline* (L13)
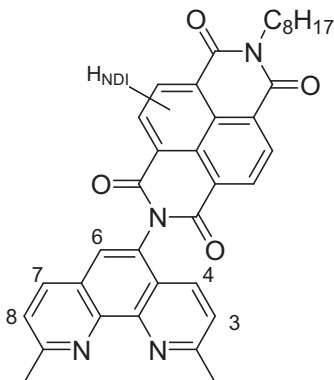
To degassed **24** (122 mg, 0.55 mmol) and **17** (263 mg, 0.69 mmol), 3.5 mL of dry DMF were added under Ar. The dark mixture was stirred at 120 ºC for 14 hours, then allowed to cool to room temperature. EtOH was added and the precipitate was collected by filtration. The sticky solid was then dissolved in CH_2Cl_2 and adsorbed on SiO_2, then purified by column chromatography on silica gel (eluant CH_2Cl_2) to obtain pure **L13** (74 mg, 23%).

^{1}H-NMR (300 MHz, CDCl$_3$): δ = 8.84 (s, 4H, H^{NDI}), 8.16 (d, 1H, J = 8.2 Hz, H^4), 7.87 (d, 1H, J = 8.4 Hz, H^7), 7.80 (s, 1H, H^6), 7.56 (d, 1H, J = 8.2 Hz, H^3), 7.45 (d, 1H, J = 8.4 Hz, H^8), 4.23 (t, 2H, J = 7.7 Hz, N-CH$_2$^{nOct}), 2.99 (s, 3H, CH$_3$), 2.95 (s, 3H, CH$_3$), 1.68-1.78 (m, 2H, CH$_2$^{nOct}), 1.50-1.20 (m, 10H, 5 CH$_2$^{nOct}), 0.90 (t, 3H, J = 6.9 Hz, CH$_3$^{nOct}) ppm.

^{13}C-NMR (75 MHz, CDCl$_3$): δ = 163.20, 162.77, 160.92, 160.20, 146.28, 145.73, 136.77, 131.86, 131.26, 130.74, 129.09, 127.46, 127.25, 127.11, 126.55, 126.45, 126.08, 124.13, 123.89, 41.26, 31.92, 29.40, 29.32, 28.22, 27.21, 26.18, 25.98, 22.76, 14.20 ppm.

HR-MS (MALDI+): m/z = 585.2512, calculated for MH$^+$ m/z = 585.2496.
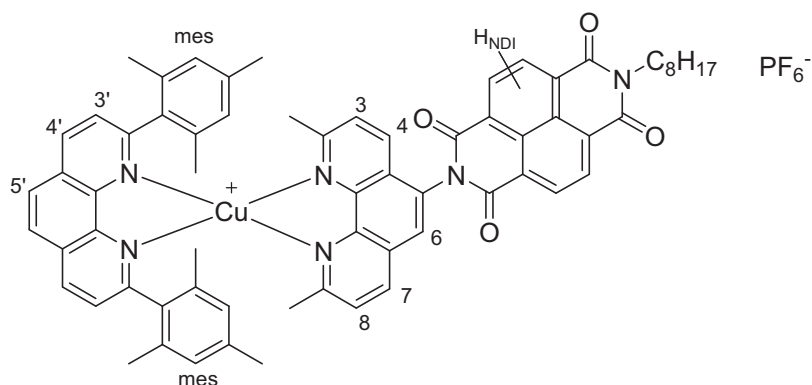
[Cu(L1)(L12^{Imi})]PF$_6$ (C14^{Imi})
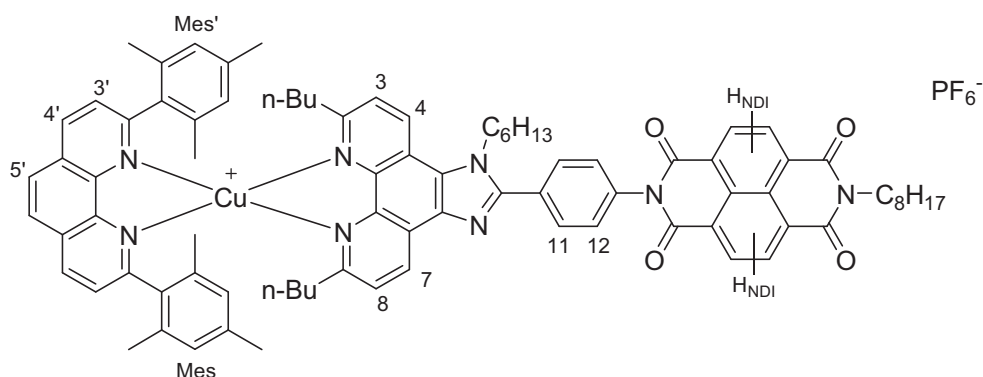
L1 (16 mg, 3.8 10^{-2} mmol) and [Cu(CH$_3$CN)$_4$]PF$_6$ (14 mg, 3.8 10^{-2} mmol) were degassed with Ar in a dry round-bottomed flask. 7 mL of dry CH$_2$Cl$_2$ were injected under Ar and the yellow solution was stirred at room temperature for 20 minutes. **L12^{Imi}** (27 mg, 3.2 10^{-2} mmol) was dissolved in 4 mL of distilled CH$_2$Cl$_2$ and degassed by Ar bubbling for 5 min, then injected dropwise into the stirring solution: the colour changed to orange. After 30 minutes the solution was turbid, so 0.5 mL of acetone were added to increase solubility. The solution was stirred for 30 more minutes before removing the solvent. The crude product was purified by preparative thin layer chromatography and afforded **C14^{Imi}** (15 mg, 29%) as an orange solid.

^{1}H-NMR (500 MHz, CDCl$_3$): δ = 9.04 (d, 1H, J = 8.4 Hz, H^7), 8.88-8.82 (m, 4H, H^{NDI}), 8.80 (d, 1H, J = 8.8 Hz, H^4), 8.70 (d, 2H, J = 8.3 Hz, H$^{4'}$), 8.24 (s, 2H, H$^{5'}$), 7.99 (d, 2H, J = 8.4 Hz, H^{12}), 7.79 (d, 2H, J = 8.2 Hz, H$^{3'}$), 7.73 (d, 1H, J = 8.7 Hz, H^3), 7.61 (d, 2H, J = 8.3 Hz, H^{11}), 7.59 (d, 2H, J = 8.4 Hz, H^8), 6.28 (s, 2H, H^{Mes}), 6.10 (s, 2H, H$^{Mes'}$), 4.86 (t broad, 2H, J = 7.1 Hz, N-CH$_2$^{nHex}), 4.23 (t broad, 2H, J = 7.6 Hz, N-CH$_2$^{nOct}), 2.50 (m, 2H, CH$_2$^{nBu}), 2.20 (m, 2H, CH$_2$$^{nBu'}$), 1.99 (m, 2H, CH$_2$^{nHex}), 1.86 (s, 6H, CH$_3$^{Mes} and CH$_3$$^{Mes'}$), 1.79 (m, 2H, CH$_2$^{nOct}), 1.68 (s, 6H, 2 CH$_3$^{Mes}), 1.51 (s, 6H, 2 CH$_3$$^{Mes'}$), 1.46-1.36 (m, 6H, 2 CH$_2$^{nBu} and CH$_2$^{nHex}), 1.36-1.24 (m, 14H, 2 CH$_2$^{nHex} and 5 CH$_2$^{nOct}), 1.05 (m, 4H, 2 CH$_2$^{nBu}), 0.89 (t, 3H, J = 7.0 Hz, CH$_3$^{nHex}), 0.85 (t, 3H, J = 6.8 Hz, CH$_3$^{nBu}), 0.80 (t, 3H, J = 7.3 Hz, CH$_3$^{nBu}), 0.55 (t, 3H, J = 7.4 Hz, CH$_3$^{nOct}) ppm.

^{13}C-NMR (125 MHz, CDCl$_3$): δ = 163.03, 162.90, 160.00, 158.92, 158.67, 153.94, 144.43, 141.37, 141.12, 138.25, 137.74, 136.52, 136.43, 136.33, 134.77, 131.67, 131.23, 131.09, 130.27, 129.74, 128.47, 127.61, 127.57, 127.54, 127.35, 127.32, 127.25, 127.09, 126.74, 125.11, 124.05, 123.05, 123.01, 119.22, 53.56, 47.23, 41.29, 39.84, 39.05, 31.96, 31.33, 30.70, 30.52, 30.38, 29.85, 29.45, 29.35, 28.27, 27.27, 26.06, 22.95, 22.79, 22.71, 22.63, 20.86, 20.40, 19.94, 14.23, 14.18, 14.02, 13.72 ppm.

HR-MS (MALDI+): m/z = 1347.6264, calculated for (M-PF$_6$)$^+$ m/z = 1347.6219.
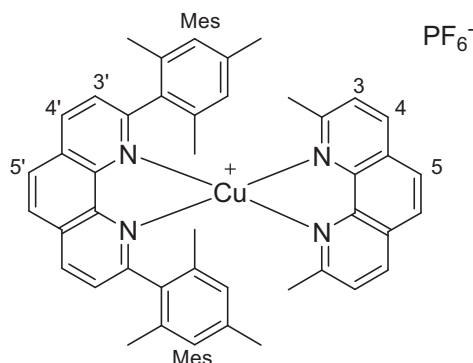
[Cu(L1)(L13)]PF$_6$ (C15)

L1 (19 mg, 4.6 10^{-2} mmol) and [Cu(CH$_3$CN)$_4$]PF$_6$ (15 mg, 3.9 10^{-2} mmol) were degassed with Ar in a dry round-bottomed flask. 5 mL of dry CH$_2$Cl$_2$ were injected under Ar and the yellow solution was stirred at room temperature for 20 minutes. **L13** (17 mg, 3.2 10^{-2} mmol) was dissolved in a mixture of 12 mL of distilled CH$_2$Cl$_2$ and 1 mL distilled CH$_3$OH and degassed by Ar bubbling for 5 min, then injected dropwise into the stirring solution: the colour changed to red. The solution was stirred at room temperature for 40 minutes and the solvents were removed. The crude product was purified by column chromatography on silica gel (eluant CH$_2$Cl$_2$: CH$_3$OH = 99:1), and by precipitation with petroleum ether from a dichloromethane solution. The pure **C15** (19 mg, 55%) was obtained as a red solid.

^{1}H-NMR (300 MHz, CDCl$_3$): δ = 8.85 (m, 4H, H^{NDI}), 8.70 (d, 2H, J = 8.2 Hz, H$^{4'}$), 8.29 (d, 1H, J = 8.4 Hz, H^4), 8.22 (s, 2H, H$^{5'}$), 8.09 (d, 1H, J = 8.5 Hz, H^7), 7.90 (s, 1H, H^6), 7.80 (d, 2H, J = 8.3 Hz, H$^{3'}$), 7.63 (d, 1H, J = 8.3 Hz, H^3), 7.49 (d, 1H, J = 8.6 Hz, H^8), 6.36 (s, 4H, H^{mes}), 4.22 (t broad, 2H, J = 7.6 Hz, NCH$_2$^{nOct}), 2.48 (s, 3H, CH$_3$), 1.96 (s, 3H, CH$_3$), 1.93 (s, 6H, 2 CH$_3$^{mes}), 1.77 (m, 8H, 2 CH$_3$^{mes} and CH$_2$^{nOct}), 1.50-1.20 (m, 16H, 2 CH$_3$^{Mes} and 5 CH$_2$^{nOct}), 0.89 (t broad, 3H, CH$_3$^{nOct}) ppm.

^{13}C-NMR (75 MHz, CDCl$_3$): δ = 163.36, 162.87, 160.03, 157.83, 144.09, 143.78, 142.92, 138.43, 137.90, 136.64, 136.42, 134.57, 134.44, 132.22, 131.95, 131.19, 130.16, 128.25, 128.05, 127.57, 127.16, 126.85, 126.43, 125.94, 125.46, 124.86, 41.27, 31.94, 29.83, 29.43, 29.35, 28.23, 27.53, 27.26, 25.14, 22.78, 20.85, 20.37, 19.51, 14.24 ppm.

HR-MS (MALDI+): m/z = 1063.3953, calculated for (M-PF$_6$)$^+$ m/z = 1063.3967.
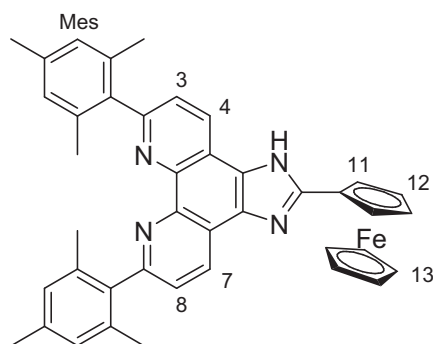

[Cu(L1)(dmp)]PF$_6$ (C18)

L1 (41 mg, 9.8 10^{-2} mmol) and [Cu(CH$_3$CN)$_4$]PF$_6$ (34 mg, 9.0 10^{-2} mmol) were dissolved in 9 mL of dry degassed dichloromethane under Ar and the yellow solution was stirred for 20 minutes at room temperature. **Dmp** (neocuproine, 18 mg, 8.6 10^{-2} mmol) was dissolved in 3.5 mL of dry dichloromethane and degassed for 5 minutes by Ar bubbling, then injected into the yellow solution that immediately turned red. After 40 minutes the solvent was removed under reduced pressure, and the crude product was purified by column chromatography on silica gel (eluant CH$_2$Cl$_2$: CH$_3$OH = 99: 1). The red solid was further crystallized by diffusion of diethyl ether vapours in a dichloromethane solution of the complex, to give pure **C18** (50 mg, 61%).

^{1}H-NMR (300 MHz, CDCl$_3$): δ = 8.69 (d, 2H, J = 8.2 Hz, H$^{4'}$), 8.28 (d, 2H, J = 8.3 Hz, H^4), 8.23 (s, 2H, H$^{5'}$), 7.81 (s, 2H, H^5), 7.78 (d, 2H, J = 8.4 Hz, H$^{3'}$), 7.54 (d, 2H, J = 8.4 Hz, H^3), 6.11 (s, 4H, H^{Mes}), 2.20 (s, 6H, CH$_3$), 1.79 (s, 6H, 2 CH$_3$^{Mes}), 1.61 (s, 12H, 4 CH$_3$^{Mes}) ppm.

^{13}C-NMR (75 MHz, CDCl$_3$): δ = 159.61, 156.93, 144.02, 142.84, 137.98, 137.74, 136.67, 136.58, 134.63, 128.29, 127.38, 127.25, 127.17, 125.72, 125.17, 26.43, 20.82, 20.02 ppm.

HR-MS (MALDI+): m/z = 687.2558, calculated for (M-PF$_6$)$^+$ m/z = 687.2543.

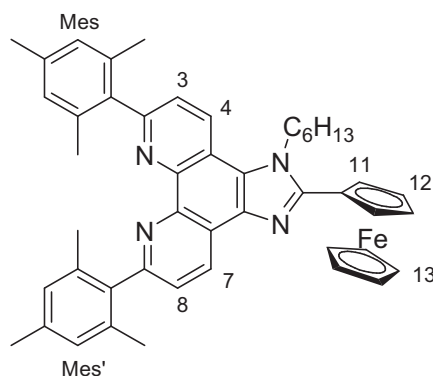## 2,9-dimesityl-1,10-phenanthroline-[a:b]imidazoferrocenyl (25)

7 (54 mg, 0.12 mmol), **Fc-CHO** (29 mg, 0.14 mmol) and NH₄OAc (200 mg, 2.59 mmol) were dissolved in 10 mL of $CHCl_3$ and 0.4 mL of acetic acid were added. The solution was heated to reflux and stirred overnight, then allowed to cool to room temperature. The solution was washed twice with water, and once with a concentrated $NaHCO_3$ aqueous solution. The organic solvent was removed and the crude product was purified by column chromatography on silica gel. The second, orange fraction was collected and the pure **25** was obtained (29 mg, 37%).

¹H-NMR (300 MHz, CD_3CN): δ = 11.48 (s broad, 1H, NH^{Imi}), 8.95 (d broad, 2H, J = 9.0 Hz, H^4), 8.78 (d broad, 2H, J = 8.1 Hz, H^7), 7.66 (d, 2H, J = 8.4 Hz, H^3 and H^8), 6.95 (s, 4H, H^{Mes}), 5.10 (t, 2H, J = 2.1 Hz, H^{12}), 4.51 (t, 2H, J = 1.8 Hz, H^{11}), 4.18 (s, 5H, H^{13}), 2.29 (s, 6H, CH_3^{Mes}), 2.02 (s, 12H, CH_3^{Mes}) ppm.

HR-MS (MALDI+): m/z = 641.2361, calculated for $(MH)^+$ m/z = 641.2362.

N-hexyl-2,9-dimesityl-1,10-phenanthroline-[a:b]imidazoferrocenyl (L14)

25 (28 mg, 4.4·10⁻² mmol) was dissolved in 5 mL of dry DMF. Cs_2CO_3 (97 mg, 0.30 mmol) was quickly added and the mixture was degassed, then heated to 110 ºC under Ar atmosphere. After 30 minutes, a solution of hexyl iodide (25 μL, 0.17 mmol) in 1.5 mL DMF was injected, and the mixture was stirred at 110 ºC for 5 hours. Removal of the solvent under reduced pressure and purification by column chromatography on silica gel afforded the pure **L14** (27 mg, 83%).

¹H-NMR (300 MHz, $CDCl_3$): δ = 9.12 (d, 1H, J = 8.4 Hz, H^7), 8.60 (d, 1H, J = 8.7 Hz, H^4), 7.67-7.62 (m, 2H, H^3 and H^8), 6.95 (s, 2H, H^{Mes}), 6.94 (s, 2H, $H^{Mes'}$), 4.94-4.86 (m, 4H, H^{11} and NCH_2^{nHex}), 4.53 (t, 2H, J = 1.6 Hz, H^{12}), 4.30 (s, 5H, H^{13}), 2.32 (s broad, 6H, CH_3^{Mes} and $CH_3^{Mes'}$), 2.19 (s, 6H, 2 CH_3^{Mes}), 2.15 (s broad, 8H, 2 $CH_3^{Mes'}$ and CH_2^{nHex}), 1.63 (m, 2H, CH_2^{nHex}), 1.51-1.39 (m, 4H, 2 CH_3^{nHex}), 0.96 (t, 3H, J = 7.0 Hz, CH_3^{nHex}) ppm.

¹³C-NMR (75 MHz, $CDCl_3$): δ = 158.30, 156.86, 152.14, 144.47, 143.98, 138.36, 137.82, 137.55, 137.31, 136.79, 136.45, 136.41, 130.34, 128.67, 128.57, 127.47, 125.30, 125.22, 124.40, 122.28, 118.18, 75.26, 69.97, 69.52, 46.63, 31.48, 30.72, 26.56, 22.72, 21.23, 20.79, 20.72, 14.10 ppm.

HR-MS (MALDI+): m/z = 725.3293, calculated for $(MH)^+$ m/z = 725.3301.

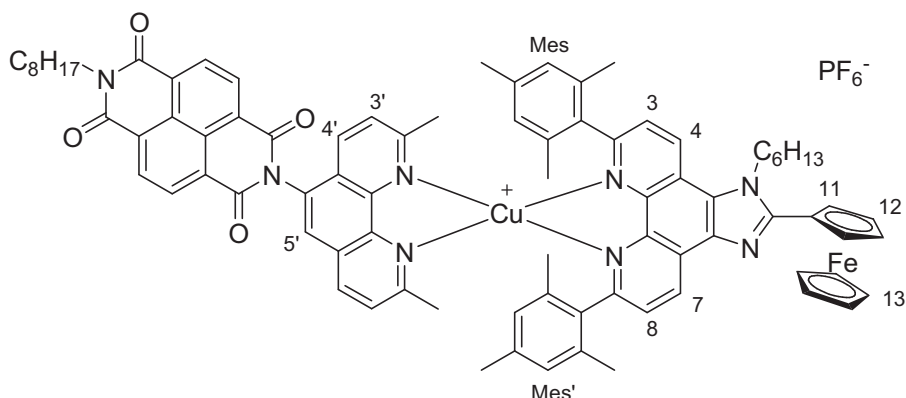## [Cu(L14)(dmp)]PF₆ (C16)

[Cu(L14)(dmp)]PF₆ (C16)

L14 (21 mg, $2.9 \cdot 10^{-2}$ mmol) and $[Cu(CH_3CN)_4]PF_6$ (10 mg, $2.7 \cdot 10^{-2}$ mmol) were dissolved in 5 mL of dry degassed dichloromethane under Ar and the orange solution was stirred for 15 minutes at room temperature. **Dmp** (neocuproine, 5 mg, $2.5 \cdot 10^{-2}$ mmol), dissolved in 2 mL of dry dichloromethane and degassed for 5 minutes by Ar bubbling, was then injected. After 40 minutes the solvent was removed under reduced pressure, and the crude product was purified by column chromatography on silica gel (eluant CH_2Cl_2: CH_3OH = 98: 2) and then by size-exclusion chromatography (BioBeads X1, THF). Pure **C16** was obtained as a red solid (14 mg, 49%).

^{1}H-NMR (300 MHz, $CDCl_3$): δ = 9.42 (d broad, 1H, J = 7.5 Hz, H^7), 8.97 (d broad, 1H, J = 6.6 Hz, H^4), 8.27 (d, 2H, J = 8.1 Hz, $H^{4'}$), 7.90 (d broad, 1H, J = 7.0 Hz, H^8), 7.84 (d, 1H, J = 8.4 Hz, H^3), 7.81 (s, 2H, $H^{5'}$), 7.53 (d, 2H, J = 7.8 Hz, $H^{3'}$), 6.14 (s, 2H, H^{Mes}), 6.00 (s, 2H, $H^{Mes'}$), 5.06 (m broad, 4H, H^{11} and NCH_2^{nHex}), 4.66 (s broad, 2H, H^{12}), 4.43 (s broad, 5H, H^{13}), 2.21 (s broad, 8H, $2CH_3^{dmp}$ and CH_2^{nHex}), 1.76 (s, 3H, CH_3^{Mes}), 1.69-1.65 (m, 5H, $CH_3^{Mes'}$ and CH_2^{nHex}), 1.63 (s, 6H, $2CH_3^{Mes}$), 1.58 (s, 6H, $2CH_3^{Mes'}$), 1.48-1.41 (m, 4H, $2CH_2^{nHex}$), 0.94 (t, 3H, J = 6.9 Hz, CH_3^{nHex}) ppm.

HR-MS (MALDI+): m/z = 995.3538, calculated for $(M-PF_6)^+$ m/z = 995.3519.

[Cu(L13)(L14)]PF₆ (C17)

[Cu(L13)(L14)]PF₆ (C17)

L14 (36 mg, $5.0 \cdot 10^{-2}$ mmol) and $[Cu(CH_3CN)_4]PF_6$ (16 mg, $4.2 \cdot 10^{-2}$ mmol) were dissolved in 5 mL of dry degassed CH_2Cl_2 under Ar. The solution was stirred for 5 minutes at room temperature, then a solution of **L13** (20 mg, $3.5 \cdot 10^{-2}$ mmol) in 7 mL CH_2Cl_2 was added dropwise. The solution was stirred for 40 minutes at room temperature, then the solvent was removed. The crude product was purified several times by column chromatography and TLC on silica gel (CH_2Cl_2: CH_3OH = 99: 1) afforded pure **C17** as a red solid (14 mg, 19%).

1H-NMR (500 MHz, CDCl$_3$): δ = 9.40 (d broad, 1H, H^7), 8.92 (d, 1H, J = 8.6 Hz, H^4), 8.87 (m, 4H, H^{NDI}), 8.27 (d, 1H, J = 8.6 Hz, H$^{7'}$), 8.07 (d, 1H, J = 8.6 Hz, H$^{4'}$), 7.88 (m, 3H, H$^{6'}$, H^3 and H^8), 7.60 (d, 1H, J = 8.4 Hz, H$^{8'}$), 7.50 (d, 1H, J = 8.4 Hz, H$^{3'}$), 6.43 (s, 1H, H^{Mes}), 6.37 (s, 1H, H^{Mes}), 6.27 (s, 1H, H^{Mes}), 6.25 (s, 1H, H^{Mes}), 5.00 (m, 4H, H^{11} and NCH$_2^{nHex}$), 4.60 (s, 2H, H^{12}), 4.36 (s, 5H, H^{13}), 4.24 (t, 2H, J = 7.8 Hz, NCH$_2^{nOct}$), 2.46 (s, 3H, CH$_3^{L13}$), 2.20 (m, 2H, CH$_2^{nHex}$), 2.01 (s, 3H, CH$_3^{L13}$), 1.94 (s, 3H, CH$_3^{Mes}$), 1.86 (s, 3H, CH$_3^{Mes}$), 1.80 (s, 3H, CH$_3^{Mes}$), 1.76 (s, 3H, CH$_3^{Mes}$), 1.67 (m, 2H, CH$_2^{nOct}$), 1.56 (s, 3H, CH$_3^{Mes}$, under H$_2$O peak), 1.47 (m, 4H, 2 CH$_2$), 1.41 (s, 3H, CH$_3^{Mes}$), 1.36-1.23 (m, 12H, 6 CH$_2$), 0.95 (t, 3H, J = 7.2 Hz, CH$_3^{nHex}$), 0.90 (t, 3H, J = 7.0 Hz, CH$_3^{nOct}$) ppm.

13C-NMR (75 MHz, CDCl$_3$): δ = 163.45, 163.28, 162.88, 158.11, 158.06, 156.74, 154.57, 143.76, 143.01, 142.10, 141.96, 138.33, 138.24, 137.29, 136.52, 136.43, 134.84, 134.79, 132.44, 132.07, 131.96, 131.22, 130.26, 129.94, 128.73, 128.10, 127.83, 127.69, 127.65, 127.35, 127.23, 127.07, 126.90, 126.75, 126.43, 126.04, 125.61, 125.34, 124.88, 123,60, 119.61, 70.33, 69.96, 69.77, 53.55, 46.90, 41.33, 31.97, 31.55, 30.79, 29.85, 29.45, 29.36, 28.27, 27.58, 27.29, 26.50, 25.35, 22.80, 22.76, 20.87, 20.81, 20.45, 20.41, 19.67, 19.52, 14.24, 14.12 ppm.

HR-MS (MALDI+): m/z = 1371.4893, calculated for (M-PF$_6$)$^+$ m/z = 1371.4942.

N-(p-benzaldehyde)-N,N-bis(p-methoxyphenyl)amine **28**[19] and 6,6'-dichloro-2,2'-bipyridine-4,4'-dicarboxylate dimethyl ester **33**[20] were synthesized according to literature procedures. **biQuiCOOK** was purchased from Alfa Aesar and used without further purification, **biQuiCOOH** was obtained from the latter by precipitation from an acidic aqueous solution.

2,9-dimesityl-1,10-phenanthroline-[a:b]imidazo-(4'-dianisylaminophenyl) (29)

7 (30 mg, $6.6 \cdot 10^{-2}$ mmol), **28** (28 mg, $8.4 \cdot 10^{-2}$ mmol) and NH$_4$OAc (125 mg, 1.63 mmol) were dissolved in 5 mL of glacial acetic ac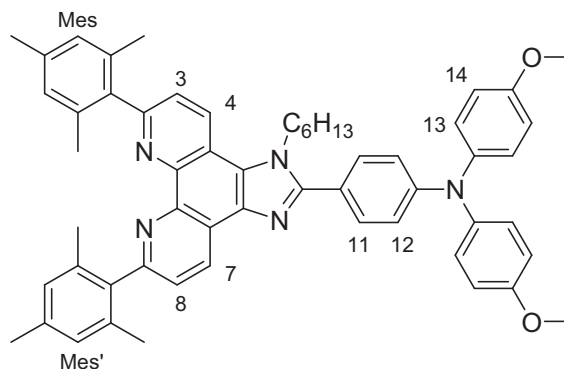id. The yellow solution was stirred at reflux overnight (the colour changed to red). After cooling to room temperature, water was added and the yellow precipitate was collected by filtration and washed with water. The crude product was dissolved in dichloromethane and washed twice with water. Purification by column chromatography on silica gel (CH$_2$Cl$_2$: CH$_3$OH = 99: 1) afforded the pure product as a yellow solid (29 mg, 58%).

^{1}H-NMR (300 MHz, DMSO-d$_6$): δ = 13.53 (s broad, 1H, NH^{Imi}), 8.96 (d broad, 2H, J = 8.4 Hz, H^4 and H^7), 8.11 (d, 2H, J = 8.7 Hz, H^{11}), 7.71 (s broad, 2H, H^3 and H^8), 7.14 (d, 4H, J = 8.7 Hz, H^{13}), 7.00-6.93 (m, 10H, H^{Mes}, H^{12} and H^{14}), 3.78 (s, 6H, OCH$_3$), 2.30 (s, 6H, CH$_3^{Mes}$), 2.02 (s, 12H, 2 CH$_3^{Mes}$) ppm.

HR-MS (MALDI+): m/z = 760.3651, calculated for (MH)$^+$ m/z = 760.3646.

N-hexyl-2,9-dimesityl-1,10-phenanthroline-[a:b]imidazo-(4'-dianisylaminophenyl) (L15)

29 (86 mg, 0.11 mmol) and Cs$_2$CO$_3$ (228 mg, 0.70 mmol) were dissolved in 10 mL of dry DMF under Ar. The yellow mixture was heated at 100 ºC for 30 minutes, and the colour turned to greenish. *N*-Hexyl iodide (0.05 mL) was injected into the flask and the mixture was further stirred at
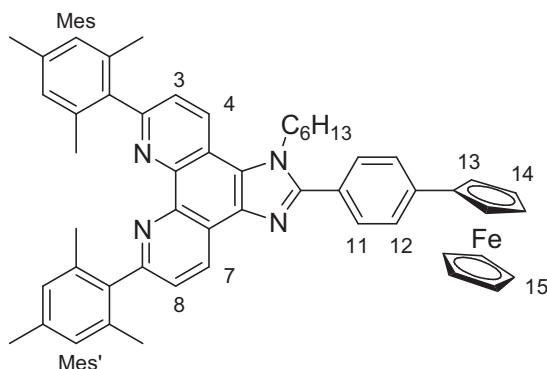
100 ºC for 4 hours, then allowed to cool. The solvents were removed and the crude product was purified by column chromatography on silica gel (CH_2Cl_2: CH_3OH = 99.5: 0.5) to give **L15** (68 mg, 72%).

^{1}H-NMR (300 MHz, $CDCl_3$): δ = 9.12 (d, 1H, J = 8.3 Hz, H^7), 8.62 (d, 1H, J = 8.6 Hz, H^4), 7.65 (d, 2H, J = 8.3 Hz, H^3 and H^8), 7.56 (d, 2H, J = 8.8 Hz, H^{11}), 7.17 (d, 4H, J = 9.0 Hz, H^{14}), 7.09 (d, 2H, J = 8.8 Hz, H^{12}), 6.95 (s, 2H, H$^{Mes'}$), 6.93 (s, 2H, H^{Mes}), 6.91 (d, 4H, J = 9.0 Hz, H^{13}), 4.69 (t broad, 2H, J = 7.3 Hz, NCH$_2$^{nHex}), 3.83 (s, 6H, 2 OCH$_3$), 2.32 (s, 3H, CH$_3$$^{Mes'}$), 2.31 (s, 3H, CH$_3$^{Mes}), 2.18 (s, 6H, 2 CH$_3$$^{Mes'}$), 2.15 (s, 6H, 2 CH$_3$^{Mes}), 2.04-1.98 (m, 2H, CH$_2$^{nHex}), 1.38-1.25 (m, 6H, 3 CH$_2$^{nHex}), 0.86 (t, 3H, J = 6.7 Hz, CH$_3$^{nHex}) ppm.

^{13}C-NMR (75 MHz, $CDCl_3$): δ = 157.12, 156.59, 154.32, 150.28, 144.54, 144.04, 140.28, 138.26, 137.74, 137.63, 137.35, 136.43, 136.36, 130.70, 130.37, 128.69, 128.58, 127.98, 127.35, 125.38, 124.97, 124.38, 122.42, 121.39, 119.45, 118.42, 115.01, 55.63, 46.94, 31.14, 30.36, 26.10, 22.55, 21.24, 20.76, 20.71, 14.04 ppm.

HR-MS (MALDI+): m/z = 844.4572, calculated for (MH)$^+$ m/z = 844.4585.

### *N-hexyl-2,9-dimesityl-1,10-phenanthroline-[a:b]imidazo-(4'-ferrocenylphenyl)* (L16)

L6' (47 mg, 6.7·10^{-2} mmol), ferroceneboronic acid (22 mg, 9.6·10^{-2} mmol) and Ba(OH)$_2$ (32 mg, 0.18 mmol) were dissolved in 4 mL of a mixture of 1,2-dimethoxyethane: H$_2$O = 9:1 and thoroughly degassed. Pd(PPh$_3$)$_4$ was quickly added and the mixture was degassed again. The reaction mixture was stirred at 105 ºC under stirring for one night. After cooling to room temperature, water was added. The mixture was extracted several times with CH_2Cl_2, until the aqueous phase was nearly colourless. After evaporation of the solvents, the crude product was purified by chromatography on silica gel (CH_2Cl_2: CH_3OH = 99.5: 0.5) affording 29 mg (54%) of pure **L16**.

^{1}H-NMR (300 MHz, $CDCl_3$): δ = 9.14 (d, 1H, J = 8.1 Hz, H^7), 8.64 (d, 1H, J = 8.4 Hz, H^4), 7.70 (s, 4H, H^{11} and H^{12}), 7.66 (d, 2H, J = 8.4, H^3 and H^8), 6.96 (s, 2H, H^{Mes}), 6.94 (s, 2H, H$^{Mes'}$), 4.77 (t, 2H, J = 1.8 Hz, H^{13}), 4.70 (m, 2H, NCH$_2$^{nHex}), 4.42 (t, 2H, J = 1.8 Hz, H^{14}), 4.10 (s, 5H, H^{15}), 2.33 (s, 3H, CH$_3$^{Mes}), 2.32 (s, 3H, CH$_3$$^{Mes'}$), 2.20 (s, 6H, 2 CH$_3$^{Mes}), 2.17 (s, 6H, 2 CH$_3$$^{Mes'}$), 2.02 (m, 2H, CH$_2$^{nHex}), 1.35-1.22 (m, 6H, 3CH$_2$^{nHex}), 0.83 (t, 3H, J = 6.9 Hz, CH$_3$^{nHex}) ppm.

^{13}C-NMR (75 MHz, $CDCl_3$): δ = 158.37, 157.10, 153.90, 144.58, 144.01, 141.44, 138.14, 137.63, 137.44, 137.17, 136.84, 136.31, 136.24, 130.05, 129.86, 128.85, 128.54, 128.43, 127.75, 126.23, 125.29, 124.98, 124.28, 122.31, 118.25, 83.81, 69.76, 69.51, 66.63, 46.80, 30.94, 30.21, 29.67, 25.96, 22.38, 21.10, 20.66, 20.62, 13.85 ppm.

HR-MS (MALDI+): m/z = 801.3636, calculated for (MH)$^+$ m/z = 801.3614.

[Cu(L15)(biQuiCOOH)]PF₆ (C22)

$[Cu(L15)(biQuiCOOH)]PF_6$ **(C22)**
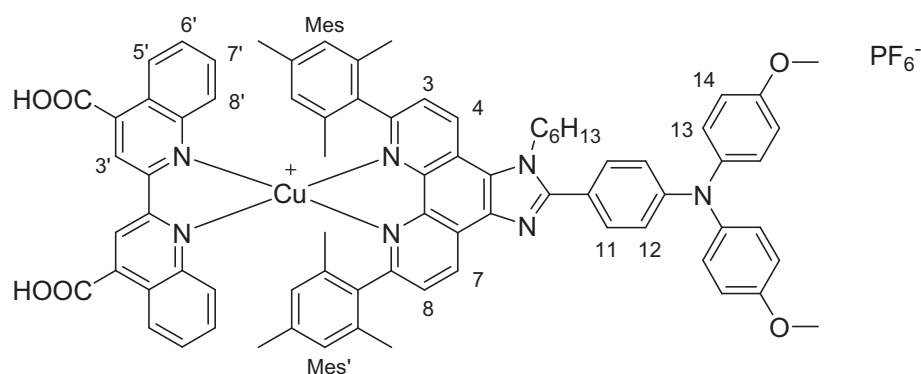
L15 (42 mg, $5.0 \cdot 10^{-2}$ mmol) and $[Cu(CH_3CN)_4]PF_6$ (17 mg, $4.5 \cdot 10^{-2}$ mmol) were dissolved in 7 mL of dry DMF, the dark orange solution was stirred under Ar for 15 minutes. **BiQuiCOOH** (14 mg, $4.1 \cdot 10^{-2}$ mmol) was suspended in 3 mL of dry DMF under Ar, sonicated and heated until dissolution. It was then injected dropwise into the stirring solution. The colour immediately changed to very dark green. After 30 minutes stirring at room temperature, the solvent was removed under reduced pressure. The crude product was purified by size exclusion chromatography (Sephadex LH20, CH_2Cl_2: CH_3OH = 50: 50) to afford pure **C22** as a dark green solid (60 mg, quantitative yield).

¹H-NMR (300 MHz, $CDCl_3$: MeOD = 4: 1): broad signals δ = 9.27 (d, 1H, J = 8.0 Hz, H^7), 8.88 (d, 1H, J = 8.6 Hz, H^4), 8.82 (d, 2H, J = 8.5 Hz, $H^{5'}$), 8.50 (s, 2H, $H^{3'}$), 7.80-7.75 (m, 2H, H^3 and H^8), 7.60 (d, 2H, J = 8.30 Hz, $H^{8'}$), 7.54 (t, 2H, J = 8.0 Hz, $H^{6'}$), 7.46 (d broad, 2H, H^{11}), 7.34-7.28 (m, 2H, $H^{7'}$), 7.06 (d, 4H, J = 8.7 Hz, H^{14}), 6.95 (d broad, 2H, H^{12}), 6.79 (d, 4H, J = 8.6 Hz, H^{13}), 5.67 (s, 4H, H^{Mes}), 4.73 (t broad, 2H, NCH_2^{nHex}), 3.69 (s, 6H, 2 OCH_3), 2.00 (m broad, 2H, CH_2^{nHex}), 1.64 (s, 3H, $CH_3^{Mes'}$), 1.62 (s, 3H, CH_3^{Mes}), 1.29 (m broad, 2H, CH_2^{nHex}), 1.16 (s, 6H, 2 $CH_3^{Mes'}$), 1.15 (s, 6H, 2 CH_3^{Mes}), 1.11-1.07 (m, 4H, 2 CH_2^{nHex}), 0.73 (t broad, 3H, CH_3^{nHex}) ppm.

HR-MS (MALDI+): m/z = 1250.4587, calculated for $(M-PF_6)^+$ m/z = 1250.4600.

[Cu(L16)(biQuiCOOH)]PF₆ (C23)

$[Cu(L16)(biQuiCOOH)]PF_6$ **(C23)**
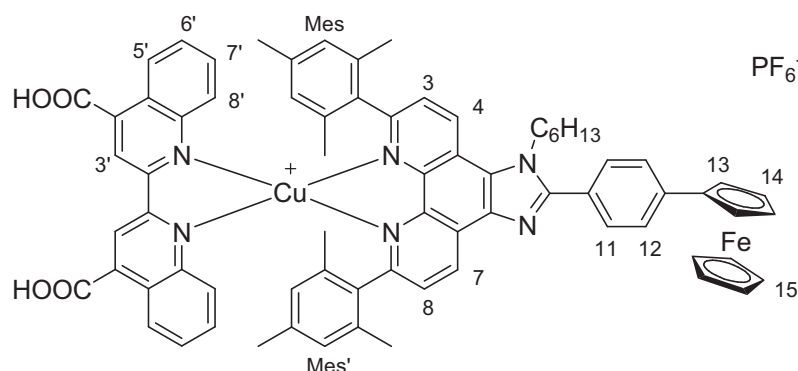
L16 (27 mg, $3.4 \cdot 10^{-2}$ mmol) and $[Cu(CH_3CN)_4]PF_6$ (11 mg, $3.0 \cdot 10^{-2}$ mmol) were dissolved in 3 mL of dry DMF, the solution was stirred under Ar for 15 minutes. **BiQuiCOOH** (9 mg, $2.6 \cdot 10^{-2}$ mmol) was suspended in 2 mL of dry DMF under Ar, sonicated and heated until dissolution. It was then injected dropwise into the stirring solution. The colour immediately changed to very dark green. After 30 minutes stirring at room temperature, the solvent was removed under reduced pressure. The crude product was purified by size exclusion chromatography (BioBeads X-1, CH_2Cl_2: CH_3OH = 60: 40) to afford pure **C23** (28 mg, 78%).

¹H-NMR (300 MHz, CDCl₃): δ = 9.31 (d broad, 1H), 8.89 (m, 3H), 8.54 (s broad, 2H), 7.86-7.78 (m, 4H), 7.61 (m, 6H), 3.36 (m, 2H), 5.73 (s, 4H), 4.73 (m, 4H), 3.74 (m), 1.99 (s, 6H), 1.70 (s, 8H), 1.19 (m), 0.76 (m) ppm.

HR-MS (MALDI+): m/z = 1207.3581, calculated for (M-PF₆)⁺ m/z = 1207.3629.

6,6'-dimesityl-2,2'-bipyridine-4,4'-dicarboxylate dimethyl ester (L17)
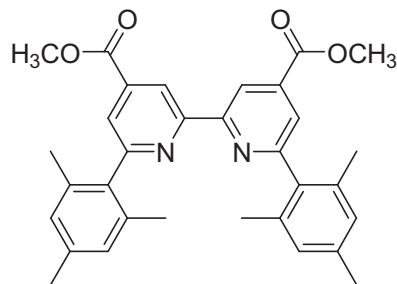
6,6'-dichloro-2,2'-bipyridine-4,4'-dicarboxylate dimethyl ester **33** (253 mg, $7.4 \cdot 10^{-1}$ mmol), mesitylboronic acid (264 mg, 1.6 mmol), Pd₂(dba)₃ (20 mg, 6%), SPhos (33 mg, $8.7 \cdot 10^{-2}$ mmol) and potassium phosphate (782 mg, 3.7 mmol) were put in a dry schlenk tube under Ar, and dry toluene was added. The mixture was refluxed overnight then allowed to cool to room temperature. Water was added and the mixture was exctracted 3 times with dichloromethane, the organic phase was then washed with brine and the solvent was removed under reduced pressure. The obtained solid was first washed with methanol, then purified by chromatography on silica gel (CH₂Cl₂) to afford **LN** (nn mg, nn%) as a white solid.

¹H-NMR (300 MHz, CDCl₃): δ = 8.93 (d, 2H, J = 1.4 Hz, H³), 7.83 (d, 2H, J = 1.4 Hz, H⁵), 7.02 (s, 4H, H^Mes), 3.96 (s, 6H, OCH₃), 2.39 (s, 6H, CH₃^Mes), 2.12 (s, 12H, CH₃^Mes) ppm.

¹³C-NMR (75 MHz, CDCl₃): δ = 166.14, 160.54, 156.82, 138.99, 138.08, 137.37, 136.09, 128.67, 124.54, 118.69, 52.78, 21.29, 20.56 ppm.

HR-MS (MALDI+): m/z = 509.2458, calculated for (MH)⁺ m/z = 509.2434.

2-chloro-6-mesitylpyridine-4-carboxylate ethyl ester (30)
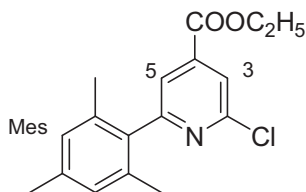
Ethyl 2,6-dichloropyridine-4-carboxylate (122 mg, 0.55 mmol), mesitylboronic acid (92 mg, 0.56 mmol) and Na₂CO₃ (290 mg, 2.74 mmol) were dissolved in 15 mL of 1,2-dimethoxyethane: H₂O = 9: 1, and thoroughly degassed. Pd(PPh₃)₄ (31 mg, 5%) was quickly added and the mixture was degassed again. The flask was heated to 110 ºC under argon for 3 hours, then allowed to cool. Water was added and the mixture was extracted with dichloromethane (x3). The organic phases were gathered and dried on Na₂SO₄, and the solvents were removed. The crude product was purified by chromatography on silica gel (CH₂Cl₂: petroleum ether = 70: 30) to give 35 mg of pure product (21%).

¹H-NMR (300 MHz, CDCl₃): δ = 7.86 (d, 1H, J = 1.2 Hz, H³), 7.74 (d, 1H, J = 1.2 Hz, H⁵), 6.93 (s, 2H, H^Mes), 4.43 (q, 2H, J = 7.1 Hz, CH₂^Et), 2.32 (s, 3H, CH₃^Mes), 2.04 (s, 6H, 2 CH₃^Mes), 1.41 (t, 3H, J = 7.1 Hz, CH₃^Et) ppm.

¹³C-NMR (75 MHz, CDCl₃): δ = 164.00, 161.66, 151.88, 140.76, 138.21, 135.64, 135.51, 128.42, 122.77, 121.69, 62.18, 29.67, 21.06, 20.14, 14.12 ppm.

HR-MS (MALDI+): m/z = 304.1097, calculated for (MH)⁺ m/z = 304.1099.

6,6'-dimesityl-2,2'-bipyridine-4,4'-dicarboxylate diethyl ester
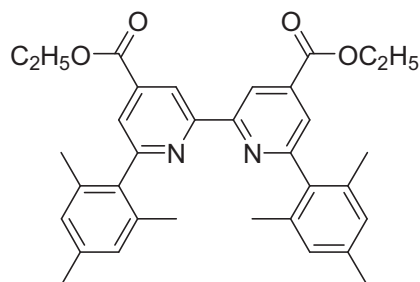
30 (148 mg, 4.8·10⁻¹) and Sn₂Bu₆ (0.14 mL, 2.8·10⁻¹ mmol) were dissolved in dry degassed DMF. Pd(PPh₃)₄ (57 mg, 10%) was quickly added and the solution was further degassed with Ar, and then heated to 110ºC for 20h. After cooling to room temperature, the solvent was removed under reduced pressure and the crude oil was purified by column chromatography on silica gel (eluent CH₂Cl₂). The product was obtained as a white powder (30 mg, 12%).

¹H-NMR (300 MHz, CDCl₃): δ = 8.90 (d, 2H, J = 1.5 Hz, H³), 7.83 (d, 2H, J = 1.5 Hz, H⁵), 7.02 (s, 4H, H^Mes), 4.43 (q, 4H, J = 7.2 Hz, CH₂^Et), 2.39 (s, 6H, 2 CH₃^Mes), 2.13 (s, 12, 4 CH₃^Mes), 1.41 (t, 6H, J = 7.2 Hz, CH₃^Et) ppm.

¹³C-NMR (75 MHz, CDCl₃): δ = 165.62, 160.43, 156.92, 139.33, 138.04, 137.37, 136.10, 128.66, 124.49, 118.76, 61.92, 21.29, 20.58, 14.42 ppm.

MS (CI, NH₃): m/z = 537.36, calculated for (MH)⁺ m/z = 536.27.

6,6'-dimesityl-2,2'-bipyridine-4,4'-dicarboxylic acid (L18)
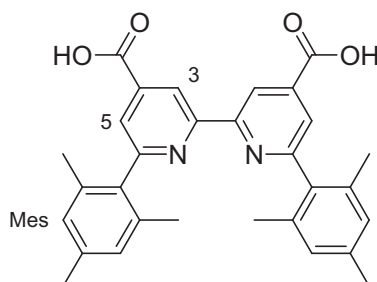
L17 (100 mg, 0.20 mmol) was suspended in 7 mL of THF, and a solution of LiOH (49 mg, 2.1 mmol) in 1 mL of water was added. The mixture is heated to reflux (**L17** dissolves completely upon heating) for 6 hours, then allowed to cool to room temperature. Water was added, and the THF was removed under reduced pressure. The mixture was acidified with HCl 1 M until a pH of 1-2 was reached, and the precipitate was collected by filtration (95 mg, quantitative).

¹H-NMR (300 MHz, DMSO-d₆): δ = 8.72 (d, 2H, J = 1.4 Hz, H³), 7.72 (d, 2H, J = 1.2 Hz, H⁵), 7.02 (s, 4H, H^Mes), 2.32 (s, 6H. CH₃^Mes), 2.03 (s, 12H, CH₃^Mes) ppm.

HR-MS (MALDI+): m/z = 481.2130, calculated for (MH)$^+$ m/z = 2122.

[Cu(L17)(dmp)]PF$_6$ (C24)
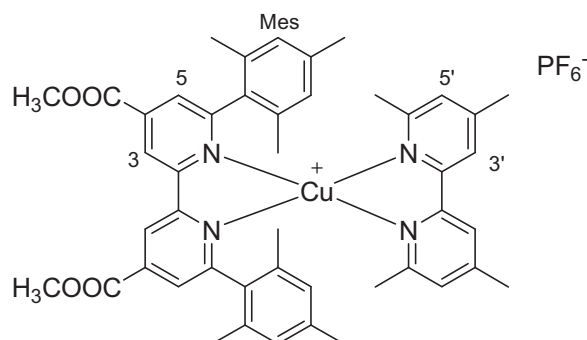
General procedure for the synthesis of the complexes **C24-C27**: **L17** (41 mg, 8.0·10^{-2} mmol) and [Cu(CH$_3$CN)$_4$]PF$_6$ (28 mg, 7.5·10^{-2} mmol) were dissolved in 4 mL of dry degassed dichloromethane and stirred under Ar at room temperature until complete dissolution. **Dmp** (4,4',6,6'-tetramethyl-2,2'-bipyridine,14 mg, 6.7·10^{-2} mmol) was dissolved in 4 mL of dry dichloromethane, degassed for 5 minutes by Ar bubbling and injected dropwise into the stirring orange-red solution. After 40 minutes the solvent was removed under reduced pressure and the crude product was purified by column chromatography on silica gel (eluent CH$_2$Cl$_2$: CH$_3$OH = 98: 2) to afford pure **C24** (52 mg, 84%) as a violet solid.

^{1}H-NMR (300 MHz, acetone-d$_6$): δ = 9.24 (d, 2H, J = 1.3 Hz, H^3), 8.17 (d, 2H, J = 1.3 Hz, H^5), 7.95 (s, 2H, H$^{3'}$), 7.20 (s, 2H, H$^{5'}$), 6.38 (s, 4H, H^{Mes}), 4.06 (s, 6H, OCH$_3$), 2.45 (s, 6H, 2 CH$_3$), 2.02 (s, 6H, 2 CH$_3$), 1.89 (s, 6H, 2 CH$_3$^{Mes}), 1.66 (s, 12H, 4 CH$_3$^{Mes}) ppm.

^{13}C-NMR (75 MHz, CDCl$_3$): δ = 165.39, 160.60, 157.31, 154.02, 152.31, 150.42, 140.54, 138.94, 137.21, 135.58, 128.31, 127.99, 126.80, 121.46, 120.54, 53.62, 25.90, 21.04, 20.82, 20.14 ppm.

HR-MS (MALDI+): m/z = 783.2951, calculated for (M-PF$_6$)$^+$ m/z = 783.2966.

[Cu(L17)(L8)]PF$_6$ (C25)
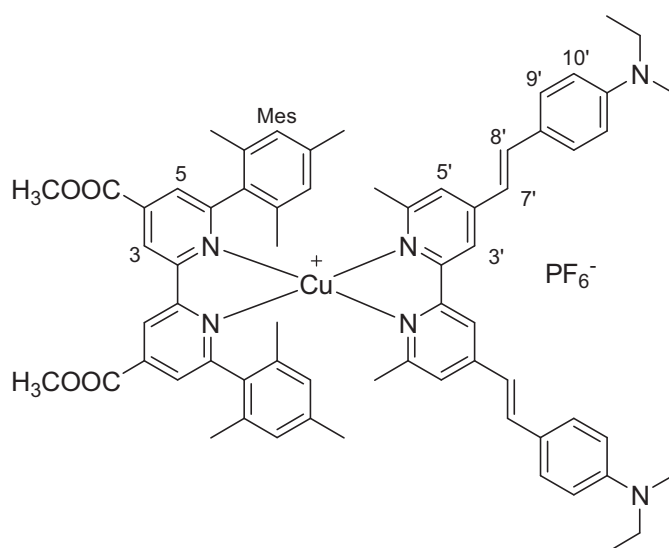
Red solid, 77% yield.

^{1}H-NMR (500 MHz, acetone-d$_6$): δ = 9.25 (d, 2H, J = 1.4 Hz, H^3), 8.24 (s, 2H, H$^{3'}$), 8.18 (d, 2H, J = 1.3 Hz, H^5), 7.62 (d, 2H, J = 16.3 Hz, H$^{7'}$), 7.53 (d, 4H, J = 8.8 Hz, H$^{9'}$), 7.42 (s, 2H, H$^{5'}$), 6.99 (d,

2H, J = 16.2 Hz, H$^{8'}$), 6.78 (d, 4H, J = 8.7 Hz, H$^{10'}$), 6.42 (s, 4H, H^{Mes}), 4.07 (s, 6H, OCH$_3$), 3.77 (s, 6H, CH$_3^{bpy}$), 3.48 (m, 8H, NCH$_2^{Et}$), 1.89 (s, 6H, CH$_3^{Mes}$), 1.71 (s, 12H, CH$_3^{Mes}$), 1.20 (t, 12H, J = 7.1 Hz, CH$_3^{Et}$) ppm.
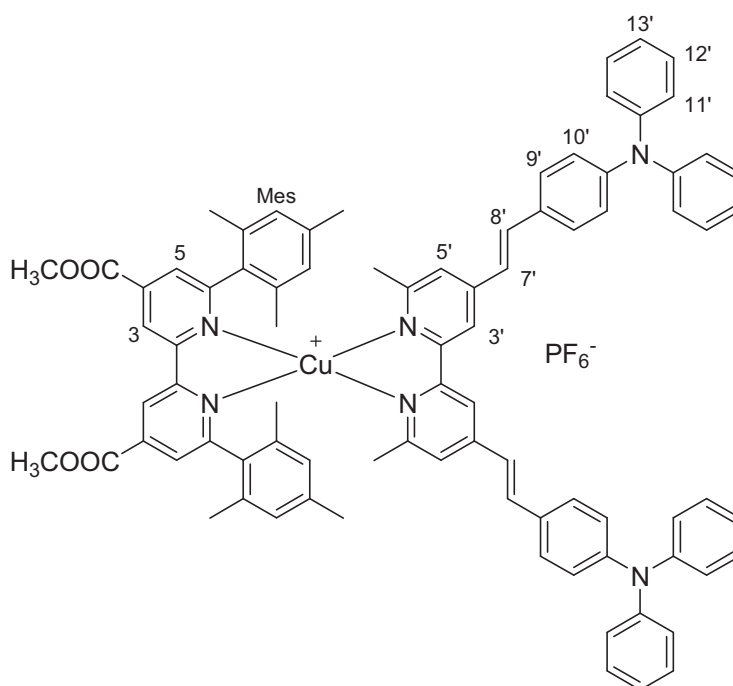
^{13}C-NMR (125 MHz, acetone-d$_6$): δ = 209.98, 198.17, 165.47, 160.68, 157.39, 155.39, 154.24, 154.07, 153.96, 152.95, 149.68, 148.71, 140.52, 139.14, 137.27, 136.40, 135.64, 129.91, 129.30, 128.45, 128.06, 126.62, 124.85, 124.66, 124.48, 124.04, 122.12, 121.47, 120.02, 116.35, 112.49, 69.35, 69.23, 53.64, 44.98, 26.04, 21.02, 20.21, 12.93 ppm.

HR-MS (MALDI+): m/z = 1101.5062, calculated for (M-PF$_6$)$^+$ m/z = 1101.5062.

[Cu(L17)(L19)]PF$_6$ (C26)

Red solid, 97% yield.

^{1}H-NMR (300 MHz, acetone-d$_6$): δ = 9.27 (d, 2H, J = 1.3 Hz, H^3), 8.32 (s, 2H, H$^{3'}$), 8.19, (d, 2H, J = 1.5 Hz, H^5), 7.70 (d, 2H, J = 16.4 Hz, H$^{7'}$), 7.60 (d, 4H, J = 8.7 Hz, H$^{9'}$), 7.52 (s, 2H, H$^{5'}$), 7.36 (t broad, 8H, J = 7.9 Hz, H$^{12'}$), 7.20 (d, 2H, J = 16.4 Hz, H$^{8'}$), 7.15-7.10 (m, 12H, H$^{11'}$ and H$^{13'}$), 7.03 (d, 4H, J = 8.6 Hz, H$^{10'}$), 6.41 (s, 4H, H^{Mes}), 4.07 (s, 6H, OCH$_3$), 2.08 (s, 6H, 2 CH$_3$), 1.89 (s, 6H, 2 CH$_3^{Mes}$), 1.71 (s, 12H, 4 CH$_3^{Mes}$) ppm.

^{13}C-NMR (75 MHz, CDCl$_3$): δ = 165.39, 160.60, 157.61, 154.01, 152.88, 149.71, 148.09, 147.92, 140.55, 139.10, 137.24, 135.60, 135.30, 130.64, 130.45, 129.28, 128.39, 128.02, 125.93, 124.74, 123.77, 123.05, 122.68, 121.49, 116.92, 53.63, 26.08, 21.01, 20.21 ppm.

HR-MS (MALDI+): m/z = 1293.5017, calculated for (M-PF$_6$)$^+$ m/z = 1293.5062.

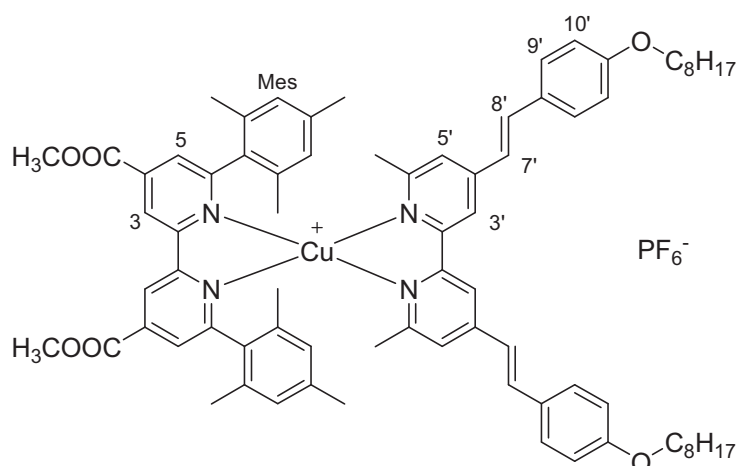## [Cu(L17)(L11)]PF₆ (C27)

[Cu(L17)(L11)]PF$_6$ **(C27)**

Violet solid, 88% yield.

^{1}**H-NMR** (300 MHz, acetone-d$_6$): δ = 9.26 (d, 2H, J = 1.1 Hz, H^3), 8.32 (s, 2H, H$^{5'}$), 8.19 (d, 2H, J = 1.0 Hz, H^5), 7.73-7.64 (m, 6H, H$^{7'}$ and H$^{10'}$), 7.51 (s, 2H, H$^{3'}$), 7.18 (d, 2H, J = 16.4 Hz, H$^{8'}$), 7.03 (d, 4H, J = 8.6 Hz, H$^{9'}$), 6.41 (s, 4H, H^{Mes}), 4.09-4.05 (m, 10H, 2 OCH$_3$ and 2 OCH$_2^{nOct}$), 2.34 (s, 6H, 2 CH$_3$), 1.88 (s, 6H, 2 CH$_3^{Mes}$), 1.86-1.76 (m, 4H, 2 CH$_2^{nOct}$), 1.70 (s, 12H, 4 CH$_3^{Mes}$), 1.53-1.43 (m, 4H, 2 CH$_2^{nOct}$), 1.42-1.30 (m, 16H, 8 CH$_2^{nOct}$), 0.89 (t, 6H, J = 6.6 Hz, 2 CH$_3^{nOct}$) ppm.

^{13}**C-NMR** (75 MHz, CDCl$_3$): δ = 165.40, 161.18, 160.63, 157.65, 154.03, 152.89, 148.02, 140.57, 139.10, 137.26, 135.60, 135.54, 129.66, 128.39, 128.03, 123.45, 122.77, 121.50, 116.82, 115.82, 68.75, 53.63, 32.57. 26.77, 26.08, 23.32, 20.99, 20.20, 14.36 ppm.

HR-MS (MALDI+): m/z = 1215.5959, calculated for (M-PF$_6$)$^+$ m/z = 1215.5994.

Complexes C24'-C27'

Complexes C24'-C27'

C24'

C25': R=NEt$_2$
C26': R=NPh$_2$
C27': R=OOct
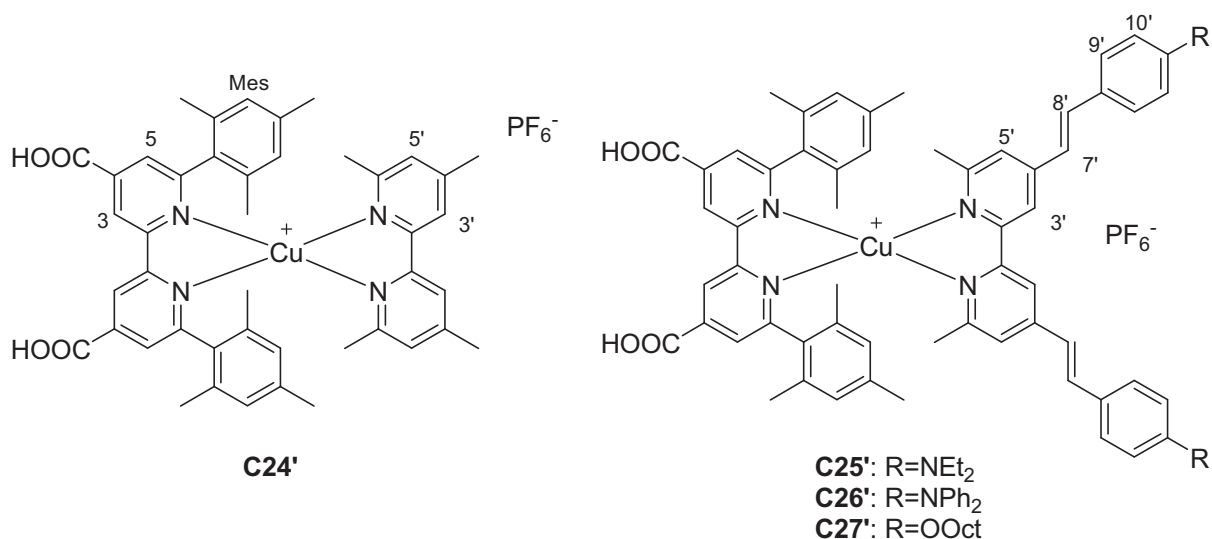
General procedure: the complexes **C24-C27** were dissolved in a 9:1 mixture of THF: H$_2$O, and 2.2 eq. of LiOH were added. The mixture was stirred at room temperature and the extent of reaction was monitored by TLC (appearance of a spot with Rf ~ 0 and disappearance of the reactant spot, eluent CH$_2$Cl$_2$: CH$_3$OH = 96: 4). The solvents are removed under reduced pressure and the product is dissolved (not completely soluble) in methanol. About 2.4 equivalents of TFA (solution in

MeOH) are added and the solvent is removed again. The crude product was purified by size exclusion chromatography (Sephadex LH20, CH₃OH: THF = 60: 40).

C24'

HR-MS (ESI+): m/z = 755.26654, calculated for (M-PF$_6$)$^+$ m/z = 755.26531.

C25'

HR-MS (ESI+): m/z = 1073.4789, calculated for (M-PF$_6$)$^+$ m/z = 1073.4749.

C26'

HR-MS (ESI+): m/z = 1265.47546, calculated for (M-PF$_6$)$^+$ m/z = 1265.47491.

C27'

HR-MS (ESI+): m/z = 1187.56982, calculated for (M-PF$_6$)$^+$ m/z = 1187.56814.

References

1.	Dietrick-Buchecker, C. O.; Marnot, P. A.; Sauvage, J. P. *Tetrahedron Lett.* **1982**, *23*, 5291-5294.
2.	Cunningham, C. T.; Cunningham, K. L. H.; Michalec, J. F.; McMillin, D. R. *Inorg. Chem.* **1999**, *38*, 4388-4392.
3.	Yamada, M.; Nakamura, Y.; Kuroda, S.; Shimao, I. *Bull. Chem. Soc. Jpn.* **1990**, *63*, 2710-2712.
4.	Frey, J.; Kraus, T.; Heitz, V.; Sauvage, J.-P. *Chem. Eur. J.* **2007**, *13*, 7584-7594.
5.	Ott, S.; Faust, R. *Synthesis* **2005**, *2005*, 3135,3139.
6.	Kubas, G. J.; Monzyk, B.; Crumblis, A. L. In *Inorg. Synth.*; John Wiley & Sons, Inc.: **2007**, p 68-70.
7.	Schmittel, M.; Lüning, U.; Meder, M.; Ganz, A.; Michel, C.; Herderich, M. In *Heterocycl. Commun.* 1997; Vol. 3, p 493.
8.	Akdas-Kilig, H.; Malval, J.-P.; Morlet-Savary, F.; Singh, A.; Toupet, L.; Ledoux-Rak, I.; Zyss, J.; Le Bozec, H. *Dyes Pigm.* **2012**, *92*, 681-688.
9.	Maury, O.; Viau, L.; Sénéchal, K.; Corre, B.; Guégan, J.-P.; Renouard, T.; Ledoux, I.; Zyss, J.; Le Bozec, H. *Chem. Eur. J.* **2004**, *10*, 4454-4466.
10.	Smith, A. P.; Lamba, J. J. S.; Fraser, C. L. *Org. Synth.* **2002**, *78*, 82-87.
11.	Hutchison, A. J.; Williams, M.; Angst, C.; De Jesus, R.; Blanchard, L.; Jackson, R. H.; Wilusz, E. J.; Murphy, D. E.; Bernard, P. S. *J. Med. Chem.* **1989**, *32*, 2171-2178.
12.	Karlsson, S.; Boixel, J.; Pellegrin, Y.; Blart, E.; Becker, H.-C.; Odobel, F.; Hammarström, L. *J. Am. Chem. Soc.* **2010**, *132*, 17977-17979.
13.	Renouard, T.; Le Bozec, H.; Brasselet, S.; Ledoux, I.; Zyss, J. *Chem. Commun.* **1999**, 871-872.
14.	Wiederrecht, G. P.; Wasielewski, M. R. *J. Am. Chem. Soc.* **1998**, *120*, 3231-3236.
15.	Blake, R. C.; Pavlov, A. R.; Khosraviani, M.; Ensley, H. E.; Kiefer, G. E.; Yu, H.; Li, X.; Blake, D. A. *Bioconjugate Chem.* **2004**, *15*, 1125-1136.
16.	Sazanovich, I. V.; Alamiry, M. A. H.; Best, J.; Bennett, R. D.; Bouganov, O. V.; Davies, E. S.; Grivin, V. P.; Meijer, A. J. H. M.; Plyusnin, V. F.; Ronayne, K. L.; Shelton, A. H.; Tikhomirov, S. A.; Towrie, M.; Weinstein, J. A. *Inorg. Chem.* **2008**, *47*, 10432-10445.
17.	Imahori, H.; Azuma, T.; Ajavakom, A.; Norieda, H.; Yamada, H.; Sakata, Y. *J. Phys. Chem. B* **1999**, *103*, 7233-7237.
18.	Hasharoni, K.; Levanon, H.; Greenfield, S. R.; Gosztola, D.; Svec, W.; Wasielewski, M. R. *J. Am. Chem. Soc.* **1995**, *117*, 8055-8056.
19.	Davies, J. A.; Elangovan, A.; Sullivan, P. A.; Olbricht, B. C.; Bale, D. H.; Ewy, T. R.; Isborn, C. M.; Eichinger, B. E.; Robinson, B. H.; Reid, P. J.; Li, X. B.; Dalton, L. R. *J. Am. Chem. Soc.* **2008**, *130*, 10565-10575.
20.	Barolo, C.; Nazeeruddin, M. K.; Fantacci, S.; Di Censo, D.; Comte, P.; Liska, P.; Viscardi, G.; Quagliotto, P.; De Angelis, F.; Ito, S.; Grätzel, M. *Inorg. Chem.* **2006**, *45*, 4642-4653.

Appendix A

Complexes C9-C13: Dipole-allowed vertical absorption wavelengths along with their oscillator strengths ($f > 0.05$) calculated in dichloromethane and their attributions.

Complex	State	ΔE (nm)	f	Exp
C9				
	$ILCT_L$ (94%)	410	1.37	439 nm
	$ILCT_L$ (90%)	397	1.95	
	$MLCT_L$ (72%) / $ILCT_L$ (14%)	325	0.07	323 nm
	$ILCT_L$ (92%)	310	0.08	
	$ILCT_L$ (67%) / $MLCT_L$ (22%)	299	0.22	
	$ILCT_L$ (83%)	291	0.25	
	$ILCT_L$ (79%)	280	0.06	
	$ILCT_L$ (70%) / $LLCT_{Phos}$ (16%)	280	0.09	
	$MLCT_{Phos}$ (65%) / $LLCT_{Phos}$ (13%)	262	0.09	
	$ILCT_L$ (39%) / $MLCT_L$ (34%)	257	0.11	259 nm
	$MLCT_{Phos}$ (57%)	252	0.07	
C10				
	$ILCT_L$ (90%)	410	2.04	445 nm
	$ILCT_L$ (84%)	398	1.64	
	$ILCT_L$ (81%)	306	0.07	
	$ILCT_L$ (50%) / $MLCT_L$ (28%)	298	0.06	
	$ILCT_L$ (67%)	294	0.08	
	$ILCT_L$ (75%)	293	0.12	290 nm
	$ILCT_L$ (79%)	287	0.28	
	$ILCT_L$ (59%)	275	0.05	
	$ILCT_L$ (49%) / $LLCT_{Phos}$ (12%)	269	0.07	
	$ILCT_L$ (41%) / $MLCT_L$ (28%)	264	0.06	
	$ILCT_L$ (63%)	260	0.09	
	$ILCT_L$ (59%)	259	0.11	
	$ILCT_L$ (26%) / $MLCT_{Phos}$ (25%) / $LLCT_{Phos}$ (11%)	258	0.18	
	$ILCT_L$ (32%) / $MLCT_{Phos}$ (21%) / $MLCT_L$ (14%)	258	0.09	
	$ILCT_L$ (78%)	257	0.23	
	$ILCT_L$ (78%)	256	0.24	
C11				
	$MLCT_{Phen}$ (43%) / $MLCT_L$ (28%) / $ILCT_L$ (12%)	442	0.35	
	$MLCT_{Phen}$ (37%) / $ILCT_L$ (23%) / $MLCT_L$ (22%)	421	0.73	
	$ILCT_L$ (87%)	419	1.51	418 nm
	$MLCT_L$ (61%) / $ILCT_L$ (22%)	404	0.61	
	$MLCT_{Phen}$ (53%) / $ILCT_L$ (26%) / $MLCT_L$ (10%)	374	0.21	

$MLCT_L$ (47%) / $MLCT_{Phen}$ (28%) / $ILCT_L$ (12%)	355	0.10	
$ILCT_L$ (63%) / $MLCT_L$ (12%)	307	0.06	
$ILCT_L$ (64%)	303	0.08	
$ILCT_L$ (79%)	302	0.10	
$MLCT_L$ (36%) / $ILCT_L$ (23%) / LLC_L (15%)	292	0.14	291 nm
$ILCT_L$ (40%) / $ILCT_{Phen}$ (21%)	273	0.05	
$ILCT_L$ (73%)	271	0.11	
$ILCT_L$ (55%) / $LLCT_{Phen}$ (21%)	271	0.13	
$ILCT_L$ (56%)	268	0.16	
$ILCT_L$ (24%) / $ILCT_{Phen}$ (17%) / $MLCT_{Phen}$ (13%)	267	0.06	
$ILCT_L$ (19%) / $ILCT_{Phen}$ (19%) / $MLCT_{Phen}$ (16%)	267	0.37	
$ILCT_L$ (65%) / $LLCT_L$ (16%)	265	0.18	
$ILCT_L$ (64%)	264	0.25	
$ILCT_L$ (71%)	264	0.09	
$ILCT_{Phen}$ (22%) / $LLCT_L$ (16%) / $MLCT_L$ (10%)	260	0.05	
$ILCT_{Phen}$ (33%) / $MLCT_{Phen}$ (17%)	255	0.39	
$ILCT_{Phen}$ (21%) / $MLCT_{Phen}$ (18%) / $ILCT_L$ (7%) / $LLCT_L$ (5%)	253	0.19	
$MLCT_{Phen}$ (51%) / $ILCT_L$ (12%)	252	0.07	
$ILCT_{Phen}$ (66%) / $LLCT_L$ (11%)	250	0.05	

C12

$MLCT_L$ (51%) / $MLCT_{Phen}$ (23%) / $ILCT_L$ (13%)	448	0.28	438 nm
$ILCT_L$ (80%)	409	1.43	
$ILCT_L$ (41%) / $MLCT_L$ (28%) / $MLCT_{Phen}$ (19%)	407	1.11	
$ILCT_L$ (34%) / $MLCT_{Phen}$ (31%) / $MLCT_L$ (18%)	373	0.75	
$MLCT_{Phen}$ (43) / $MLCT_L$ (37)	363	0.13	
$ILCT_L$ (41%) / $MLCT_L$ (13%)	317	0.07	
$MLCT_L$ (54%) / $ILCT_L$ (14%)	309	0.05	
$MLCT_L$ (52%) / $ILCT_L$ (23%)	302	0.09	
IL_{Phen} (21%) / $MLCT_L$ (14%) / $ILCT_L$ (14%) / $MLCT_{Phen}$ (12)	299	0.06	
IL_L (46%) / $MLCT_L$ (30%)	294	0.07	
$ILCT_L$ (65%)	290	0.08	
$MLCT_L$ (38%) / $ILCT_L$ (36%)	289	0.08	
IL_{Phen} (25%) / $MLCT_{Phen}$ (21%) / $LLCT_{Phen}$ (10%)	281	0.21	
IL_L (33%) / $MLCT_{Phen}$ (18%) / $LLCT_{Phen}$ (13%)	276	0.09	
$LLCT_{Phen}$ (28%) / IL_L (22%) / $MLCT_{Phen}$ (10%)	275	0.06	
$LLCT_{Phen}$ (32%) / $MLCT_{Phen}$ (26%)	271	0.06	
IL_L (58%)	269	0.15	
$LLCT_{Phen}$ (23%) / $ILCT_L$ (16%) / $MLCT_L$ (11%) / $MLCT_{Phen}$ (10%)	269	0.06	
IL_L (68%)	267	0.18	
IL_L (21%) / $LLCT_L$ (13%)	257	0.05	
IL_L (30%) / $MLCT_L$ (11%) / $LLCT_L$ (10%)	250	0.17	

C13

$MLCT_{Phen}$ (53%) / $MLCT_L$ (38%)	447	0.11	484 nm

MLCT$_L$ (56%) / MLCT$_{Phen}$ (32%)	421	0.10	
MLCT$_L$ (45%) / MLCT$_{Phen}$ (43%)	395	0.42	
ILCT$_L$ (52%) / MLCT$_L$ (34%)	362	1.48	
MLCT$_{Phen}$ (52%) / MLCT$_L$ (33%)	359	0.07	344 nm
MLCT$_L$ (26%) / ILCT$_{Phen}$ (24%) / LLCT$_L$ (19%) / ILCT$_L$ (13%)	332	0.45	
ILCT$_{Phen}$ (40%) / MLCT$_L$ (26%) / ILCT$_L$ (14%)	330	0.43	
LLCT$_L$ (56%) / ILCT$_{Phen}$ (16%)	324	0.06	
LLCT$_L$ (40%) / MLCT$_{Phen}$ (13%) / ILCT$_{Phen}$ (11%) / MLCT$_L$ (10%)	306	0.14	
MLCT$_{Phen}$ (51%) / LLCT$_L$ (16%) / ILCT$_{Phen}$ (15%)	303	0.06	297 nm
MLCT$_L$ (56%)	279	0.05	
ILCT$_{Phen}$ (70%) / MLCT$_{Phen}$ (16%)	275	0.10	
ILCT$_{Phen}$ (52%)	271	0.26	
LLCT$_L$ (51%) / ILCT$_L$ (14%) / MLCT$_L$ (12%)	268	0.09	
MLCT$_L$ (41%) / LLCT$_L$ (22%) / ILCT$_L$ (20%)	267	0.06	
ILCT$_L$ (41%) / LLCT$_L$ (21%) / MLCT$_L$ (13%)	264	0.24	
ILCT$_{Phen}$ (42%) / LLCT$_L$ (16%)	262	0.08	
ILCT$_L$ (58%)	260	0.05	
ILCT$_L$ (59%)	259	0.06	
MLCT$_{Phen}$ (58%) / ILCT$_{Phen}$ (14%)	254	0.05	
ILCT$_{Phen}$ (44%)/ LLCT$_{Phen}$ (33%)	253	0.05	253 nm
ILCT$_{Phen}$ (58%)/ MLCT$_{Phen}$ (10%)	252	0.09	
ILCT$_{Phen}$ (55%)	251	0.20	
ILCT$_{Phen}$ (33%)/ LLCT$_{Phen}$ (13%) / ILCT$_L$ (13%)	250	0.06	